Tensile Membrane Action of Reinforced Concrete Slabs at Ambient and Elevated Temperatures

Samantha J Foster

A Thesis presented for the partial fulfilment
of the requirements for the degree of
Doctor of Philosophy

Department of Civil and Structural Engineering
University of Sheffield
July 2006

Declaration

The work in this thesis is based upon research carried out at the Department of Civil and Structural Engineering, The University of Sheffield, UK. No part of this thesis has been submitted elsewhere for any other degree or qualification and is all my own work unless referenced to the contrary in the text.

The author gratefully acknowledges sponsorship by the Engineering and Physical Sciences Research Council of the United Kingdom, and by Arup Fire Ltd. Many thanks to Professor Colin Bailey, Professor Ian Burgess and Professor Roger Plank who gave me inspiration.

Abstract

The aim of this research was to extend the knowledge of the performance of slabs at ambient and elevated temperatures, to look at their failure mechanisms and the influence of temperature on their performance. This involved undertaking a programme of experimental work in which a series of slabs were tested in a custom made loading rig at ambient and elevated temperatures. An in depth investigation of the BRE Simplified Design Method was undertaken.

This thesis presents the results from 15 small-scale tests conducted on horizontally unrestrained slabs at ambient temperature which were subjected to large vertical displacements. All the tested slabs showed a load-carrying capacity far greater than the design capacity using the well-established yield-line theory. The results of the tests have been compared to the Simple Design Method which incorporates membrane action of composite floor slabs into the estimation of their load capacity in fire and shows that the design method compares well with experimental results and is generally conservative. The numerical results at ambient temperature showed that tensile strength of concrete is significant at low deflections and not a significant factor at high displacements as the strength and type of wire used is important as it affects the load capacity of the slab.

This thesis also presents the results from a series of tests conducted on horizontally unrestrained slabs at elevated temperatures. The purpose of these tests was to investigate the influence of thermal curvature on the failure mechanisms of rectangular slabs, since this is not explicitly allowed for in the simplified design method. Observations from the high-temperature tests have shown that the mechanism of failure differs from that assumed in the Simplified Design Method. The observed slab behaviour at high temperatures is that high double-curvature deflection is created quickly, and this leads to full-depth cracking across the short span of the slab, but the association with a yield-line mechanism is much less obvious. The results from the numerical study showed that up to temperatures of 200°C, the influences of concrete tension, load ratio, type of wire on the displacements is negligible, and that thermal gradient dominates the slab behaviour.

The studies have proven that the proposed design method is not always conservative and is only based on one pre-determined collapse mode. At high temperatures, the experimental and numerical work has shown that the slab behaviour is dominated by different

mechanisms. The design method is based a final failure mechanism of the slab which was observed in the tests during the latter stages of the heated tests which questions the applicability of the method. The *Vulcan* predictions were accurate at elevated temperatures even though it does not consider bond effects.

Contents

Notation

a	aspect ratio (L/l).
b	parameter defining magnitude of membrane force.
d	effective depth of reinforcement.
E	Youngs Modulus
e	enhancement of yield-line load due to membrane action.
e_{1m}	enhancement of Element 1 due to membrane forces.
e_{2m}	enhancement of Element 2 due to membrane forces.
e_{1b}	enhancement of Element 1 due to bending action.
e_{2b}	enhancement of Element 2 due to bending action.
f_c	Compressive strength of concrete.
f_t	Tensile strength of concrete.
fy	Strength of reinforcement.
g_o	parameter defining the compressive stress block in flexural action.
h	Heat transfer coefficient
h_c	Convective heat transfer coefficient
h_r	Radiant heat transfer coefficient
k	parameter defining magnitude of membrane force.
KT_0	force in steel per unit width in the shorter span.
L	largest span of rectangular slab.
l	shortest span of rectangular slab.
M_0	moment of resistance when no membrane force is present.
M_{1m}	moment about support due to membrane forces for Element 1.
M_{2m}	moment about support due to membrane forces for Element 2.
n	parameter defining yield-line (refer Figure 3).
S	in-plane shear at yield-line.
T_0	force in steel per unit width in the longer span.
w	deflection of yield line.
φ	angle defining yield line pattern (refer Figure 3).
μ	coefficient of orthotropy.
t	actual measured depth of slab

f_y yield strength

f_c compressive cube strength

d_x effective depth of reinforcement in x-direction

d_y effective depth of reinforcement in y-direction

Chapter 1

Introduction

1.0 Developments in Fire Engineering

Over the past twenty years, tremendous progress has been made in the fire engineering design of composite structures. Significant development has been achieved through analytical and experimental research projects that have helped to increase our knowledge of the global structural behaviour of buildings. From this research has flowed various design codes, the most significant advances being to the British Standard BS5950 and the Eurocodes. The Building Research Establishment (BRE) has produced additional guidance for the practising engineer in the form of digests which are intended to act as quick sources of reference for structural engineers involved in the fire-resistant design of buildings.

The Building Regulations for England and Wales, within the United Kingdom, attempt to ensure the safety of the occupants of a building and their safe escape in the event of a fire. Life safety is of primary importance and consideration of threats to life safety; smoke and heat are embodied in this document. It is crucial therefore that the fire is contained for a sufficient period whilst giving occupants time to evacuate a building. This is achieved through the concept of fire resistance, which ensures for a building in the event of a fire that its stability will be maintained for a reasonable period. Fire safety in buildings is concerned with achieving two fundamental objectives;

- To reduce the loss of life in, or in the neighbourhood of, building fires.
- To reduce the consequent property loss or financial loss.

To achieve these objectives the designer has to consider the following;

- Choice of materials to be used in a building; the use of non-flammable products to reduce or prevent ignition and smoke.
- Ensure safe exits to facilitate escape and time to evacuate.

- The boundary walls should be designed with sufficient stability, integrity and insulation to providing compartmentation.

1.1 Development of an Uncontrolled Fire

The development of a natural fire requires three sources to be present at the same time,

- Oxygen.
- Heat source.
- Combustible material.

If one of these forms is not present, the fire will burn itself out. Fire is usually represented by a temperature-time curve. The response of the curve is related to the size and the type of the compartment under fire, the quantity of combustible material and the air supply available for combustion. A natural fire is considered to consist of three phases, the growth phase (pre-flashover), the fully developed phase and then the decay phase (post-flashover), Figure 1.1.

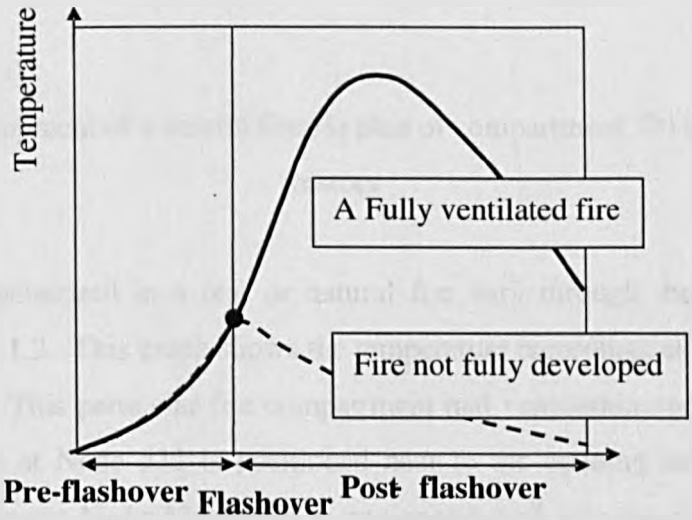

Figure 1.1: Development of a natural fire

Once the combustible material ignites the fire starts to develop, and its duration may be long or short depending on the combustible material burning. During the pre-flashover stage, active measures such as automatic sprinklers or fire brigade action will usually be able to prevent flashover; this is represented by the dashed curve in Figure 1.1. The critical point is flashover, which is the transition from a locally contained fire to a fully developed fire in which all the combustible material in the compartment burns uncontrollably. The gas temperature at which flashover occurs depends on the combustibility of the material,

but tends to be in the range 500°C to 600°C. The post-flashover fire will have temperatures in excess of 1000°C, followed by the decay of the fire.

1.2. The Nature of a Fire

A natural fire consists of the three phases defined above. The heat release generated by the fire depends on the type of combustible material and its ventilation. Figure 1.2 shows the time- history of a typical natural fire.

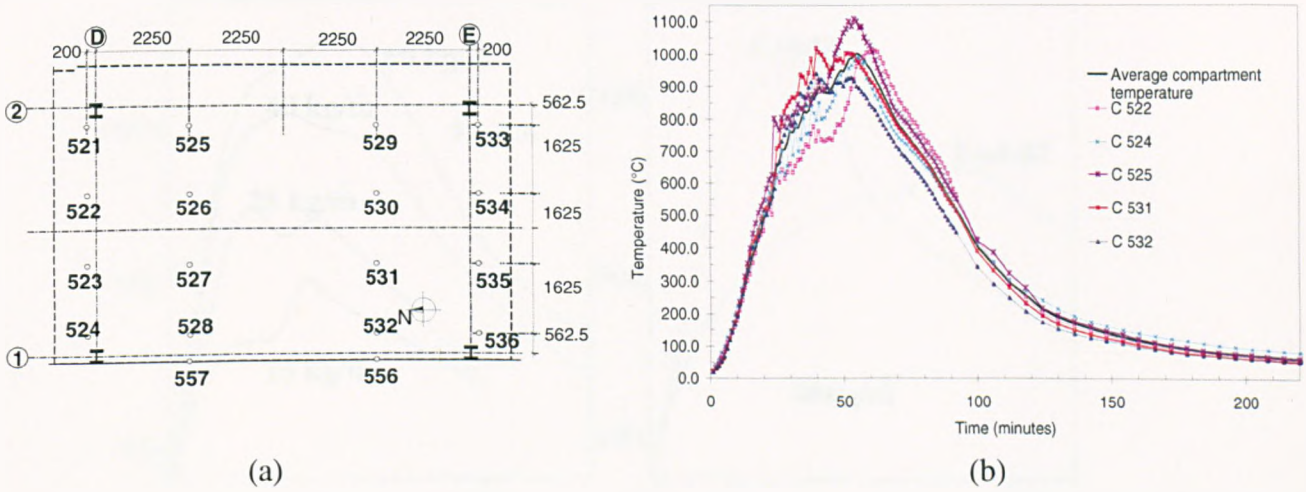

(a) (b)

Figure 1.2: Development of a natural fire (a) plan of compartment, (b) temperature-time history

The temperatures generated in a real or natural fire vary through the compartment, as presented in Figure 1.2. This graph shows the temperature recordings at different locations in a compartment. This particular fire compartment had ventilation openings along Grid-line 1. The gauge at Node 532 is positioned near to the opening and the temperature reading is lower than at Node 525 which is positioned well into the compartment. This particular fire was generated by using wooden cribs with a fire load density of 40 kg/m^2 of timber. For comparison, a typical value for hotels and offices is 45 kg/m^2 timber equivalent. As mentioned previously, ventilation and the type of combustible material determines the nature of the fire curve developed. Figure 1.3 shows the effect of varying the fire load and ventilation on the fire curve developed. The proportion of ventilation in a compartment may-be defined by a ventilation factor [equn.1.1]. This factor is calculated by multiplying the area of the open windows by the square root of the height of the opening and dividing this by the total boundary surface area. The effect of increasing the fire load for a constant size of opening produces a hotter and longer-lived fire. Varying the

size of the window opening also determines what fire is generated; fires that are controlled by ventilation burn faster and hotter than fires with little ventilation, which burn for longer.

$$F_v = A_v\sqrt{H_v / At} \qquad 1.1$$

Where A_v is the area of the window opening (m^2), H_v is the height of the window opening (m) and A_t is the total internal area of the boundary surfaces (m^2). Fv is the ventilation factor ($m^{0.5}$).

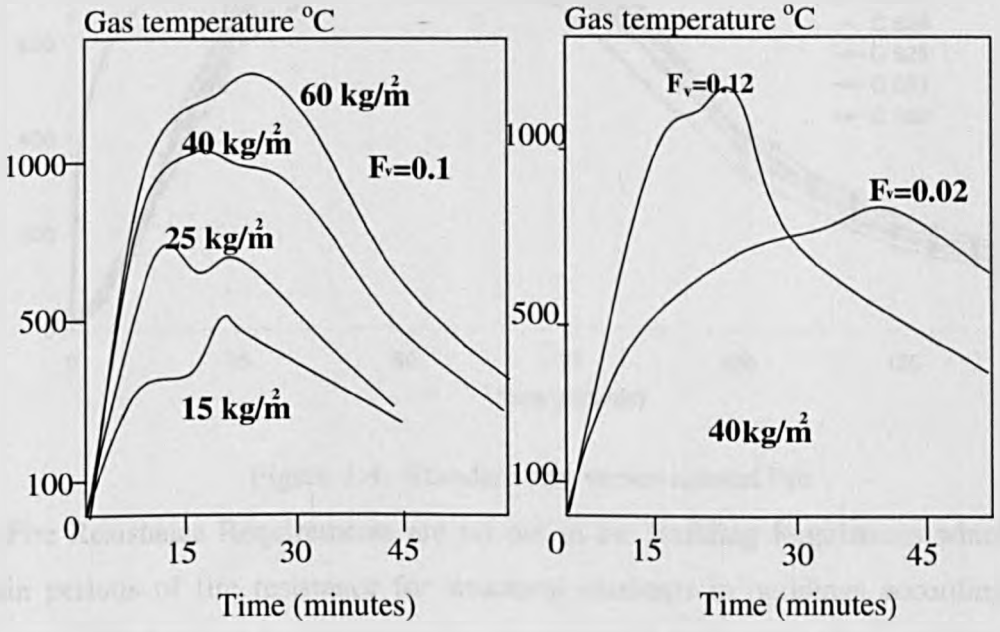

Figure 1.3: Influence of fire load and ventilation on the gas temperatures within a compartment

1.2.1 Standard Fires

When a fire develops in a building, it must be contained within its compartment. This requires the structural elements in buildings to retain their integrity so that compartmentation is maintained. The main elements of a structure must also maintain their load bearing capacity for a sufficient period to safeguard both life and property. The fire resistance of building components is prescribed in the building codes and is expressed in units of time. To determine the fire resistance of the building components, controlled tests are undertaken on singular structural elements. These controlled tests are known as the Standard Fire Tests and are carried out to a specified standard, ISO834 [1], which is the international standard. The gas temperature-time relationship of the ISO834 fire curve is

compared to natural fire temperatures in Figure 1.4.

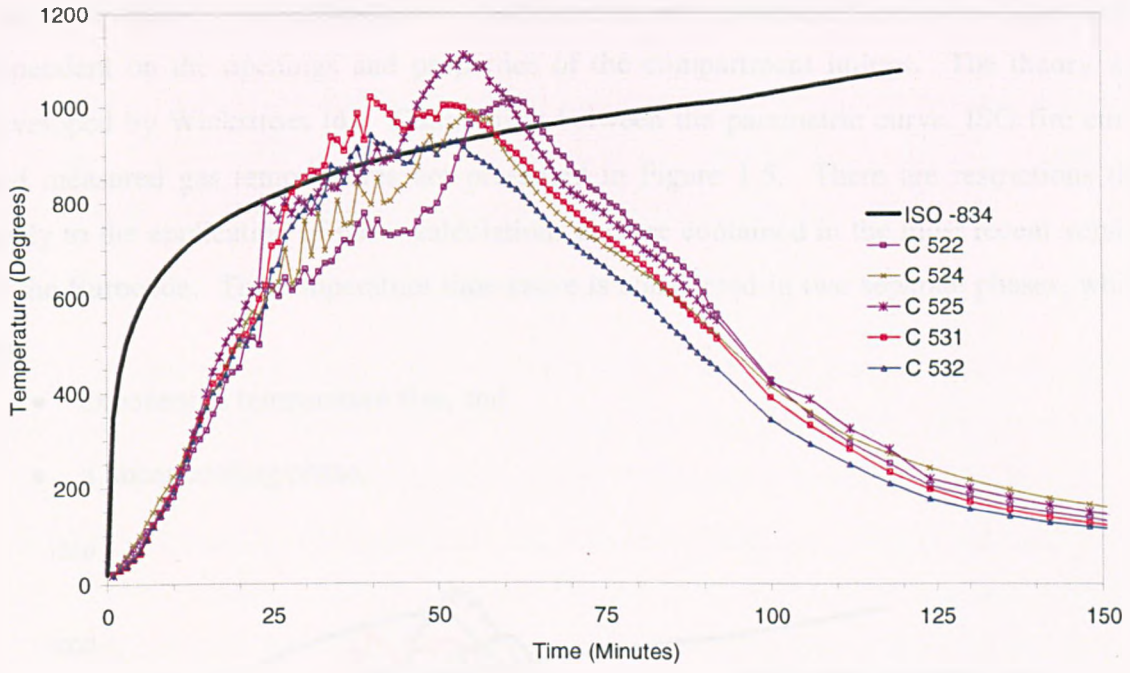

Figure 1.4: Standard fire versus natural fire

The Fire Resistance Requirements are set out in the Building Regulations which specify certain periods of fire resistance for structural elements in buildings according to their function. The level of fire resistance is governed by the building type, height, and fire load. The required time of fire resistance is usually expressed in terms of multiples of 30 minutes (for example 30, 60, 90) and relate to the ISO834 fire curve. This means that a structural component must satisfy criteria for structural stability, integrity, and insulation (the last two only for separating elements) during the required time under fire temperatures according to the ISO834 fire. The ISO834 temperature rise is calculated by;

$$\theta_g = 20 + 345 \log (8t + 1) \qquad 1.2$$

Where θ_g is the furnace temperature (^{0}C) and t is the time in minutes.

The test methodology has been criticised for its simplicity but has contributed to our understanding of the behaviour of structural elements in fire. In an attempt to relate to natural behaviour of fires, a new concept was introduced and this was known as the Time-Equivalent concept [2]. This concept relates the temperature generated in a protected structural component exposed to a particular real fire with the time taken to produce the same temperature when the same beam is exposed to a Standard Fire.

The most widely used method for calculating the time-temperature response of a fire compartment is the parametric approach [3]. This approach has been incorporated into the Eurocode drafts. The temperature is calculated as an exponential function of time and is dependent on the openings and properties of the compartment linings. The theory was developed by Wickstrom [4]. Comparison between the parametric curve, ISO fire curve and measured gas temperatures are presented in Figure 1.5. There are restrictions that apply to the application of these calculations and are contained in the most recent version of the Eurocode. The temperature time curve is considered in two separate phases, which are:

- exponential temperature rise, and
- a linear cooling phase.

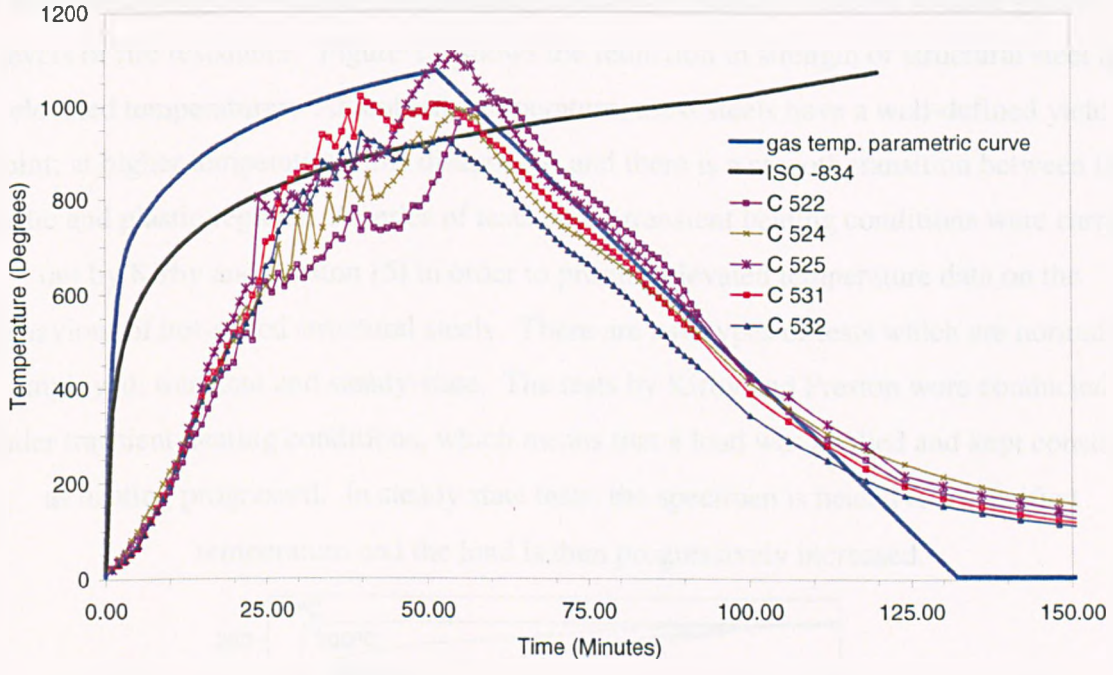

Figure 1.5: Comparison of parametric fire curve with ISO curve 834 with a 'real' fire.

It can be seen from Figure 1.5 that the parametric approach provides a good estimate of the maximum temperature and linear decay but greatly over estimates the severity of the beginning of the fire. The Parametric approach assumes a uniform temperature within the fire compartment at any time. As shown in Figure 1.5, there is actually some variation between the actual gas readings measured at different positions in a compartment.

1.3 Material Behaviour at Elevated Temperatures

The mechanical properties of all materials decrease with large increases in temperature. Modern buildings are mainly composite in that they are composed of steel and concrete. This research focuses on the fire performance of modern office/apartment type composite buildings. Neither material is combustible, but steel is an excellent conductor of heat and can follow the fire curve closely. Concrete is a much better insulator than steel.

1.3.1 Steel at Elevated Temperatures

It is imperative when designing steel members to know how the steel properties change at elevated temperatures. Unprotected steel beams can reach up to 1000°C in a fire, at which temperature loaded structural elements would be in danger of collapse. The Building Regulations require that any load-bearing structural element is shown to have specific levels of fire resistance. Figure 1.6 shows the reduction in strength of structural steel at elevated temperatures. At ambient temperature, most steels have a well-defined yield point; at higher temperatures this disappears, and there is a smooth transition between the elastic and plastic regions. A series of tests under transient heating conditions were carried out by Kirby and Preston [5] in order to provide elevated temperature data on the behaviour of hot-rolled structural steels. There are two types of tests which are normally employed; transient and steady-state. The tests by Kirby and Preston were conducted under transient heating conditions, which means that a load was applied and kept constant as heating progressed. In steady state tests, the specimen is heated to a specified temperature and the load is then progressively increased.

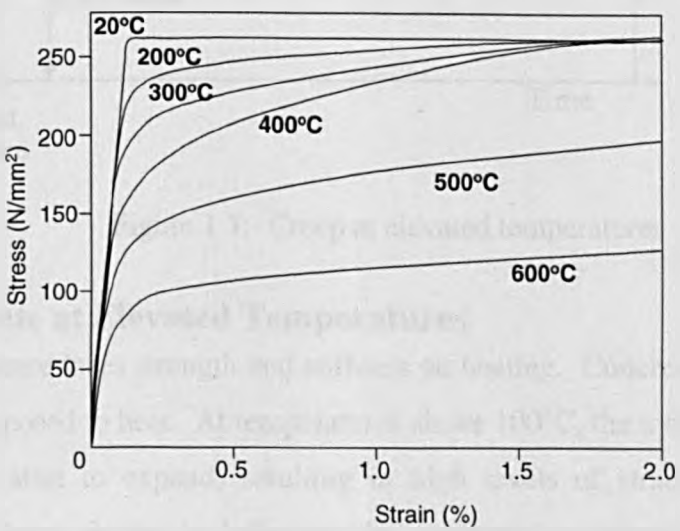

Figure 1.6: Stress-Strain relationship of steel at elevated temperatures

The stress-strain relationship which has been adopted in Eurocode 3 Part 1.2 [6] consists of three parts; a straight line, part of an ellipse, and then a plateau.

Thermal and creep strains

As the steel is subjected to a temperature rise, temperature-induced strains develop; these are known as thermal and creep strains. Thermal strains develop when the steel is heated and the material expands, in relation to the increase in temperature. The thermal strains can produce large internal forces if the expansion of the steel is restricted. These forces can occur in buildings where there are complex structural interactions between elements which are not free to expand. Creep strains can also form during long-term deformation of materials under constant load. Creep can be significant for highly stressed members which are subject to high temperatures, as there is a marked reduction in the material strength which can accelerate creep which could ultimately lead to failure of a member (Figure 1.7). Kirby and Preston investigated the creep strains which develop for heated steel as the material degrades.

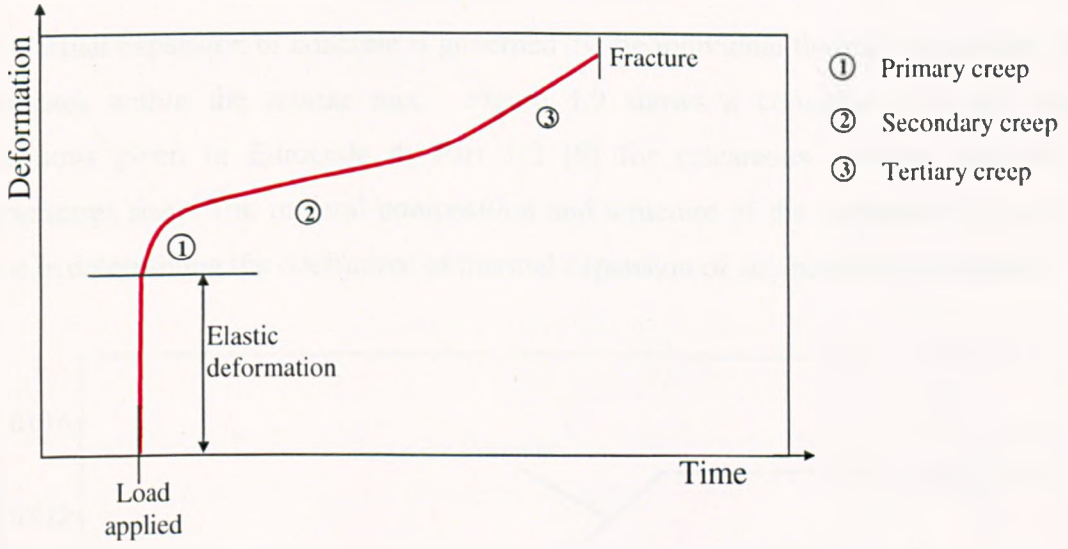

Figure 1.7: Creep at elevated temperatures

1.3.2 Concrete at Elevated Temperatures

Like steel, concrete loses strength and stiffness on heating. Concrete goes through several phases when exposed to heat. At temperatures above 100°C, the moisture is driven out and the aggregates start to expand, resulting in high levels of strain. The nature of the aggregate has been shown to influence the compressive strength of concrete at high temperatures [7]. Concrete made with calcareous (limestone) or lightweight aggregates

perform much better than siliceous (gravel) aggregates which break down above 350°C. The stress/strain relationships for concrete at elevated temperatures are shown in Figure 1.8.

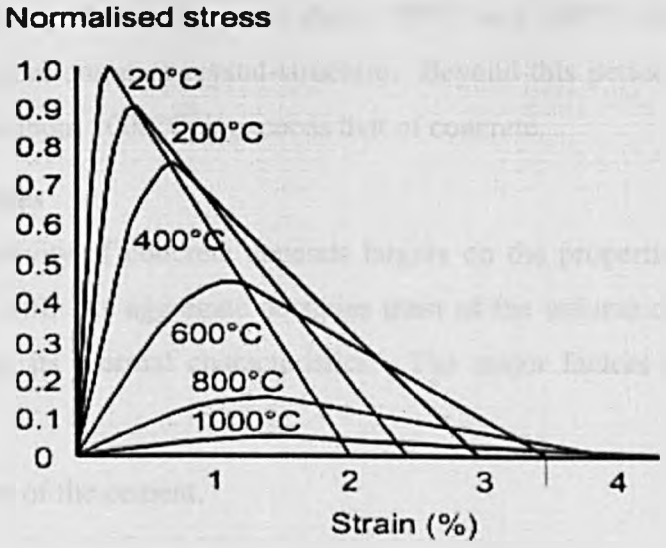

Figure 1.8: Stress-strain relationship of concrete at elevated temperature according to Eurocode 2: Part 1.2 [8].

The thermal expansion of concrete is governed by the individual thermal expansions of the aggregates within the mortar mix. Figure 1.9 shows a comparison of the thermal expansions given in Eurocode 4: Part 1:2 [9] for calcareous concrete and steel as temperatures rise. The mineral composition and structure of the aggregates is the major factor in determining the coefficient of thermal expansion of any particular concrete.

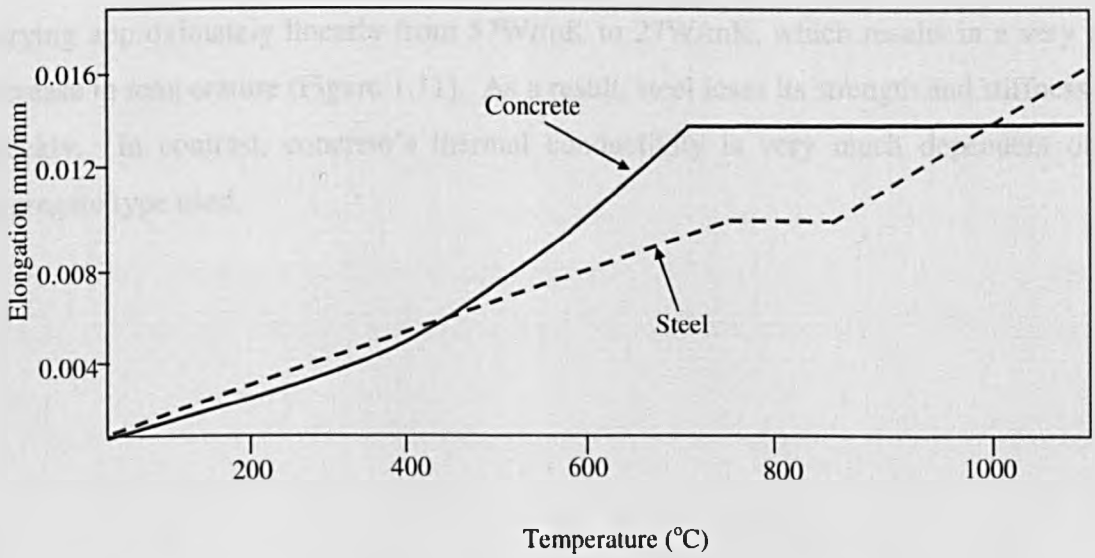

Figure 1.9: Comparison of the thermal expansion of steel and concrete

Figure 1.9 shows that between 20-450°C steel has slightly higher thermal strain, although the orders of magnitude are very similar, but at temperatures greater than 400°C concrete progressively expands more than steel. At about 700°C, concrete undergoes an irreversible chemical breakdown which causes its expansion effectively to stop. This parallels a break down in the expansion of steel between about 720°C and 850°C while it undergoes a phase-change to a more compact crystal-structure. Beyond this period, the steel resumes its expansion, and at about 1000°C, it exceeds that of concrete.

Thermal conductivities

The thermal conductivity of concrete depends largely on the properties of the aggregate type used (Figure 1.10). As aggregate occupies most of the volume of concrete, it is the main determinant of its thermal characteristics. The major factors that influence heat conduction are:

- Conductivity of the cement,
- Conductivity of the aggregate,
- Mix proportions,
- Compactness of the cast concrete,
- Moisture content.

The results in Figure 1.10 indicate that conductivity decreases rapidly with a rise in temperature, and at 800°C, the coefficient of thermal conductivity has fallen to approximately 50% of that at normal temperature. Steel has a high thermal conductivity, varying approximately linearly from 57W/mK to 27W/mK, which results in a very rapid increase in temperature (Figure 1.11). As a result, steel loses its strength and stiffness very quickly. In contrast, concrete's thermal conductivity is very much dependent on the aggregate type used.

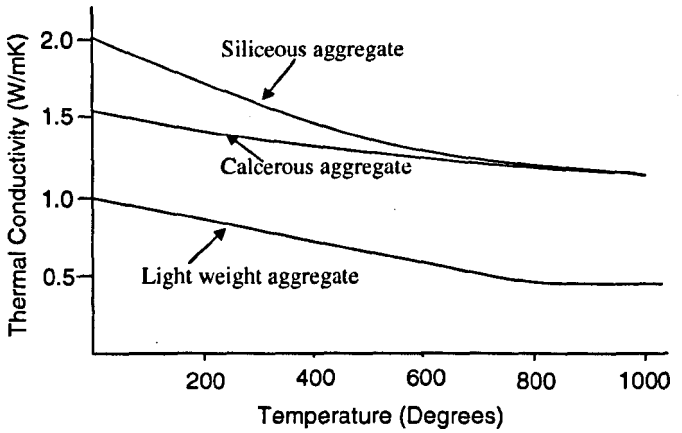

Figure 1.10: Comparison of thermal conductivity with various types of aggregate

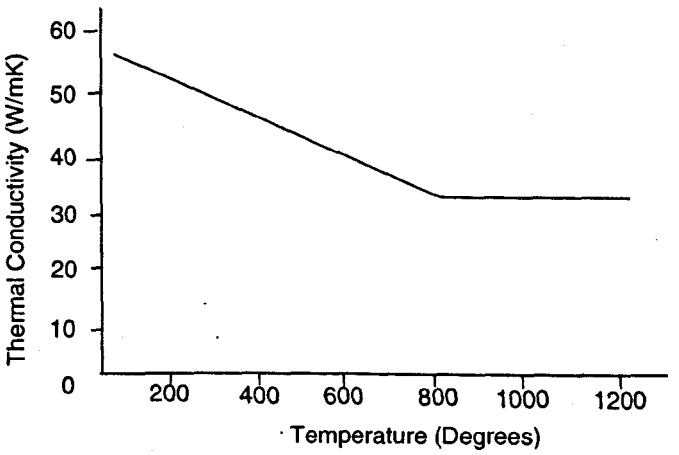

Figure 1.11: Thermal conductivity of steel with increasing temperature.

Figure 1.12 illustrates the reduction in ambient-temperature compressive strength with increasing temperature. It can be seen that lightweight concrete performs better than normal-weight concrete at any given temperature; this is mainly due to the increase in porosity, which reduces the concrete's density and at the same time its conductivity. The lightweight concrete is therefore a better insulator due to its low thermal conductivity. Steel has high thermal conductivity and if exposed will heat up more rapidly than concrete; because of this, it is common practice to apply fire protection to exposed steel elements.

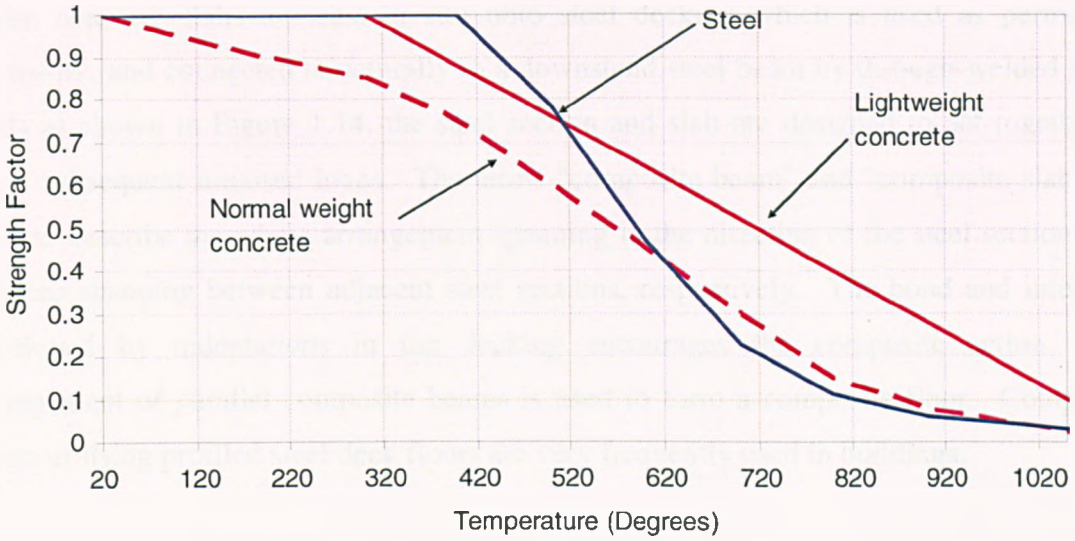

Figure 1.12: Reduction in strength with temperature

Spalling of Concrete

Spalling of concrete in fire involves pieces of concrete breaking off from the surface of the concrete as it is heated. Concrete spalling is much debated, and no definitive guidance exists to estimate the extent to which it will occur. It is, however, of great concern, as the reinforcement can be left with no protection, and exposed to extreme temperatures and ultimately failure of beams, columns or slabs.

Strains

The assessment of the total strain of concrete at elevated temperature is complex. According to Anderberg [10] the total strain is made up of:

- Thermal strain; the thermal expansion of the concrete. Not important in simply supported members subject to heat as the member can expand without any restraint. Thermal strains are important when modelling complex frames where members are restrained by other parts of the structure therefore the thermal strains can induce large internal forces.
- Stress related strain (mechanical strain).
- Creep strain, the long deformation of concrete under load.
- Transient strain; caused by decomposition of the cement paste when it is heated for the first time under load. They are permanent, unrecoverable and only occur under initial heating. The magnitude of transient strain can be of the same order as that of thermal strain.

1.4 Composite Slabs

When concrete slabs are cast in situ onto steel decking which is used as permanent formwork, and connected structurally to a downstand steel beam by through-welded shear studs as shown in Figure 1.14, the steel section and slab are designed to act together to resist subsequent imposed loads. The terms "composite beam" and "composite slab" are used to describe the whole arrangement spanning in the direction of the steel section, and the slab spanning between adjacent steel sections, respectively. The bond and interlock developed by indentations in the decking encourages the composite action. An arrangement of parallel composite beams is used to form a composite floor. Composite floors utilising profiled steel deck floors are very frequently used in buildings.

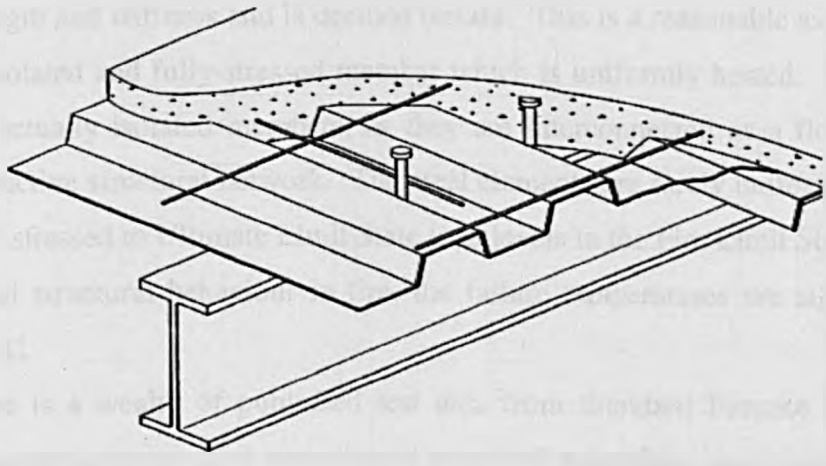

Figure 1.14: Composite steel deck floor

1.5 Developments in Structural Fire Engineering Design

Large-scale fire tests have shown that the fire performance of complete composite structural systems is much better than the Standard Test would suggest, and indicates that the amount of fire protection applied to such structural systems is excessive.

Fire engineering design of steel structures has developed from the traditional prescriptive approach, in which reliance was placed on the behaviour of individual structural elements based on the Standard Time-Temperature curves, to the full-scale testing or modelling of structural systems subject to a range of natural fires.

The design codes such as BS 5950: Part 8 [11] and the structural Eurocodes were developed from Standard Fire Tests on isolated elements. The perception of structural fire

resistance began to change after 1990, when a fire developed on the Broadgate development [12]. The building, which had large areas of unprotected steel, did not suffer any overall structural collapse, although there was considerable local distortion.

For the safety of occupants in a building, the designer must ensure that if a fire occurs it will not collapse within a reasonable period. In steel-framed buildings this has traditionally been achieved by protecting all areas of exposed steel, to provide fire resistance for a period specified by Approved Document B [13] of the Building regulations for England and Wales. This traditional method, although it has proved to be adequate, is conservative. It is based on Standard Fire Tests on isolated elements, and unprotected I and H sections are expected to achieve 15 to 20 minutes' fire resistance. The use of protection systems requires an insulation thickness such that the steel's temperature will not exceed 550°C, on the basis that at this temperature the steel has lost 60 percent of its strength and stiffness and is deemed unsafe. This is a reasonable assumption if the steel is an isolated and fully-stressed member which is uniformly heated. The steel elements are not actually isolated members, as they are interconnected as a floor system to form an interactive structural network. The steel elements are rarely uniformly heated, and are not fully stressed to Ultimate Limit State load levels in the Fire Limit State. When considering actual structural behaviour in fire, the failure temperatures are significantly higher than 550°C.

There is a wealth of published test data from Standard Furnace Fire Tests on isolated elements; tests on more complicated structural assemblies have been rare due to the costs and complexity of such projects. Early work on fire tests of sub-assemblies was undertaken by Kruppa [14], and by Rubert & Schaumann [15], which were followed later by full-scale testing on a steel framed building subject to various natural fires. The construction of the eight-storey steel-framed building at Cardington provided the opportunity to observe the reaction of a multi-storey building to a real fire (Figure 1.14). This building was designed to BS 5950 standards, and incorporated a braced central lift-shaft and two stair-wells providing the necessary resistance to lateral wind loads. The floor construction incorporated a steel decking used as permanent formwork to a lightweight in-situ concrete composite floor. The erection and fabrication of the structure was carried out in accordance with normal British practice.

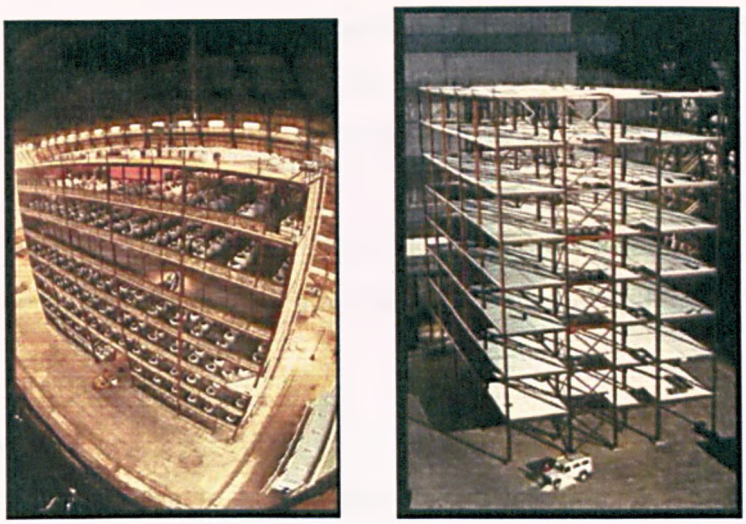

Figure 1.14: The eight-storey building at the Cardington Laboratory

Six full-scale fire tests were conducted inside the building at various locations (Figure 1.15). The aim of these tests was to assess the global structural behaviour of a multi-storey office building to a "real" fire.

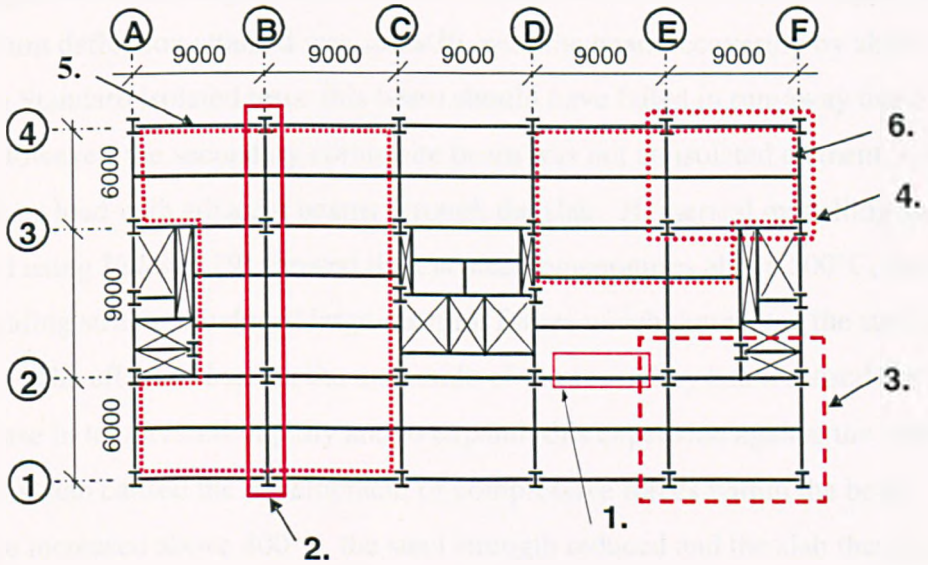

Level 7; Restrained beam test	*Level 3; Corner bay test*
Level 4; Plane frame test	*Level 3; Large compartment test*
Level 2; Corner bay test	*Level 2; Office demonstration test*

Figure 1.15: Original test locations in the office building at Cardington.

The tests were extensively instrumented with thermocouples, strain gauges, and displacement transducers. The imposed floor load in all of these tests was 2.663 kN/m^2,

and included an allowance for the services, false ceilings, and partitions. The load was applied using sand-bags distributed evenly on each of the floors. The Cardington building has a 45m x 21m footprint of five 9m x 21m bays, with an overall concrete slab thickness of 130mm.

These tests have been well documented [16, 17 and 18] and the results have been useful in rationalising the complex behaviour of three-dimensional structural fames in fire.

Restrained Beam Test

This was the first test to be undertaken on the building, and involved the heating of a single secondary composite beam (305x165UB40) over 8m of its 9m span using a purpose-built furnace. The purpose of this test was to gain an understanding of the structural behaviour of the beam, and the restraining effect from the surrounding, unheated floor slab. The maximum recorded steel temperatures were 834°C (lower flange), 816°C (web) and 764°C (upper flange) with slab temperatures of 481°C (lower surface) and 129°C (upper surface). The maximum deflection attained was *span/39*, with the beam recovering by about 30% on cooling. In Standard isolated tests, this beam should have failed in run-away due to loss of strength. However, the secondary composite beam was not an isolated element, being able to share its load with adjacent beams through the slab. Numerical modelling studies conducted using *Vulcan* [19] showed that, at steel temperatures above 500°C, the cooler surrounding structure induced large restraint forces which dominated the structural behaviour. The effect of heat on the underside of the secondary beam caused the steel to increase in temperature rapidly and to expand; this expansion against the cooler surrounding slab caused the development of compressive forces within the beam. As the temperature increased above 400°C, the steel strength reduced and the slab then dominated the structural behaviour, as can be seen in Figure 1.16(a). As the slab/beam deflections rose, the slab increasingly resisted the applied loads through tensile membrane action as is

shown in Figure 1.16(b). This mechanism will be discussed in more detail later.

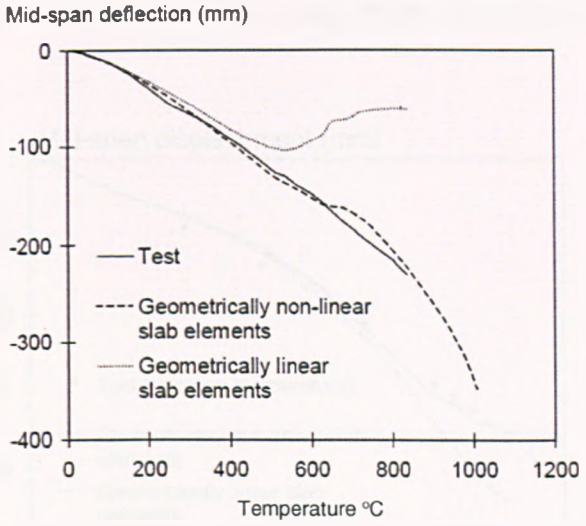

(a)

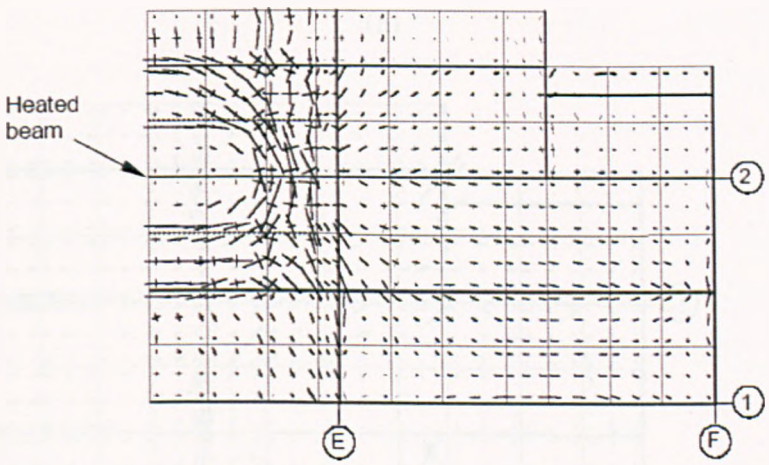

(b)

Figure 1.16: The load-deflection behaviour for the restrained secondary beam in Test 1 (a) comparison of test results with numerical model *Vulcan* (b) Membrane traction plots at 1000°C [19]

Corner Compartment Tests

This was the first fire test to use a full corner bay of the building, incorporating a floor area of 70m^2. In this test the perimeter beams and columns were fire protected whilst the internal secondary beams remained unprotected. The steel temperatures measured were in excess of 1000°C, with a maximum slab deflection of 425mm. The composite floor performed well, and there was no observed integrity failure of the slab. The test results were again compared with numerical models, and similar results were obtained to the restrained beam test (Figure 1.17(a)). At temperatures up to 600°C there was little

influence from membrane action of the slab, but at temperatures in excess of this the steel has a marked reduction in strength and the loads were carried by the floor slab (Figure 1.17(b)).

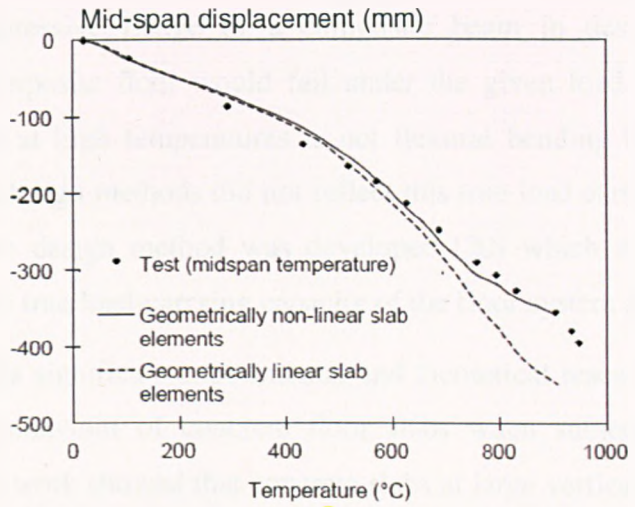

(a)

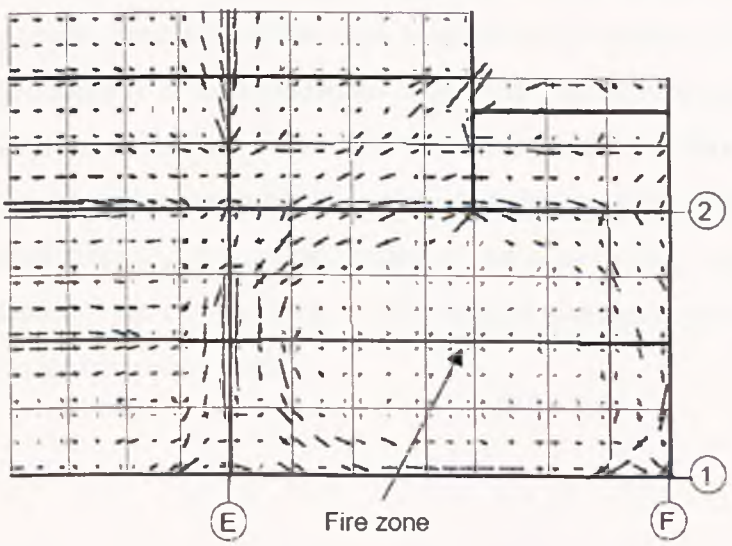

(b)

Figure 1.17: The load-deflection behaviour for the restrained secondary beam in Test 3 (a) comparison of test results with numerical model *Vulcan* (b) Membrane traction plots at 1000°C [19]

1.5 Background to the Research

The full-scale tests at Cardington showed that there is an inherent strength in the floor slabs which is not considered in ambient-temperature design. The concrete slab is assumed to act as the compressive flange of a composite beam in design, so that at high temperatures the composite floor would fail under the given load. However the load-carrying mechanism at high temperatures is not flexural bending but tensile membrane action. The current design methods did not reflect this true load carrying behaviour of the slab, and a new fire design method was developed [20] which was a significant step towards assessing the true load-carrying capacity of the floor system at high deflections.

During the late 1960s significant experimental and theoretical research work [21-25] was conducted on the behaviour of concrete floor slabs when subjected to large vertical displacements. This work showed that concrete slabs at large vertical displacements could support loads considerably greater than those calculated using the well-established yield-line approach. The mechanism for supporting the load was shown to be tensile membrane action, which could form within the slab irrespective of whether it was restrained or unrestrained horizontally at its boundaries. For a slab which was unrestrained around its boundaries compressive in-plane membrane forces were shown to form within the depth of the slab around its perimeter, and these provided the required support to the in-plane tensile membrane forces in the central region of the slab (Figure 1.18). The supporting ring of compression force can only occur if the vertical displacements around the perimeter remain small under increasing load.

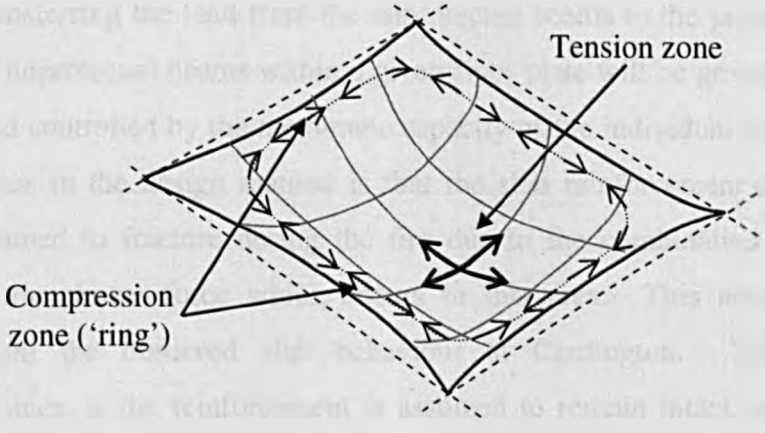

Figure 1.18: Membrane action in horizontally unrestrained concrete slab.

Although the early work provided an insight into the behaviour of slabs at large displacements, and some tentative design methods were proposed, no practical use for the research was found and the work was not developed significantly. However, following the fire tests conducted on the steel-framed building at Cardington, in which composite floor slabs were used, interest in the behaviour of concrete slabs at large displacements has been revived. During a fire, large displacements of the structure are acceptable if the fire is contained within the compartment of origin, so that the risk of fire spread throughout the building is low. Based on a combination of previous research work, the results from the Cardington fire tests and a large-scale ambient-temperature test conducted by the Building Research Establishment (BRE), a design method [26-27] was developed, based on a simplified model of the membrane action of composite floor slabs at large displacements subjected to elevated temperatures. The design method was a significant improvement on previous calculations of load capacity, which were limited to flexural behaviour. By using membrane action, it is possible to design composite floors for a defined fire resistance period, in which a large proportion of the steel beams within a given floor-plate can be left unprotected. Previously, considering only flexural action, all the supporting steel beams within a given floor-plate generally required some form of passive fire protection to achieve the required fire resistance.

The new design method divides the floor-plate of a building into square or rectangular slab panels, which are surrounded by protected beams (Figure 1.19), located on the column grid. The beams within each defined panel are left unprotected. During a fire, the unprotected beams lose a significant proportion of their strength and stiffness, and this, coupled with thermal effects, results in large vertical displacements of the composite slab. The applied load is then mainly supported by membrane action in the composite slab, effectively transferring the load from the unprotected beams to the protected beams. The proportion of unprotected beams within a given floor plate will be governed by the size of the panels, and controlled by the membrane capacity of the individual slab panels. One of the assumptions in the design method is that the slab reinforcement over the protected beams is assumed to fracture during the fire due to the combination of large hogging moment and membrane force which occurs in this area. This assumption has been supported from the observed slab behaviour at Cardington. This assumption is conservative since, if the reinforcement is assumed to remain intact, the induced tensile membrane forces in the slab, and thus its load-carrying capacity, would be significantly increased. With the assumption that reinforcement fractures over the protected steel

beams, the slab panels are assumed to be unrestrained horizontally, so that the compressive in-plane forces around the slab's perimeter provide support to the tension field in its central region.

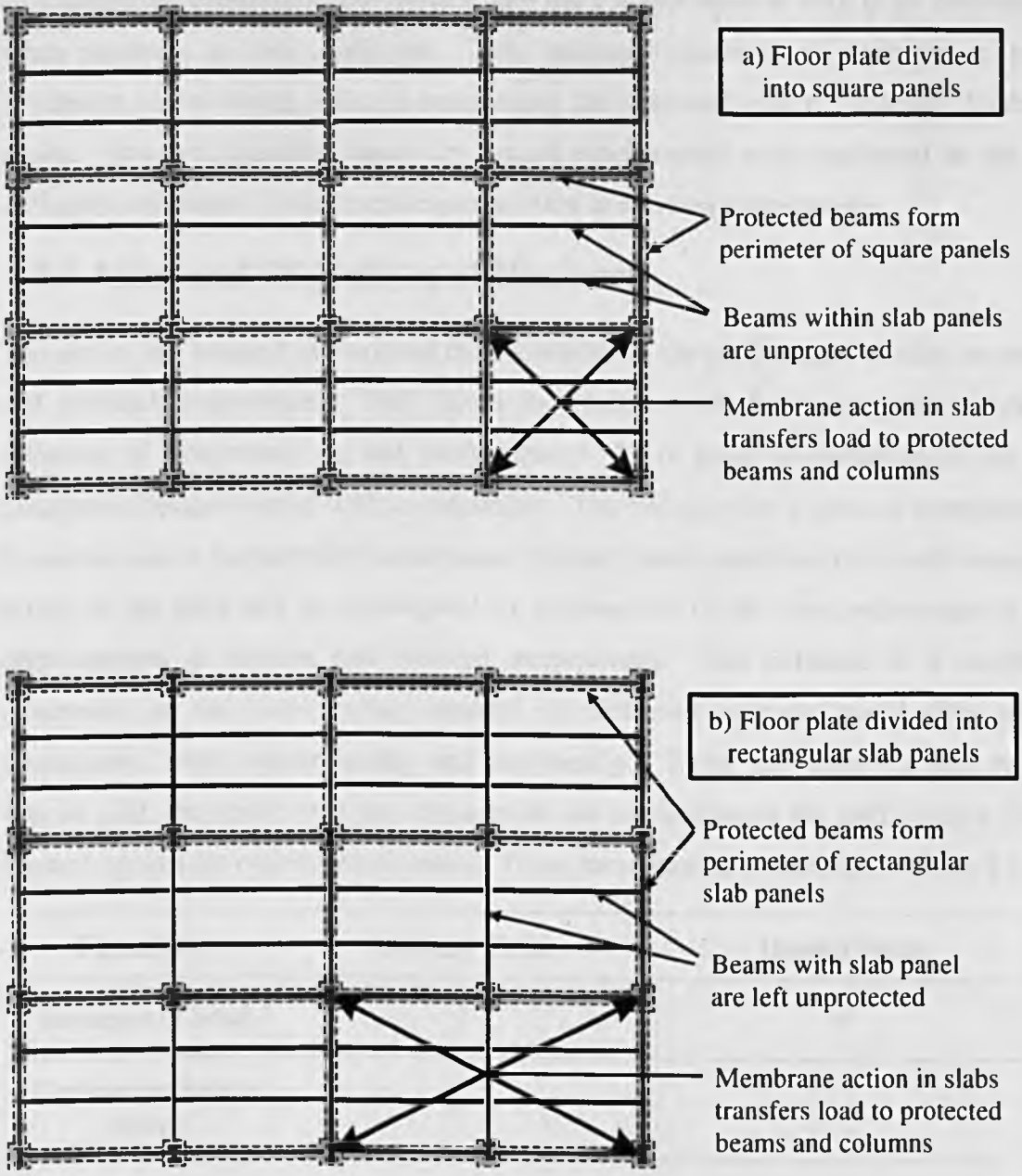

Figure 1.19: Two options for dividing the floor plate into slab panels to ensure membrane action in the floor slab during a fire, (a) Floor plate divided into square panels and (b) Floor plate divided into rectangular slab panels.

1.6 Impetus of Research

Full-scale fire tests in the multi-storey steel framed building at Cardington have shown that an unprotected composite floor system may not collapse even at very large deformations when subjected to fire conditions. This enhanced resistance is attributed to tensile membrane forces which assist in maintaining the structural integrity through diaphragm action. However, there has been very limited experimental work conducted on the large deflection behaviour of reinforced concrete slabs at elevated temperatures.

1.6.1 Aims and Objectives of Research

The aim of this research is to extend the knowledge of the performance of slabs at ambient and elevated temperatures. Slab failure mechanisms will be investigated as will the influence of temperature on slab performance. An in depth investigation of the BRE Simplified Design Method will be undertaken. This will involve a series of experiments to be carried out on horizontally unrestrained concrete model slabs and the tensile membrane action of the slabs will be investigated by examination of the slab performance at large displacements at ambient and elevated temperatures. The influence of a number of parameters on the load-carrying capacity of reinforced concrete model slabs will be investigated, both experimentally and analytically. Using the finite element package *Vulcan* [28], the results will be compared to the predictions of the BRE Simple Design Method against the experimental results. These parameters are presented in Table 1.1.

Parameter	Ambient Tests	Heated Tests
Influence of bond	√	√
Orthotropic nature of slab	√	
Area of reinforcement		√
Slab aspect ratio	√	√
Slab thickness		√

Table 1.1: Parameters investigated in experimental work

The tests will firstly be carried out at ambient temperature to allow the basic engineering principles embodied in the developed design method to be checked, and to validate the

small-scale test methodology against theory and the finite element approach. The purpose of these tests is to investigate the influence of isotropic and orthotropic reinforcement, together with reinforcement bond strength on the degree of mobilisation of tensile membrane action, and thus on the load carrying capacity of the slab. The effects of scaling are not applicable in this research, as the mechanics involved is scale-independent. The design method assumes that the basic behaviour observed at ambient temperature (Figure 1.20) will remain the same at elevated temperatures, and comparison with limited data from the Cardington fire tests does not seem to support this assumption.

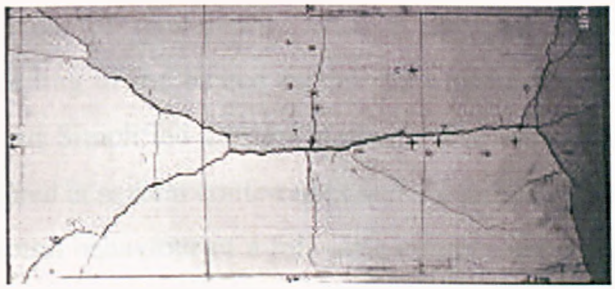

Figure 1.20: Cracking pattern observed in slabs due to tensile membrane action at ambient temperature.

The experimental work will then be extended and a series of tests conducted at elevated temperatures. This will require the design and construction of a purpose built furnace.

The purpose of these tests is to investigate the influence of thermal curvature on the failure mechanisms of rectangular slabs, since this is not explicitly allowed for in the Simplified Design Method. The more detailed issues being studied include the influence of slab geometry, reinforcement percentage and reinforcement bond strength at high temperatures on the final integrity failure caused by tensile cracking. Numerical modelling studies will be carried out in conjunction with the experimental work, and comparisons will be made with the Simplified Method. Further studies will follow using *Vulcan* to further understand the mechanics involved when a slab is subjected to high temperatures.

From the above investigations, a better understanding will be gained of concrete slab behaviour at large displacements at both ambient and elevated temperatures.

1.6.2 Structure of Thesis

Chapter 2 provides a review of the literature related to this project and derivation of a revised Simple Design Method for orthotropic slabs. Chapter 3 summarises the experimental results and slab behaviour of the model-slabs at ambient conditions. This Chapter forms part of a published paper to the Engineering Structures Journal.

Chapter 4 describes *Vulcan* and discusses the verification of a 3D model representative of the ambient slab test. The 3D analyses of the tested slabs are undertaken and comparisons are made with the experimental results and Simple Design Method.

Experimental fire tests on model-scale slabs are described in Chapter 5. This Chapter also investigates the behaviour of model-scale slabs at elevated temperatures. Chapter 6 describes the 3D modelling of the heated model-slabs and compares the results with the experimental results and Simplified Design Method. The work presented in Chapters 5 and 6 have been presented at several conferences and are published in their proceedings.

The thermal and structural behaviour of a full-scale composite building subject to a severe compartment fire are presented in Chapter 7. This Chapter forms part of a paper submitted to the Fire Safety Journal and is awaiting publication.

The discussion, conclusions and recommendations from this research can be found in Chapter 8.

Chapter 2

Response of RC slabs to Imposed Loads

2.0 Introduction

In the design of reinforced concrete slabs there are two main approaches used, based on either elastic or limit analysis theory. The former uses classical small deflection elastic bending theory of thin plates to calculate the deflection response under load and subsequently the maximum elastic stresses; this will not be considered here. The main impetus of the work is the investigation of slab behaviour at large displacements that have already formed failure mechanisms.

Limit analysis calculates the ultimate load of the slab and the internal distribution of the moments on the basis of assumed hinge patterns. There are two methods of calculating the ultimate load; a lower-bound and an upper-bound method. The difference between the two methods is that in the lower-bound case, the slab never enters a collapse mechanism, so the ultimate load calculated is a safe estimate. For the upper-bound approach, a collapse mechanism must be determined for the slab, and the most commonly used method is so-called Yield Line Theory [29].

2.1 Yield Line Theory

Yield line theory can be used to predict the ultimate load-carrying capacity of concrete slabs. The method assumes a collapse mechanism defined by a pattern of yield lines (hinges which include concrete cracking) across which the reinforcing bars have yielded and about which plastic rotation occurs. The flat concrete plate facets between the yield lines are assumed to remain rigid and perfectly planar, with the pattern of the yield lines governed by the type of loading, the geometry of the slab, and the boundary conditions (Figure 2.1).

Yield Line Design is a method of designing reinforced concrete slabs. It uses the yield line theory to investigate failure mechanisms at the ultimate limit state and establishes the load in a loaded slab at the point of assumed failure.

Figure 2.1: Yield line patterns of a rectangular slab.

Considering the slab shown in the photograph of Figure 2.1, the slab was subjected to a uniform load which was increased until collapse occurred. Initially, as the load was applied, the response was elastic with the maximum steel stress and deflection occurring at the centre of the slab. During this stage hairline cracks occurred where the tensile capacity of the concrete had been exceeded at the mid span. Increasing load caused further increases in the size of the cracks and yielding of the reinforcement, which initiated the formation of larger cracks emanating from the point of maximum deflection. On further loading, these cracks developed towards the edges of the slab, at which stage all the tensile reinforcement passing across these yield lines had yielded. The yield lines develop into continuous plastic hinges, and these hinges constitute a small deflection mechanism generally referred to as the yield line pattern. The yield lines divide the slab into individual regions, which pivot about their axis of rotation. There may be several possible yield line patterns, which can apply to a slab depending on the particular boundary conditions and loading applied.

Yield Line theory is generally considered to be an upper-bound approach. The results can either be correct or theoretically unsafe, so it is essential to ensure that the most critical collapse mechanism has been selected. The work balance method has been the most popular way of applying Yield Line theory. The principle is that internal and external work must balance. In plastic deflection the work done by the imposed load is equal to the internal energy dissipated by rotations about the yield lines.

$$\sum(N.\delta) = \sum(m.l.\phi) \qquad 2.1$$

Where; N = Loads

δ = Corresponding vertical displacement

ϕ = Relative rotation of regions about yield line

m =Moment of resistance of the slab

l = Length of yield line

2.1.1 Isotropy

Consider the slab shown in Figure 2.1; which has isotropic reinforcement (with identical cross sectional areas of reinforcement per unit length in the two directions, X and Y (Figure 2.2 (a)). Orthotropic slabs have different amounts of reinforcement area per unit length in the two directions (Figures 2.2 (b) and (c)). Johansen, Wood and Park [29, 30, 31] derived a theorem which enabled solutions for orthotropic slabs to be determined from that of an isotropic slab; the lengths of the sides of the slab and the loading are altered by ratios depending on the ratio of the ultimate moments of resistance per unit width in the two directions. This ratio of moments of resistance is commonly known as the coefficient of orthotropy (μ).

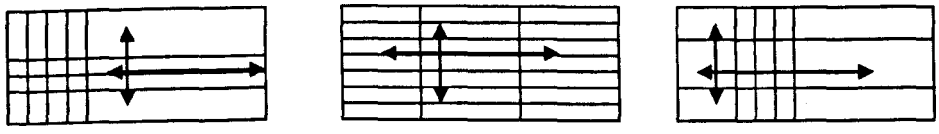

(a) (b) (c)

Figure 2.2: Isotropic and orthotropic reinforcement layouts

In Figure 2.2:

(a) Is an isotropic slab, μ=1, where $\mu=\frac{m_x}{m_y}$

(b) Is an orthotropic slab of μ<1

(c) Is an orthotropic slab of μ>1

In design, there is often no need for the reinforcement to be the same in both directions, and in the design of two-way slabs the shorter direction will usually have the greater amount of reinforcement; such slabs will have coefficient of orthotropy greater than 1.

2.1.2 Deflection and Ductility

The British Standards [32] limit the deflection of beam/slabs to certain permissible (*span/20, span/30*) ratios at elevated temperatures.

At ambient temperature, Yield Line theory also assumes that there is sufficient ductility in the reinforcement to maintain its ultimate moment of resistance as rotation proceeds about the yield lines. In the design codes there is strict guidance on the type of reinforcement which may be used and the minimum permissible elongation ("ductility") of the steel. For reasons of durability the code specifies limits in respect of:

- Minimum reinforcement areas.
- Spacing of reinforcement.

2.2 Development of Membrane Action

Yield Line theory only considers the moments and shear forces at the yield lines without considering the development of in-plane forces as displacements increase. These in-plane forces are known as membrane forces and develop due to the boundary conditions imposed and the changes in the geometry of the slab as it deflects. The two extremes, of full in-plane restraint and no in-plane restraint for rectangular slabs that are vertically supported cause either compressive membrane action or tensile membrane action. Research work into membrane action was undertaken by Ockleston [33] in the test to destruction of the Dental Hospital in Johannesburg. Ockleston investigated the development of compressive membrane forces within a slab. If the edges are restrained against expansion then compressive forces are induced within the slab. The compressive force acts above mid-depth at the centre span of the slab and below the mid-depth at the edges of the slab. This creates an arching action, which when combined with the bending resistance, enhances the load carrying capacity of the slab. Compressive membrane action throughout the entire slab occurs at small deflections. With increasing load, collapse takes place violently by instability at an approximate displacement of 0.4 to 0.5 times the depth of the slab [33]. If the collapse is not too violent it is followed by a tensile phase where the loads increase once more.

In steel-framed composite buildings, membrane action has been identified as a primary mechanism which accounts for the stability of a structure at high deflections (Chapter 1).

It has been shown to increase the ultimate load capacity of many reinforced concrete slabs significantly, but has not yet been incorporated into design procedures.

Figure 2.3 shows the enhancements with deflection of load capacity above the initial yield load, for a uniformly loaded two-way rectangular reinforced concrete slab with simple supports. The rapid initial rise to point A represents the increase in load as the moment of resistance of the largely uncracked slab resists the load. At point A the slab rapidly develops its yield lines and there is a rapid decrease in load capacity as the slab loses stability and is represented by the decrease in load capacity of the slab. At point B the central zone of the slab begins to develop tension, with the reinforcement across the full-depth crack acting mainly in tension.

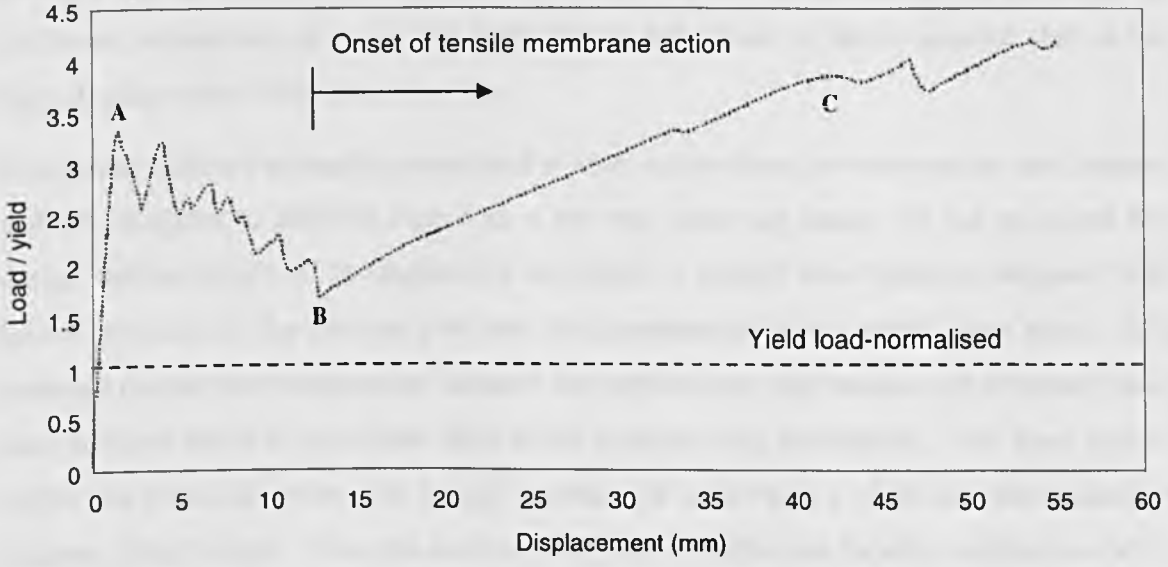

Figure 2.3: Load deflection response for simply supported slab of aspect ratio 2.09.

The membrane forces start to develop at approximately *span/36*, and at *span/15*, the slab is succeeding in carrying more load than its actual capacity in small deflection bending action. Also shown in this figure is the yield line mechanism prediction which is represented by the dashed straight line at normalised load level 1.0. This is predicated on the assumption that the concrete has no tensile strength, and that only plastic bending contributes to the slab's strength. In fact, the load level never returns to this level after the initial loading phase; this would be an indication of failure if it occurred. It can be seen that the yield line design limit is very conservative in its assumptions, and the slab has an inherent strength which is not considered in design methods.

This has a reflection at elevated temperatures. Designers have perceived that structural materials perform badly at high temperatures, resulting in the general practice of protecting

or partially protecting exposed parts of a steel frame against fire. Steel, in common with other materials, loses strength and stiffness as its temperature rises, and if the building structure is considered on an element by element basis, the general perception of poor performance of exposed steel members in fire is reasonable. However, tests and observations from accidental fires in real structures which incorporate a composite flooring system with downstand steel beams have shown that these types of structures perform far better than current design methods suggest. It is possible, by considering the true inherent fire performance of these structures, that a significant amount of passive fire protection which is currently specified for the steel beams is unnecessary. Analysis of test results has shown that the load path mechanisms of a steel structure, supporting a composite slab, during a fire are different from those assumed during the normal use of the building. In particular, membrane action is the predominant behaviour of the composite slab at the large displacements encountered in fire.

Composite slabs are normally considered to span in one direction between the steel beams, and are designed to BS5950 Part 8 as a one-way spanning beam. In the proposed fire design method which is investigated in this thesis, a typical floor layout is designed with beams protected on the column grid-lines and unprotected beams within these zones. It is assumed that as the temperatures increase the unprotected steel beams will ultimately lose their strength and will contribute little to the load-carrying mechanism. The floor system within the protected beam grid layout is presumed to develop a yield line mechanism of discrete plastic hinges. It is also assumed that there is sufficient ductility within the slab to maintain the full moment of resistance simultaneously along the entire length of each yield line. However, many factors effect ductility and it cannot be assumed, especially in fire design, that ductility can be maintained when increasing temperature is reducing the strength of the reinforcement. Observations of the deflected floor slab at Cardington have raised questions about this assumed failure pattern of the floor zones and the applicability of the method to floor slabs at high temperatures. The deflected floor systems at Cardington did not show any signs of developing a well defined yield line mechanism. There were, however, apparent cracks across the short span of the floor system, but these did not extend to full-depth cracking, suggesting that the yield line mechanism could not have been fully 'developed'. The deflected profile of the floor system for square compartments was a biaxial curve, tending in the mid-zones of rectangular compartments towards single curvature between protected beams. Around the edges of the

compartments, due to large hogging moments, the concrete slab had full depth cracking and the reinforcement was often observed to have fractured, as shown in Figure 2.4.

Figure 2.4: Cardington Test 7, photograph of full depth cracking around the compartment edges.

Further tests have been carried out in New Zealand [34] which showed that initially, as the steel beams lost their load-carrying capacity, the concrete slab increasingly utilised its own load-carrying capacity. The slabs were also noted to deflect into double curvature, developing transverse cracks. Figure 2.5 illustrates the deflection profile of a slab under load at increasing temperature; initially it resists the applied loads through bending, but as the temperatures rises and the steel beam loses strength the slab goes into membrane action, carrying the required tension in its reinforcement.

Figure 2.5: Behaviour of floor slab with increasing deflection.

2.3 Early Investigations into Membrane Action.

The theory of membrane action in slabs has been the subject of research since the 1960's, when Ockleston showed from tests to complete destruction of a building that loads greater than those indicated by yield line theory could be sustained by continuous floors.

Hayes and Taylor [35] carried out load-testing of reinforced concrete slabs to investigate membrane action within the slab. Tests were carried out on 11 model-sized slabs of varying rectangularity reinforced with smooth plain bars which had been annealed to give a long yield plateau. Hayes and Taylor concluded that reinforced slabs can sustain higher loads than the collapse loads predicted by yield line theory, the phenomenon being attributed largely to membrane action. From tests on different geometries, it was found that the increase in load-bearing capacity depended upon slab rectangularity.

Tests were conducted on three series of varying spans, each with varying isotropic and orthotropic reinforcement.

2.3.1 Summary of Tests by Hayes and Taylor

The first series of tests were conducted on square slabs with varying percentages of total reinforcement. It was observed during the tests that the slabs reinforced with the heaviest reinforcement had the highest cracking load, which is to be expected. The cracks were widest near the mid-span. The observations during loading of the slab showed that up to cracking, the mid-span deflections were small, but dramatically increased, with a marked discontinuity in the load-deflection curve at cracking. Observing the slabs at the loads predicted by yield-line theory as collapse, the slabs had the diagonal yield pattern, but showed no signs of imminent collapse. It is interesting to note from the test data that the lightly reinforced slabs had much higher enhancements than the heavily reinforced slabs.

The second and third sets of tests were performed on rectangular slabs. In these sets of tests, the reinforcement was increased across the short span and consequently decreased in the long span to maintain a constant amount of reinforcement. Increasing the percentage of reinforcement in the short span of the slab will increase the flexural capacity of the slab. A summary of the test results are presented in Table 2.1.

Aspect Ratio	Slab	$\frac{Actual\ \max.load}{Yieldload}$
1	Isotropic-light	2.07
	Isotropic-heavy	1.60
1.5	Isotropic	1.8
	orthotropic	1.56
2	Isotropic	1.54
	orthotropic	1.26

Table 2.1: Summary of Hayes and Taylor's experimental results.

The test results indicated that the enhancements decreased as the slab's aspect ratio increased. The distribution of the reinforcement also had an influence on the enhancement factors.

Two-way spanning square reinforced concrete slabs sustain much higher loads than the collapse loads predicted by yield-line theory due to tensile membrane action. Rectangular slabs also sustain loads higher than predicted by yield-line theory, but the enhancements are smaller than for square slabs. As the slab approaches a one way spanning slab spanning between two edges and the slab aspect ratio increases therefore, lesser enhancements are attained. For rectangular slabs having the same total amount of reinforcement, the load-carrying capacity decreases as the coefficient of orthotropy increases.

In 1968 Taylor and Hayes [36] further investigated the phenomenon of less reinforcement giving more enhancement, referring back to theories developed by Westergaard and Slater [37] in 1921. These researchers had shown that the effects of the tensile strength of the concrete are considerable for a lightly reinforced section. The contribution of concrete tensile strength of course is not taken into account in the yield line method.

Taylor [38] went on to postulate a new method for ultimate load design of reinforced concrete slabs. He derived a possible method for calculating the design ultimate load incorporating membrane action by using a k factor on the deflection which relates back to a factored ultimate load.

Further experimental work undertaken by Powell [39] and Park [23] further supported the findings from the experiments undertaken by Taylor. Powell investigated the effects of varying the reinforcement percentages for slabs of aspect ratio 1.75 whilst Park investigated the orthotropic nature of the slab. The results were very similar to Taylor's in

finding that lightly reinforced slabs attained higher enhancement than heavily reinforced slabs and an increase in reinforcement in the slab resulted in lower enhancements.

Kemp [40] developed an upper-bound yield approach for simply supported square slabs, based on previous work undertaken by Wood. The method assumed rigid-plastic behaviour and the results tied in closely with Wood's predictions for a circular slab. The derived equations depended only on the relative deflection of the slab, the reinforcement percentage and yield strength of the reinforcement. The results showed that the membrane effect is quite small up until the stage when full-depth cracking occurs, then is more pronounced as slab displacement increases. For displacements greater than this, a greater increase in membrane force results, and is more pronounced in lightly reinforced slabs than those with higher percentages of reinforcement.

Sawczuk [24] undertook an investigation of the load-deflection relationship for simply supported rectangular concrete slabs. He considered two modes of failure, as shown in Figure 2.6.

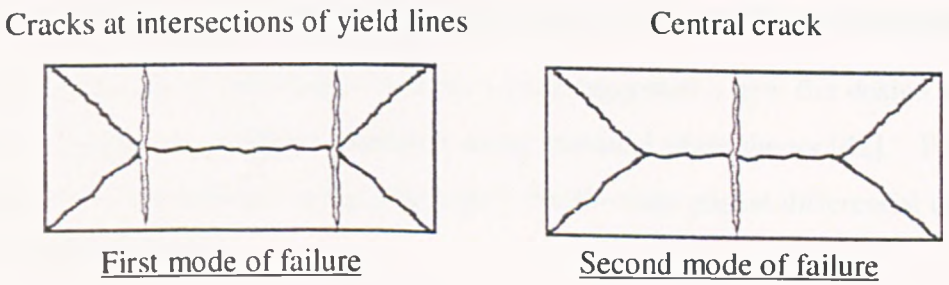

Figure 2.6: Sawczuk failure mechanisms

Hayes' [25] new equilibrium method was based on theories by Kemp and Wood. It attempted to tie-in closely with Kemp's method for square slabs, and is applicable to both isotropically and orthotropically reinforced rectangular slabs with a failure mode of two transverse cracks at the intersections of the yield lines (Figure 2.7).

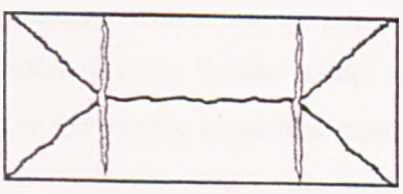

Figure 2.7: Hayes' failure mechanism for rectangular slabs

Hayes' method was developed for rectangular slabs based on the typical collapse mechanism shown in Figure 2.7. Hayes' approach assumed that the neutral axes along the yield lines would remain straight and the membrane forces would be linearly distributed. For the collapse mechanism shown in Figure 2.7, a critical distribution of membrane forces was found which causes in-plane bending hinges to form at the intersections of the yield lines with the transverse cracks. Comparison of this method with Kemp's and Sawczuk's shows that at large slab displacements Hayes' predictions lie close to Sawcuk's method, but Kemp's enhancements are much lower than Hayes' and Sawcuk's at low displacements and much higher at larger displacements. Kemp's method ignores the possibility of in-plane hinges forming.

2.4 Membrane Action at Elevated Temperatures

The fire tests conducted at Cardington resulted in slabs showing no signs of a well-defined yield line. It has generally been thought that the slabs did not closely approach failure in these tests. However, this does bring into question whether a design method based on ambient-temperature yield line theory is applicable to slabs at elevated temperatures.

A research project at Edinburgh University [41] suggested a new fire design method. The theory is based on an elastic approach using classical plate theory [42]. The membrane stresses have been derived using Lagrange's fourth-order partial differential equation (2.2) for thin elastic plates:

$$\frac{\partial^4 w}{\partial x^4}+2\frac{\partial^4 w}{\partial x^2 \partial y^2}+\frac{\partial^4 w}{\partial y^4}=\frac{q}{D} \qquad 2.2$$

This method assumes elastic deformations of an isotropic plate. The analysis examines the large-deflection behaviour of a laterally restrained floor slab. When the heated slab deflects due to thermal and load-induced effects at some point the composite slab will suffer considerable cracking due to hogging over the protected beams. This may easily result in fracture of the reinforcement and a loss of lateral restraint at these edges. The Edinburgh method only considers this one failure mode, and is therefore not a practical design method in the absence of the simply supported case. This method is also confined to isotropic slabs, which may be over-restrictive for design.

2.5 Calculation of Membrane Strength for Reinforced Slabs

The development of membrane forces within a slab is dependent on the slab geometry and support conditions. For tensile membrane action to develop in a slab system, vertical support at the grid lines must be maintained in order to induce membrane forces within the slab.

The Simplified Fire Design method considers the behaviour of composite floor slabs and their supporting grillage of steel beams at elevated temperatures. The derivation of the design method to predict the load-displacement response of concrete slabs in tensile membrane action has been published [26-27] for isotropically reinforced slabs. The derivation for orthotropically reinforced slabs is based on the observation from previously published test results [43] that a full-depth tension crack forms across the shorter span of the slab. The failure collapse mechanism of a slab is shown in Figure 2.8, where full-depth cracking occurs across the central region of the slab.

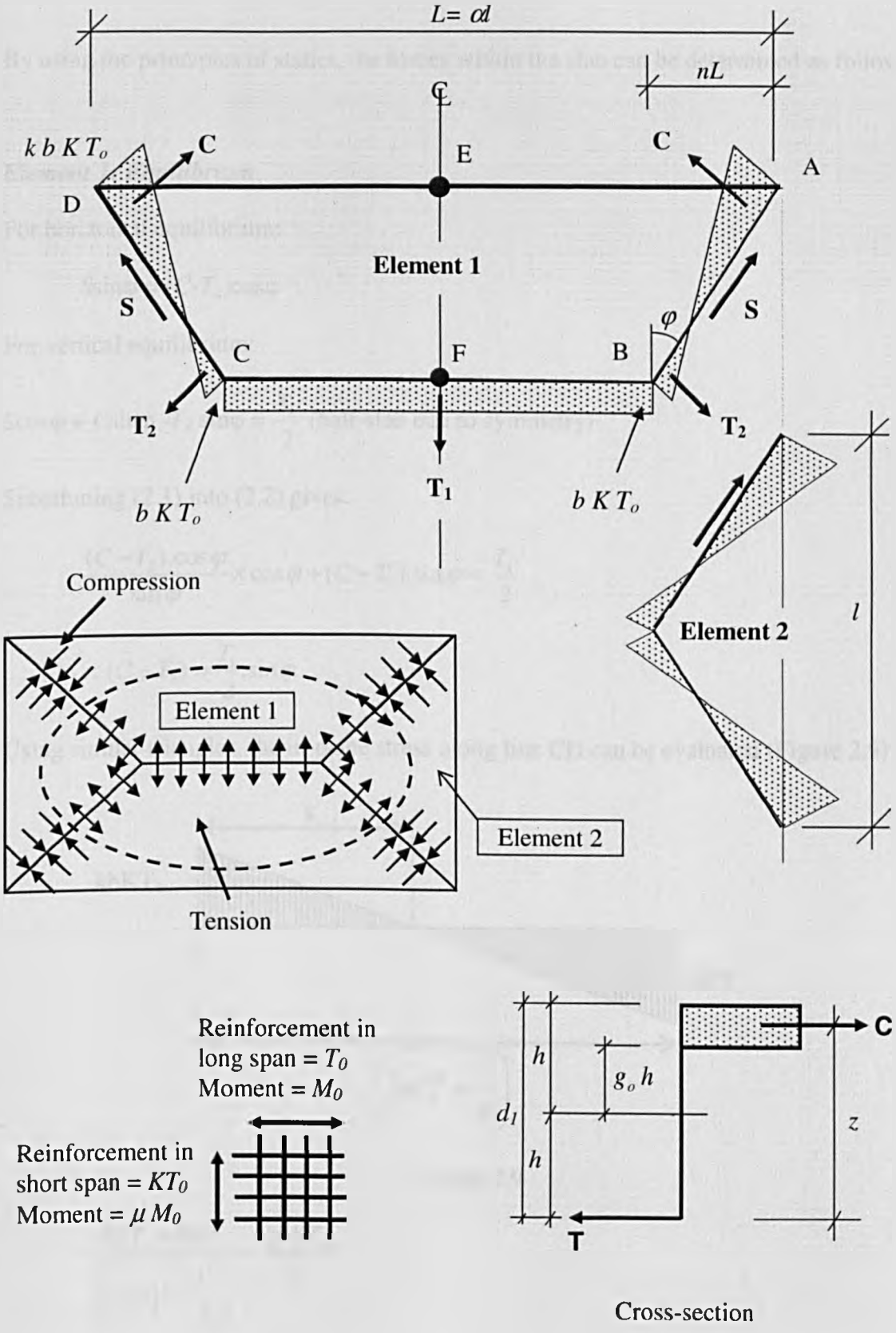

Figure 2.8: Assumed in-plane stress distributions for the equilibrium of orthotropic slabs.

By using the principles of statics, the forces within the slab can be determined as follows:

Element 1: Equilibrium

For horizontal equilibrium:

$$S\sin\varphi = (C\text{-}T_2)\cos\varphi \qquad 2.3$$

For vertical equilibrium:

$$S\cos\varphi + C\sin\varphi - T_2\sin\varphi = \frac{T_1}{2} \text{ (half-slab due to symmetry)} \qquad 2.4$$

Substituting (2.1) into (2.2) gives:

$$\frac{(C-T_2).\cos\varphi}{\sin\varphi}\times\cos\varphi + (C-T_2).\sin\varphi = \frac{T_1}{2}$$

$$\therefore (C-T_2) = \frac{T_1}{2}.\sin\varphi \qquad 2.5$$

Using similar triangles, the in-plane stress along line CD can be evaluated (Figure 2.9):

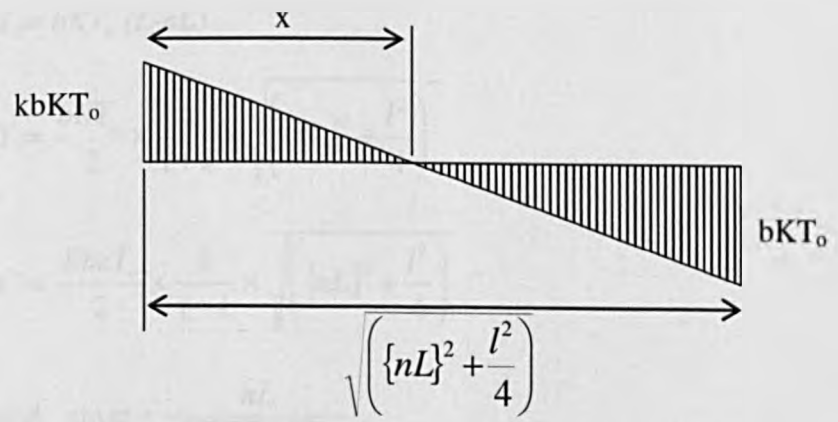

Figure 2.9

$$\frac{kbKT_o + bKT_o}{\sqrt{\left(\{nL\}^2+\frac{l^2}{4}\right)}} = \frac{kbKT_o}{x}$$

$$\therefore x = k.\frac{1}{(k+1)}\sqrt{(\{nL\}^2+\frac{l^2}{4}}$$

The dimension b (Figure 2.10) is therefore: $\frac{1}{(k+1)}\sqrt{(\{nL\}^2+\frac{l^2}{4}}$.

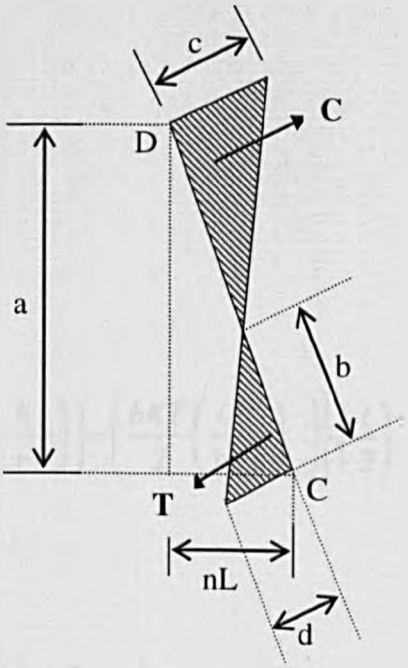

Figure 2.10

Where $a=\frac{l}{2}$, $c= kbKT_o$ and $d=bKT_o$

$$T_1= bKT_o\,(L-nL)$$

$$T_2= \frac{bKT_o}{2}\times\frac{1}{1+k}\times\sqrt{\left(\{nL\}^2+\frac{l^2}{4}\right)}$$

$$C = \frac{KbkT_o}{2}\times\frac{k}{1+k}\times\sqrt{\left(\{nL\}^2+\frac{l^2}{4}\right)}$$

and: $\sin\varphi = \frac{nL}{\sqrt{(nL)^2+(\frac{l}{2})^2}}$.

Substitute for C and T_2 into Equation (2.3):

$$\frac{SnL}{\sqrt{\left(\{nL\}^2+\frac{l^2}{4}\right)}}=\left\{\left(\frac{kbKT}{2}{}_o\left(\frac{k}{1+k}\right)\sqrt{\left(\{nL\}^2+\frac{l^2}{4}\right)}\right)-\left(\frac{bKT}{2}\left(\frac{1}{1+k}\right)_o\sqrt{\left(\{nL\}^2+\frac{l^2}{4}\right)}\right)\right\}.$$

$$\frac{l}{2}.\frac{1}{\sqrt{\left(\{nL\}^2+\frac{l^2}{4}\right)}}$$

Hence:

$$\frac{SnL}{\sqrt{\left(\{nL\}^2+\frac{l^2}{4}\right)}}=\left\{\left(\frac{kbKT}{2}{}_o\left(\frac{k}{1+k}\right)\right)-\left(\frac{bKT}{2}\left(\frac{1}{1+k}\right)_o\right)\right\}.\left(\frac{l}{2}\right)$$

Rearranging the formulae:

$$\frac{SnL}{\sqrt{\left(\{nL\}^2+\frac{l^2}{4}\right)}}=\left\{\frac{bKT_o}{4}\frac{(k^2-1)}{(k+1)}\right\}.(l)$$

$$\frac{SnL}{\sqrt{\left(\{nL\}^2+\frac{l^2}{4}\right)}}=\left\{\frac{bKT_o}{4}\frac{(k^2-1)}{(k+1)}\right\}.(l)$$

$$\frac{SnL}{\sqrt{\left(\{nL\}^2+\frac{l^2}{4}\right)}}=\left\{\frac{bKT_o}{4}\frac{(k\ -1)(k+1)}{(k+1)}\right\}.(l) \qquad 2.6$$

Re-arranging Equation (2.7) to find S:

$$S=\frac{bKT_0l}{4nL}\times(k-1)\times\sqrt{(nL)^2+(\frac{l}{2})^2}$$

Substituting T_1, T_2 and C into Equation (2.6) gives;

$$\frac{bKT_o}{2}\times\frac{1}{1+k}\times\sqrt{(nL)^2+(\frac{l}{2})^2}\times(k^2-1)=\frac{bKT_0}{2}\times(L-2nL)\times\frac{bKT_0}{2}\times(L-2nL)\times\frac{nL}{\sqrt{(nL)^2+(\frac{l}{2})^2}}$$

The parameter k is a proportion of the membrane force and is determined by:

$$k-1=\frac{nL(L-2nL)}{(nL)^2+(\frac{l}{2})^2}$$

$$k=\frac{4na^2\times(1-2n)}{4n^2a^2+1}+1, \text{ where } a=\frac{L}{l} \qquad 2.7$$

Taking moments about E:

$$-\frac{T_1}{2}\times(\frac{L}{2}-nL)\times\frac{1}{2}+S\times\frac{L}{2}\cos\varphi+T_2\times(\sqrt{(nL)^2+(\frac{l}{2})^2}-\frac{L}{2}\sin\varphi-$$
$$\frac{1}{3}\times\frac{1}{1+k}\sqrt{(nL)^2+(\frac{l}{2})^2})+C\times\frac{L}{2}\sin\varphi-\frac{k}{3(1+k)}\sqrt{(nL)^2+(\frac{l}{2})^2}=\frac{1.1Tol^2}{8}$$

Substituting for T_2, C and S leads to:

$$b=\frac{1.1l^2}{8K(A+B+C-D)} \qquad 2.8$$

where:

$$A=\frac{1}{2}\left(\frac{1}{1+k}\right)\left[\frac{l^2}{8n}-\frac{(L/2-nL)}{nL}\left((nL)^2+\frac{l^2}{4}\right)-\frac{1}{3}\left(\frac{1}{1+k}\right)\left((nL)^2+\frac{l^2}{4}\right)\right]$$

$$B=\frac{1}{2}\left(\frac{k^2}{1+k}\right)\left[\frac{nL^2}{2}-\frac{k}{3(1+k)}\left((nL)^2+\frac{l^2}{4}\right)\right]$$

$$C=\frac{l^2}{16n}(k-1)$$

$$D=\left(\frac{L}{2}-nL\right)\left(\frac{L}{4}-\frac{nL}{2}\right)$$

Slab capacity due to membrane force

The load bearing capacity of the slab can be found by considering moment equilibrium about the axis of rotation for elements 1 and 2. The moment about the support due to membrane forces, for a maximum vertical displacement (w) can be found.

Element 1:

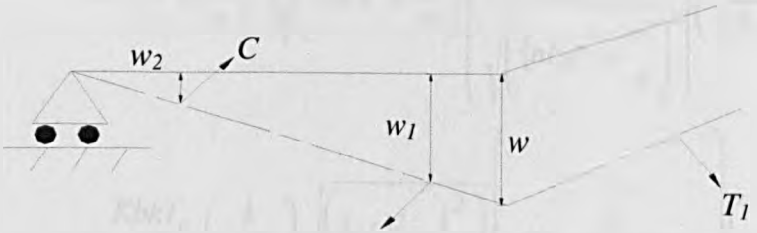

By similar triangles:

$$\frac{w}{\sqrt{\left(\{nL\}^2+\frac{l^2}{4}\right)}}=\frac{w_1}{\sqrt{\left(\{nL\}^2+\frac{l^2}{4}\right)}.\left(1-\frac{1}{3(1+k)}\right)}$$

$$w_1=\frac{3k+2}{3(1+k)}.w$$

Again by similar triangles:

$$\frac{w}{\sqrt{\left(\{nL\}^2+\frac{l^2}{4}\right)}}=\frac{w_2}{\sqrt{\left(\{nL\}^2+\frac{l^2}{4}\right)}.\left(\frac{1}{3}\times\frac{k}{1+k}\right)}$$

$$w_2=\frac{k}{3(1+k)}.w$$

$$\therefore M_{1m}=T_1.w+T_2.\sin\varphi.2.w_1-C.\sin\varphi.2.w_2$$

$$=KT_oLbw[(1-2n)+\frac{n(3k+2)}{3(1+k)^2}-\frac{nk^3}{3(1+k)^2}] \qquad 2.9$$

Element 2:

Again by similar triangles:

$$M_{2m}=2T_2.\cos\varphi.w_1-2C.\cos\varphi.w_2$$

$$= \frac{bkT_0}{2}\left(\frac{1}{1+k}\right)\sqrt{\left(\{nL\}^2+\frac{l^2}{4}\right)}\left(\frac{\frac{l}{2}}{\sqrt{\left(\{nL\}^2+\frac{l^2}{4}\right)}}\right)\left(\frac{3k+2}{3(1+k)}\right).w -$$

$$= \frac{KbkT_o}{2}\left(\frac{k}{1+k}\right)\sqrt{\left(\{nL\}^2+\frac{l^2}{4}\right)}\left(\frac{\frac{l}{2}}{\sqrt{\left(\{nL\}^2+\frac{l^2}{4}\right)}}\right)\left(\frac{k}{3(1+k)}\right).w$$

$$M_{2m} = KT_o lbw\left[\frac{2+3k}{6(1+k)^2} - \frac{k^3}{6(1+k)^2}\right] \qquad 2.10$$

M_{1m} and M_{2m} represent the moments about the supports due to membrane forces, where KT_o is the force in the steel per unit width in the shorter span and n is the parameter defining the yield line pattern (Figure 2.8). In addition:

$(g_0)_1$ and $(g_0)_2$ are coefficients defining the depth of the compressive stress blocks in flexural action in the shorter and longer spans respectively,

d_1 and d_2 are the effective depths of the reinforcement in the shorter and longer spans respectively.

Refer to Figure 2.8 for a diagram of the compressive stress block.

In order to determine the enhancement factors due to membrane forces e_{1m} and e_{2m} in elements 1 and 2, the above moments are divided by $\mu M_o L$ when membrane forces are absent.

Element 1

Taking moments about T (stress block in Figure 2.8),

The value of M_o can be calculated when there is no axial force;

$$M_o = KT_o d_1.(\frac{3+g_{o1}}{4}) \qquad 2.11$$

$$e_{1m} = \frac{M_{1m}}{\mu M_o L} = \frac{4b}{3+g_{o1}} \times \frac{w}{d_1}\left[(1-2n)+\frac{n(3k+2)}{3(1+k)^2} - \frac{nk^3}{3(1+k)^2}\right] \qquad 2.12$$

Element 2:

$$M_{2m} = T_2 \times \cos\varphi \times 2 \times w_1 - C \times \cos\varphi \times 2 \times w_2$$

$$= \frac{bkT_0}{2} \times \frac{1}{1+k} \sqrt{(nL)^2 + (\frac{l}{2})^2} \times \frac{\frac{l}{2}}{\sqrt{(nL)^2 + (\frac{l}{2})^2}} \times \frac{3k+2}{3(1+k)} \times w -$$

$$\frac{KbkT_o}{2} \times \frac{k}{1+k} \times \sqrt{(nL)^2 + (\frac{l}{2})^2} \times \frac{\frac{l}{2}}{\sqrt{(nL)^2 + (\frac{l}{2})^2}} \times \frac{k}{3(1+k)} \times w$$

$$= KT_o lbw \left[\frac{2+3k}{6(1+k)^2} - \frac{k^3}{6(1+k)^2} \right]$$

$$M_o = T_o d_2 . (\frac{3+g_{o2}}{4}) \quad , \qquad 2.13$$

Where; M_o is the moment of resistance when no axial force is present for the longer span.

Dividing M_{2m} by $M_o l$ provides the enhancement factor for the membrane force:

$$e_{2m} = \frac{M_{2m}}{M_o l} = \frac{4bK}{3+g_{o2}} \times \left(\frac{w}{d_2} \right) \times \left[\frac{2+3k}{6(1+k)^2} - \frac{k^3}{6(1+k)^2} \right] \qquad 2.14$$

Capacity due to enhancement of bending resistance

The enhancements to the yield line capacity due to increased bending resistance caused by the membrane forces in Elements 1 and 2 can also be determined.

The yield criterion must be established:

Wood derived a relationship between M and T, at yield based on theories set out in C.P.114, the British Code of Practice at the time [44]. Using principles of equilibrium, the moment of resistance of the section can be found if an axial force is present, see below for derivation.

The stress distribution on the slab sections in the longer span at yield subject to compressive force at mid depth is shown in Figure 2.11.

The yield moment M and axial force N can be found by:

$$M = T_o\left(d_1 - \frac{d}{2}\right) + C\left(\frac{d}{2} - k_2 d_n\right)$$

where $T_o = A_s f_y$ and $C = k_1 k_3 u d_n$, and

$$N = k_1 k_3 u d_n - T_o$$

$$d_n = \frac{N + T_o}{k_1 k_3 u}$$

Substitution of the neutral axis depth into above equation gives:

$$M = T_o\left(d_1 - \frac{d}{2}\right) + C\left(\frac{d}{2} - k_2\left(\frac{N + T_o}{k_1 k_3 u}\right)\right)$$

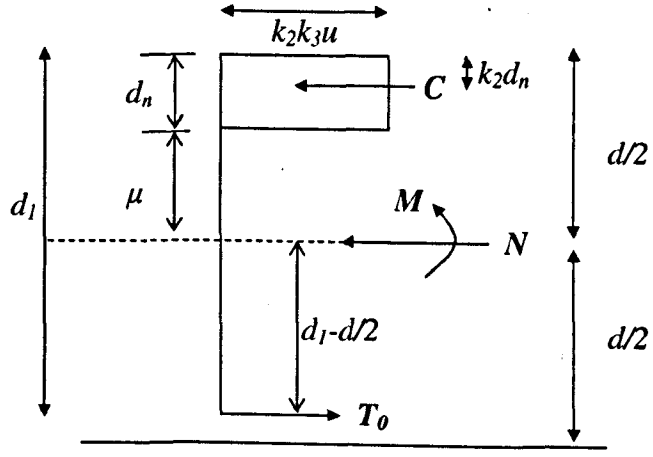

Figure 2.11

Substitution of C into the above equation gives:

$$M = T_o\left(d_1 - \frac{d}{2}\right) + \left\{(N + T_o)\left[\frac{d}{2} - \left(\frac{k_2 N}{k_1 k_3 u}\right) - \left(\frac{k_2 T_o}{k_1 k_3 u}\right)\right]\right\}$$

$$M = T_o\left(d_1 - \frac{k_2 T_o}{k_1 k_3 u}\right) + N\left(\frac{d}{2} - \frac{2k_2 T_o}{k_1 k_3 u}\right) - \frac{N^2 k_2}{k_1 k_3 u}$$

The yield moment corresponding to N=0 is

$$M_o = T_o\left(d_1 - \frac{k_2 T_o}{k_1 k_3 u}\right)$$

Wood's terminology used the term P for the overall axial force but in the methods presented by Kemp and Hayes used N. The values of k_1, k_2 and k_3 relate to the concrete stress block.

In non-dimensional form the equation relating moment capacity for the reinforcement in the long span to axial force is:

$$\frac{M}{M_o} = 1 + \alpha_2\left(\frac{N}{T_o}\right) - \beta_2\left(\frac{N}{T_o}\right)^2 \qquad 2.15$$

and a similar equation exists for the reinforcement in the short span direction:

$$\frac{M}{\mu M_o} = 1 + \alpha_1\left(\frac{N}{KT_o}\right) - \beta_1\left(\frac{N}{KT_o}\right)^2 \qquad 2.16$$

The symbols α and β are the parameters in the yield criterion and are a function of the stress block, therefore for the assumed stress block in Figure 2.8, the parameters are:

$$\alpha_1, \alpha_2 = \frac{2(g_0)}{3+(g_0)}$$

$$\beta_1, \beta_2 = \frac{1-(g_0)}{3+(g_0)}$$

Element 1:

The enhancements for the individual yield lines are considered separately. For line BC, the membrane force is constant and equal to $-bKT_o$, and thus;

$$\left(\frac{M}{\mu M_o}\right)_{BC} = 1 - \alpha_1 b - \beta_1 b^2$$

For line AB, the membrane force across the yield line at a distance x from B is given by:

$$N_x = -bKT_o + \frac{x}{nL}(k+1)bKTo = bKT_o\left[\frac{x(k+1)}{L} - 1\right]$$

For line AB and CD, the moment contribution is;

$$2\int_0^{nL}\frac{M}{\mu M_o}dx = 2\int_0^{nL}\{1+\alpha_1 b[\frac{x(k+1)}{nL}-1]-\beta_1 b^2[\frac{x(k+1)}{nL}-1]^2\}dx$$

So;

$$e_{1b}=\frac{M}{\mu M_o L}=2n\left[1+\frac{\alpha_1 b(k-1)}{2}-\frac{\beta_1 b^2}{3}\left(k^2-k+1\right)\right]+(1-2n)(1-\alpha_1 b-\beta_1 b^2) \quad 2.17$$

Element 2:

$$\left(\frac{M}{M_o}\right)=1+\alpha_2\left(\frac{N}{T_o}\right)-\beta_2\left(\frac{N}{T_o}\right)^2,$$

where $\alpha_2=\frac{2g_{o2}}{3+g_{o2}}$ and $\beta_2=\frac{1-g_{o2}}{3+g_{o2}}$

The membrane force across the yield line, at a distance y from A is given by:

$$N_y=-bKT_o+\frac{y}{l/2}(k+1)bKT_o=bKT_o[\frac{2y(k+1)}{l}-1]$$

Substituting for Element 2:

$$2\int_0^{\frac{l}{2}}\frac{M}{M_o}dy=2\int_0^{\frac{l}{2}}\{1+\alpha_2 b\ K[\frac{2y(k+1)}{l}-1]-\beta_2 b^2K^2[\frac{2y(k+1)}{l}-1]^2\}dy$$

Therefore, the enhancement factor due to the effect of membrane forces on the bending resistance for Element 2 is given by:

$$e_{2b}=\frac{M}{M_0 l}=1+\frac{\alpha_2 bK}{2}(k-1)-\frac{\beta_2 b^2K^2}{3}\left(k^2-k+1\right) \quad 2.18$$

The net enhancements are assumed to be given by combining the individual enhancements of bending capacity and due to membrane forces:

$$e_1=e_{1m}+e_{1b}$$
$$e_2=e_{2m}+e_{2b}$$

Therefore; $e=e_1-\frac{e_1-e_2}{1+2\mu a^2}$ 2.19

In which;

μ is the coefficient of orthotropy,

a is defined in Figure 2.9

2.5.1 Factors Influencing Enhancement Factor

The theory outlined in the previous section may be used to compute enhancement factors for various scenarios. It is found that the enhancement factor is dependent on several parameters, which are:

- The geometry of the slab.
- The yield strength of the reinforcement.
- The compressive strength of the concrete.
- The distribution of the reinforcement within the slab.
- The effective depth of the reinforcement.

A comparison of computed enhancements with respect to orthotropy is illustrated in Figure 2.12. Slabs reinforced with more reinforcement in the long span (μ=0.2) increase their membrane capacity, which increases the load carrying capacity of the slab. In the case of increased reinforcement across the short span (μ>1), the moment of resistance of the slab is increased but the increase in enhancement is less than for slabs reinforced with isotropic reinforcement.

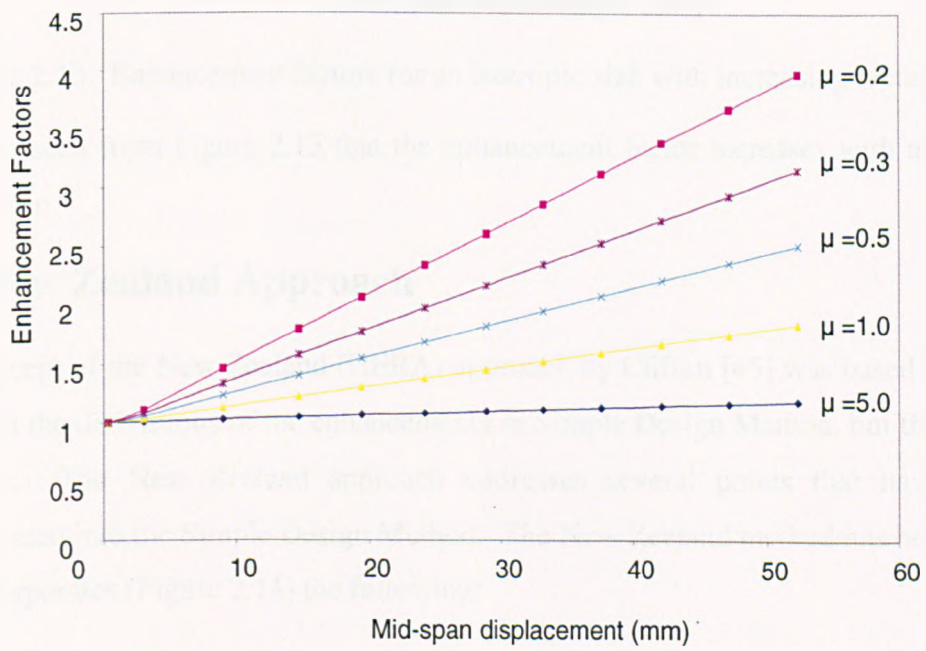

Figure 2.12: Comparison of enhancement factors with coefficient of orthotropy.

Enhancement factors are also influenced by the aspect ratio of the slab. As the slab's rectangularity increases, it becomes increasingly one-way-spanning and this decreases the tensile membrane forces generated. At the other limit, as the slab tends towards square the enhancement factors are greatly increased due to the increase in membrane forces. A comparison of aspect ratio with computed enhancement factors is shown in Figure 2.13.

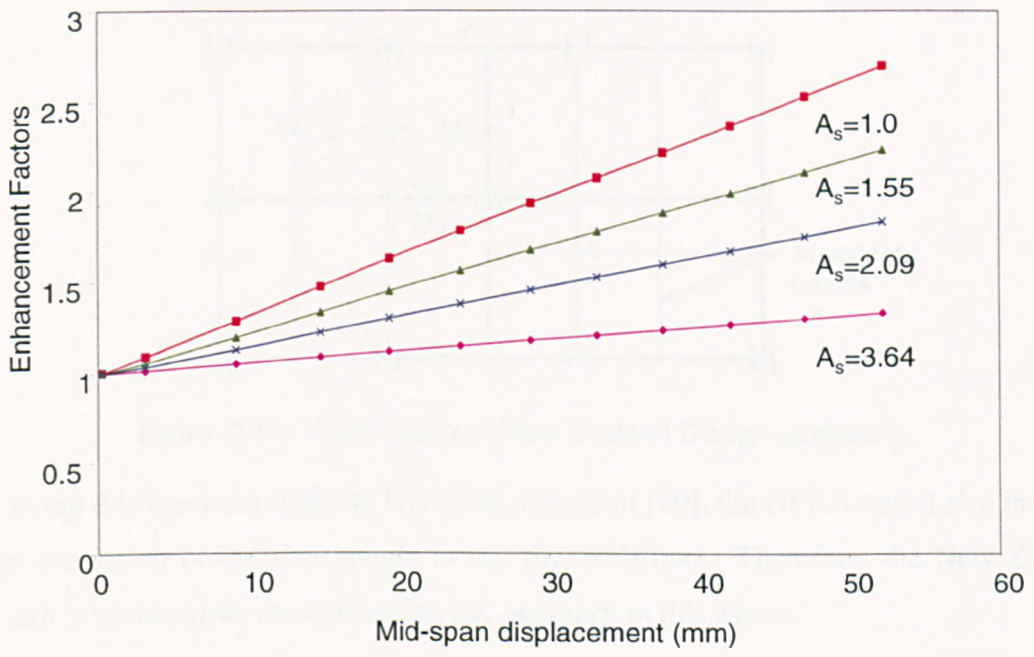

Figure 2.13: Enhancement factors for an isotropic slab with increasing rectangularity.

It can be seen from Figure 2.13 that the enhancement factor increases with a decrease in aspect ratio.

2.6 New Zealand Approach

The concept of the New Zealand (HERA) approach by Clifton [45] was based on the same theory in the derivations of the enhancements in Simple Design Method, but the scope was widened. The New Zealand approach addresses several points that have not been incorporated into the Simple Design Method. The New Zealand method has been extended and incorporates (Figure 2.14) the following:

- Contribution of secondary beams to the moment capacity of the slab (M_x).
- Contribution of any deck trough bars, if installed (M_y).
- Determination of the moments over the supports (M_x^*).

- Determination of the Yield Line Load carrying capacity for actual support conditions at ambient conditions.
- The shear capacity of the slab panel is checked for adequacy;

  a) Through the slab.

  b) Through the secondary beam to primary beam connection.

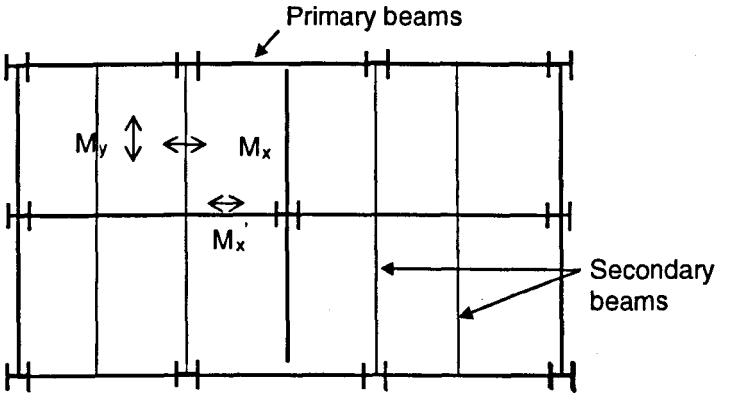

Figure 2.14: Application of New Zealand Design Approach.

Comparing this approach with the UK P288 document [20], the HERA report also includes design checks on connection details in the fire condition. Therefore, the New Zealand approach is more conservative than the UK approach in this aspect.

The New Zealand approach allows unprotected secondary beams to be connected to columns. In the UK approach, P288, for a fire resistance period of 60 minutes all beams connected to columns should be fire-protected to provide adequate restraint for fires of this severity. The New Zealand approach takes on board the evidence from the Cardington tests, and recommends insulating the ends of an unprotected beam connecting into a protected beam or column at least 200mm into the span of the unprotected beam from its end.

The assumed boundary condition to all slab edges in the Simple Design Method is "simply supported", as evidence from the full-scale tests conducted at Cardington has shown that full depth cracking of the slab, and reinforcement fracture, occurs around the peripheral region of the compartment. The calculation of the yield load in the New Zealand approach is based on the slab's behaviour in ambient conditions and not the behaviour at high temperature.

2.7 Enhancement Factors for Square Slabs

The derivation above can easily be altered so that membrane forces and enhancement factors can be calculated for a square slab.

Because the slab is square, the stress distribution is altered to that shown in Figure 2.15.

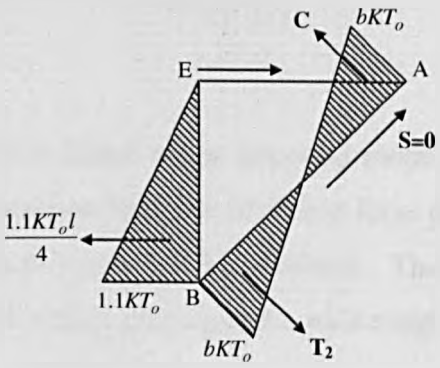

Figure 2.15: Calculation of in-plane moment of resistance along line EF for a square slab

For a square slab $k=1$ (Eqn. 2.4) because $nl= L/2$, so $n= 0.5$, and $\alpha= L/l=1$;

Hence;

$$b=\frac{1.1l^2}{12(A+B)}$$

where:

$$A=\frac{1}{4}\left[\frac{L^2}{8n}-\frac{1}{6}\left((nL)^2+\frac{L^2}{4}\right)\right]$$

$$B=\frac{1}{4}\left[\frac{nL^2}{2}-\frac{1}{6}\left((nL)^2+\frac{L^2}{4}\right)\right]$$

Substituting n=0.5 into A and B for square slab, these both become $A=B=\frac{L^2}{24}$.

Hence, for Element 1, $e_{1m}=\frac{4b}{3+g_0}\left(\frac{w}{d_1}\right)\left(\frac{1}{6}\right)$ and $e_{1b}=1-\frac{\beta b^2}{3}$.

Similarly, for Element 2 $e_{2m}=\frac{4b}{3+g_0}\left(\frac{w}{d_1}\right)\left(\frac{1}{6}\right)$ and $e_{2b}=1-\frac{\beta b^2}{3}$.

Chapter 3

The Response of Model-Scale Concrete Slabs at Ambient Temperature

3.1 Introduction

The Simplified Design Method is based on an assumed mode of failure; the previous tests (discussed in Chapter 2) conducted on this type of slab at large displacements were conducted in the 1960's and full test details could not be obtained. Therefore, a series of tests were undertaken on model scale slabs which investigated a wide range of parameters.

This chapter presents the results from a series of small-scale tests conducted on horizontally unrestrained slabs which were subjected to large vertical displacements to allow the basic engineering principles embodied in the developed design method to be checked, and to validate the small-scale test methodology against theory and the finite element approach. Scale (or 'size') effects have not been investigated in detail in this research project. However, the underlying mechanical principles of tensile membrane action are scale-independent, and hence the mechanical models can be validated using data collected from experiments on specimens of any scale. The purpose of these tests was to investigate the influence of isotropic and orthotropic reinforcement, together with type of wire, on the degree of mobilisation of tensile membrane action, and thus on the load-capacity of the slab. The results of the tests have been compared to an extension of the Simplified Design Method. The main objective of conducting tests at small scale was to enable a large body of data to be generated at relatively low cost. The number of uncertainties which accompany concrete in tension and the bonding of low percentages of reinforcement across cracks make it essential that a statistical approach is taken.

The results of the small-scale tests conducted on horizontally unrestrained slabs presented in this Chapter has been summarised and published within the Engineering Structures Journal [46].

3.2 Material Properties

3.2.1 Concrete

The materials used to produce the sample slabs were mortar and steel wire. A concrete mix study was initially undertaken; and Table 3.1 summarises the results of this study. After some testing a cement-sand ratio of 1:3 was adopted, using a gritty sand containing fine aggregate ranging between 1mm and 4mm. The water-cement ratio was 0.47 without plasticiser and the mix had good workability, with a 14-day cube strength in the range of 33-38 N/mm^2.

Mix Design	7-day Compressive Cube Strength (N/mm^2)	Curing Technique
1 part cement: 3 parts builders sand Water content 0.58	12.6	Hessian
1 part cement: 3 parts gritty sand Water content 0.58	19.2	Hessian
1 part cement: 3 parts builders sand Water content 0.75	12.9 - 13.9	Hessian Water bath (20°C)
1 part cement: 3 parts gritty sand Water content 0.47	26.5 - 29.2	Hessian Water bath (20°C)
1 part cement: 3 parts builders sand (1% plasticier); Water content 0.63	16.4 - 16.8	Hessian Water bath (20°C)

Table 3.1: Results of concrete mix study.

Figure 3.1 shows the variation of the 14-day cube strength of the concrete. The concrete mix was designed to a nominal strength of 35N/mm^2. The results show some variation, with increases in strength corresponding closely to days when the weather was hot.

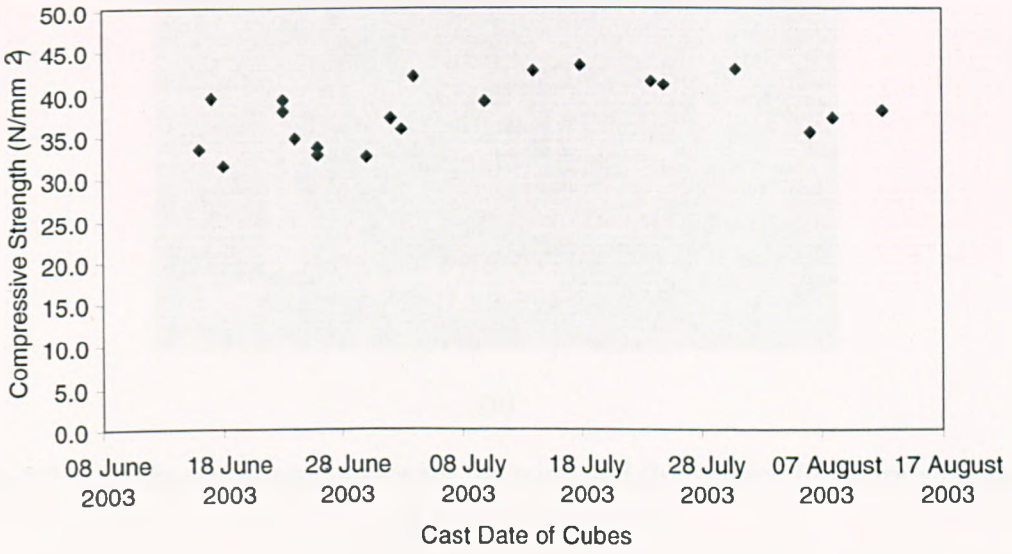

Figure 3.1: Variation of 14-day compressive strength of the concrete used in tests.

3.2.2 Reinforcing Steel

The reinforcement comprised 0.71mm diameter smooth or deformed (ribbed) wire. The deformed wire was created by indenting the smooth wire using a purpose-built machine (Figure 3.2 (a) and (b)).

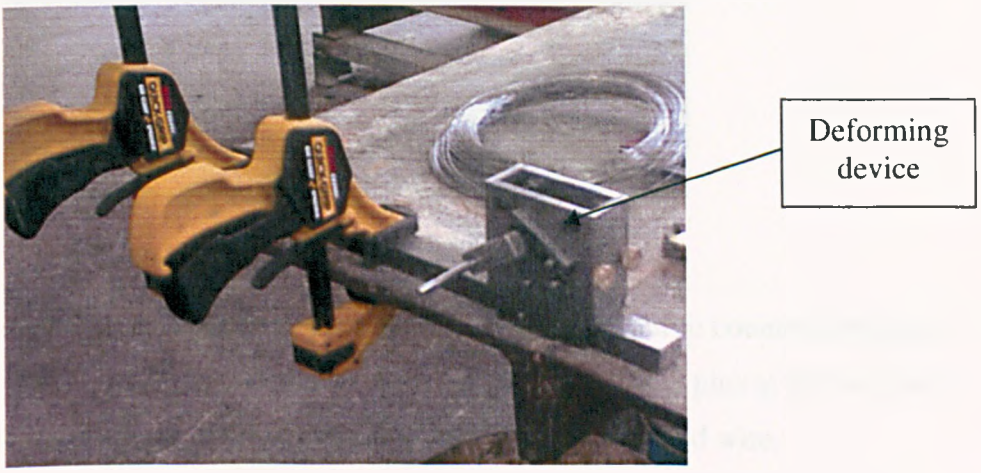

(a)

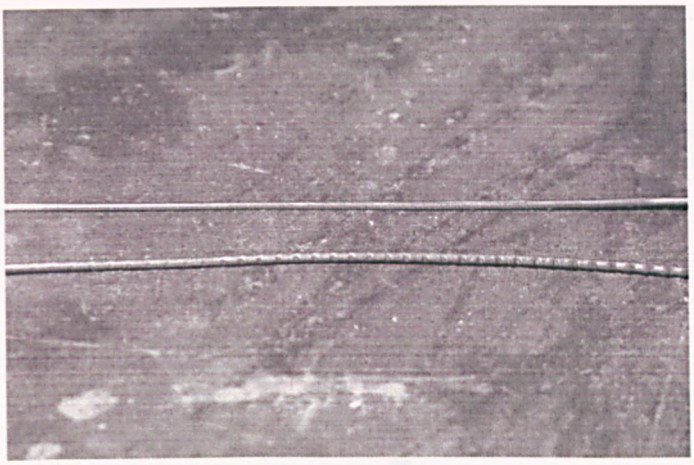

(b)

Figure 3.2: (a) The deforming device for the wire, and (b) Surface finish for smooth and deformed wire.

The yield strength of the smooth wire the yield strength ranged from 255-265N/mm^2, and for the deformed wire varied between 245-255N/mm^2. Tensile tests were conducted on both the smooth and deformed wire using the tensile testing machine shown in Figure 3.3.

Figure 3.3: View of tensile testing machine.

The steel wire was originally held in the grips at either end, but in order to counter slipping of the wire in the grips these were removed and the wire was looped around pins at the two ends. Figure 3.4, shows the variation of yield stress for the smooth and deformed wire.

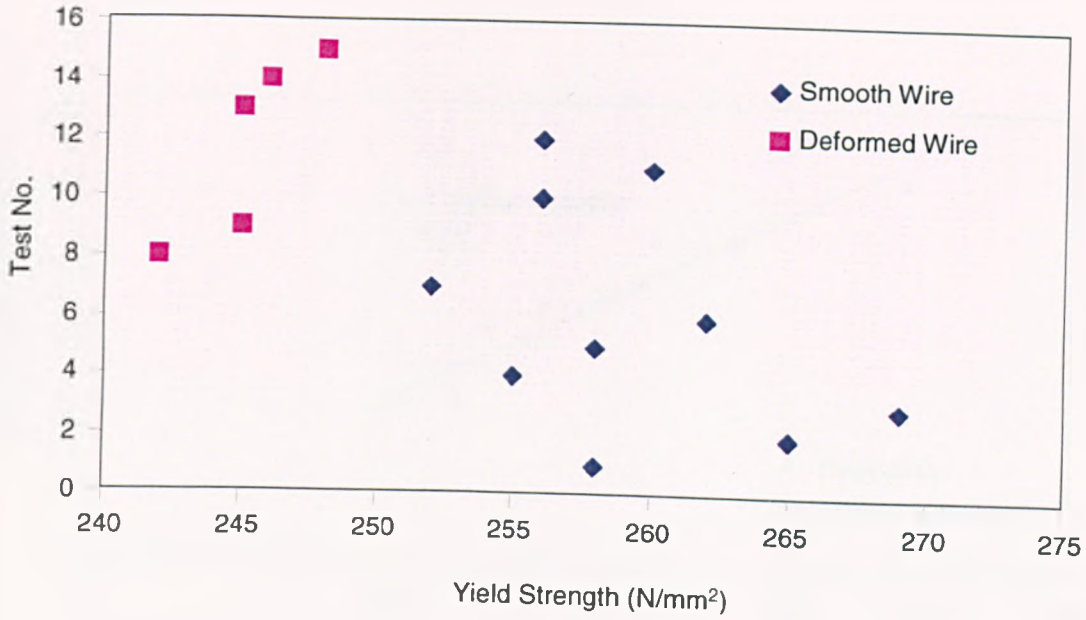

Figure 3.4: Variation of Yield Strength for Smooth and deformed Wire.

The results in Figure 3.4 show that the smooth wire from the yield strength ranged from 252-269 N/mm^2, and for the deformed wire be taken 248-250 N/mm^2.

The tested ductility was 20.3% for the smooth wire and 11.4% for the deformed wire, as shown in Figure 3.5. The deformation of the wire surface increased the bond between the concrete and reinforcement, but clearly had the effect of reducing the reinforcement's ductility. Figure 3.2 shows the wire after indenting by the deforming machine compared to the smooth wire.

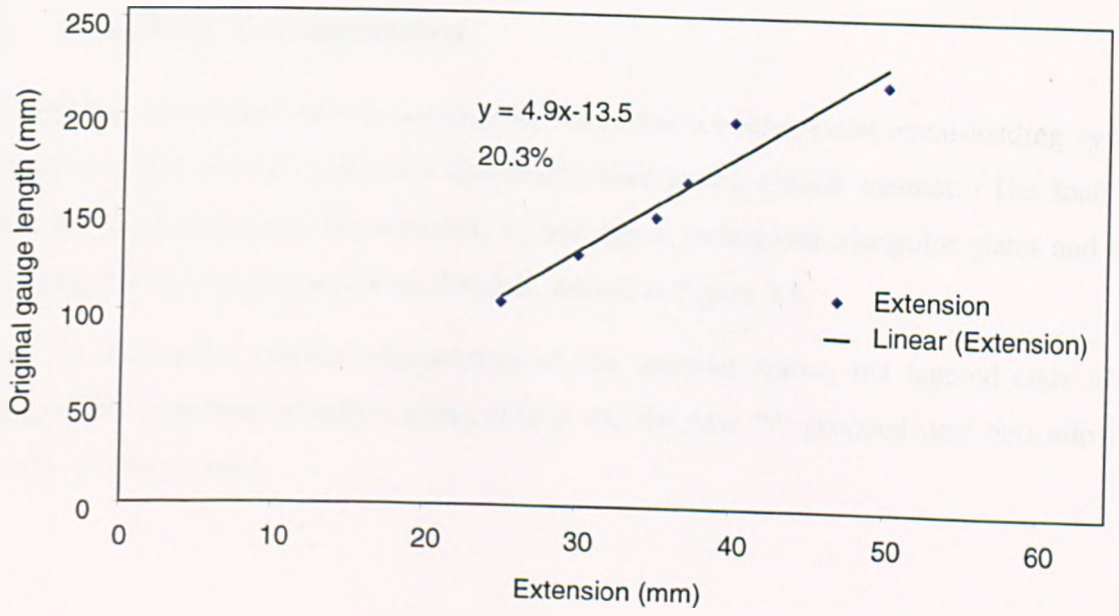

(a)

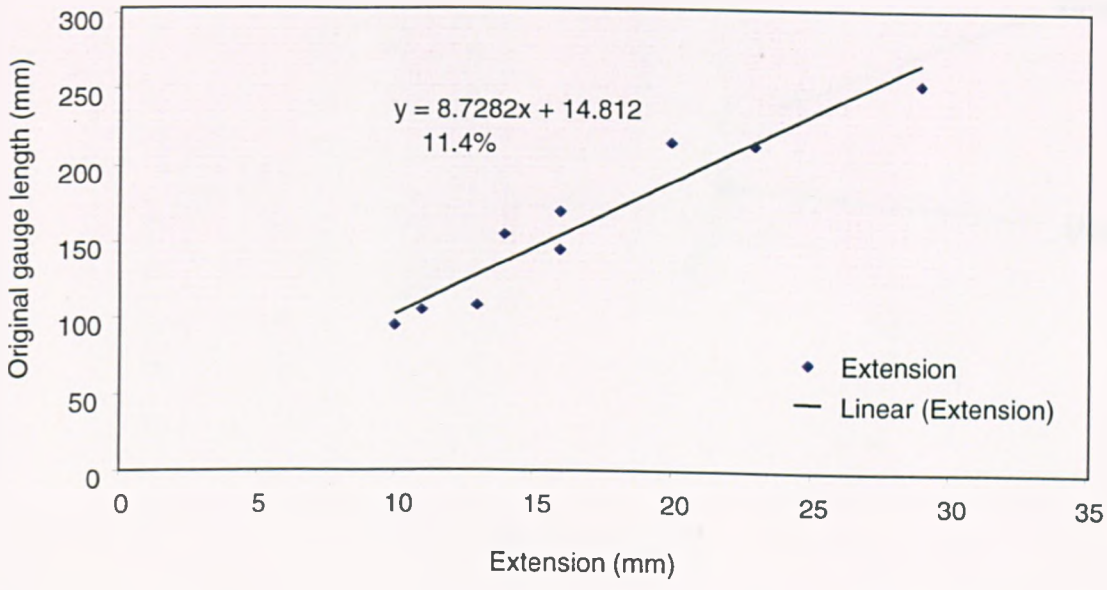

(b)

Figure 3.5: Tested ductility for (a) smooth wire; and (b) deformed wire (Extension of wire to failure).

3.3 Loading Arrangement

The loading arrangement for the rectangular slabs was a twelve-point equal-loading system, intended to represent the uniformly distributed load in the closest manner. The load was transferred from the jack to the centroids of four equal orthogonal triangular plates and from there to the twelve loading points on the slab, shown in Figure 3.6.

Figure 3.6 shows the general arrangement of the spreader frame, the tapered ends of the loading screws, notched circular loading platens and the new 'V' grooved steel bars allow the bars and screws to rotate.

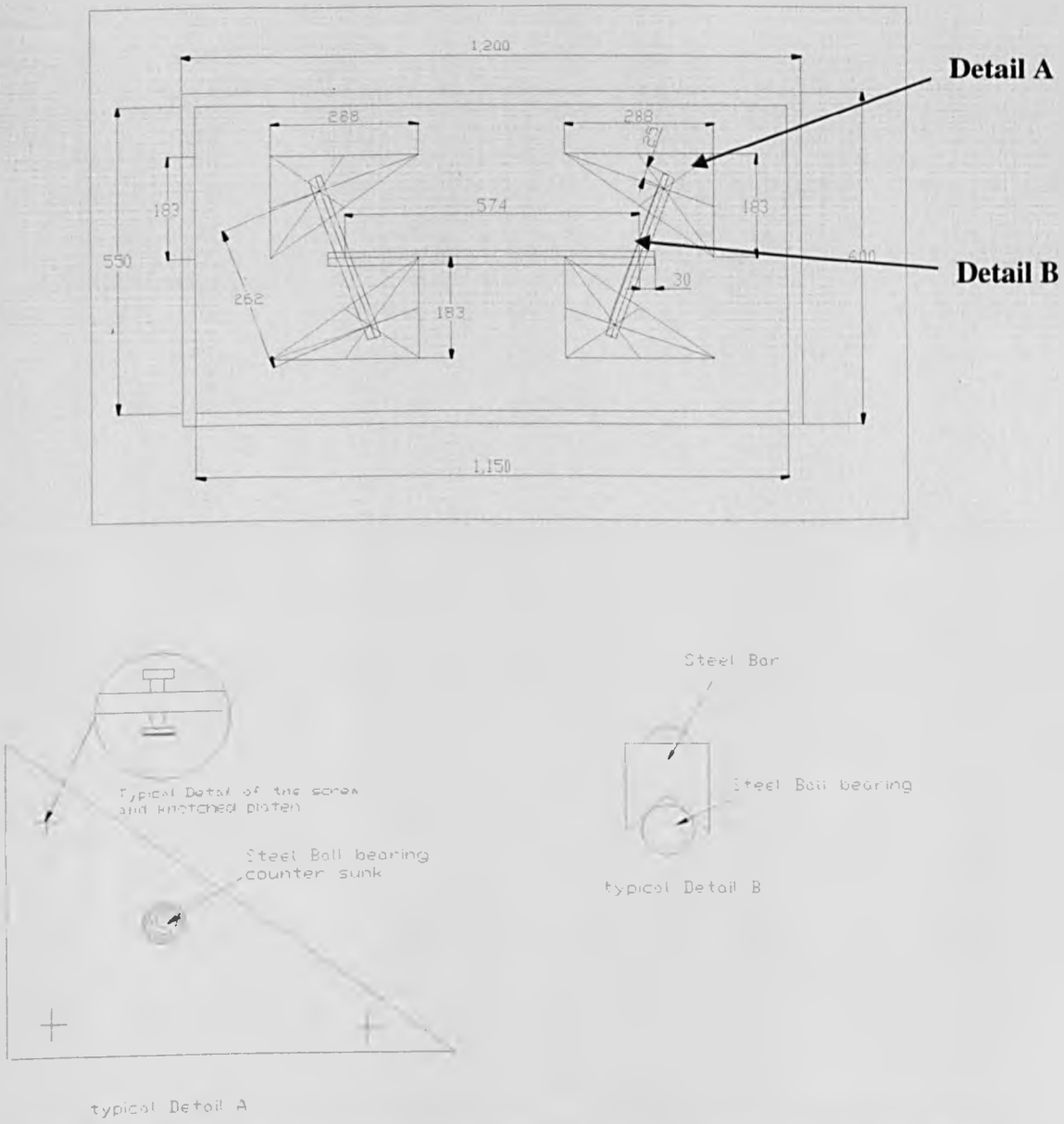

Figure 3.6: Typical detail of triangular platen and steel bars for rectangular slabs.

3.3.1 Supporting Frame

The supporting frame had round steel bars welded to its perimeter so that the slab could be placed on top of these bars. An early idea was to use plastic ties which were cast into the slab when the concrete was poured into the mould. However, the plastic ties proved to be ineffective, as they loosened and allowed corner lifting to occur. They were replaced by g-clamps, as can be seen in Figure 3.7, for better performance.

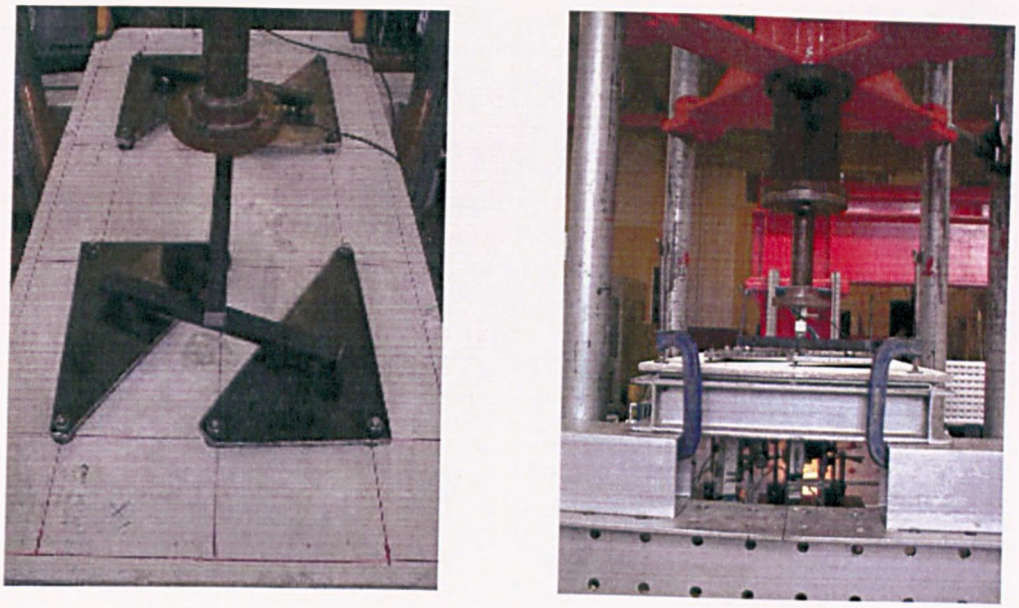

Figure 3.7: Loading system and supporting frame.

The main problem with this type of arrangement was the danger of instability of the frame, but this was overcome by steadying the frame in place until an initial load had been applied by the jack to the slab.

Instrumentation

The load was applied to the centroids of four equal right-angled triangles of steel plate and from there to the twelve load points on the slab. Transducers were placed at key points, in order to measure the out-of-plane displacement.

3.4 Experimental Procedure

The procedures for casting and testing of each slab were as follows:

1. The mould was cleaned then greased with oil and silicone so that the slab could be taken out easily when cast. The first set of wooden strips was screwed onto the mould surface, and the positions of the nails were then measured and marked (Figure 3.8).

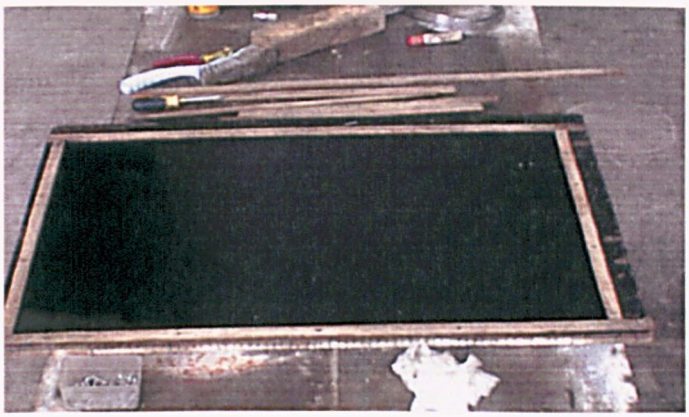

Figure 3.8: Preparation of mould.

2. The nails to which the wires would be tied were hammered into the positions marked on all sides of the mould. One end of each wire was tied to a nail, and the wire was then cleaned in order to decrease the possibility of de-bonding (Figure 3.9). It was then gently tensioned and tied around the opposite nail at its other end.

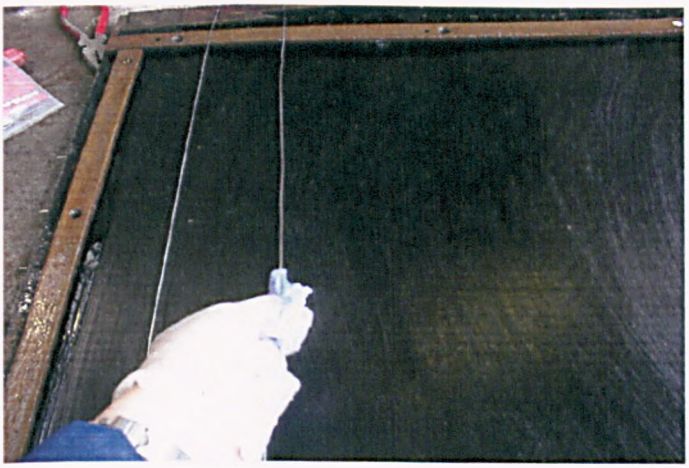

Figure 3.9: Degreasing the reinforcement.

3. The wires in the x-direction were placed first, followed by the y-direction, and wires were interwoven at three locations to stop separation of the mesh during casting (Figure 3.10).

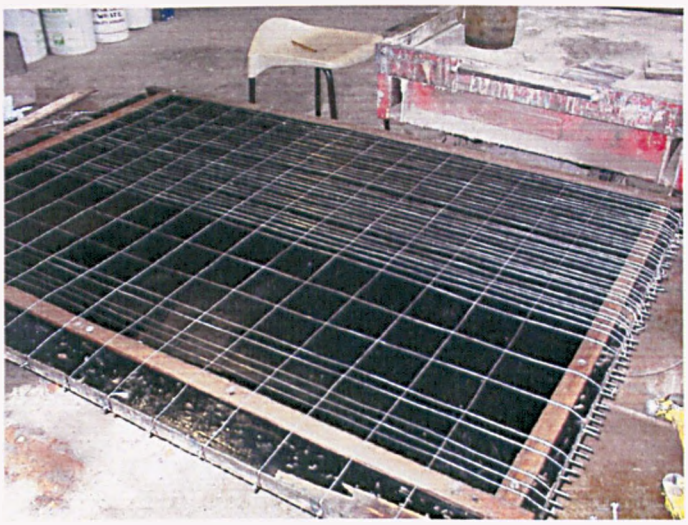

Figure 3.10: Placement of reinforcement wire within the mould.

4. The wire was then straightened by applying a small tension. The wooden strips forming the upper part of the edge of the slab were screwed onto the lower set of strips. The concrete was mixed and poured into the mould, and was then compacted on a vibrating table before being left to cure for several days (Figure 3.11). Six concrete cubes were also cast in order to establish the strength of the mix at different times.

5. The slabs were then tested after 28 days, once the "full" strength had been achieved.

(a)

(b)

Figure 3.11: (a) Casting the slab, and (b) Curing of the slab and cubes.

Problems with test procedure

As mentioned earlier, one of the main concerns in testing was the stability of the loading mechanism. The whole frame tended to move inwards and the triangular plates could slip from the pads on the slab. This actually happened in only two of the tests conducted, and these slabs did not reach the *span/10* (=55mm) displacement.

Another problem experienced was some variability in the load cell performance. In some of the experiments the load channel exhibited a scatter ("noise") which can be observed in some of the test results.

3.5 Outline of Work

Tests were conducted on two sizes of slabs whose nominal dimensions (in mm) were 1200×600×15 and 900×600×15, with the supported areas being 1150×550 and 850×550 respectively. Table 3.2 shows the testing schedule.

	Slab Size (Supported) (mm)	As*	Area of reinf in X direction (mm^2/m)	Area of reinf in Y direction (mm^2/m)	Coeff of orthotropy μ	Smooth/ Deformed rebar	Test Repeated
1	850x950	1.5	6.60	32.99	0.2	Smooth	
2	850x950	1.5	18.69	18.69	1	Smooth	✓
3	850x950	1.5	32.99	6.60	5	Smooth	
4	850x950	1.5	6.60	32.99	0.2	Deformed	
5	850x950	1.5	18.69	18.69	1	Deformed	
6	850x950	1.5	32.99	6.60	5	Deformed	
7	1150x550	2.0	6.60	32.99	0.2	Smooth	
8	1150x550	2.0	18.69	18.69	1	Smooth	✓
9	1150x550	2.0	32.99	6.60	5	Smooth	
10	1150x550	2.0	6.60	32.99	0.2	Deformed	
11	1150x550	2.0	18.69	18.69	1	Deformed	
12	1150x550	2.0	32.99	6.60	5	Deformed	✓

*As= Aspect Ratio

Table 3.2: Test Schedule.

The actual depth of the slab varied slightly between tests, and measurements were made after each test. The slabs were tested in a loading rig in which the load was applied at 12 points (Figure 3.12).

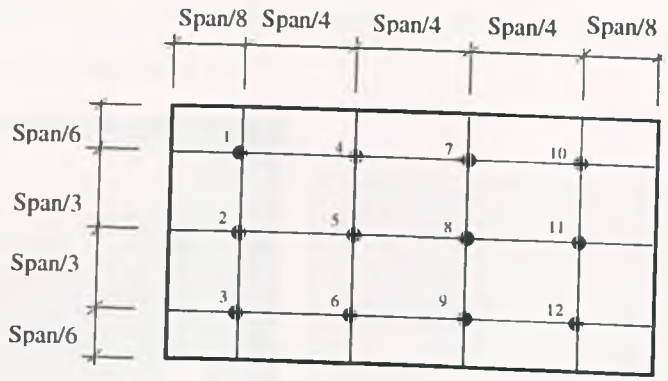

Figure 3.12: Loading positions.

The loading frame is shown in Figure 3.13. With the aid of ball-joints the applied load remained vertical as the slab deflected. The slab was placed on a supporting frame, which provided vertical support around its perimeter. The four corners of the slab were restrained from lifting by lightly clamping them to the supporting frame. No horizontal restraint was provided to the slab at the supported edges.

Figure 3.13: Slab and loading system in loading frame.

The total reinforcement percentage used in each slab was kept constant at 0.3%. The concrete mix used a gritty sand with fine aggregate particle sizes ranging between 1-4 mm, a cement-sand ratio of 1:3 and a water-cement ratio of 0.47, as previously discussed. The measured yield strength of the reinforcement and the compressive strengths of the concrete are shown in

Table 3.1 and Figure 3.8. The instrumentation consisted of a load cell and several displacement transducers (Figures 3.14).

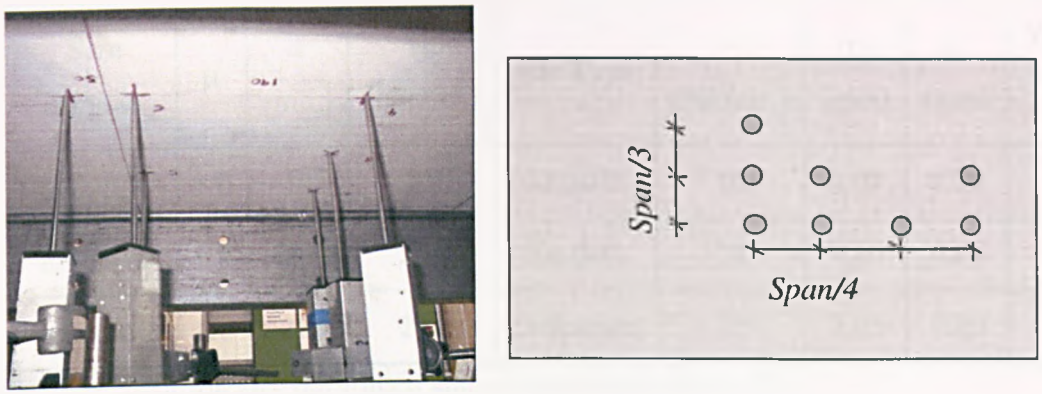

Figure 3.14: Location of displacement transducers.

3.6 Test Results

In total 15 tests were conducted on small-scale wire-reinforced slabs.

3.6.1 Isotropically Reinforced Slabs

Six tests were carried out on isotropically reinforced slabs, three at aspect ratio 2.09 and three at 1.55. For each aspect ratio, two of the tests used smooth reinforcement with the other test using deformed reinforcement. The properties of the six slabs with isotropic reinforcement are shown in Tables 3.3(a) and 3.3(b). The yield line capacity was calculated assuming that the 12-point loading system acted as a uniformly distributed load. The yield load calculated assuming distributed loading over -estimates the actual yield by 14.7% for the slabs of aspect ratio 2.05 and by 11% for slabs of aspect ratio 1.55 (see Appendix A for calculations).

Isotropically Reinforced Slabs (Spacing in long span 20mm, spacing in short span 20mm). **Aspect Ratio = 2.09**

Test	Size (mm)	μ	t (mm)	fy (N/mm^2)	Bar Type	fc (N/mm^2)	dx (mm)	dy (mm)	Yield-line capacity (kN/m^2).
2	1150×550	1.0	20	265	Smooth	28	9.65	9.29	2.25
5	1150×550	1.0	18	258	Smooth	38	8.65	8.29	1.97
16	1150×550	1.0	15	240	Deformed	34	7.15	6.79	1.54

Table 3.3(a): Isotropically reinforced slabs with aspect ratio 2.09.

Isotropically Reinforced Slabs. (Spacing in long span 20mm, spacing in short span 20mm) **Aspect Ratio = 1.55**									
Test	Size (mm)	μ	t (mm)	fy (N/mm^2)	Bar Type	fc (N/mm^2)	dx (mm)	dy (mm)	Yield-line capacity (kN/m^2).
4	850×550	1.0	14	265	Smooth	16	6.65	6.29	1.81
10	850×550	1.0	19.5	256	Smooth	28	9.40	9.04	2.54
15	850×550	1.0	16	248	Deformed	25	7.65	7.29	1.99

Table 3.3(b): Isotropically reinforced slabs with aspect ratio 1.55.

Observation of Slab Behaviour

In these tests it was seen that the slabs achieved ultimate loads greater than those predicted by yield line theory. In all tests carried out, flexural cracking was observed first, with the highest cracking loads occurring on the slabs of aspect ratio 1.55 and reinforced with deformed wire. The cracks were widest near the mid-span for the uniformly reinforced slabs reinforced with deformed wire, whilst for the slabs reinforced with smooth wire, the slabs had remained intact.

Tests 2, 5 and 16

In the first set of tests (Tests 2 and 5), of aspect ratio 2.09 and isotropically reinforced with smooth wire, the slabs showed initial cracking parallel to the longer sides near the centre of the slab (Figure 3.15).

Figure 3.15: Initial cracking of rectangular slab under increasing load.

Under increased load, the cracks extended towards the corners (Figure 3.16) of the slab. When the cracks had formed the typical yield pattern, a marked reduction in the total load was observed.

Figure 3.16: Formation of diagonal cracks with increasing load.

An additional crack formed later into the test across the central region of the underside of the slab parallel to the short span direction, as shown in Figure 3.17.

Figure 3.17: Formation of transverse crack.

The photographs in Figures 3.18 and 3.19 show the top and bottom slab faces of Tests 5 and 16. These were tested with a uniform load (UDL) over the slab surface. Figure 3.18 shows Test 5, a rectangular slab reinforced isotropically with smooth wire. The edges were supported at the corners to prevent vertical movement but offered minimal resistance to rotation ('simply supported edges').

Test 5: Plan view of top face.

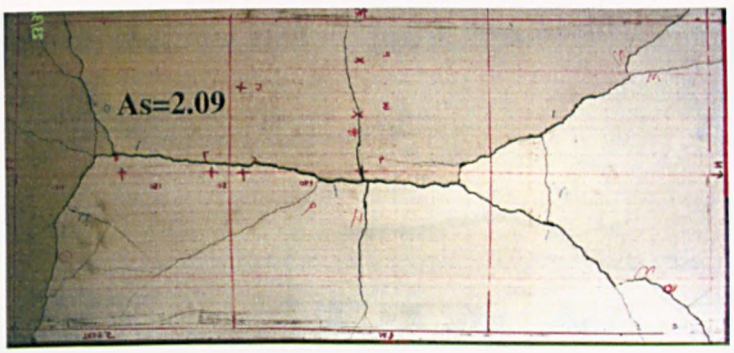

Test 5: Plan view of bottom face.

Figure 3.18: Test on a rectangular slab reinforced with isotropic smooth wire.

On the tension side of the slab (the bottom face in Figure 3.18) the cracks have developed in the typical yield line pattern; these cracks formed at relatively low loads. On the compression face of the slab, the concrete had wedged where the cracks had opened up on the tension face. There are also cracks on the compression face across the corners of the slab due to vertical restraint by the clamps.

The photographs of Test 16 in Figure 3.19 show the aftermath of a test on a slab reinforced with deformed wire. The cracks have opened up wider because of fracturing of the reinforcement across the longitudinal crack. This test was stopped when the slab had reached a deflection of *span/8* as run-away failure had started. On comparing the slab in Figure 3.19 with that in Figure 3.18, it can clearly be seen that the slab reinforced with smooth wire remained intact, whereas the slab reinforced with deformed wire essentially formed complete fractures along its yield lines.

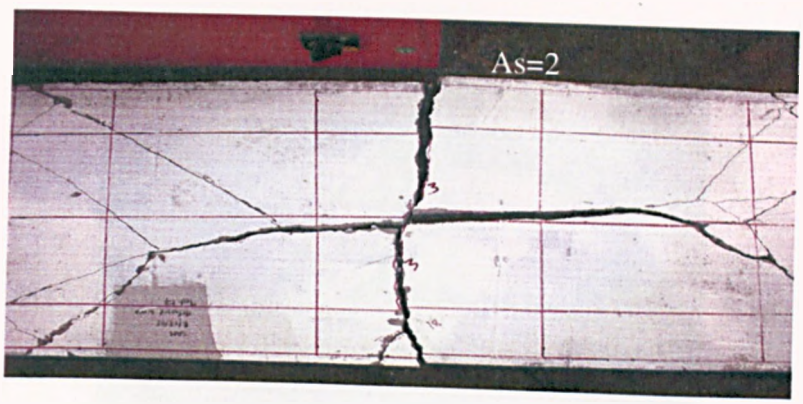

Test 16: Plan view of top face.

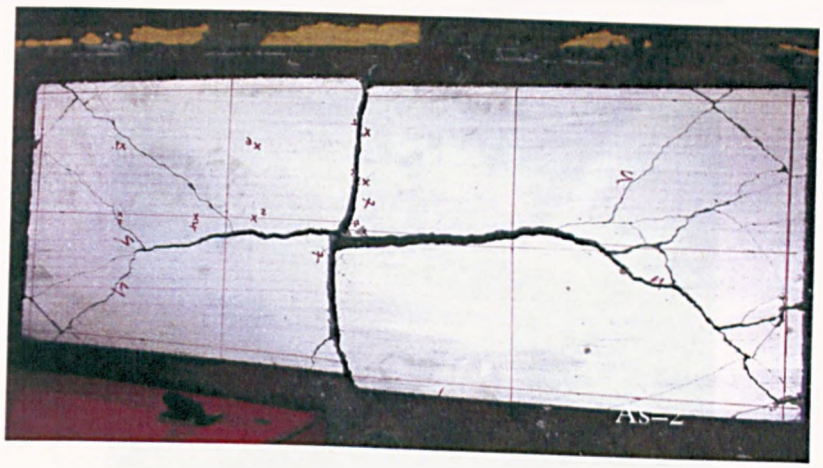

Test 16: Plan view of bottom face.

Figure 3.19: Test on a rectangular slab reinforced with isotropic deformed wire.

In both Tests 5 and 16, the slab initially started to crack in the longitudinal direction, as a one-way spanning slab would behave. As the deflections increased and the geometry changed, diagonal cracks began to form as the slab folded. The development of the short span transverse crack occurred after the yield lines had fully developed. The slab failure was dominated by fracture of the reinforcement across the transverse crack. The development of the transverse crack and the influence of the type of reinforcement can be seen clearly in Figures 3.20 and 3.21.

Figure 3.20: Transverse crack in Test 16.

Figure 3.21: Transverse crack in Test 5.

Figures 3.22 and 3.23 shows the experimental results of Tests 2 and 5. Test 5 was terminated at a deflection of *span/15* due to the instability of the loading rig. A peak load of 4.5kN/m^2 was attained, which was more than double the yield line prediction. Both sets of results show similarities, in that there are two definite peaks at relatively small displacements, which correspond to the noted time of appearance of the yield lines and the transverse crack. The yield line patterns quickly formed as the load rapidly increased. This was followed by a sharp decline, then another sharp rise in the load corresponding to the formation of the transverse tension crack across the short span of the slab.

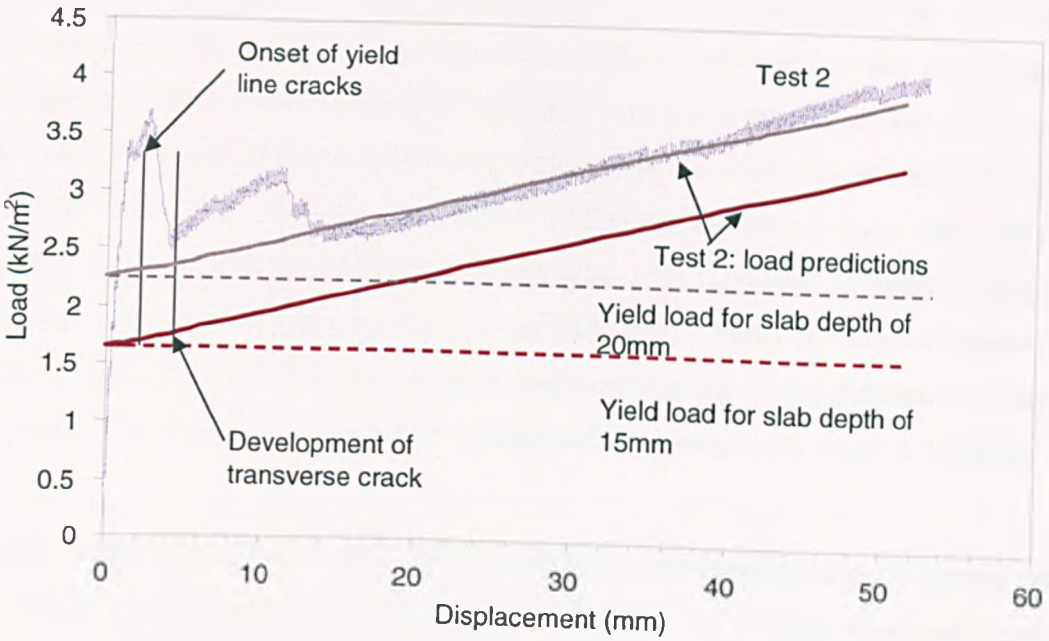

Figure 3.22: Load-deflection curves for Test 2 with theoretical predictions.

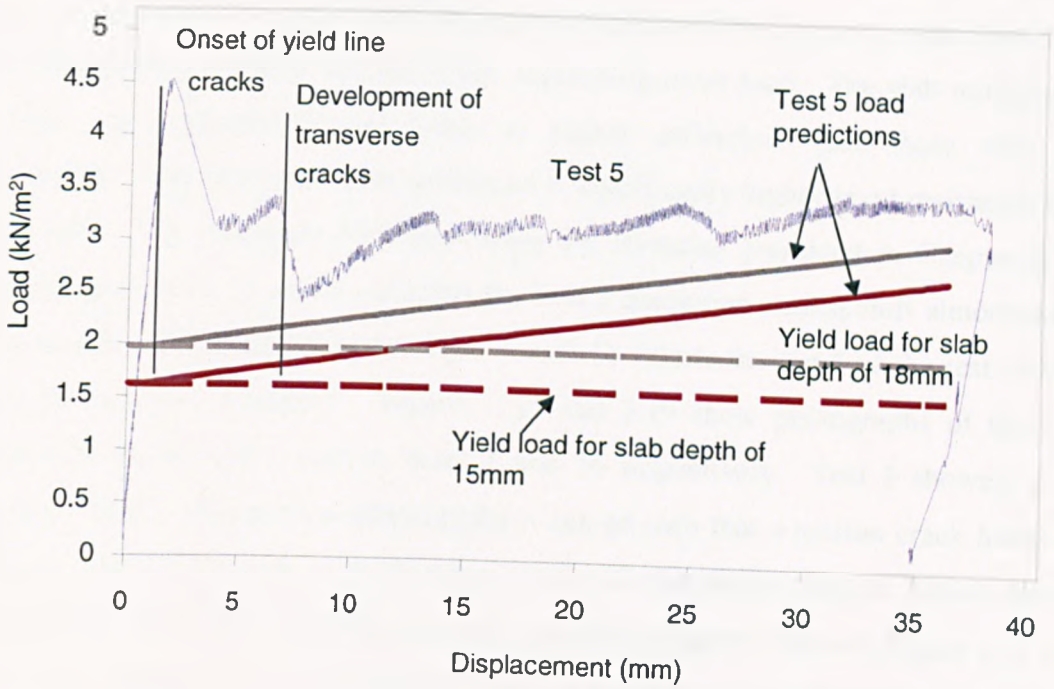

Figure 3.23: Load-deflection curves for Test 5 with theoretical predictions.

The thickness of the slab was initially estimated at 15mm as this was the depth of the concrete casting mould. At the end of each test, several measurements were taken along the yield lines of the actual depth of the slab. When the actual depth of the slab was entered into the theoretical model, the theoretical prediction was brought closer to the experimental. The experimental and theoretical calculations also tend to converge as deflections increase.

Comparisons can be made between Tests 16 and 5, remembering that the only difference between these two tests is the surface condition (plain or deformed) of the wire. Figure 3.24 shows comparisons between Tests 2, 5 and 16. Test 5 is a replica of Test 2; the concrete strength being the only difference between these two tests. The concrete strength for Test 2 was 28.30N/mm^2; the concrete mix had a higher water-cement ratio than adopted for subsequent tests, resulting in much lower strength. The concrete strength for Test 5 was measured at 38.20N/mm^2 and for Test 16 at 34N/mm^2. From the load-deflection plot in Figures 3.22 and 3.23 the difference in peak loads corresponds to the difference in strength of the concrete; Test 5 had a peak load of 4.5kN/mm^2 compared with about 3.7kN/mm^2 in Test 2.

The load-displacement responses of Tests 2, 5 and 16, representing slabs of aspect ratio 2.09 with isotropic reinforcement, are shown again in Figure 3.24, in which the load is normalised with respect to the yield line capacity of the individual slabs, which was calculated using material properties and dimensions measured on the day of the test. The main difference between Tests 2 and 5 is due to the measured strength of the concrete, with Test 5 having higher compressive strength and therefore, supporting more load. The slab reinforced with deformed wire supported greater loads at higher deflections than those with smooth reinforcement. The deformed wire developed a significantly higher bond resistance than the smooth wire. The predicted behaviour using the formulae presented in Chapter 2 is also shown in Figure 3.24. It can be seen that the Test 2 prediction corresponds almost exactly to the test results. The predictions for Tests 5 and 16 follow the trend of the test results and provide conservative estimates. Figures 3.18 and 3.19 show photographs of the top and bottom faces of the slabs used in Tests 5 and 16 respectively. Test 2 showed a similar response to Test 5. From these photographs it can be seen that a tension crack forms across the shorter span of the slab, corresponding well with the theory used to derive the Simple Design Method. It is also of interest to note, comparing Figure 3.20 with Figure 3.21 that the slab remained integral in Test 5 whereas in Test 16 it had to be 'pieced' together after the test, due to fracture of the deformed reinforcing wires along the full-depth tension cracks.

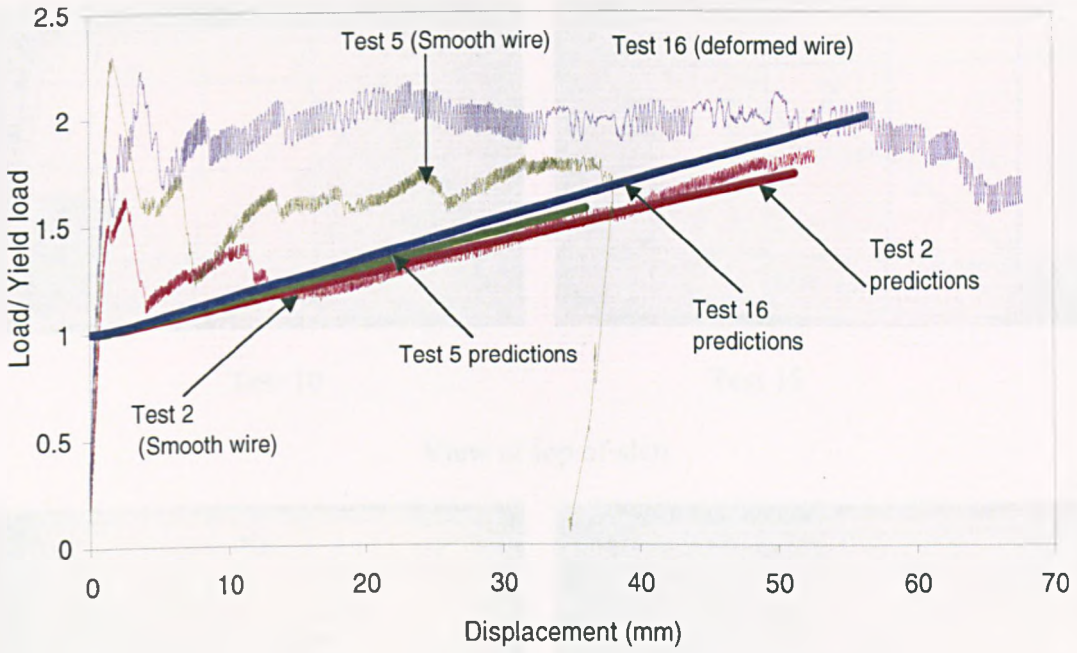

Figure 3.24: Comparison of enhancement factors for Tests 2, 5 and 16 with Simple Design Method.

The higher enhancements for Test 16 are indicative of the better bond between the concrete and reinforcement which is developed using the deformed wire. Test 16 also shows that there is little, if any, deflection induced enhancement and a plateau is maintained. This may be due to progressive fracture of the reinforcement across the yield line crack, causing the enhancements to decrease.

Tests 4, 10 and 15

These slabs had dimensions of 900x600mm with a supported area of 850x550mm. Tests 4 and 10 were reinforced with smooth wire and Test 15 with deformed wire. Figure 3.25 shows photographs of the top and bottom surfaces of the slabs used in Tests 10 and 15 respectively.

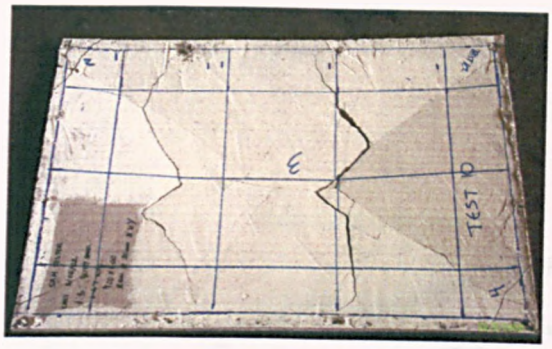

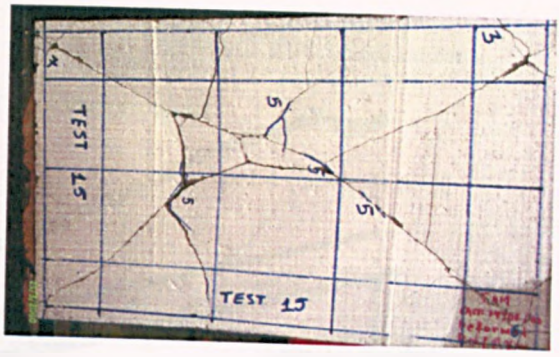

Test 10 Test 15

View of top of slab

Test 10 Test 15

View of bottom of slab

Figure 3.25: View of slabs in Test 10 and 15.

In both tests, the transverse tension cracks formed at the intersections of the diagonals and not in the central zone of the slab, as in the case of the 1200x600mm slabs. Figure 3.26 shows the load-deflection plots for Tests 4, 10 and 15. Tests 10 and 4 were identical apart from the concrete strength, Test 4 being lower than for Test 10 (Table 3.3). The slabs reinforced with smooth wire behaved very differently from those reinforced with deformed wire in previous tests. In these tests, the smooth wire gave higher load capacity than the deformed wire, and this could be related to the concrete strengths of the slabs. It can be seen from Table 3.3 that Test 10 had a higher concrete strength than Tests 15 and 4.

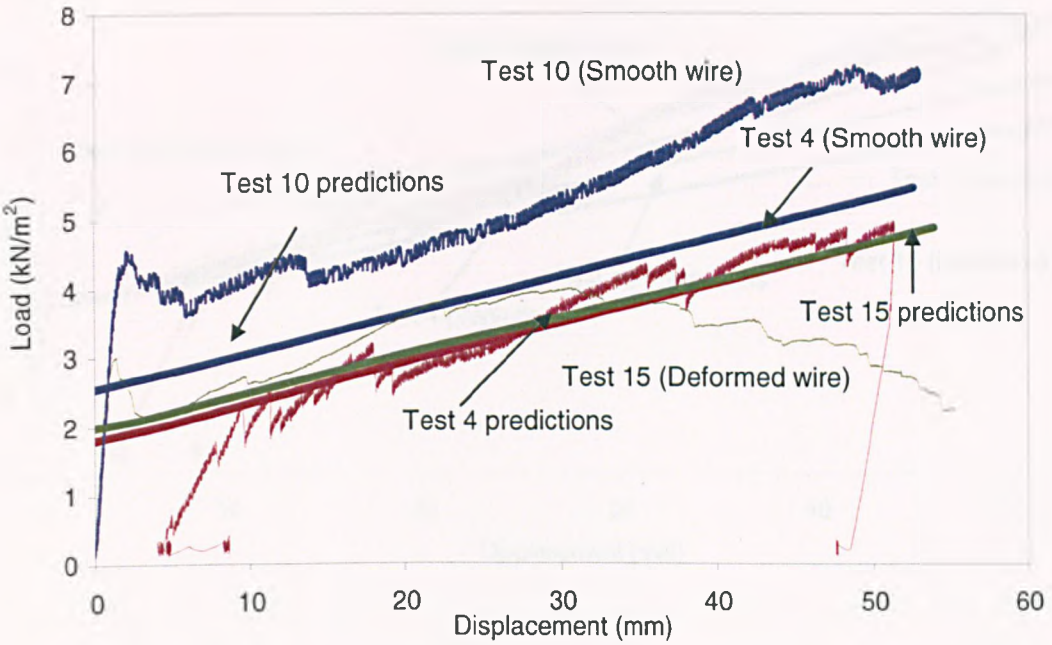

Figure 3.26: Comparison of load Displacement plots for Tests 4, 10 and 15.

Figure 3.27 shows the load displacement responses for Tests 4, 10 and 15, together with the predictions using the Simple Design Method. It can be seen that the predictions correlate very well with the test results for Tests 4 and 10, which have smooth reinforcement. For Test 15 the prediction is very good up to a vertical displacement of 30mm, beyond which the actual load carrying capacity decreased, whereas the predicted load increased. It was observed at a deflection of 30mm that the reinforcement had started to fracture, so it is possible that the decrease in load capacity was caused by fracture of the reinforcement. For the slab in Test 10, no fracture of the reinforcement in the transverse crack was noted, and the Test was terminated at a deflection of *span/10*. At the end of the test, the slab was integral when removed from the loading rig; the transverse cracks had opened out but the central longitudinal crack had not fully opened and the two regions of the slab either side had jammed.

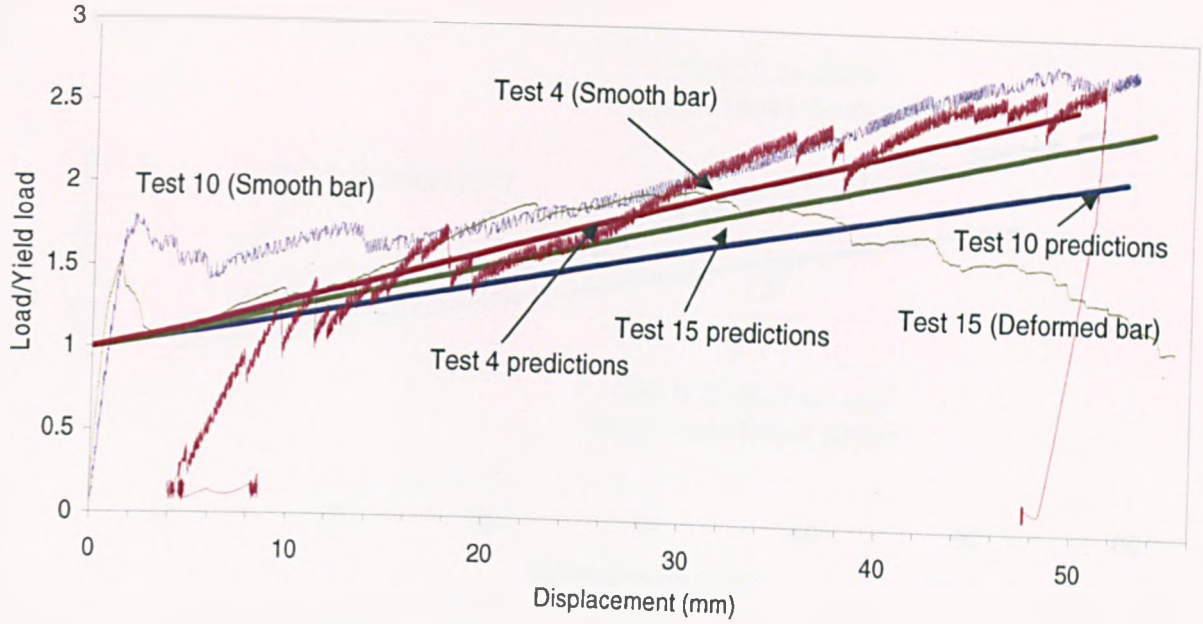

Figure 3.27: Comparison of enhancement factors for Tests 4, 10 and 15

Figure 3.26 shows photographs of the top and bottom surfaces of the slabs used in Tests 10 and 15 respectively. It was observed during the tests that the flexural cracks developed differently in these tests from those in the 1200x600mm slabs, forming diagonally across the slab (Figures 3.28). In Test 10, two tension cracks occurred across the shorter span at the intersections of the yield lines. The in-plane membrane forces can be predicted based on this mode of deformation, but the estimated membrane forces are higher in this case than those estimated on the basis of a single tension crack occurring across the shorter span at the centre of the slab (Figure 3.29).

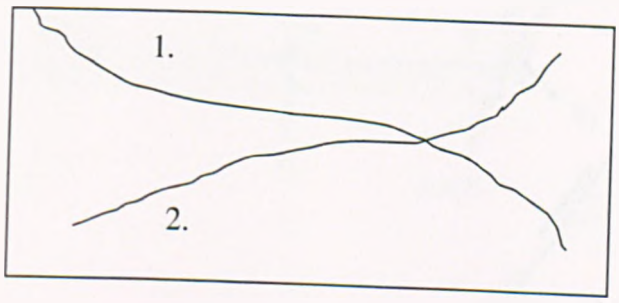

Figure 3.28: Development of cracks for slabs of aspect ratio 1.55

The cracks developed in the same order as for the 1200x600mm slabs. Figures 3.30 and 3.31 highlight the development of cracks over the duration of the tests. Once again, in the early stages the diagonal yield lines form as the flexural capacity of the slab is reached, followed later by development of the transverse crack.

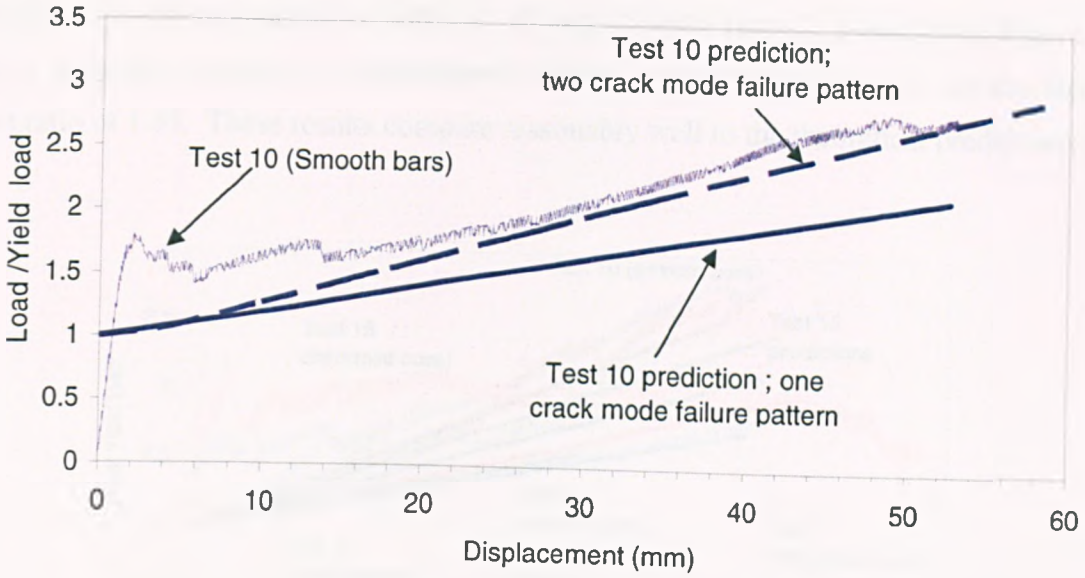

Figure 3.29: Comparison between predicted load displacement responses for two failure modes for the slab in Test 10

The revised formulation is based on an in plane stress distribution for the development of two cracks at the intersections of the yield lines, as shown in Figure 3.30.

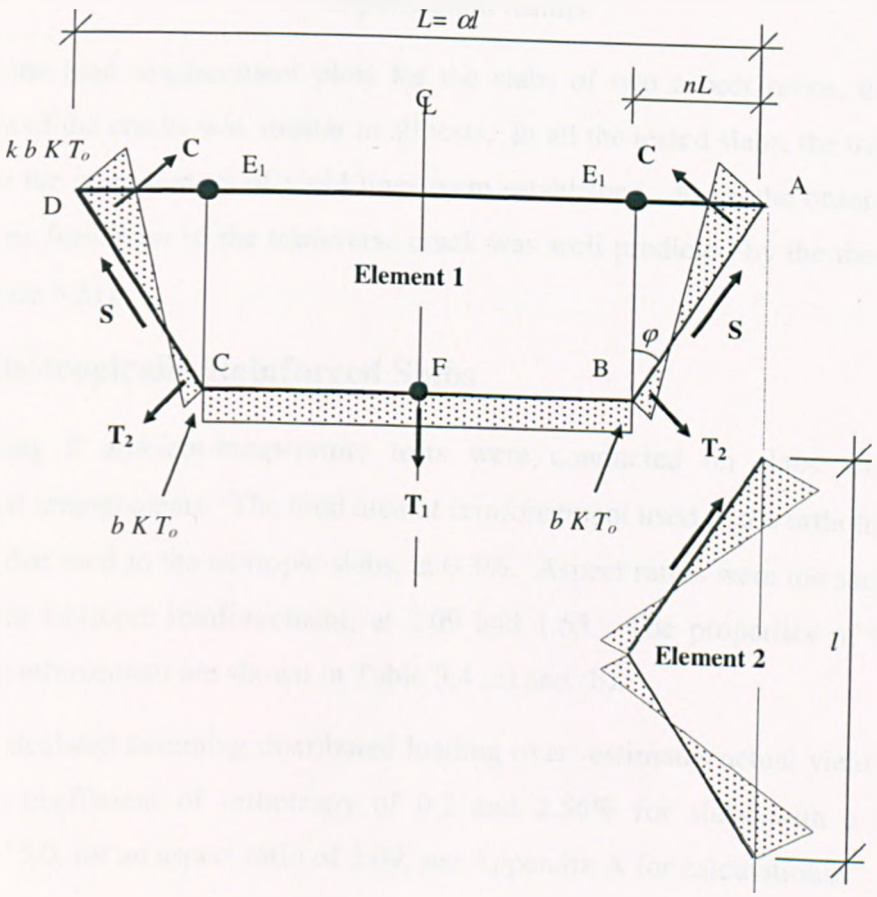

Figure 3.30: In plane stress distribution for development of two transverse cracks

Comparing the enhancements for Tests 4, 10 and 15 with Tests 2, 5 and 16 in Figure 3.31 there is a definite increase in enhancement factors at high displacements for the slabs of aspect ratio of 1.55. These results compare reasonably well to the theoretical predictions.

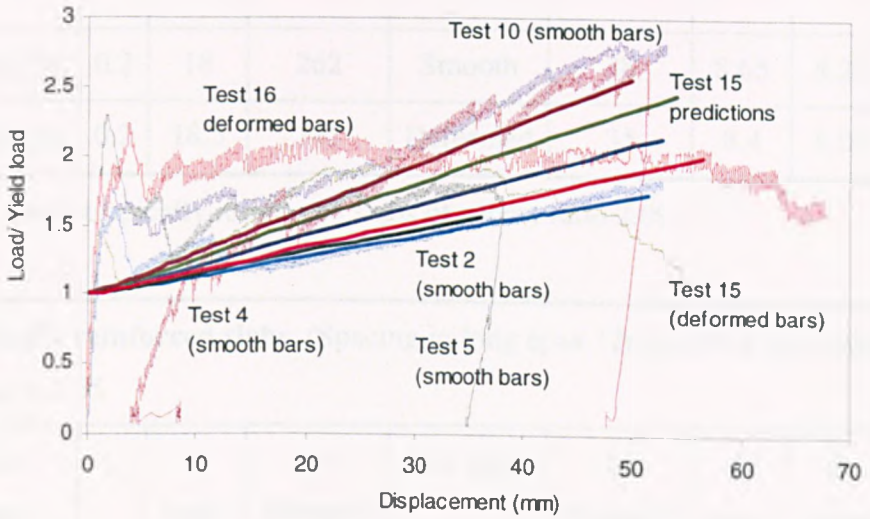

Figure 3.31: Comparison of enhancement factors for Tests 2, 4, 5, 10 and 15 with experimental results.

Comparing the load displacement plots for the slabs of two aspect ratios, the sequence of development of the cracks was similar in all tests. In all the tested slabs, the transverse cracks formed after the main pattern of yield lines were established. From the observations of slab behaviour, the formation of the transverse crack was well predicted by the theoretical failure criteria (Figure 3.31).

3.6.2 Orthotropically Reinforced Slabs

The remaining 9 ambient-temperature tests were conducted on slabs with orthotropic reinforcement arrangements. The total area of reinforcement used in the orthotropic slabs was the same as that used in the isotropic slabs, at 0.3%. Aspect ratios were the same as those for the slabs with isotropic reinforcement, at 2.09 and 1.55. The properties of the slabs with orthotropic reinforcement are shown in Table 3.4 (a) and (b).

Yield load calculated assuming distributed loading over -estimates actual yield by 0.26% for slabs with a coefficient of orthotropy of 0.2 and 2.56% for slabs with a coefficient of orthotropy of 5.0, for an aspect ratio of 2.09; see Appendix A for calculations.

Orthotropically reinforced slabs. (Spacing in long span 12mm, short span 60mm) Aspect Ratio = 2.09									
Test	Size (mm)	μ	t (mm)	fy (N/mm^2)	Bar Type	fc (N/mm^2)	dx (mm)	dy (mm)	Yield-line capacity (kN/m^2).
6	1150x550	0.2	18	262	Smooth	38	8.65	8.29	1.23
8	1150x550	0.2	18.5	242	Deformed	35	8.4	8.04	1.10

Table 3.4(a): Orthotropically reinforced slabs of aspect ratio 2.09.

Orthotropically reinforced slabs. (Spacing in long span 12mm, short span 60mm) Aspect Ratio = 1.55									
Test	Size (mm)	μ	t (mm)	fy (N/mm^2)	Bar Type	fc (N/mm^2)	dx (mm)	dy (mm)	Yield-line capacity (kN/m^2).
11	850x550	0.2	14	260	Smooth	36	6.65	6.29	1.31
14	850x550	0.2	15	255	Deformed	41	7.15	6.79	1.39

Table 3.4(b): Orthotropically reinforced slabs of aspect ratio 1.55.

The reinforcement ratio μ defined as ratio of the area per unit width in the shorter span to that in the longer span, is a measure of the degree of orthotropy of each slab. Four of the tests had greater reinforcement in the longer span (μ=0.2), with five having greater reinforcement in the shorter span (μ=5).

Tests 6 and 8

These 1200x600mm slabs had a coefficient of orthotropy of 0.2. In Test 6, the slab was reinforced with smooth wire and the load displacement of this slab is shown in Figure 3.32. The peaks in the load displacement plot correspond well to the observed development of cracks.

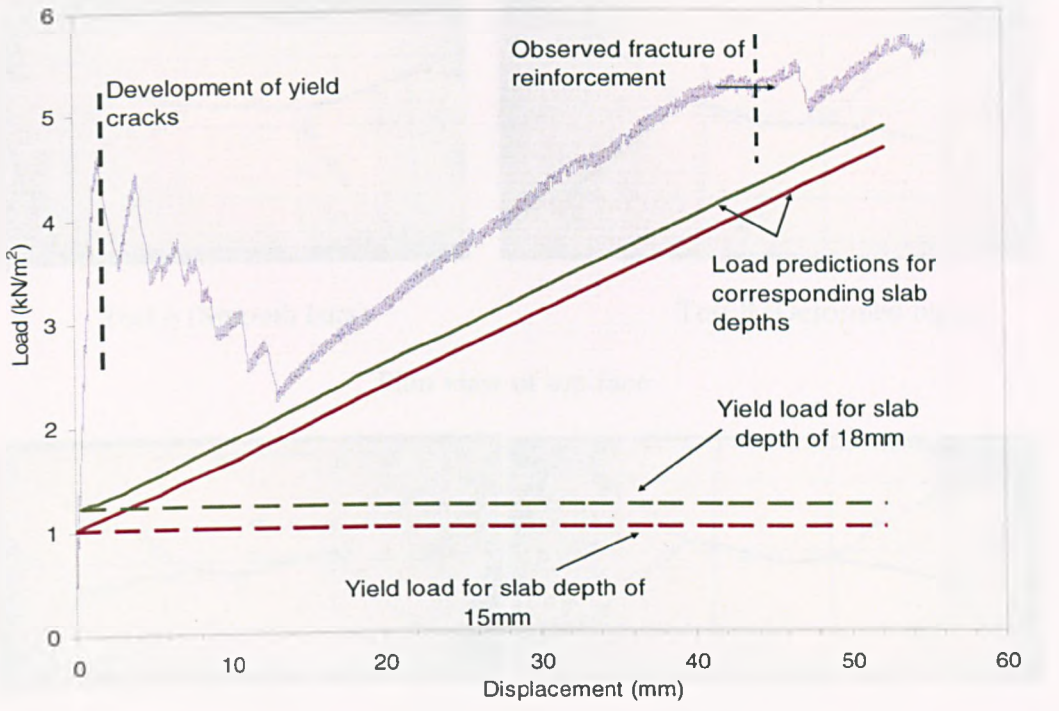

(a)

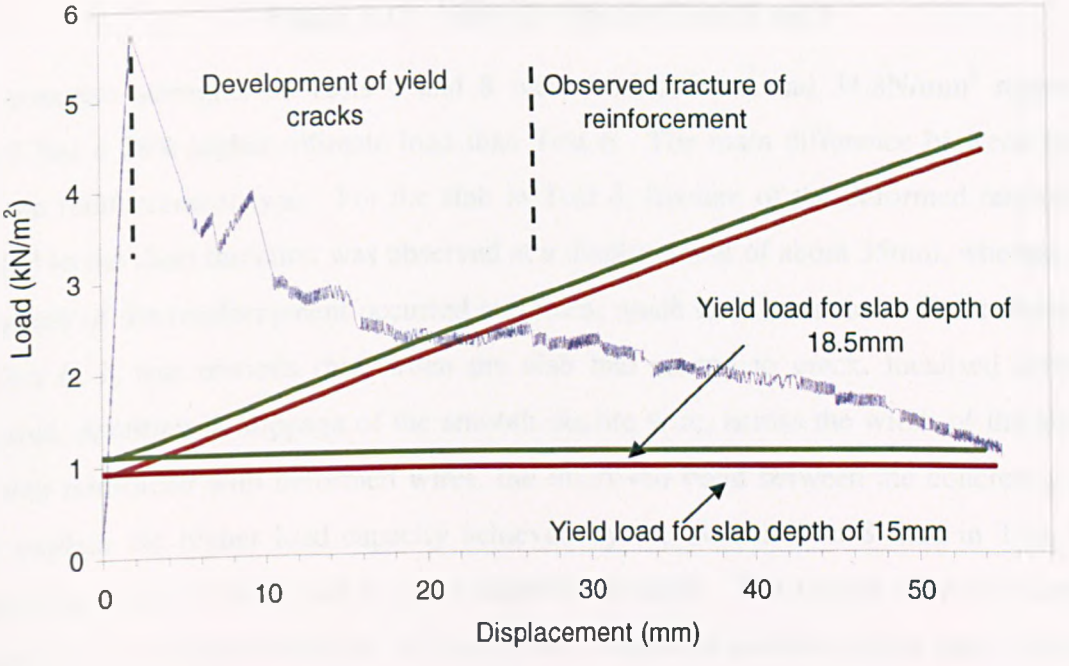

(b)

Figure 3.32: Load-displacement plots for (a) Test 6 and (b) Test 8.

In the isotropic set of tests, the formation of the transverse crack was clear, but in Tests 6 and 8, this did not form across the short span of the slab. The photographs in Figure 3.33 display the slabs at the end of the tests, and the absence of the transverse crack can clearly be seen.

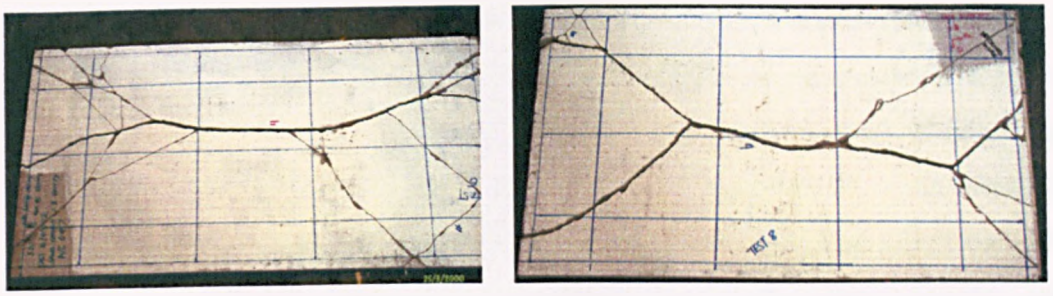

Test 6 (Smooth bars) Test 8 (Deformed bars)

Plan view of top face

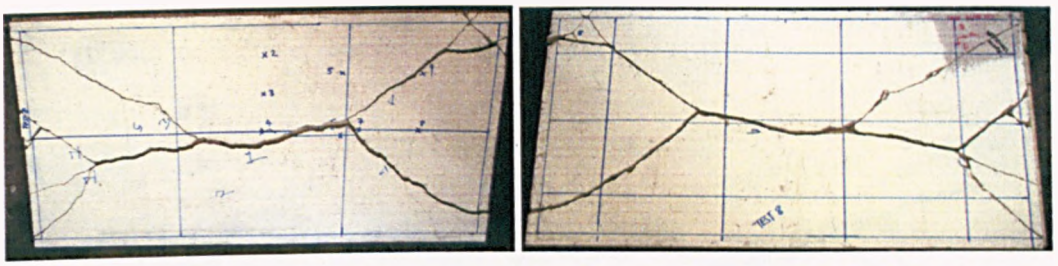

Test 6 Test 8

Plan view of bottom face

Figure 3.33: View of slabs for Tests 6 and 8

The concrete strengths in Tests 6 and 8 were 38.20N/mm^2 and 34.8N/mm^2 respectively. Test 8 had a 28% higher ultimate load than Test 6. The main difference between the slabs was the reinforcement type. For the slab in Test 8, fracture of the deformed reinforcement parallel to the short direction was observed at a displacement of about 35mm, whereas in Test 6 fracture of the reinforcement occurred at 47mm, much later in the test. From observations of Test 6, it was obvious that, when the slab had started to crack, localised de-bonding occurred, resulting in slippage of the smooth ductile wire, across the width of the slab. For the slab reinforced with deformed wires, the improved bond between the concrete and wire may explain the higher load capacity achieved by the slab in Test 8 than in Test 6, even though the slab in Test 8 had a lower concrete strength. The results from the Cambridge model tests on bond behaviour of short-span reinforced concrete slabs have shown that smooth ductile reinforcement will produce lower than expected ultimate loads [47]. These results correlate well with the test results, and seem to indicate that the structure needs to be ductile to allow the membrane mechanism to develop.

The load displacement responses of Tests 6 and 8, for which the aspect ratio was 2.09 and μ=0.2, are shown in Figure 3.34 together with predictions using the Simple Design Method.

It can be seen that for the slab with smooth wire (Test 6) the prediction, albeit as a lower-bound, follows the trend of the test. However, for Test 8 the test result shows a progressive decrease of load with increase of deflection, whereas the analysis predicts an ever-increasing load capacity. After a displacement of 20mm, the test load-carrying capacity was unconservative. Observations from the test showed that the deformed wires had fractured across the cracks in the slab, resulting in a reduction of load-carrying capacity whereas, because of their lower bond and greater ductility, the smooth wires did not fracture.

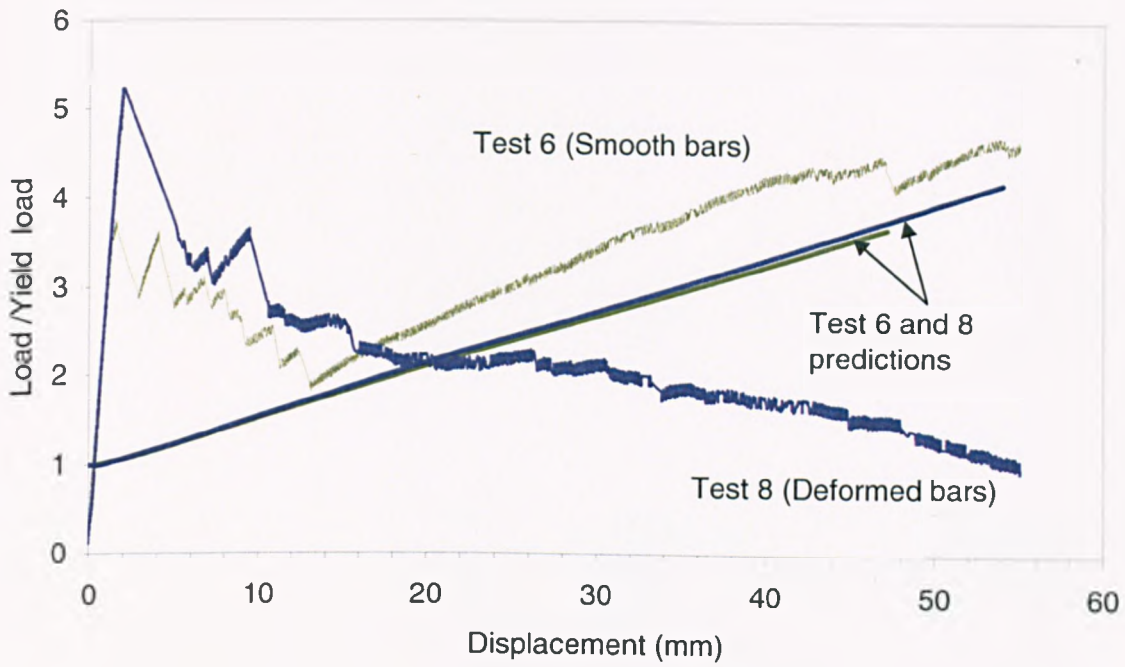

Figure 3.34: Comparison between the slab behaviour for smooth and deformed wire

It can be seen that no tension cracking occurred across the shorter span (Figure 3.33) due to the greater area of reinforcement placed in the longer span.

Tests 11 and 14

These 850x550mm slabs of Tests 11 and 14 were reinforced respectively with smooth and deformed wire and had a coefficient of orthotropy of 0.2. Figure 3.35 shows the slabs after the tests. In all tests of this orthotropic nature, the tension crack across the short span did not develop (Figure 3.35). The development of the cracks differed for the two different aspect ratios, in that the smaller aspect-ratio slabs developed diagonal cracks first, whereas for the higher aspect ratio the longitudinal crack developed first followed by the formation of the diagonal cracks.

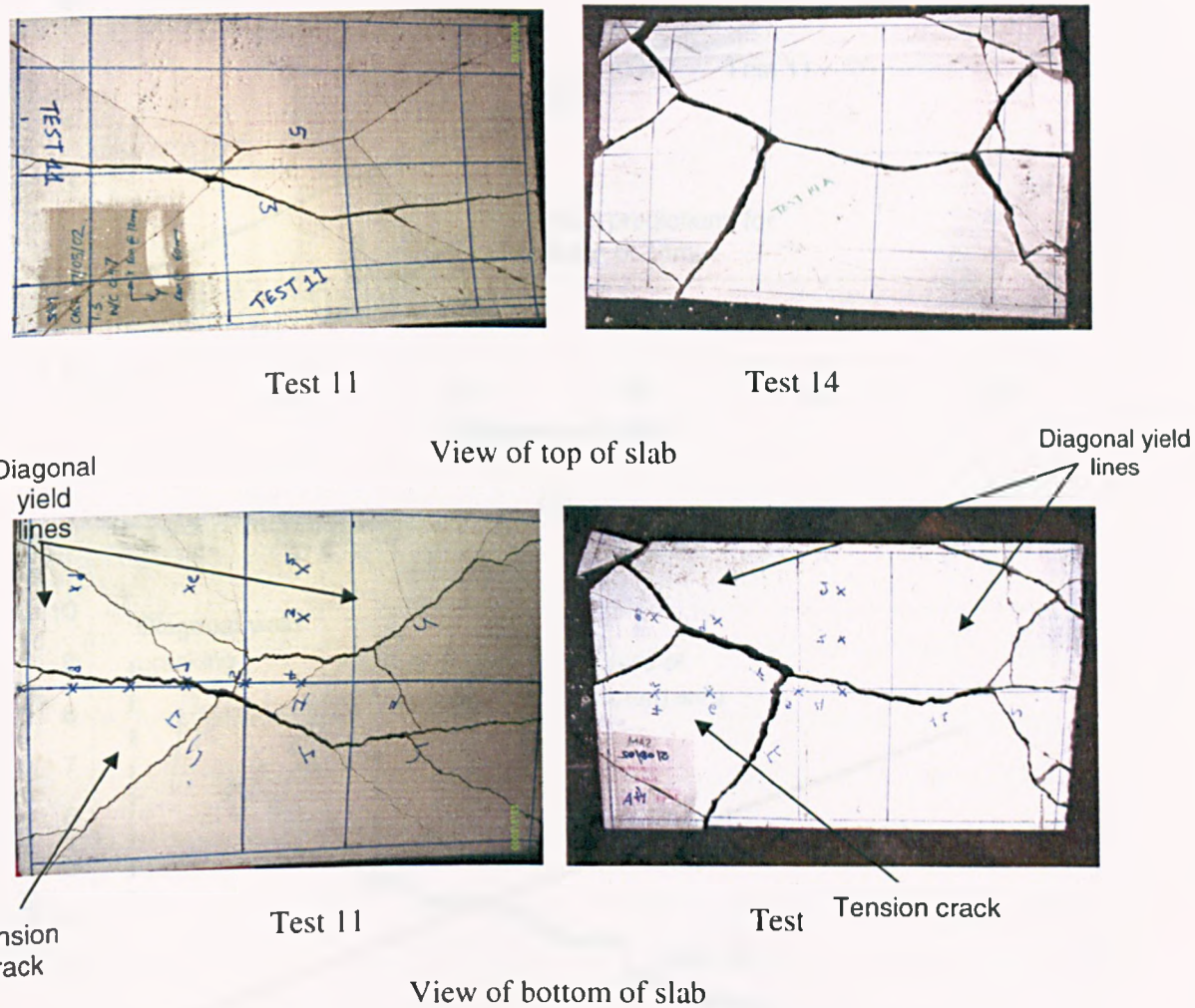

Figure 3.35: View of Test 11 and Test 14 slabs surface.

There was no observed fracture of the reinforcement in Test 11 (smooth wire), whilst in Test 14 reinforcement fracture was observed at a deflection of 29mm (Figure 3.36). Test 14 achieved an ultimate load of 9kN/m^2 whilst in Test 11 the slab achieved only 5kN/m^2. The concrete strength in Test 14 was 41.4N/mm^2 compared to that of Test 11, 36.2N/mm^2. The increased concrete and bond strengths may explain the increased ultimate load for the slab

(Figure 3.36). The deformed wire clearly increased the flexural performance of the slab at relatively low deflections, but at the onset of full depth cracking, the decreases in load with increasing deflection are probably due to fracture of the deformed wire. This would occur quickly, since the increased bond strength would strain the reinforcement over a smaller de-bonded gauge length.

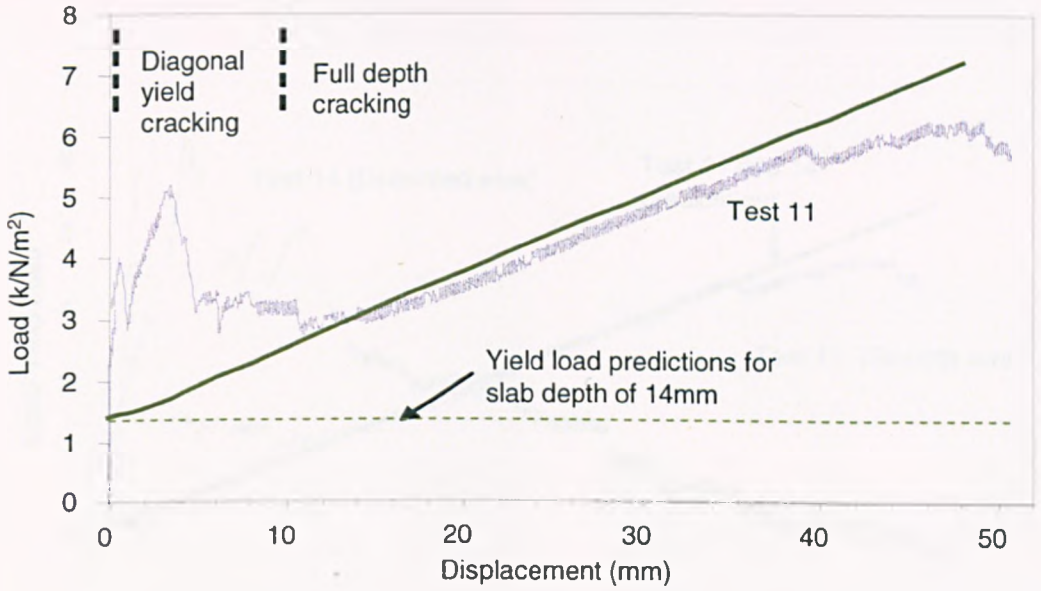

(a)

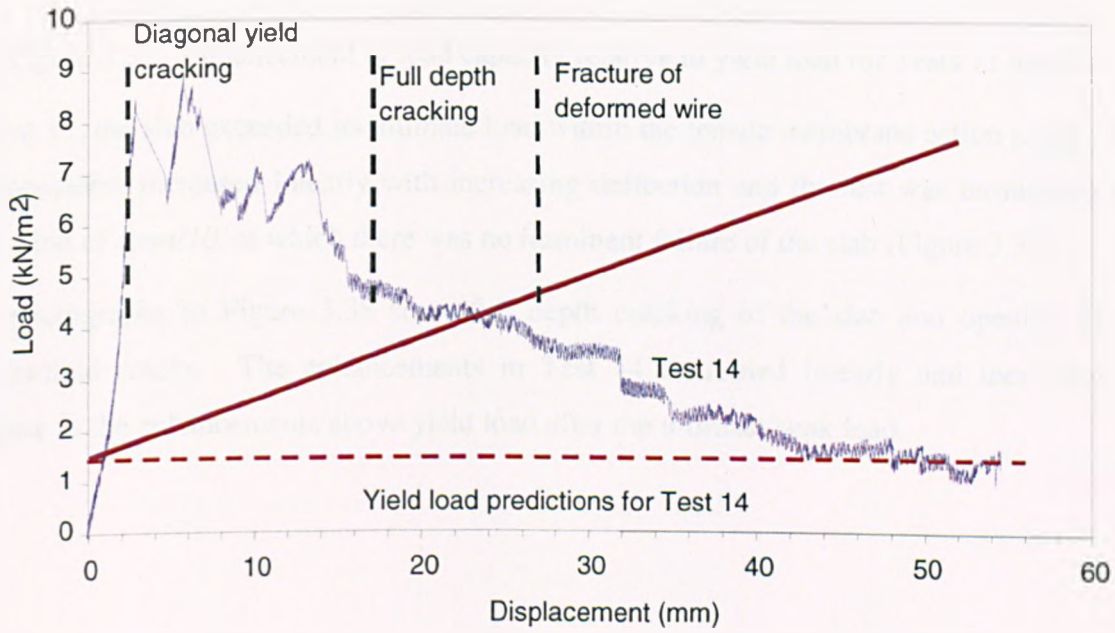

(b)

Figure 3.36: Load deflection plots for (a) Test 11, and (b) Test 14

Figure 3.37 shows the enhancement-displacement responses of Tests 11 and 14, for which the aspect ratio was 1.55 and μ=0.2, together with predictions for the tests. Test 11, with smooth wires, correlates well with the theoretical response. However Test 14, with deformed wires, did not compare well with the predicted response, and beyond a vertical displacement of 16mm the test results indicate that the theoretical enhancement-displacement response is unconservative.

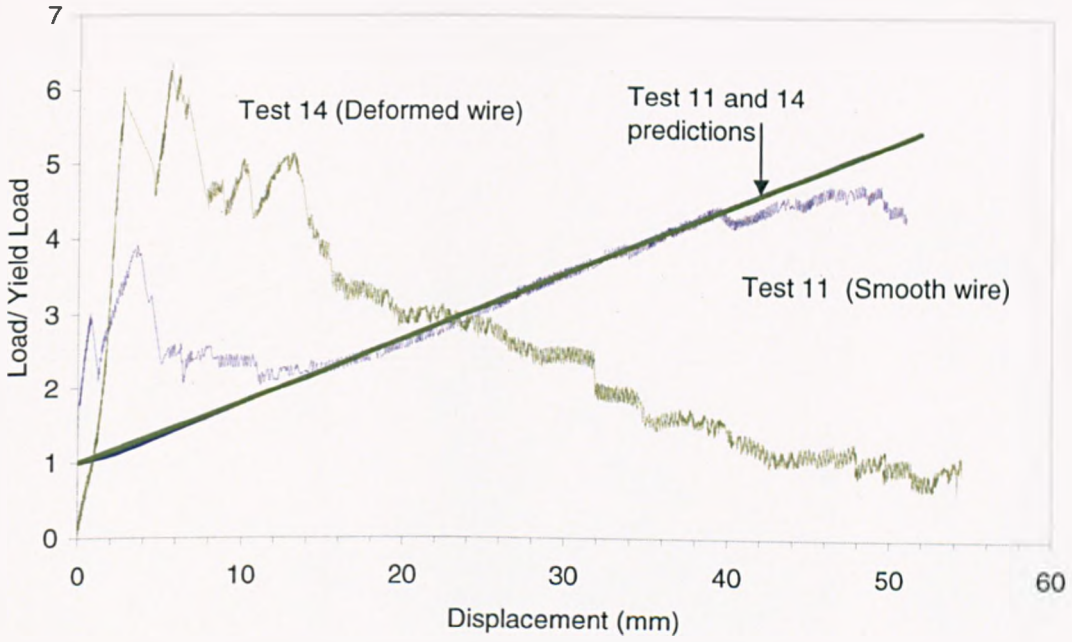

Figure 3.37: Enhancement of load capacity relative to yield load for Tests 11 and 14

In Test 11, the slab exceeded its ultimate load within the tensile membrane action range. The enhancements increased linearly with increasing deflection and the test was terminated at a deflection of *span/10*, at which there was no imminent failure of the slab (Figure 3.37).

The photographs in Figure 3.38 show full depth cracking of the slab and opening of the longitudinal cracks. The enhancements in Test 14 decreased linearly and there was no increase in the enhancements above yield load after the ultimate peak load.

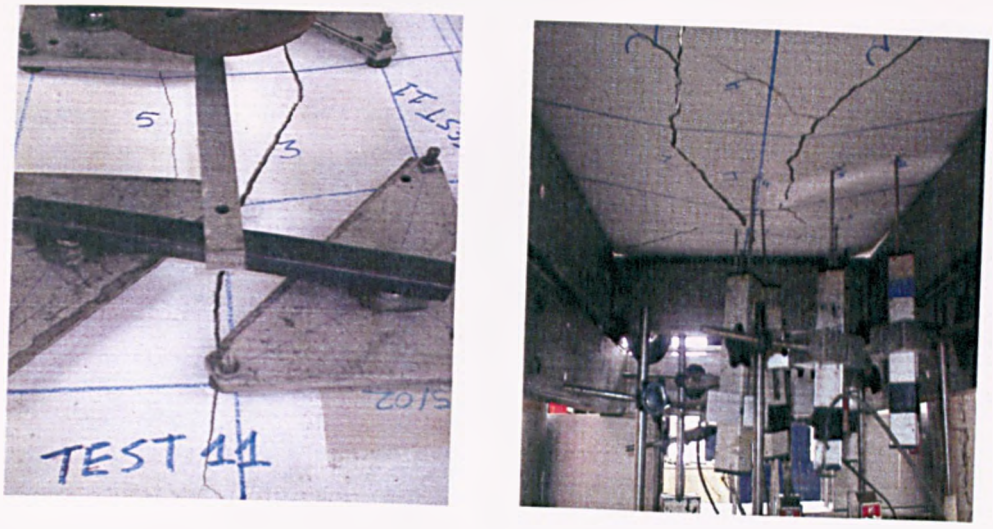

(a) Test 11

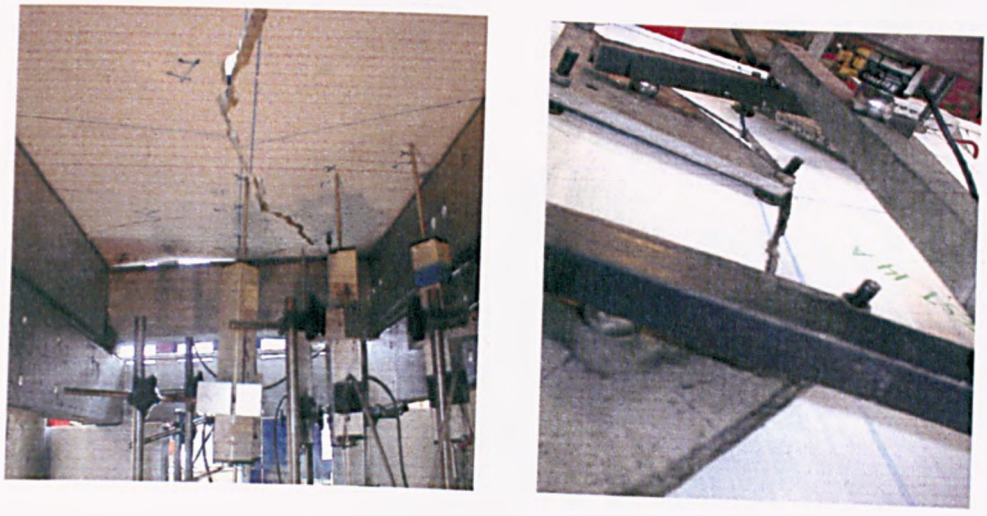

(b) Test 14

Figure 3.38: View of the cracks for the slabs in (a) Test 11, and (b) Test 14.

Tests 7, 9 and 9A

Tests 7, 9 and 9A used orthotropically reinforced slabs, with more reinforcement placed in the shorter span (μ=5) and an aspect ratio of 2.09. The slab in Test 7 was reinforced with smooth wire and in Tests 9 and 9A reinforced with deformed wire. The slabs in Tests 9 and 9A were nominally identical, and the case was repeated as a reliability check, but their measured thicknesses differed, as can be seen in Tables 3.4 (a) and (b).

Orthotropically reinforced slabs. (Spacing in long span 60mm, in short span 12mm) Aspect Ratio = 2.09									
Test	Size (mm)	μ	t (mm)	fy (N/mm^2)	Bar Type	fc (N/mm^2)	dx (mm)	dy (mm)	Yield-line capacity (kN/m^2).
7	1150×550	5.0	18.5	252	Smooth	38.2	8.90	8.54	2.45
9	1150×550	5.0	17.5	245	Deformed	31.5	8.40	8.04	2.24
9A	1150×550	5.0	20.0	245	Deformed	32.6	9.65	9.29	2.58

Table 3.4(a): Orthotrpically reinforced slabs of aspect ratio 2.09.

Orthotropically reinforced slabs. (Spacing in long span 60mm, in short span 12mm) Aspect Ratio = 1.55									
Test	Size (mm)	μ	t (mm)	fy (N/mm^2)	Bar Type	fc (N/mm^2)	dx (mm)	dy (mm)	Yield-line capacity (kN/m^2).
12	850×550	5.0	20	256	Smooth	41.2	9.65	9.29	2.94
13	850×550	5.0	15	245	Deformed	38.0	7.15	6.79	2.07

Table 3.4(b): Orthotropically reinforced slabs of aspect ratio 1.55

Considering the difference in measured thickness, and the variability which might be expected from such concrete elements under test (particularly in the reinforcement depth), the comparison between Tests 9 and 9A is reasonable. Figures 3.39 and 3.40 are photographs of the bottom and top surfaces of the slabs in Tests 7 and 9. Tests 9 and 9A developed a full central tension crack, while in Test 7 the tension crack formed at the intersection of the yield lines.

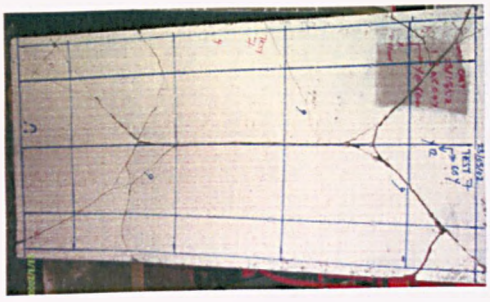

Test 7

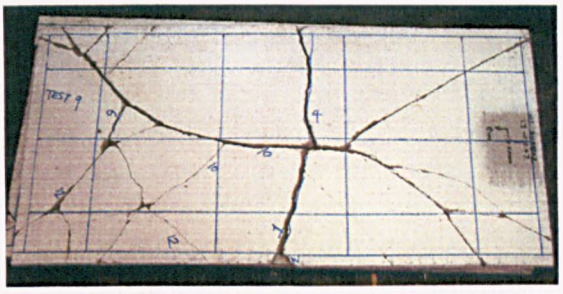

Test 9

Test 9A

Figure 3.39: View of top of slabs in Tests 7, 9 and 9A.

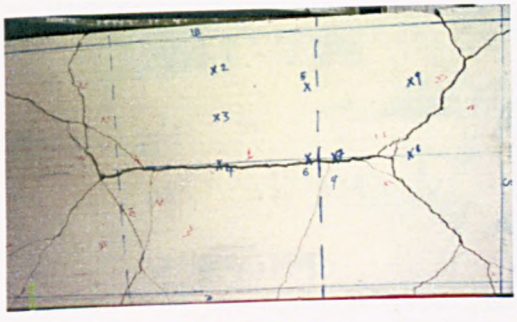

Test 7

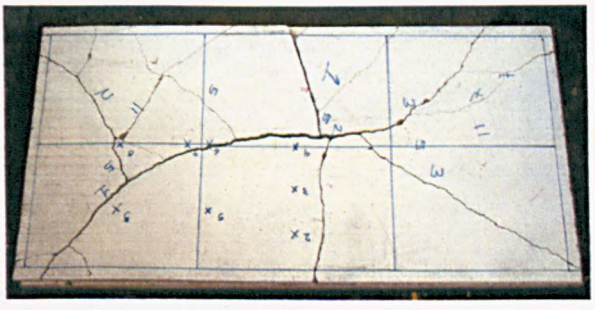

Test 9

Test 9A

Figure 3.40: View of bottom of slabs in Tests 7, 9 and 9A.

Figure 3.41 shows the test results and predictions for Tests 7, 9 and 9A. It can be seen that for Test 7, for which smooth wire was used, the prediction is always conservative and follows the trend of the test results. For Tests 9 and 9A, for which deformed wire was used, the prediction becomes unconservative beyond a vertical displacement of 39mm. As previously mentioned, the essential difference between the observed behaviour of slabs with deformed and smooth reinforcement is that the deformed wire was observed to fracture during the tests.

The initial peak load close to the start of the tests seems to indicate that the bond between the concrete and steel has an influence on the behaviour of the slab at early stages. The deformed wire can develop significantly higher bond resistance than the smooth wire. In the case of the smooth wire, the frictional resistance at the interface between the concrete and steel will be lower than that of the deformed wire. This may explain the higher load capacity achieved by the slab in Tests 9, 9A than in Test 7, even though the slabs of Tests 9 and 9A had a lower concrete strength. The enhancements for Test 7 increase linearly as the slab deflections increase, and correspond well with the theoretical prediction. At a deflection of 29mm the enhancements for the deformed slab decrease linearly to below that of Test 7, and at a deflection of 39mm decrease below that of the theoretical prediction.

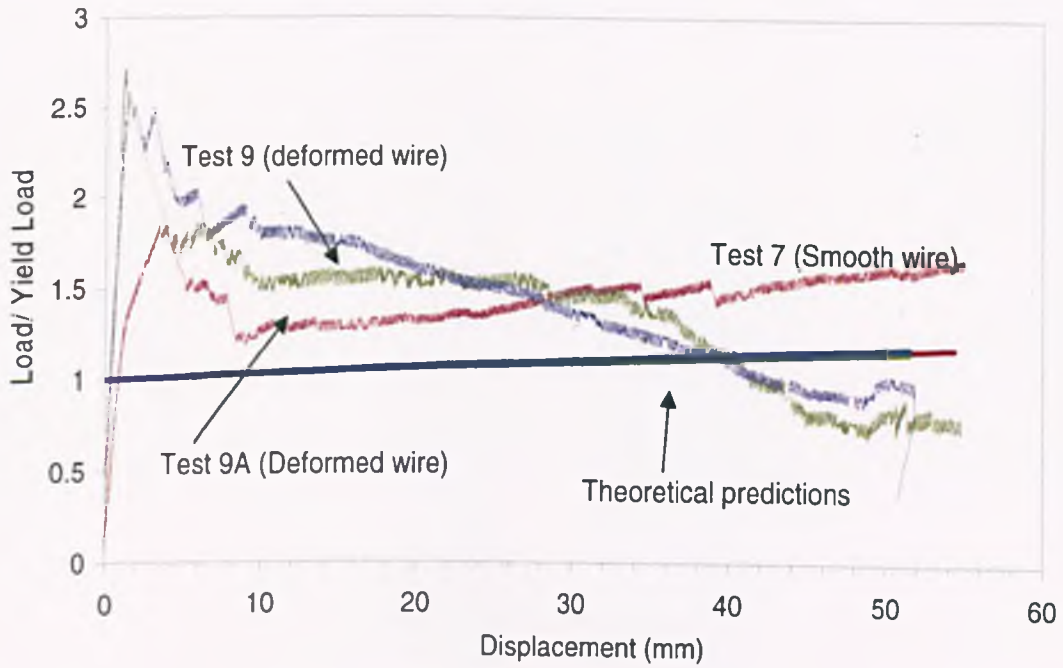

Figure 3.41: Enhancement relative to yield line load for Tests 7, 9 and 9A

Tests 12 and 13

These slabs had an aspect ratio of 1.55 and a coefficient of orthotropy of 5. The slab in Test 12 was reinforced with smooth wire and that in Test 13 with deformed wire. The photographs in Figure 3.42 show the results of these tests. The slabs formed two transverse cracks at the intersections of the yield lines, and the development of the cracks proceeded in a similar manner to that of the isotropic slabs. From the photographs in Figure 3.42, the transverse crack in Test 13 had opened out more than in Test 12. Two tension cracks developed in both slabs at the intersections of the yield lines.

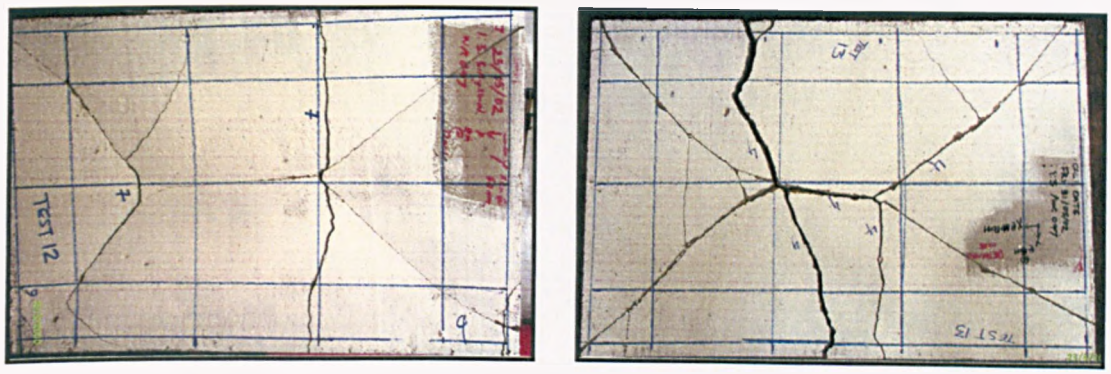

Test 12 Test 13

View of the top of the slab

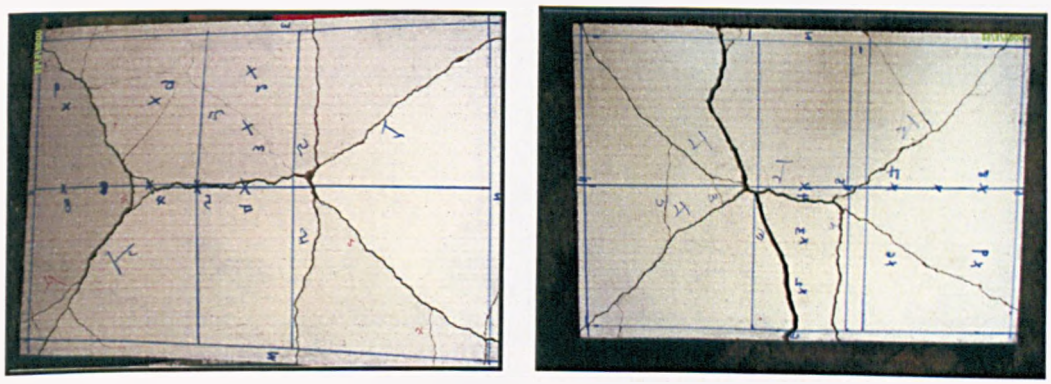

Test 12 Test 13

View of bottom of the slab

Figure 3.42: View of slabs after testing for Tests 12 and 13.

The load displacement responses of Tests 12 and 13 are shown in Figure 3.43, together with predictions for the tests using the Simple Design Method. These slabs had orthotropic reinforcement (μ=5) and an aspect ratio of 1.55. Comparison of the theory with Test 12, which had smooth bars, is very good. For Test 13, which was reinforced with deformed bars,

the comparison is very good up to a displacement of 35mm. Above this displacement, the prediction is unconservative. Again, it is thought that the reduction in load carrying capacity is due to fracture of the deformed bars.

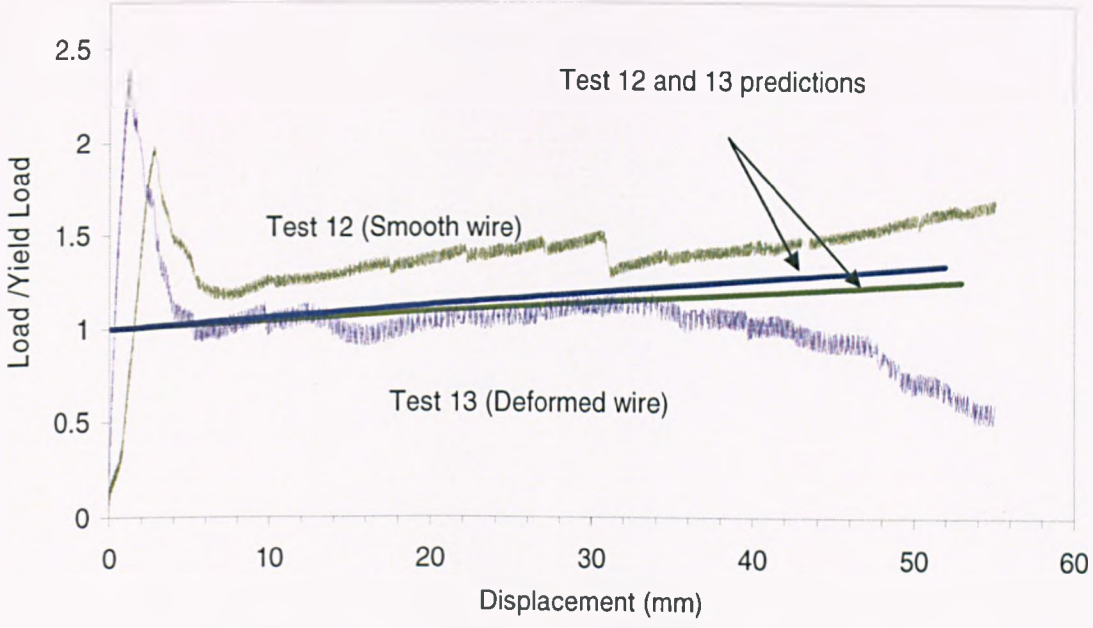

Figure 3.43: Comparison between smooth and deformed wire for Tests 12 and 13.

3.7 Tensile Tests on Small Sawn Slab Specimens

In order to investigate the bond behaviour of the smooth and deformed wire as part of the concrete slab, tensile tests were carried out on sawn sections of slabs.

3.7.1 Test Set-Up

The test set-up involved placing pre-sawn sections of slabs reinforced with smooth and deformed wire into a tensile testing device. Figure 3.44 shows the typical test set-up of the tension test. The pre-cut sections were notched in the middle in order to generate crack propagation along this weak point. The section sizes were cut to 300x75mm in which each section contained 4 wires running parallel to the longitudinal direction of the section.

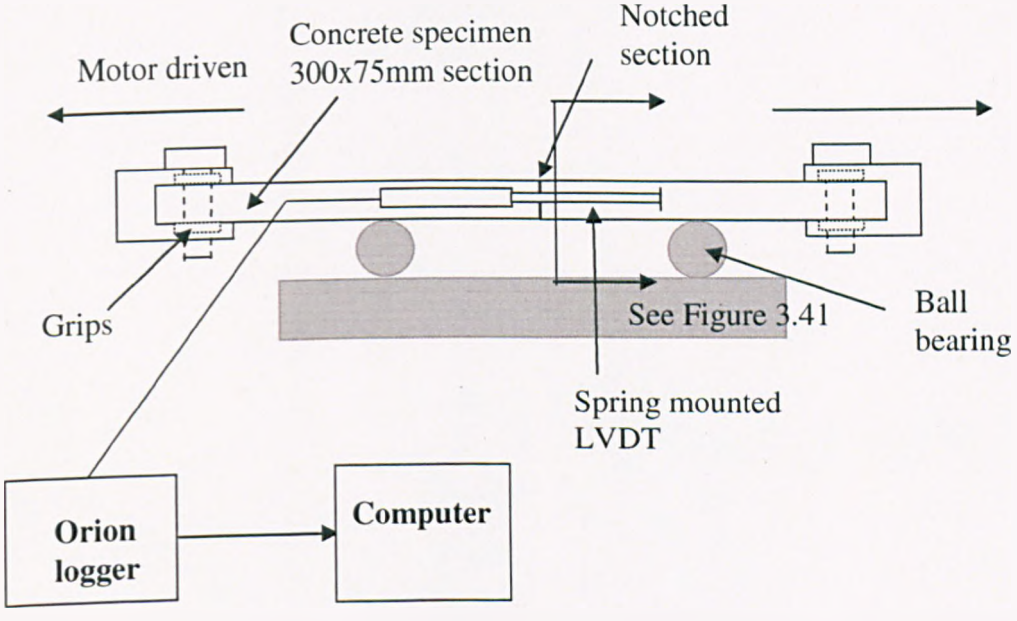

Figure 3.44: Test set-up for tension tests on sawn sections of slab.

Horizontal displacements were measured by the use of two displacement gauges placed at either end of the longitudinal section; the load was measured by the use of strain gauges placed on the load platen of the tensile machine. Uniform tension was created by the use of a motor and ball bearings which were placed under the specimen in order to maintain tension throughout the specimens. The grips placed at the bolt holes provided sufficient friction around the bolt hole reducing any stress concentrations near to the bolts. Figure 3.45(a) shows a plan view of a typical specimen, note the notch across the specimen.

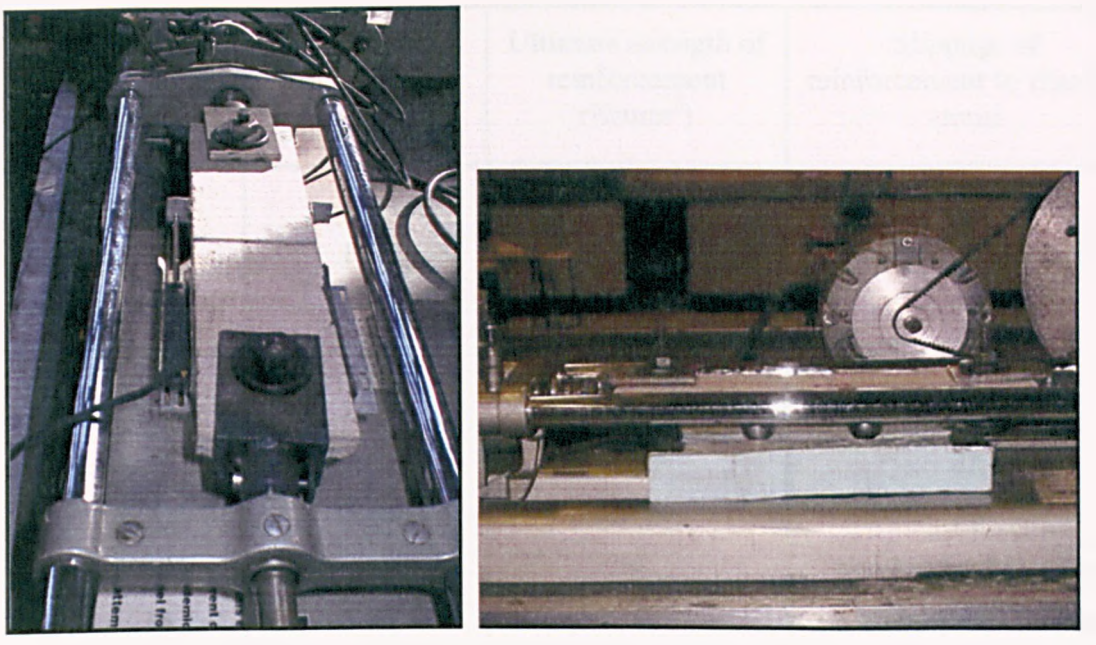

(a) (b)

Figure 3.45 a) Plan view of section within test rig, and b) side view of test rig.

Behaviour of smooth reinforced sections

Table 3.5 shows the results of the tension tests carried out on the sawn sections of a concrete slab reinforced with smooth wire. The concrete tensile strength, on the basis of Eurocode 2 [8], Table 3.1, gives lower bound tensile strength of 1.9N/mm^2 for cube strength of 35N/mm^2. In the design of reinforced concrete the contribution of the tensile strength is ignored which of course is conservative. The results from the experiments showed that concrete does in fact utilise its tensile strength and the maximum moment capacity of the section is not just a combination of concrete compression and tensile strength of the reinforcement.

The formulas for determining the necessary amount of reinforcement within a slab assume that there is no contribution from tensile strength of the concrete and is assumed to be zero. Therefore, as the amount of reinforcement within a slab is reduced we are in fact relying on the tensile strength of the concrete. Tables 3.6 and 3.7 below compare the bond-slip behaviour for smooth and deformed wire. In some of the smooth wire tests, the wire fails to fracture as the wire is de-bonding and the straining over a larger length than for the case of the concrete sections reinforced with deformed wire.

Test	f_c (N/mm$^{2)}$ Cube strength	f_t (N/mm^2) Measured tensile strength	Ultimate strength of reinforcement (N/mm^2)	Slippage of reinforcement to fracture (mm)
1	35	2.5	253	8
3	35	1.52	-	No observed fracture
4	35	1.86	284	19
5	35	2.02	290	10
7	35	1.88	295	9
8	35	1.90	253	23
9	35	2.10	278	10
10	35	1.9	-	No observed fracture
12	35	1.66	-	No observed fracture

Table 3.6: Data for smooth wire tests

Test	f_c (N/mm$^{2)}$	f_t (N/mm^2)	Ultimate strength of reinforcement (N/mm^2)	Slip of reinforcement to fracture (mm)
2	35	2.10	290	1.86
6	35	1.95	286	3
11	35	1.43	315	0.9

Table 3.7: Data for deformed wire tests

Figure 3.46 shows the recorded load versus horizontal travel of the sawn sections for Tests 1 and 3. The initial peak is the failure of the concrete in tension, followed by the opening of the transverse crack due to the loss of bond between the concrete and steel leading to fracturing of the reinforcement. It has been confirmed by these set of tests the behaviour between the concrete and steel once the slab had cracked. In the tests, the slabs reinforced with smooth wire, large crack widths were observed as the reinforcement progressively de-bonded from the concrete and an 'unzipping' effect occurred where the reinforcement fractured and the remaining reinforcement carried the load and de-bonded. This can be seen in these tension tests, Figures 3.46 and 3.47.

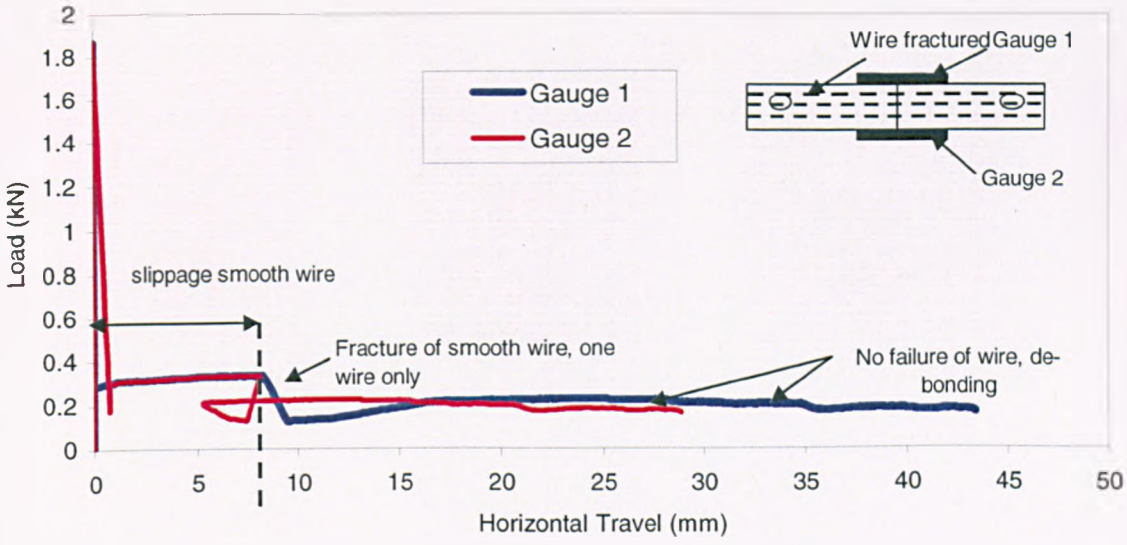

Test 1

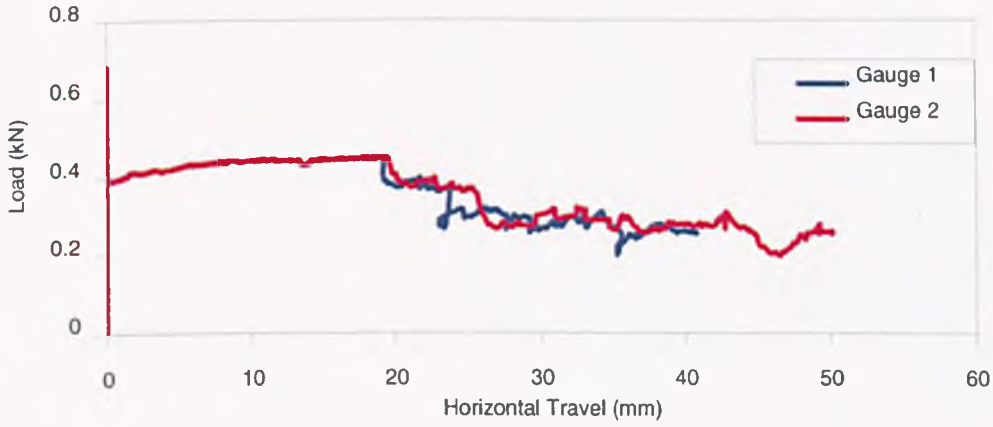

Test 3

Figure 3.46: Load displacement plots for Tests 1 and 3 reinforced with smooth wires.

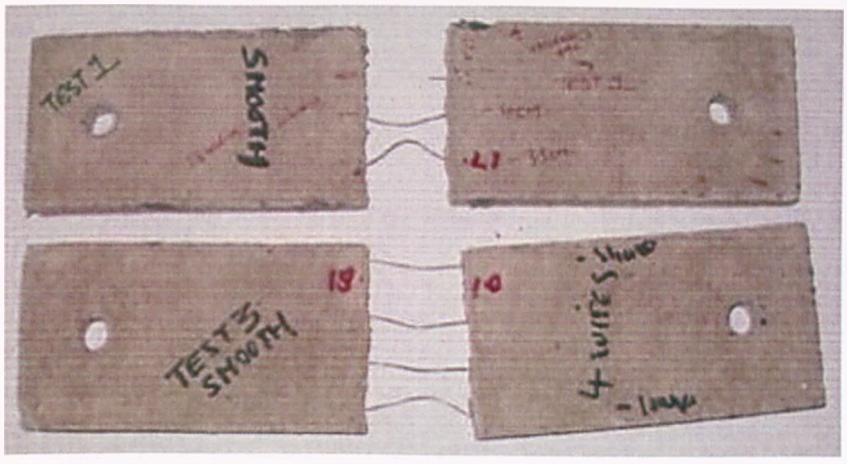

Tests 1 and 3

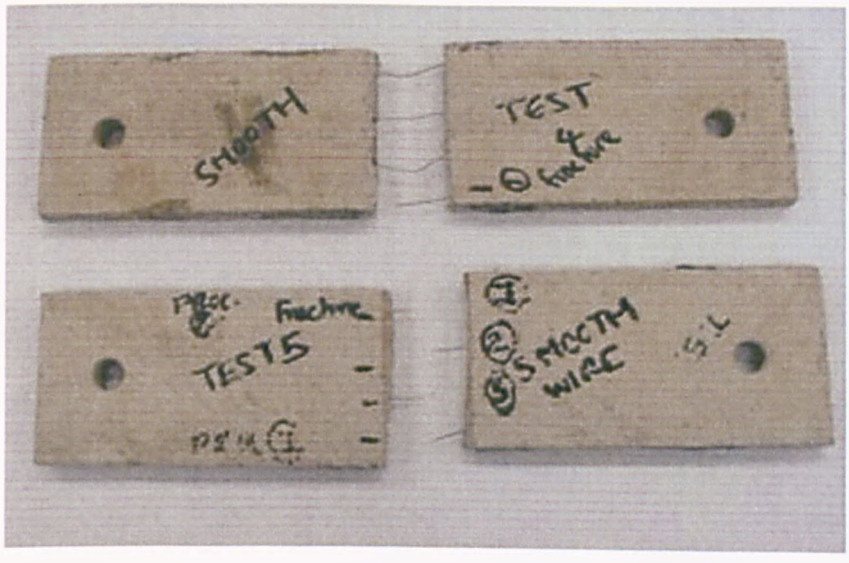

Tests 4 and 5

Figure 3.47: Tests 1, 3, 4 and 5 reinforced with smooth wires.

The sections in Tests 1 and 3 are shown in Figure 3.47 above. The slippage of the reinforcement is clearly seen as well as fracture of the reinforcement. It can be seen from the tests carried out on sections reinforced with smooth wire that slippage of the wire had reached up to 30mm, Figure 3.48. In Tests 3, 10 and 12 there was no observed fracture of the smooth wire, Figure 3.49.

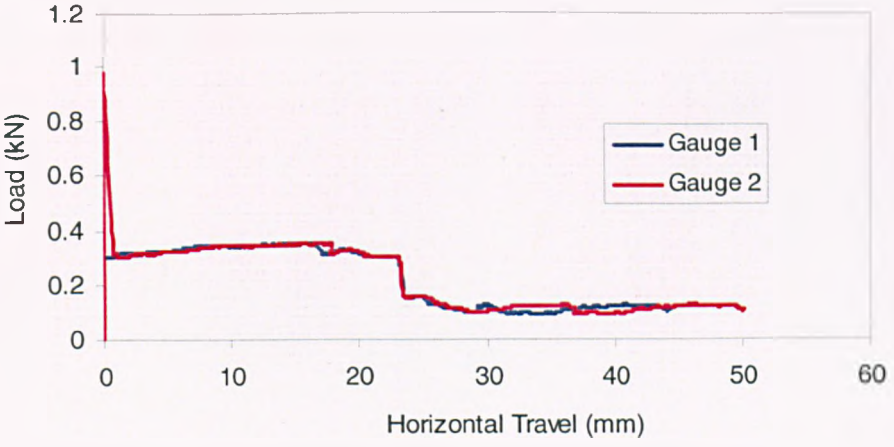

Test 8

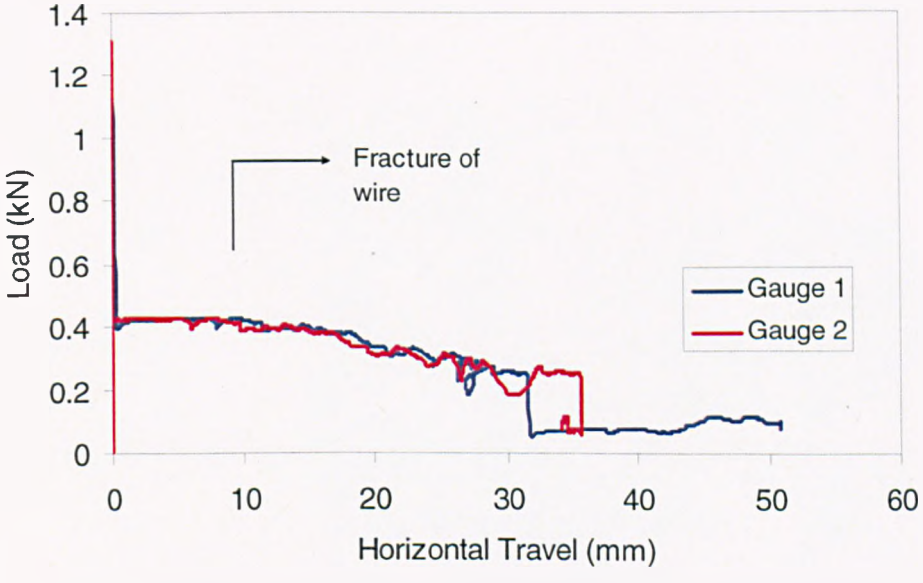

Test 9

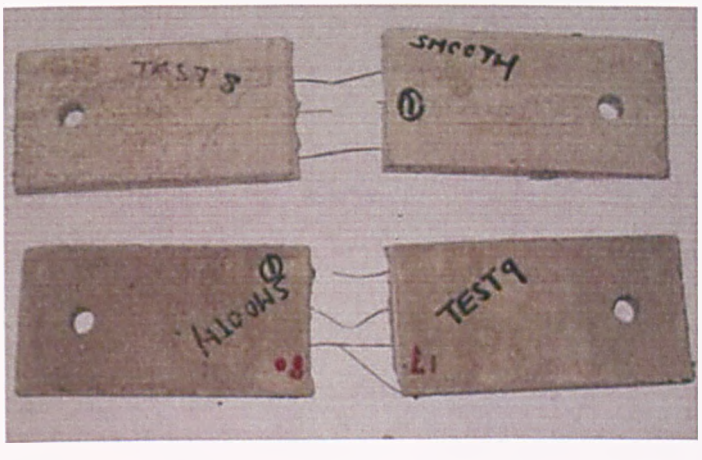

Figure 3.48: Tests 8 and 9 reinforced with smooth wires.

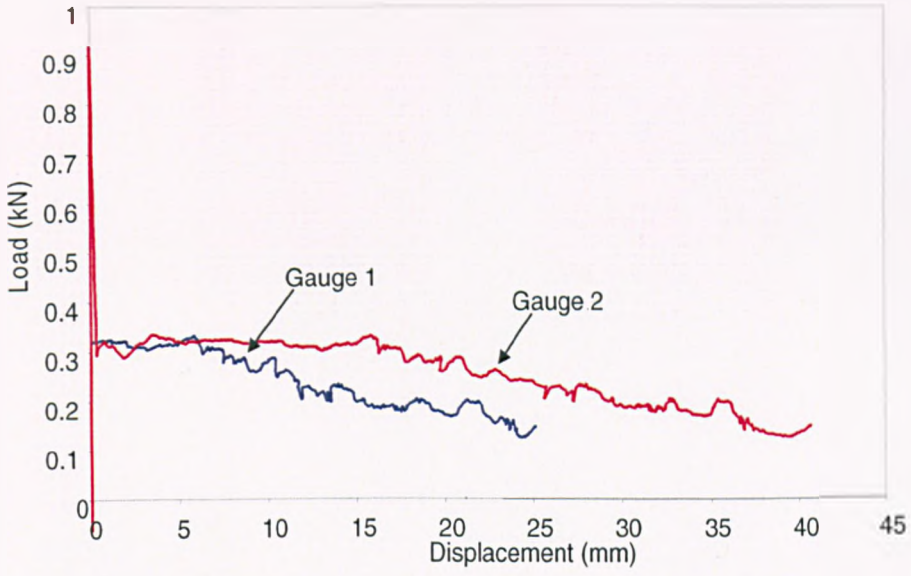

Test 12

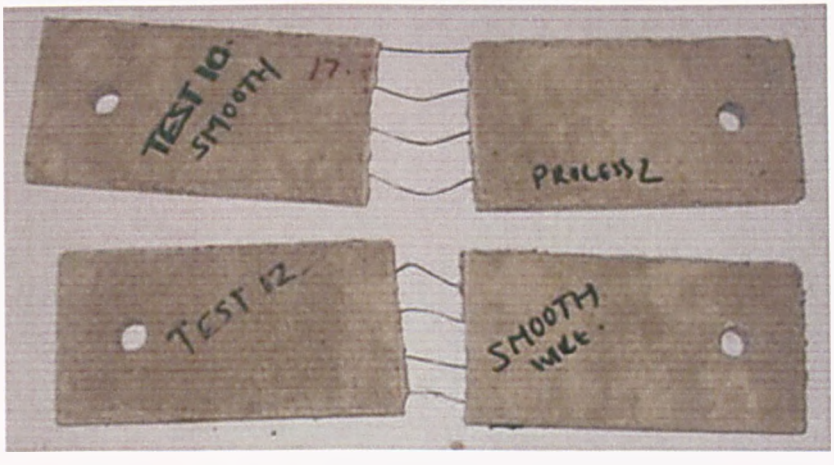

Figure 3.49: Tests 10 and 12 reinforced with smooth wires.

The mechanism of de-bonding differs for the deformed wire case; the indentations on the surface of the wire anchors the wire to the concrete, thus once the concrete has cracked, the reinforcement is strained over a shorter aperture length. Figures 3.50 and 3.51, shows the reduced slip and fracture of the reinforcement which correlated well with the observed behaviour in the tests. The horizontal travel of the wires attained in Tests 2, 6 and 11 are approximately 50% less than the horizontal travel of the deformed wire.

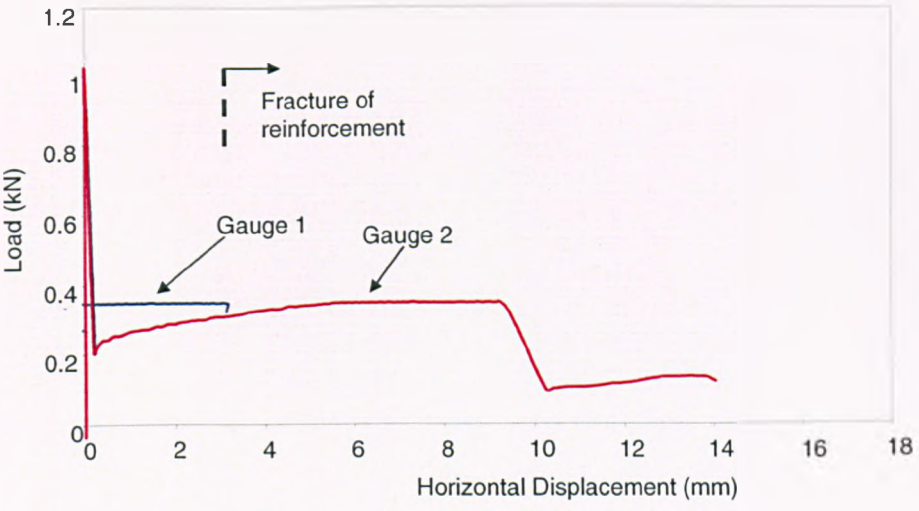

Test 2

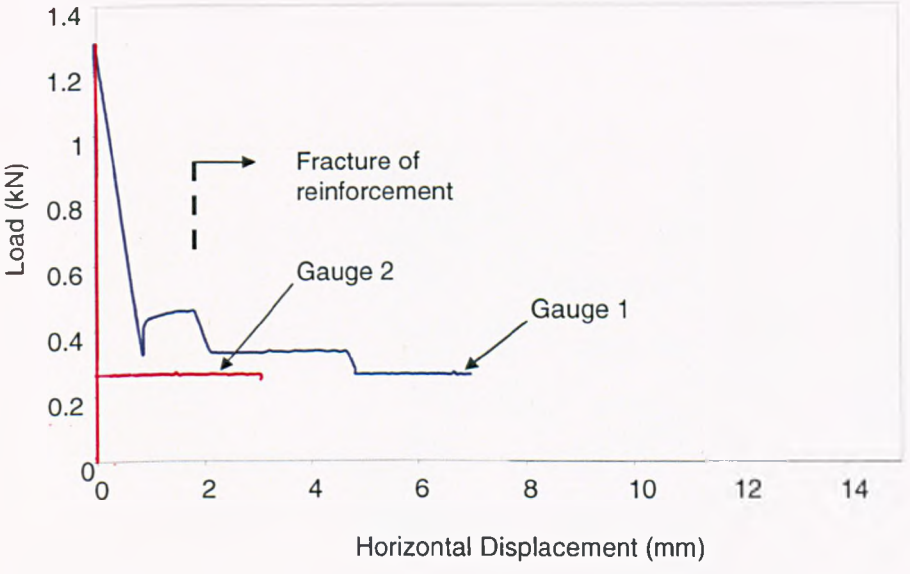

Test 6

Figure 3.50: Tests 2 and 6 reinforced with deformed wires.

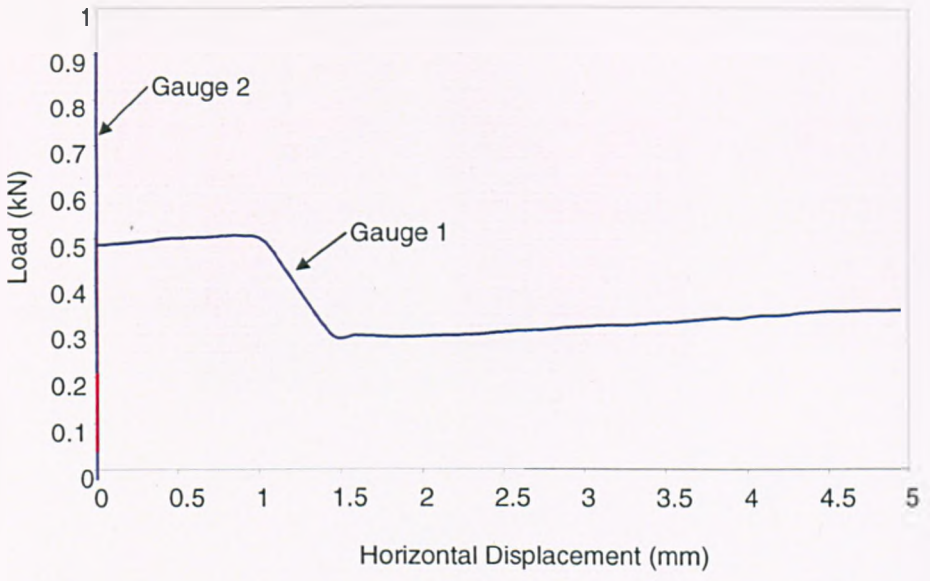

Test 11

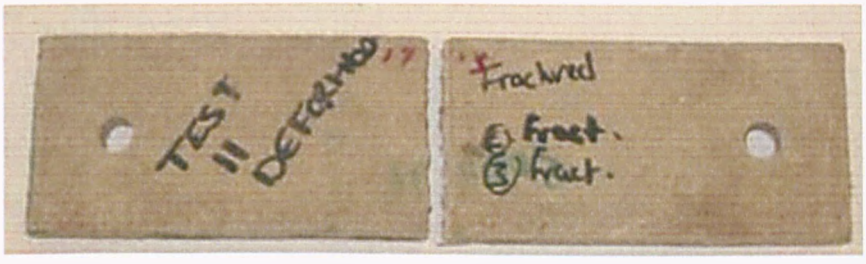

Figure 3.51: Test 11 reinforced with deformed wire.

Numerous studies [48] have been conducted on the bond-slip behaviour of concrete and the main factors influencing the bond slip have been identified as follows;

- Temperature.
- Concrete strength, aggregate type, water-cement ratio, and cement type.
- Bar diameter.
- Surface of reinforcement, deformed or smooth finish.

3.8 Comparison of Test Performance

The slabs reinforced with deformed wire performed much better at small deflections than those with smooth wire. In the slabs which used deformed wire it can be seen from the test records that the initial peaks of the load-deflection curves were higher and more prolonged than in the corresponding cases which used smooth wire. The initial path up to the peak load is associated with the whole cross-section of the slab, including fully bonded reinforcement, acting compositely and the sudden loss of strength at the peak is the result of a large amount of simultaneous cracking when the concrete's limiting tensile strain is exceeded at the lower surface of the slab. The progressive loss of load capacity beyond the peak happens as the reinforcement loses bond-length around the cracks, allowing it to spread the crack-width into straining over an adequate de-bonded length. The higher degree of interaction between the concrete and deformed reinforcement has the effect that the load capacity undergoes a less dramatic fall immediately after the peak, but progressive fracture of the wires at the cracks causes the loss of capacity to continue as the slab deforms. Figures 3.52–3.55 compare the test results for the 1200x600mm and 900x600mm slabs reinforced with smooth and deformed wire.

The experimental results compare well with predictions for smooth wire, and by increasing the reinforcement in the longer span the tensile membrane capacity, and hence the load-carrying capacity of the slab, are increased.

Figure 3.56 compares the slab enhancements attained in the tests which have a coefficient of orthotropy of 5 (more reinforcement placed across the short span), with varying aspect ratio. The results show that the slabs of aspect ratio 2.09 generally exhibit a more pronounced peak in load at initial deflections but at a displacement of approximately 24mm, the slabs enhancements decrease with increasing load. The slabs of aspect ratio 1.55 exhibit a lesser pronounced peak at initial deflections but after approximately 10mm displacement the slabs recover and the enhancement factors for these slabs increase with increasing deflection. It can be seen that the slabs that have an aspect ratio 2.09 have increased bending resistance at initial deflections but the overall slab performance is very good with the load capacity decreasing below the yield load at the latter stages of the test.

Figure 3.57 compares the slab enhancements attained in the tests which have a coefficient of orthotropy of 1, with varying aspect ratio. The results show that the slabs of aspect ratio 2.09 perform better at initial deflections when the slab is initially in bending. Towards the

latter stages of the test, the slabs of aspect ratio 1.55 perform better as these slabs attain higher enhancement factors.

As well as predicting the permissible load-capacity with deflection, the design method also provides a maximum allowable displacement, which at ambient temperature is given by,

$$\Delta = \sqrt{\left(\frac{0.5 f_y}{E}\right)_{Reinf't} \frac{3L^2}{8}} \qquad 3.1$$

A comparison between the predicted and the actual load-carrying capacity of the tested slabs at this maximum vertical displacement is shown in Table 3.8. It can be seen that the design capacity only exceeds the test load in 3 cases (Tests 2, 4 and 13) and by less than 10% in all of these. It is also of interest to note that, although the load-displacement responses of slabs with deformed wires can drop below the method's prediction with increasing vertical displacement, the maximum permissible design vertical displacement is generally effective in ensuring that the predicted design capacity corresponds well with the actual test load. The test results do, however, indicate that a more rational limiting displacement should be dependent on the bond strength between the reinforcing bar and the concrete.

Recent studies [49, 50] have been carried out on the behaviour of lightly reinforced concrete members, with the obvious potential for extension to composite floor slabs. The work is restricted to one-dimensional lightly reinforced concrete beam elements, with the assumption that the reinforcement is continuous across the perimeter, which is not assumed in the simplified method used here. The studies however present a potentially useful model for bond-slip at cracks at ambient and elevated temperatures, and for rupture of steel reinforcement. This may lead to the development of a more justifiable model for ultimate failure of slabs by tension cracking.

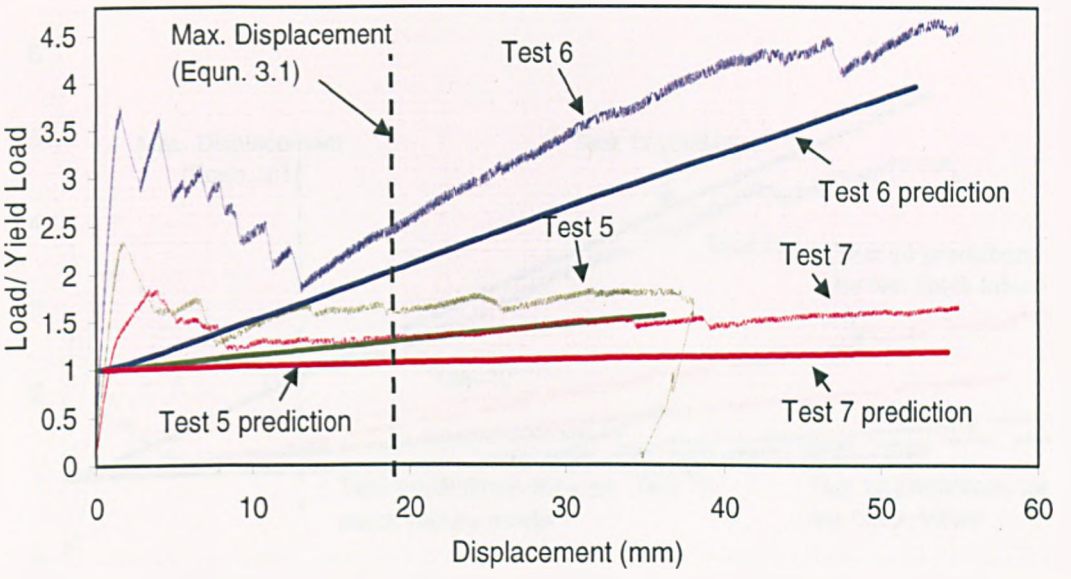

Figure 3.52: Comparison of load-deflection response for 1200mmx 600mm orthotropic slabs reinforced with smooth wire.

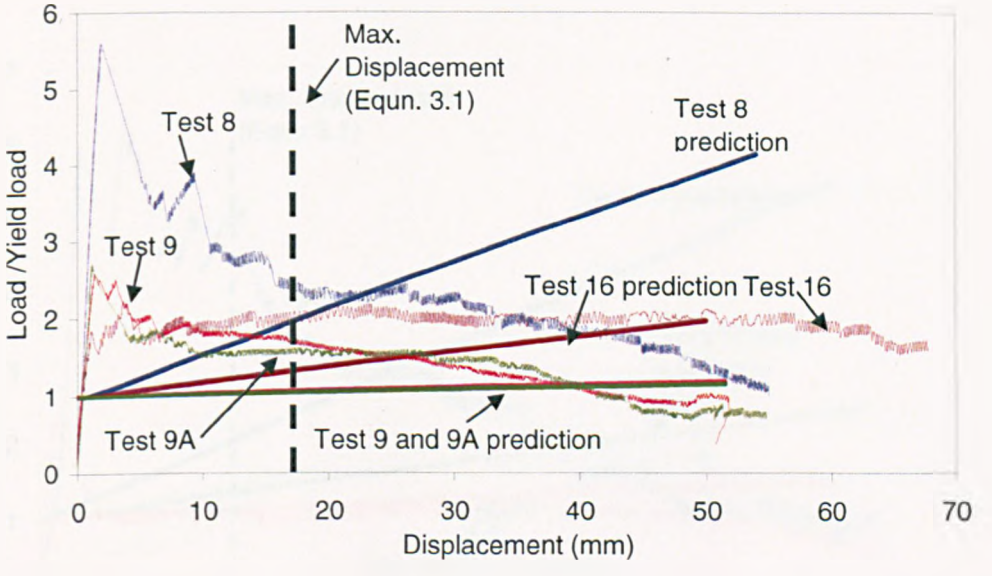

Figure 3.53: Comparison of load-deflection response for 1200 mm x 600 mm orthotropic slabs reinforced with deformed wire.

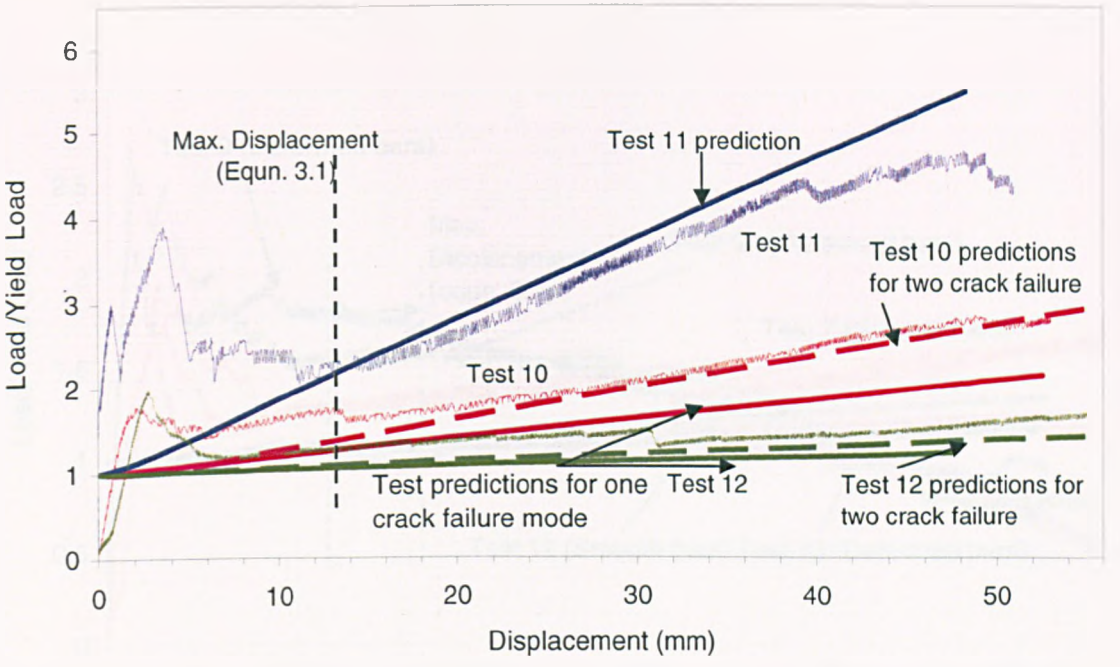

Figure 3.54: Comparison of load-deflection response for 950x600 mm orthotropic slabs reinforced with smooth wire.

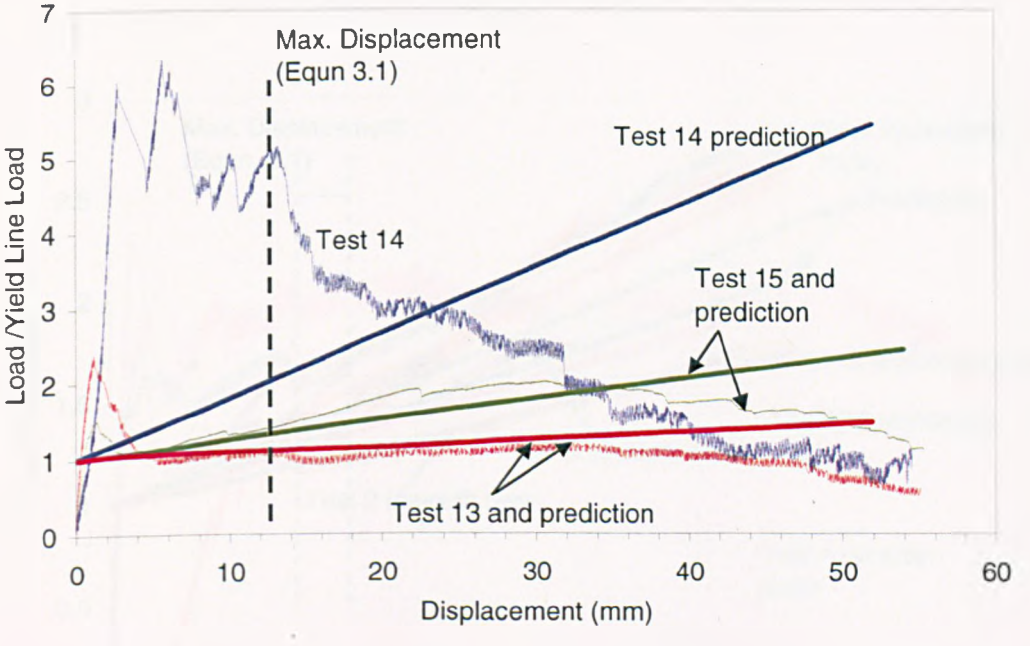

Figure 3.55: Comparison of load-deflection response for 950x600 mm orthotropic slabs reinforced with deformed wire.

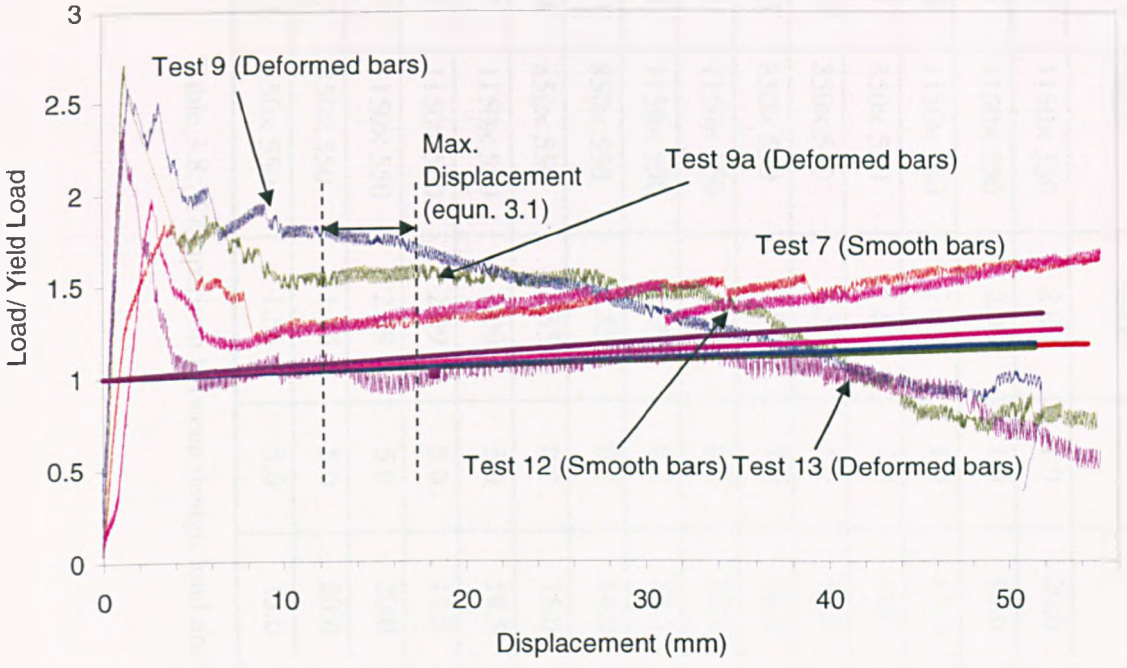

Figure 3.56: Comparison of load-deflection response for orthotropic slabs of aspect ratio 1.55 and 2.09 (μ=5.0).

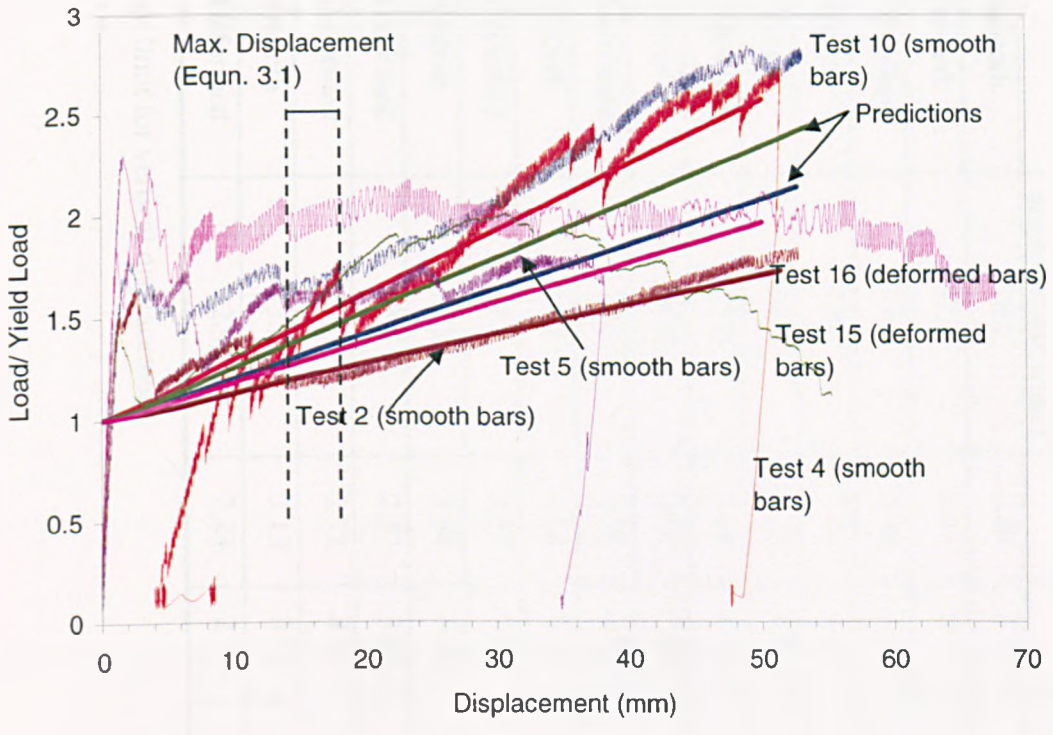

Figure 3.57: Comparison of load-deflection response for orthotropic slabs of aspect ratio 1.55 and 2.09 (μ=1.0).

Test	Size (mm)	Aspect Ratio	μ	t (mm)	fy (N/mm^2)	Bar Type	Design limit on vertical displacement (mm)	Design load	Test load	Design / Test
2	1150× 550	2.09	1.0	20.0	265	Smooth	18.1	2.89	2.76	**1.05**
5	1150× 550	2.09	1.0	18.0	258	Smooth	17.9	2.51	3.17	0.79
16	1150× 550	2.09	1.0	15.0	240	Deformed	17.3	2.00	3.18	0.63
4	850× 550	1.55	1.0	14.0	265	Smooth	13.4	2.53	2.30	**1.10**
10	850× 550	1.55	1.0	19.5	256	Smooth	13.2	3.23	4.41	0.73
15	850× 550	1.55	1.0	16.0	248	Deformed	13.0	2.65	2.81	0.94
6	1150× 550	2.09	0.2	18.0	262	Smooth	18.0	2.43	3.00	0.81
8	1150× 550	2.09	0.2	18.5	242	Deformed	17.3	2.16	2.52	0.86
11	850× 550	1.55	0.2	14.0	260	Smooth	13.3	2.83	2.86	0.99
14	850× 550	1.55	0.2	15.0	255	Deformed	13.1	2.87	7.09	0.40
7	1150× 550	2.09	5.0	18.5	252	Smooth	17.7	2.59	3.23	0.80
9	1150× 550	2.09	5.0	17.5	245	Deformed	17.4	2.37	3.83	0.62
9A	1150× 550	2.09	5.0	20.0	245	Deformed	17.4	2.72	4.07	0.67
12	850× 550	1.55	5.0	20.0	256	Smooth	13.2	3.13	3.72	0.84
13	850× 550	1.55	5.0	15.0	245	Deformed	12.9	2.24	2.10	**1.07**

Table 3.8: Comparison between design load and test load at design limit for vertical displacement

3.8.1 Revisions to Simple Design Method

The Simple Design Method can be modified to take account of the observed failure mode for the orthotropic slabs reinforced with more reinforcement in the long span and less reinforcement across the short span. Figure 3.58 shows the modified failure mode for two transverse cracks and Figure 3.59 plots the predictions. The modified failure mode shows a central long-direction yield-line crack that has developed into a tension crack.

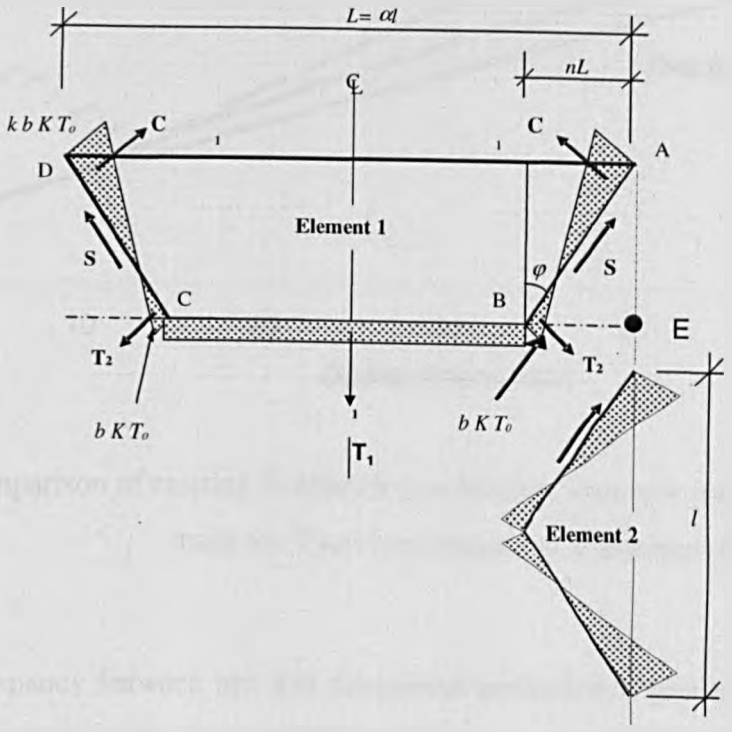

Figure 3.58: Modified failure mode for orthotropic slabs with less reinforcement across the shorter span.

Figure 3.59 compares the predicted enhancement factors for the existing and for the new modified failure mode. In comparison with the results of Test 6, the new mode of failure predicts higher enhancements than actual. There are a number of possible reasons for the discrepancy between test and experimental results. These are;

- The 'ring' of compression is not considered in the simple design method; see Chapter 2 for details on derivation of enhancement factors for orthotropic slabs.
- The assumed development of a uniform peak yield strength along the tension crack.

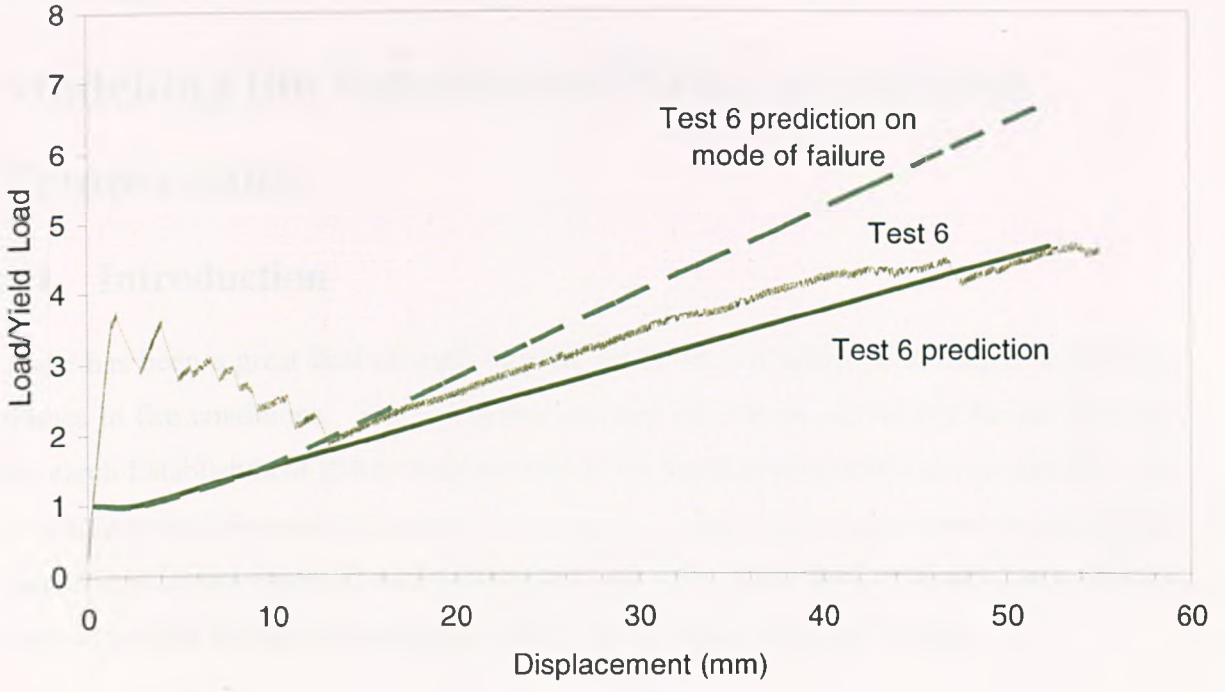

Figure 3.59: Comparison of existing Simple Design Method with new proposed failure crack mode for Test 6, coefficient of orthotropy of 0.2.

The overall discrepancy between test and theoretical prediction is greater for this particular failure mode compared with the comparisons between the Simple Design Method and isotropically reinforced slabs. The revised Simple Design Method becomes unconservative as it is predicting more enhancement than the test.

Chapter 4

Modelling the Behaviour of Slabs at Ambient Temperature

4.1 Introduction

There has been a great deal of work carried out in the numerical modelling of composite frames in fire conditions. The full scale tests that have been carried out by the Building Research Establishment (BRE) have prompted the development of numerical models. It is advantageous if the real behaviour of composite slabs can be represented by numerical models and comparison will be made between the ambient model test results, the yield-line method and the Simple Design Method with the numerical software *Vulcan*.

4.2 *Vulcan*

The numerical software *Vulcan* was created at the University of Sheffield, and models the 3-D structural behaviour of composite steel frames in fire. It has been extensively validated over the years with experimental data collated from the full scale tests carried out at Cardington. *Vulcan* successfully models the complicated factors that arise in fire conditions such as thermal expansion of the elements, change of material properties with temperature and concrete cracking and crushing. Figure 4.1 shows how the slab elements are configured.

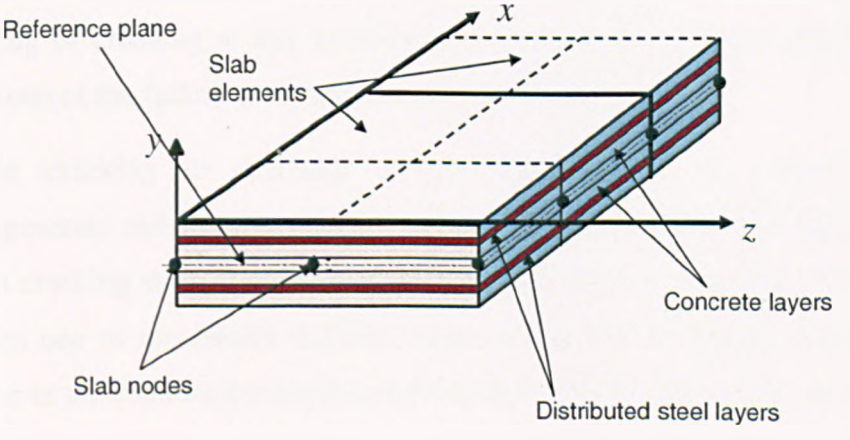

Figure 4.1: The distribution of slab elements

The main features of the program are summarised below, and further details are given in references [51, 52]:

- The element nodes for the slab, beam and column lie within the same plane, which is located at the mid-depth of the slab and is referred to as the common reference plane. The beams are offset from this common reference plane at a distance of half the beam depth plus half the slab depth. These locations are fixed throughout the analyses.

- The cross-section of the slab depth is divided into a number of layers; material properties in each layer are temperature-dependent. The reinforcing steel bars are modelled by an equivalent smeared steel layer, with the thickness of each layer determined so that its cross-sectional area is equal to the total area of the reinforcement per metre width. Perfect bond is assumed between the reinforcing steel layers and the surrounding concrete.

- In *Vulcan* the concrete failure models at ambient-temperature conditions are extended to elevated temperatures by considering all the relevant parameters of the material to be temperature-dependent. The proposed failure envelope by Barzegar-Jamshidi [53] was adopted with the compressive strength $f_c^{'}$ and tensile strength $f_t^{'}$, considered as temperature dependent. This is illustrated in Figure 4.2. The failure surfaces of the biaxial strength envelope are divided into four regions, each region depending on the stress state as represented by the principal stress ratio $\alpha = f_{c1}/f_{c2}$. The compressive stresses are assumed negative, tensile stresses positive and the principal directions are chosen so that $f_{c1} \geq f_{c2}$. The initiation of cracking or crushing at any location occurs when the concrete principal stresses reach one of the failure surfaces of the failure envelope.

- Before cracking or crushing occurs, the concrete is assumed isotropic, homogeneous and linearly elastic. A smeared crack model has been adopted in which cracking at any Gauss point is identified when the concrete principal stress reaches one of the failure surfaces, either in the biaxial tension region (segment AB) or in the combined tension-compression region (segment BC) shown in Figure 4.2.

- After the initiation of cracking in a single direction, the concrete is treated as an orthotropic material with the principal axes normal and parallel to the crack direction. The concrete parallel to the crack is capable of resisting both tensile and compressive stresses. When it is subjected to tension, linear elastic behaviour is assumed, and when the concrete parallel to the crack is subjected to compression, the uniaxial stress-strain relationship is applied. Upon further loading of singly-cracked concrete, a second set of cracks can be formed in the direction normal to the first set of smeared cracks. If the stress in that particular direction is less than $f_t^{'}$, then concrete remains singly cracked. If it is greater than $f_t^{'}$ then the second set of cracks form.

- Concrete exhibits linear elastic behaviour up to its ultimate tensile strength. Beyond this, the tensile stress gradually decreases with increasing tensile strain, rather than dropping to zero abruptly as a brittle material does. This phenomenon is known as tensile strain-softening. In *Vulcan*, the model suggested by Rots *et al.* [54] has been used to model tensile strain-softening, Figure 4.3.

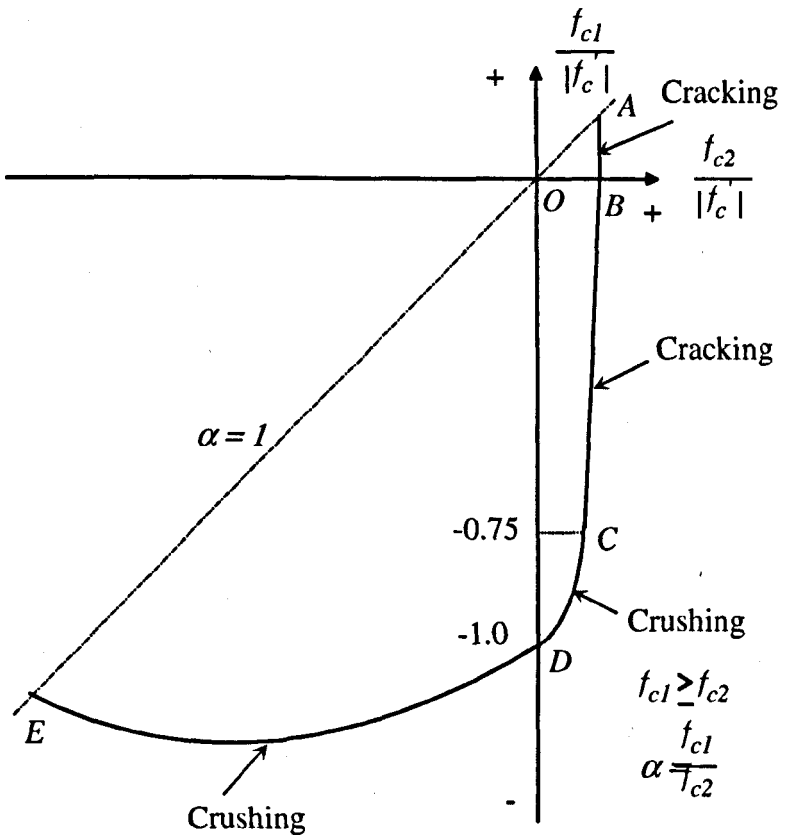

Figure 4.2: Concrete biaxial failure envelope [53]

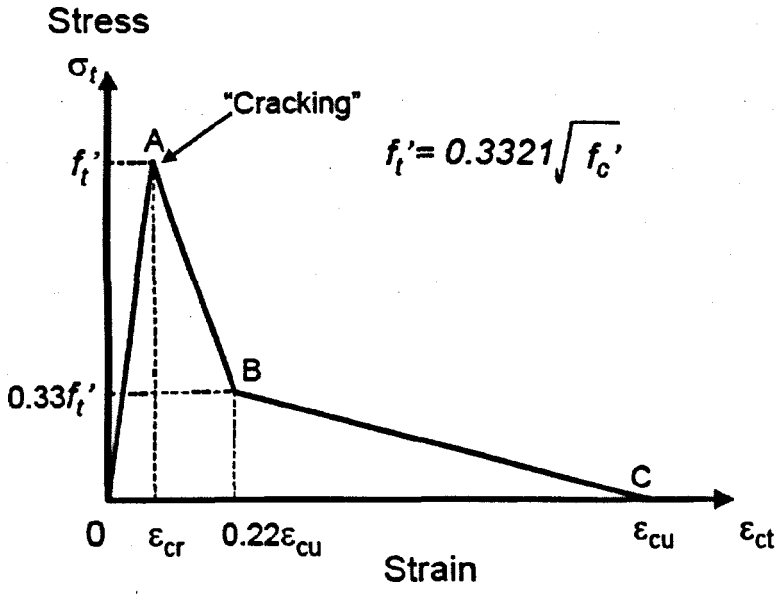

Figure 4.3: Adopted tension strain softening, [54].

- In *Vulcan,* the reinforcement is modelled using equivalent steel layers so that the thickness of the layer is equal to the slab's cross-sectional area of reinforcement. The bond between the steel and concrete layer is assumed to be perfect. The stress-strain curve that has been adopted in the model for the reinforcing steel is taken from Eurocode 4, and is shown in Figure 1.6.

4.3 Validation of Model

The model-scale slabs were recreated in *Vulcan* using an assemblage of finite plate elements that use a quadrilateral 9-noded element. The elements were divided into several layers which represented the concrete and reinforcing steel (Figure 4.1). In order to develop a representative model at ambient temperature of the tested slabs a series of mesh studies were undertaken. The models were based on the 1200x600x20mm slab with a supported area of 1150x550x20mm and applied uniform load of 8kN/m^2. The material properties used in the modelling, were based on tested values measured in Test 2, which were as follows:

- The yield strength of steel was 265N/mm^2 (smooth wire).
- The total area reinforcement was 0.3%.
- The average compressive strength of concrete test samples was 28N/mm^2.

- The Eurocode 4 model for normal-weight concrete was used.

The mesh study involved creating models of dimensions 1150x550x20mm with varying element numbers ranging from 10 elements up to 300 elements. The maximum deflections at the mid-span for each of these models are compared in Figure 4.4.

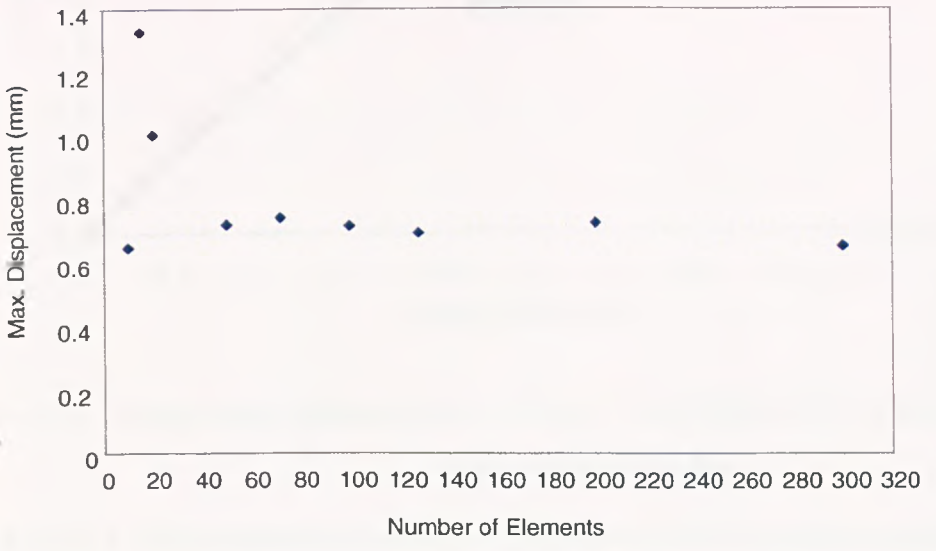

Figure 4.4: comparison of the maximum deflection with increasing slab element numbers.

In Figure 4.4, it is shown that above 100 elements there is little change in the maximum displacement. The plot of applied load against mid-span deflection for the models is shown in Figure 4.5; it can be seen that the results start to converge at approximately 6.4kN/m^2 with slab elements in excess of 128, but for 300 elements the analysis led to convergence problems and early termination.

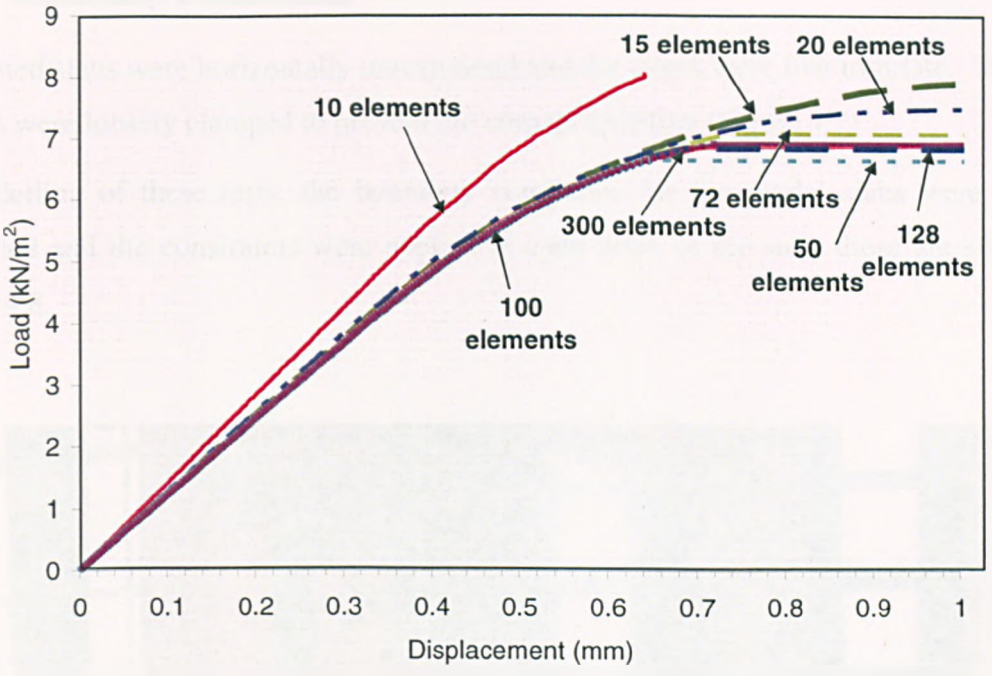

Figure 4.5: Applied load-deflection plots for the 1150x50x20mm slab with increasing slab element numbers.

A mesh size of 128 elements was adopted to model the ambient-temperature tests, as the computational effort for modelling with 200 elements (Figure 4.6) was greatly increased, but yielded the same accuracy.

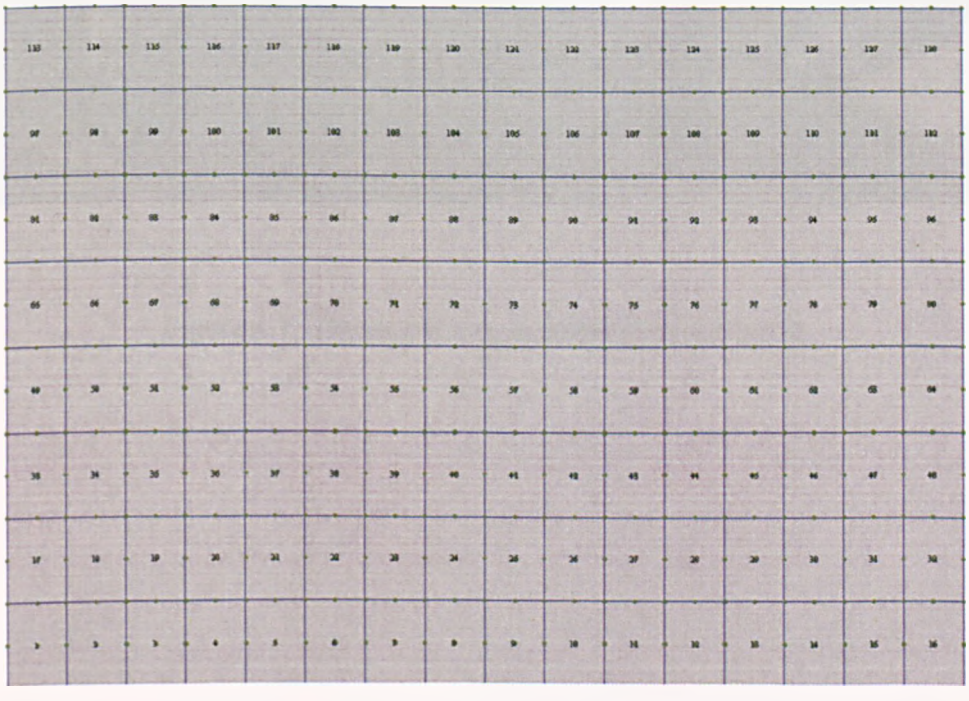

Figure 4.6: Model slab with 128 elements (16x8mesh).

4.3.1 Boundary Conditions

The tested slabs were horizontally unrestrained and the edges were free to rotate. The four corners were loosely clamped to prevent the corners uplifting (Figure 4.7).

In modelling of these tests, the boundary conditions for the model slabs were simply supported and the constraints were applied at each node of the slab; these are shown in Figure 4.8.

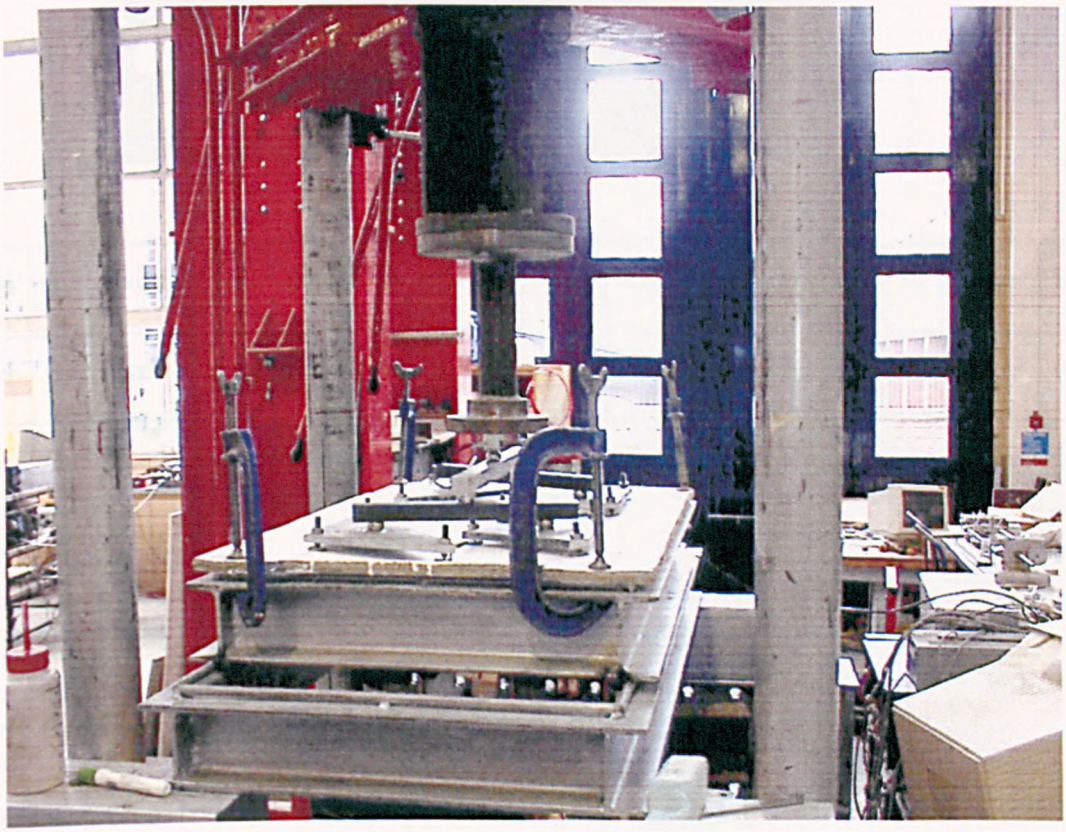

Figure 4.7: The test set-up at ambient temperature.

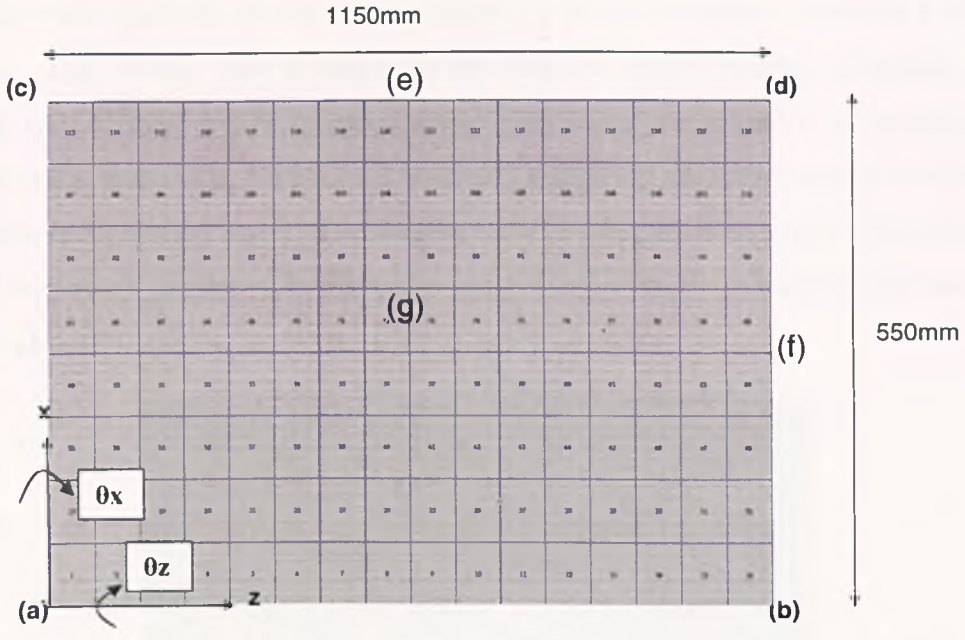

δ_x	fixed	θ_x	fixed
δ_y	fixed	θ_y	fixed
δ_z	fixed	θ_z	fixed

(a)

δ_x	fixed	θ_x	free
δ_y	fixed	θ_y	fixed
δ_z	free	θ_z	free

(b)

δ_x	free	θ_x	free
δ_y	fixed	θ_y	fixed
δ_z	free	θ_z	free

(c)

δ_x	free	θ_x	free
δ_y	fixed	θ_y	fixed
δ_z	free	θ_z	free

(d)

δ_x	free	θ_x	fixed
δ_y	fixed	θ_y	fixed
δ_z	free	θ_z	free

(e)

δ_x	free	θ_x	free
δ_y	fixed	θ_y	fixed
δ_z	free	θ_z	fixed

(f)

δ_x	free	θ_x	free
δ_y	free	θ_y	fixed
δ_z	free	θ_z	free

(g)

Figure 4.8: Boundary conditions for simply supported model scale slab.

The concrete model is based on the smeared crack approach in which cracking of the concrete is identified when the concrete's principal stress reaches one of the failure boundaries and represented by the single lines shown diagrammatically in Figure 4.9. These plots will be referred to as 'crack patterns'. To check that the boundary conditions adopted in the models were representative of the tested slabs, which were simply

supported, crack patterns for the bottom layer of the slab (Figures 4.9 and 4.10) were analysed. The critical load intensity in the test was approximately 3.3kN/m^2, which compares well to the 3.64kN/m^2 predicted by *Vulcan* for the initiation of cracking. The predicted crack patterns in Figures 4.9 and 4.10 reflect the idealised yield line pattern for that of simply supported slabs. The development of the predicted crack patterns (bottom layer of concrete), Figure 4.9, compares very closely to the observed slab behaviour (Chapter 2).

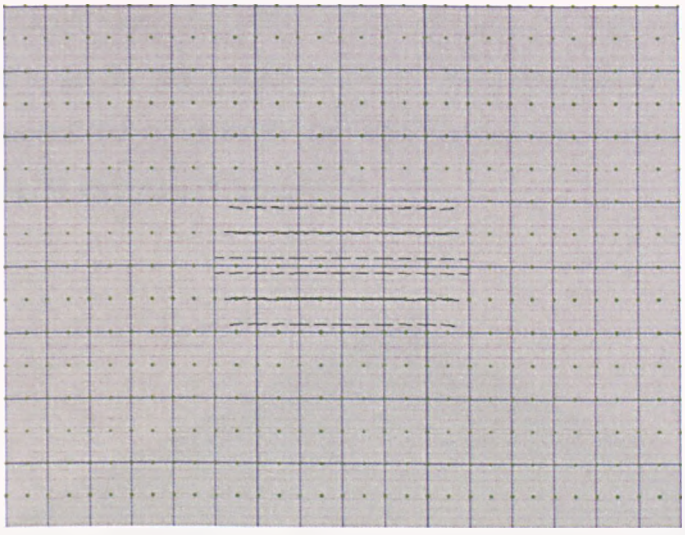

Figure 4.9: Test 2, crack pattern for bottom layer of slab (1150x550mm) at a load level of 3.72kN/m^2.

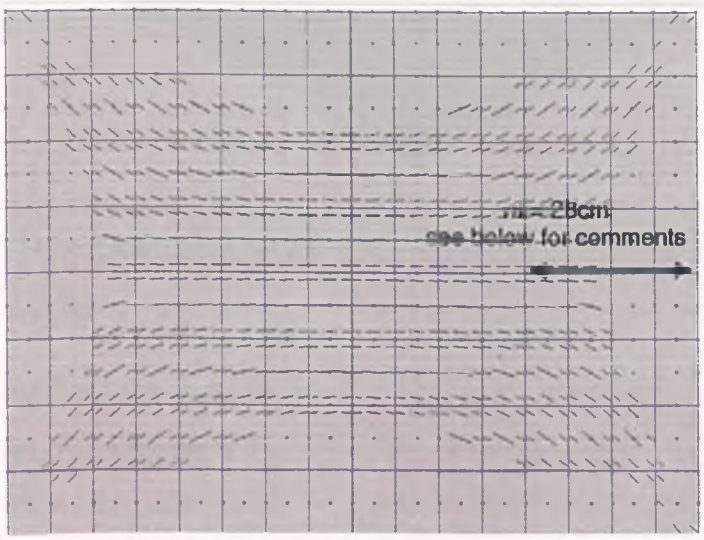

Figure 4.10: Test 2, crack pattern for bottom layer of slab (1150x550mm) at a load level of 4.96kN/m^2.

Comparing the predicted yield capacities attained in Test 2, Figures 4.9-4.10, with the theoretical yield capacity of 2.25kN/m^2, both *Vulcan* and Test 2 experimental results exceed these factors by 1.5 and 1.6 respectively. Figure 4.10 also shows the predicted distance of the hinge between the intersection of the diagonal yield line crack with the longitudinal yield line crack (*nL*), to be 28cm (to the edge of the slab). The theoretical calculations of *nL* (Chapter 2) gives 30.5cm, which closely tie in with the Vulcan predictions of *nL*.

Due to the computational time and effect of the modelling a full sized slab (1150x550 mm), it was decided to model one quarter of a slab. By using lines of symmetry, X-X and Z-Z, the full sized model slab (1150x550 mm) was divided into 4 equal quarters (575x275 mm), each containing 32 elements, Figure 4.11.

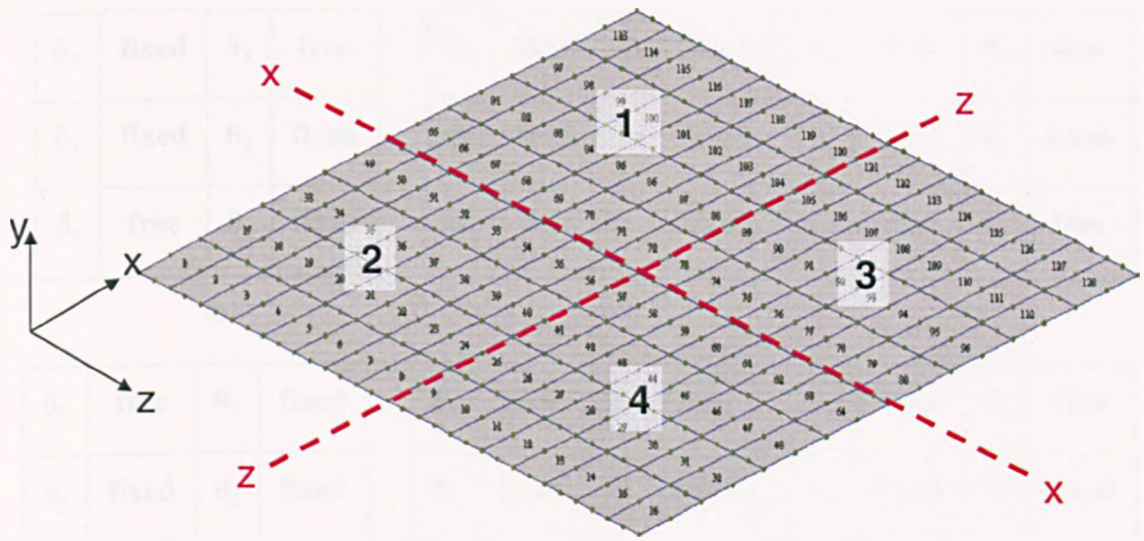

Figure 4.11: 3-D isometric view of full test slab (1150x550mm) with 128 elements.

The boundary conditions for Area 1 have to take into consideration the two lines of symmetry, X-X and Z-Z (Figure 4.11). The boundary conditions on these two lines of symmetry must allow the slab to move vertically but keep it fixed against moving horizontally across a symmetry line or rotating about it. At point (b) in Figure 4.12, where the two symmetry lines intersect, only vertical movement is allowed and all other rotations and movements are fixed. The edges of the slab were vertically supported by a steel frame,

but horizontal movement and rotation about the edges remained free. The boundary conditions for Area 1 are listed in Figure 4.12.

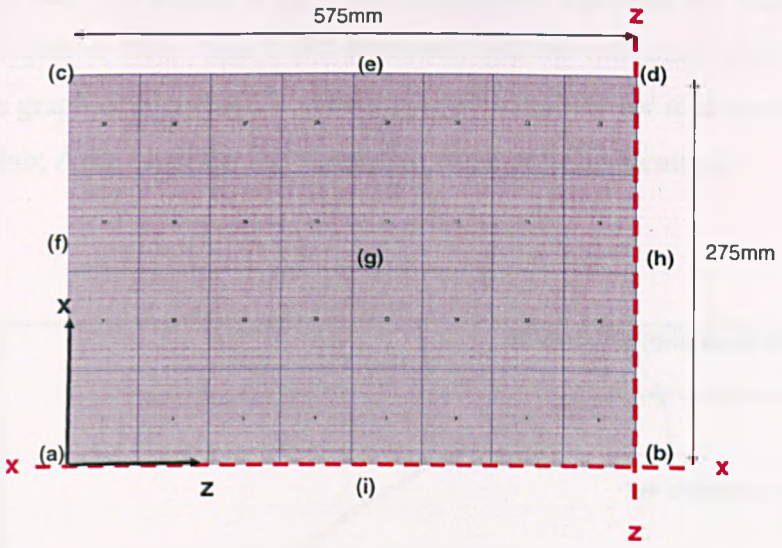

δ_x	fixed	θ_x	free
δ_y	fixed	θ_y	fixed
δ_z	free	θ_z	fixed

(a)

δ_x	fixed	θ_x	fixed
δ_y	fixed	θ_y	fixed
δ_z	free	θ_z	fixed

(b)

δ_x	free	θ_x	free
δ_y	fixed	θ_y	fixed
δ_z	free	θ_z	free

(c)

δ_x	free	θ_x	fixed
δ_y	fixed	θ_y	fixed
δ_z	fixed	θ_z	free

(d)

δ_x	free	θ_x	fixed
δ_y	fixed	θ_y	fixed
δ_z	free	θ_z	free

(e)

δ_x	free	θ_x	free
δ_y	fixed	θ_y	fixed
δ_z	free	θ_z	fixed

(f)

δ_x	free	θ_x	free
δ_y	free	θ_y	fixed
δ_z	free	θ_z	free

(g)

δ_x	free	θ_x	fixed
δ_y	free	θ_y	fixed
δ_z	fixed	θ_z	free

(h)

δ_x	fixed	θ_x	free
δ_y	free	θ_y	fixed
δ_z	free	θ_z	fixed

(i)

Figure 4.12: Boundary conditions for Area 1, quarter of a slab (525x275mm).

To validate using a quarter model (Area 1) in Figure 4.11 vertical displacements at point (b) of the concrete slab was compared with the vertical displacements at the centre point of the full-sized slab, see Figure 4.13. The comparison between the mid-span deflections given by the quarter slab; Area 1 (32 elements) and the full sized slab (128 elements) is shown in the graph of Figure 4.13. The predicted solutions for mid-span displacements of the quarter slab; Area 1 and the full sized slab are seen to be identical.

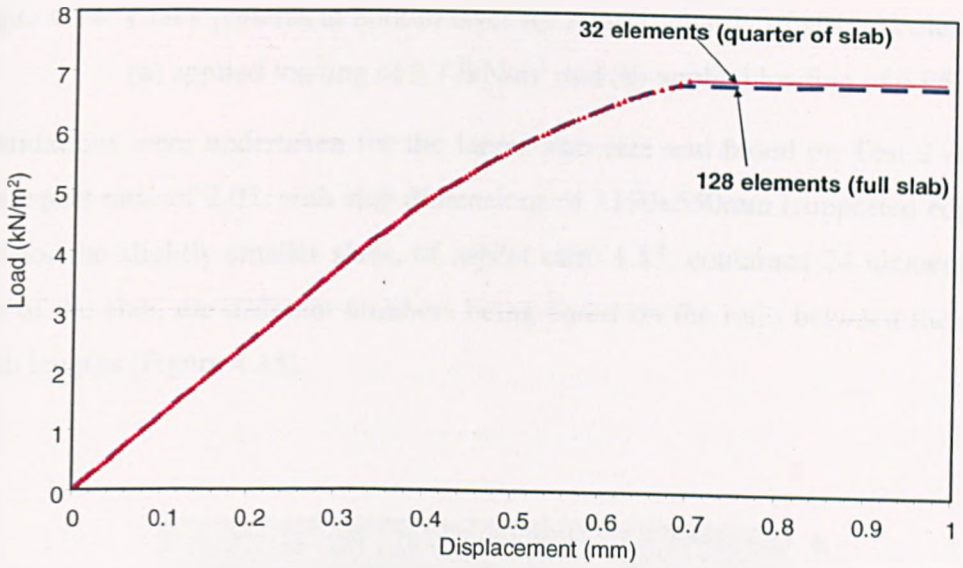

Figure 4.13: Comparison of the mid-span displacements for full size slab (1150x550 mm) and quarter size slab (575x275 mm) models.

The predicted crack patterns for the bottom layer of the quarter slab are presented in Figure 4.14 (a) and (b). It is shown that Area 1 shows identical development of crack patterns to those of the full size slab in Figures 4.9 and 4.10.

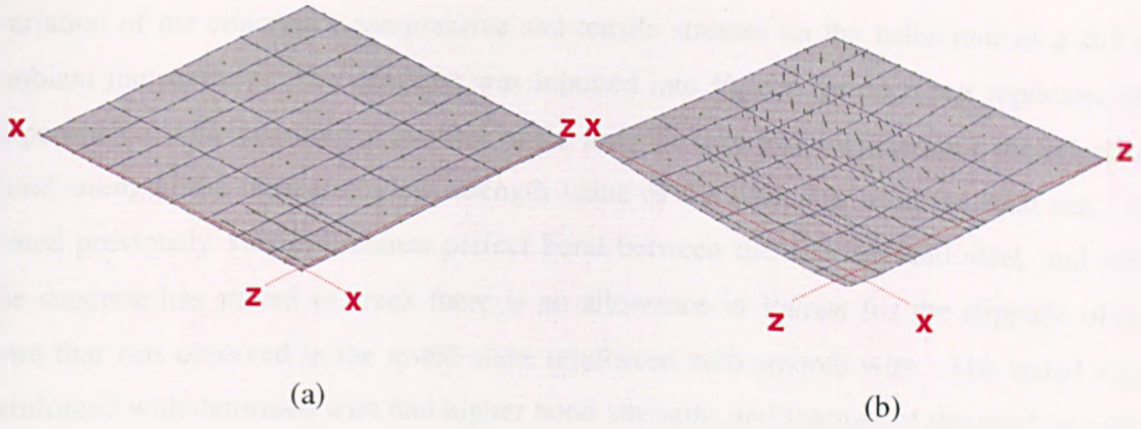

Figure 4.14: Crack patterns at bottom layer for Area 1, quarter of slab (32 elements) for (a) applied loading of 3.72kN/m^2 and (b) applied loading of 4.96kN/m^2.

The validations were undertaken for the larger slab size and based on Test 2 data which had an aspect ratio of 2.05, with slab dimensions of 1150x550mm (supported edges). The models for the slightly smaller slabs, of aspect ratio 1.55, contained 24 elements for one quarter of the slab, the different numbers being based on the ratio between the two areas and slab lengths (Figure 4.15).

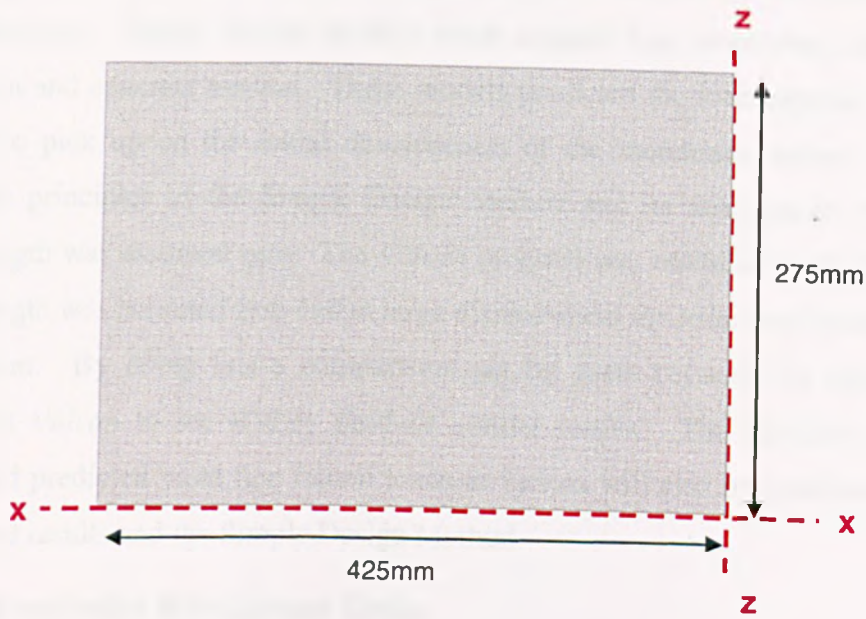

Figure 4.15: Representation of model slab of aspect ratio 1.55 using the symmetry case.

4.4 Results

This section presents the predicted results from *Vulcan* and the comparisons with the Simple Design Method and experimental data. The major objective of this work was to study the effects of orthotropic reinforcement on the slab behaviour and the effect of

variation of the concrete's compressive and tensile stresses on the behaviour of a slab at ambient temperature. The data that was inputted into *Vulcan* for each test replicated the experimental data measured at the time of the test. To take into consideration the effects of bond strength, the measured yield strength value of the wire was used for each test. As stated previously *Vulcan* assumes perfect bond between the concrete and steel, and once the concrete has started to crack there is no allowance in *Vulcan* for the slippage of the wire that was observed in the tested slabs reinforced with smooth wire. The tested slabs reinforced with deformed wire had higher bond strengths and fracture of the reinforcement progressed quickly after the initiation of cracking. It can be concluded that the tested slabs reinforced with deformed wire are more in line with *Vulcan*'s perfect bond assumptions.

As discussed in Chapter 3, bond strength is a function of several parameters, including material properties of concrete and the surface of the reinforcement. However, even though *Vulcan* cannot model bond slippage it can model with accuracy the overall sub-frame behaviour of a building.

The concrete tensile strength is not considered within the Simple Design Method, as the slab has formed the yield line cracks and the tension is carried by the reinforcement at large deflections. Initial *Vulcan* models were created that considered both concrete compression and concrete tension. These models predicted the load capacity of the slabs but failed to pick up on the initial development of the membrane action. In order to validate the principles of the Simple Design Method and its assumptions, the concrete tensile strength was assumed zero. The *Vulcan* program was modified so that the concrete tensile strength was assumed zero and at large displacement the tension to be carried by the reinforcement. By doing this a comparison can be made between the Simple Design Method and *Vulcan* to see if they produce similar results. The initiation of concrete cracking and predicted yield line failure loads in *Vulcan* will also be compared with both experimental results and the Simple Design Method.

4.4.1 Isotropically Reinforced Slabs

Using the validated finite element mesh in Figure 4.12, 3-D quarter models were created for Tests 2, 5, and 16. The material properties used in the models were based on data collected from each test (Table 4.1). The measured slab depth was used instead of the nominal slab depth to create a finite element model which was a true representation of the tested slabs. The experimental slabs were tested in a displacement-controlled rig, and the

resulting load resistance of the slab was plotted. In *Vulcan*, a uniform load of 8kN/m^2 was applied to the whole slab area and this was applied in a series of load increments of 0.04kN/m^2. The resulting load-deflection plots from *Vulcan* (full concrete model) and the modified version of *Vulcan* (*Vulcan 1*) which has zero concrete tension were compared with the experimental results and the Simple Design Method. Figure 4.16 shows the comparison between *Vulcan* and *Vulcan 1* with the experimental and simple theoretical results. The predicted crack patterns for the bottom layer of the slab have already been presented in Figure 4.14.

In Table 4.1, the concrete tensile strengths have been calculated for each test using the equation from tensile softening model that is used in *Vulcan*, Figure 4.3. On comparison of the predicted tensile strengths in Table 4.1 with the measured concrete tensile strengths of the sawn section tests in Chapter 3, the results of the predicted tensile strengths are within the same range and compare well.

Isotropically Reinforced Slabs.
Aspect Ratio = 2.09
(Spacing in long span 20mm, spacing in short span 20mm)

Test	Size (mm)	μ	t (mm)	fy (N/mm^2)	Bar Type	fc (N/mm^2)	ft (N/mm^2)	Yield line capacity (kN/m^2).
2	1150x550	1.0	20	265	Smooth	28	1.76	2.25
5	1150x550	1.0	18	258	Smooth	38	2.05	1.97
16	1150x550	1.0	15	240	Deformed	34	1.94	1.54
Aspect Ratio = 1.55								
Test	Size (mm)	μ	t (mm)	fy (N/mm^2)	Bar Type	fc (N/mm^2)	ft (N/mm$^{2)}$	Yield-line capacity (kN/m^2).
4	850x550	1.0	14	265	Smooth	16	1.33	1.81
10	850x550	1.0	19.5	256	Smooth	28	1.76	2.54
15	850x550	1.0	16	248	Deformed	25	1.66	1.99

Table 4.1: Isotropically reinforced slabs with aspect ratios 2.09 and 1.55

The peak load predicted by *Vulcan* in Figure 4.16 which incorporates the tensile strength of concrete is significantly higher than the peak load attained in the test. The *Vulcan* prediction dramatically increases from zero to 5.8kN/m^2 and the peak is approximately 1.5 times that of the peak load in the test (3.8kN/m^2). After this peak value has been reached

the *Vulcan* predictions do not follow the post peak behavior of the test results. As discussed in Chapter 3, once the peak load is reached, the slab which is cracked dramatically loses its stiffness and the load dramatically decreases. The load is then carried by the reinforcement. *Vulcan* cannot model this 'dramatic decrease in load' but shows the large loss of stiffness in the slab by the straight horizontal line, which can be seen in Figure 4.16.

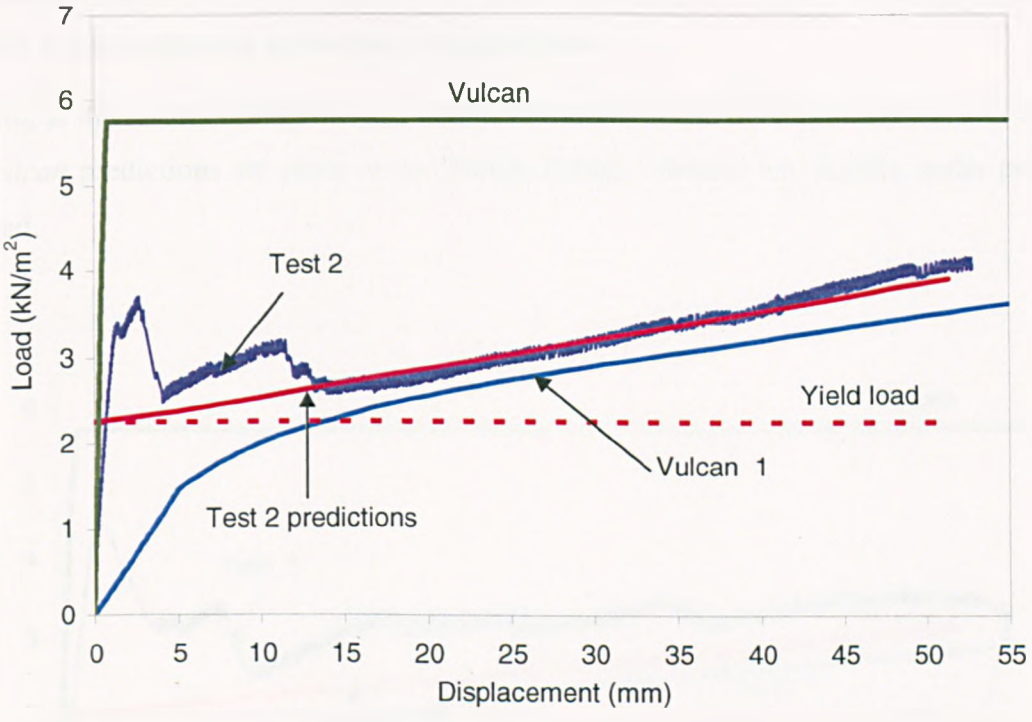

Figure 4.16: Comparison of Test 2 with *Vulcan* and the Simple Design Method.

The load predictions by *Vulcan 1*, which has zero concrete tension, shows no initial peak as the concrete is assumed to have cracked, however, the initial stage of when the slab in bending is not being investigated. The *Vulcan 1* plot does start to predict with some accuracy at slab displacements greater than 15mm and shows that the tension forces within the slab is being carried by the reinforcement. It is interesting to note that when the assumption of zero tensile strength is made in the analysis which is shown as *Vulcan* 1, the results are very close to the Simple Design Predictions but under predicts the load at any given displacement.

The peak load (5.8kN/m^2) attained in the *Vulcan* model which considers concrete tension, is approximately 1.5 times the peak load attained in the test (3.8kN/m^2). On comparison of

these results with the *Vulcan 1* predictions, which has zero concrete tensile strength, there is a large difference between the two *Vulcan* predictions when the slab is initially in bending. The *Vulcan* prediction, which considers concrete tension, seems to overestimate the load capacity of the slab and predict a much higher ultimate load than what the actual slab yields in the test.

It is also shown in Figure 4.16, that the yield line method under predicts the load capacity of a slab but this is due to the fact that the yield line method does not take into account the in-plane forces within the slab at large displacements.

Looking at the results in Figures 4.17 and 4.18, for the slabs in Tests 5 and 16, it is shown the *Vulcan* predictions are close to the Simple Design Method but slightly under predicts the load.

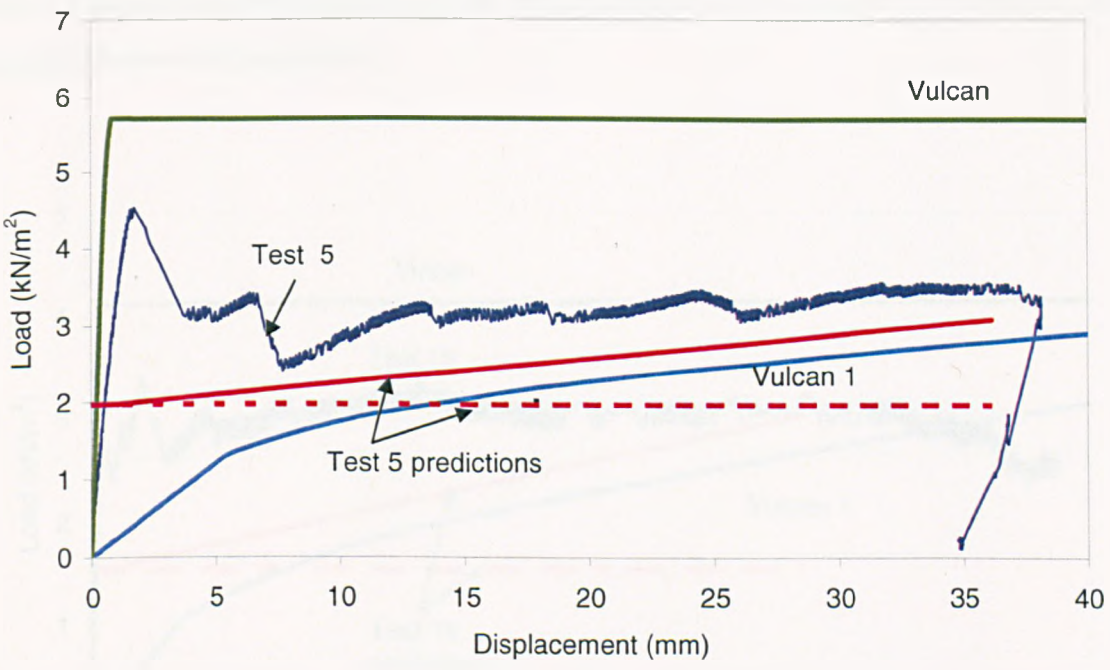

Figure 4.17: Comparison of Test 5 with *Vulcan* and the Simple Design Method.

The *Vulcan* prediction of the peak load in Test 5 is approximately 1.2 times the peak load achieved in the test. The peak load predicted by *Vulcan* in Test 5 is similar to that attained in Test 2, which seems surprising as Test 2 had a lower concrete strength. The only differences between these two slabs in Tests 2 and 5 were the thickness of the slab and type of reinforcement used.

Test 16 comparisons are shown in Figure 4.18. A peak load value of approximately 3.4kN/m^2 was achieved in the test with a resulting peak load predicted by *Vulcan* of approximately 4.2kN/m^2.

There could be a number of plausible reasons for the variation between the peak load attained in the test and that predicted by *Vulcan*, these could be:

1. The slab will have some initial micro cracks; these will develop under increasing load and weaken the slab.
2. The actual concrete tensile strength of the slab.

The *Vulcan 1* predictions in Test 16 under predict the load at any given displacement compared to the load estimated by the Simple Design Method, Figure 4.18. The type of wire used in Test 16 was deformed. The test slab did perform better than that predicted by *Vulcan 1* and the Simple Design Method, but at displacements in excess of 50mm the load decreased below the predictions.

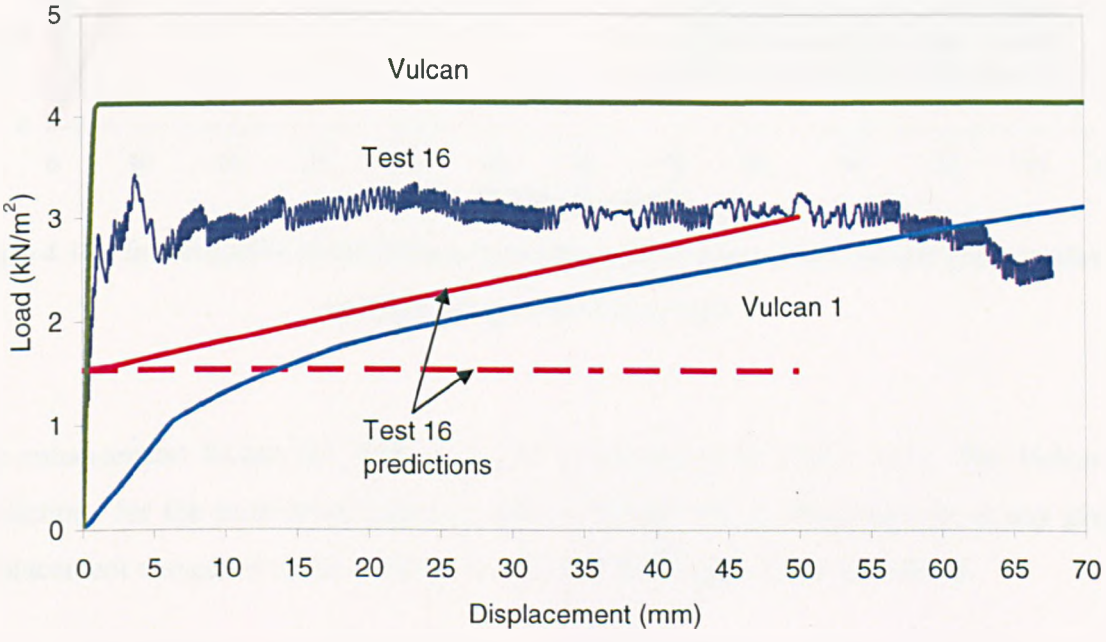

Figure 4.18: Comparison of Test 16 with *Vulcan* and the Simple Design Method.

A study was carried out using measured data from Test 16 to investigate the variation of the yield strength of the wire and the compressive and tensile strength of concrete, Figure 4.19. A range of concrete strengths were investigated from very low concrete compressions (F_{cube}=6N/mm^2) to the measured concrete strength on the day of the test as

well as the influence of the type of reinforcement used. The results of this study are presented in Figure 4.19. The parametric study undertaken showed that;

- At initial deflections, the concrete tensile strength is very important.
- At large deflections, the tensile strength of the reinforcement is important in deciding the load capacity of the slab.

The load-displacement curves shown in Figure 4.19 converges at large displacement which indicates that concrete strength does not affect the enhancement factor.

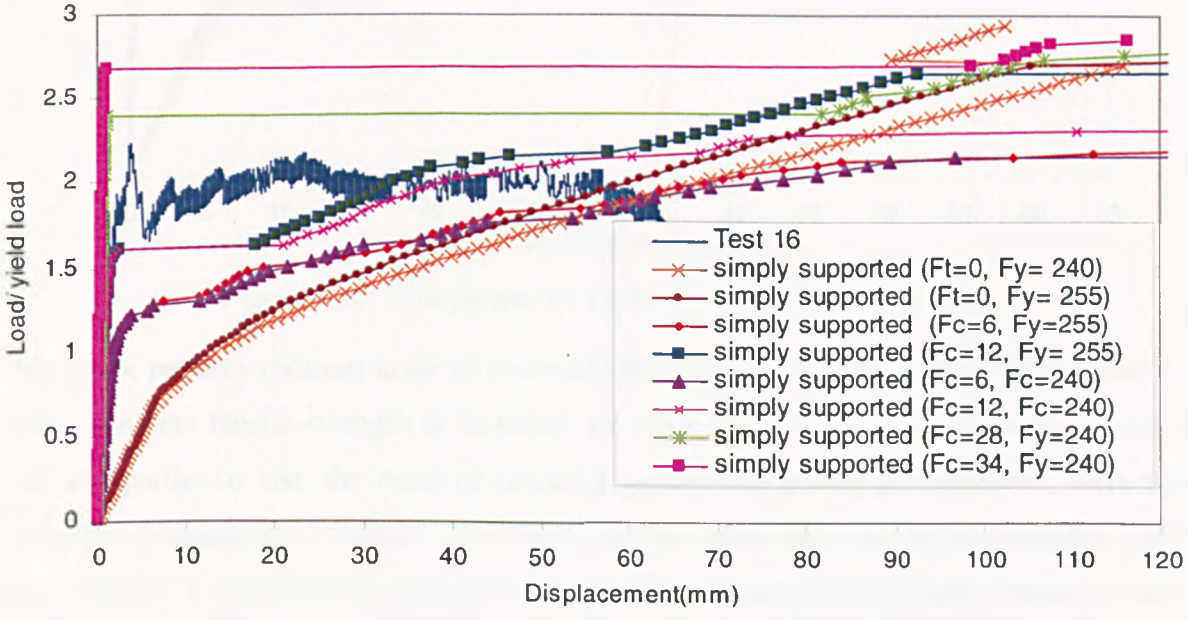

Figure 4.19: Investigation of the influence of the yield strength and concrete compressive strength using Test 16 test data.

The enhancement factors for Tests 2, 5 and 16 are shown in Figure 4.20. The *Vulcan* 1 predictions for the tests have shown to have achieved lesser enhancements at any given displacement compared to the predictions given by the Simple Design Method.

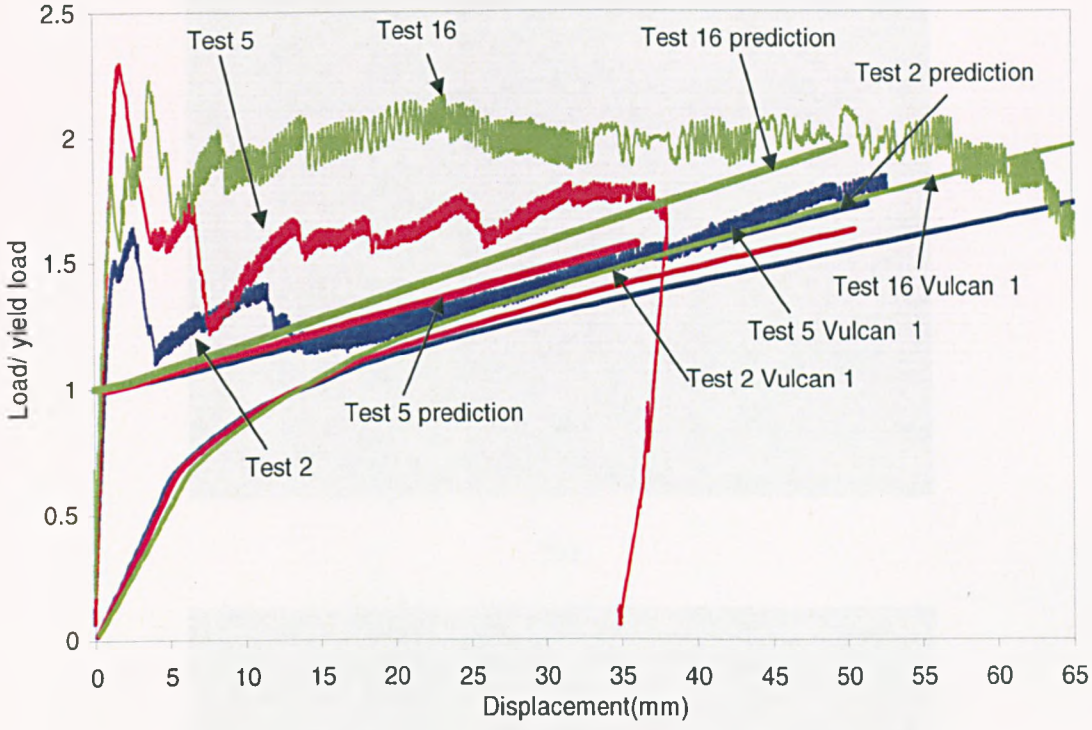

Figure 4.20: Comparison of Tests 2, 5 and 16 with *Vulcan*

The crack patterns (bottom layer of concrete) predicted by *Vulcan* for the slab in Test 5, when concrete tensile strength is included, are shown in Figure 4.21 at two load levels. For this particular test, the onset of cracking occurred at a load of 3.41kN/m^2, with the yield line forming at 5.76kN/m^2. The crack patterns once again reflect the idealised yield line pattern. It is evident from these results that the concrete tension failure criterion used in *Vulcan* predicts a higher ultimate load than that given in the tests, but both are considerably above the methods which neglect concrete tension.

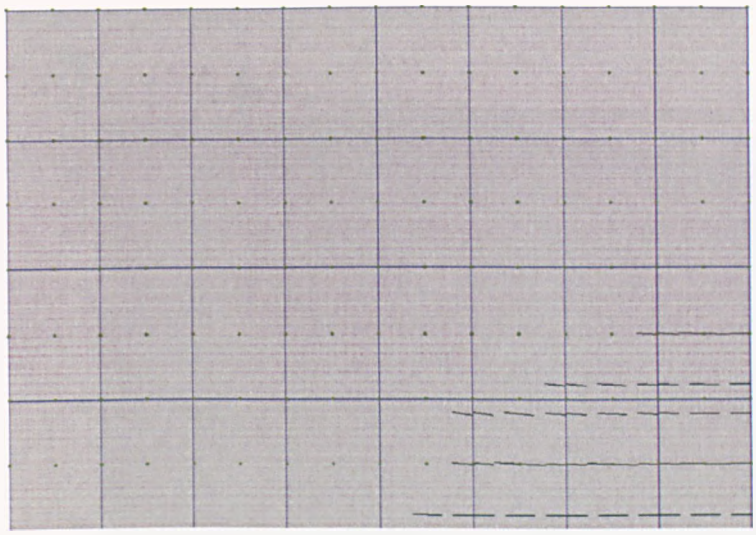

(a)

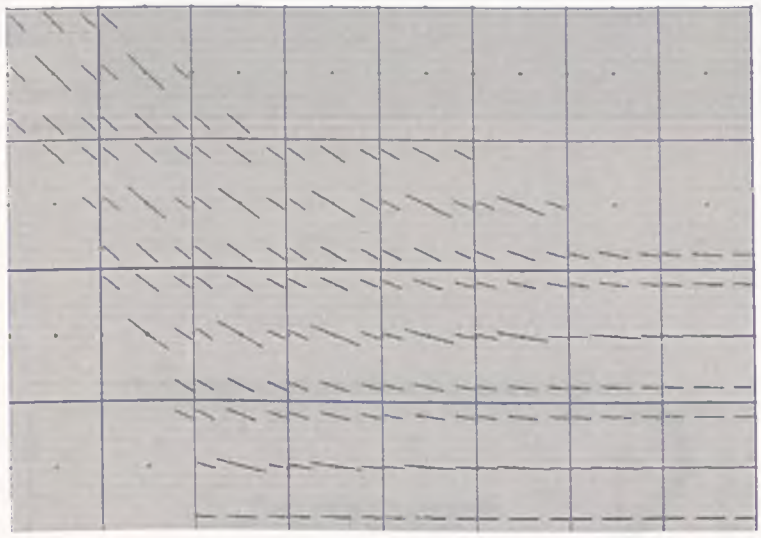

(b)

Figure: 4.20: Test 5 (quarter slab), bottom layer crack patterns for applied loads of (a) 3.73kN/m^2 and (b) 5.76kN/m^2.

The horizontal edge movements for the slab in Test 2 have been plotted and are shown in Figure 4.21. The edges of the slab move initially outwards then inwards. The edge parallel to the z-axis moves inwards by a horizontal distance of 4.5mm at a vertical mid-span displacement of 56mm. These horizontal edge movements tie in well with the observed slab movements at ambient temperature. As the slab edges move inwards, compression is observed to develop within the central zone (normal to the z-axis) of the slab, as the slab effectively shortens and 'jam' in the middle.

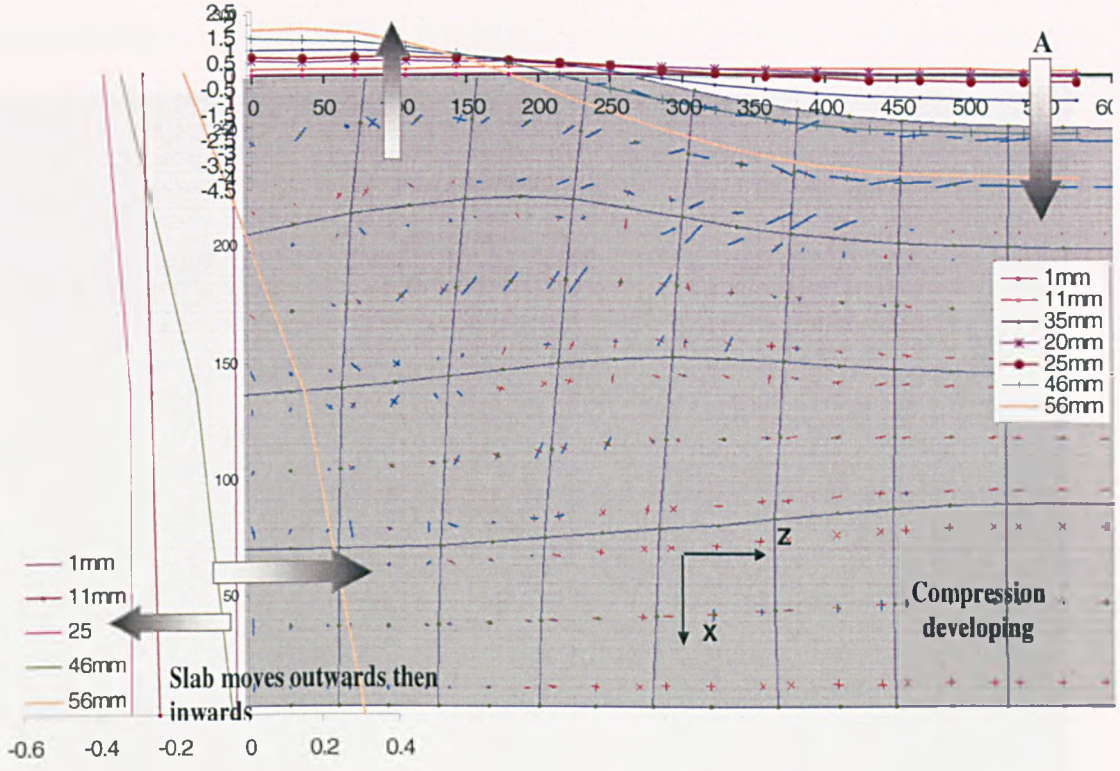

(a)

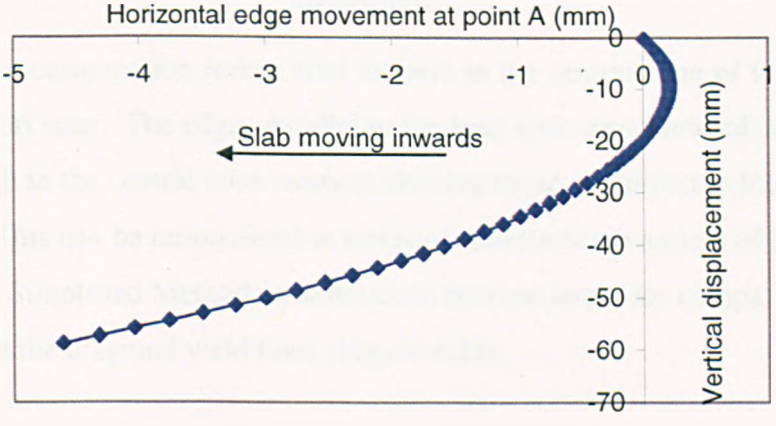

(b)

Figure 4.21: Test 2, (a) Horizontal movement at the edges for zero tensile strength, (b) Predicted edge movements at Point A by *Vulcan* (ft=0N/mm^2).

The distribution of the membrane forces for Test 2 is plotted for a mid-span displacement of 9.9mm at a load of 2kN/m^2, in Figure 4.22. The plot shows the development of tensile forces in the central zone of the slab with an outer compression ring around the peripheral

edges. The values of the membrane forces at each Gauss point are the average over the full depth of the slab.

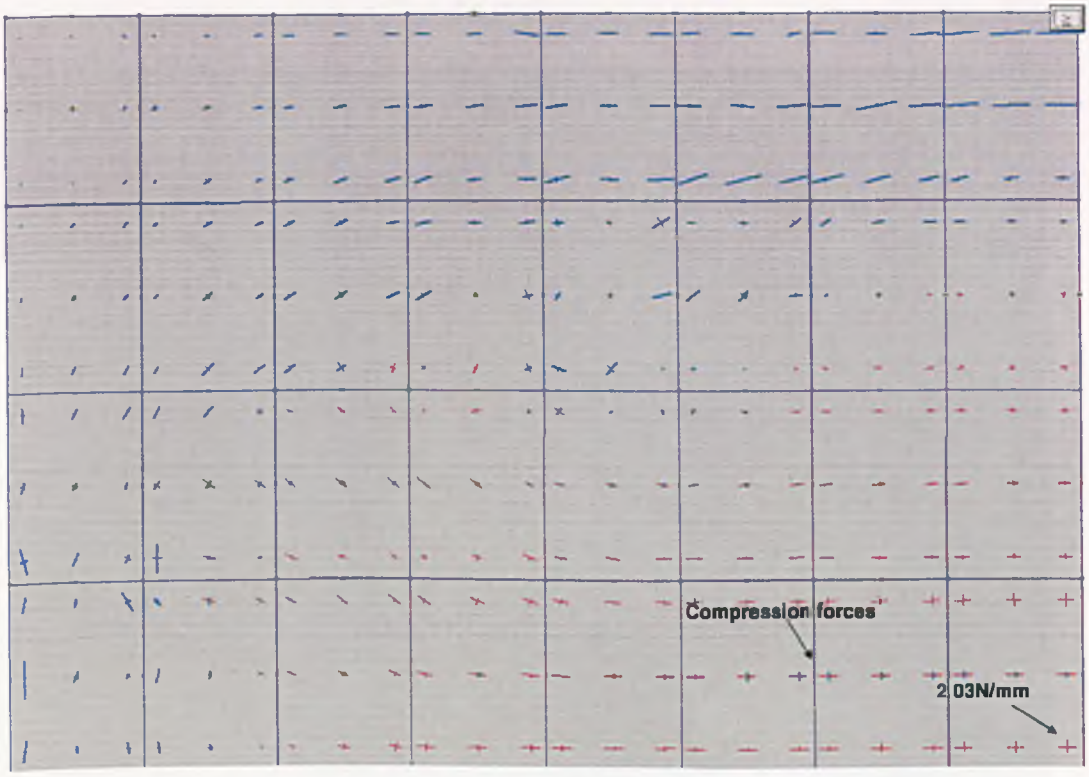

Figure 4.22: Test 2 (quarter slab) membrane tractions at 9.9mm deflection, load of 2kN/m^2 (ft=0N/mm^2).

It can be seen that compression forces start to form in the central zone of the slab quarter, parallel to the short span. The edges parallel to the long span move inwards and as the slab displaces, the slab in the central zone starts to develop these compressive forces as the slab starts to 'Jam'. This can be rationalised in terms of rotational movement of the trapezoidal slab facets in the Simplified Method as deflections become large, for compatibility with the triangular facet at the diagonal yield lines (Figure 4.23).

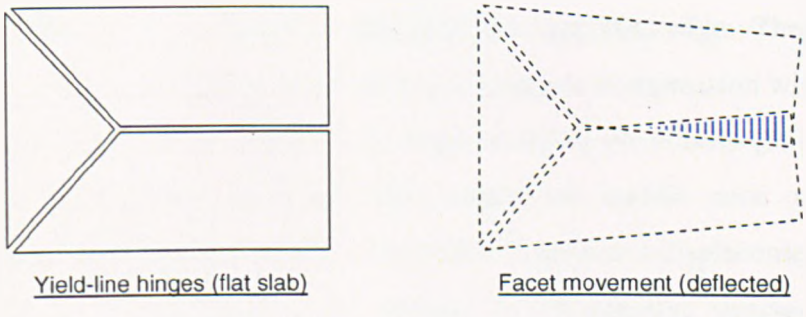

Figure 4.23: Schematic of development of transverse compression tractions.

Figure 4.24 shows the further development of the membrane tractions for Test 2 at a mid-span displacement of 33mm. The slab deflection is now at *span/17* and the compressive forces normal to the long span within the central region of the tension zone have increased.

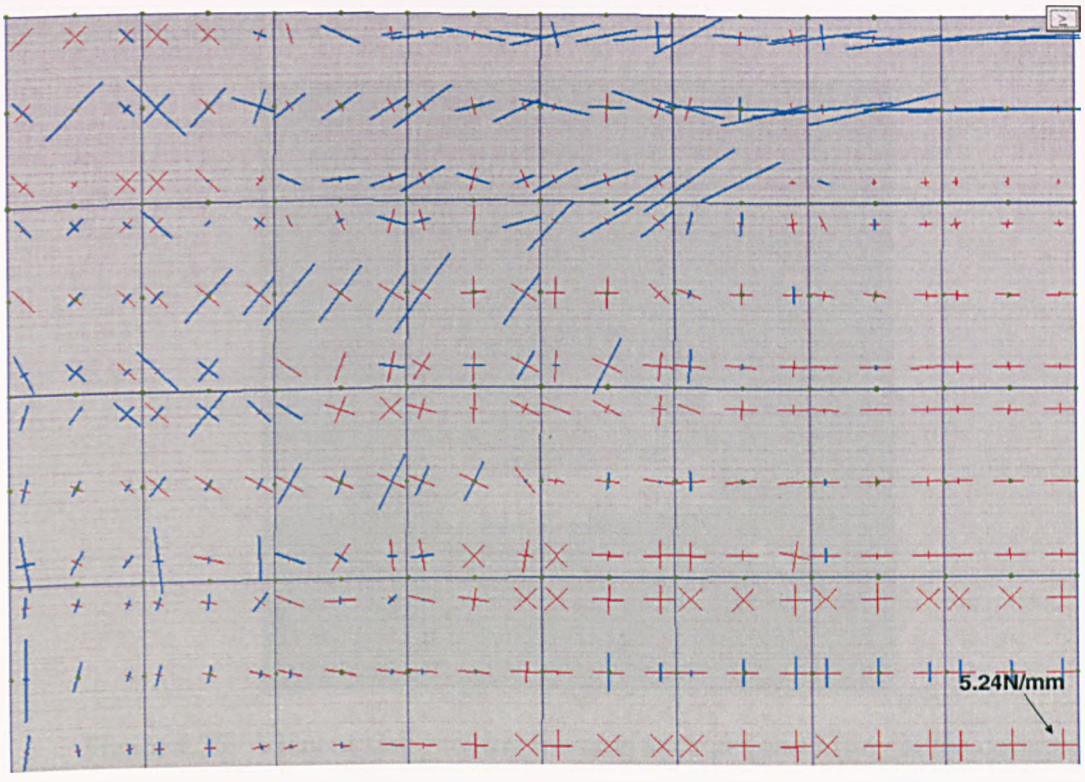

Figure 4.24: Test 2 (quarter slab), membrane tractions at 33mm deflection, load of 3kN/m^2 (f_t=0N/mm^2)

Comparing the membrane plot predictions with the Simple Design Method and the observed slab behaviour, the development of the compression forces within the central region of the slab is not taken into consideration within the existing Simple Design Method. It is also seen in Figures 4.23 and 4.24, the area of concrete that is in compression along the edge of the long span. As the applied load increases, the compression forces around the peripheral edges increases. The area of concrete in compression within the Simple Design Method is considered a point along the supported edge. Theoretical studies previously carried out have shown the inclusion of concrete compression within the Simple Design Method to have no significant effect on the resulting predictions [55]. However, by considering the development of compression within the middle zone of the slab, the resulting enhancements decrease by approximately 0.5 units at a displacement of 50mm, as the tensile stresses decrease due to the increase in compressive stresses. This is too conservative of an assumption to adopt within the BRE Simplified Method. The compressive forces start to develop once the slab has deflected and increase in magnitude

but the central zone is not fully 'in compression'. However, it seems that the Simplified Method is not representing the true slab behaviour.

Figure 4.25, shows the observed slab edge movements along the z-axis. The slab edges can be seen moving inwards.

Figure 4.25: View of slab moving inwards at centre and lifting at the corners.

Test 2, *Vulcan* predictions (ft=0N/mm^2) for the tensile membrane force normal to the long span at the mid-span of the slab gives values of 2.03N/mm at 9.9mm deflection and 5.24N/mm at 33mm deflection.

The *Vulcan* predictions with and without the inclusion of concrete tension for Tests 4, 10 and 15 are shown in Figures 4.26-4.28. The measured cube strength on the day of Test 4 was 16N/mm^2. The slab thickness was measured at 14mm (Table 4.1) which resulted in a lower yield line capacity. It is shown in Figure 4.26 that because of the lower concrete strength, the *Vulcan* model which incorporates concrete tension, recovers and the load capacity of the slab increases as the load is carried by the reinforcement.

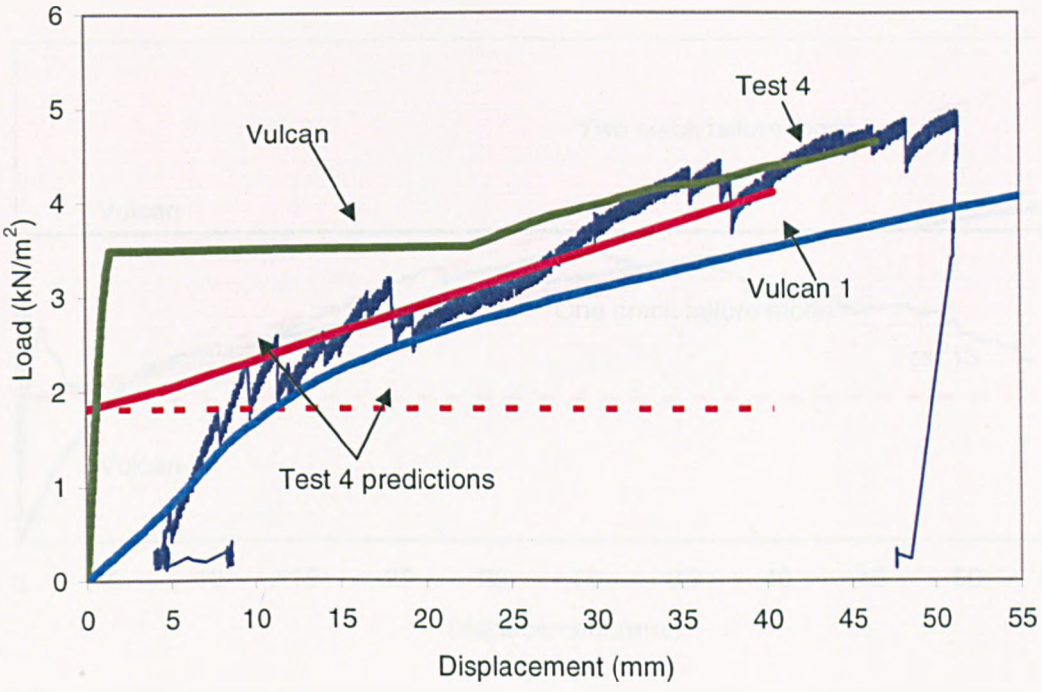

Figure 4.26: Comparison of Test 4 with *Vulcan* and the Simple Design Method.

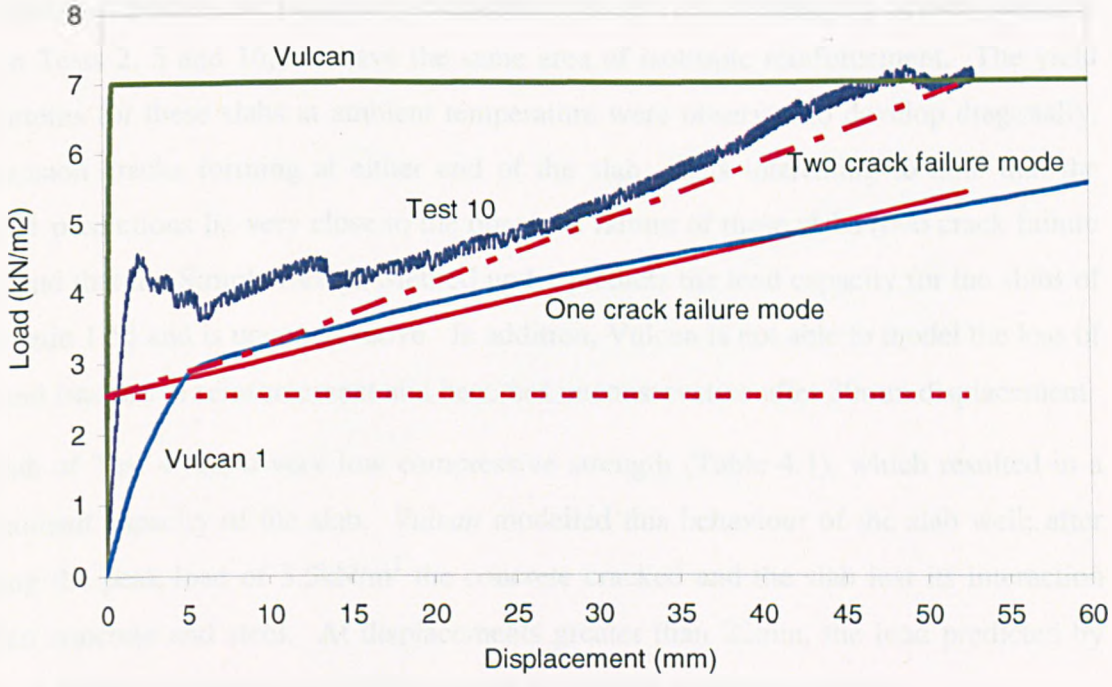

Figure 4.27: Comparison of Test 10 with *Vulcan*, the Simple Design Method and the new failure criteria.

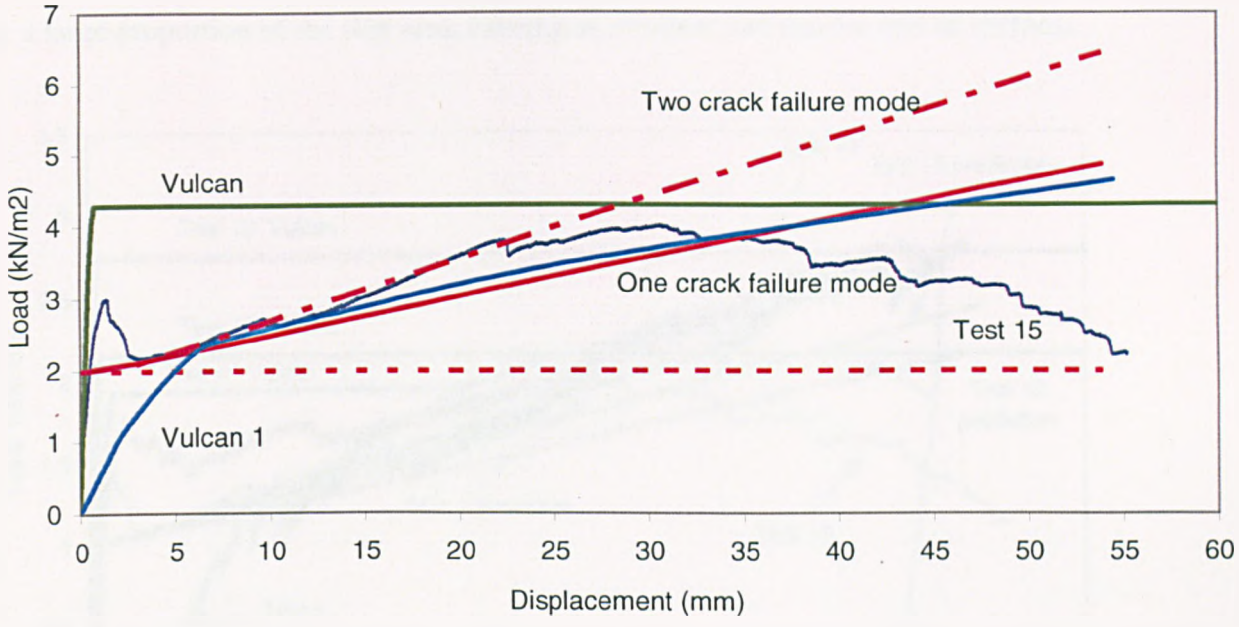

Figure 4.28: Comparison of Test 15 with *Vulcan*, the Simple Design Method and the new failure criteria.

The slabs in Figures 4.26-4.28, have an aspect ratio of 1.55, so they are squarer than the slabs in Tests 2, 5 and 16, but have the same area of isotropic reinforcement. The yield line patterns for these slabs at ambient temperature were observed to develop diagonally, with tension cracks forming at either end of the slab. It is interesting to note that the *Vulcan* 1 predictions lie very close to the observed failure of these slabs (two crack failure mode) and that the Simple Design Method under predicts the load capacity for the slabs of aspect ratio 1.55 and is unconservative. In addition, Vulcan is not able to model the loss of bond and fracture of reinforcement and becomes unconservative after 30mm displacement.

The slab of Test 4 had a very low compressive strength (Table 4.1), which resulted in a low moment capacity of the slab. *Vulcan* modelled this behaviour of the slab well; after reaching the peak load of 3.5kN/m^2 the concrete cracked and the slab lost its interaction between concrete and steel. At displacements greater than 22mm, the load predicted by *Vulcan 1* started to increase as the slab started to develop membrane action.

Figures 4.29 and 4.30, shows the comparison between these three tests and the *Vulcan* cases including and neglecting concrete tension. The graphs show that *Vulcan* modelled the tests with some accuracy in either case; removing concrete tensile strength tends to produce lower-bound solutions. Its inclusion produces a more complex relationship, with a sudden loss of strength which does not recover within the practical range of displacements;

this is essentially a modelling issue caused by the simultaneous appearance of cracking over a large proportion of the slab area, causing an extreme and sudden loss of stiffness.

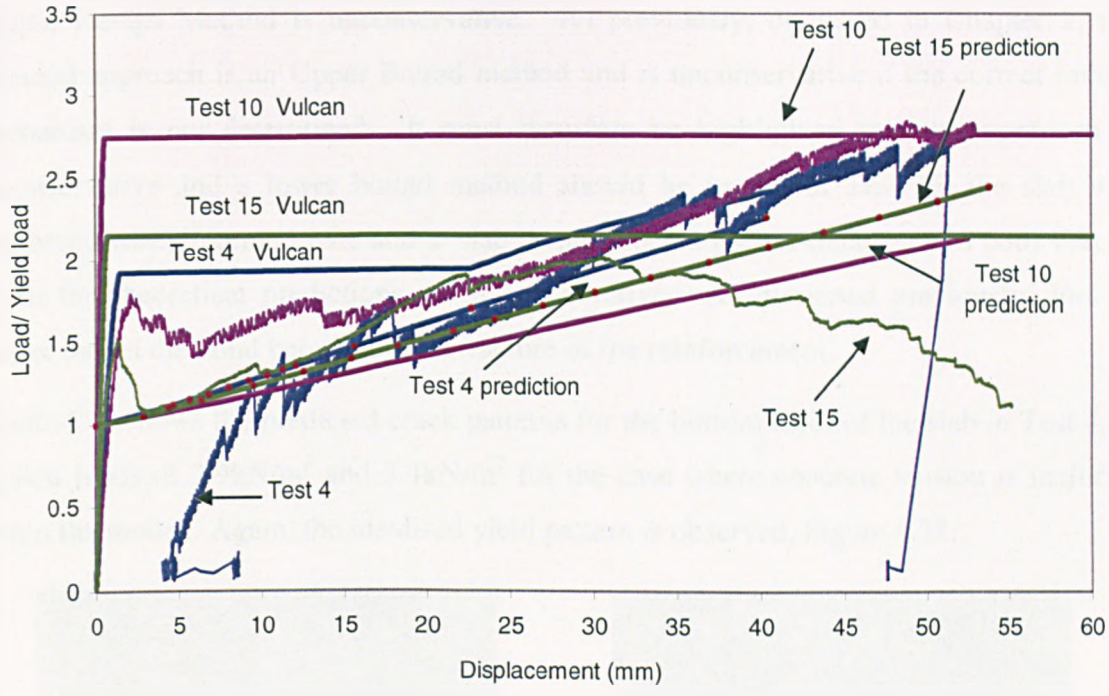

Figure 4.29: Comparison of test results with *Vulcan* and Simple Design Method.

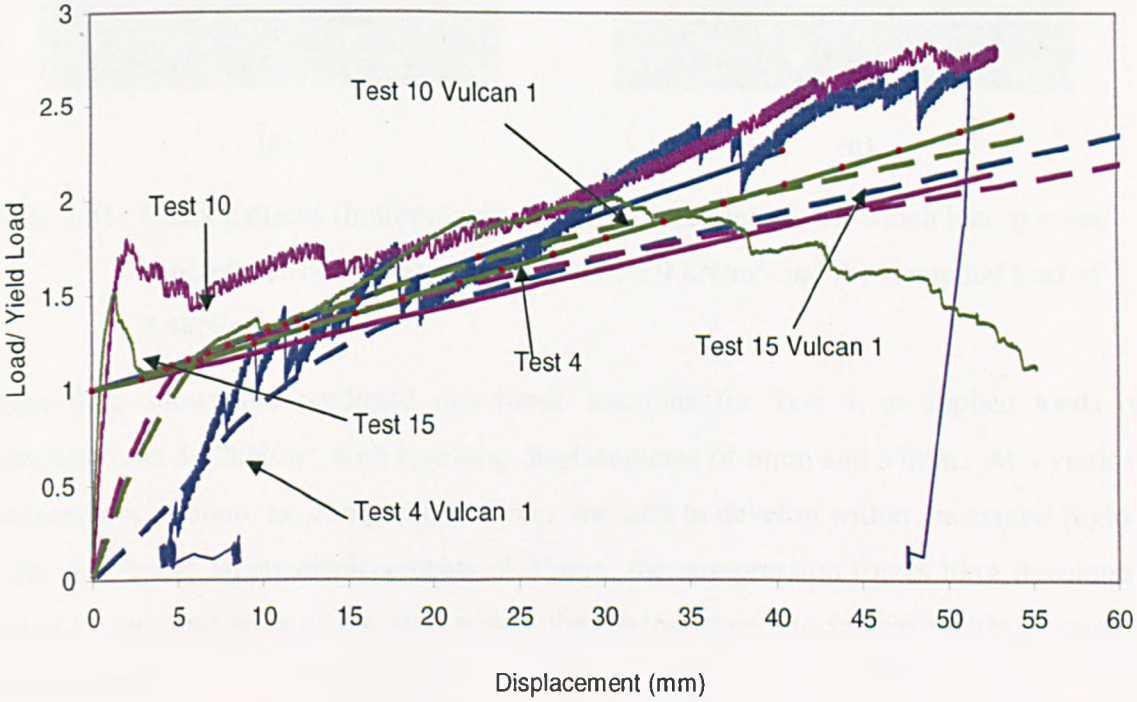

Figure 4.30: Comparison of test results with *Vulcan* 1 (zero concrete tensile strength) and Simple Design Method.

Figure 4.30 shows that for the slabs reinforced with smooth wire, the predictions by *Vulcan* and the simple method are conservative and under predict the test results. The results also show that the correct mode of failure must be predicted, if it is not as shown here, the Simple Design Method is unconservative. As previously, discussed in Chapter 2, the assumed approach is an Upper Bound method and is unconservative if the correct failure mechanism is not determined. It must therefore be highlighted that this approach is unconservative and a lower bound method should be used. In Test 15, the slab was reinforced with deformed wire and at slab displacements greater than *span/18* both *Vulcan* 1 and the theoretical predictions are unconservative. As discussed previously, *Vulcan* cannot model the bond behaviour and fracture of the reinforcement.

Figure 4.31 shows the predicted crack patterns for the bottom layer of the slab in Test 4, at applied loads of 2.9kN/m^2 and 3.4kN/m^2 for the case where concrete tension is included within the model. Again, the idealised yield pattern is observed, Figure 4.31.

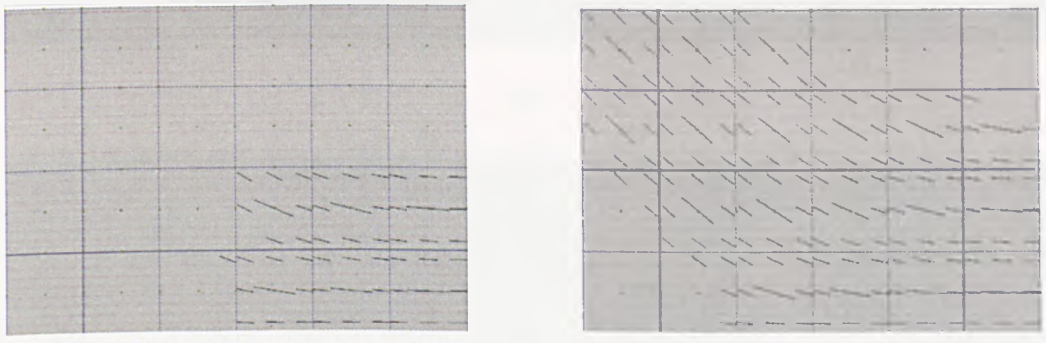

(a) (b)

Figure 4.31: Crack patterns (bottom layer of slab) for quarter of slab which incorporates concrete tension (a) at applied load of 2.9 kN/m^2 and (b) at applied load of 3.4kN/m^2.

Figure 4.32 shows the predicted membrane tractions for Test 4, at applied loads of 1.08kN/m^2 and 3.32kN/m^2, with resulting displacements of 6mm and 35mm. At a vertical displacement of 6mm, no compression forces are seen to develop within the central region of the slab but at larger displacements of 35mm, the compression forces have developed normal to the long span of the slab within the central zone and increase with increasing displacement.

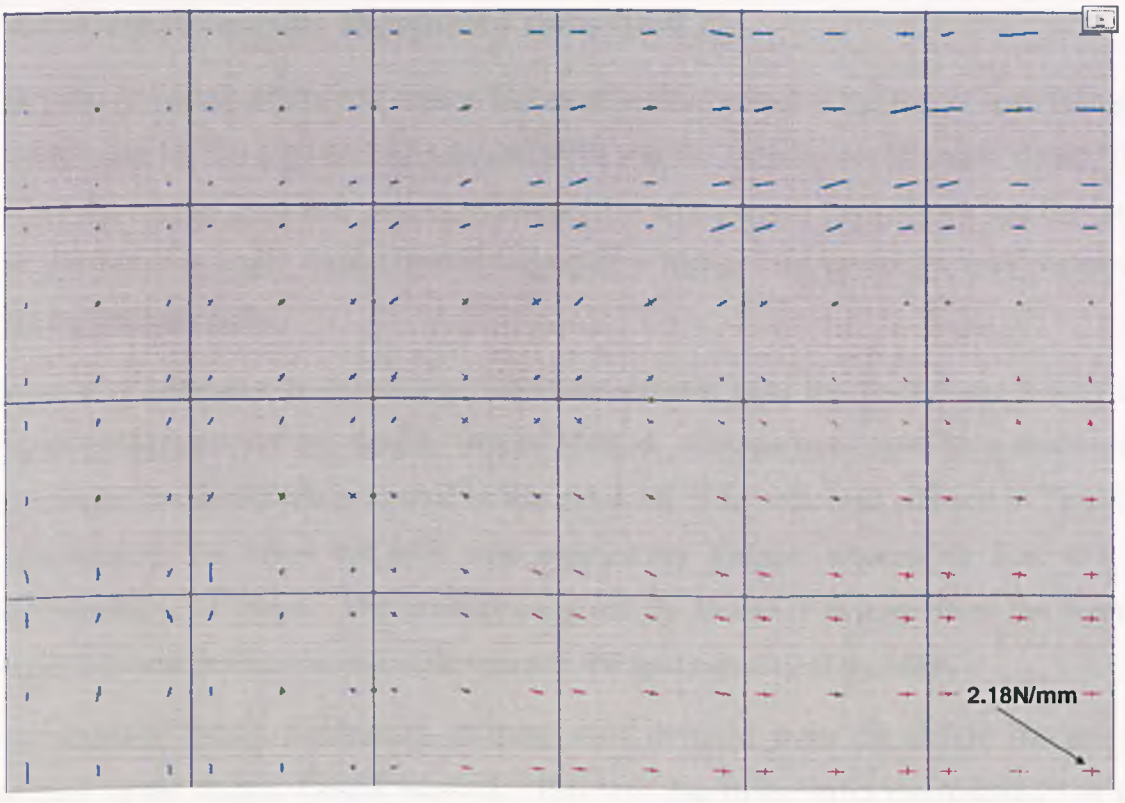

(a)

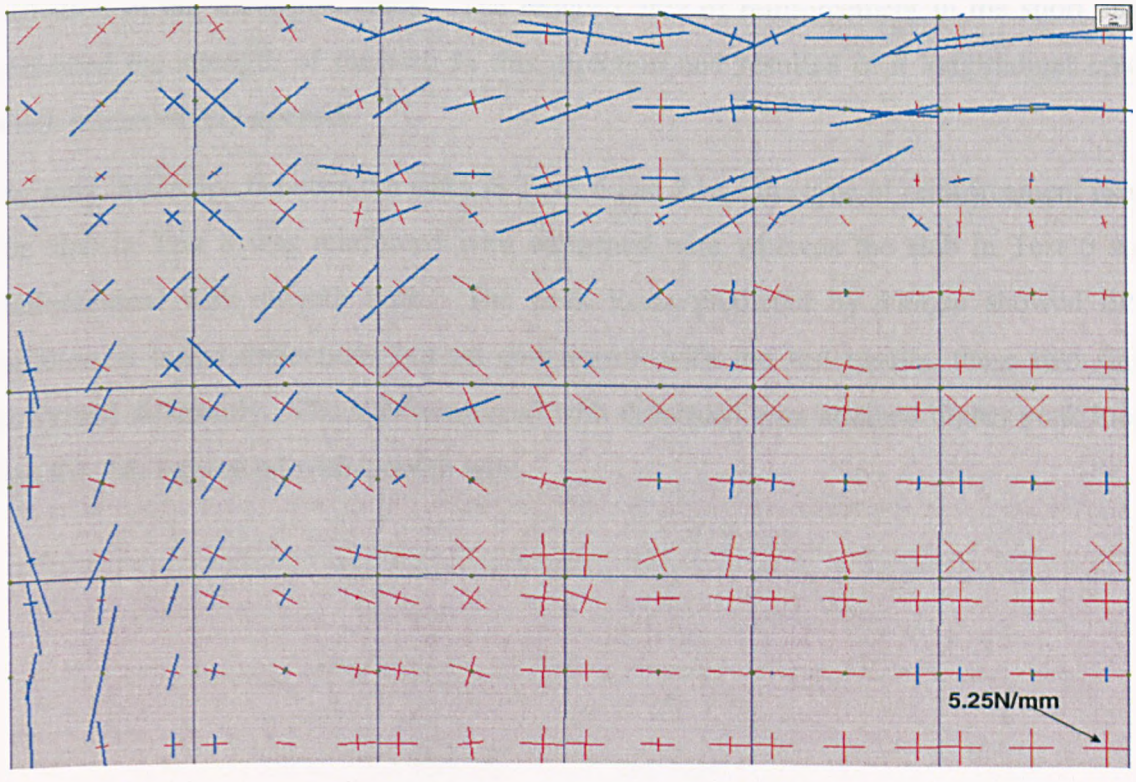

(b)

Figure 4.32: Distribution of membrane tractions at (a) an applied load of 1.08kN/m^2 and (b) an applied load of 3.32kN/m^2.

4.4.2 Orthotropically Reinforced slabs (μ=0.2)

The slabs presented within this section had more reinforcement in the longer span than the shorter span, but the total area of reinforcement was the same as the isotropic slabs. The test results for this particular type of reinforcement arrangement have shown that the slabs perform better at larger displacements and achieve higher load capacities than compared with the isotropic slabs.

Figure 4.33 compares the normalised load-displacement plots for Tests 6 and 8 with the *Vulcan* predictions and the Simple Design Method. Comparisons have been made with *Vulcan* and the results are presented in Figures 4.33. The peak load attained in Test 8 is approximately 1.6 times the peak load attained by *Vulcan,* whereas in Test 6 it is approximately 1.1 times. The predictions given by *Vulcan* 1 diverge from the Simple Design Method predictions and underestimate the load capacity of the slabs.

The observed failure mechanism in these tests deviated from the failure mechanism assumed in the Simple Design Method. This was due to the extra reinforcement in the longer span strengthening the slab in this particular direction which resulted in no formation of the transverse crack. The reduced area of reinforcement in the short span weakened the strength of the slab in this direction and resulted in a longitudinal crack which progressively opened.

The only difference between the slabs in Tests 6 and 8 was the type of reinforcement used. The slab in Test 8 was reinforced with deformed wire whereas the slab in Test 6 was reinforcement with smooth wire. The peak loads predicted by *Vulcan* showed little variation at initial deflections but on comparison with the test results, these two slabs performed differently. The slab reinforced with deformed wire attained higher peak loads than the slab reinforced with smooth wire.

Orthotropically reinforced slabs. Aspect Ratio = 2.09 (Spacing in long span 12mm, spacing in short span 60mm)										
Test	Size (mm)	μ	t (mm)	fy (N/mm^2)	Bar Type	fc (N/mm^2)	ft (N/mm^2)	dx (mm)	dy (mm)	Yield-line capacity (kN/mm^2)
6	1150×550	0.2	18	262	Smooth	38	2.05	8.65	8.29	1.23
8	1150×550	0.2	18.5	242	Deformed	35	1.96	8.4	8.04	1.10

Table 4.2: Orthotropically reinforced slabs of aspect ratio 1.55.

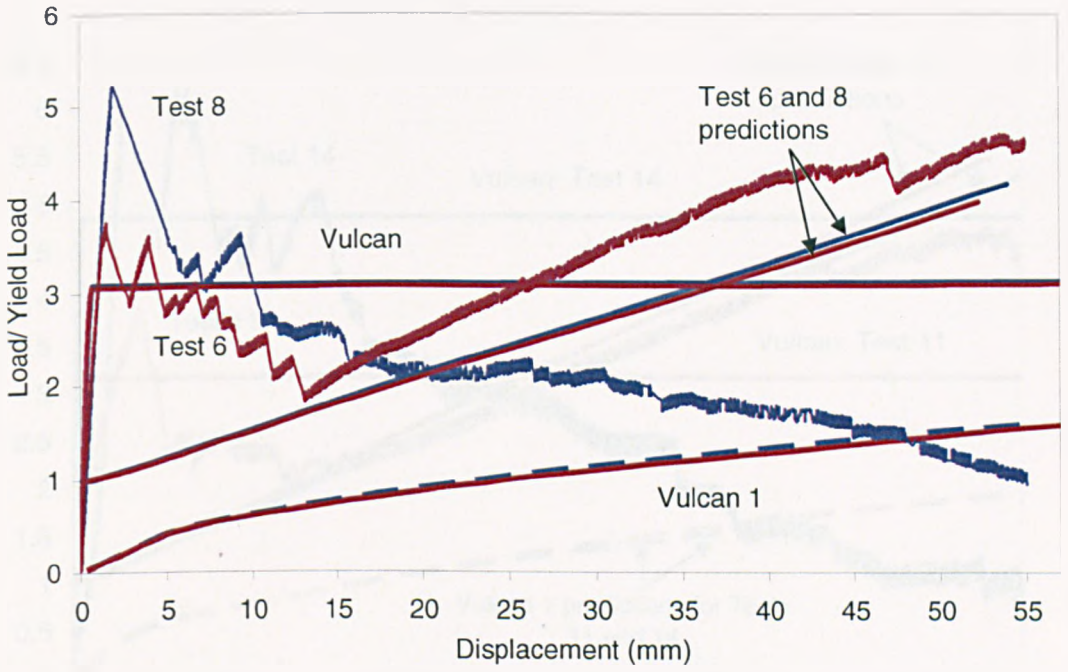

Figure 4.33: Comparison of Tests 6 and 8 with *Vulcan* and the Simple Design Method.

The results presented in Figure 4.34 reinforces the theory presented earlier that when the slab is in bending (small vertical deflections), the slab behaviour is dominated by the slab's concrete tensile strength. At vertical displacements greater than *span/30*, the slab's behaviour is dominated by the tensile strength and type of reinforcement used.

Orthotropically reinforced slabs. Aspect Ratio = 1.55 (Spacing in long span 12mm, spacing in short span 60mm)										
Test	Size (mm)	μ	t (mm)	fy (N/mm^2)	Bar Type	fc (N/mm^2)	ft (N/mm^2)	dx (mm)	dy (mm)	Yield-line capacity (kN/mm^2)
11	850×550	0.2	14	260	Smooth	36	1.99	6.65	6.29	1.31
14	850×550	0.2	15	255	Deformed	`41	2.13	7.15	6.79	1.39

Table 4.3: Orthotropically reinforced slabs of aspect ratio 1.55.

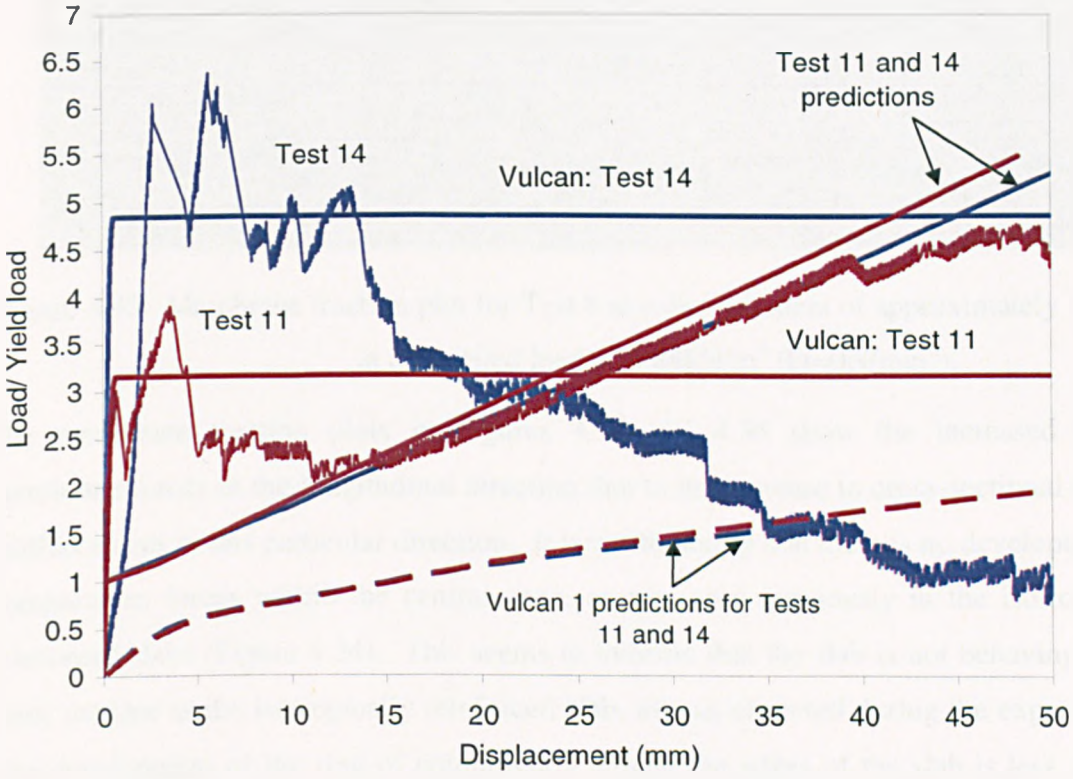

Figure 4.34: Comparison of Tests 11 and 14 with *Vulcan* and the Simple Design Method.

The membrane traction plot for Test 8 is shown in Figure 4.35 for a mid-span displacement of approximately 15mm. The traction plots are very different from that of Tests 2 and 4, which were reinforced with isotropic reinforcement.

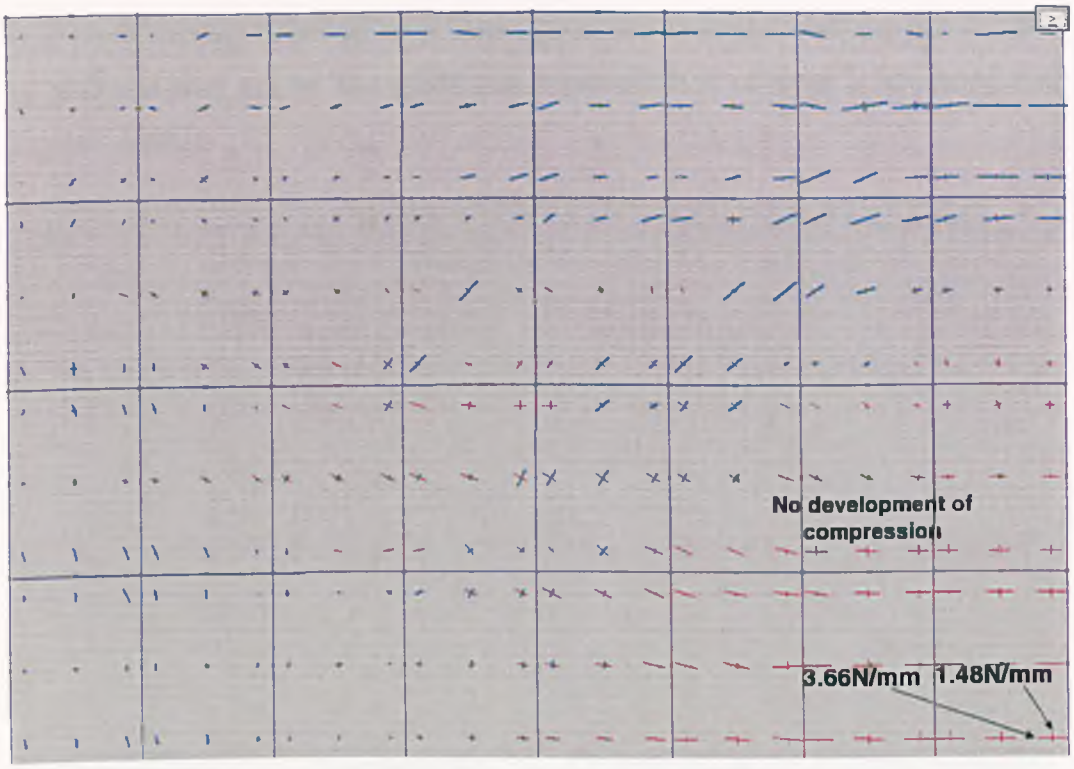

Figure 4.35: Membrane traction plot for Test 8 at a displacement of approximately 15mm at an applied load of 0.88kN/m^2 (Ft=0N/mm^2).

The membrane traction plots in Figures 4.35 and 4.36 show the increased tensile membrane forces in the longitudinal direction due to the increase in cross-sectional area of reinforcement in this particular direction. It is worth noting that there is no development of compression forces within the central zone, as was seen previously in the isotropically reinforced slabs (Figure 4.24). This seems to indicate that the slab is not behaving in the same manner as the isotropically reinforced slab, as was observed during the experiments. The development of the ring of compression around the edges of the slab is less defined and there are compression forces that have developed diagonally across the quarter slab, Figure 4.36. Possible reasons for these diagonals of compression could be:

1. A slab reinforced with this particular reinforcement arrangement develops no transverse crack across the short span of the slab. Therefore, the slab behaviour under increasing displacement is different. For isotropic slabs, the slab segment rotates in plane and 'jams' in the middle which causes compression forces to occur. For these types of orthotropic slabs, due to absence of the transverse crack there will be no 'jamming' of the slabs within the middle of the slab hence no development of compressive forces. The slab behaviour is different.

2. The membrane forces at each Gauss point are averaged over the full depth of the slab and may not be an overall true representation of what is occurring over the slab depth.

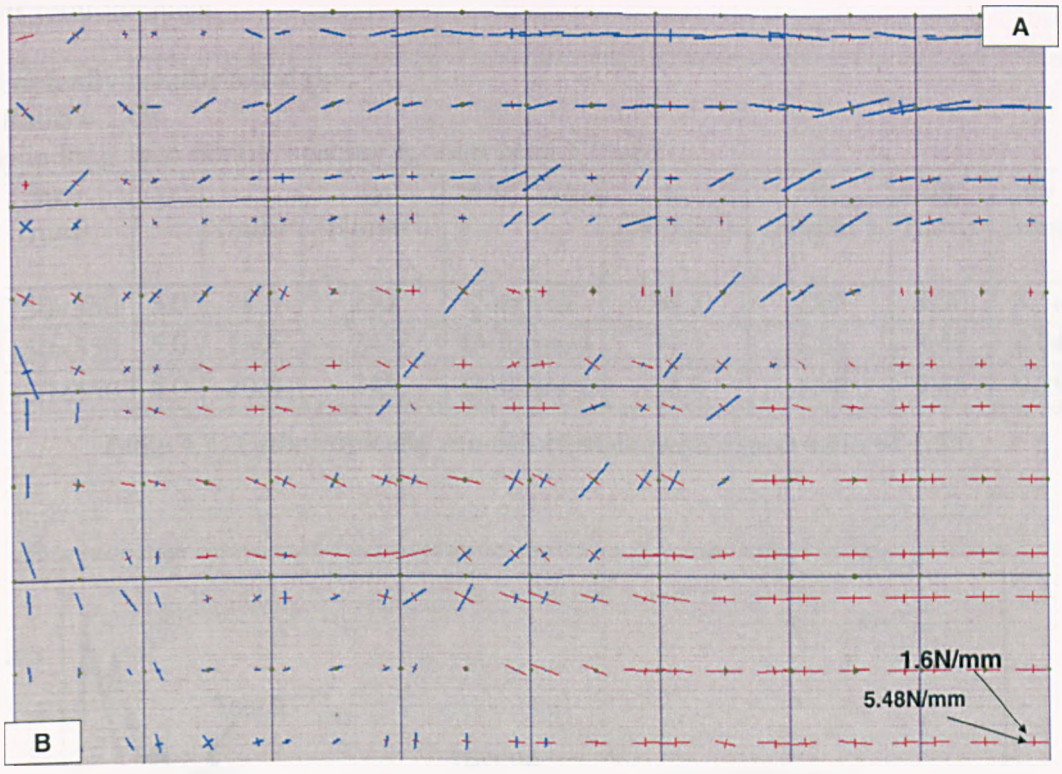

Figure 4.36: Membrane traction plot for Test 8 at a displacement of approximately 27mm at an applied load of 1.2kN/m^2 (Ft=0N/mm^2).

4.4.3 Orthotropically Reinforced Concrete Slabs (μ=5.0)

The slabs in these tests had more reinforcement across the short span (μ=5.0), which gave an initial increase in the yield-line moment resistance capacity of the slab. Figures 4.37-4.38 show the comparisons between the results of these tests with the Simple Design Method and *Vulcan*. It is interesting that, at small deflections when the slab is initially in bending, the increase in reinforcement across the short span increases the slab resistance; this is shown in Figure 4.37, for the *Vulcan* 1 predictions. Comparing this with the plot for orthotropic slabs with μ=0.2 (Figure 4.33) the initial enhancements were much lower for these slabs in comparison with the orthotropic slabs of μ=5.0. The enhancement factors in Figure 4.37 for *Vulcan* 1 (ignoring concrete tensile strength) are close to those predicted by the Simple Design Method and the test results. They also increase at a similar rate, as is verified in Figure 4.38.

The slabs reinforced with deformed wire behaved similarly to Tests 9 and 9A, in that progressive failure of the slab occurred after formation of the yield cracks. The mechanism of failure for these slabs was the opening of the transverse crack and fracture of this reinforcement.

Orthotropically reinforced slabs.
Aspect Ratio = 2.09
(Spacing in long span 60mm, spacing in short span 12mm)

Test	Size (mm)	μ	t (mm)	fy (N/mm^2)	Bar Type	fc (N/mm^2)	ft (N/mm^2)	dx (mm)	dy (mm)	Yield-line capacity (kN/mm^2)
7	1150×550	5.0	18.5	252	Smooth	38.2	2.05	8.90	8.54	2.45
9	1150×550	5.0	17.5	245	Deformed	31.5	1.86	8.40	8.04	2.24
9A	1150×550	5.0	20.0	245	Deformed	32.6	1.90	9.65	9.29	2.58

Table 4.4: Orthotropically reinforced slabs with aspect ratio of 1.55.

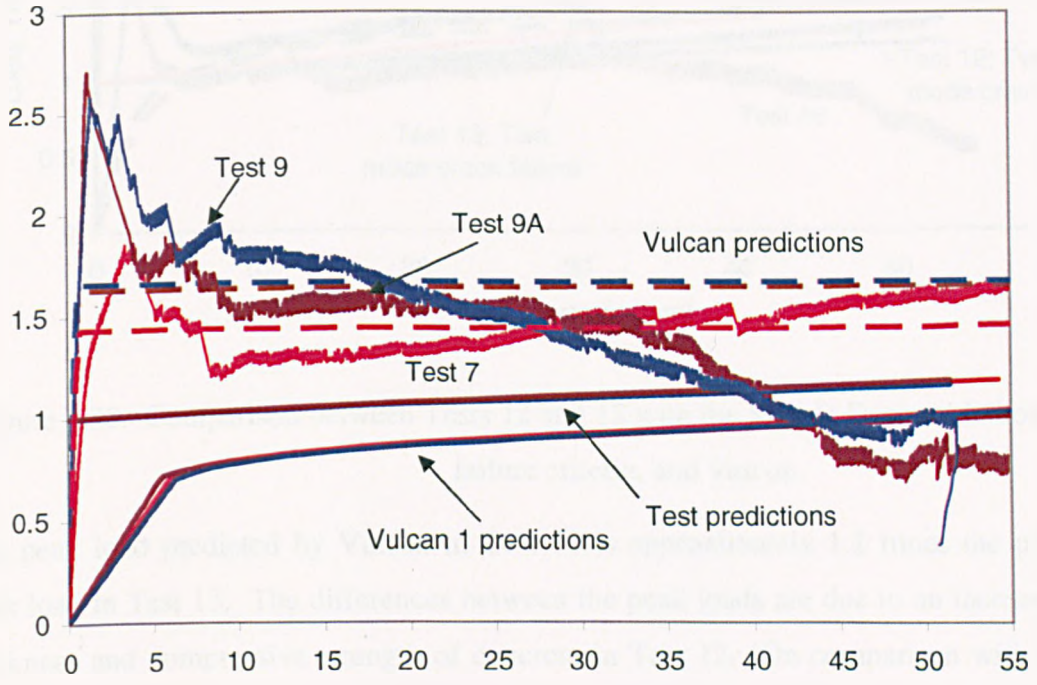

Figure 4.37: Comparison between Tests 7, 9 and 9A with the Simple Design Method and *Vulcan*.

Figure 4.38 presents the comparisons between experimental and *Vulcan* for Tests 12 and 13. The tested slabs had an aspect ratio of 1.55 and formed two transverse cracks. The predictions based on the two mode crack failure has also been plotted in Figure 4.38 but the predictions lie beneath the *Vulcan* predictions (ft=0N/mm^2). Therefore, the Simple Design Method is under predicting the enhancements.

Orthotropically reinforced slabs. Aspect Ratio = 1.55 (Spacing in long span 60mm, spacing in short span 12mm)										
Test	Size (mm)	μ	t (mm)	fy (N/mm^2)	Bar Type	fc (N/mm^2)	ft (N/mm^2)	dx (mm)	dy (mm)	Yield-line capacity (kN/mm^2)
12	850×550	5	20	256	Smooth	41.2	2.13	9.65	9.29	2.94
13	850×550	5	15	245	Deformed	38.0	2.05	7.15	6.79	2.07

Table 4.5: Orthotropically reinforced slabs with aspect ratio of 2.09.

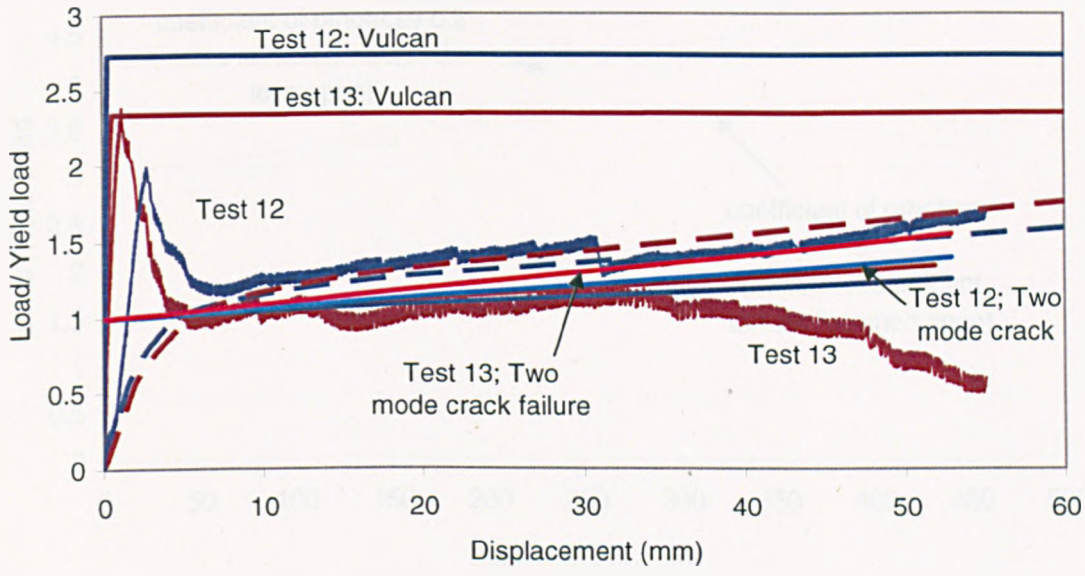

Figure 4.38: Comparison between Tests 12 and 13 with the Simple Design Method, new failure criteria, and *Vulcan*.

The peak load predicted by Vulcan in Test 12 is approximately 1.2 times the predicted peak load in Test 13. The differences between the peak loads are due to an increased slab thickness and compressive strength of concrete in Test 12. On comparison with the test results, Test 13 attained a higher initial peak load which seems to indicate that the type of wire used did have an influence on the bond achieved and resulting peak load attained. In all the tests in which the slabs were reinforced with deformed wire, a higher peak load was attained. This behaviour was not predicted by *Vulcan*.

Sensitivity Study

A numerical study was carried out using the measured data from Test 6 but varying the distribution of reinforcement within the slab and investigating the overall slab performance. Figure 4.39 shows the enhancements predicted by *Vulcan* for two

reinforcement distributions of μ= 0.2 and μ= 5. The predictions correspond well to the theory in that more enhancements are gained by increasing the reinforcement in the long span than the short span. The plot shows that there is little difference in the performance of the slabs up to 60mm displacement, after which only at large displacements it is apparent that the slabs reinforced with additional reinforcement in the long span perform better than with additional in the shorter span. At displacements above 125mm, the slab reinforced with more wire in the long span direction has higher enhancements than the slab reinforced with more steel across the short span.

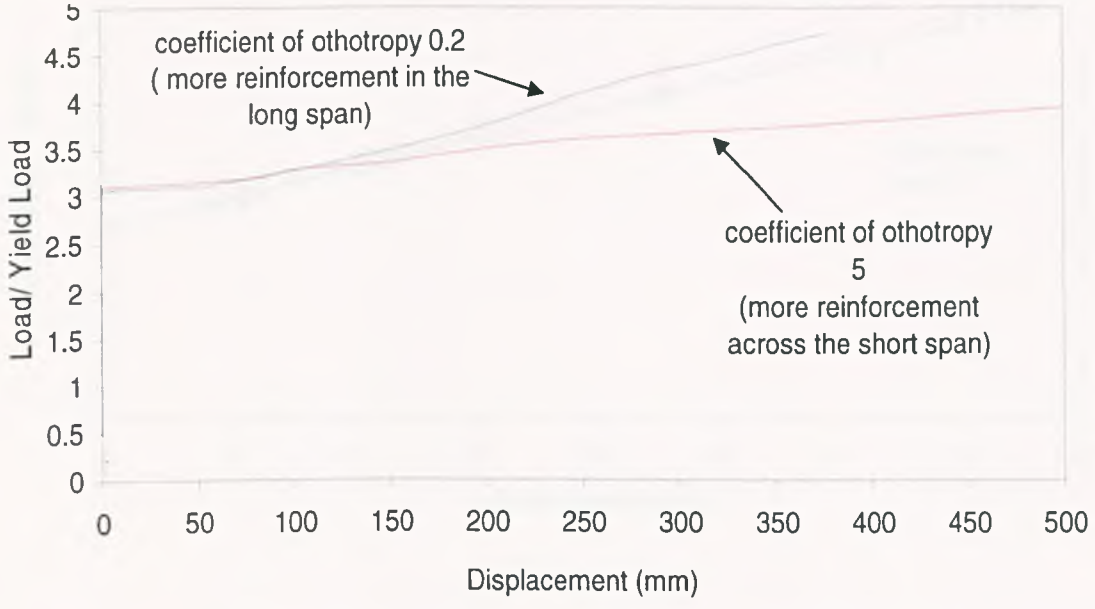

Figure 4.39: Numerical study based on Test 6 tests data.

4.5 Isotropically Reinforced Slabs with Increased Area of Reinforcement

Numerical studies were undertaken to investigate the influence on slab behaviour of increased areas of total reinforcement, and also to facilitate comparisons with the Simple Design Method. The slab model used in these studies was based on the material properties for the isotropic slab of Test 4. The cross-sectional reinforcement area was varied from 0.05% to 0.7% whilst other variables remained constant. The enhancements predicted by the Simple Design Method are presented in Figure 4.40, which shows that, as the reinforcement area increases the predicted enhancements increase at any given slab displacement. The Simple Design Method cannot be used for reinforcement greater than

0.7% as the slab is effectively 'over-reinforced' and the Simple Method yields negative values for g_o. The method limits the maximum allowable area of reinforcement as the formulation limits the compressive stress block to half the effective depth. It must be noted that the Simplified Method is based on the yield line approach which is based on the slab being 'under-reinforced'. The limits on steel ratios given in design codes is to ensure reasonable ductile sections and that the reinforcement yields first.

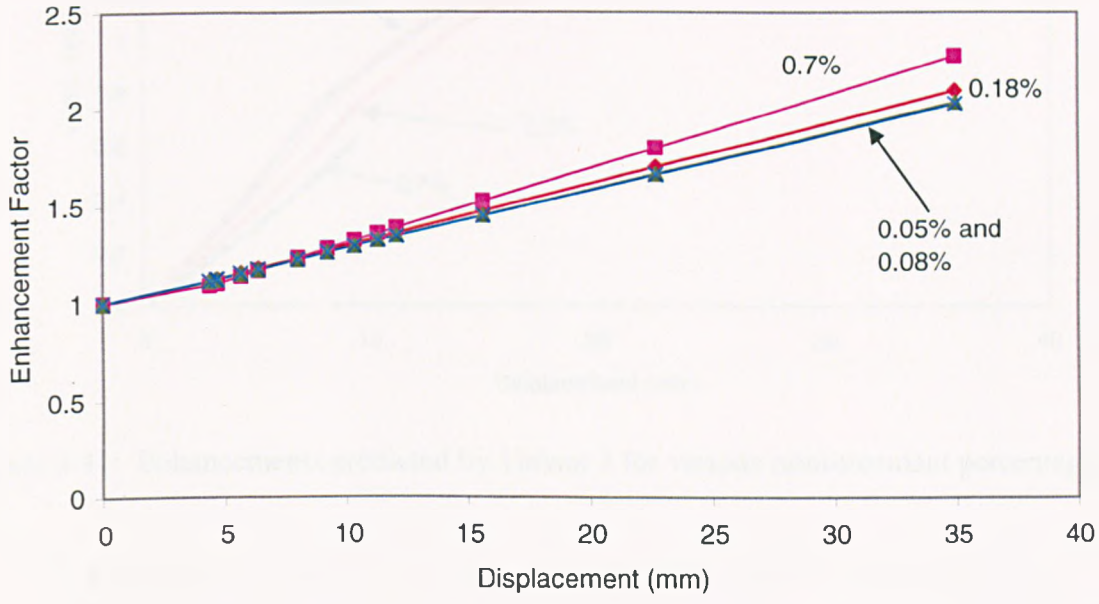

Figure 4.40: Enhancements predicted by the Simple Design Method for various reinforcement percentages.

For comparison, the predictions made by using the modified version of *Vulcan* which considered no contribution from the concrete's tensile strength are presented in Figures 4.41 and 4.42. On comparison of Figure 4.41 with Figure 4.40, the slabs that had a cross sectional area of reinforcement between 0.08%-0.18% yielded similar enhancements from 0-40mm displacement. The model slabs with 0.3% and 0.7% reinforcement yielded lesser enhancement at low displacements due to the increased yield load capacity for these slabs. At vertical displacements of 40mm, the *Vulcan* prediction for the slab which has 0.3% reinforcement converges with the slabs that have less reinforcement. It can be concluded that the slab reinforced with 0.7% would have followed this behaviour if the model had not terminated early. Figure 4.42 shows the results of the *Vulcan* predictions for slab displacement up to 250mm. It is shown that after 120mm displacement, the slabs

reinforced with less reinforcement attain higher enhancements compared to those reinforced with higher reinforcement percentages.

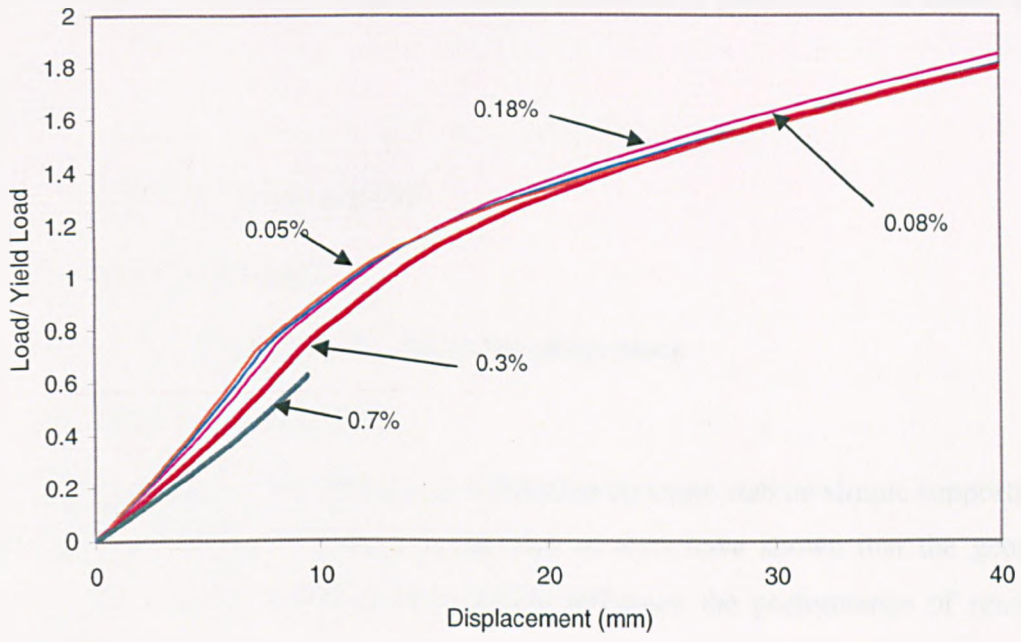

Figure 4.41: Enhancements predicted by *Vulcan 1* for various reinforcement percentages.

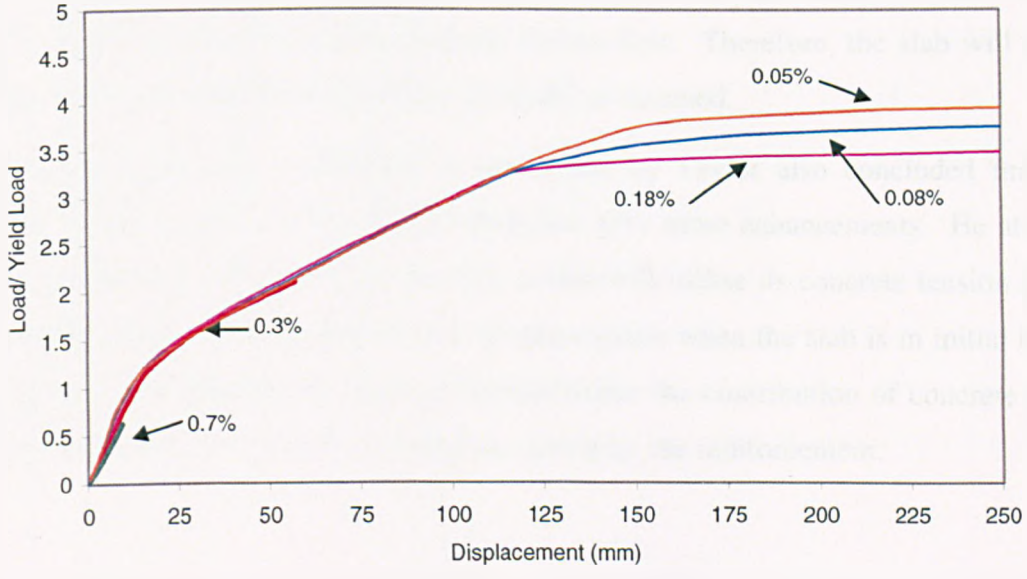

Figure 4.42: Enhancements predicted by *Vulcan 1* for various reinforcement percentages.

The enhancements predicted by *Vulcan* seem to tie in with the predictions made by Wood and Kemp that slabs with small percentage of reinforcement the enhancements are greatest. Kemp stated that the increase in the yield load due to membrane action is small up to the stage when cracking throughout the depth of slab occurs. This is plausible, as the slab

deflections up to cracking are quite small and the slab is initially in bending, so that only after cracking will the displacements increase more rapidly. Kemp theorised that the onset of membrane action in the slab depends on the reinforcement percentage (see Equn. 4.1).

$$\frac{\omega_o}{d_1} \geq \frac{8k_2}{k_1 k_3} t \qquad 4.1$$

Where: ω_o = The relative displacement

d_1= The effective depth

k_1, k_2 and k are variables relating to the stress block

t = reinforcement percentage

These predictions were based on a square reinforced concrete slab on simple supports. The method, however, requires further investigation as tests have shown that the geometry, distribution, and type of reinforcement greatly influence the performance of reinforced concrete slabs.

The yield line method is based on pre-determined collapse mechanism in which the slab is under-reinforced. As the percentage of the reinforcement increases, the slab becomes 'over reinforced' in that concrete crushing occurs first. Therefore, the slab will not fail into the typical pre determined collapse mechanism assumed.

The experimental work undertaken in the 1960s by Taylor also concluded that slabs reinforced with small amounts of reinforcements give more enhancements. He attributed the increased enhancements to the fact that a slab will utilise its concrete tension if it has less reinforcement. This is true at small displacements when the slab is in initial bending but once the slab has cracked at large displacements the contribution of concrete tension will be minimal as the tension force will be carried by the reinforcement.

Chapter 5

High-Temperature Experiments on Model –Scale Concrete Slabs at Large Displacements

5.1 Introduction

A limited number of tests have been conducted on reinforcement concrete slabs at high temperatures. The full scale tests carried out at Cardington have shown that modern composite steel/concrete type multi-storey structures have an inherent strength due to the load carrying mechanism at elevated temperatures changing from that of 'bending action' to tensile membrane action within the concrete slab. The ambient test conducted at the British Research Establishment did not consider the thermal effects on the slab behaviour [26].

The slab behaviour at ambient temperature has been investigated and the results compared with the Simple Design Method and *Vulcan*. The assumptions embodied within the simple method are based on the slab behaviour at ambient temperatures. The experimental results presented in Chapter 3 compared reasonably well to the predictions by the Simple Method. The numerical investigations presented in Chapter 4 highlights that the upper bound method may be unconservative for some particular types of slab.

The influence of bond was also investigated by comparing the results from slabs using smooth and deformed (ribbed) reinforcing bars. However, it cannot be assumed that the basic behaviour observed at ambient temperature will necessarily remain the same at elevated temperatures. The test series was therefore extended to investigate the slab and bond behaviour at elevated temperatures.

The experimental work was undertaken on horizontally unrestrained rectangular and square concrete slabs with varying percentages of isotropic reinforcement, for a range of temperatures. The influence of bond was considered by comparing the results from slabs using smooth and deformed (ribbed) reinforcing wires.

The experimental fire tests on model scale slabs of aspect ratio 1.55 and 1 with varying reinforcement percentages and slab depths are presented in Chapter 5. The main objective of the work was to investigate the slab behaviour at elevated temperatures in a controlled

furnace. This Chapter summarises the experimental work undertaken and compares the test results with those from the Simple Design Method. Comparisons of the fire test results with *Vulcan* will be described in Chapter 6.

The results of the heated tests conducted on horizontally unrestrained slabs presented in this Chapter have been summarised and published within Proceedings of the Third International Workshop of Structures in Fire [56] and at the Second International Conference on Steel and Composite Structures [57].

5.2 Test Configuration and Instrumentation

Two slab sizes were tested, with nominal dimensions (in mm) 920x620, and 600x600 with the supported areas being 850x550 and 550x550 respectively. Two nominal thicknesses – 15mm and 22mm, were tested in which the actual thickness varied slightly, and was measured for each test (Tables 5.1). The test arrangement was very similar to the previous tests at ambient temperature (Chapter 3). The loading rig enabled equal constant concentrated loads to be maintained at 12 points for the rectangular slabs and 4 points for the square slabs (Figure 5.1).

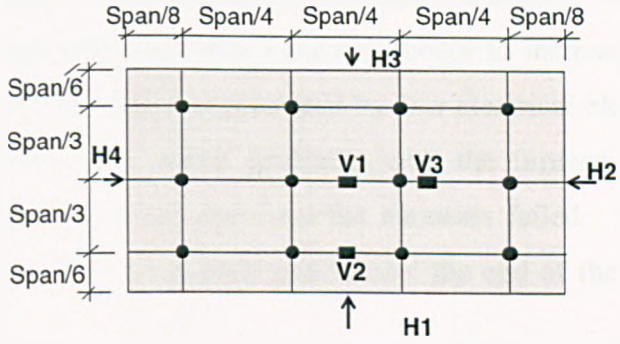

(a)

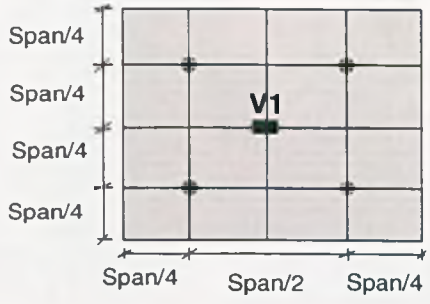

(b)

Figure: 5.1: Location of load and displacement gauges for (a) rectangular and (b) square slabs.

The loading frame and test set-up are shown in Figure 5.2. The slab was supported vertically around the perimeter on an adjustable frame to allow the testing of the square slabs. The applied load remained vertical with the aid of ball-joints which allowed the loading system to rotate as the slab deflected.

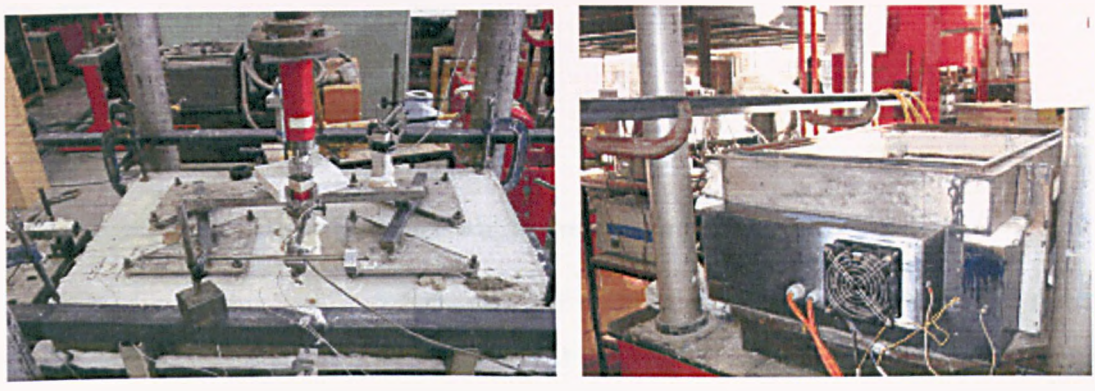

(a) (b)

Figure 5. 2: Typical arrangement of test set-up and supporting frame, (a) Loading fame and (b) View of gas furnace.

The four corners of the slab were loosely clamped to restrain vertical upward movement, but no horizontal restraint was provided at the supported edges. The heating device was constructed from a steel box lined with insulation board to increase the heating rate and protect the steel casing. Heating was generated by four electrical elements within the steel box, Figure 5.3. There were initial problems with the furnace in that the electrical elements were over heating at the ends and the elements failed. The furnace was later modified to include in-built fans at each end to cool the end of the elements is shown in Figure 5.2 (b).

Figure 5.3: Arrangement of heating elements.

The slabs were reinforced with 0.71mm diameter smooth or deformed (ribbed) steel wire, distributed isotropically. The orthotropic slabs were not included within the test schedule due to time constraints and should be investigated in the future. It was decided to investigate the slab behaviour of slabs of aspect ratio of 1.55 and 1, varying certain parameters:

- Type of wire: smooth and deformed.
- Area of reinforcement.
- Position of the reinforcement within the slab depth.

The deformed wire was made by indenting the smooth wire using a purpose-built machine that was used in the ambient tests, see Chapter 3. The percentage of reinforcement in any slab cross-section varied between 0.05% and 0.25%. The concrete mix used in these tests was the same mix used in the ambient tests, which was composed of gritty sand with fine aggregate with particle sizes ranging between 1 and 4mm, a cement-sand ratio of 1:3, and a water-cement ratio of 0.47, see Figure 5.4. The concrete mould also changed, with the reinforcement fixed to an independent frame which was placed over the mould, Figure 5.4. The measured moisture content for the slabs varied between 3 to 4 percent (measured). The measured yield strength of reinforcement and the compressive strength of concrete are shown in Tables 5.1-5.3. The concrete slabs were cast in a similar way to the ambient temperature slabs but incorporated plugs cast into the concrete to accommodate thermocouples.

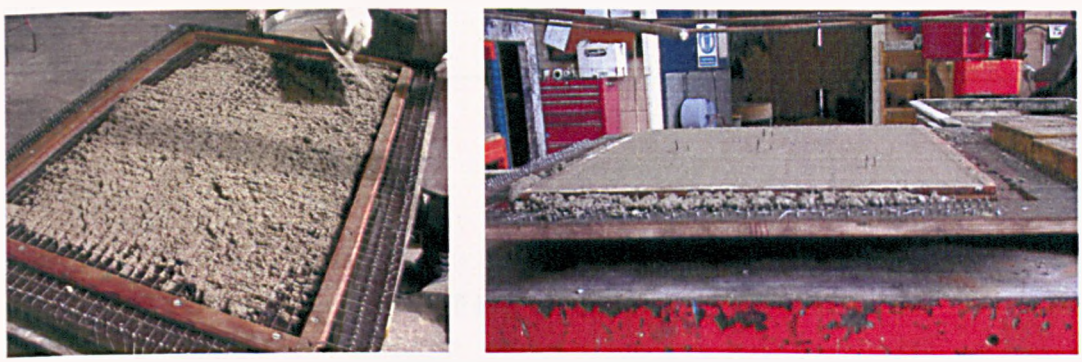

Figure 5.4: Casting of the slabs

The logged instrumentation included a load cell and several displacement transducers to measure both the horizontal and vertical displacements during the test (Figure 5.1). The

temperatures of the slab were measured at 4 key locations, Figure 5.5, at 3 levels through the slab section - underside, reinforcement level, and topside.

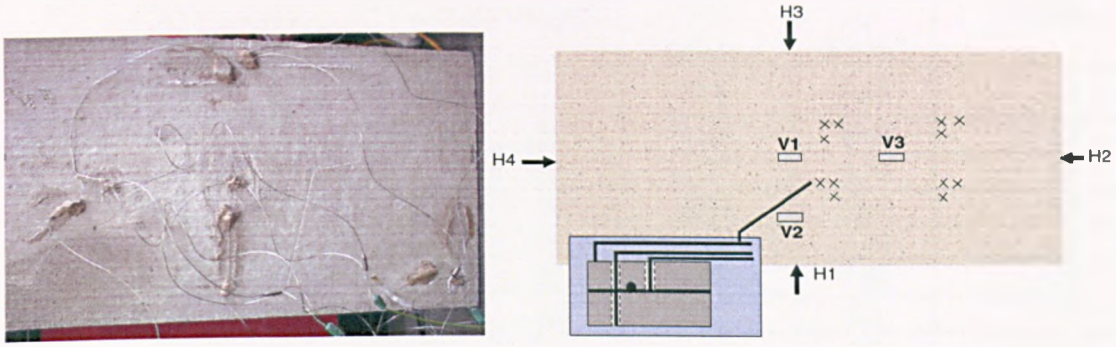

Figure 5.5: Placement of the thermocouples within the slab.

Figure 5.6, shows the temperature history at these locations for a typical test, and demonstrates good consistency between the temperatures at various locations in the slab.

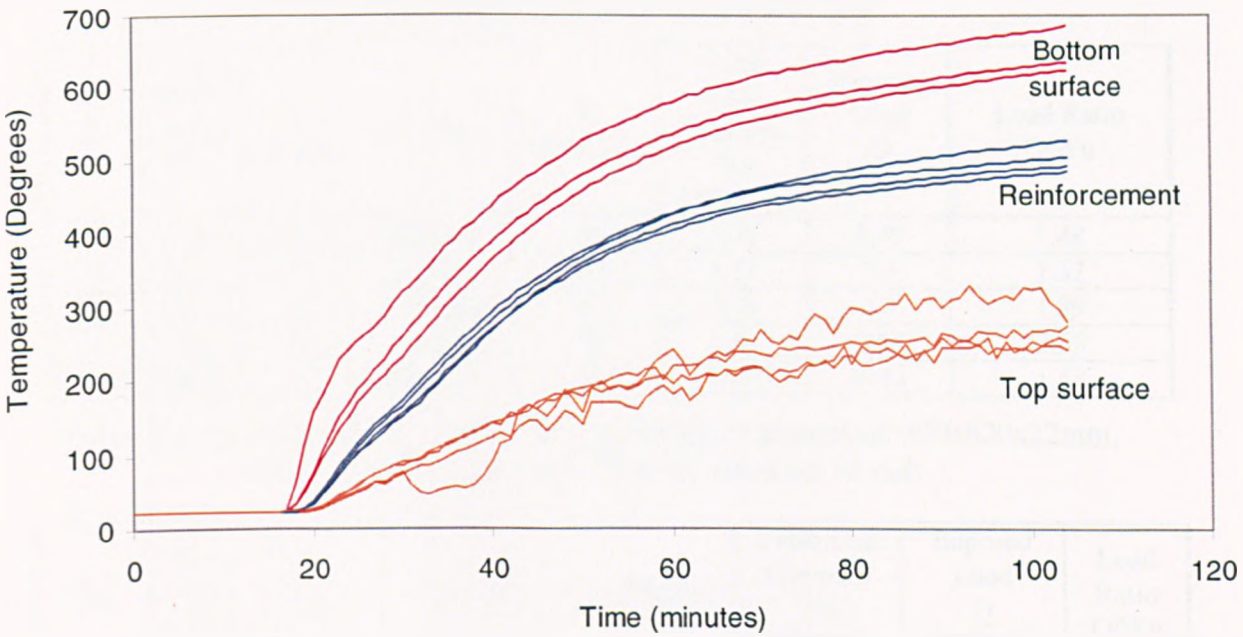

Figure 5.6: Temperature profiles through the slab depth.

The yield line capacity was calculated assuming that the 4 point loading system acted as a uniformly distributed load. The Yield load calculated assuming distributed loading over – estimated the actual yield by 33% (see Appendix A for calculations).

The same margin of error previously calculated for rectangular will still apply to the calculated yield line capacity.

Test	Reinf. Area (%)	t (mm)	Bar Type	fc (N/mm^2)	Yield Line Capacity Wu (kN/m^2)	Imposed Load Q (kN/m^2)	Load Ratio Q/Wu
4	0.15	17	Smooth	37	2.34	4.46	1.9
5	0.15	13	Deformed	40	1.58	4.58	2.9
7	0.15	17	Deformed	40	2.21	3.30	1.5
6	0.05	17	Smooth	44	0.94	2.67	2.8
15	0.05	16	Smooth	40	0.89	1.50	1.7
17	0.05	17	Deformed	39	0.89	1.66	1.87
12	0.25	14.6	Deformed	38	3.62	6.4	1.77
13	0.25	16	Smooth	38	4.63	6.8	1.47
22	0.25	17	Smooth	40	4.94	9.60	1.94
14	0.1	16.8	Deformed	40	1.47	2.54	1.73
16	0.1	17	Smooth	38	1.57	2.76	1.76
19	0.1	17	Smooth	37.5	2.34	4.90	2.09
18	0.1	24	Smooth	37.1	4.60	4.87	1.06

Table 5.1: Summary of test results for tested slabs of dimension 920x620x15mm, with reinforcement placed at half depth of slab

Test	Reinf. Area (%)	t (mm)	Bar Type	fc (N/mm^2)	Yield Line Capacity Wu (kN/m^2)	Imposed Load Q (kN/m^2)	Load Ratio Q/Wu
9	0.1	23	Deformed	42	4.32	6.39	1.48
20	0.1	26	Smooth	40	5.17	7.1	1.37
10	0.05	24	Deformed	39	2.49	4.7	1.89
11	0.05	23	Smooth	39	2.48	5.92	2.39
21	0.05	26	Deformed	40	2.79	4.42	1.58

Table 5.2: Summary of test results for tested slabs of dimension 920x620x22mm, reinforcement placed at 7.5mm from bottom of slab.

Test	Reinf. Area (%)	t (mm)	Bar Type	fc (N/mm^2)	Yield Line Capacity Wu (kN/m^2)	Imposed Load Q (kN/m^2)	Load Ratio Q/Wu
3	0.25	15	Smooth	38	5.95	8.90	1.50
4	0.15	15.1	Deformed	40	2.87	4.61	1.61
5	0.05	15.1	Deformed	39	1.16	2.76	2.38
6	0.1	15	Smooth	38	2.04	5.40	2.65
7	0.05	15	Smooth	40	1.23	3.87	3.15
600x600x22mm, reinforcement placed at 7.5mm from bottom of slab							
8	0.05	24	Deformed	39	3.62	6.10	1.69
9	0.05	24	Smooth	39	3.83	6.00	1.57

Table 5.3: Summary of test results for tested slabs of dimension 600x600x15mm, reinforcement placed at half depth of slab and 7.5mm from bottom of slab.

5.3 Observations of Slab Behaviour

The slabs were subjected to a constant imposed load before the heating elements were switched on; values for each test are shown in Tables 5.1, 5.2 and 5.3. The rectangular and square slabs behaved in a similar way; approximately 10-15 minutes after the furnace was switched on, diagonal cracking occurred across the corners as the slab deflected into double curvature. After 20 minutes, a single transverse crack could be seen forming on the upper surface of the slab in its central region (Figure 5.7). This crack develops irrespective of load. Subsequently, this crack extended outwards in the short-span direction towards the long edges of the slab. Most of the slabs developed crack patterns resembling a yield line mechanism towards the end of the test, usually after about 2 hours. The crack patterns were similar to those of the equivalent slabs tested at ambient temperature (Chapter 3), except that the diagonal yield lines tended to align more in the long direction of the slab (Figure 5.8), giving a much shorter central yield line. The formation of these yield lines seems to depend on the applied load level, while the development of the initial transverse crack after the slab has deflected into double curvature appears to be associated with its thermal bowing.

Test 1 has not been included, as it was used only to check the temperature distributions in the slab at various key locations. Test 3 was a re-test of the slab in Test 2, to which no load was applied and showed little damage although it had some residual distortion due to thermal bowing.

5.3.1 Isotropically Reinforced Slabs of Aspect Ratio 1.55 with Reinforcement Placed at Half Depth

Test 4, 5 and 7

These slabs measured 920x620x15mm with supported edges of 850x550mm, and had a cross sectional area of reinforcement of 0.15%. The slab in Test 4 was reinforced with smooth wire and in Tests 5 and 7 with deformed wire. The measured data is shown in Table 5.1. The development of the transverse crack in Test 4 approximately 20 minutes after the heating elements were switched on can be seen in Figure 5.7. The relative movement of the edges can be seen in Figure 5.10, which shows the edge curving inwards. The slab in Test 5 failed quickly due to the combination of a high imposed load and type of reinforcing wire used (deformed) (Figure 5.8). The increased load forced the slab into a

yield line mechanism and the exposed deformed wire fractured quickly (see Chapter 3 for discussion). The mechanism by which the slabs deformed seemed to be affected by the applied load. This can be seen in Test 7, Figure 5.11, in which the slab deformed into double curvature with the formation of a transverse crack but there was no development of the yield line pattern. Comparing Test 7 with Tests 5 and 4, Figures 5.8-5.11, these slabs developed yield line patterns but only towards the end of the test.

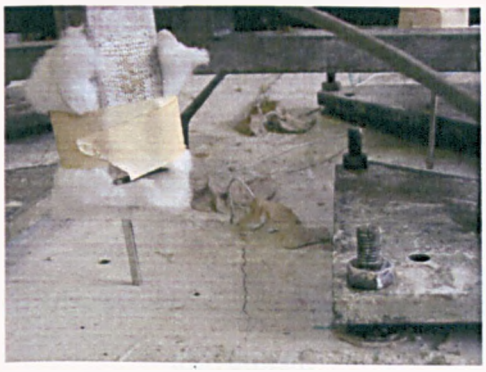

Figure 5.7: Development of transverse crack in Test 4.

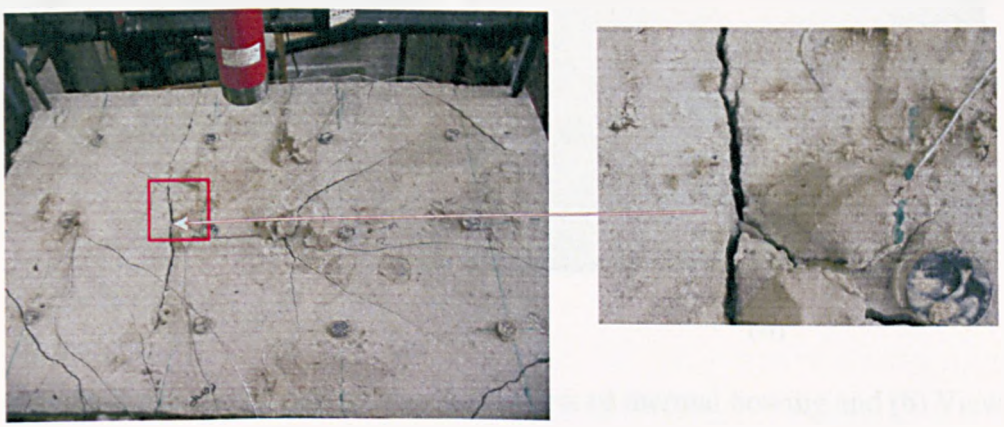

Figure 5.8: View of top face of slab in Test 4.

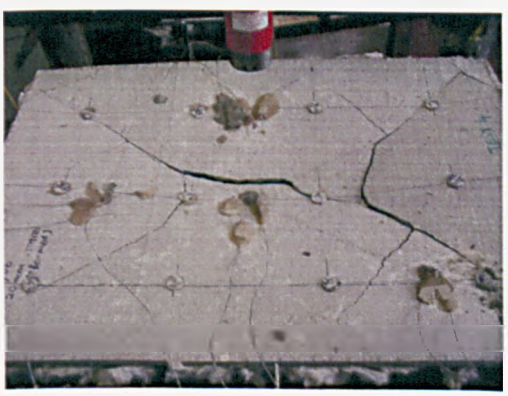

Figure 5.9: View of top face of slab in Test 5.

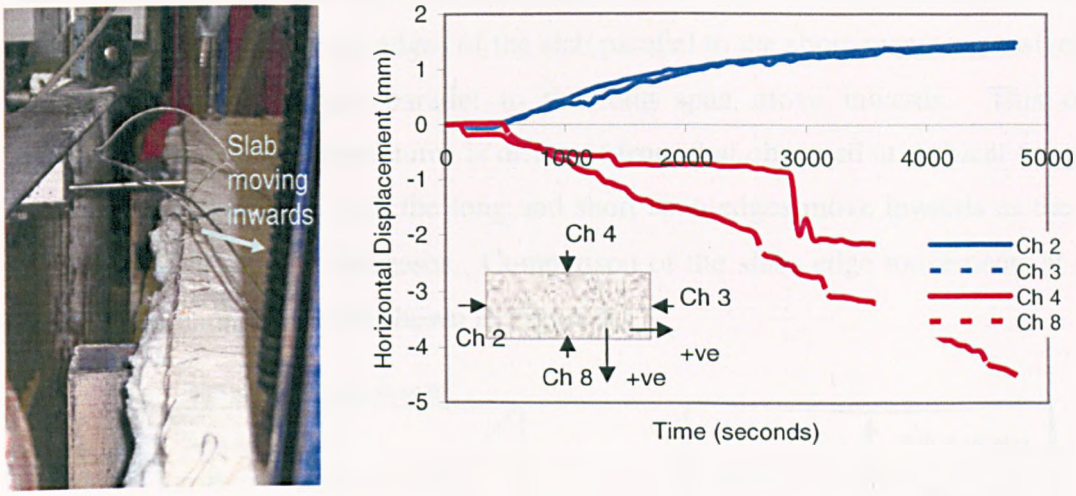

(a) (b)

Figure 5.10: Test 4: (a) Observed horizontal edge movement (b) Recorded edge movement.

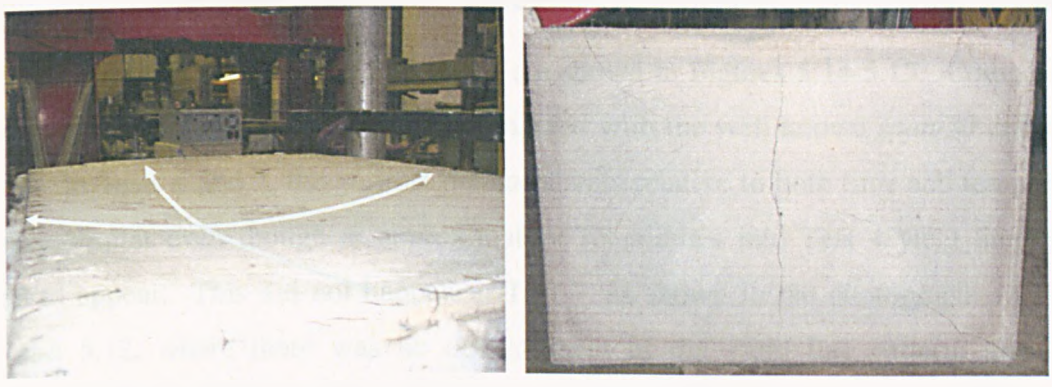

(a) (b)

Figure 5.11: Deformation of slab in Test 7, (a) View of thermal bowing and (b) View of bottom of slab.

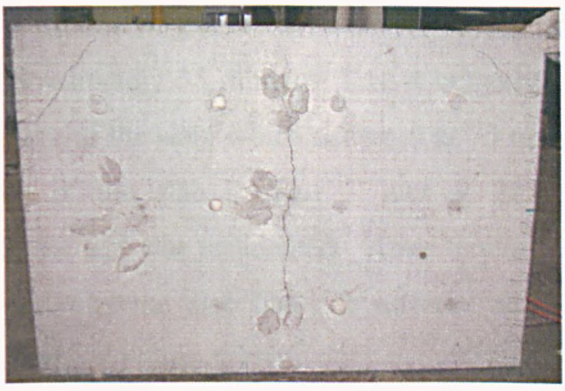

Figure 5.12: View of top face of slab in Test 7.

The recorded horizontal edge movements for the slab in Test 4 are shown in Figure 5.10(b). It is shown that the edges of the slab parallel to the short span progressively move outwards whilst the edges parallel to the long span move inwards. This observed behaviour at elevated temperatures is different from that observed at ambient temperature. At ambient temperature, both the long and short span edges move inwards as the vertical displacement of the slab increases. Comparison of the slabs edge movements at ambient and elevated temperature are shown in Figure 5.13.

Figure 5.13: Comparison of slab edge movements at ambient and elevated temperatures.

Vertical displacements for Tests 4, 5 and 7 are shown in Figures 5.14-5.15. Comparisons of the vertical displacements have been compared with the well known *span/30* deflection criteria. In Tests 4 and 7, the vertical displacements relative to both time and temperature are very similar even though at approximately 75 minutes into Test 4 yield line cracks started to appear. This did not happen in Test 7, as shown in the photographs in Figure 5.11 and 5.12, where there was no development of the yield line pattern; this could possibly be due to the load ratio. Test 7 had a lower load ratio than Test 4 which could have affected the mechanism in which the slab was forced into towards the latter stages of the tests. There is a difference in the rate of displacement between Tests 4 and 7 during the first 35 minutes; in Test 4 the rate of displacement is faster at any given displacement than Test 5 which seems to be related to the lower measured compressive strength and higher imposed load. After approximately 35 minutes, Test 4 behaved in a very similar way to Test 7, until runaway failure of the slab, which occurred at 75 minutes into the test. There was no observed failure of the slab in Test 7, and at 225 minutes at a mid-span displacement of *span/12*, the test was terminated. After 'cooling', the slab in Test 7 was lifted off the furnace, and that the slab had not suffered any major cracking but had deformed into double curvature, Figure 5.11(a).

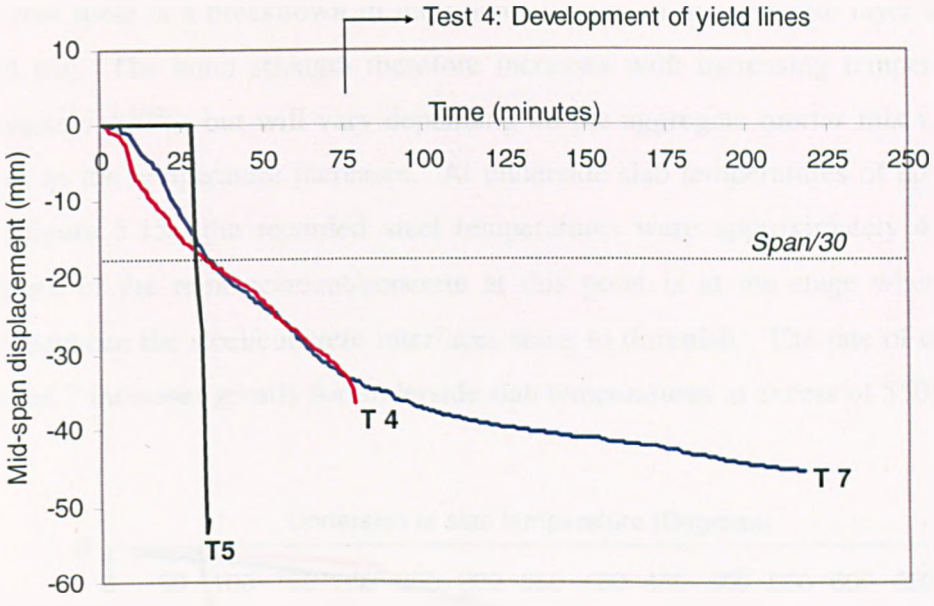

Figure 5.14: Comparison of the mid-span displacements with respect to time in Tests 4, 5 and 7.

The temperature of the bottom surface of the slab reached 650°C in Tests 4 and 7 (Figure 5.15). The slab in Test 4 suffered major cracking before runaway failure occurred and the reinforcement was exposed to the hot furnace temperatures. The cracks had widened due to the slippage of the wire and breakdown of the bond between the concrete and steel, which led to the reinforcement exposed to hot furnace temperatures. The steel of course fractured due to the reduction in strength at high temperatures, which led to the integrity failure of the slab in Test 4. In Test 7, in which the reinforcement temperatures reached approximately 450°C, the slab did not experience any major cracking apart from the transverse crack which did not open up. At ambient temperature, membrane action was apparent after the formation of yield lines. After concrete cracking, there was a progressive loss of bond between the concrete and steel which led to the steel wire hanging between the slab facets (see Chapter 3). The slab facets remained flat and rotated about the edges of the slab. At elevated temperatures, the bond between the concrete and the steel will be different to that at ambient conditions due to the difference in thermal strains of the two materials. For temperatures up to approximately 400°C, the thermal strain of steel is slightly greater than concrete but at higher temperatures concrete expands more than steel and beyond 1000°C, steel expands more than concrete. From extensive experimental work carried out on bond strength at elevated temperatures [48], it is apparent during the heating

process that there is a breakdown in the microstructure in the concrete layer surrounding the steel bar. The bond strength therefore increases with increasing temperature up to approximately 400°C, but will vary depending on the aggregate mortar mix used; it then decreases as the temperature increases. At underside slab temperatures of approximately 550°C (Figure 5.15), the recorded steel temperatures were approximately 450°C. The temperature of the reinforcement/concrete at this point is at the stage where the bond strength between the steel/concrete interfaces starts to diminish. The rate of deflection in Tests 4 and 7 increases greatly for underside slab temperatures in excess of 550°C.

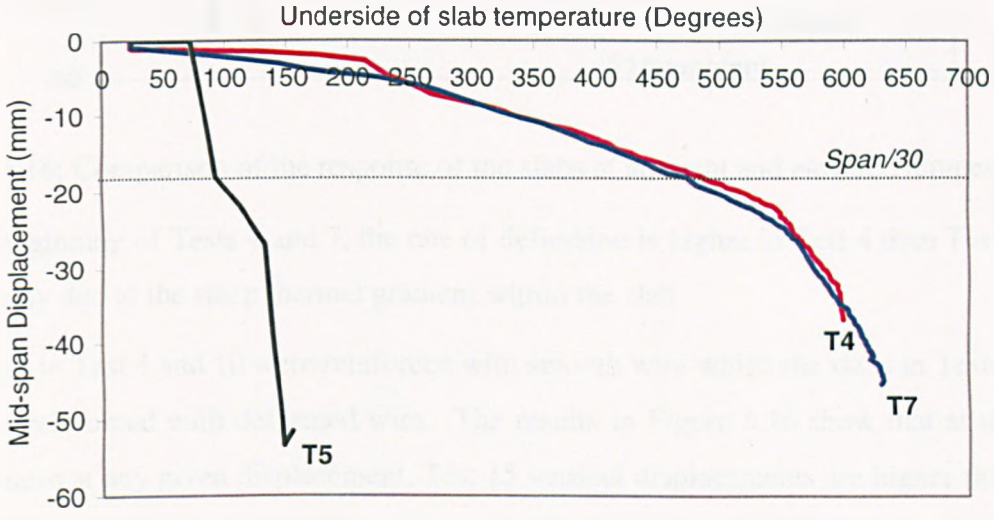

Figure 5.15: Comparison of the mid-span displacements with respect to temperature in Tests 4, 5 and 7.

Comparisons have been made between Tests 4, 5 and 7 with the ambient temperature tests, Tests 15 and 10; the results are presented in Figure 5.16. The rate of deflection of the slabs at elevated temperatures is similar to the ambient temperature tests but after 100 minutes, the ambient tests deflections linearly increased whilst the slab in Test 4 was terminated and the slab in Test 7 reached *span/12*. The ambient temperature slabs increased in displacement due to the increased load, and at 100 minutes had an applied load/yield load ratio in excess of 2 increasing to 2.75 towards the end of the test.

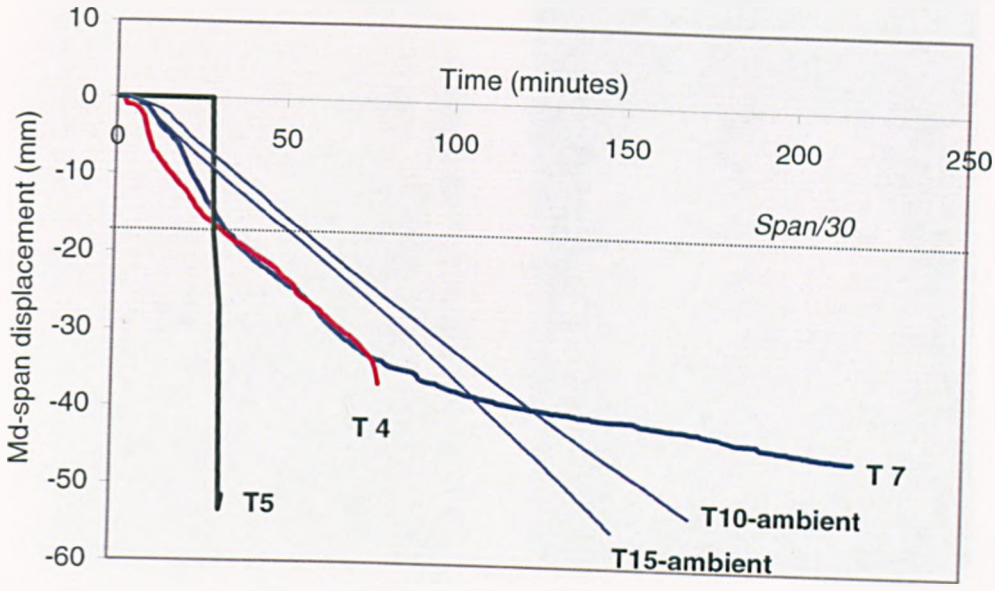

Figure 5.16: Comparison of the response of the slabs at ambient and elevated temperatures.

At the beginning of Tests 4 and 7, the rate of deflection is higher in Test 4 than Test 7 and is probably due to the steep thermal gradient within the slab

The slabs in Test 4 and 10 were reinforced with smooth wire whilst the slabs in Tests 7 and 15 were reinforced with deformed wire. The results in Figure 5.16 show that at ambient temperature at any given displacement, Test 15 vertical displacements are higher than Test 10 and the increased rate of displacements is due to the type of reinforcement. Comparing the rate of displacement between Tests 4 and 7, the results show that the type of reinforcement does not influence the slab's performance. The response of the slabs at elevated temperatures is of course very different in that initially there would be no major cracking of the slab and the bond strength would increase then progressively decrease with increasing temperature.

Test 6, 15 and 17

These slabs measured 920x620x15mm with a supported area of 850x550mm, and had a cross sectional area of reinforcement of 0.05%. The slabs in Tests 6 and 15 were reinforced with smooth wire and in Test 17 with deformed wire. The measured test data is shown in Table 5.1. Figures 5.17 and 5.18 show the slabs after testing. In both tests, the transverse cracks appeared 20 minutes into the test and this was followed by the development of poorly defined yield line cracks.

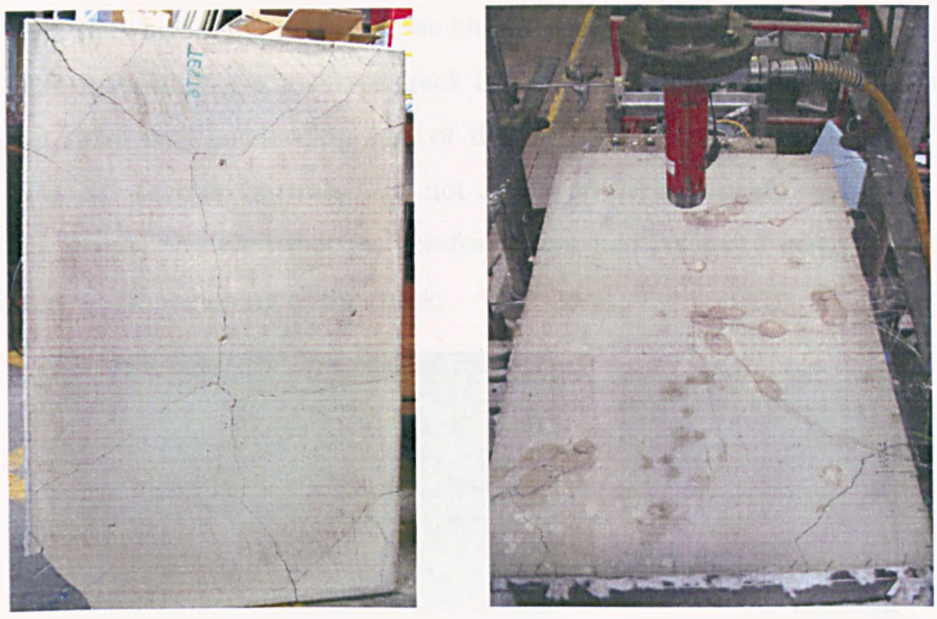

(a) (b)

Figure 5.17: Test 6:(a) View of bottom face of slab (b) View of tope face of slab.

The load ratio in Test 6 was 2.8 and in Test 15 was 1.7 (Table 5.1). The underside views of the slabs show that in Test 6, the yield line cracks had extended full depth of the slab but in Test 15 only the transverse cracking and part of the diagonal cracks are apparent, Figure 5.18. Figure 5.19 shows the view of the slabs in Test 17, which was reinforced with deformed wire and had a load ratio of 1.87 (see Table 5.1).

(a) (b)

Figure 5.18: Test 15: (a) View of top surface of slab (b) View of bottom surface.

Figure 5.19(a) shows the slab profile at the end of testing in Test 17, which shows double curvature deformation. The transverse crack formed after 20 minutes into the test (Figure 5.19 (b)) but there was no development of the full depth yield cracks (Figure 5.19(c)); surface cracks did develop but these did not extend to the full depth. After the slab had cooled down it was observed that the reinforcement had fractured across the transverse crack resulting in the widening of the crack.

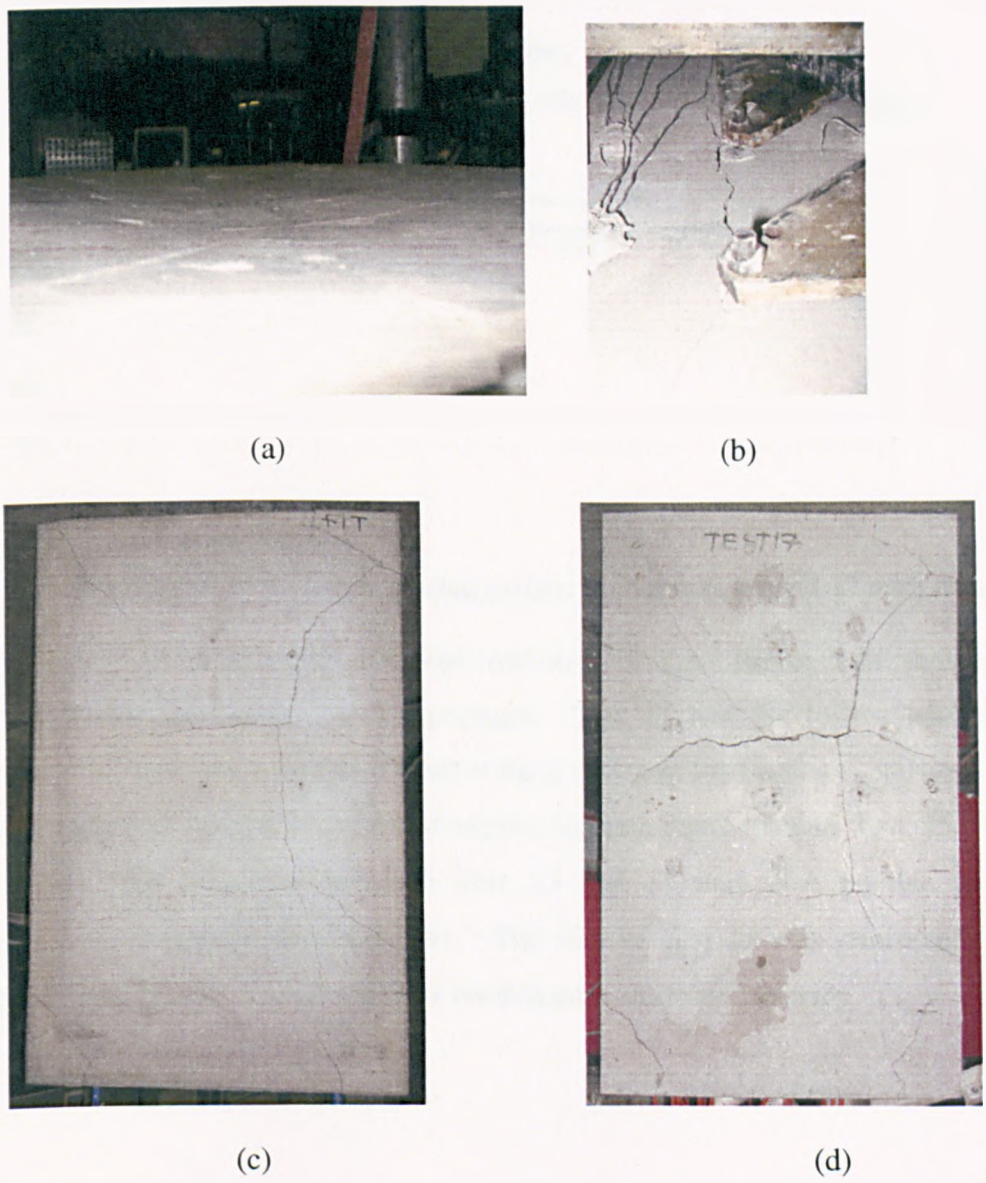

(a) (b)

(c) (d)

Figure 5.19: Test 17: (a) Slab profile after test, (b) Transverse crack, (c) Bottom surface of slab and d) Top surface of slab.

In Tests 6 and 15, the transverse cracks remained closed and the wire intact whereas in Test 17 the transverse crack opened up on cooling leading to subsequent fracture of the reinforcement, Figure 5.19(d).

Figures 5.20 and 5.21 compares the mid-span displacements of the three tests with respect to time and temperature. These slabs reached maximum displacements of approximately *span/18*, after 150 minutes of start of test. The rates of deflection for the three tests are very similar for the first 50 minutes and after approximately 60 minutes the rate of defection for Tests 15 and 17 is still very similar.

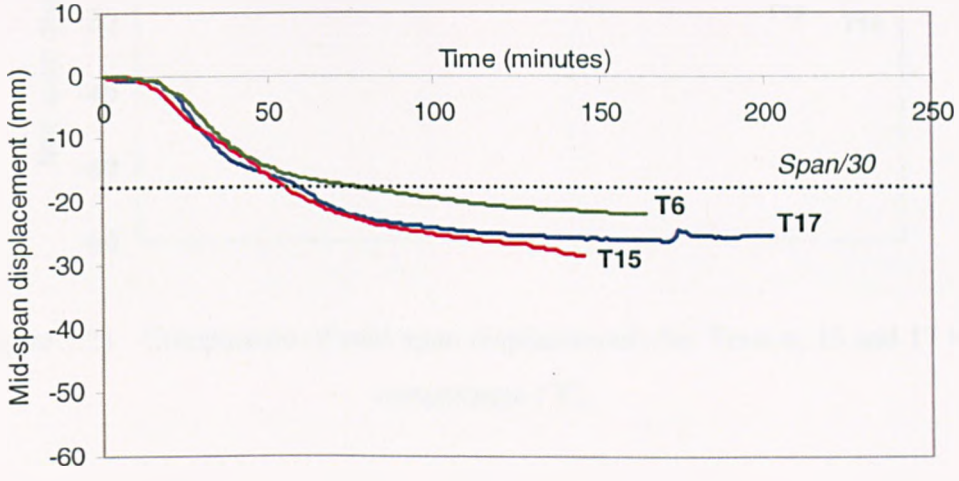

Figure 5.20: Comparison of mid-span displacements for Tests 6, 15 and 17 with time.

The slab in Test 6 was loaded with a higher load ratio of 2.8. Figure 5.21 shows the response of the slabs with respect to temperature. Test 15 had the lowest load ratio followed by Test 17 and Test 6, and the effect of these different load ratios is apparent. At any given temperature, Tests 6 and 17 had higher displacements than in Test 15. The difference in the slab behaviour between Test 15 and 17 may also be due to the reinforcement type but cannot be conclusive. The slab in Test 15 was reinforced with smooth wire whereas in Test 17, the slab was reinforced with deformed wire.

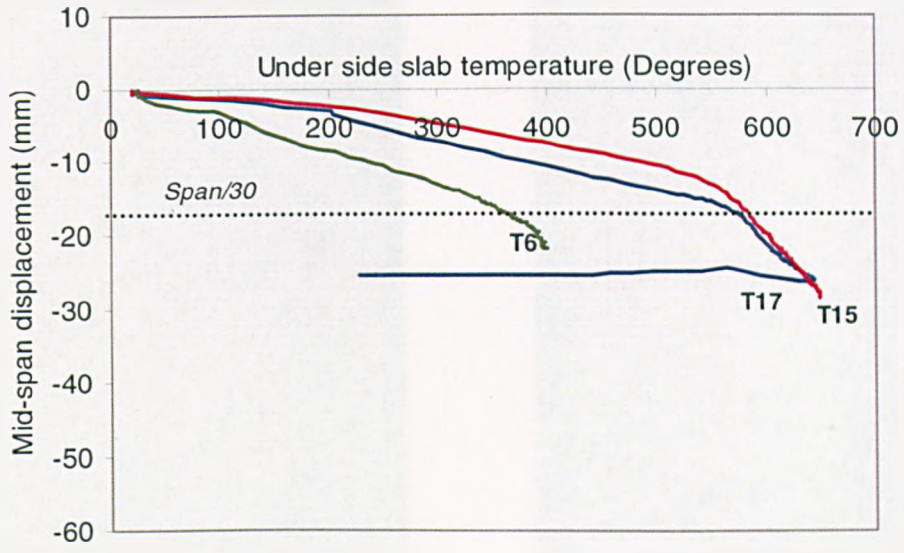

Figure 5.21: Comparison of mid-span displacements for Tests 6, 15 and 17 with temperature (^{o}C).

Tests 12, 13 and 22

These slabs measured 920x620x15mm with a supported area of 850x550mm, and a cross sectional area of reinforcement of 0.25%. The slabs in Tests 13 and 22 were reinforced with smooth wire and in Tests 12 with deformed wire. The measured data is shown in Table 5.1. Test 12 had to be terminated after 45 minutes as collapse of the slab was imminent; the transverse crack had progressively widened, and the reinforcement exposed, revealing fracture of the wire (Figure 5.22(b)). At the time when the heaters were switched off, the slab in Test 12 showed no signs of the development of the yield line cracks, but on cooling these cracks were apparent (Figure 5.22(a)). The slab in Test 13 developed two transverse cracks across the short span of the slab after approximately 30 minutes into the test, Figure 5.23. Figures 5.22 and 5.23 show the top and bottom surface of the slabs in Tests 12 and 13 after testing.

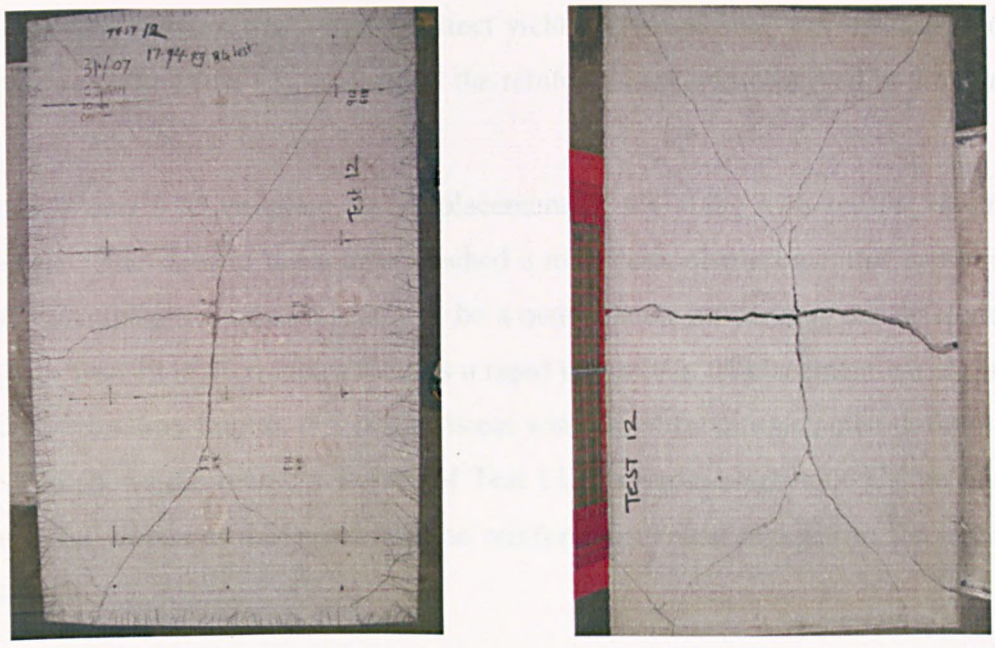

(a) (b)

Figure 5.22: Test 12: (a) View of top surface of slab and (b) View of bottom surface of slab.

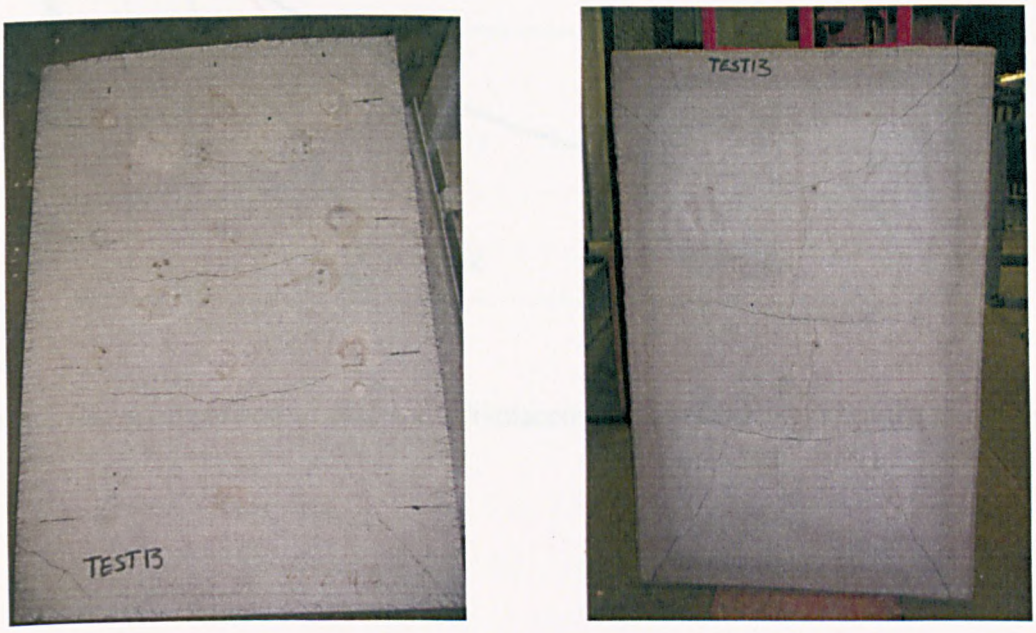

(a) (b)

Figure 5.23: Test 13: (a) View of top surface of slab and (b) View of bottom surface of slab.

The slab in Test 12 was tested at a higher load compared to Test 13, which may explain the absence of the yield line cracking in Test 13 (Figure 5.23). As seen in Figure 5.23, diagonal cracks started to form but did not developed fully due to the lower load ratio.

whereas in Test 12 there was a more distinct yield line formation. For the slab reinforced with deformed wire (Test 12), fracture of the reinforcement was observed in the transverse crack.

Figures 5.24 and 5.25 compare the displacement of the slabs with respect to time and temperature. The slabs in these tests reached a maximum displacement of approximately *span/10*. The influence of load seems to be a major factor influencing the deflection rate, although in Test 12 at 50 minutes there is a rapid increase in displacement which indicates the onset of runaway failure; this is consistent with the observations noted during the test. Figure 5.25 shows the runaway failure of Test 12 at approximately 600°C; the transverse crack was fully open at this point and the reinforcement was exposed to the hot furnace temperatures.

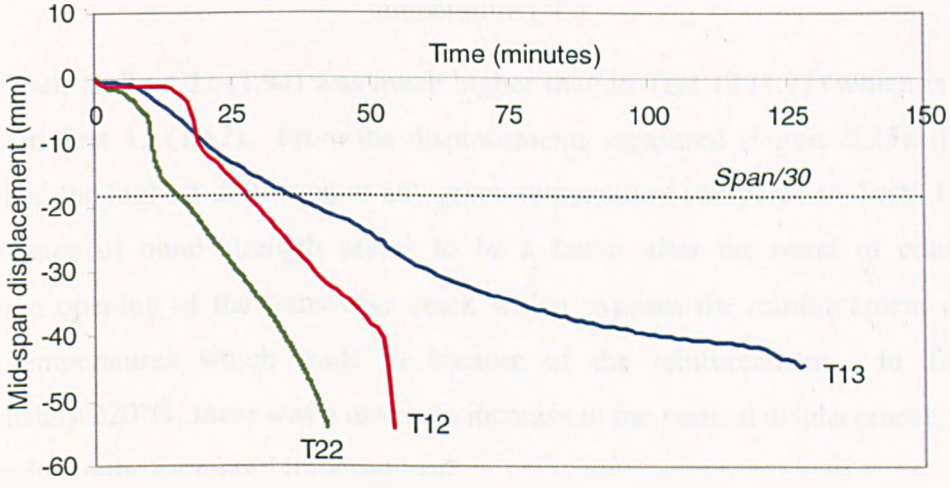

Figure 5.24: Comparison of mid-span displacements for Tests 12, 13 and 22 with time.

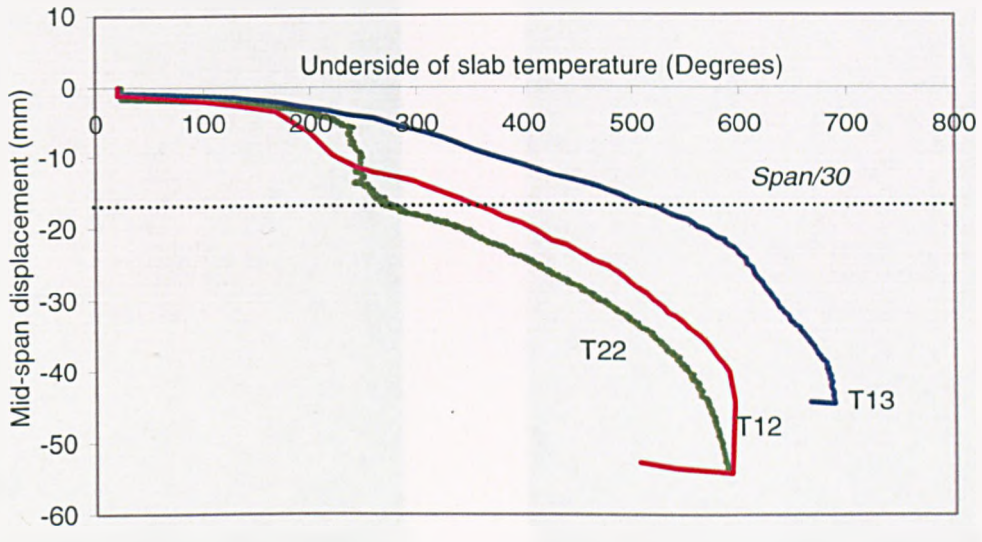

Figure 5.25: Comparison of mid-span displacements for Tests 12, 13 and 22 with temperature (°C).

The load ratio in Test 22 (1.94) was much higher than in Test 12 (1.77) which in turn was higher than Test 13 (1.47). From the displacements measured (Figure 5.25), the slab in Test 22 had the highest deflection at any given temperature compared to Tests 12 and 13. The influence of bond strength seems to be a factor after the onset of cracking and progressive opening of the transverse crack which exposes the reinforcement to the hot furnace temperatures which leads to fracture of the reinforcement. In Test 22 at approximately 220°C, there was a dramatic increase in the vertical displacement. This was probably due to the increased imposed load.

Tests 14, 16, 19 and 18

These slabs measured 920x620x15mm with a supported area of 850x550mm, and a cross sectional area of reinforcement of 0.1%. The slab in Test 14 was reinforced with smooth wire and in Tests 16, 19 and 18 with deformed wire. The measured data is shown in Table 5.1 and photographs of Tests 14 and 16 taken after testing are shown in Figure 5.26.

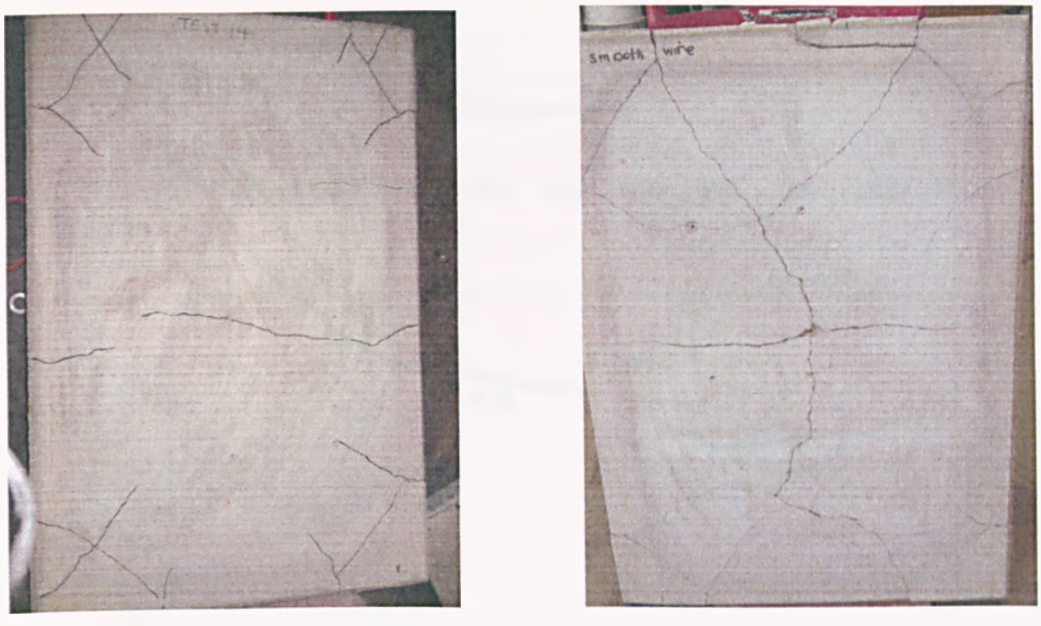

(a) (b)

Figure 5.26: (a) Test 14, bottom surface of slab, and (b) Test 16, bottom surface of slab.

In Test 16, the slab reinforced with deformed wire developed yield line cracks whereas in Test 16 the slab reinforced with smooth wire only developed the central transverse crack. Test 16 had a slightly higher load ratio (1.76) than Test 14 (1.73). The yield line cracks were observed to form whilst the slab cooled; there was no evidence of fracture of the reinforcement though the slab reinforced with deformed wire (Test 14) showed evidence that the wire had become debonded. Figures 5.27 and 5.28 show the mid-span displacements with respect to time and temperature. Test 19 had the highest load ratio (2.09) and attained the highest displacements (Figure 5.28). It was observed in Test 16, that the yield line cracks developed in the cooling phase.

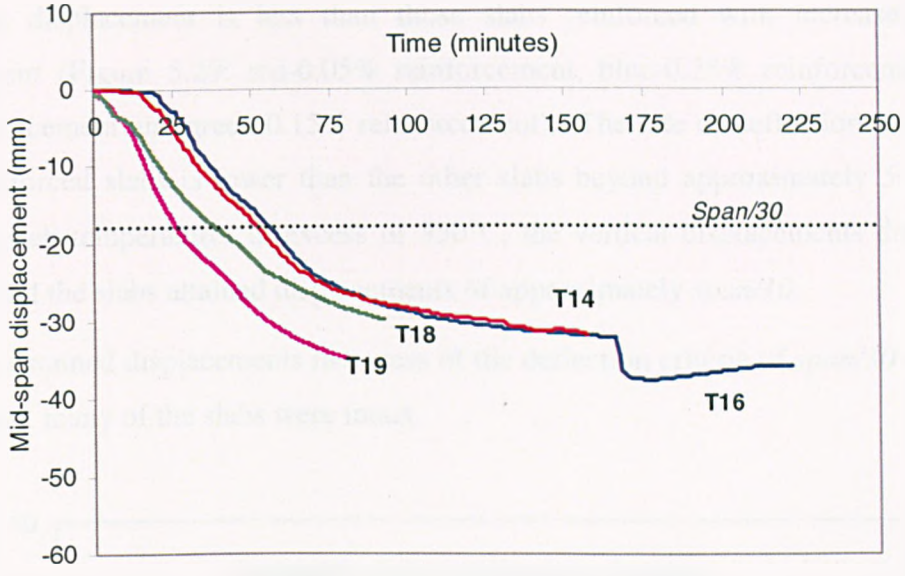

Figure 5.27: Comparison of mid-span displacements for Tests 14, 16, 18 and 19 with time.

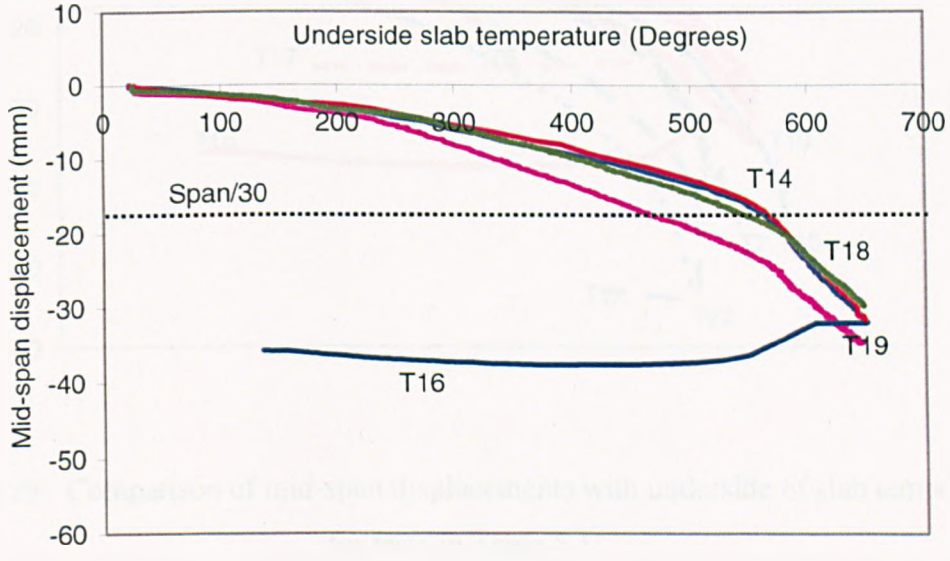

Figure 5.28: Comparison of mid-span displacements for Tests 14, 16, 18 and 19 with temperature (^{o}C).

5.3.2 Comparison of Tests

The mid-span displacements of the tests in Table 5.1 are compared and presented in Figures 5.29 and 5.30. Overall, the results show that between 20°C-300°C similar displacements are attained irrespective of type reinforcement, percentage of reinforcement and applied load After 300°C, the displacements are still clustered together but is shown

that for the slabs reinforced with lower percentages of reinforcement (Tests 5, 15, and 17), the overall displacement is less than those slabs reinforced with increased area of reinforcement (Figure 5.29: red-0.05% reinforcement, blue-0.25% reinforcement, pink-0.1% reinforcement and green-0.15% reinforcement). The rate of deflection for the more lightly reinforced slabs is lower than the other slabs beyond approximately 50 minutes. Underside slab temperatures in excess of 550°C, the vertical displacements dramatically increased and the slabs attained displacements of approximately *span/10*.

The slabs sustained displacements in excess of the deflection criteria of *span/30* and at this displacement many of the slabs were intact.

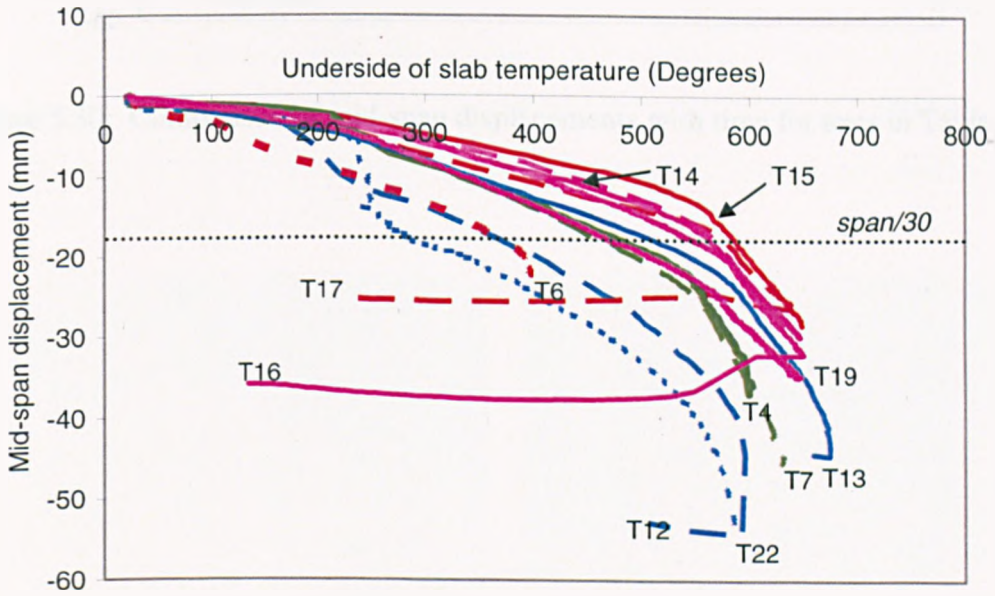

Figure 5.29: Comparison of mid-span displacements with underside of slab temperature for tests in Table 5.1

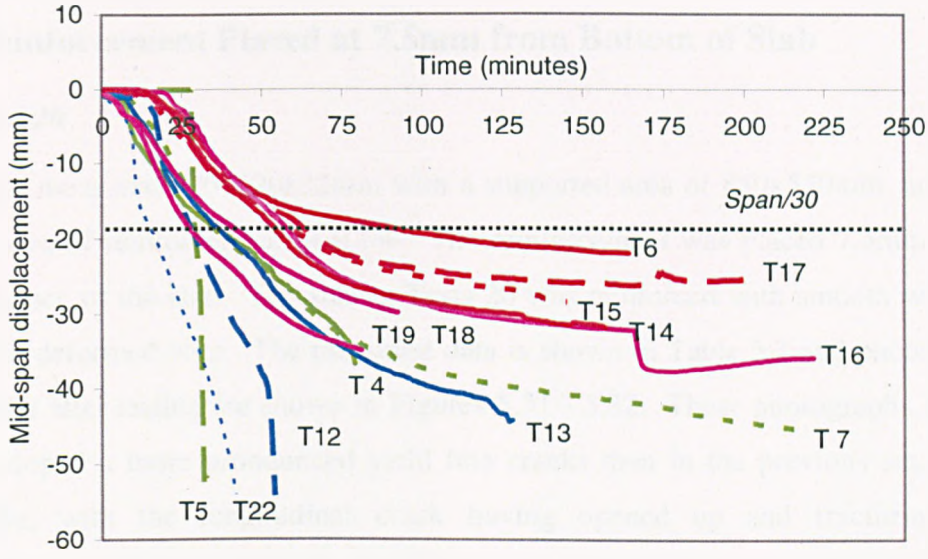

Figure 5.30: Comparison of mid-span displacements with time for tests in Table 5.1.

5.3.3 Istropically Reinforced Slabs of Aspect Ratio 1.55 with Reinforcement Placed at 7.5mm from Bottom of Slab

Tests 9 and 20

These slabs measured 920x620x22mm with a supported area of 850x550mm, and a cross sectional area of reinforcement of 0.1%. The reinforcement was placed 7.5mm from the bottom surface of the slab. The slab in Tests 20 was reinforced with smooth wire and in Test 9 with deformed wire. The measured data is shown in Table 5.2 and photographs of Test 9 taken after testing are shown in Figures 5.31 - 5.32. These photographs shows the slabs developed a more pronounced yield line cracks than in the previous set of 15mm thick slabs, with the longitudinal crack having opened up and fracturing of the reinforcement. The crack patterns were similar to the thinner heated slabs, in that after approximately 20 minutes into the test, the slab had developed the transverse crack as the slab bowed into double curvature. The slab also bowed significantly less than the thinner slabs as can be seen in Figure 5.31.

Figure 5:31: Test 9, view of top surface of slab after test

The slab in Test 9 was reinforced with deformed wire and towards the end of the test, after the formation of the yield line cracks, the reinforcement quickly fractured in the longitudinal crack leading to runaway failure of the slab (Figure 5.32). Figure 5.33 compares the mid-span displacement for Tests 9 and 20 with respect to time. The runaway deflection for Test 9 can be seen to occur just after 120 minutes.

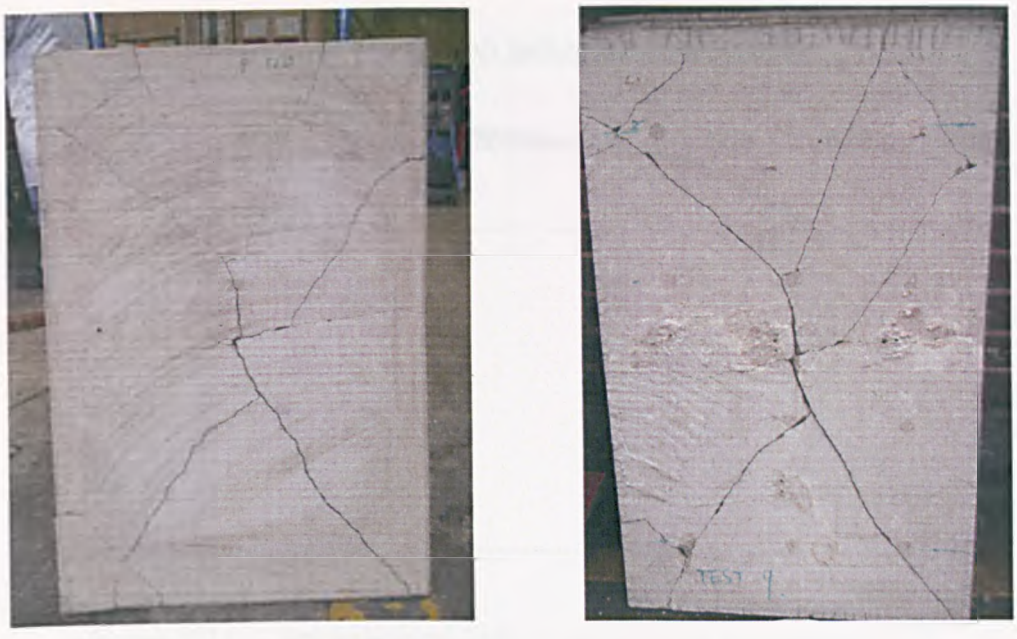

(a) (b)

Figure 5:32: Test 9: (a) View of bottom surface of slab after test (b) View of top surface of slab

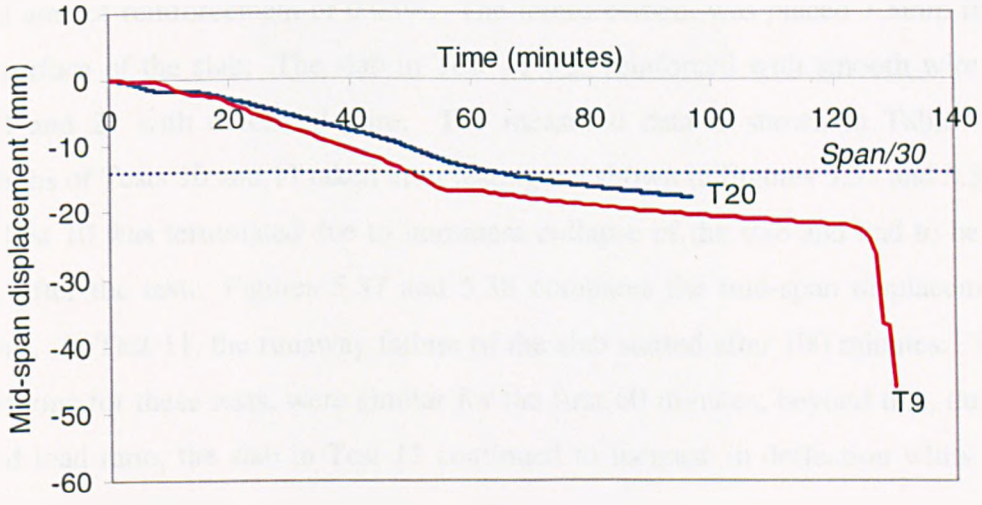

Figure 5.33: Comparison of Tests 9 and 20 with time.

The test deflections with respect the underside slab temperatures are compared in Figure 5:34. The runaway failure of the slab in Test 9 occurs at approximately 600°C with reinforcement temperatures of 445°C. As previously discussed, the bond strength at these temperatures is very low which quickly leads to progressive opening of the cracks, exposing the reinforcement to the furnace temperatures. The slab in Test 20 did not experience runaway failure, and this is clear from Figures 5.33-5.34.

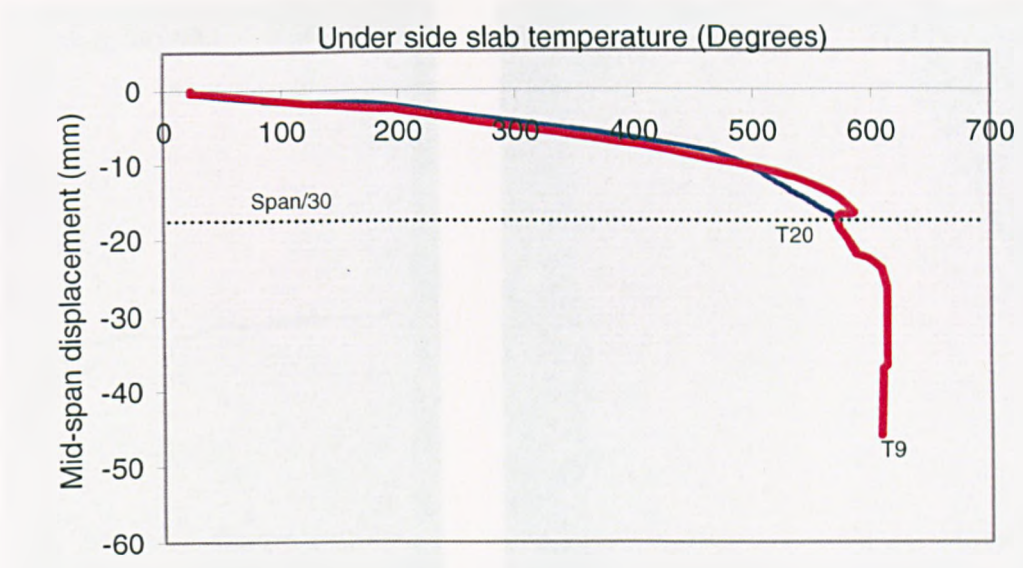

Figure 5.34: Comparison of Tests 9 and 20 with temperature (°C).

Tests 10, 11 and 21

These slabs measured 920x620x22mm with a supported area of 850x550mm, and a cross sectional area of reinforcement of 0.05%. The reinforcement was placed 7.5mm from the bottom surface of the slab. The slab in Test 11 was reinforced with smooth wire and in Tests 10 and 21 with deformed wire. The measured data is shown in Table 5.2 and photographs of Tests 10 and 11 taken after testing are shown in Figures 5.35 and 5.36. The slab in Test 10 was terminated due to imminent collapse of the slab and had to be pieced together after the test. Figures 5.37 and 5.38 compares the mid-span displacements of these tests. In Test 11, the runaway failure of the slab started after 100 minutes. The rate of deflections for these tests, were similar for the first 60 minutes; beyond this, due to the increased load ratio, the slab in Test 11 continued to increase in deflection whilst that in Test 21 seems to plateau.

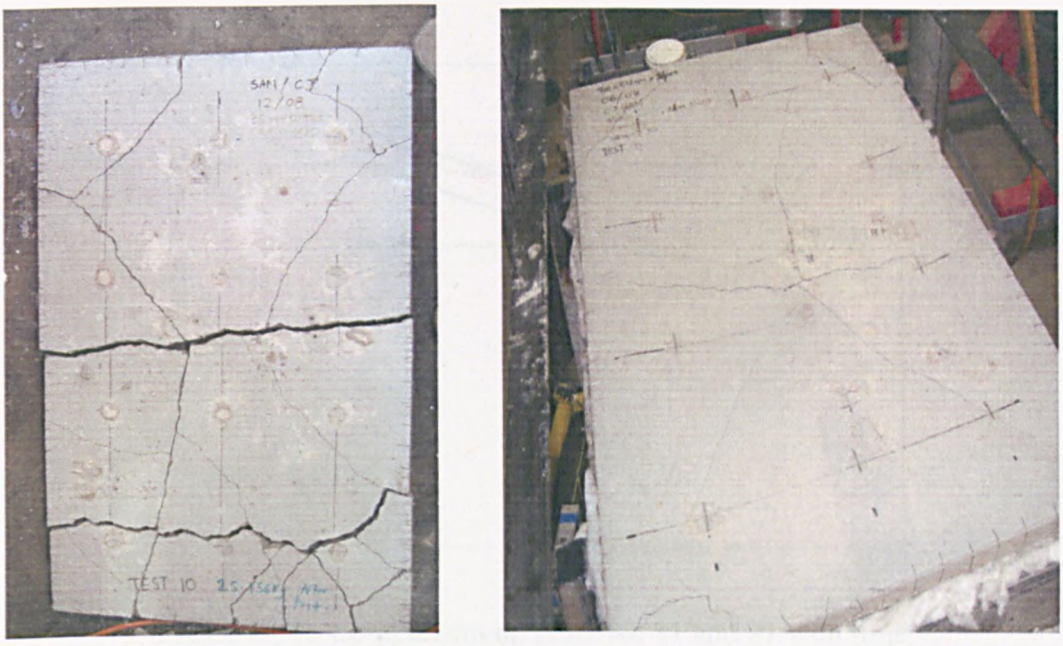

(a) (b)

Figure 5.35: View of top surface of slab for (a) Test 10 and (b) Test 11.

Figure 5.36: View of bottom surface of slab in Test 11.

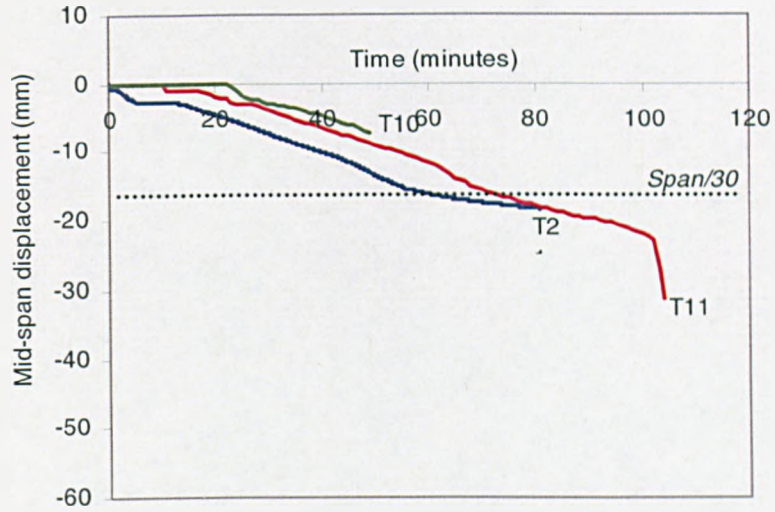

Figure 5.37: Comparison of Tests 10, 11 and 21 with time.

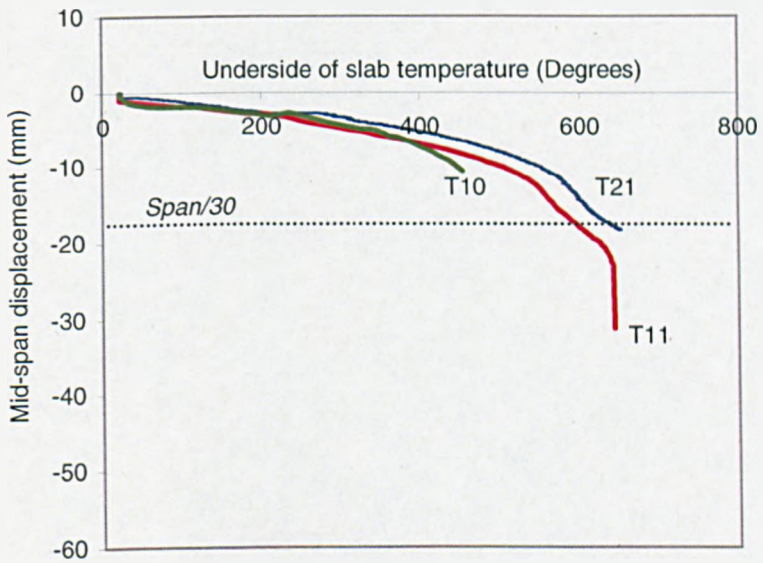

Figure 5.38: Comparison of Tests 10, 11 and 21 with temperature.

5.3.4 Comparison of Tests

The slabs in Table 5.2 have been compared with respect to time and temperature. The results are presented in Figures 5.39 and 5.40. The load ratio for Test 21 was 1.58 and in Test 9 was 1.48, with cross sectional areas of reinforcement of 0.05% and 0.1%. Again the rates of deflection for these tests were similar, Figure 5.39. Comparing these tests with the previous tests of thinner depth, it can be seen that at any given displacement the thicker slabs displace less. The increased slab depth leads to the slabs having reduced thermal

bowing, also the increased effective depth and compression zone in the concrete leads to reduced enhancements.

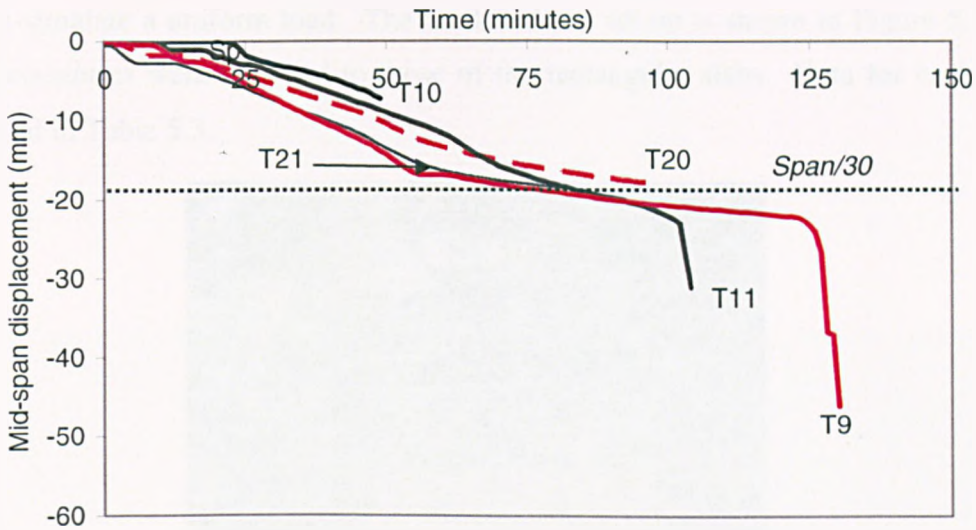

Figure 5.39: Comparison of Tests 9, 10 11, 20 and 21 with time.

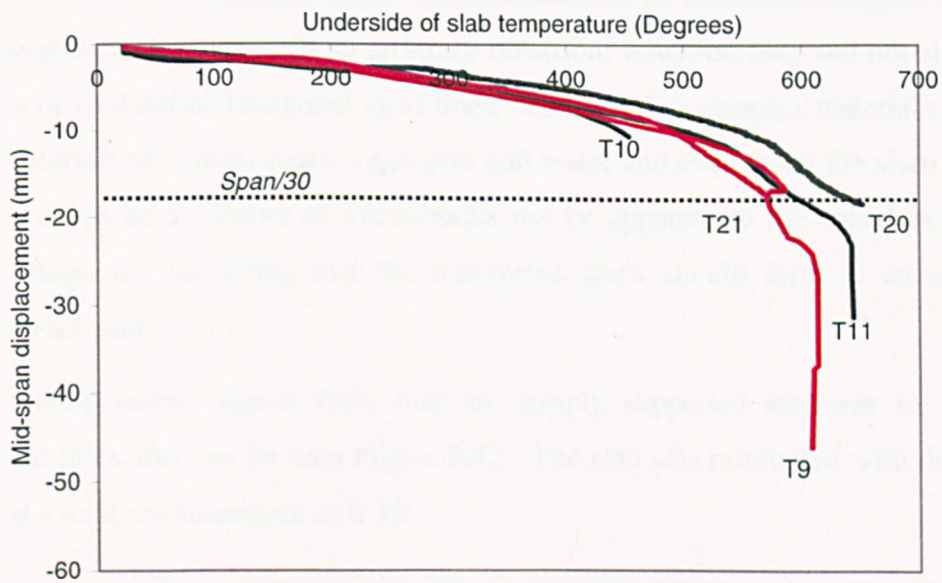

Figure 5.40: Comparison of Tests 9, 10 11, 20 and 21 with temperature.

The slabs performed similar to previous tests in that up to 550°C all slabs behaved very similar irrespective of reinforcement percentage. After 550°C, the rate of deflections for all slabs increased dramatically leading to runaway failure in some tests.

5.4 Square Tests

5.4.1 Observations of Slab Behaviour

The test rig was adapted for the testing of the square slabs, with a new 4 point loading system to simulate a uniform load. The modified test set up is shown in Figure 5.41, but the test procedures were identical to those of the rectangular slabs. Data for each test is summarised in Table 5.3.

Figure 5.41: Test set-up for the heated square slabs

In general, the tests on the square slabs were characterised by thermal bowing of the slab with a transverse crack forming in an arbitrary direction; however, they did not show the development of well defined diagonal yield lines. Concrete is a complex material made up of several materials of cement paste, aggregate and water and even when the slabs are not loaded there could be a number of microcracks not be apparent to the naked eye. It is therefore perhaps not surprising that the transverse crack should form in an arbitrary direction for each slab.

At ambient temperature, square slabs that are simply supported are seen to develop diagonal yield lines, this can be seen Figure 5.42. The slab was reinforced with deformed wire and had a total reinforcement of 0.3%.

Figure 5.43 shows different views of the Test 3 slab after testing. The slab dimensions were 620x620x15mm with the reinforcement placed at mid-depth. This slab was reinforced with smooth wire which had a cross sectional area of reinforcement equivalent to a ratio of 0.25%. The slab initially developed the transverse crack which grew progressively through the test. Figure 5.43(a) shows the diagonal folds of the slab but these have not formed full-depth yield line cracks that are apparent at ambient temperature (Figure 5.42).

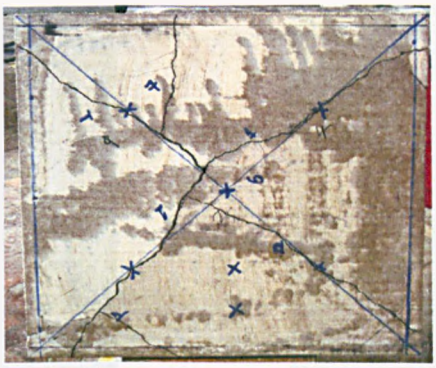

Figure 5.42: Ambient temperature testing of a square slab reinforced with deformed wire (bottom surface view).

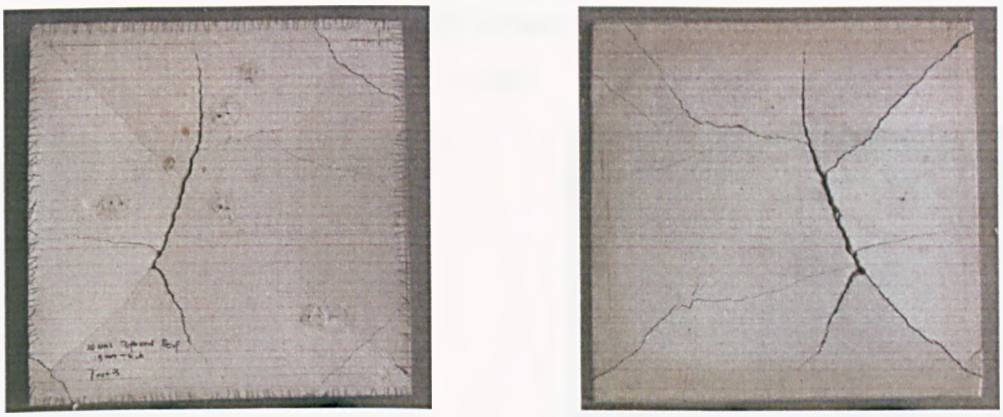

(a) (b)

Figure 5.43: Test 3: (a) View of top surface of slab, and (b) View of bottom surface of slab.

In Test 4, the slab had a cross sectional area of reinforcement of 0.15% and the wire was deformed; the load ratio was also higher (1.61). Photographs taken after the test are shown in Figure 5.44; again the transverse crack developed initially and progressively widened. However, unlike the previous test, yield line cracks also formed but were not as well defined as in the ambient test. The transverse crack had opened exposing the deformed wire to the hot furnace temperatures which lead to the fracturing of the reinforcement.

The slab in Test 5 was reinforced with deformed wire and the cross sectional area of reinforcement equivalent to a ratio of 0.05%. This slab was subject to a high load ratio of 2.38. During the test, the slab did not develop any major cracks, other than the transverse crack, and the yield lines were characterised by diagonal folds, Figure 5.45.

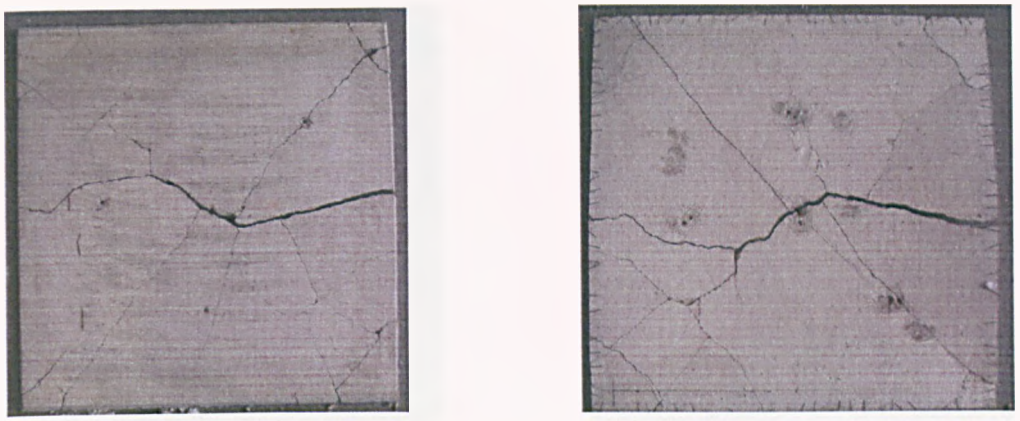

(a) (b)

Figure 5.44: Test 4: (a) View of bottom surface of slab and (b) View of top surface of slab.

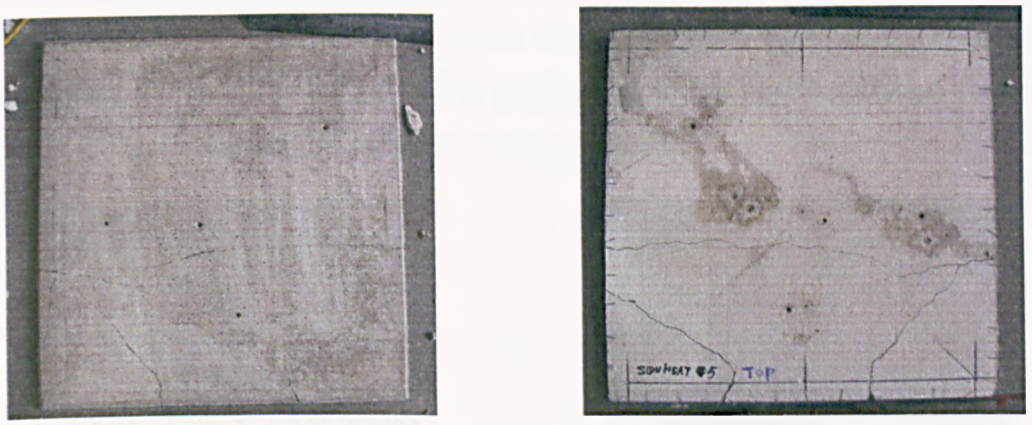

(a) (b)

Figure 5.45: Test 5: (a) View of bottom surface of slab and (b) View of top surface of slab.

The slab in Test 6 developed extensive cracking with the formation of two transverse cracks. This slab was reinforced with smooth wire with a reinforcement ratio of 0.1%. As can be seen in Figure 5.46, the transverse and diagonal cracks are apparent.

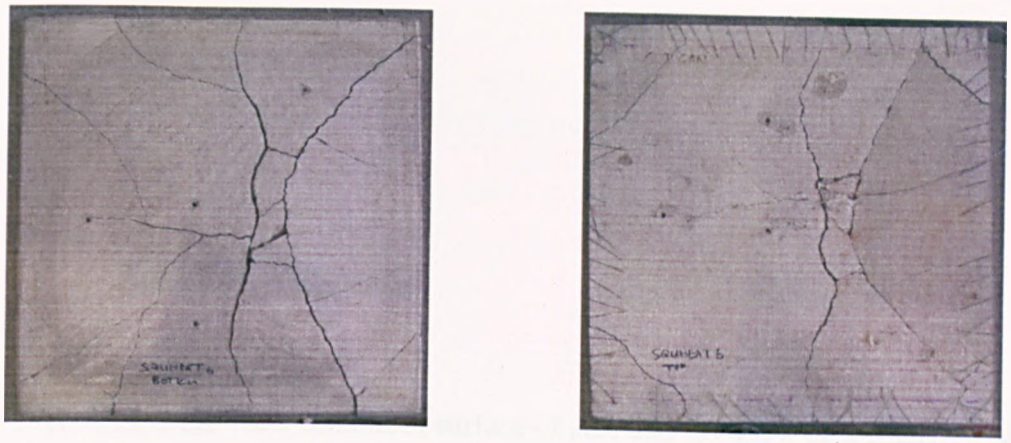

(a) (b)

Figure 5.46: Test 6 (a) View of bottom surface of slab and (b) View of top surface of slab

The slab in Test 7 was reinforced with smooth wire with a reinforcement ratio of 0.05%. The load ratio for this slab was 3.15 and the formation of the transverse crack and yield line cracks are shown in Figure 5.47. The diagonal yield line cracks had also formed and are similar to those found in the ambient test (Figure 5.42).

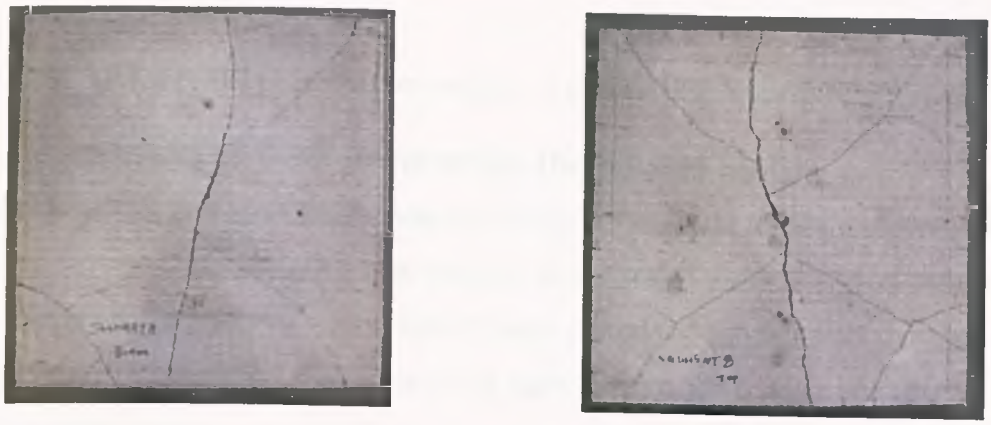

(a) (b)

Figure 5.47: Test 7 (a) View of bottom surface of slab and (b) View of top surface of slab.

The next set of tests was conducted on square slabs of dimensions 620x620x22mm with reinforcement placed at 7.5mm from the bottom surface of the slab. The total cross sectional reinforcement in Tests 8 and 9 was 0.05%. In Test 8, the slab was reinforced with deformed wire and in Test 9 with smooth wire. Figures 5.48 and 5.49 show the slabs after testing; both slabs exhibited cracking with Test 9 forming just the transverse and corner cracks and Test 8 random top surface cracking.

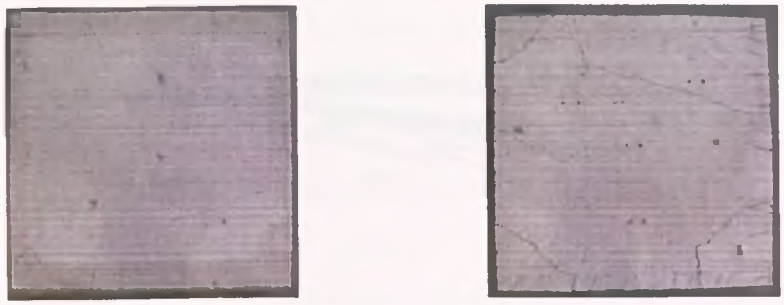

(a) (b)

Figure 5.48: Test 8 (a) View of bottom surface of slab and (b) View of top surface of slab.

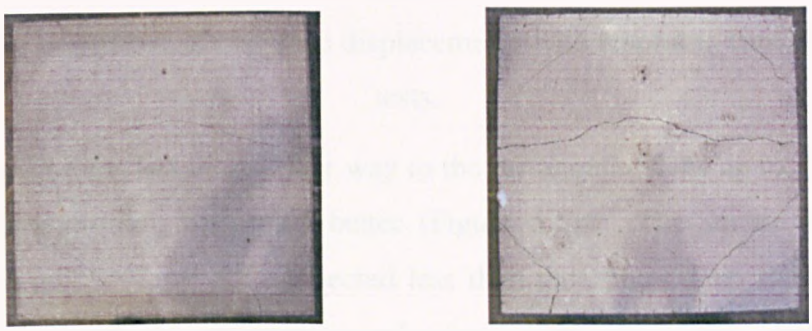

(a) (b)

Figure 5.49: Test 9 (a) View of bottom surface of slab and (b) View of top surface of slab.

5.4.2 Comparison of Displacement for the Square Slabs

Comparisons of the mid-span displacements for all of the square tests are shown in Figures 5.50 and 5.51. Similar behaviour was attained to the tested slabs of aspect ratio 1.55, in that the slabs of depth 22mm with reinforcement placed 7.5mm from the bottom surface (Tests 8 and 9) deflected less the 15mm thick slabs (Figure 5.50). Runaway deflections of the slabs can be seen to occur in Tests 3, 4 and 6. Most of the slabs reached maximum deflections in excess of *span/30.*

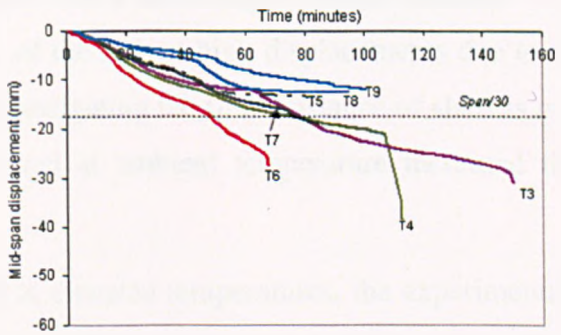

Figure 5.50: Comparison of mid-span displacements with respect to time for the square tests.

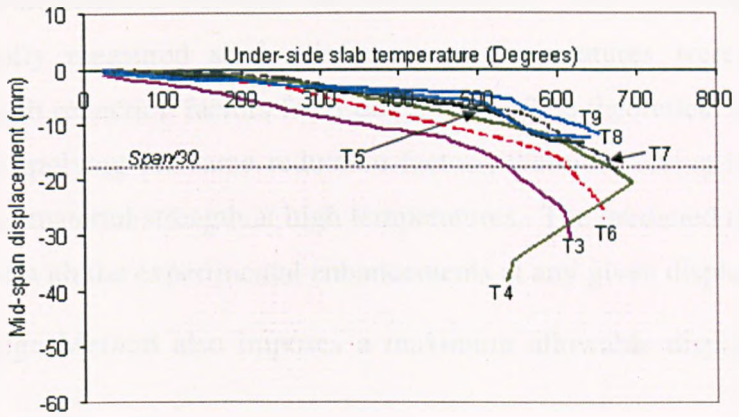

Figure 5.51: Comparison of mid-span displacements with respect to time for the square tests.

The square slabs performed in a similar way to the rectangular slabs up to about 300°C; at higher temperatures, they performed better (Figure 5.51). The square slabs of depth 24mm, Tests 8 and 9 (Table 5.3) deflected less than the 15mm deep slabs at any given temperature. For both the rectangular and square slabs, the results show that, as the percentage of reinforcement decreases, the deflections towards the latter stages of the test reduce (Figure 5.51).

5.5 Comparisons with the Simple Design Method

At ambient temperature, the enhancements for each test were calculated by dividing the load capacity of the slab by the calculated yield line capacity of the slab at ambient temperature. The test results were then compared with results from the Simple Design Method at ambient temperature. It was shown that two-way slabs have increased load capacity at high displacements due to the presence of membrane forces. This next section presents the predicted load capacity of the tested slabs and the enhancements attained above the yield line load using the Simple Design Method. The method accounts for increased load capacity of the slab at high displacements due to in-pane forces within the slab. The purpose of investigating the fire resistance of slabs is to investigate if the tensile membrane action observed at ambient temperature increased the fire resistance of the tested slabs.

For the tests conducted at elevated temperatures, the experimental enhancements for each test can be deduced by dividing the applied load by a reduced yield line capacity with increasing temperature. A reduced, high-temperature yield-line load capacity can be

calculated using the reduced strengths of the reinforcing steel at elevated temperatures. The experimentally measured steel reinforcement temperatures were used to assign appropriate strength reduction factors from Eurocode 3. The theoretical enhancements are then deduced by applying the same reduction factors, therefore taking into consideration the degradation of material strength at high temperatures. The predicted enhancements can then be compared with the experimental enhancements at any given displacement.

The Simple Design Method also imposes a maximum allowable displacement which is given by;

$$v = \frac{\alpha(T_2 - T_1)l_2}{16h} + \sqrt{\left(\frac{0.5f_y}{E}\right)_{\text{Reinf'r}20^oC} \frac{3L^2}{8}} \qquad 5.1$$

where: v = Vertical displacement

α = Coefficient of thermal expansion

T_2 = Bottom temperature

T_1 = Top temperature

h = Slab depth

l = length of shorter span

L = length of longer span

The first part of the equation considers the thermal expansion of the slab and the second part of the equation considers the mechanical strains in the reinforcement.

5.5.1 Isotropically Reinforced Slabs of Aspect Ratio of 1.55

Tests 4 and 7

In order to compare Tests 4 and 7, the theoretical enhancement factors given by the Simple Design Method are plotted on Figure 5.52 as lines eT4 and eT7 respectively. Test 4 reached factors of nearly 2.4 times the yield line load compared to Test 7 which only reached 2.1.

Test 5 has not been presented due to the immediate failure of the slab shortly after the start of the test. The BRE deflection limit (equation 5.1) is also shown and it can be seen that at this point the slab has not progressed into membrane action and gives a similar result to the well known deflection criteria of *span/30*. The slabs had the same amount of cross

sectional reinforcement of 0.15%, but differ only in the reinforcement type used (Table 5.1). Whilst the two slabs had different types of reinforcement and different load ratios, the enhancement rate is very similar. Figure 5.53 compares the predicted load capacities of the slab calculated using the Simple Design Method, in that the enhancement factors are multiplied by the reduced yield line load. The enhancement factor is directly proportional to the displacements because increasing displacement increases the lever arm between the in-plane membrane forces and thus increases the enhancements.

In comparing the predicted load capacity of the slabs in Test 4 and 7 with the imposed test load and yield load capacity, it can be seen that the predicted load capacities increased above the yield line predictions and reached a maximum peak at approximately 25mm displacement. After that, the predicted load capacities decreased due to the decreasing strength of the reinforcement. Further increases in displacement did not increase the load capacities. It is shown in Test 7, that at displacements greater than 20mm, the yield load progressively decreased due to reduction in the strength of the reinforcement though the predicted load capacity of the slab shows that the slab maintains the load even though there is a reduction in the strength of the reinforcement. Test 4 had a higher load ratio and the slab did resist the load initially but then there was a rapid decline in the load capacity at a displacement of 30mm followed by a slight increase, at which point the test was terminated due to imminent collapse of the slab.

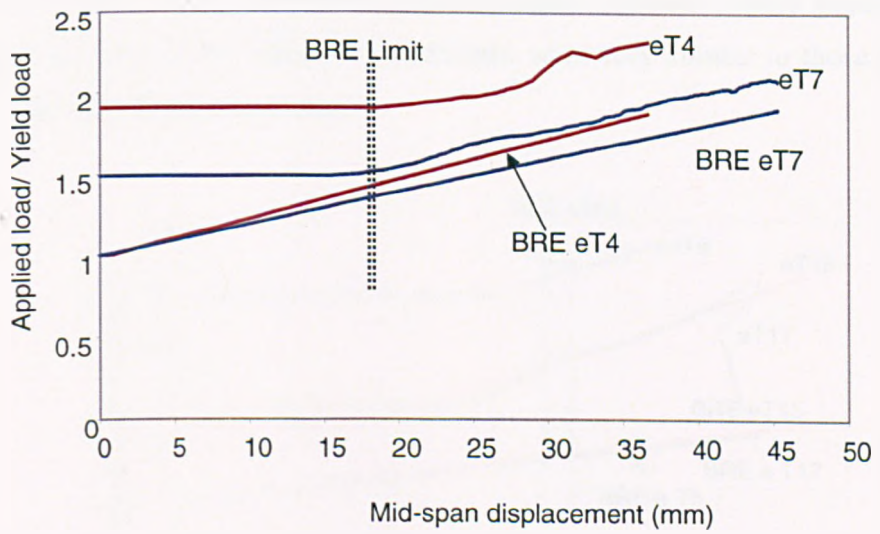

Figure 5.52: Variation of applied load/yield load for Tests 4 and 7.

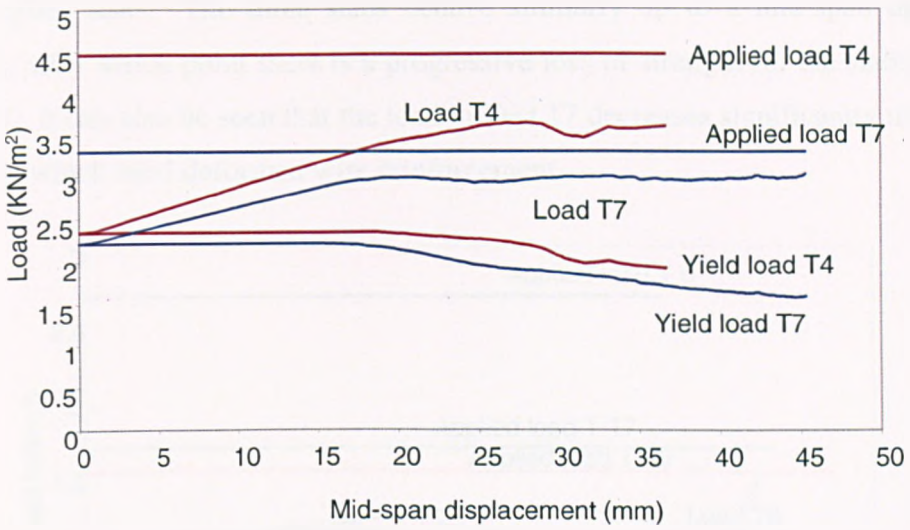

Figure 5.53: Comparisons of the load and yield-line capacities for Tests 4 and 7 from the Simple Design Method with the actual load levels as deflections increase.

Tests 6, 15 and 17

The slabs in this set of tests were reinforced with lower percentages of reinforcement, 0.05% (Table 5.1); the enhancement plots for these tests are shown on Figure 5.54. The slab in Test 17 was reinforced with deformed wire and at a deflection of approximately 24mm, the enhancement factor increases slightly relative to Test 15 which had a similar load ratio. Test 6 used smooth wire reinforcement and had a much higher load ratio, but the linear increase in the enhancement factors were very similar to those in Test 15, even though this had a lower load ratio.

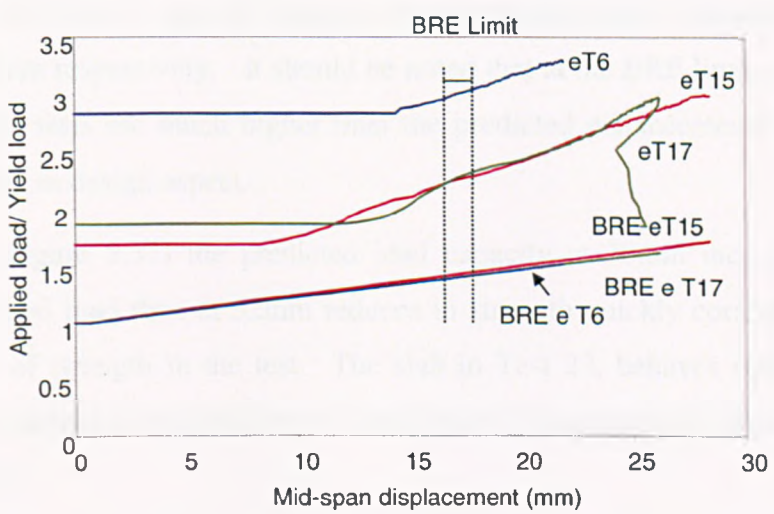

Figure 5.54: Variation of applied load/yield load for Tests 6, 15 and 17.

Figure 5.55 compares the load capacities calculated using the Simple Design Method with the applied load. The three slabs behave similarly up to a mid-span displacement of 14mm, after which point there is a progressive loss of strength for the slabs in Tests 6, 15 and 17. It can also be seen that the load in Test 17 decreases significantly more for Tests 6 and 15, which used deformed wire reinforcement.

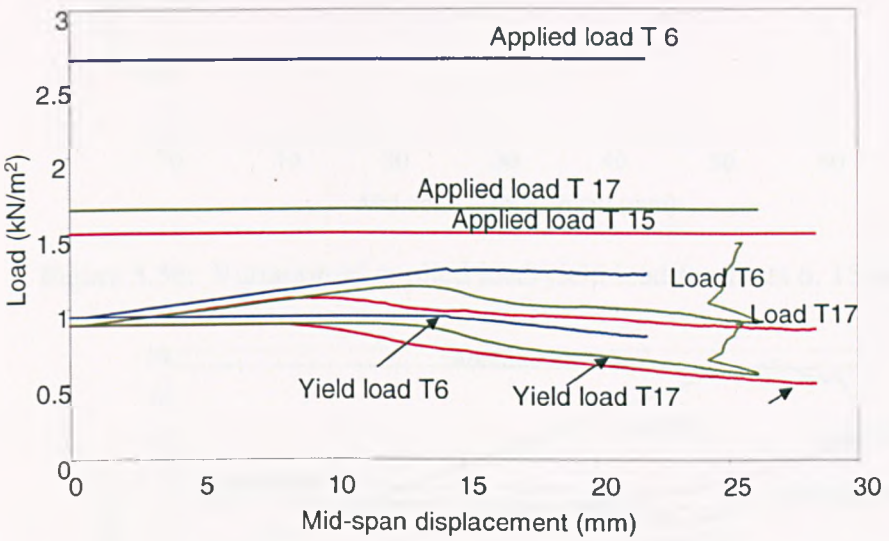

Figure 5.55: Comparison of the load and yield-line capacities for Tests 6, 15 and 17 from the BRE design method with the actual load levels as deflections increase.

Tests 12, 13 and 22

These tests had a total cross sectional area of reinforcement of 0.25%. Figures 5.56 and 5.57 plot the enhancement factors and the predicted load capacities against mid-span displacement. The predicted enhancement factors given by the Simplified Design Method for the slabs in Tests 12 and 22 become unconservative above mid-span deflections of 32mm and 45mm respectively. It should be noted that at the BRE limit, all enhancements indicated in the tests are much higher than the predicted enhancements which ensures a margin of safety in design aspect.

For Test 12 (Figure 5.57) the predicted load capacity at 30mm increases significantly above the applied load then at 52mm reduces in strength quickly corresponding with the observed loss of strength in the test. The slab in Test 22, behaves similarly to Test 12 whilst Test 13 maintains this load up to a mid-span displacement of 30mm when there is a noted reduction.

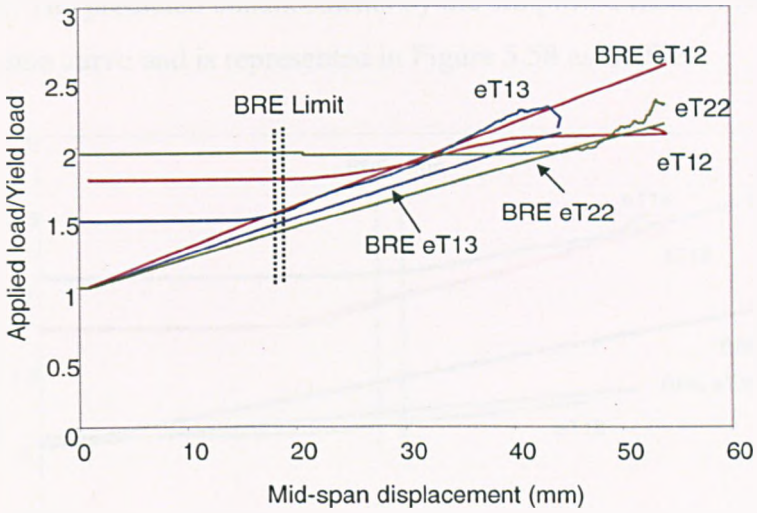

Figure 5.56: Variation of applied load/yield load for Tests 6, 15 and 17.

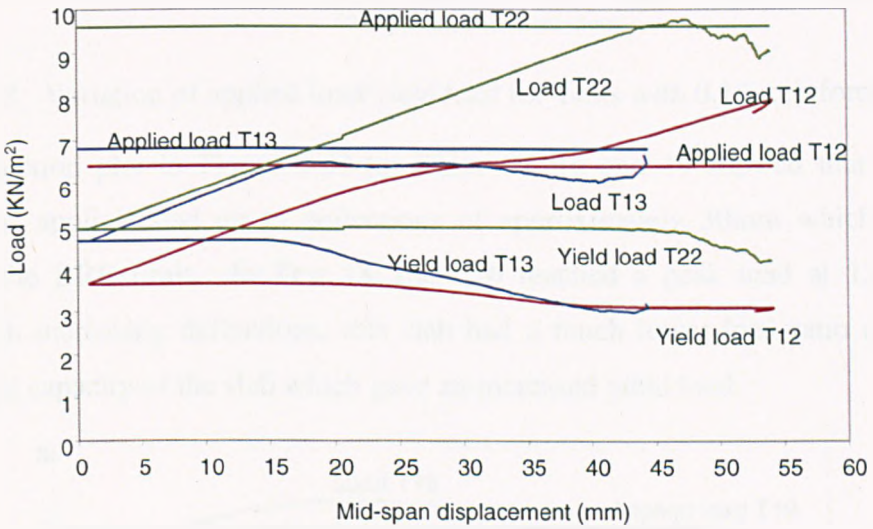

Figure 5.57: Comparison of the load and yield-line capacities for Tests 12, 13 and 22 from the BRE design method with the actual load levels as deflections increase.

Tests 14, 16, 18 and 19

The slabs in these set of tests had total cross sectional area of reinforcement of 0.1%, and the enhancement factors are plotted in Figure 5.58. The enhancement factors in Tests 14, 16 and 19 are quite close and increase at a similar rate to the predicted enhancements by the Simple Design Method. The predicted enhancements in Test 18 are much lower than the other tests due to the increased slab thickness. The slab in Test 18 yields lower enhancements than predicted by that of the Simple Design Method. This slab did have a low load ratio but the test enhancements increased at a similar rate to the predicted

enhancements. The predicted enhancements by the simplified method for Tests 14, 16 and 19 lie on the same curve and is represented in Figure 5.58 as BRE e.

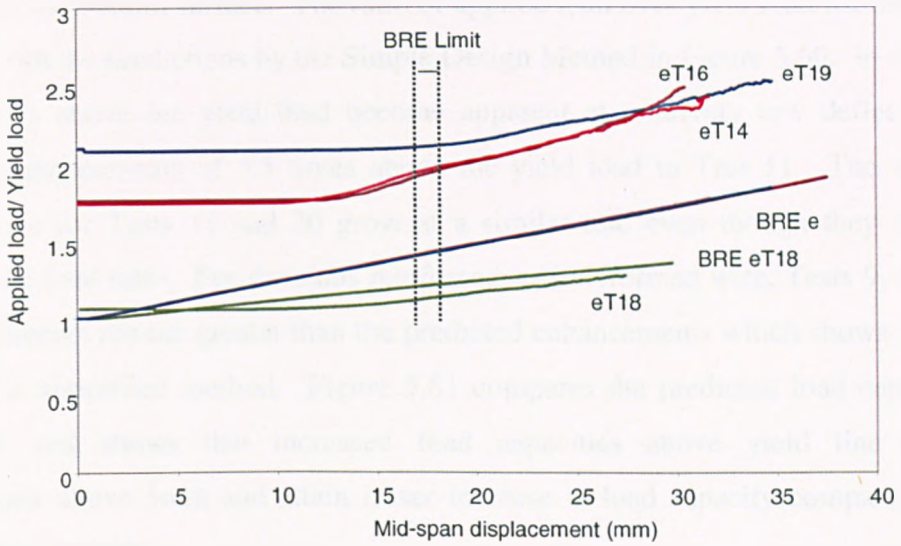

Figure 5.58: Variation of applied load/yield load for Tests with 0.1% reinforcement

The load-deflection plot in Figure 5.59 for Tests 14, 16 and 19 showed that the slabs maintained the applied load up to deflections of approximately 30mm which is much greater than the BRE limit. In Test 18, the slab reached a peak load at 15mm then decreased with increasing deflections; this slab had a much lower load ratio due to the increased yield capacity of the slab which gave an increased yield load.

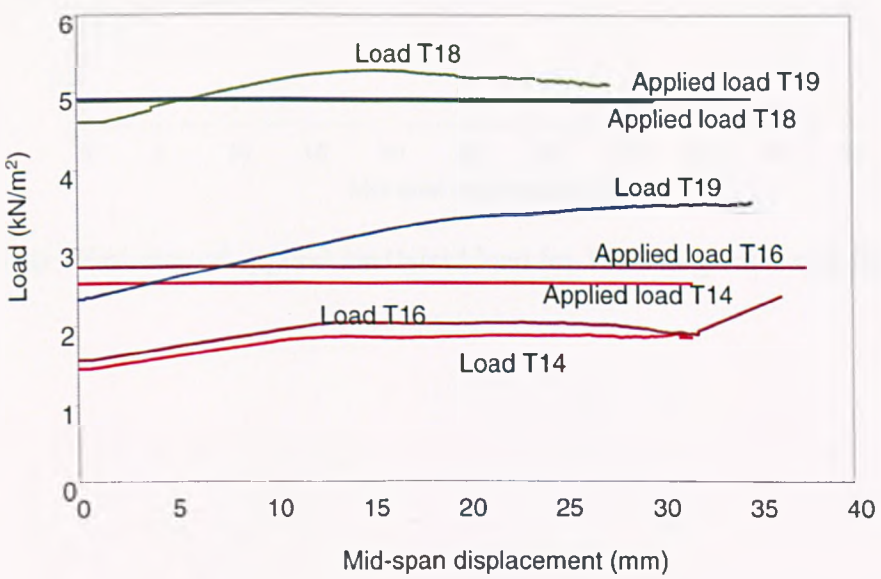

Figure 5.59: Comparison of the load and yield-line capacities for Tests with 0.1% reinforcement from the Simple Design Method with the actual load levels as deflections increase.

Tests with slabs of thickness 22mm

The thicker slabs (Table 5.2) of theoretical depth 22mm had the reinforcement placed at 7.5mm from the bottom surface. The ratio of applied load over yield load for these tests is compared with the predictions by the Simple Design Method in Figure 5.60. In all tests the enhancements above the yield load become apparent at relatively low deflections with maximum enhancements of 3.5 times above the yield load in Test 11. The increase in enhancements for Tests 11 and 20 grow at a similar rate even though they differ with respect to the load ratio. For the slabs reinforced with deformed wire, Tests 9, 10 and 21, the enhancements remain greater than the predicted enhancements which shows a margin a safety in the simplified method. Figure 5.61 compares the predicted load capacities for these tests and shows that increased load capacities above yield line occurs at displacements above 5mm and attain lesser increase in load capacity compared with the slabs of thinner depth.

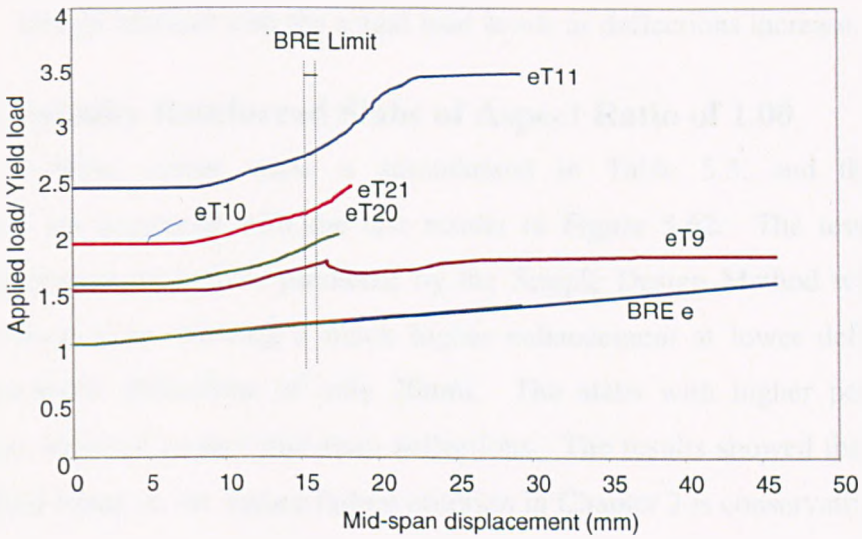

Figure 5.60: Variation of applied load/yield load for Tests of greater slab thickness.

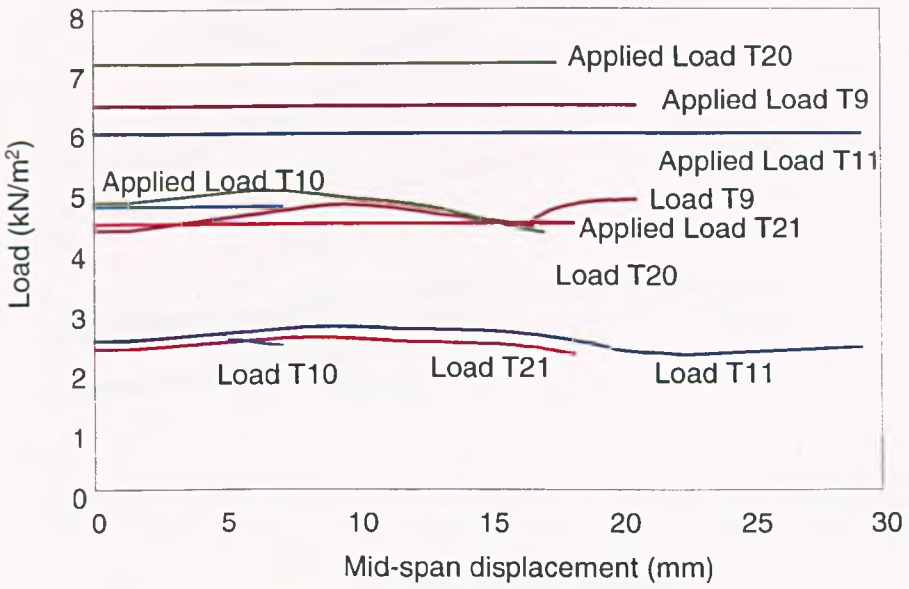

Figure 5.61: Comparison of the load and yield-line capacities for Tests from the Simple Design Method with the actual load levels as deflections increase.

5.5.2 Isotropically Reinforced Slabs of Aspect Ratio of 1.00

The data for these square slabs is summarised in Table 5.3, and the predicted enhancements are compared with the test results in Figure 5.62. The tests indicate a greater enhancement than those predicted by the Simple Design Method with the more lightly reinforced slabs showing a much higher enhancement at lower deflections, but reaching maximum deflections of only 20mm. The slabs with higher percentages of reinforcement achieved greater mid-span deflections. The results showed that the Simple Design Method based on the square failure criterion in Chapter 2 is conservative.

Figure 5.62 compares the predicted load capacities for the square slabs; in general, all of the slabs reached a peak load followed by a reduction in strength, although this is more pronounced in some cases than others.

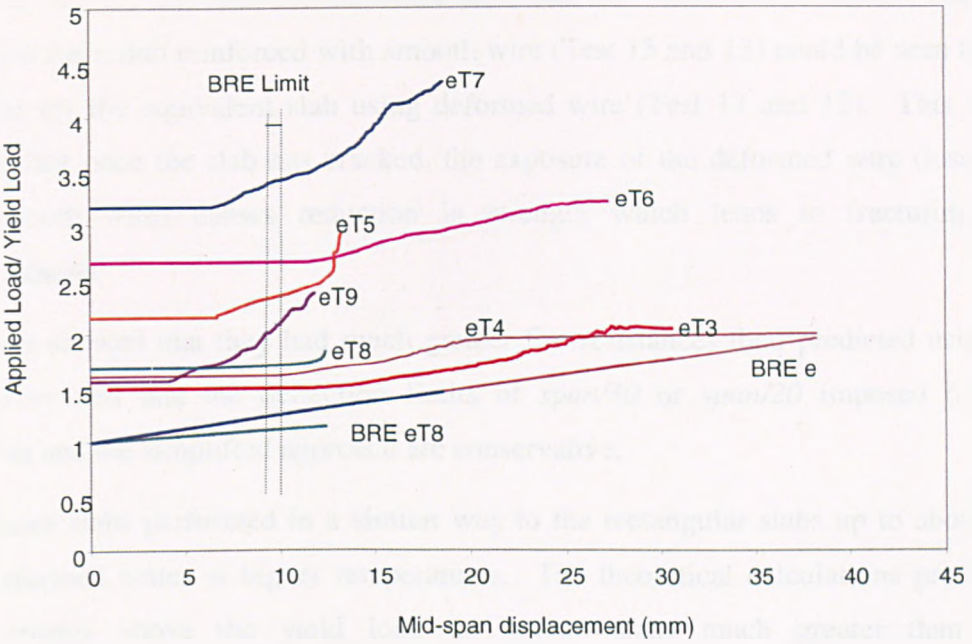

Figure 5.62: Variation of applied load/yield load for Tests of greater slab thickness.

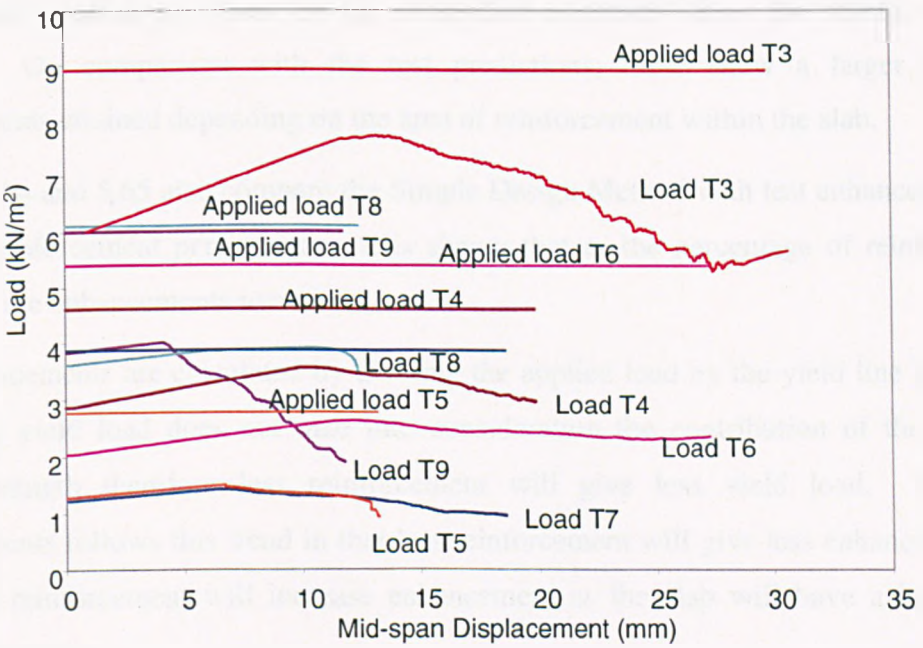

Figure 5.63: Comparison of the load and yield-line capacities for Tests from the Simple Design Method with the actual load levels as deflections increase.

5.6 Concluding remarks

The mid-span vertical deflections for the rectangular and square slabs tested have been presented and show that mid-span deflections of up to *span/12* were achieved without integrity failure of the slab. All the slabs showed similar rates of deflection between 20°C-300°C. The 22mm thick slabs with reinforcement placed 7.5mm from the bottom surface

(Tests 9, 10, 11, 20, and 21) deflected less than the 15mm thick slabs. The rate of deflection for a slab reinforced with smooth wire (Test 15 and 13) could be seen to be less than that for the equivalent slab using deformed wire (Test 17 and 12). This seems to indicate that once the slab has cracked, the exposure of the deformed wire (less ductile) than smooth wire) causes reduction in strength which leads to fracturing of the reinforcement.

The slabs showed that they had much greater fire resistances than predicted using yield-line theory and that the deflection limits of *span/30* or *span/20* imposed by current standards and the simplified approach are conservative.

The square slabs performed in a similar way to the rectangular slabs up to about 300°C, and performed better at higher temperatures. The theoretical calculations predicted the enhancements above the yield load for square slabs much greater than for the corresponding rectangular slabs, Figure 5.64.

The overall predictions given by the simplified approach show the results clustered together. On comparison with the test predictions, these show a larger range of enhancements attained depending on the area of reinforcement within the slab.

Figures 5.64 and 5.65 also compare the Simple Design Method with test enhancements for varying reinforcement percentages. It is shown that as the percentage of reinforcement decreases the enhancements increase.

The enhancements are calculated by dividing the applied load by the yield line load. The calculated yield load does not take into consideration the contribution of the concrete tensile strength therefore less reinforcement will give less yield load. The BRE enhancements follows this trend in that less reinforcement will give less enhancement and increased reinforcement will increase enhancement as the slab will have a higher load carrying capacity.

The heated loaded slabs will utilise their concrete tensile strength as the slabs do not suffer any major cracking. These slabs tended to perform better than the slabs with more reinforcement and this could possibly be due to the contribution of the concrete tensile strength. Therefore, the predicted enhancements are not a true representation of the actual slabs performance in fire.

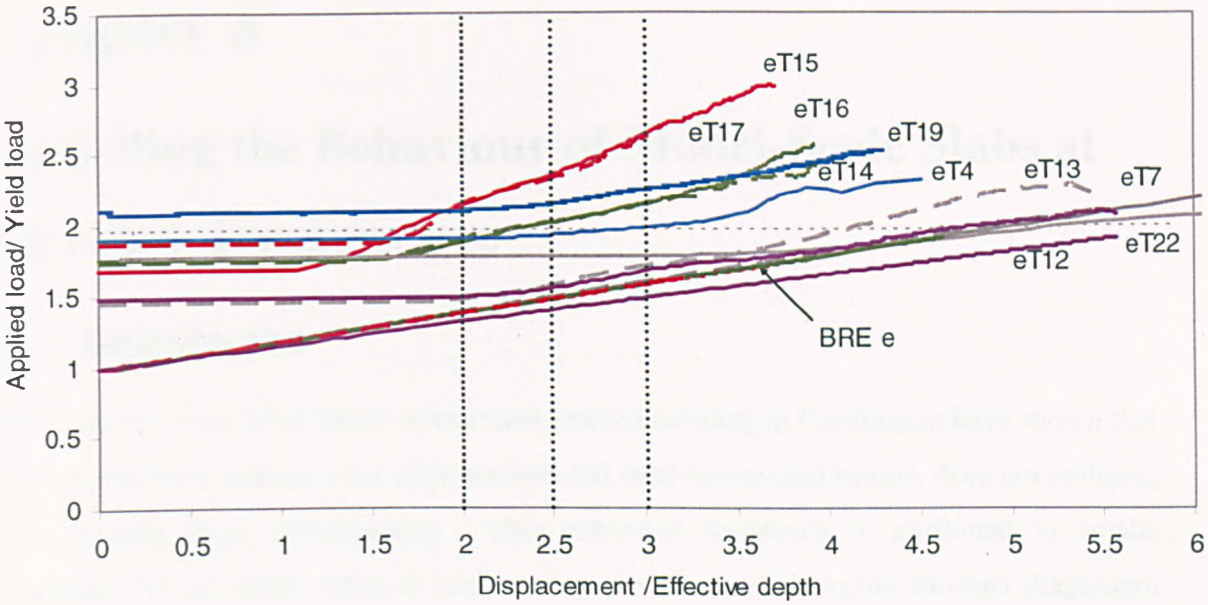

Figure 5.64: Comparison of the applied load/yield load ratio for Tests and comparisons with Simplified Design Method.

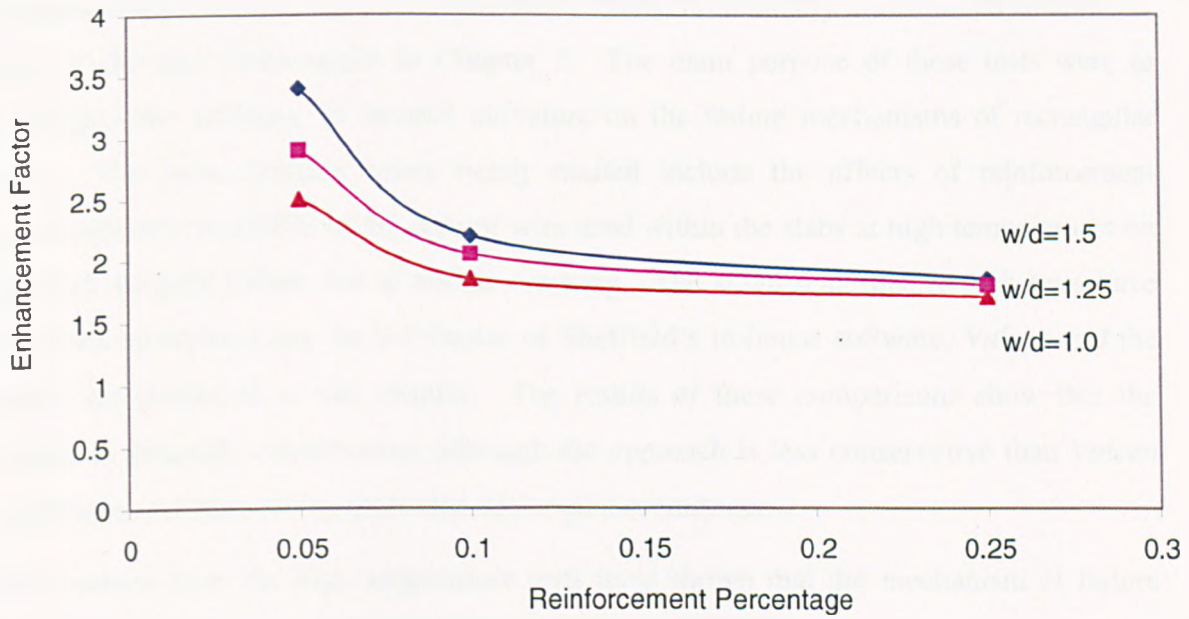

Figure 5.65: Comparison of the applied load/yield load ratio with percentage reinforcement with displacement/effective depth (w/d).

Chapter 6

Modelling the Behaviour of Model-Scale Slabs at Elevated Temperature

6.1 Introduction

Full-scale fire tests in the multi-storey steel framed building at Cardington have shown that a composite floor system, even with unprotected steel downstand beams, does not collapse, even at very large deformations. This enhanced resistance is attributed to tensile membrane forces which assist in maintaining the structural integrity through diaphragm action.

The BRE Simplified Design Method for composite floors in fire is based on a simplified model of membrane action in rectangular slabs. The method has been tested against experimental results from tests on a number of loaded horizontally unrestrained small-scale slabs at elevated temperatures in Chapter 5. The main purpose of these tests were to investigate the influence of thermal curvature on the failure mechanisms of rectangular slabs. The more detailed issues being studied include the effects of reinforcement percentage and the effects of the type of wire used within the slabs at high temperatures on the final integrity failure due to tensile cracking. The small-scale heated slab tests have also been modelled using the University of Sheffield's in-house software, *Vulcan* and the results are presented in this chapter. The results of these comparisons show that the method is generally conservative, although the approach is less conservative than *Vulcan* predictions and may not be applicable under all circumstances.

Observations from the high-temperature tests have shown that the mechanism of failure may differ from that assumed in the Simplified Design Method.

The results of the heated tests conducted on horizontally unrestrained slabs presented in this Chapter have been summarised and published in a paper in the Proceedings of the Fourth International Conference on Advances in Steel Structures [57].

6.2 Numerical Modelling

Numerical studies have been carried out using the University of Sheffield software *Vulcan*. See Chapter 4 for details. Three dimensional models have been created of the model-scale slabs (Chapter 4) and these form the templates for the heated models. The slab elements are sub-divided into 10 layers of which 8 layers represent the concrete and two layers the steel reinforcement. The number of layers used in these models were based on a previous study undertaken which recommended using between 10-20 layers to model the depth of the concrete slab [51]. The recorded temperatures through the depth of the slab have been used to calculate the temperature history for each layer.

6.3 Summary of Model Set-Up

Four slab sizes, of nominal dimensions (in mm) 920x620x15, 920x620x22, 600x600x15, and 600x600x22, were tested with the supported areas being 850x550mm and 550x550mm respectively. The actual depth of the slab varied slightly between tests, and measurements were made after each test (Chapter 5).

The numerical models that were created reflected the true nature of the slab in that the measurements of slab depth and material properties were used as the input data. The uniform load that was applied to the slabs by the loading piston was measured at regular intervals and this value was used in the model input data, so that the model underwent the same level of load as the slab in test. The measured yield strengths of reinforcement and the compressive strengths of concrete are shown in Chapter 5 and these values were used as data for the model.

The temperatures of the lower surface, the reinforcement level and the upper surface of the slab were measured using 12 thermocouples placed at key locations (Figure 6.1). The average temperatures for the three positions were measured and were used as the temperature input to the model. Each model test had a different temperature input data and the aim of the numerical work was to create unique models for each test so that a representative model could be achieved.

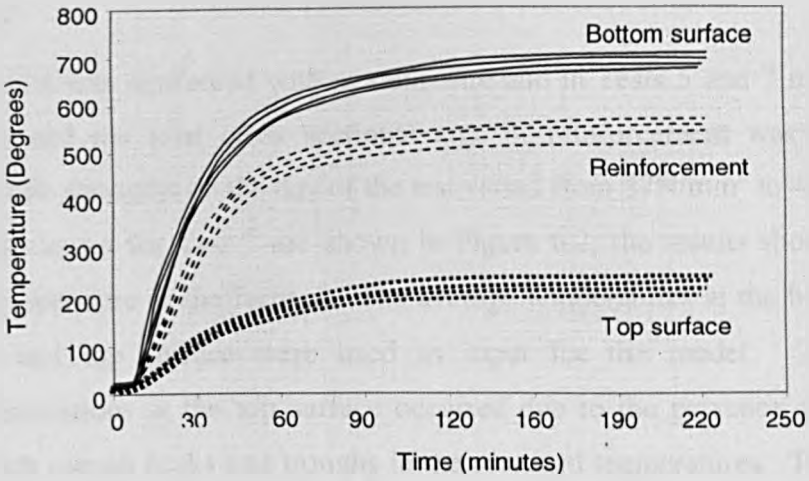

Figure 6.1: Temperature profiles.

6.4 Numerical Modelling

6.4.1 Rectangular Slabs with Reinforcement at Mid-Depth

The rectangular and square slabs were modelled using *Vulcan*. Table 5.1 (Chapter 5) shows a summary of the test results for the rectangular tests; Table 6.1 compares the maximum test displacement with the calculated displacement using the Simple Design Method.

Test	BRE Limit		BRE Limit Δ_{Total}	$\frac{span}{30}$	Max. Reinforcement temperature °C	Max. Test displacement (mm)	$\frac{\text{BRE Limit}}{\text{Max.Test}}$
	$\Delta_{thermal}$	$\Delta_{mechanical}$					
4	4.55	13.27	17.82	18.33	446	37	0.48
5	1.85	12.88	14.73	18.33	194	52	0.28
7	3.85	13.27	16.52	18.33	520	45	0.37
6	3.25	13.27	16.52	18.33	427	22	0.75
15	2.84	13.27	16.11	18.33	564	28	0.37
17	3.7	12.80	14.86	18.33	572	32	0.46
12	3.98	12.88	16.86	18.33	443	41	0.41
13	4.5	13.27	17.77	18.33	574	44	0.4
22	3.41	12.88	16.30	18.33	430	55	0.30
14	1.98	12.88	14.86	18.33	572	32	0.46
16	4.89	13.27	18.16	18.33	445	34	0.53
19	4.03	13.27	14.30	18.33	475	35	0.41
18	2.4	13.27	16.01	18.33	415	30	0.53

Table 6.1: Comparison of maximum test displacements with predictions for slabs of dimensions 920x620x15mm, with reinforcement placed at mid-depth of slab.

Tests 4, 5 and 7

The slab in Test 4 was reinforced with smooth wire and in Tests 5 and 7 reinforced with deformed wire and the total cross sectional area of reinforcement was 0.15%. The measured concrete strengths on the day of the test varied from 37N/mm^2 to 40N/mm^2. The measured temperatures for Test 7 are shown in Figure 6.2; the results show consistency and uniform temperature in the furnace. The average temperatures at the bottom surface, reinforcement and top surface were used as input for the model. The measured temperature fluctuations at the top surface occurred due to the presence of surrounding cooler air, which caused peaks and troughs in the recorded temperatures. The top surface recorded temperatures for the slab were 'smoothed' before use; the new profile is shown in Figure 6.2 below.

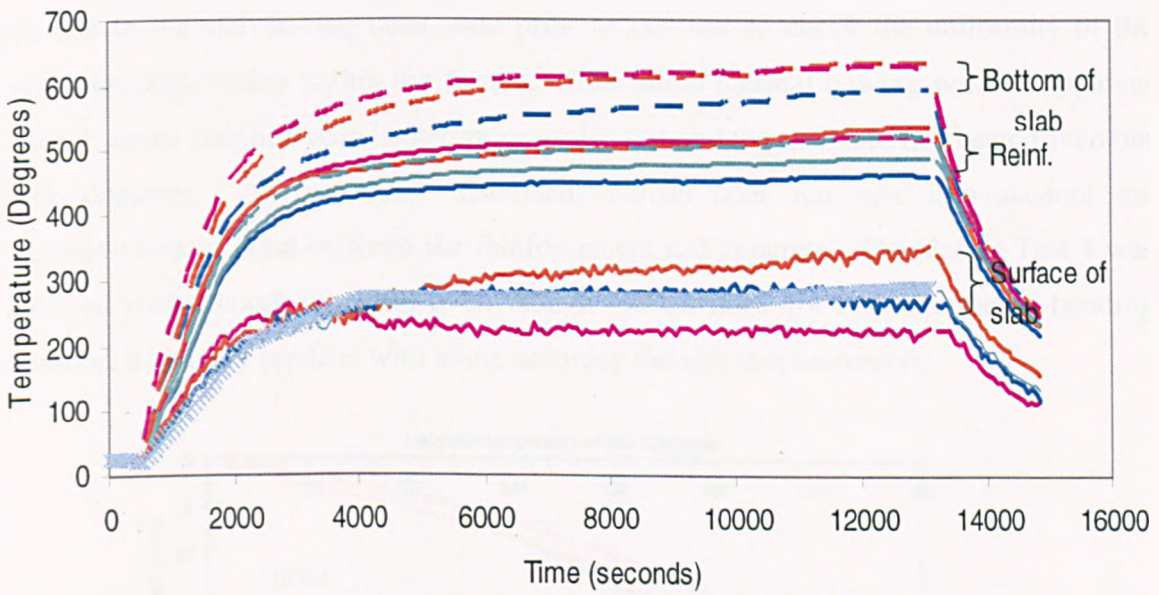

Figure 6.2: Temperature profiles for Test 7.

The mesh layout for the rectangular slabs was based on the same layout used in the ambient-temperature tests (see Chapter 4). Figure 6.3 shows the typical grid layout adopted; the model is based on one quarter of the rectangular slab. The boundary conditions imposed are simply supported with two cut lines which are axes of symmetry.

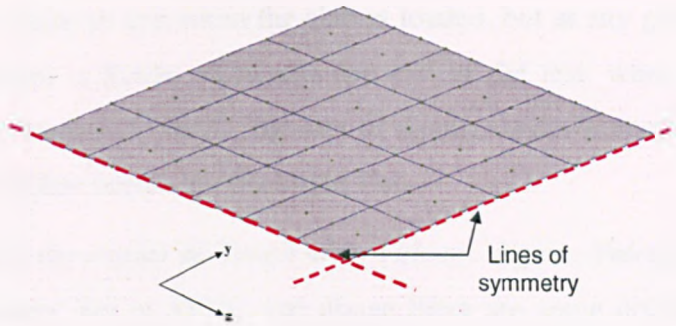

Figure 6.3: Typical mesh layout for rectangular slab of dimensions 850x550mm.

Figure 6.4 compares the measured displacements with the results from *Vulcan*. It can be seen that *Vulcan* slightly under estimates the tested displacements and at approximately *span/30* the slab was intact. The initial discrepancies from the start of the test up to 200°C, were due to the slab having been used prior to this test to check the uniformity of the temperature distribution within the furnace. The initial thermal bowing was not apparent in Test 4, as the slab had been heated prior to this test and the moisture had been driven out of the concrete. As previously discussed, *Vulcan* does not take into account the progressive loss of bond between the reinforcement and concrete. The slab in Test 4 was reinforced with smooth wire and even though *Vulcan* does not consider the de-bonding behaviour, it actually predicts with some accuracy the slab displacements.

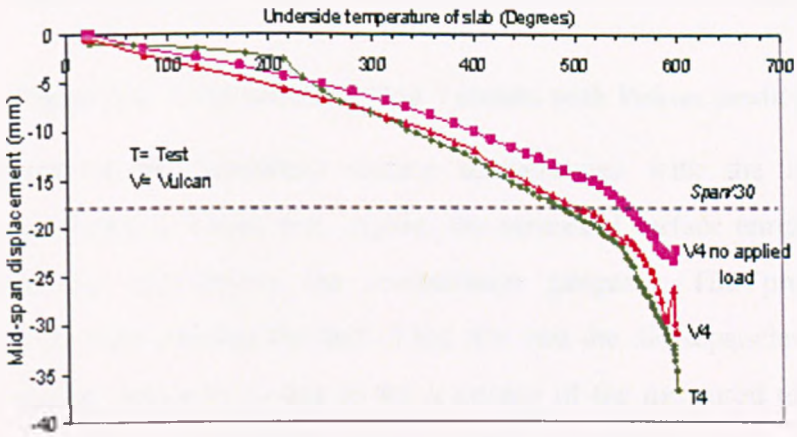

Figure 6.4: Comparison of Test 4 results with *Vulcan* predictions.

The maximum displacement calculated using the Simple Design Method always gives lower-bound values compared with *span/30* and the actual deflection. In order to investigate the influence of the thermal strains in the slab without the influence of the applied load the model was re-run with zero applied load. Figure 6.4 compares the *Vulcan*

results for the cases with and without applied load. It is interesting to note that the overall slab behaviour is similar to that when the slab is loaded, but at any given temperature, the resulting displacement is lower. Towards the end of the test, when the slab underside temperatures are in excess of 500°C, the rate of displacement dramatically increases until at 600°C runaway failure occurs for the tested slab.

Figure 6.5 compares the results of Test 7 with *Vulcan*. Again, *Vulcan* accurately predicts the slab displacements, but at 550°C and above there are some discrepancies due to the measured temperature profiles towards the end of the test. The test was modelled using the recorded surface temperature profiles, which resulted in a scatter of displacements towards the end of the test.

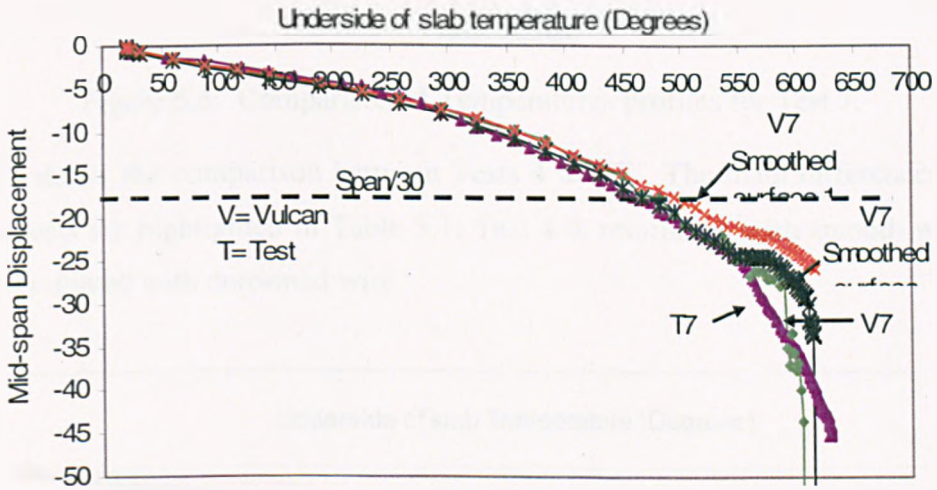

Figure 6.5: Comparison of Test 7 results with *Vulcan* predictions

The comparison of the smoothed surface temperatures with the measured surface temperatures is shown in Figure 6.6. Again, the measured surface temperatures fluctuate due to cooler air surrounding the temperature gauges. The predicted mid-span displacements do vary towards the end of the test and the discrepancies between *Vulcan* and the test results appear to be due to the accuracy of the measured temperatures. It is shown that the displacements using smoothed surface 1 profile are lower at any given point compared with the actual and smoothed profiles due to the difference between the top surface and lower surface temperatures being lower, therefore producing less thermally-induced deflection.

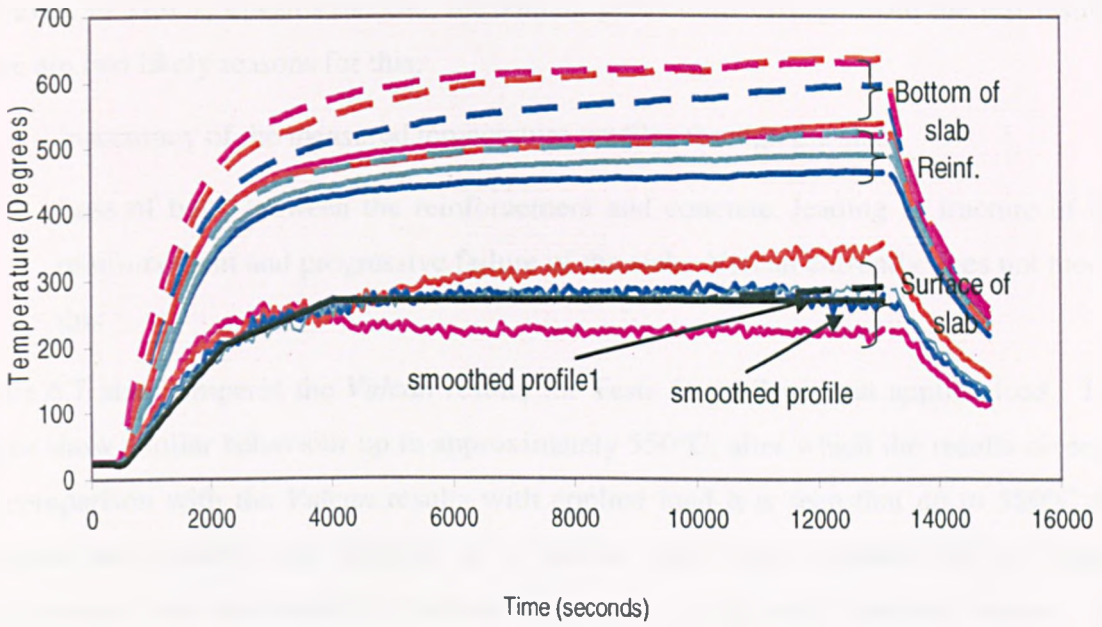

Figure 6.6: Comparison of Temperatures profiles for Test 7.

Figure 6.7 shows the comparison between Tests 4 and 7. The main differences between these two tests are highlighted in Table 5.1; Test 4 is reinforced with smooth wire whilst Test 7 is reinforced with deformed wire.

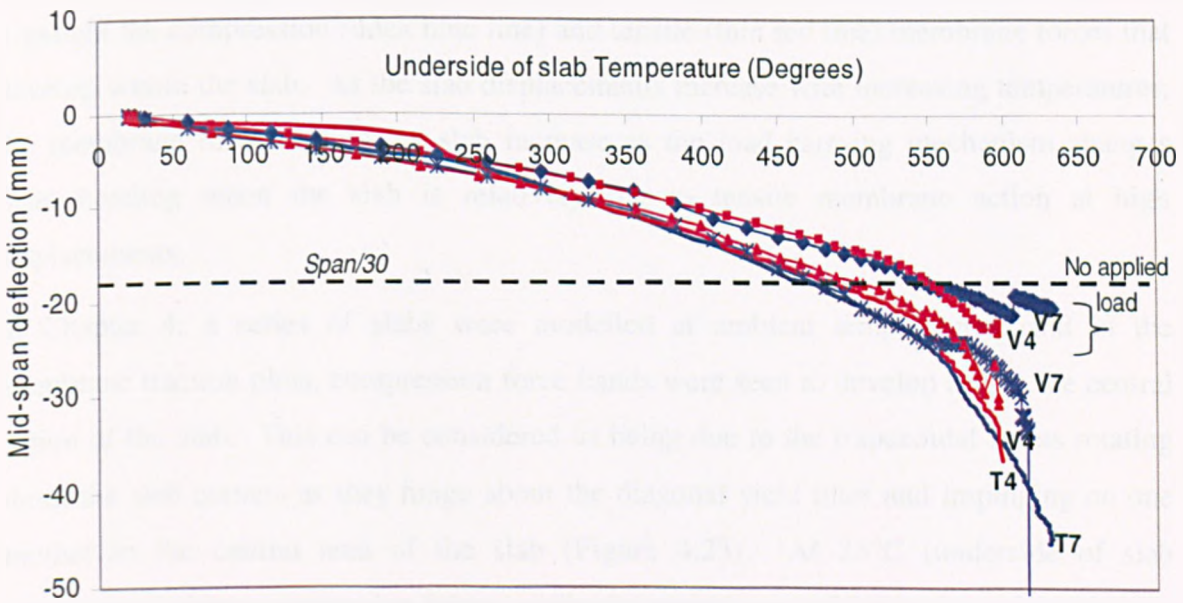

Figure 6.7: Comparison of Test 7 with Test 4 results with Vulcan predictions.

The *Vulcan* predictions for both tests show a very good degree of accuracy, with slight discrepancies at temperatures in excess of 600°C. The *Vulcan* predictions for Test 4 towards the end of test are in close agreement with the measured mid-span displacements.

However, in Test 7, towards the end, the *Vulcan* predictions diverge from the test results. There are two likely reasons for this:

- Inaccuracy of the measured temperature profiles through the slab,
- Loss of bond between the reinforcement and concrete, leading to fracture of the reinforcement and progressive failure of the slab. Vulcan currently does not model this.

Figure 6.7 also compares the *Vulcan* results for Tests 4 and 7 without applied load. The results show similar behaviour up to approximately 550°C, after which the results diverge. On comparison with the *Vulcan* results with applied load it is seen that up to 550°C the unloaded and loaded slabs displace at a similar rate which indicate that the initial displacements are dominated by thermal expansion of the slab (thermal strains). In Chapter 5, comparisons were made between the displacements attained in ambient and heated tests; the results seem to tie in with the *Vulcan* results presented here indicating that thermal bowing of the slab influences the initial displacements.

The membrane force plots for Tests 4 and 7 have been plotted at various exposed-face slab temperatures. Figures 6.8-6.12 show the membrane traction plots for Test 4. These figures highlight the compression (thick blue line) and tensile (thin red line) membrane forces that develop within the slab. As the slab displacements increase with increasing temperatures, the membrane forces within the slab increase as the load carrying mechanism changes from bending when the slab is relatively flat to tensile membrane action at high displacements.

In Chapter 4, a series of slabs were modelled at ambient temperatures, and in the membrane traction plots, compression force bands were seen to develop across the central region of the slab. This can be considered as being due to the trapezoidal facets rotating about the slab corners as they hinge about the diagonal yield lines and impinging on one another in the central area of the slab (Figure 4.23). At 23°C (underside of slab temperature), these compression forces within the central zone of the quarter of the slab are clearly seen to have developed (Figure 6.8). As the temperatures increase these initial compressive forces that had developed within the central zone of the slab were relieved by the increasing slab displacements. Figure 6.9 shows the membrane forces that have developed within the slab at 177°C (underside of slab temperature).

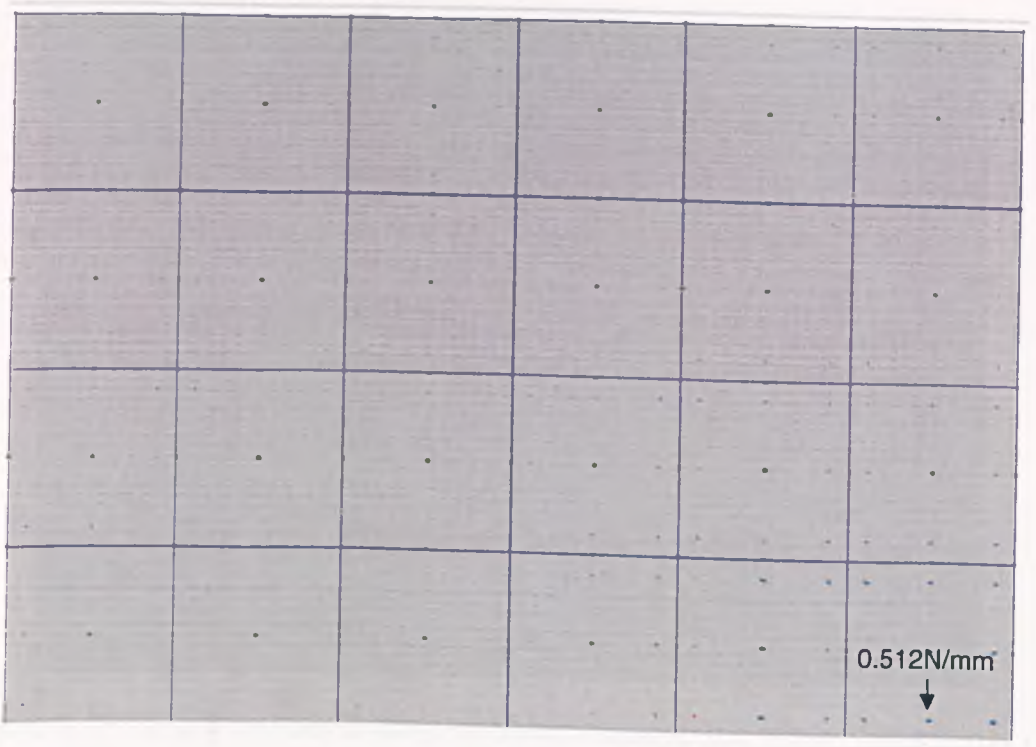

Figure 6.8: Test 4 (quarter of slab), membrane traction plot at 23.5°C (load ratio 1.9).

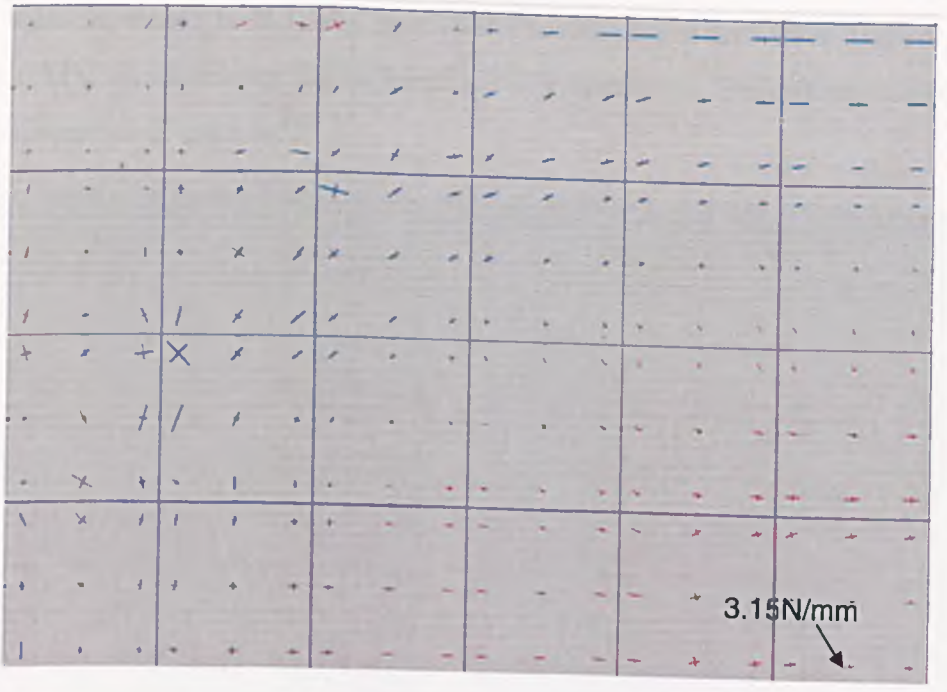

Figure 6.9: Test 4 (quarter of slab), membrane traction plot at 177°C (load ratio 1.9).

At approximately 231°C, the tensile forces within the central region are seen to develop with a peripheral 'ring' of compression. In any cross section through the slab, these forces will balance out and the slab is in a state of equilibrium (Figure 6.10). The development of compressive forces parallel to the short span is seen to develop within the central zone.

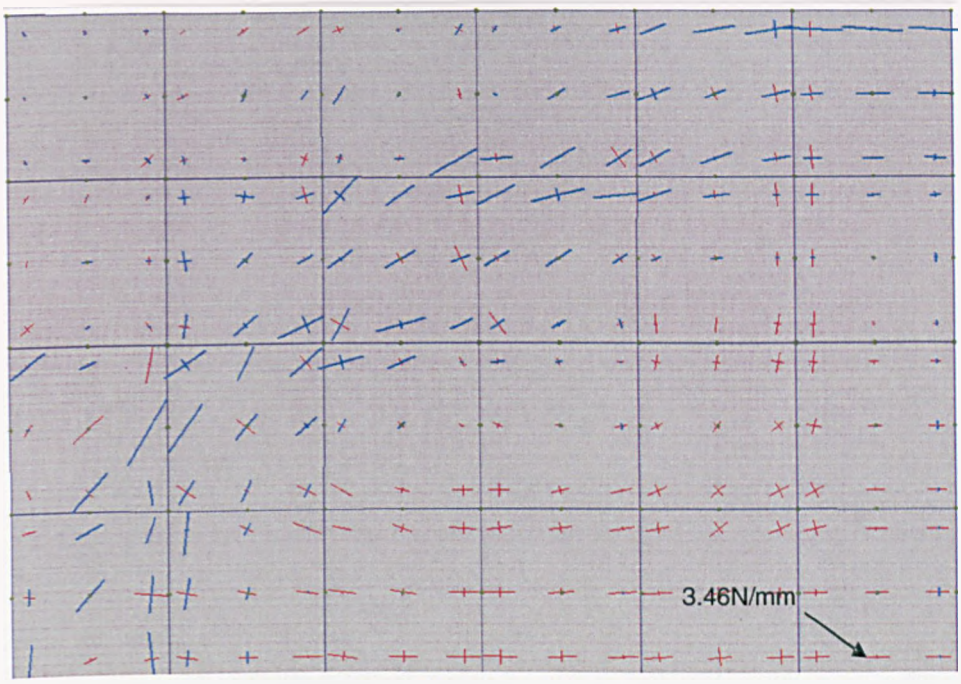

Figure 6.10: Test 4 (quarter of slab), membrane traction plot at 231°C (load ratio 1.9).

At 342°C, the slab displacements are approximately 10mm, the tensile and compressive forces have increased in the long span and compressive forces have started to develop (Figure 6.11). At increasing displacements and temperatures, these compressive forces are more pronounced (Figure 6.12).

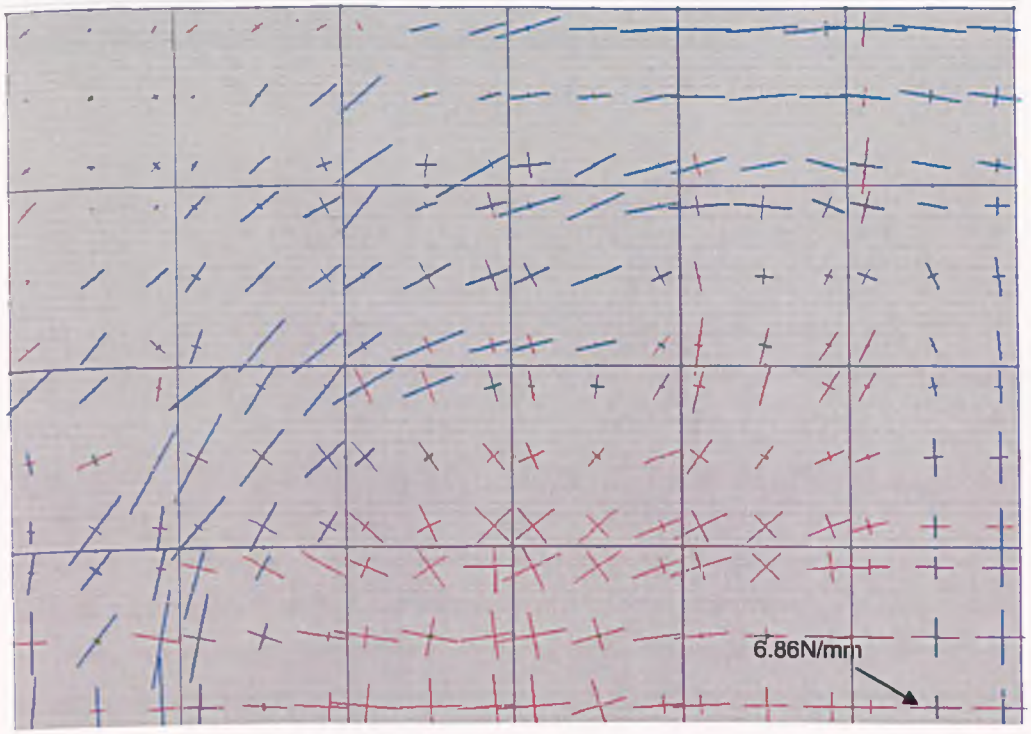

Figure 6.11: Test 4 (quarter of slab), membrane traction plot at 342°C (load ratio 1.9).

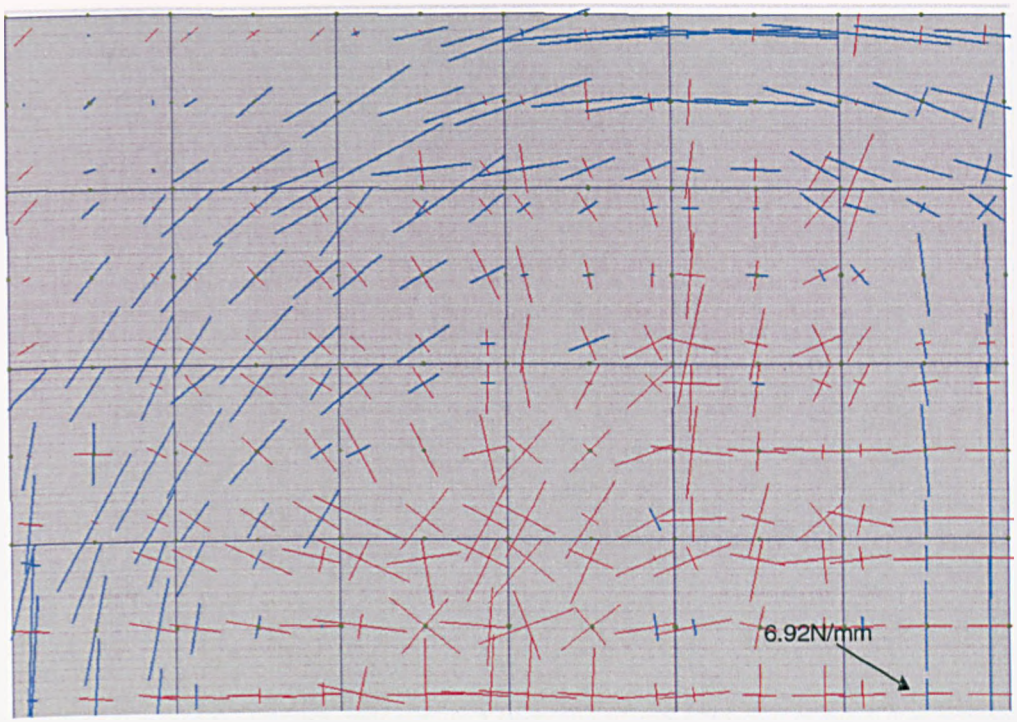

Figure 6.12: Test 4 (quarter of slab), membrane traction plot at 542°C (load ratio 1.9).

Test 4 with the applied test load (Figure 6.12) is now compared with the case in which no load is applied, Figure 6.13. Figure 6.13 shows the membrane forces for the latter case at a temperature of 522°C, at which the mid-span displacement is approximately 20mm. Compared with Figure 6.12 the membrane forces are reduced and the development of compressive forces within the central zone is more pronounced.

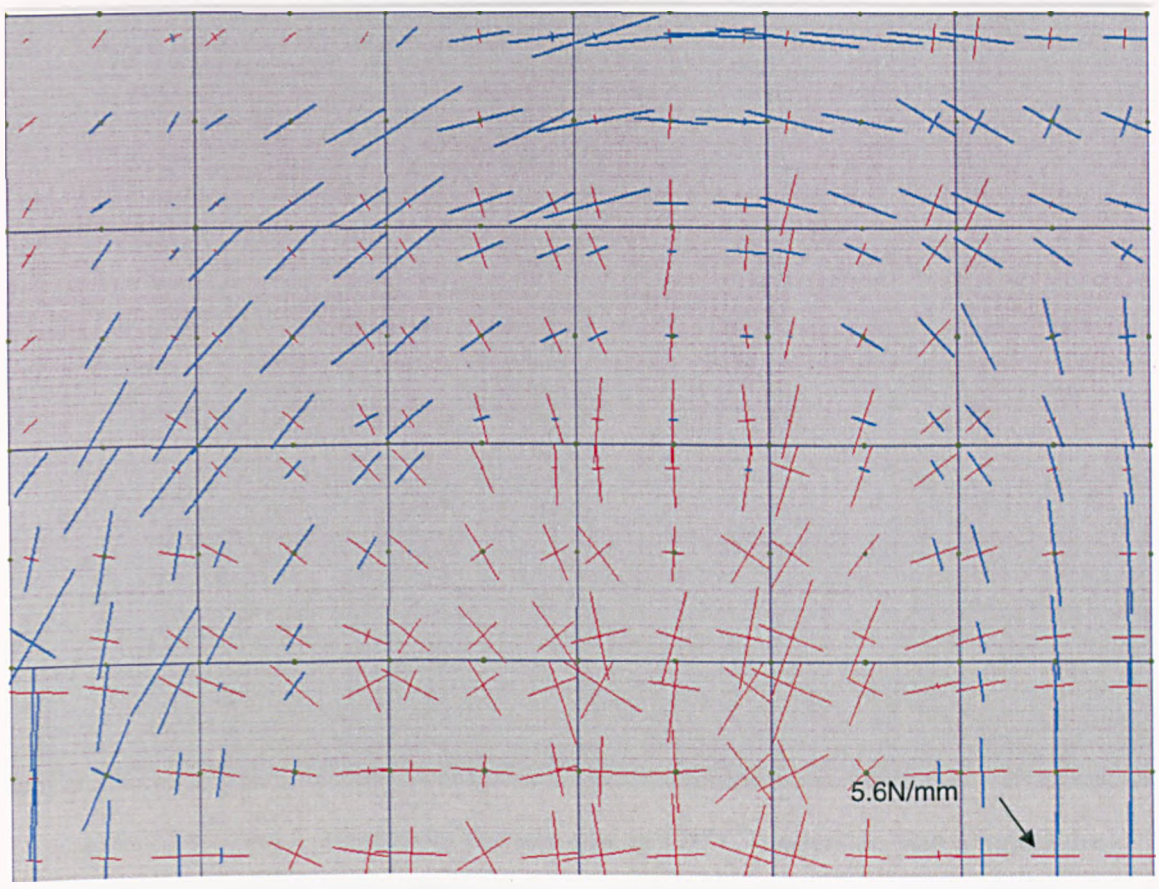

Figure 6.13: Test 4, membrane traction plot at 522°C (underside slab temperature) with no applied load.

Test 7 was a replica of Test 4 apart from the type reinforcement used within the slab, which was deformed and had a lower yield strength. The load ratio was slightly lower than in Test 4, reducing from 1.9 to 1.5. Figures 6.14-6.17 show the membrane traction plots for Test 7 at increasing temperatures and displacements. The reduced yield strength in Test 7 results in increased mid-span displacement. The development of compressive forces within the central zone is apparent at 341°C but at temperatures over 500°C these become less marked. The compression forces are probably relieved due to increasing slab displacements.

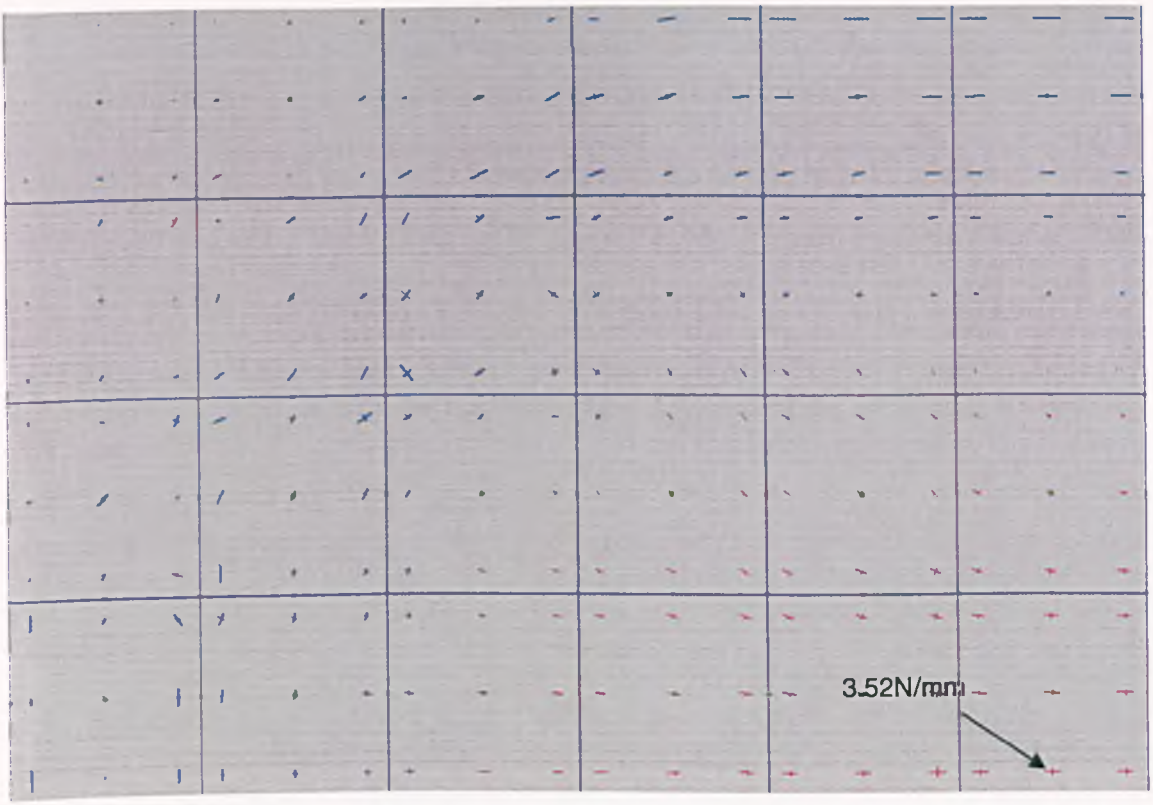

Figure 6.14: Test 7, membrane traction plot at 120°C (underside slab temperature).

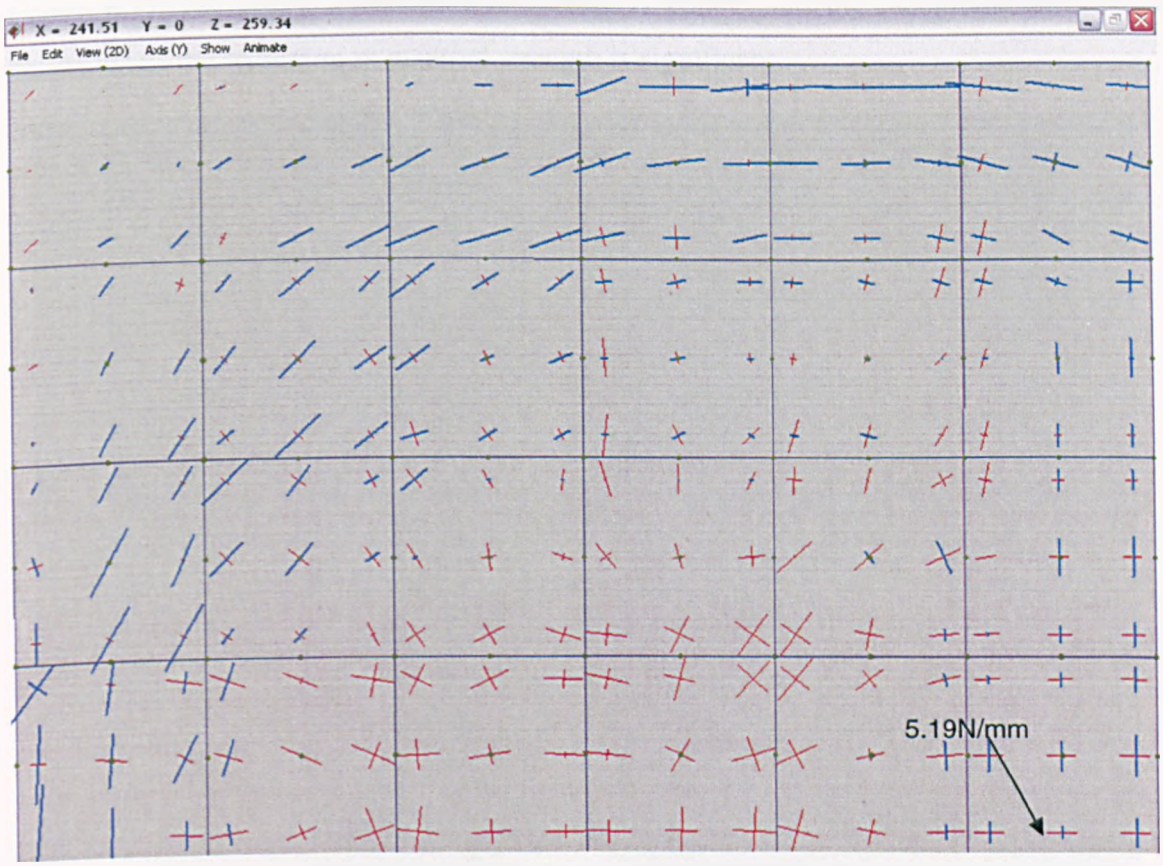

Figure 6.15: Test 7, membrane traction plot at 341°C (underside slab temperature).

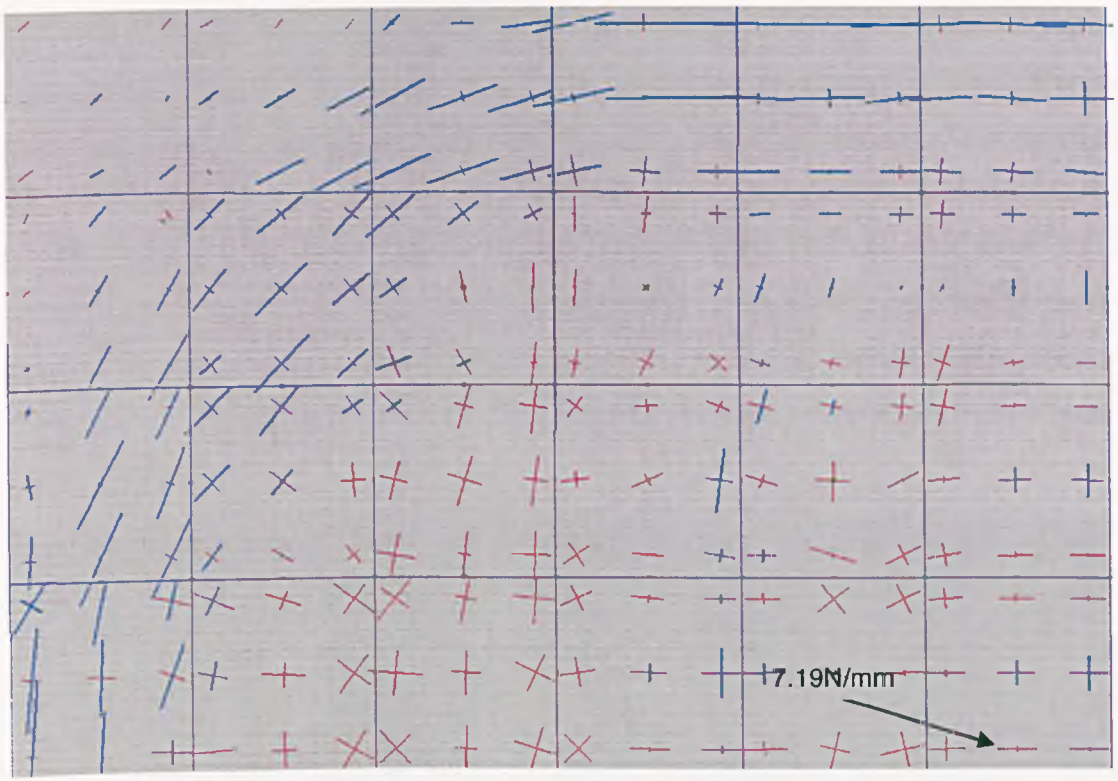

Figure 6.16: Test 7, membrane traction plot at 582°C (underside slab temperature).

Figure 6.17, the slab's underside temperature is 630°C and the membrane forces have decreased as the reduction in material strength is significant.

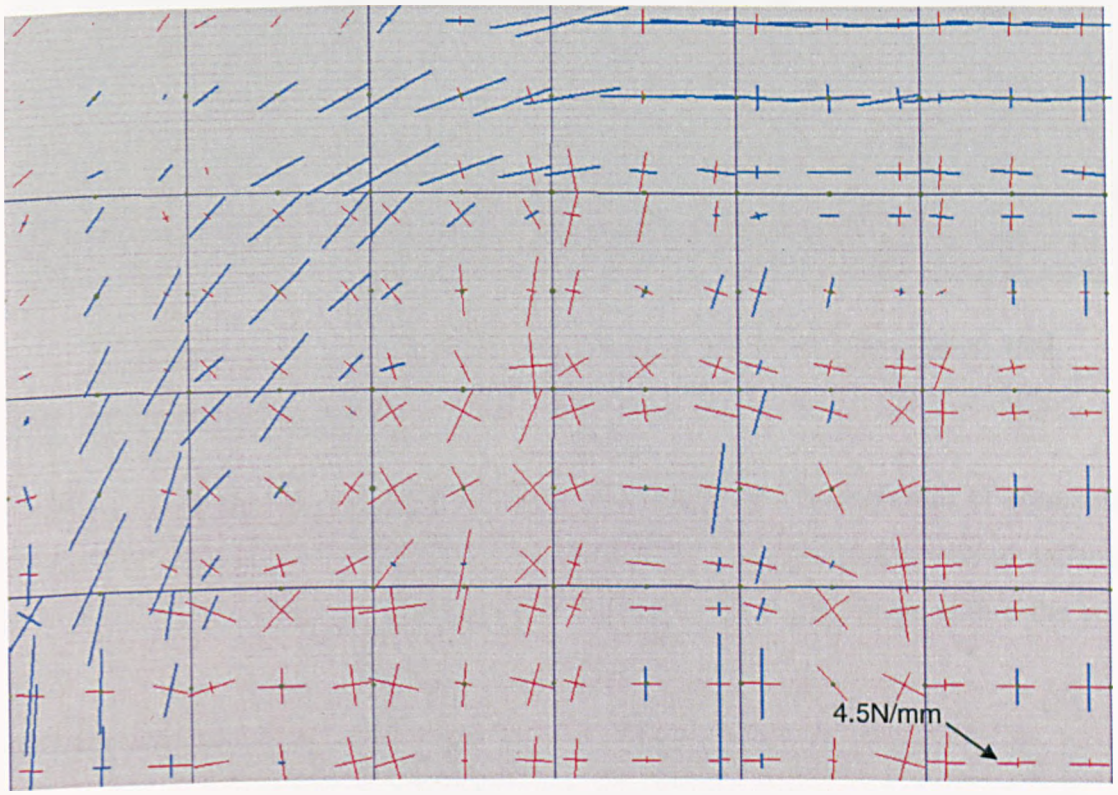

Figure 6.17: Test 7, membrane traction plot at 630°C (underside slab temperature).

The model of Test 7 was run again but without any applied load, and the development of the membrane forces within the slab at a lower-surface temperature of 589°C is shown in Figure 6.18 below. The compressive tractions can clearly be seen to have developed across the short span. The values of the membrane forces in Figure 6.18 are less than for the loaded case as the displacements at any given displacement are less therefore less membrane force. It is interesting that the developments of the compressive tractions across the short span are more pronounced in the unloaded slab than the loaded slab which seems to indicate that the non linear thermal expansion of the slab is causing these compressive forces to develop.

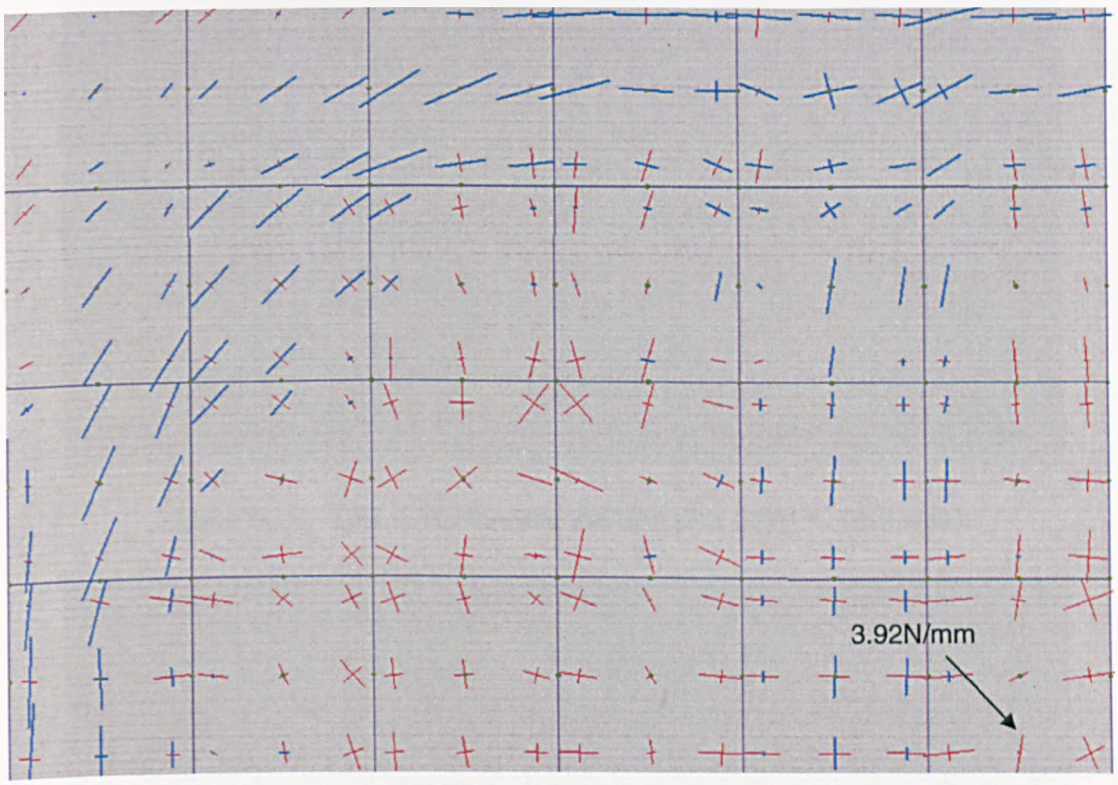

Figure 6.18: Test 7, membrane traction plot at 589°C with no applied load.

6.4.2 Sensitivity Studies

A number of studies have been conducted to investigate the development of compressive forces within the central zone of the slab. The aim of the investigation was to understand the controlling factors in the development of these compressive forces within the central region.

Boundary Conditions

It seemed possible that the use of symmetry in the boundary conditions might have influenced the membrane forces indicated, therefore a full slab was analysed using a 12 x 8

grid of elements based on measured data of Test 4. Figure 6.19 shows the principal membrane tractions given at a bottom-surface temperature of 99°C, at which point the tensile zone within the central region and the peripheral 'ring' of compression are clearly seen. As the temperatures increase, the band of compression forces is seen in Figures 6.20 to develop across the short span of the slab.

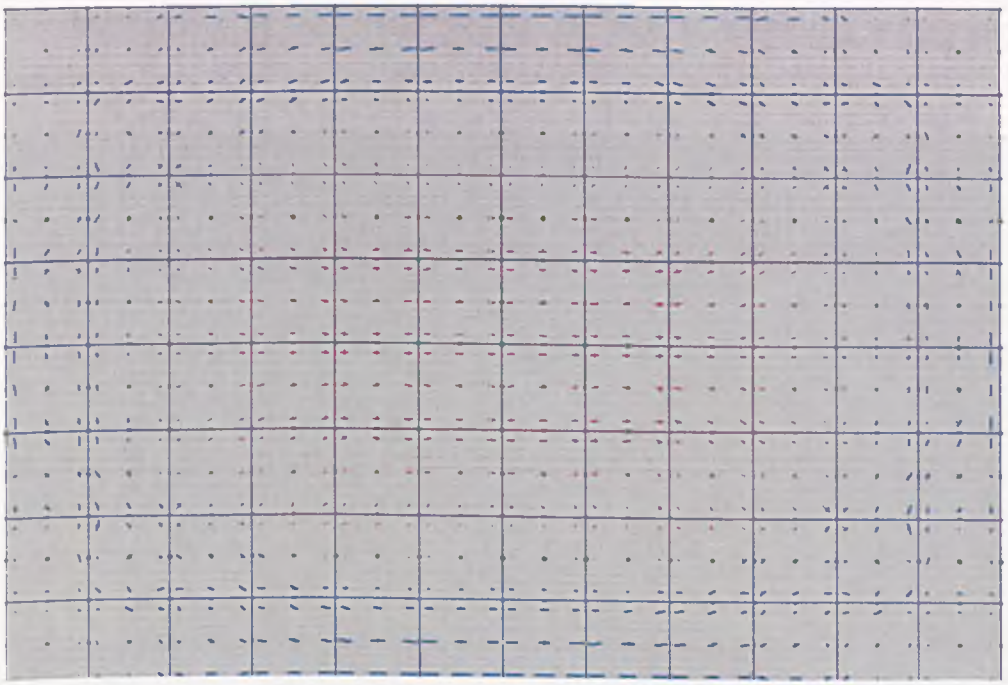

Figure 6.19: Test 2, membrane traction plot at 99°C (full slab).

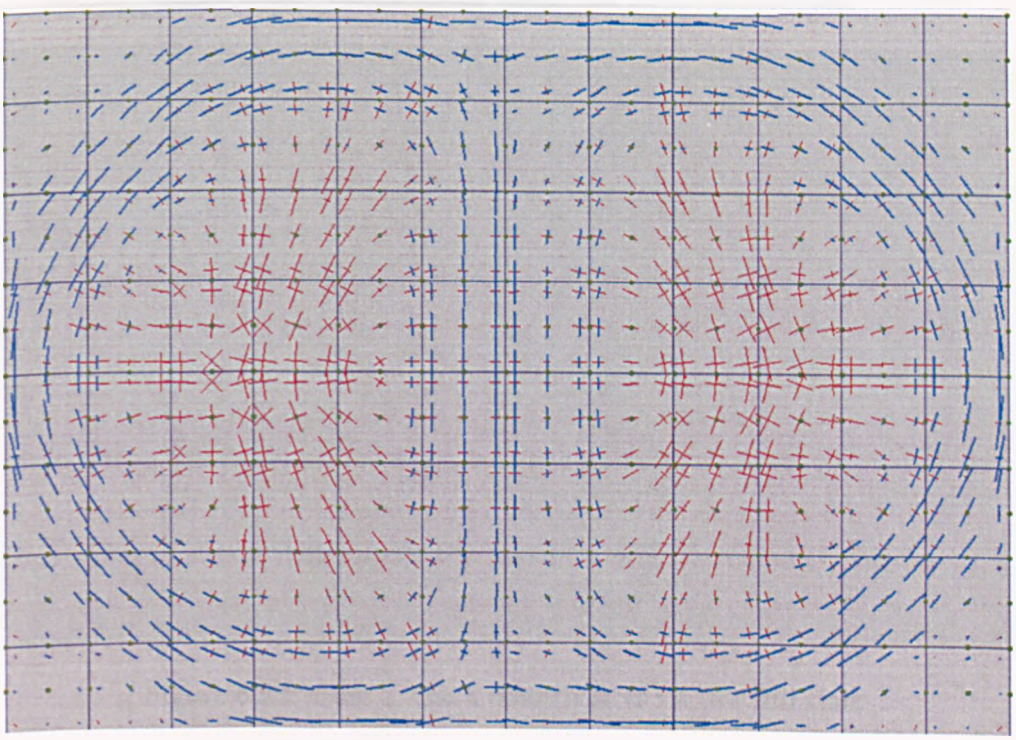

Figure 6.20: Test 2, membrane traction plot at 357°C

Crack Development

The crack pattern on the bottom surface was plotted at various temperatures for the fully-modelled slab in Test 4. The initiation of crack development is at the corners of the slab (Figure 6.21) and it then proceeds across the central mid-span of the slab, with concrete crushing towards the ends of the span in the later stages of the test. Figures 6.21- 6.23 show the development of the cracks within the slab at increasing temperature and displacement.

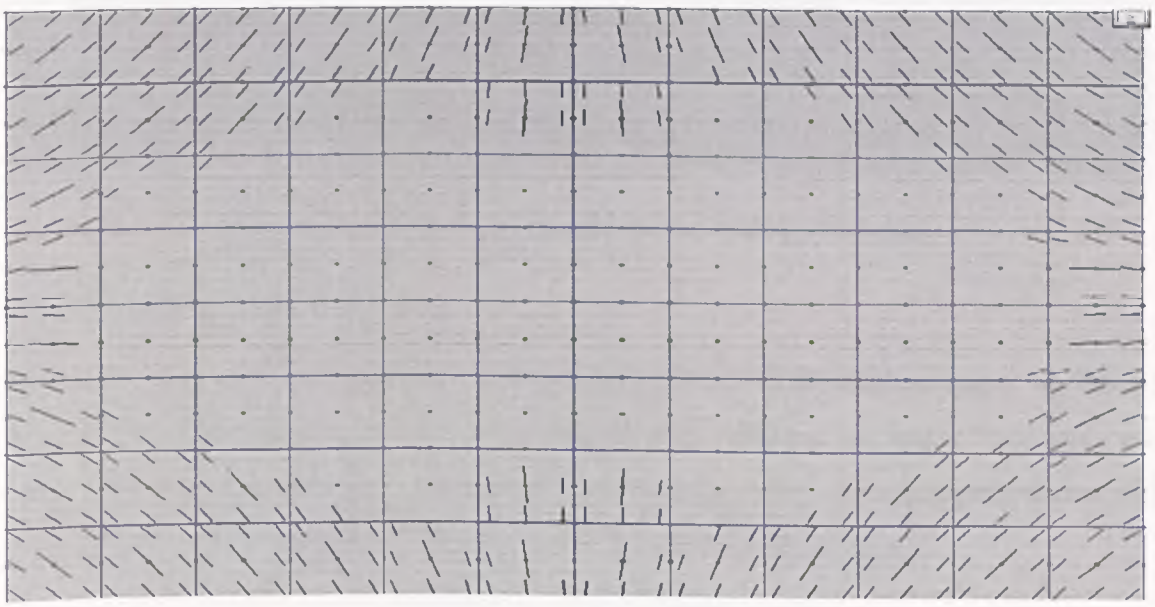

Figure 6.21: Test 2, crack pattern at 99°C for full slab.

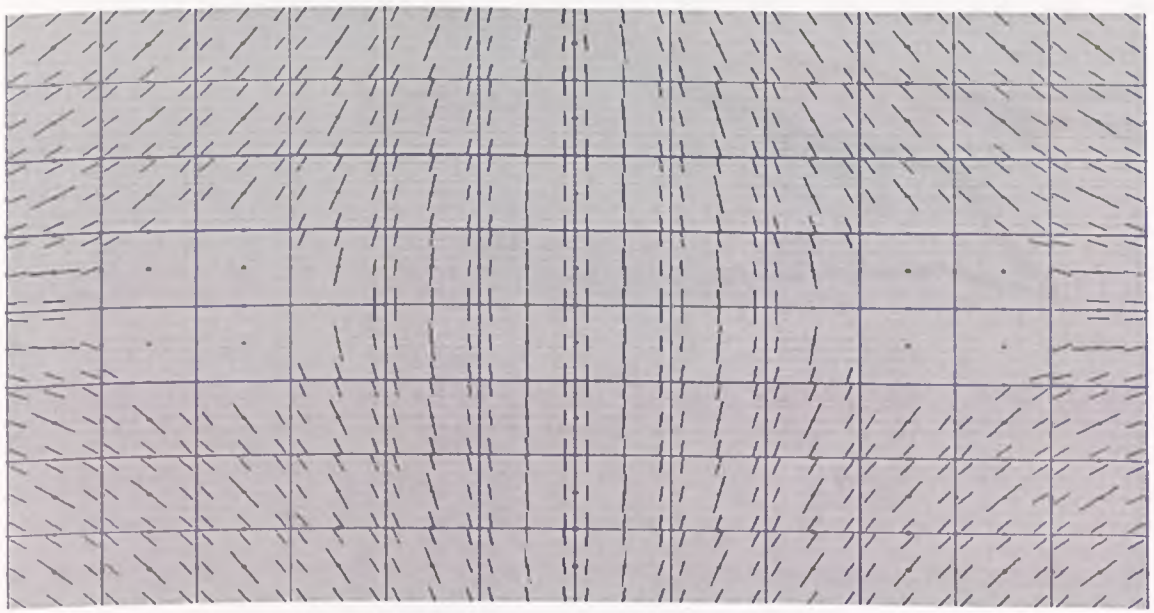

Figure 6.22: Test 2, crack pattern at 153°C for full slab.

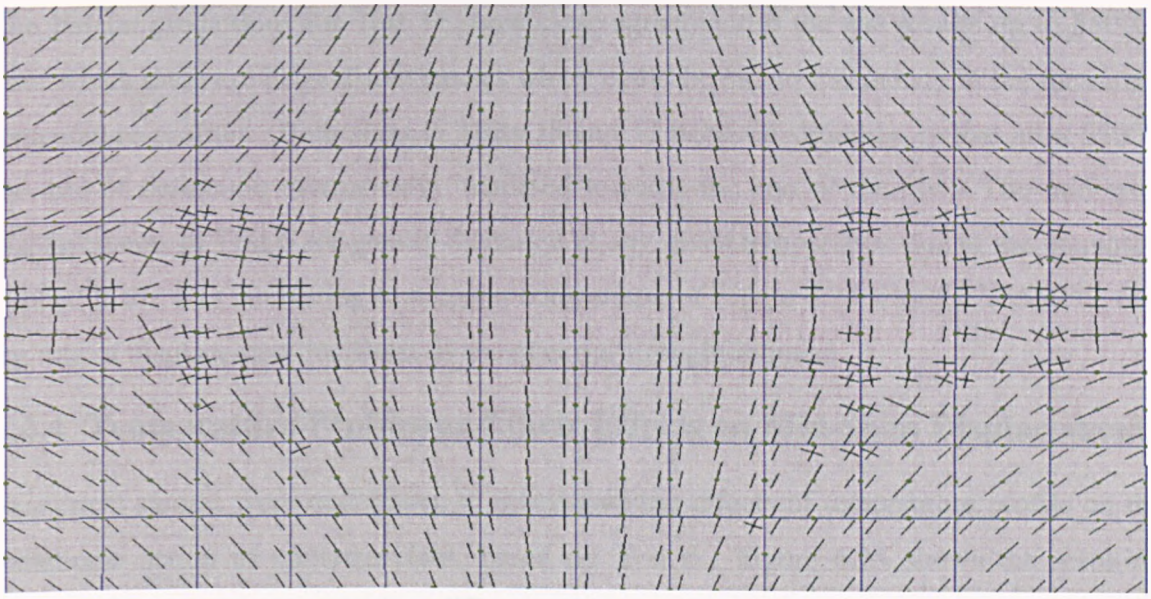

Figure 6.23: Test 2, crack pattern at 516°C for full slab.

6.4.3 Tests 6, 15 and 17

The slabs in this set of tests had a cross sectional area of 0.05% reinforcement. In Tests 6 and 15, the slabs were reinforced with smooth wire, whereas in Test 17 the slab was reinforced with deformed wire. Figure 6.24 shows the resulting mid-span deflections with respect to the bottom surface slab temperatures for the three set of tests.

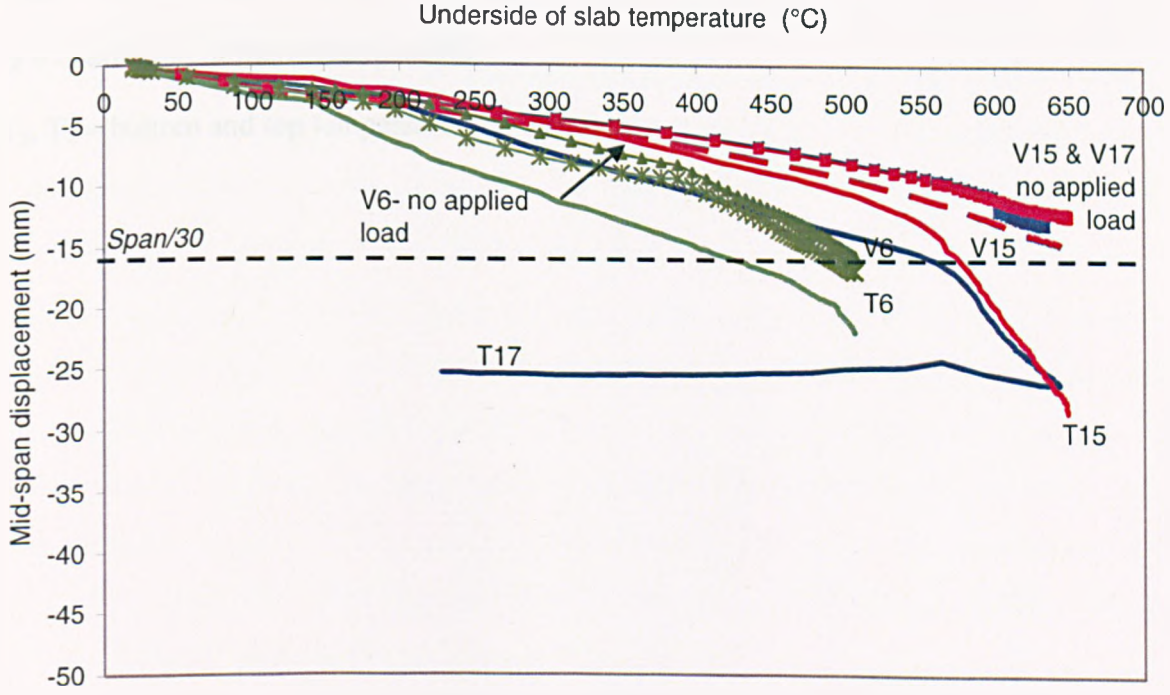

Figure 6.24: Comparison of mid-span displacements for Tests 6, 15,17 results with Vulcan predictions.

The *Vulcan* predictions for Test 17 show close agreement to the test results up to 550°C, after which there are large discrepancies which could be due to inaccuracy in the measured temperature profiles. Both slabs in Tests 15 and 17 behaved similarly, in that after 550°C the rate of deflection dramatically increased towards the end of the test. The mid-span displacements in Test 6 are greatly increased at any given temperature due to the increased applied load. It is interesting to note, on comparison of Figure 6.24 with 6.7 at 550°C, that the rate of displacement increases as the material strength reduced.

6.4.4 Temperature Profiles and their Effects on Mid-Span Displacements

Numerical studies were undertaken to investigate the effects of temperature profile on the membrane action of concrete slabs, based on Test 6. Figure 6.25 shows the resulting vertical displacements assuming different linear temperature gradients across the slab depth. The displacements due to thermal effects can be calculated using the equation from the Simple Design Method, Equation 6.1.

$$v_{therm} = \frac{\alpha(T_2 - T_1)l^2}{16h} \qquad 6.1$$

In which

v_{therm} = vertical displacement

α = coefficient of thermal expansion

T_2, T_1 = bottom and top temperature of concrete

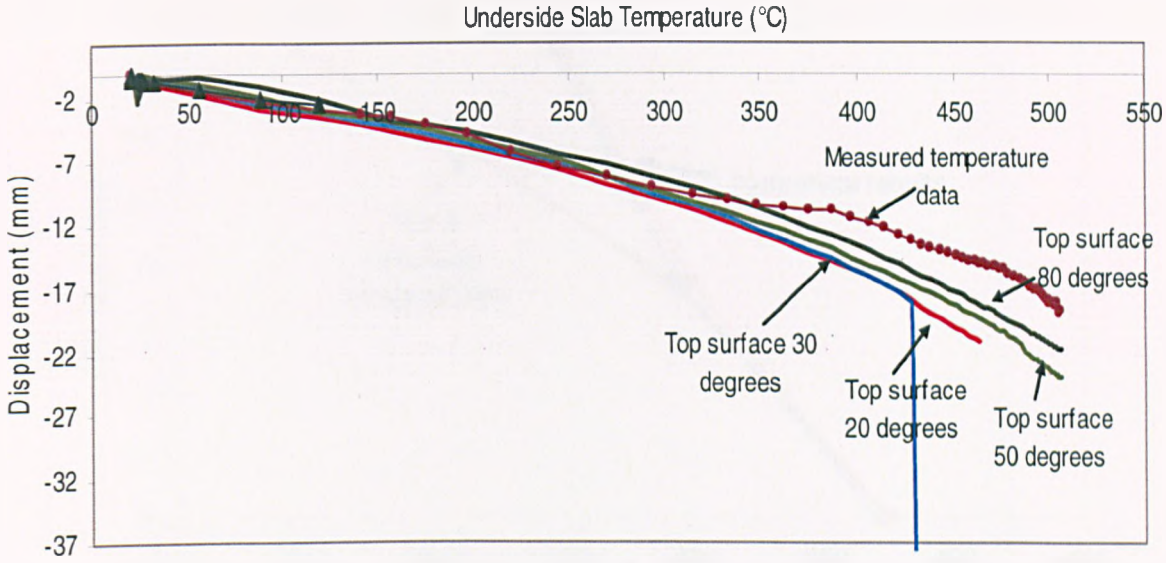

Figure 6.25: Comparison of mid-span displacements with *Vulcan* predictions for various linear temperature gradients.

The calculated slab displacements are mainly dependent on the difference in temperatures between the bottom and top surfaces of the slab. It was observed during the experiments that the top surface temperature fluctuated quite significantly and on comparison with predictions from the thermal analysis program FPRCBC-T [59] (Figure 6.25), the actual top surface temperatures are much lower than predicted. The reason for this difference is of course the set-up of the actual test. The thermocouples were placed on the slab surface, but with the cooler surrounding environment, some recorded temperatures reflected mainly the surrounding air temperature and not the true slab temperature. The slab's top surface was exposed to cooler temperatures since no insulation was provided above the slab and this could have influenced the low top surface temperatures measured.

Between temperatures of 20-300°C, the rates of displacements for all the temperature profiles were similar. After 300°C, the rate of displacement for the measured temperature profile decreased compared to the other temperature profiles. It can be concluded that at the beginning of the test, the steep increase in rate of displacements are due to the large thermal gradients in the slab which become less steep as the top surface temperatures of the slab increases which decreases the thermal bowing. The initial steep thermal gradients are due to the poor conductivity of the concrete.

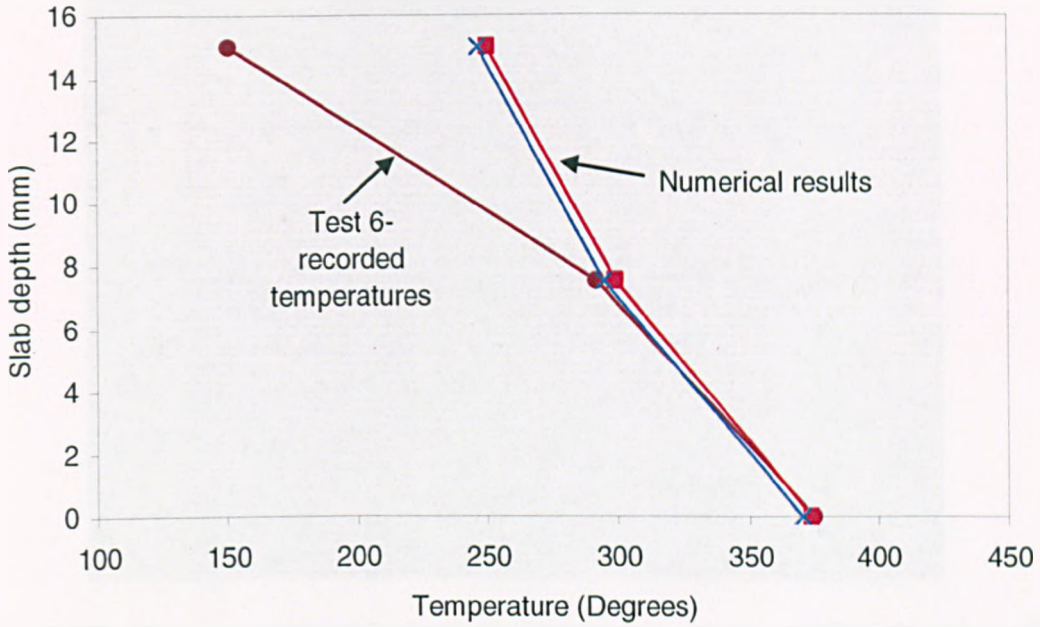

Figure 6.26: Comparison of the measured temperature distribution through the slab depth with numerical predictions.

Membrane Traction Plots

The development of the membrane forces within the slab and the effects of the thermal gradients on the resultant membrane forces for Test 6, is shown in Figures 6.27-6.30.

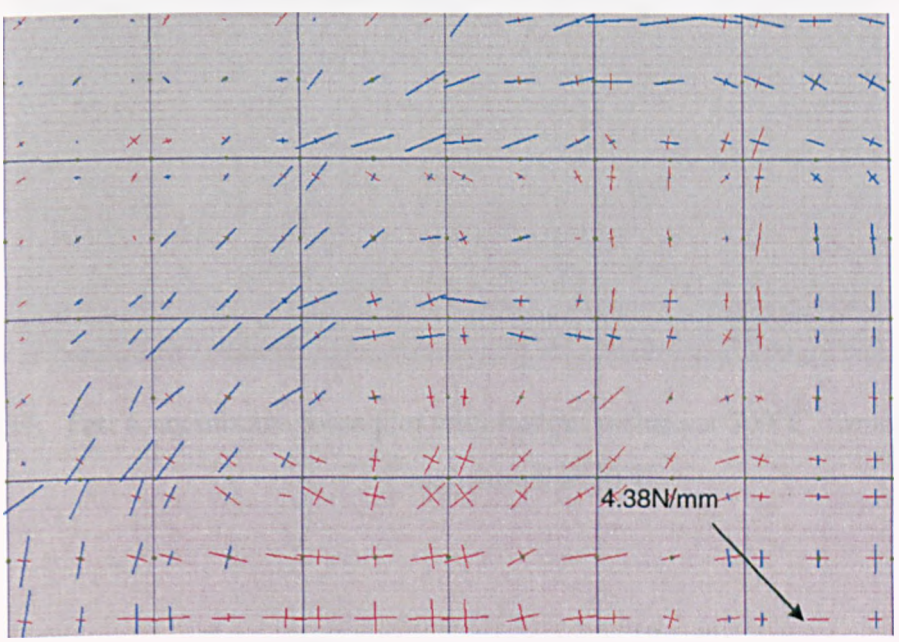

Figure 6.27: Test 6, membrane force plot with bottom surface at 341°C, for top surface maintained at 30°C.

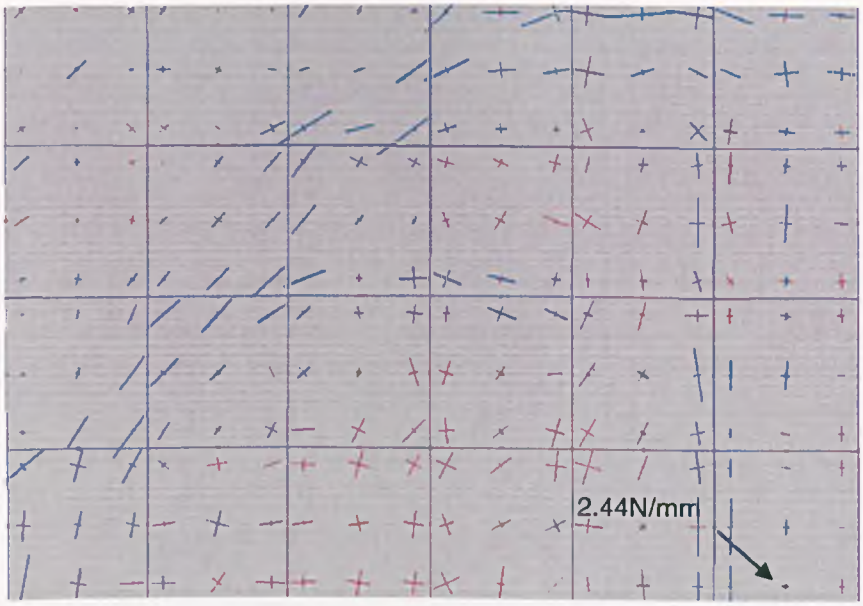

Figure 6.28: Test 6, membrane force plot with bottom surface at 505°C, for top surface maintained at 50°C.

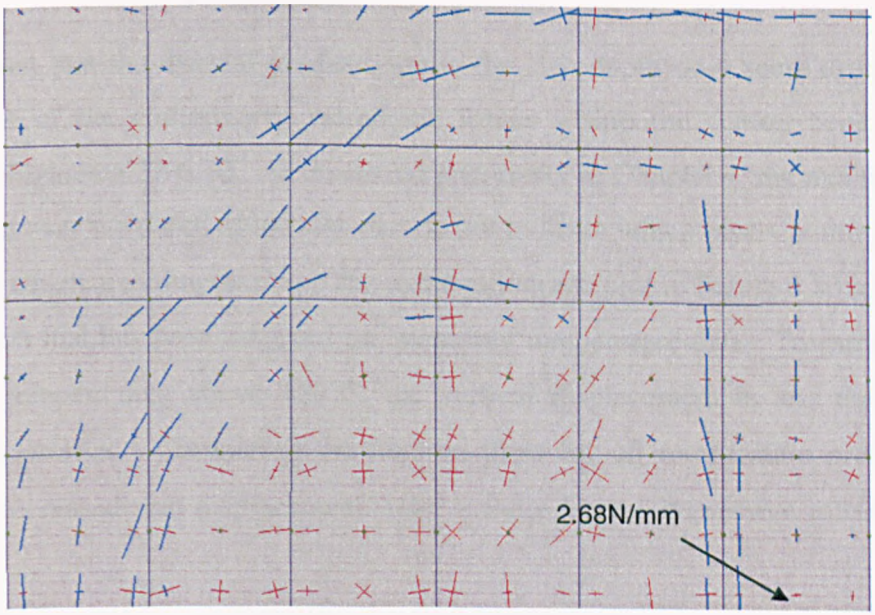

Figure 6.29: Test 6, membrane force plot with bottom surface at 509°C, for top surface maintained at 80°C.

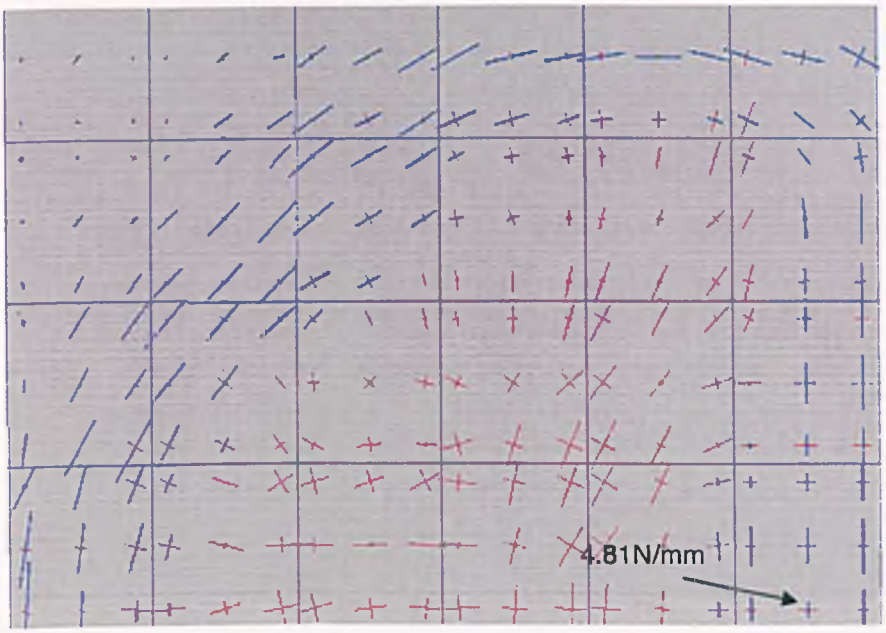

Figure 6.30: Test 6, membrane force plot for measured data temperature profile at 505°C

It can be seen that the thermal gradient across the slab depth does seem to influence the development of the compressive membrane forces within the central zone, which are apparent in Figures 6.27-6.30. As discussed previously in Chapter 4, the membrane forces are averaged over the depth of the slab and do not indicate which layers within the slab are tension and which are compression. The membrane force plot in Figure 6.30 represents the slab in Test 6 that has been assigned the measured temperature data. Towards the end of the test at temperatures above 450°C, the vertical displacement is less than the other temperature profiles. Comparing the traction plots for all temperature profile cases it seems that increased slab displacements relieve these large compressive forces within the slab.

The membrane traction plots for Tests 15 and 17 are shown in Figures 6.31-6.33, the temperature profiles assigned to these models are the measured temperature data.

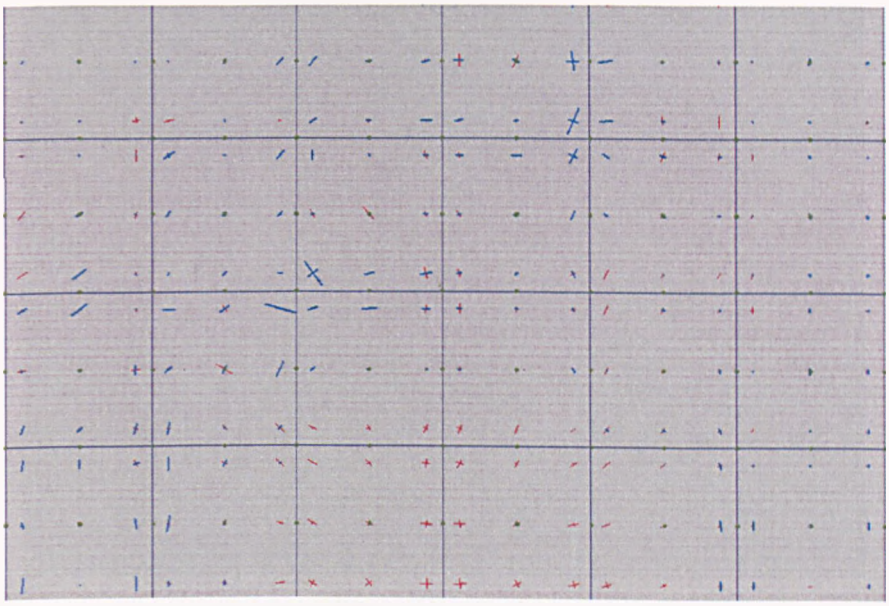

Figure 6.31: Test 15, membrane force plot for bottom surface temperature of 283°C.

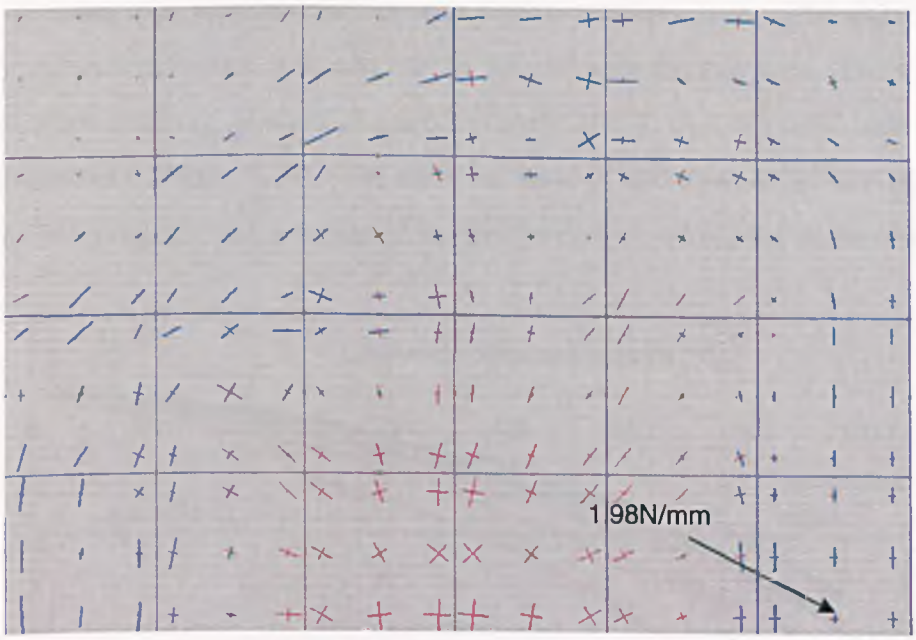

Figure 6.32: Test 15, membrane force plot for bottom surface temperature of at 594°C

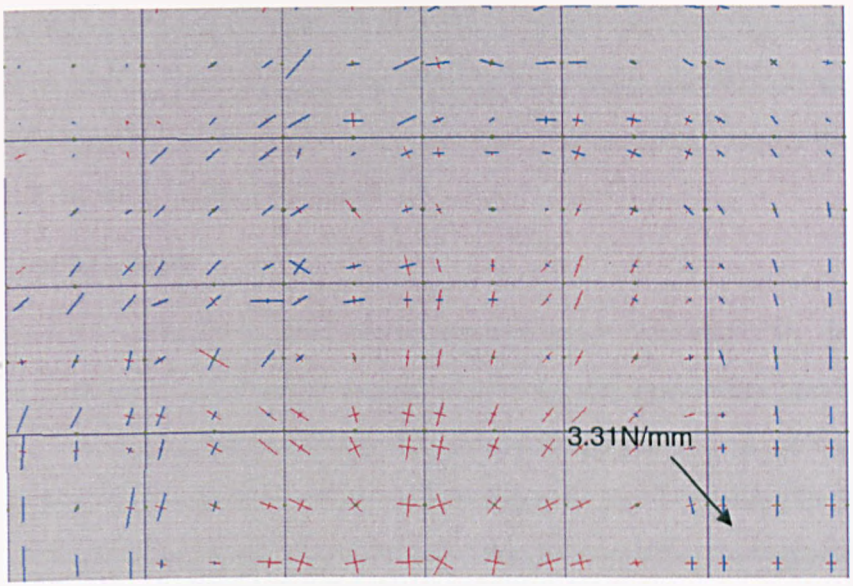

Figure 6.33: Test 17, membrane force plot for bottom surface temperature of at 547°C

6.4.5 Tests 12 and 13

The slabs in these tests were reinforced with 0.25% reinforcement. The slab in Test 12 was reinforced with deformed wire and that in Test 13 with smooth wire. The slab in Test 12 had extensive cracking, leading at approximately 200°C to a dramatic increase in the rate of displacement (Figure 6.34). The rapid increase in mid-span deflection is due to the loss of bond and progressive fracturing of the deformed wire across the transverse crack.

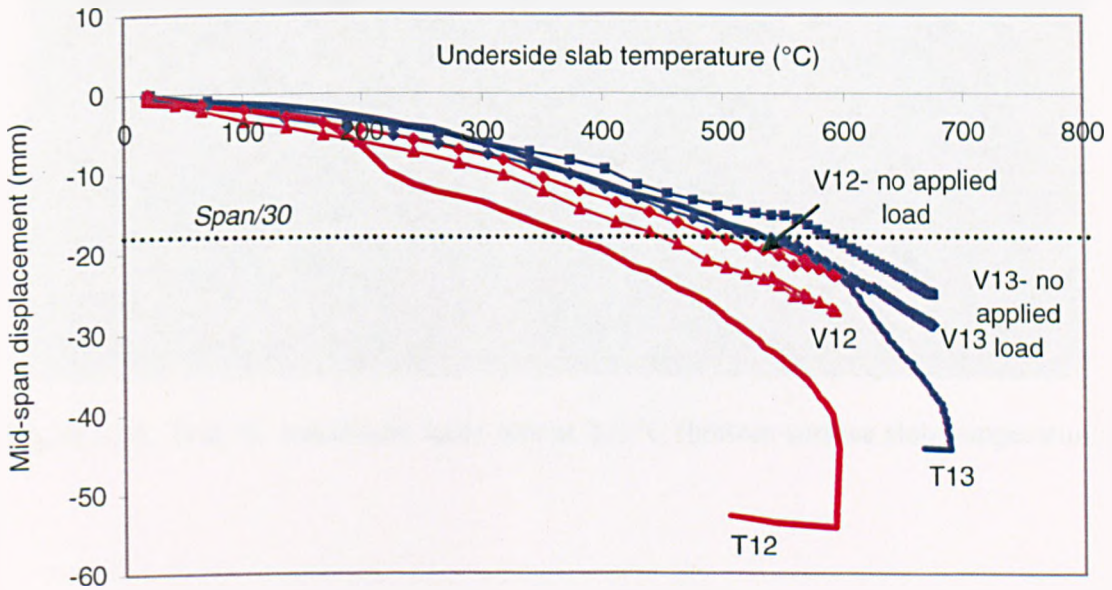

Figure 6.34: Comparison of mid-span displacements for Tests 12 and 13 with *Vulcan* predictions.

It is interesting that the displacements in Test 13 compare well with *Vulcan* predictions but in Tests 12 after 200°C, the comparisons between test results and *Vulcan* are not in close agreement. The reason for this is due to the fact that *Vulcan* cannot model the loss of bond and progressive fracture of the deformed wire.

Membrane Traction Plots

The membrane force plots for Test 12 are shown in Figures 3.35 and 3.36. It is interesting to note that the internal compressive forces are not as pronounced as previously seen in Tests 4, 7, 6, 15 and 17. The resulting slab displacements at any given temperature are higher than in Tests 6.15 and 6.17. The slabs in Tests 12 and 13 had higher reinforcement percentages, of 0.25% and larger displacements therefore resulting in higher tension forces within the slab, which could explain the absence of compressive forces within the central zone of slab.

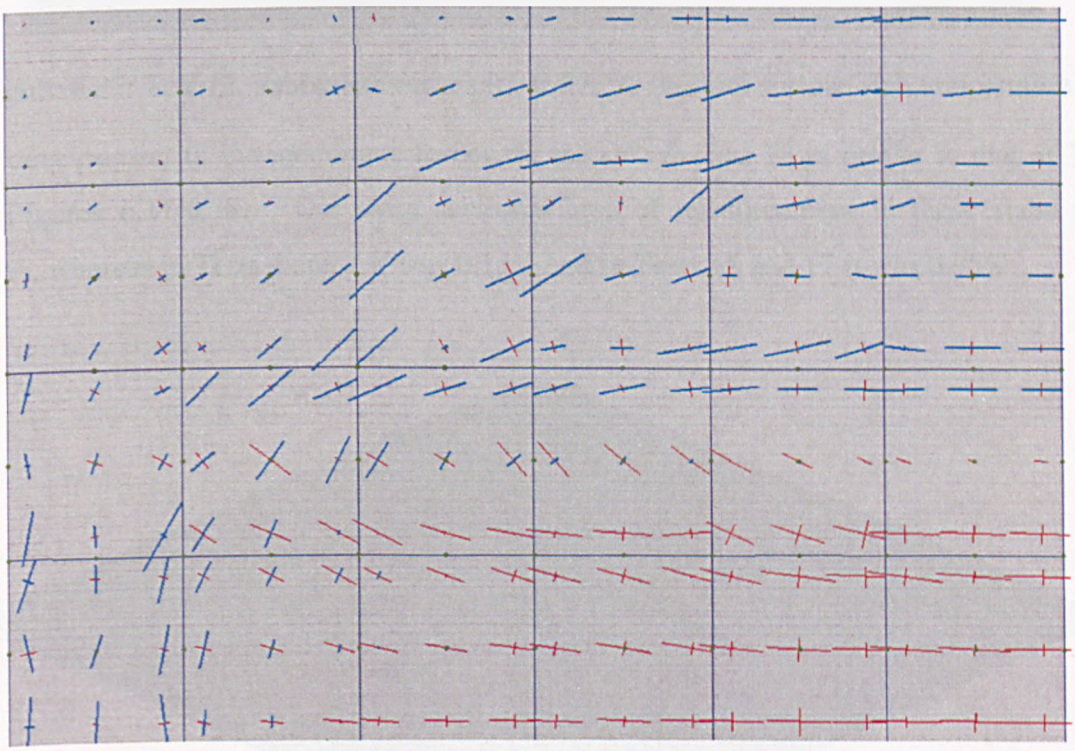

Figure 6.35: Test 12, membrane force plot at 221°C (bottom surface slab temperature).

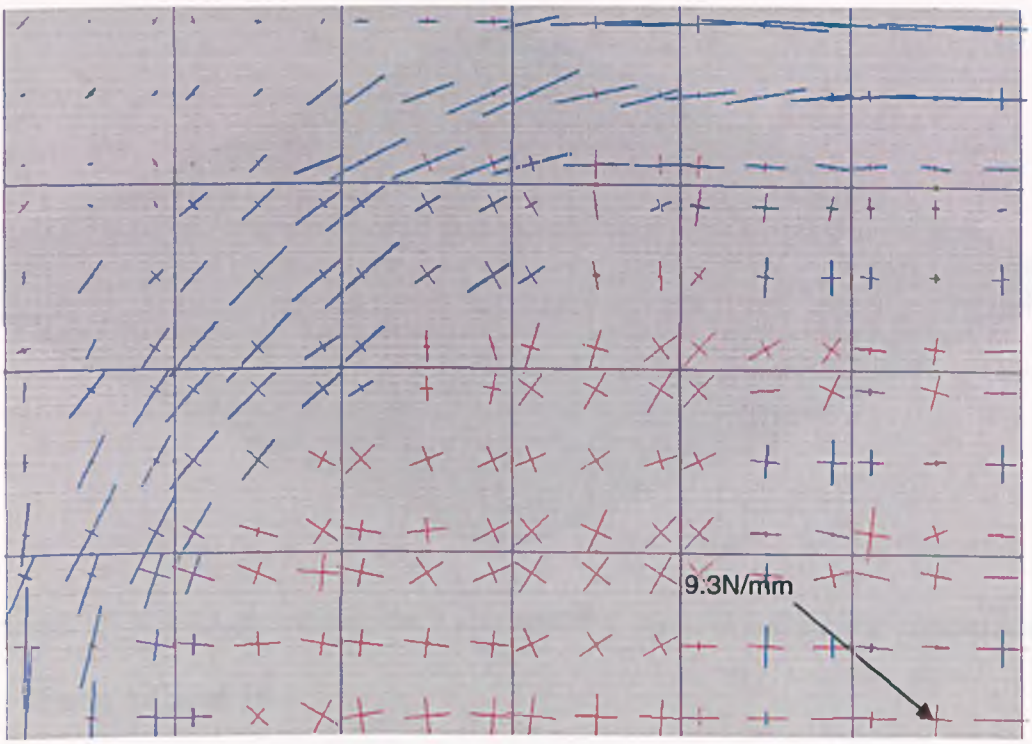

Figure 6.35: Test 12, membrane force plot at 579°C (bottom surface slab temperature).

The development of the membrane forces for the slab in Test 13 is similar to that of Test 12 (Figures 6.37-6.38). The cross sectional area of reinforcement in these slabs was 0.25%, whereas in Tests 4 and 7 it was 0.15% and in Tests 15 and 17 it was 0.05%.

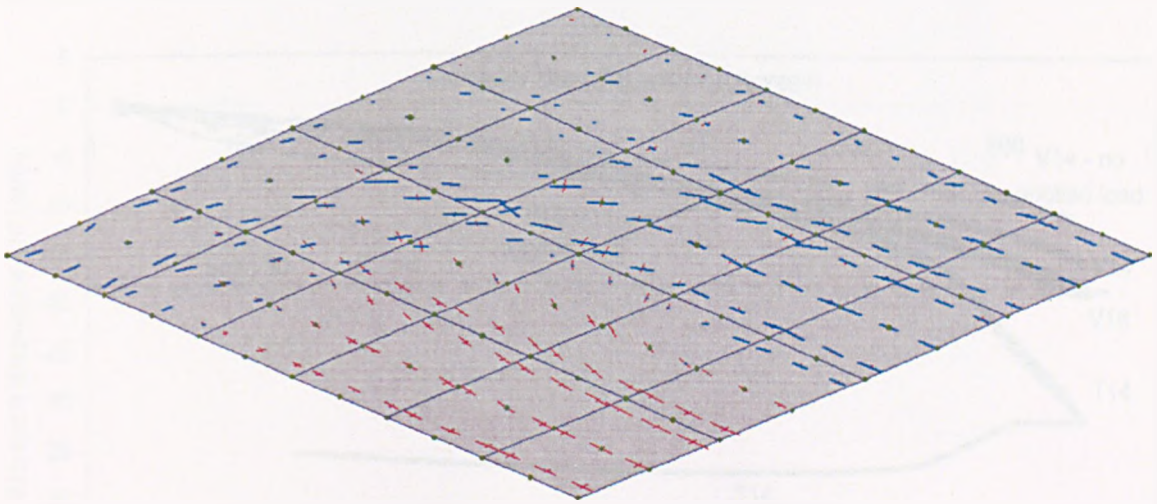

Figure 6.37: Test 13, membrane force plot at 208°C (bottom surface slab temperature).

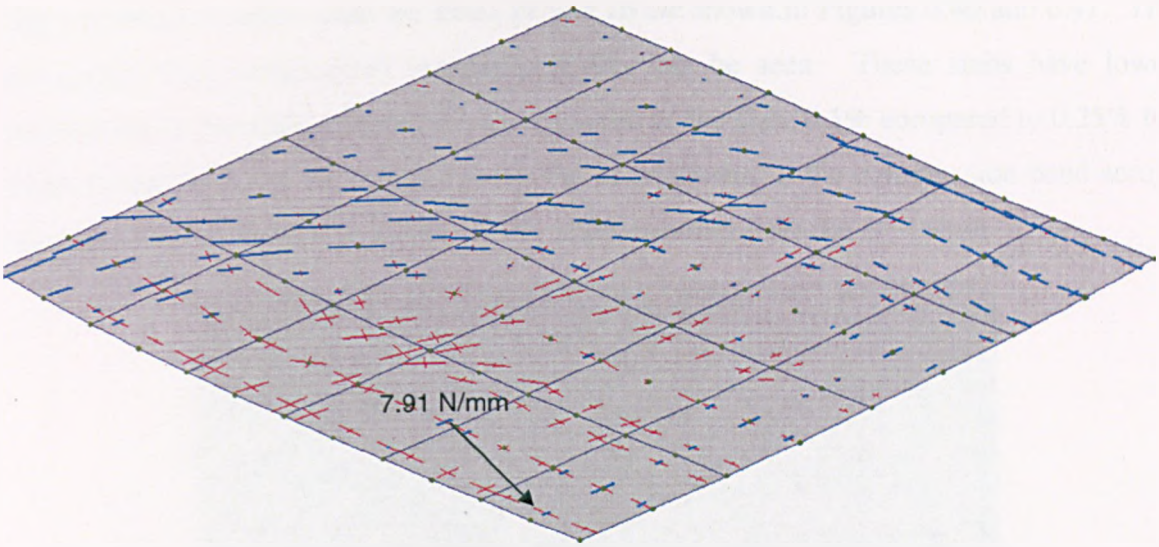

Figure 6.38: Test 13, membrane force plot at 608°C (bottom surface slab temperature).

6.4.6 Tests 14 and 16

The slabs in these tests were reinforced with 0.1% reinforcement. The reinforcement used in Test 14 was deformed whereas in Test 16 smooth wire was used. Figure 6.39 compares the measured mid-span displacements with *Vulcan* predictions. The comparisons between test and *Vulcan* are good up to 550°C. After this point, the *Vulcan* predictions are more conservative and the resulting rates of deflection are lower. The test results also show that the type of reinforcement used seems to have no influence.

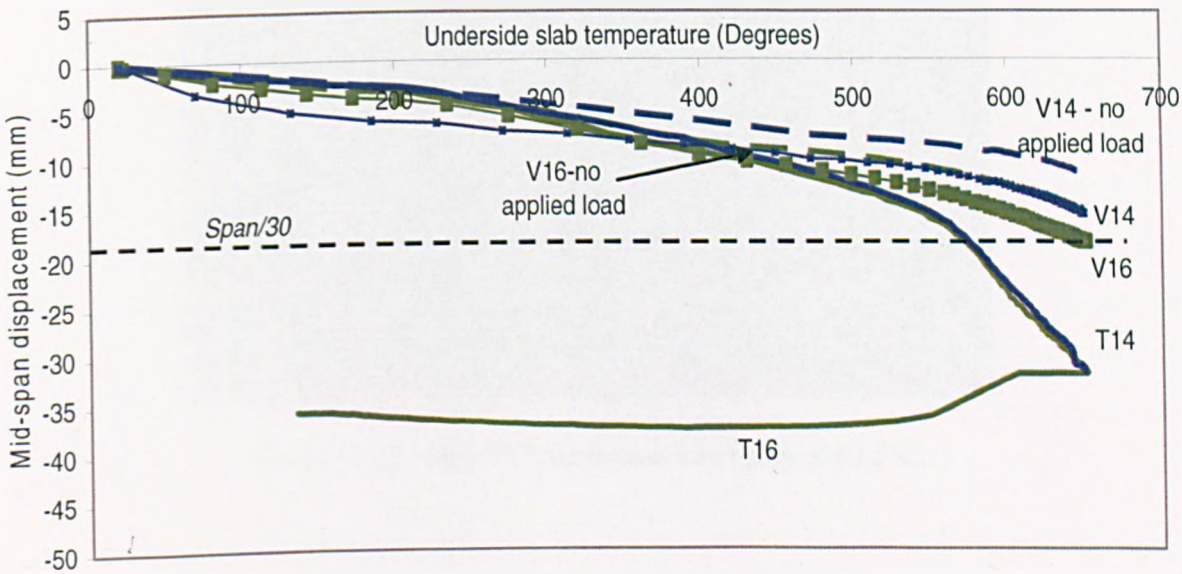

Figure 6.38: Comparison of mid-span displacements for Tests 14 and 16 with *Vulcan* predictions.

The membrane traction plots for Tests 14 and 16 are shown in Figures 6.40 and 6.41. The development of compressive membrane forces can be seen. These slabs have lower reinforcement percentage across the cross section of the slab, 0.1% compared to 0.25% for Tests 12 and 13. It is interesting to note the development of the compression band across the short span of the slab at displacements approximately between 15-18mm.

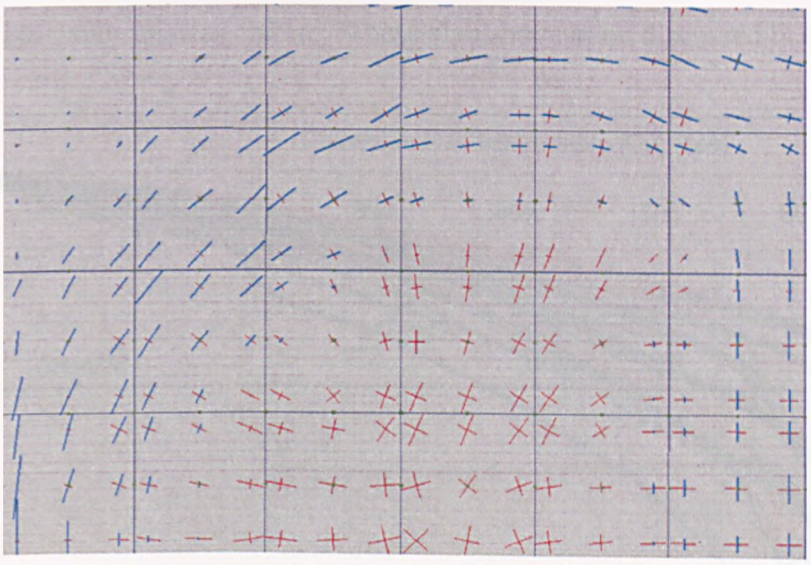

Figure 6.40: Test 14, membrane force plot at 608°C.

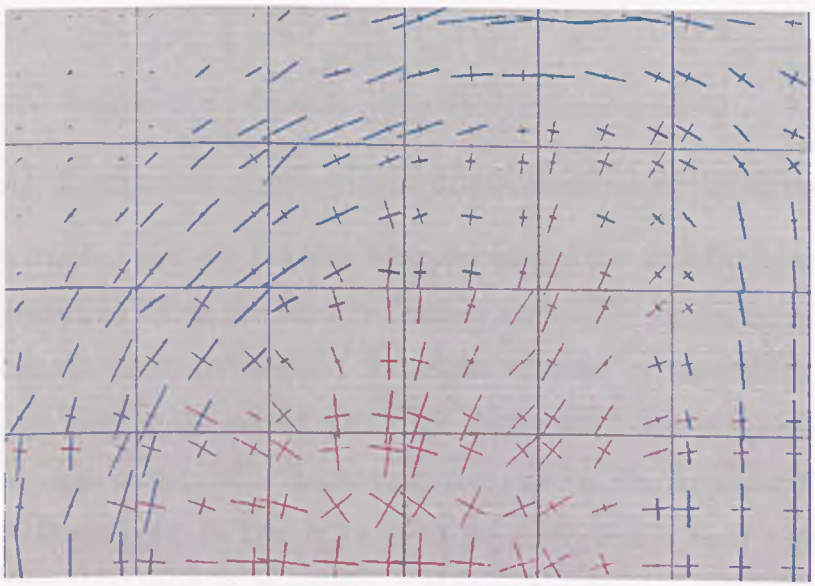

Figure 6.41: Test 16, membrane force plot at 612°C.

6.4.7 Effect of Reinforcement Percentage on Slab Performance

Comparisons have been made between the tests in Table 5.1 and their results are summarised in Figure 6.42. The tests follow a similar pattern, even though the slabs are reinforced with varying reinforcement percentages, in that after 550°C the rate of deflection increases depending on the extent of cracking. Some of the slabs suffered extensive cracking and runaway failure. These slabs have been discussed in Chapter 5.

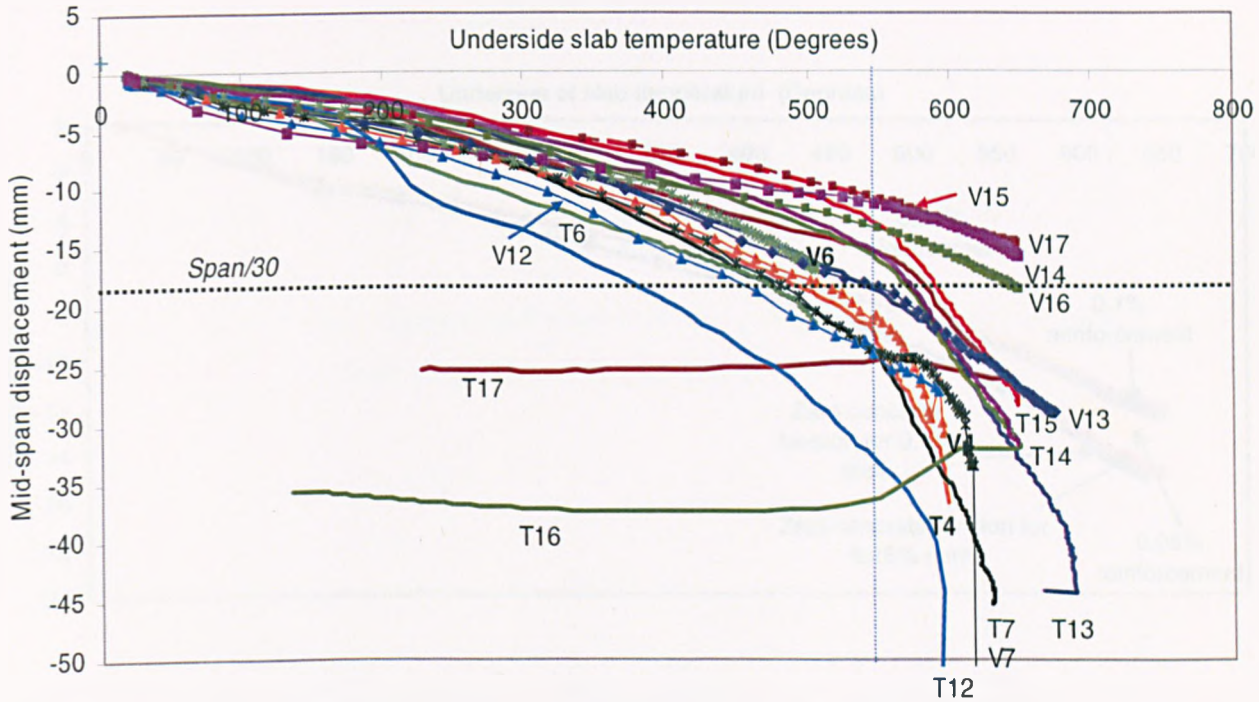

Figure 6.42: Comparison of the mid-span displacements with *Vulcan* predictions.

The membrane traction plots for the tests have shown that for slab displacements between 10-15mm, compressive forces are seen to develop across the short span of the slab. At larger displacements, these compressive forces are relieved as the slab develops tensile membrane action, with tensile forces within the central zone and compressive peripheral ring around the edges of the slab. The compressive band is also influenced by the area of reinforcement, for example, in Tests 12 and 13 the compressive band within the central zone of the slab was not as distinct as compared with the tested slabs of lesser reinforcement.

Influence of concrete tension on slab performance

A numerical study was carried out using Test's 17 measured data. Comparisons were made between slabs of different reinforcement area, 0.1% and 0.25% with zero applied load and models were run with and without the inclusion of concrete tension, Figure 6.43.

As discussed in Chapter 4, concrete tension seems to contribute to the load carrying capacity of the slab at initial displacements, when the slab is in bending. The numerical results showed that as the slab temperatures increased the model slabs where concrete tension was ignored displaced more than the model slabs where concrete tension was included. At initial displacements, the influence of concrete tension does not become apparent until after 200°C when the numerical results start to diverge between the slabs that include tension and the slabs that do not include tension.

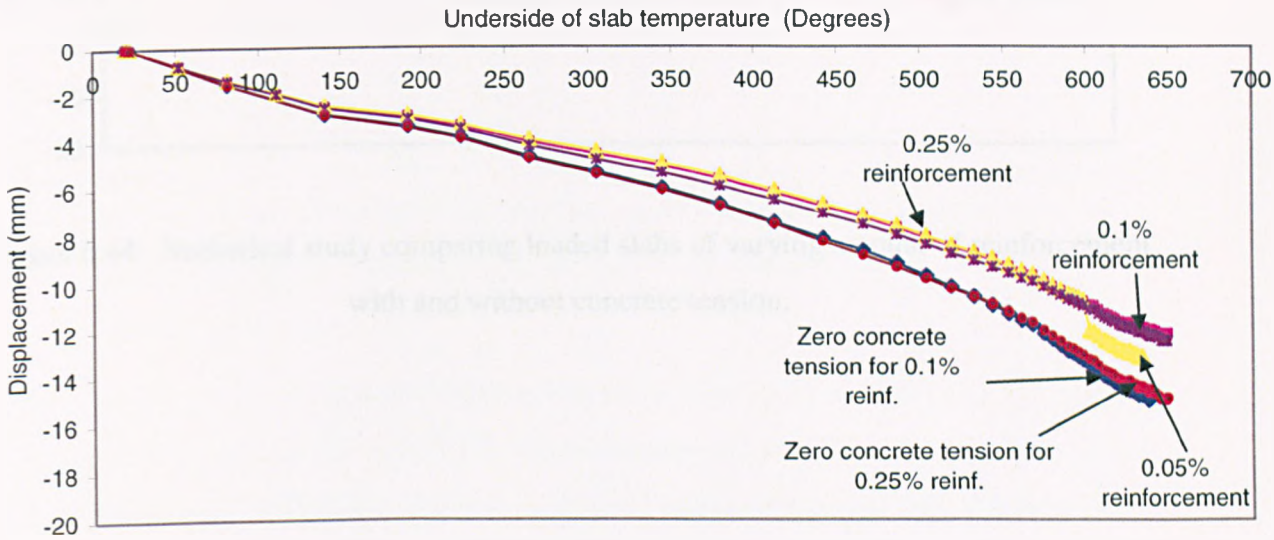

Figure 6.43: Numerical study comparing the displacements of models with varying amount of reinforcement with zero applied load.

Figure 6.44 compares the numerical results between slabs of different reinforcement percentages with applied load (Test 17 measured data used). It can be seen that after 200°C, the rate of displacements for the *Vulcan* prediction with zero concrete tension for a slab of 0.1% reinforcement is higher than the *Vulcan* prediction with zero concrete tension for a slab of 0.25% reinforcement. Therefore, as the percentage of reinforcement in the slab increases the influence of concrete tension is less.

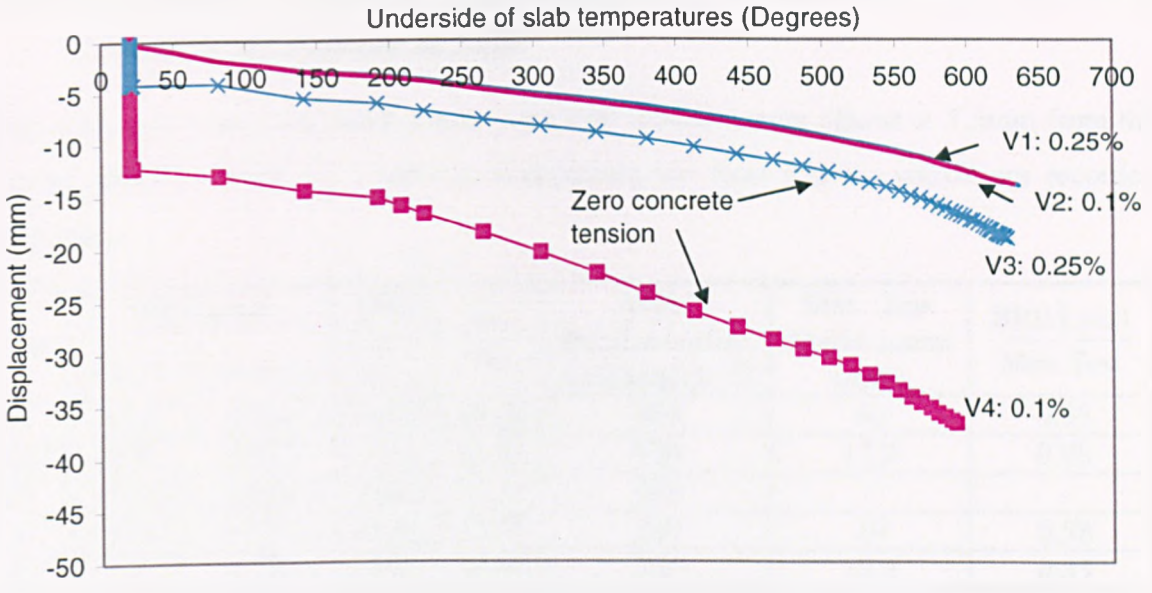

Figure 6.44: Numerical study comparing loaded slabs of varying amount of reinforcement with and without concrete tension.

6.4.8 Rectangular Slabs of Depth 22mm with Reinforcement Placed at 7.5mm from Bottom of Slab

Four slabs were cast with depth 22mm, and with reinforcement placed at 7.5mm from the bottom surface. Tables 5.2 and 6.2 summarises the tests and the maximum recorded deflections.

Test	BRE Limit		BRE Limit Δ_{Total}	$\frac{span}{30}$	Max. Reinforcement temperature °C	Max. Test displacement (mm)	$\frac{\text{BRE Limit}}{\text{Max.Test}}$
	$\Delta_{thermal}$	$\Delta_{mechanical}$					
9	3.12	12.88	16.01	18.33	480	46	0.35
20	4.04	13.27	17.31	18.33	520	17.7	0.98
10	2.55	12.88	15.43	18.33	459	-	-
11	3.44	13.27	16.71	18.33	526	29	0.58
21	2.66	12.88	15.55	18.33	500	18.4	0.85

Table 6.2: Comparison of maximum test displacements with predicted displacements for slabs of dimension 920x620x22mm, with reinforcement placed 7.5mm from bottom of slab.

Figure 6.45 shows the comparison between test and *Vulcan* in Tests 9 and 20. The slabs in these tests were reinforced with 0.1% reinforcement and the load ratio in Test 9 was slightly higher than in Test 20. The slab in Test 9 was also reinforced with deformed wire. The slabs performed similarly up to 500°C, after which point the rate of displacement in Test 9 dramatically increased, ultimately leading to runaway failure of the slab. Figure 6.46 shows the slab in Test 9 after testing; the major crack development is notable. On comparison of Test results with *Vulcan* predictions it is shown that *Vulcan* accurately predicts the slab behaviour up to 500°C after which point *Vulcan* predictions do not correlate well with the test results. As previously discussed in Chapter 4, the layered slab elements within *Vulcan* are based on the structural mechanics principle 'plane sections remain plane'; the layer of reinforcement remains fully bonded to the concrete. Therefore, neither bond slip nor fracture of the reinforcement is modelled, which explains the deviations between experimental and numerical results. In addition, what is not easily seen is the difference in slab behaviour due to the type of reinforcement used. Up to 500°C, irrespective of load ratio, the slabs perform very similarly but then diverge, with Test 9 showing signs of run-away failure. This could be due to the slightly higher load ratio experienced by this particular slab, but upon cracking, the deformed wire behaved in a less ductile manner because of its better bond with the concrete and this could have led to the failure of the wire.

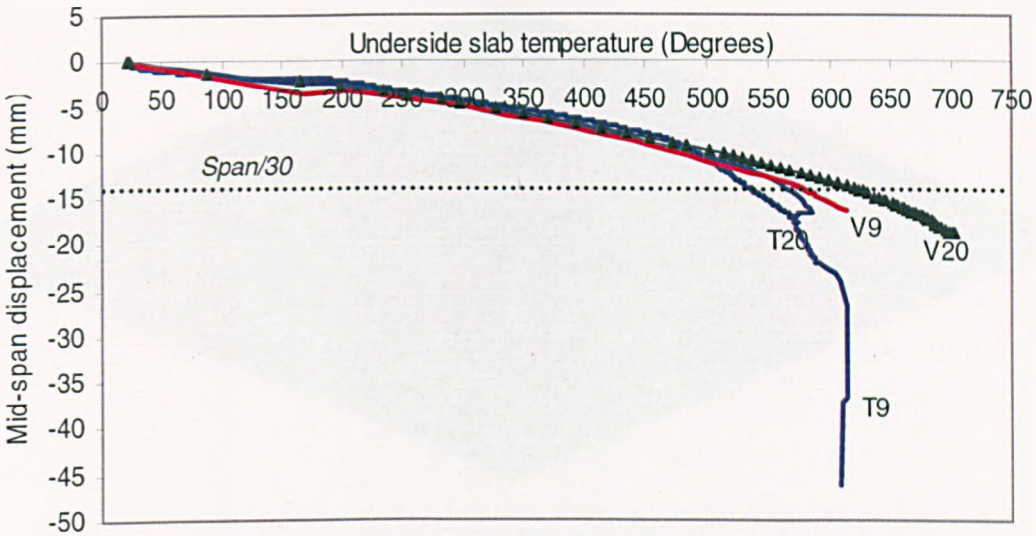

Figure 6.45: Comparison of Tests 9 and 20 with Vulcan predictions.

Figure 6.46: Test 9; View of top surface after test.

Figures 6.47 and 6.48 show the development of the membrane forces within the slab. The compressive forces within the central zone can clearly be seen.

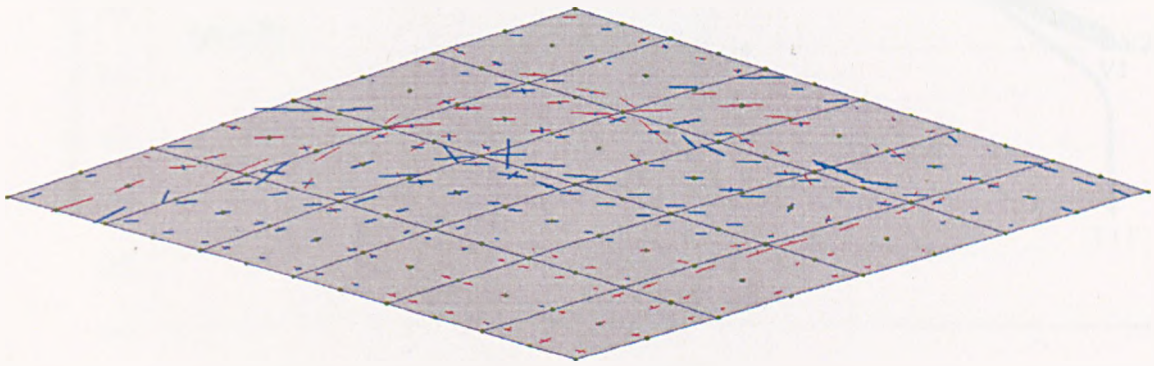

Figure 6.47: Test 9, membrane force plot at 221°C (underside slab temperature).

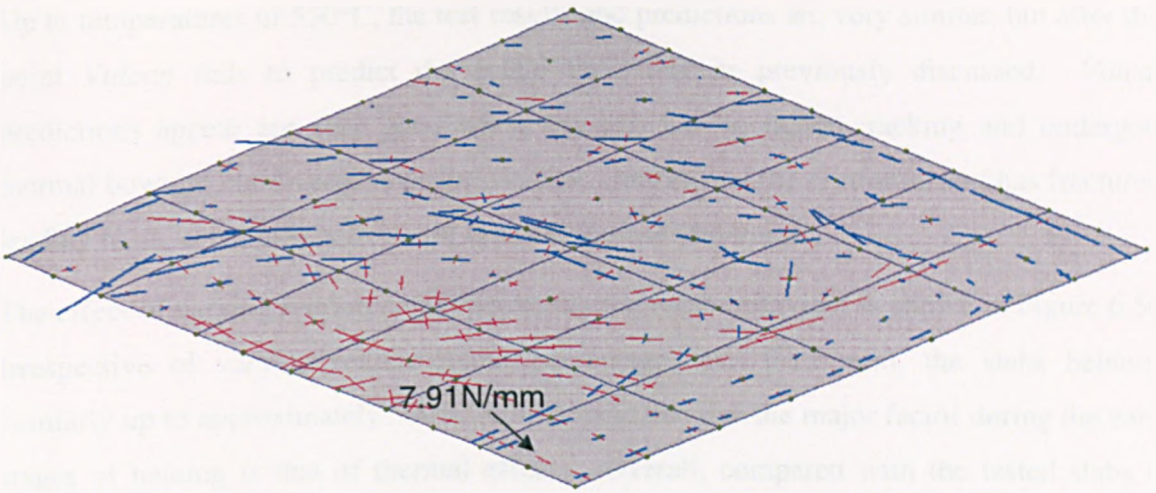

Figure 6.48: Test 9, membrane force plot at 576°C.

The slab displacement in Test 9 at 576°C is approximately 15mm; it seems that the slab has not developed the full tensile membrane forces within the central zone of the slab.

The graph presented in Figure 6.49 compares the identical slabs of Tests 10, 11 and 21 with *Vulcan*. Tests 10 and 11 performed similarly up to 450°C, at which point Test 10 had to be terminated due to problems with the test rig. Test 21 is a replica of Test 10 but was tested at a lower load ratio. It is interesting to see from this graph that, in the early stages of Test 21, the slab had lower deflections compared with the numerical analysis results, when no load was applied, which could be due to the measured temperature distributions within the temperature data file not accurately picking up the slab's thermal behaviour.

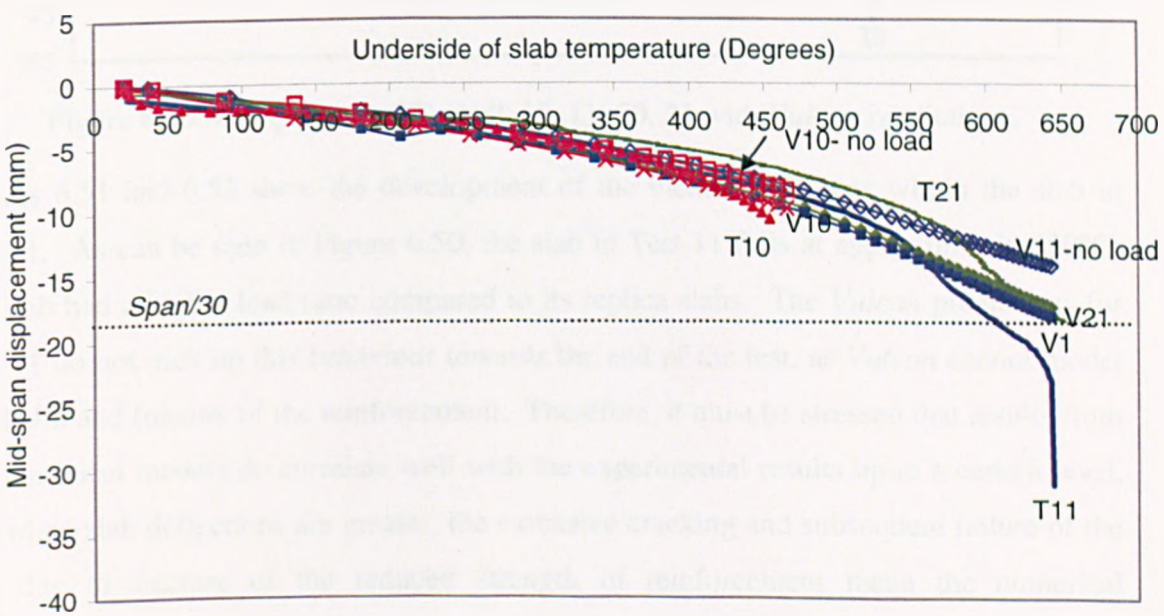

Figure 6.49: Comparison of Tests 10, 11 and 21 with *Vulcan* predictions.

Up to temperatures of 550°C, the test results and predictions are very similar, but after this point *Vulcan* fails to predict the actual behaviour as previously discussed. *Vulcan* predictions appear are very good when the slab has no major cracking and undergoes thermal bowing, but diverge once the slab has cracked and the reinforcement has fractured, leading to an 'unzipping' effect and runaway failure of the slab.

The effect of varying reinforcement percentages on slab behaviour is shown in Figure 6.50. Irrespective of varying reinforcement percentages and load ratio, the slabs behaved similarly up to approximately 500°C, which indicated that the major factor during the early stages of heating is that of thermal effects. Overall, compared with the tested slabs of lower depth, the thicker slabs deflected less in the early stages, which corresponds well with theory (Equation 6.1). The thinner slabs achieved higher displacements than the thicker slabs due to their increased thermal bowing.

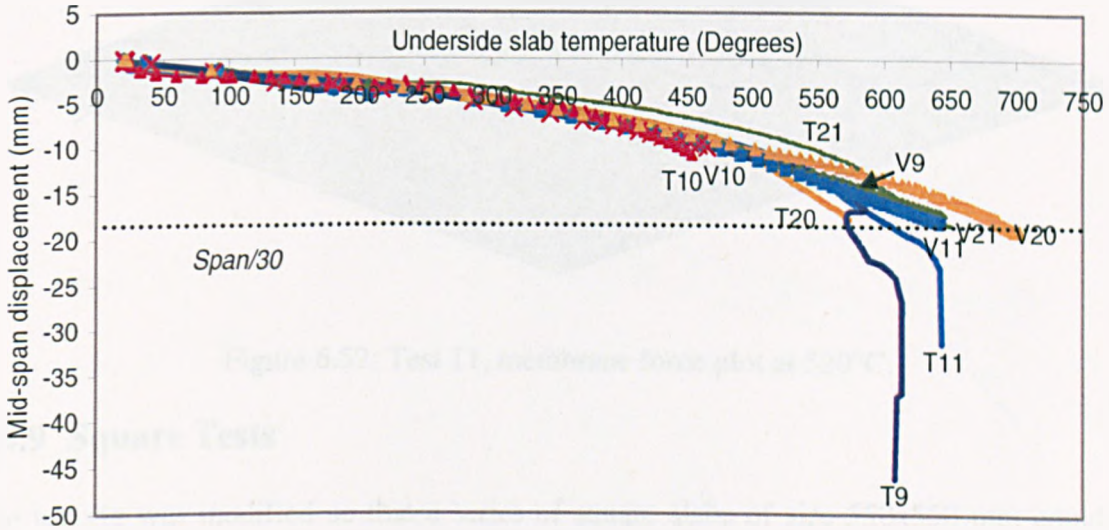

Figure 6.50: Comparison of Tests 9, 10, 11, 20, 21 with *Vulcan* predictions.

Figures 6.51 and 6.52 show the development of the membrane forces within the slab in Test 11. As can be seen in Figure 6.50, the slab in Test 11 fails at approximately 650°C; this slab had a higher load ratio compared to its replica slabs. The *Vulcan* predictions for Test 11 do not pick up this behaviour towards the end of the test, as *Vulcan* cannot model bond-slip and fracture of the reinforcement. Therefore, it must be stressed that results from the numerical models do correlate well with the experimental results up to a certain level, but, when slab deflections are greater, the extensive cracking and subsequent failure of the slab due to fracture of the reduced strength of reinforcement mean the numerical predictions cannot be relied upon.

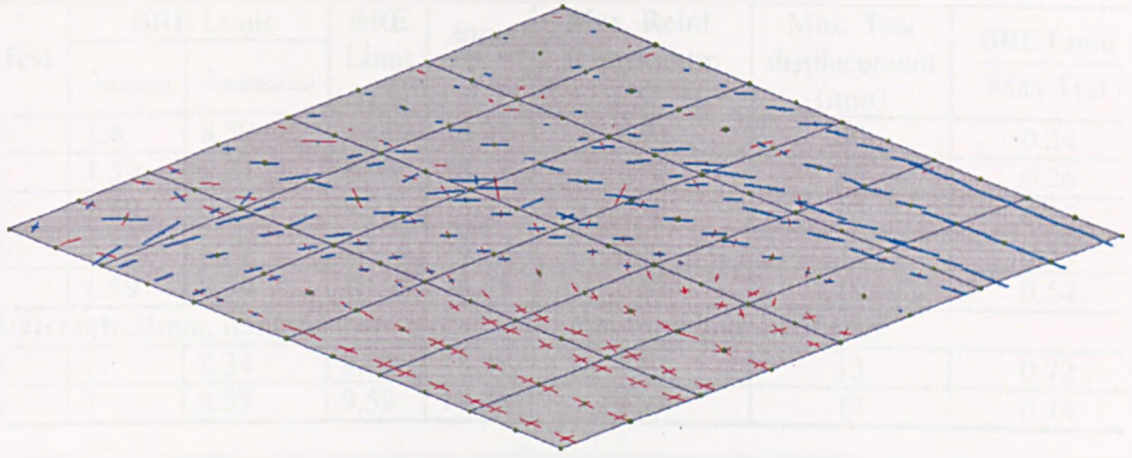

Figure 6.51: Test 11, membrane force plot at 220°C (underside slab temperature).

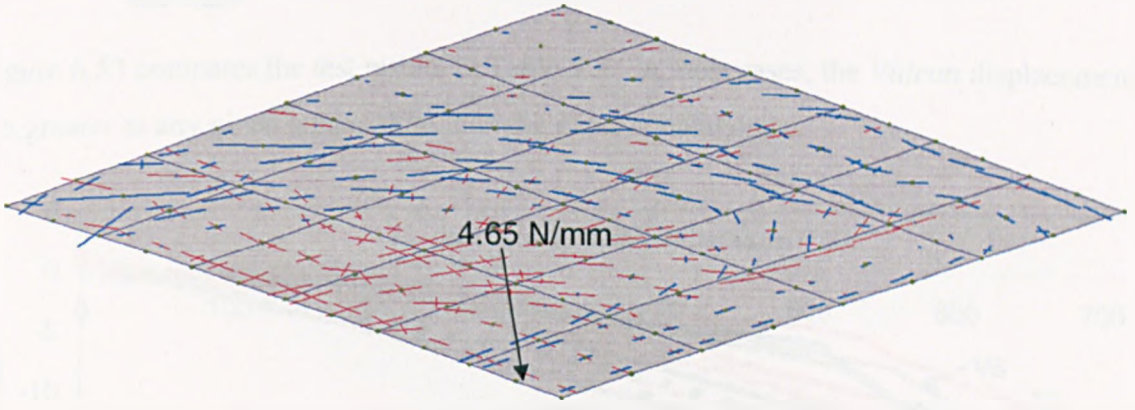

Figure 6.52: Test 11, membrane force plot at 520°C.

6.4.9 Square Tests

The test rig was modified so that a series of square slabs of size 550x550 mm could be tested. The test series is presented in Table 5.3 and a summary of the results of the tests is shown in Table 6.3. The tested slabs had total cross sectional areas of reinforcement varying from 0.05% to 0.25%. The slabs in Tests 4-7 had overall depth of 15mm and in Tests 8 and 9, this depth was increased to 22mm.

Test	BRE Limit		BRE Limit	$\frac{span}{30}$	Max. Reinf. temperature °C	Max. Test displacement (mm)	BRE Limit / Max.Test
	$\Delta_{thermal}$	$\Delta_{mechanical}$	Δ_{Total}				
3	1.6	8.59	10.19	18.33	530	30	0.34
4	1.59	8.34	9.93	18.33	530	38	0.26
5	1.59	8.34	9.93	18.33	530	13	0.26
6	1.59	8.59	10.18	18.33	530	27	0.37
7	1.59	8.59	10.18	18.33	530	19	0.54
600x600x22mm, reinforcement placed at 7.5mm from bottom of slab							
8	1	8.34	9.34	18.33	530	13	0.72
9	1	8.59	9.59	18.33	530	13	0.74

Table 6.3: Comparison of maximum test displacements with predicted displacement for slabs of dimension 920x620x15mm, with reinforcement placed at half depth of the slab.

Figure 6.53 compares the test results in Table 5.3. In most cases, the *Vulcan* displacements are greater at any given temperature than the experimental ones.

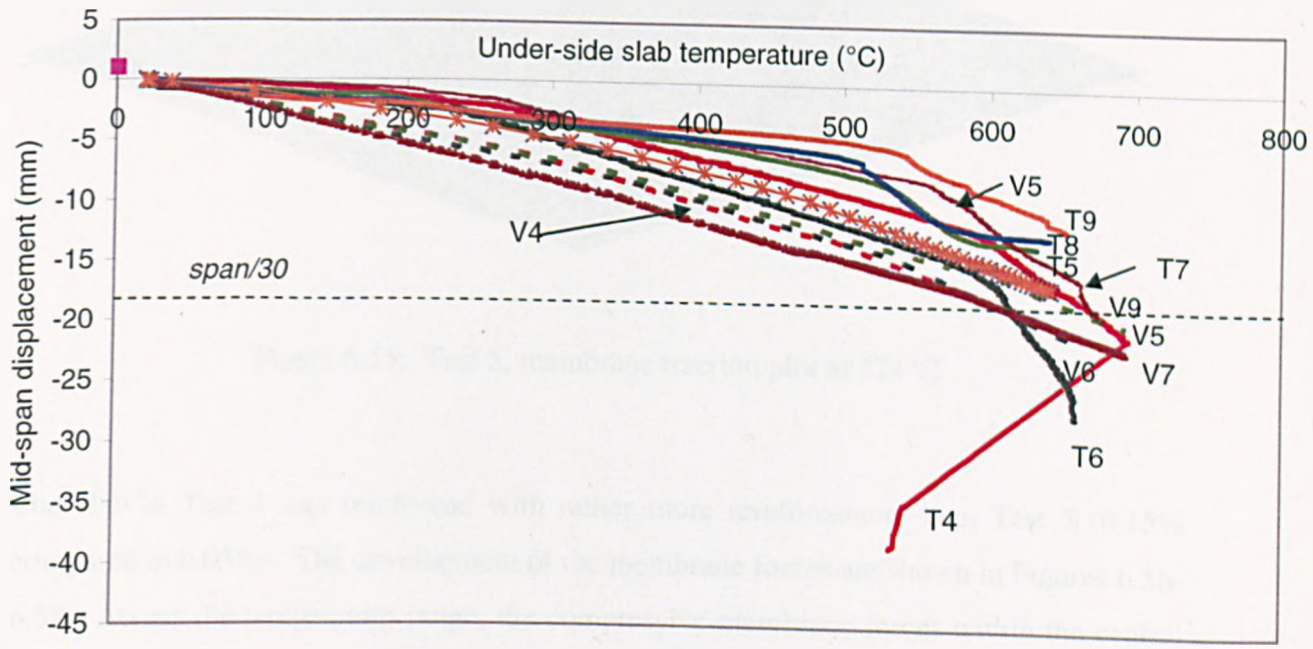

Figure 6.53: Comparison of test results with *Vulcan* predictions for the square slabs.

Figures 6.54 and 6.55 show the membrane traction plots for Test 5 at 332°C and 574°C. The distribution of the membrane forces is symmetrical about the diagonal axis, which is perfectly logical. The tensile membrane forces within the central zone are balanced by the peripheral 'ring' of compressive forces at the surrounding edge. At 574°C, compressive forces have not developed within the central region of the slab.

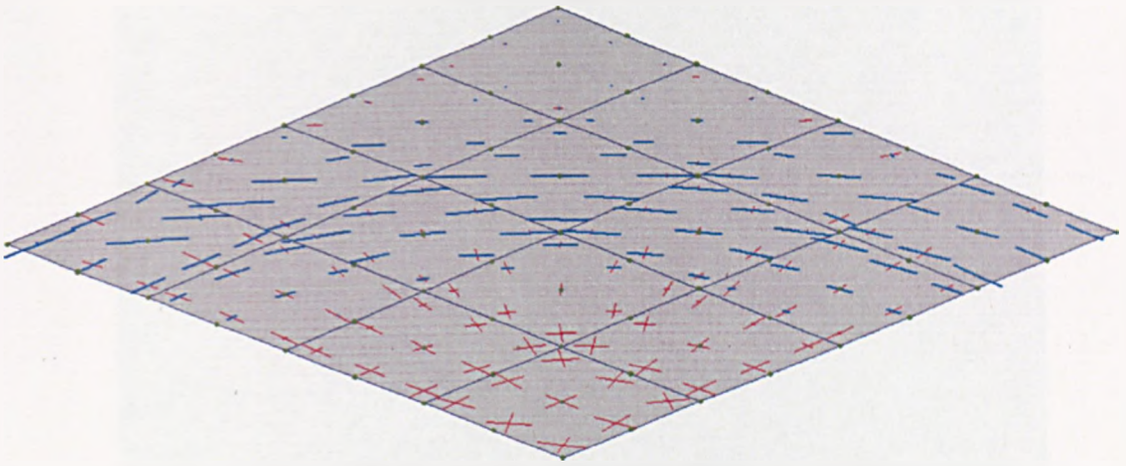

Figure 6.54: Test 5, membrane traction plot at 332°C (bottom surface temperatures).

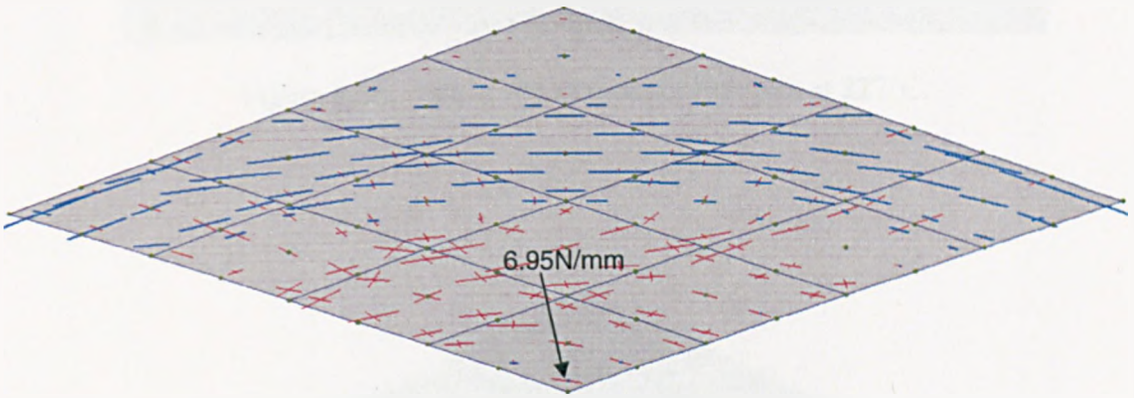

Figure 6.55: Test 5, membrane traction plot at 574°C.

The slab in Test 4 was reinforced with rather more reinforcement than Test 5 (0.15% compared to 0.05%). The development of the membrane forces are shown in Figures 6.56-6.58. Across the temperature range, the compressive membrane forces within the central zone that were present in the rectangular slabs are not apparent for the square slab in Test 4.

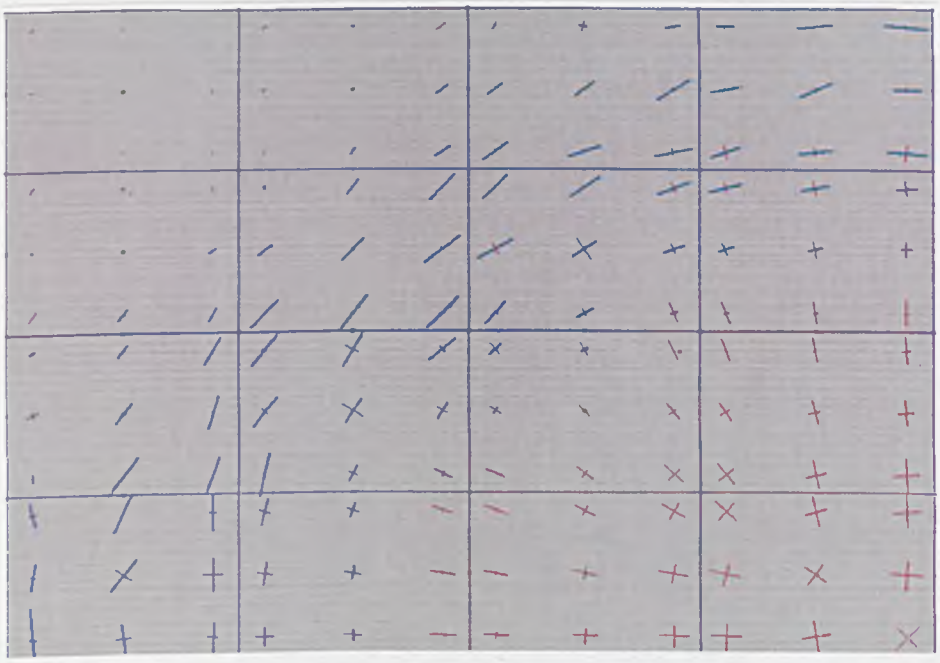

Figure 6.56: Test 4, membrane traction plot at 227°C.

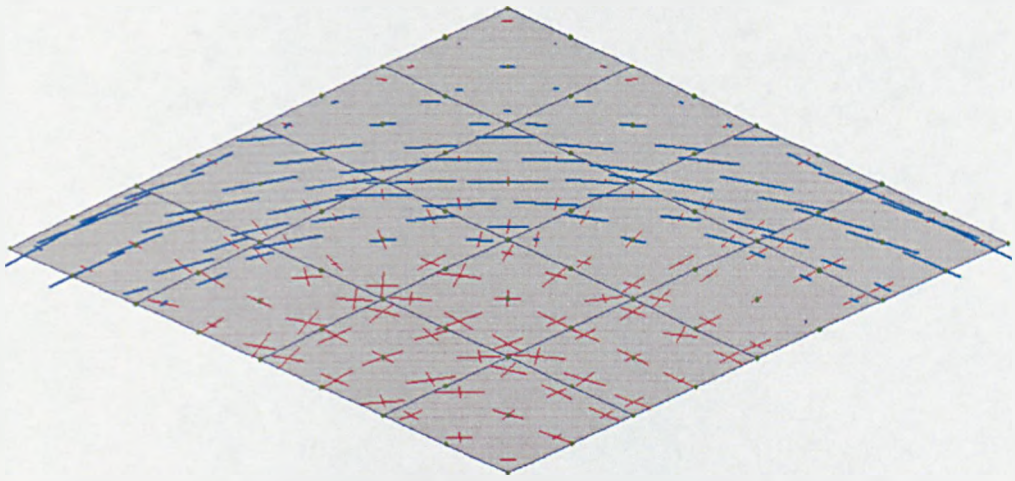

Figure 6.57: Test 4, membrane traction plot at 572°C.

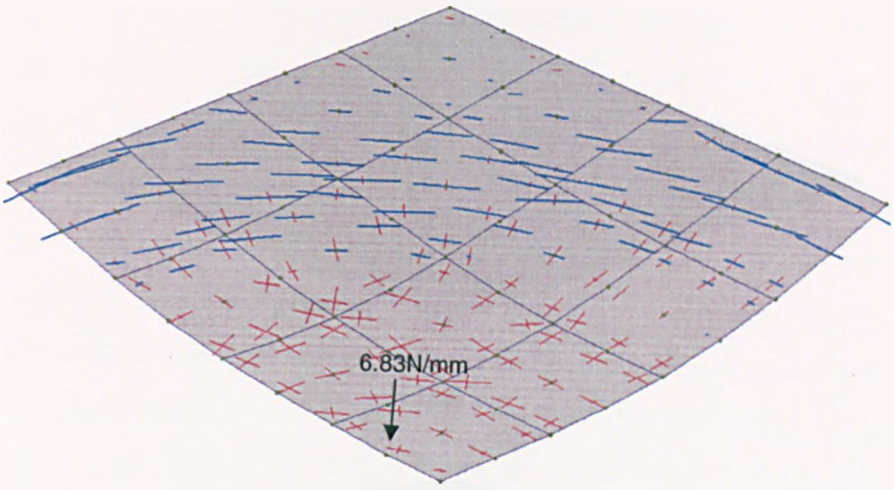

Figure 6.58: Test 4, membrane traction plot at 581°C (vertical displacement scaled by 50).

The square slabs in Tests 4, 5 and 7 (Figures 6.56-6.58) did not develop any compressive bands across within the central zone of the slab for the full range of slab temperatures. These tests had variable loads and differing reinforcement percentages, which seems to indicate that the geometry of the slab had some influence on the initial development of the compressive band within the rectangular slabs.

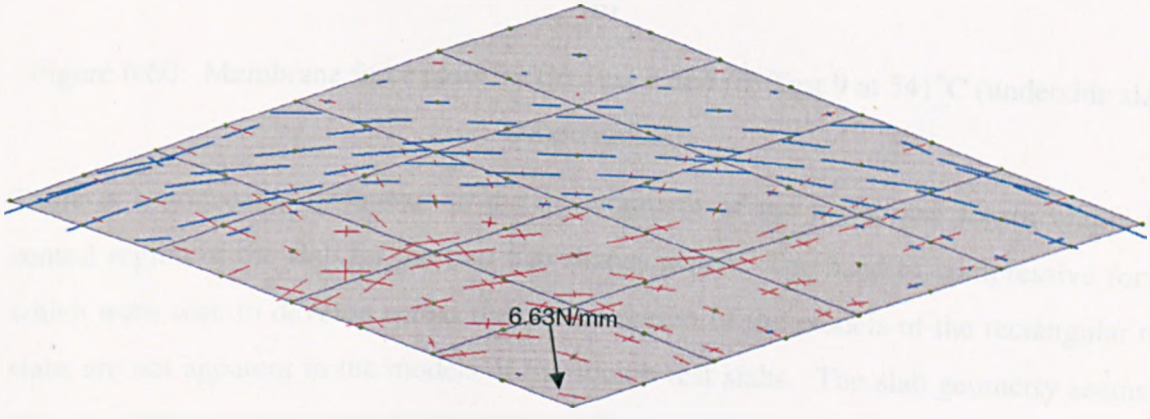

Figure 6.59: Test 7, membrane traction plot at 645°C.

The membrane force plots for Tests 8 and 9 are shown in Figure 6.60, below. These slabs were of greater depth, with the reinforcement placed 7.5mm from the bottom surface. The tensile zone is clearly seen and the absence of compressive membrane forces in the central area is notable.

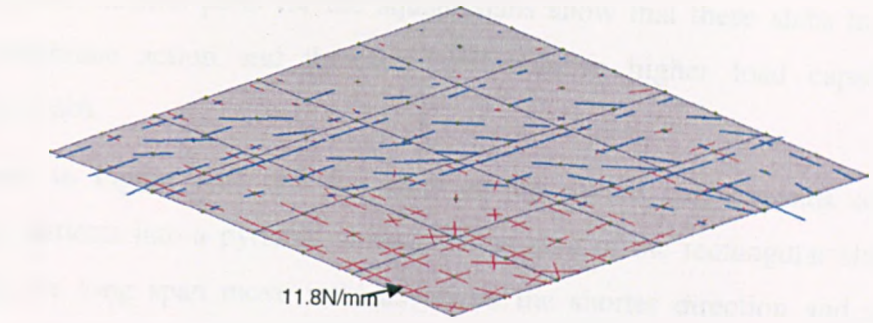

(a)

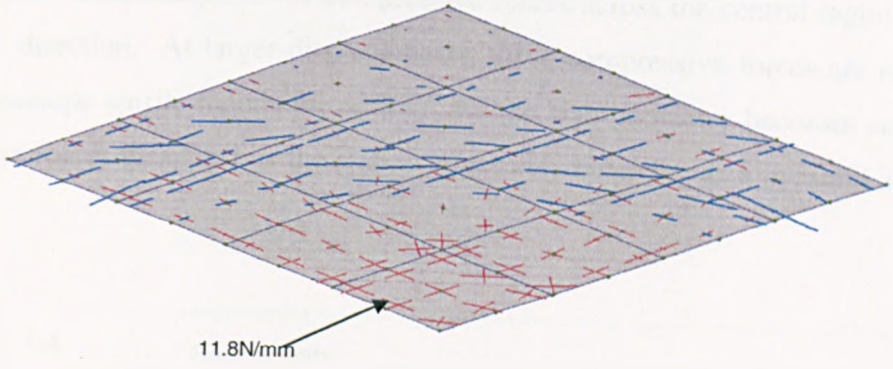

(b)

Figure 6.60: Membrane force plots for (a) Test 8 and (b) Test 9 at 541°C (underside slab temperatures).

There is a noticeable difference in the development of the membrane forces within the central region of the slab for the two slab shapes tested. The band of compressive forces which were seen to develop across the central region of the models of the rectangular test slabs are not apparent in the models of the square test slabs. The slab geometry seems to play an important part in the development of these membrane forces. In Chapters 3 and 4, it was observed at ambient temperature that the trapezoidal slab facets caused by a typical yield line hinge pattern for rectangular slabs rotated on plan and 'butted' in the middle of the slab. For square slabs, of course, there are no trapezoidal facets in the yield-line mechanism, and the triangular facets simply move apart in the central area of the slab. The compressive band across the short span in the rectangular slabs are seen to occur at low displacements (approximately 15mm) and seem to be due to a combination of the rectangularity of the slab and the thermal bowing of the slab. At large displacements, the compressive band disappears as the slab progresses into tensile membrane action.

The membrane traction plots for the square slabs show that these slabs have developed tensile membrane action and therefore will achieve higher load capacity than the rectangular slabs.

It is shown in Figure 6.61 that the edge of the square slab expands outwards as it effectively deflects into a pyramid shape. In the case of the rectangular slabs, the edges parallel to the long span move inwards across the shorter direction and push the slab outwards in the longer direction, Figure 6.62. As the slab moves inwards and deflections increase, the trapezoidal facets will still rotate in plan due to the change of geometry and this will cause the development of compressive forces across the central region parallel to the shorter direction. At larger displacements, these compressive forces are relieved and the slab develops tensile membrane action. As the slab geometry becomes square, these compressive forces disappear as the slab is effectively behaving as a pyramid and pushing outwards.

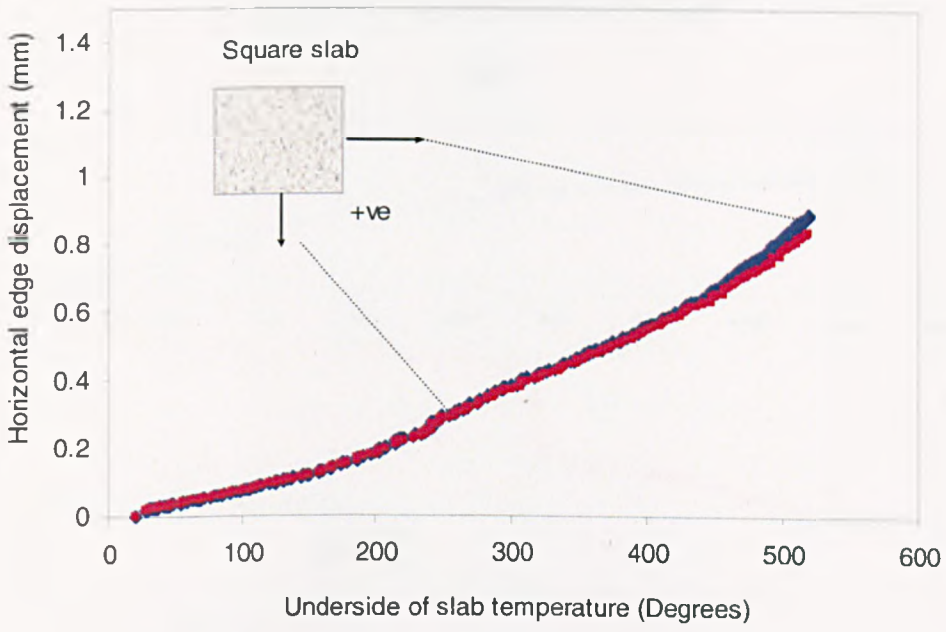

Figure 6.61: Predicted edge movements from *Vulcan* for square slabs of isotropic reinforcement.

(a) Movement at the edge of the slab

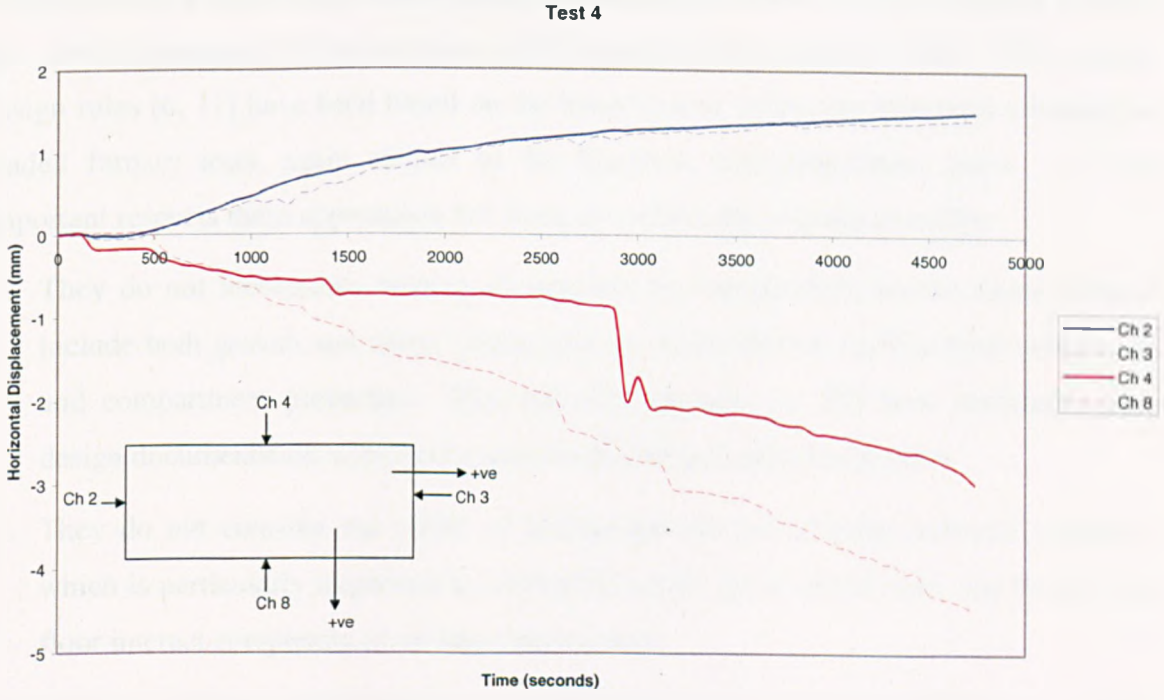

(b)

Figure 6.62: Typical movements at the edges of rectangular slabs (Test 4 experimental data).

Chapter 7

Thermal and Structural Behaviour of a Full-Scale Composite Building Subject to a Severe Compartment Fire

7.1 Introduction

Over the past decade, the fire engineering design of steel structures has developed considerably. The traditional prescriptive approach has placed reliance simply on limiting the temperature achieved by any structural component when subjected to a prescribed "Standard Fire" heating regime [32] up to the required fire resistance time, but taking no account of the influence of other elements of the building construction or its loading condition. It has therefore been normal practice to protect steel beams and columns by using prescribed thicknesses of fire protection materials, whose purpose is simply to limit the steel temperatures for the duration of the specified fire resistance time. More recent design rules [6, 11] have been based on the behaviour of individual structural elements in loaded furnace tests, again subject to the Standard time-temperature curve. In two important respects these approaches fall short of realistically relating to reality:

1. They do not incorporate heating of structure by natural fires, whose characteristics include both growth and decay phases and are controlled by the fire load, ventilation and compartment properties. This has only recently [3, 59] been introduced into design documentation with limitations on allowable compartment sizes.
2. They do not consider the effect of interaction and load-sharing between elements, which is particularly important in composite construction where slabs and beams in a floor interact completely as an integrated system.

Perhaps the key point overall is that, while design codes based on isolated member tests in Standard Fire conditions [6, 11] give the critical steel temperature for runaway failure of unprotected secondary beams in the region of 670°C for all the Cardington tests all temperatures experienced were above this level yet no structural failure was observed in any of them. Deflections of the floor system in most cases exceeded the normal furnace-test limit of *span/30* during the heating phase, reducing somewhat as cooling took place.

Subsequent numerical analyses of the tests [60, 61] have shown that this unexpected resilience of the floor system derives from combinations of:

- ***Three-dimensional flexural bridging*** due to continuity of the slabs, both directly above fire compartments and with surrounding cool areas. This mechanism is more dominant at lower deflections.
- ***Catenary tension*** in both slabs and composite beams when deflections reach high levels and the curvatures are predominantly unidirectional. For this action to provide substantial support the edges of the zone in catenary must be capable of resisting the largely horizontal tensile forces generated.
- ***Tensile membrane action*** in slabs at high deflections. This is a self-equilibrating action [62] in which an individual slab in biaxial curvature generates a multi-directional tension field in its central region, which is resisted by a ring of compression around its edge zone. The necessary condition for this action to be effective is that vertical support to the edges of the slab should be maintained, and that its aspect ratio should be reasonably "square".

A seventh fire test was carried out on the building in January 2003. The main emphasis in undertaking this work was to collect more detailed data on the performance of typical beam-to-column and beam-to-beam frame connections in fire, a considerable spur to the work being the documented failures [63] of connections in some buildings of the New York World Trade Center complex on 11 September 2001, and subsequent recommendations for investigation. This test also provides further opportunities both to investigate the behaviour of the composite floor system in the multi-storey building and to use the results to check the capability of specialised numerical modelling software.

This Chapter presents comparisons of the results from "Test 7" on the Cardington composite frame with the results of thermo-structural numerical modelling using *Vulcan*. Three-dimensional non-linear analyses of the fire compartment and surrounding cold structure have been carried out, using measured temperatures where available, but in other cases using either simplified temperature calculation or numerical thermal analysis of structural components.

The results of this Chapter has been summarised and are awaiting publication in the Fire Safety Engineering Journal [64].

7.2 The Fire Compartment of Test 7

The rectangular 11m x 7m fire compartment, a little larger than one bay of the column grid, was situated on the third floor of the eight-storey composite building, and differed from those of similar size in the original series by having just one edge at the perimeter of the building. The fire compartment location is shown in Figure 7.3.

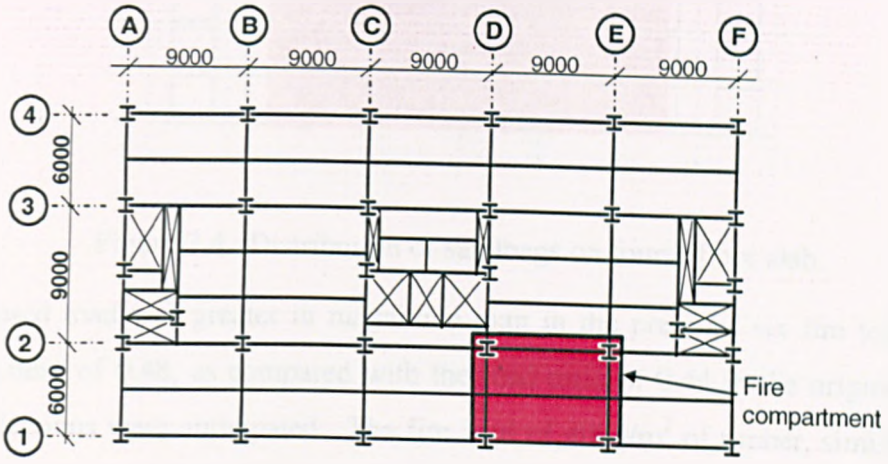

Figure 7.3: Floor plan and location of fire "Test 7" compartment.

The internal walls were constructed using fire-resistant boards, which were not fixed to the composite floor soffit above, and thus allowed some vertical movement of the slab without damage. The external edge of the compartment was left unglazed, but two wind-posts were left in place. These connected the upper and lower edge-beams and were continuous over the height of the building, but allowed some vertical relative movement of the edge-beams by being connected to them at slotted holes. A uniform imposed load of 3.19kN/m^2 was simulated by the use of 11kN sandbags distributed evenly over an area of 18m by 10.5m at fourth floor level see Figure 7.4.

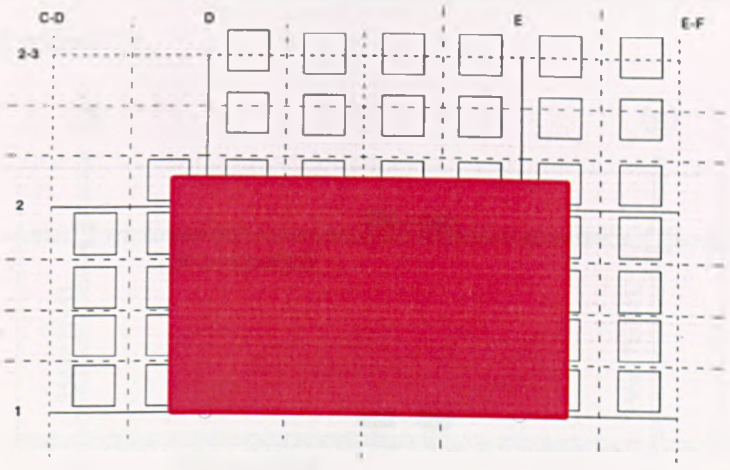

Figure 7.4. Distribution of sandbags on fourth floor slab.

This imposed load was greater in magnitude than in the previous six fire tests, giving a total load ratio of 0.48, as compared with the load ratio of 0.44 in the original series, so larger deflections were anticipated. The fire load of 40kg/m^2 of timber, similar to two of the original tests, was provided by wooden cribs distributed within the compartment area. The compartment dimensions and properties of the materials used are given in Table 7.2.

Fire Compartment	
Height H = 4 m	**Floor area A_f = 77 m^2**
Length L = 11 m	**Total area of compartment A_t = 298 m^2**
Depth D = 7 m	
Fire load:	
Wooden cribs 40 kg/m^2	**Fire load density q_f = 720 MJ**
Openings:	
Height h_v = 1.27 m	**Opening factor O = 0.043**
Length l_v = 9 m	
Boundaries:	
Plasterboard b_p = 520 J/m^{2}s$^{1/2}$K	**Total b = 801 J/m^{2}s$^{1/2}$K**
LW concrete b_c = 1120 J/m^{2}s$^{1/2}$K	

Table 7.2: Compartment dimensions.

For the purposes of the fire test both the primary and secondary beams were unprotected, with cementitious spray protection applied only to the columns and to a short length (1m) of the primary beams at the building edge, including the whole of the external joints. The

displacements and temperatures of the steel beams, joints and concrete slab were measured at key locations (Figure 7.5).

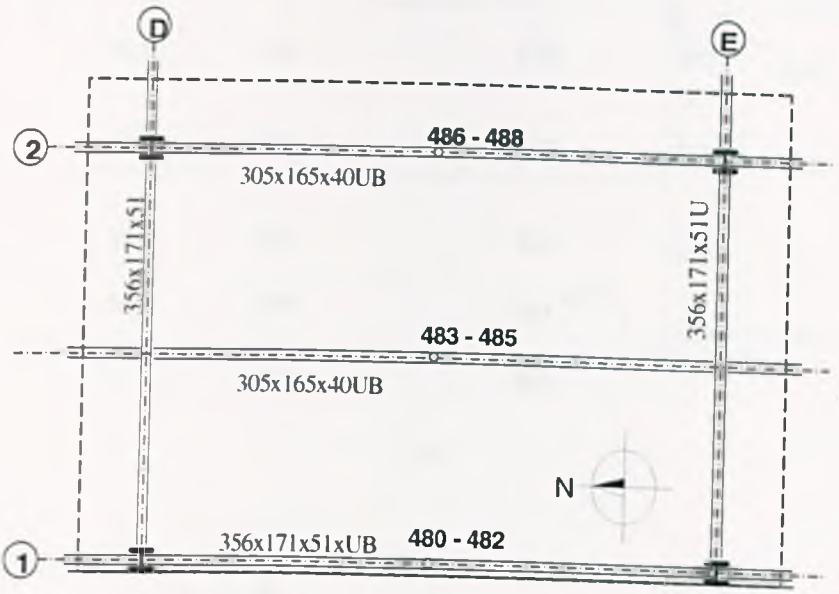

(a)

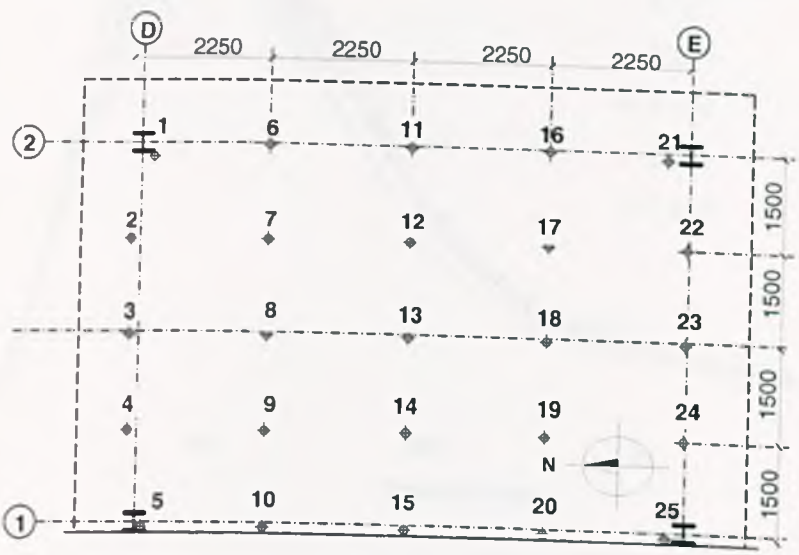

(b)

Figure 7.5: (a) Arrangement of members and thermocouples and (b) Position of displacement transducers

The maximum depth of the composite slab was 130mm with a continuous upper part of 70mm over the troughs in the decking. The temperatures within the compartment were measured at several key locations (Figure 7.6) which shows also their measured variations. The average measured fire temperatures were calculated throughout the fire period, and these were used as input into thermal analysis.

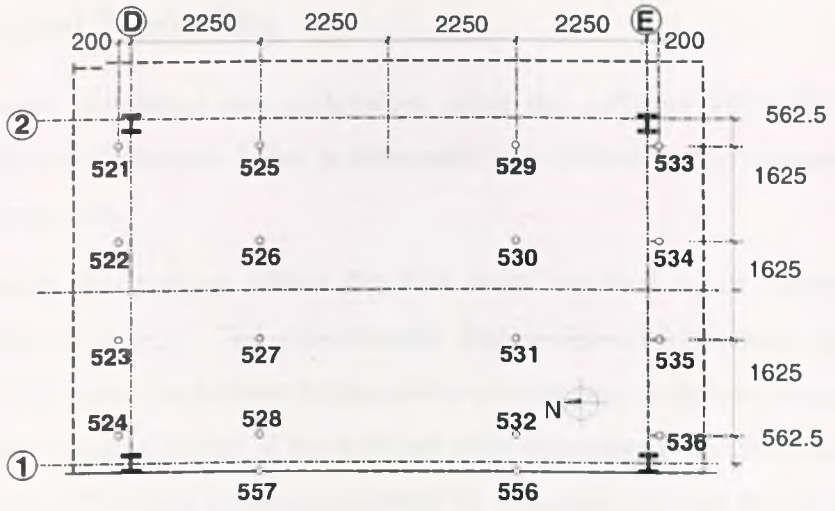

(a)

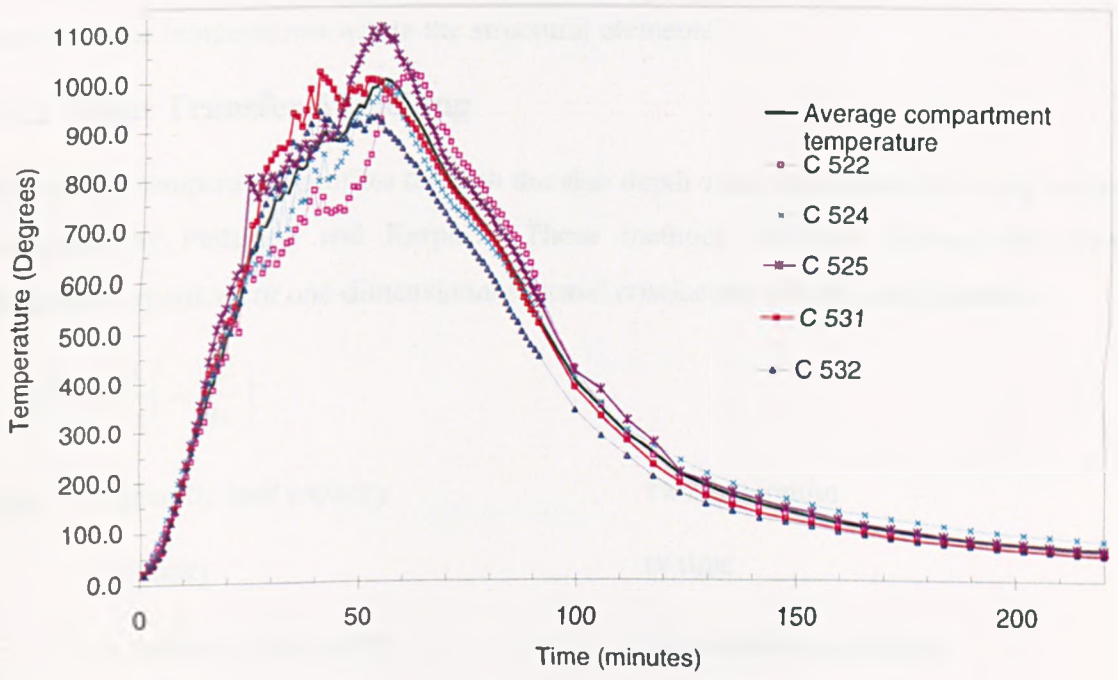

(b)

Figure 7.6: (a) Location of the air thermocouples on the 3rd floor hung 300 mm below the ceiling and (b) Recorded fire temperatures within the compartment and average calculated fire temperature.

7.3 Thermal Modelling

The heat transfer modelling was undertaken using the software FPRCBC-T [58], and simplified calculation methods given in Eurocode 3, to determine the temperatures within the structural elements.

The temperature distributions across the slab were required to be inputted into the numerical software *Vulcan*. The experimental data measured from these thermocouples could not be relied upon as the heat destroyed the instruments in the later stages of the test. A comprehensive thermal model of the slab had to be determined. Initial calculations were undertaken using differential methods presented by Petterson [65] and Karpas [66]. Due to the complexity of concrete, further analyses were undertaken using the finite element software FPRCBC-T, and simplified calculation methods given in Eurocode 3, to determine the temperatures within the structural elements.

7.3.1 Heat Transfer Modelling

Preliminary temperature profiles through the slab depth were determined by using methods developed by Petterson and Karpas. These methods involved solving the general conduction equation for one-dimensional thermal conduction which is expressed as:

$$c\gamma\frac{\partial v}{\partial t}=\frac{\partial}{\partial x}\left(\lambda_x\frac{\partial T}{\partial x}\right) \qquad 7.1$$

where: c = specific heat capacity — T= temperature

γ = density — t= time

λ_x = thermal conductivity — x = coordinate position

The slab is divided into a number layers and each layer has a thickness Δx_i (see Figure 7.7). Over a time interval Δt, the temperatures for each layer can be determined using the following equations derived by Petterson : The thickness of the layer is related to density of the material and the maximum layer thickness is limited to 30mm. The time interval is calculated by:

$$\Delta t \le \frac{c\gamma\Delta x_n^2}{2\lambda} \qquad 7.2$$

The temperature of the external layer exposed to fire is calculated as:

$$\Delta x_1 c(x,T)\gamma\frac{\Delta T_1}{\Delta t}=\frac{1}{\left(\frac{1}{\alpha(T)}+\frac{\Delta x_1}{2\lambda(x,T)}\right)}(T_i-T_1)-\frac{1}{\left(\frac{\Delta x_1}{2\lambda(x,T)}+\frac{\Delta x_2}{2\lambda(x,T)}\right)}(T_1-T_2) \qquad 7.3$$

where: Δx_1 = Thickness of inner layer which is exposed to fire (m)

$c(x,T)$ = Specific heat capacity at section x_1 at temperature υ (J/kg°C)

γ = Density of the section x (kg/m^3)

T_i = Gas temperature in the fire compartment (°C)

$T_{1,2}$ = Temperature in centre of inner layers 1 and 2

$\alpha(T)$ = Heat transfer coefficient at surface exposed to fire (W/m^2 °C)

$\lambda(x,T)$ = Thermal conductivity of section x at the temperature T (W/m^2 °C)

The temperature of the internal layers is calculated as:

$$\Delta x_k c(x,T)\gamma\frac{\Delta T_k}{\Delta t}=\frac{1}{\left(\frac{\Delta x_{k-1}}{2\lambda(x,T)}+\frac{\Delta x_k}{2\lambda(x,T)}\right)}(T_{k-1}-T_k)-\frac{1}{\left(\frac{\Delta x_k}{2\lambda(x,T)}+\frac{\Delta x_{k+1}}{2\lambda(x,T)}\right)}(T_k-T_{k+1}) \qquad 7.4$$

where: Δx_k = Thickness of internal layer k (m)

The temperature of the external layer exposed to outside air is calculated as:

$$\Delta x_n c(x,T)\gamma\frac{\Delta T_n}{\Delta t}=\frac{1}{\left(\frac{\Delta x_{n-1}}{2\lambda(x,T)}+\frac{\Delta x_n}{2\lambda(x,T)}\right)}(T_{n-1}-T_n)-\frac{1}{\left(\frac{\Delta x_1}{2\lambda(x,T)}+\frac{\Delta x_2}{\alpha_o(T)}\right)}(T_n-T_o) \qquad 7.5$$

where: Δx_n = Thickness of last layer (m)

T_o = Temperature of outside layer (°C)

α_o = Heat transfer coefficient at the outer surface (W/m^2 °C)

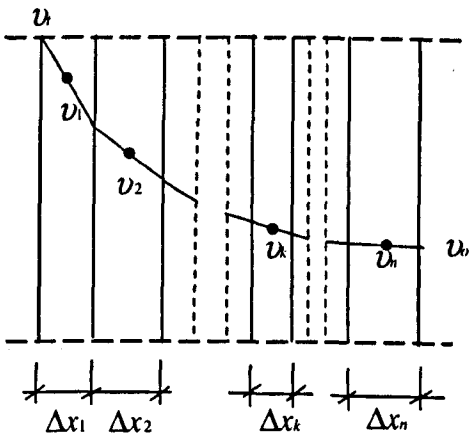

Figure 7.7: Temperature distribution through the cross section of an element

The equations presented above [7.1-7.5] calculate the temperatures per unit of time for each layer of the slab thickness. The temperature distributions at the exteriors to the slab are determined by imposing boundary conditions. These boundary conditions are defined by using appropriate heat transfer coefficients at the interface between the surface and the external air temperature. The heat transfer coefficient for the boundary exposed to the fire contains two parts: radiation component and a convective component [7.6].

$$\alpha_i = \alpha_r + \alpha_k \qquad 7.6$$

The radiation component is the dominant mode of heat transfer at high temperatures and the convective component is simplified to a constant.

The heat transfer coefficient at the inner surface is calculated by:

$$\alpha_i = \frac{5.77\varepsilon}{T_f - T_i}\left[\left(\frac{T_f + 273}{100}\right)^4 - \left(\frac{T_i + 273}{100}\right)^4\right] + 23 \qquad 7.7$$

where: ε = resultant emissivity

The heat transfer coefficient at the outer surface is expressed as:

$$\alpha_u = 8.7 + 0.033T_u$$

where: T_u = Temperature of outside air (°C)

The prediction of temperatures through the depth of a concrete slab is complex due to the thermal properties and water content of the concrete. Further temperature distributions were performed using the differential method by Karpas. These calculations are based on the simplified one dimensional heat conduction equation [7.1]. The boundary conditions

are defined by the temperature of the fire and the external air temperature. The heat transfer coefficient equation for the exposed and not exposed surface of the concrete differ slightly from that of Petterson equations.

The heat transfer coefficients derived by Karpas are:

For the surface exposed to the fire is calculated as:

$$\alpha_i = \frac{3{,}75}{T_t - T_i} \cdot \left[\frac{(T_t + 273)^4}{100^4} - \frac{(T_i + 273)^4}{100^4} \right] + 16.7 \qquad 7.8$$

For the surface not exposed to the fire is calculated as:

$$\alpha_i = \frac{4.64}{T_t - T_i} \cdot \left[\frac{(T_t + 273)^4}{100^4} - \frac{(T_i + 273)^4}{100^4} \right] + 11.4 \qquad 7.9$$

The temperature of the surface layer is calculated as

$$T_{t+1} = \frac{2\alpha\lambda_1\Delta t}{\Delta x_1 c_1 \gamma_1 (\alpha\Delta x_1 + \lambda_1)} T_t + \left(1 - \frac{2\lambda_1\Delta t}{\Delta x_1^2 c_1 \gamma_1}\right) T_{1,t} + \frac{2\lambda_1^2 \Delta t}{\Delta x_1^2 c_1 \gamma_1 (\alpha\Delta x_1 + \lambda_1)} T_{2,t} \qquad 7.10$$

where:

$T_{1,t}$ and $T_{2,t}$ = The temperatures of boundary layers 1 and 2.

The temperature calculations for the inner layers of the slab take into consideration the evaporation of water and moisture content of the concrete [7.11]. The temperature increment [7.12] is expressed as the amount of heat necessary to evaporate the water.

$$T_{m,t+1} = \frac{\lambda_1\Delta t}{c_1\gamma_1\Delta x_1^2} T_{m-1,t} + \left(1 - 2\frac{\lambda_1\Delta t}{c_1\gamma_1\Delta x_1^2}\right) T_{m,t} + \frac{\lambda_1\Delta t}{c_1\gamma_1\Delta x_1^2} T_{m+1,t} \qquad 7.11$$

Where: $T_{m,t+1}$ = The temperatures of the inner layers.

$$\Delta T_m = \frac{\overline{E}}{100} 2{,}26.10^6 \frac{v}{100.c} \qquad 7.12$$

Where: ΔT_m = The temperature increment

$\overline{E}$ = The evaporating water (%), taken as 40%

v = The moisture content

$2.26.10^6$ = The heat required for the evaporation of water

7.3.2 Development of a Slab Model to Determine Temperature Distributions

The calculated average fire temperature curve from Figure 7.6(b), based on the atmosphere temperatures measured within the fire compartment, was used to carry out a two-dimensional thermal analysis of the composite slab. The thermal analysis was undertaken using Fire Performance of Reinforced Concrete Building Components-Thermal (FPRCBC-T) software. The cross section was modelled using quadrilateral finite elements, Figure 7.8.

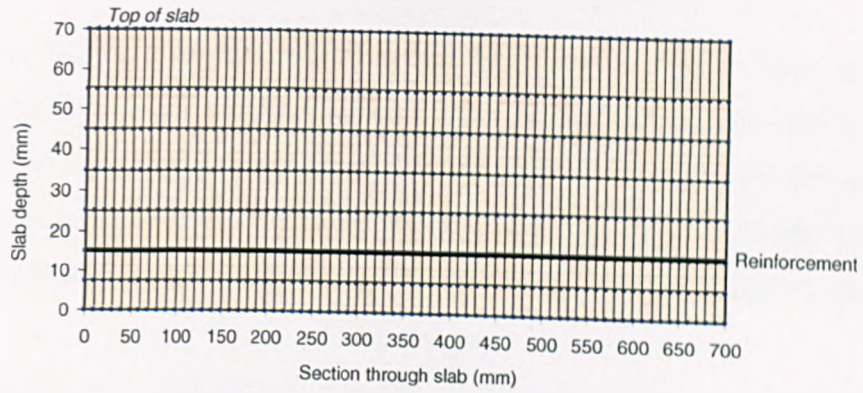

Figure 7.8: Finite element mesh for 2-D thermal analysis (not to scale)

The temperature distributions produced by this thermal model were validated against the temperature distributions measured by thermocouples embedded in the slab. The total nominal thickness of the composite slabs in the test building was 130mm, with a 70mm upper continuous portion. The temperatures were measured at different depths through the slab thickness at various locations for both the 70mm (trough) and 130mm (rib) sections (Figure 7. 9(a)).

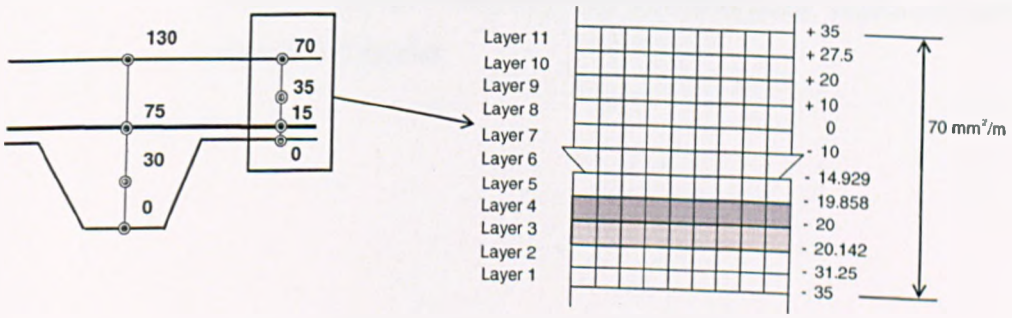

(a) (b)

Figure 7.9: (a) Position of thermocouples; and (b) Temperatures layers through the cross section.

The assumptions made for the thermal analysis were as follows:

- The average compartment temperatures of Fig 7.6(b) were assumed to apply to the whole of the fire compartment.
- The slab was assumed to have 3% water content.
- The Eurocode 4 thermal characteristics for lightweight concrete were used.
- The thermal analysis was carried out on the upper 70mm continuous portion of the slab. This was subdivided into 7 temperature layers for modelling in FPRCBC-T as shown in Figure 7.8, extending to 11 layers by interpolation Figure 7.9.

The measured slab temperatures could not themselves be used as input data for the structural modelling, as the thermocouples were destroyed during the later stages of the test, so reliance had to be placed on an accurate thermal model. The predictions from the thermal analysis were compared with the experimental results in the earlier stages of the fire and the comparisons were used to tune the input parameters to obtain the best possible agreement.

Figure 7.10 shows the comparative study and the results of three cases modelled which were as follows:

1. Case 1: The concrete was assumed to have no water content.
2. Case 2: A water content of 3% was chosen, this was based on previous studies at Cardington.
3. Case 3: The radiation view factor for horizontal surfaces was reduced from a default 1 to 0.75. They were reduced as the temperatures were measured across the shorter section of the slab and some shadowing from the ribs would be expected.

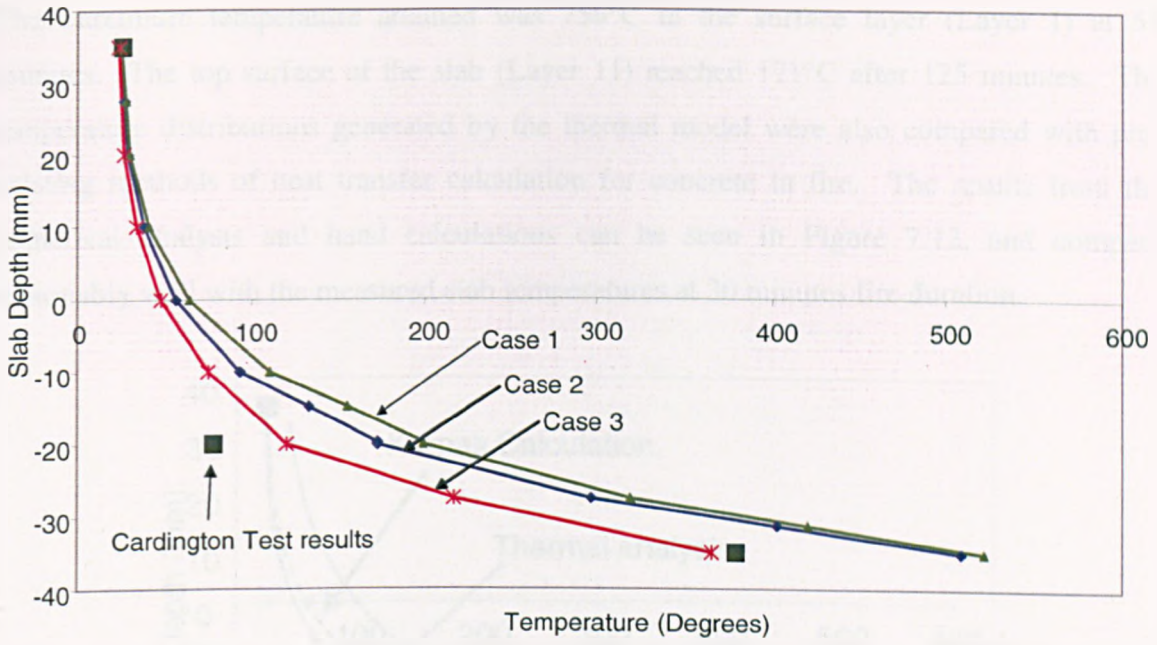

Figure 7.10: Comparative study between Cardington and the thermal analysis, at 30 minutes fire duration.

Figure 7.11 displays the results from the thermal analysis at each of the 11 layers across the 70mm slab, subject to the fire curve of Figure 7. 6(b).

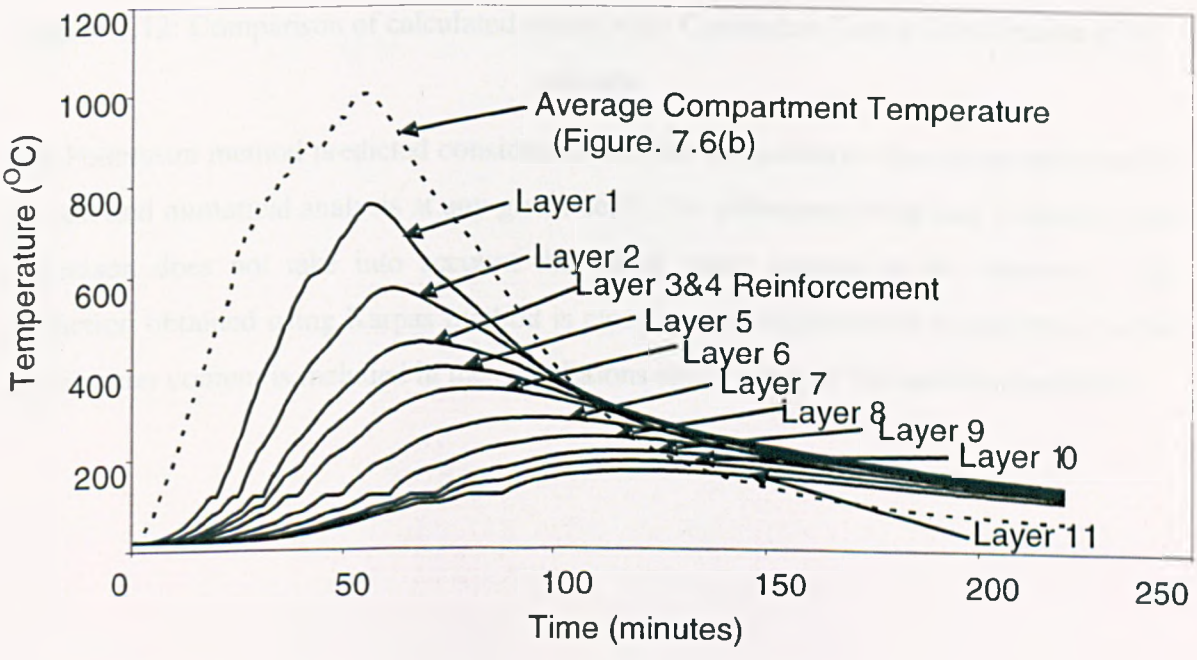

Figure 7.11: Calculated temperature distribution through depth of slab

The maximum temperature attained was 756°C in the surface layer (Layer 1) at 57 minutes. The top surface of the slab (Layer 11) reached 171°C after 125 minutes. The temperature distributions generated by the thermal model were also compared with pre-existing methods of heat transfer calculation for concrete in fire. The results from the numerical analysis and hand calculations can be seen in Figure 7.12, and compare reasonably well with the measured slab temperatures at 30 minutes fire duration.

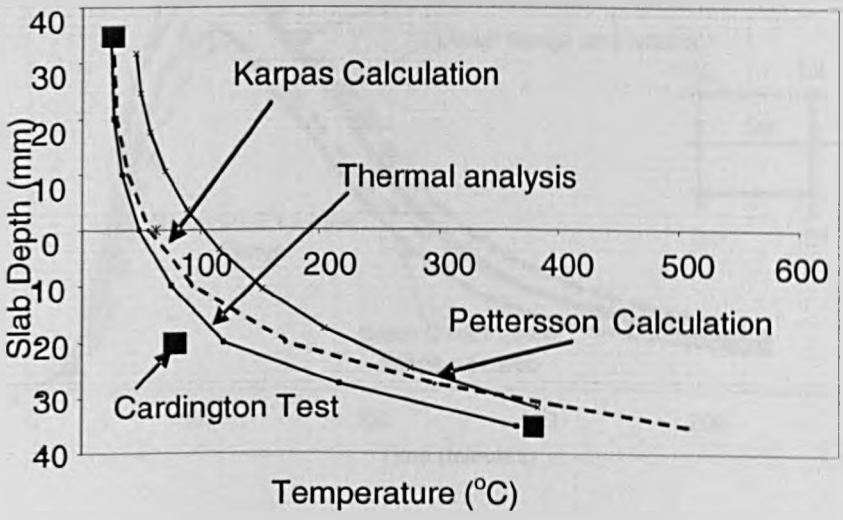

Figure 7.12: Comparison of calculated results with Cardington Test at fire duration of 30 minutes.

The Pettersson method predicted considerably higher temperatures than those measured in the test and numerical analysis at any given depth, the difference being due to the fact that Pettersson does not take into account the initial water content of the concrete. The prediction obtained using Karpas method is closer to the experimental results because the initial water content is included in the calculations and a value of 3% has been assumed.

7.3.2 Steel Downstand Beams

The temperatures of the 305x165x40UB and 357x171x51UB secondary beams were recorded during the test, and the results are presented in Figure 7.13.

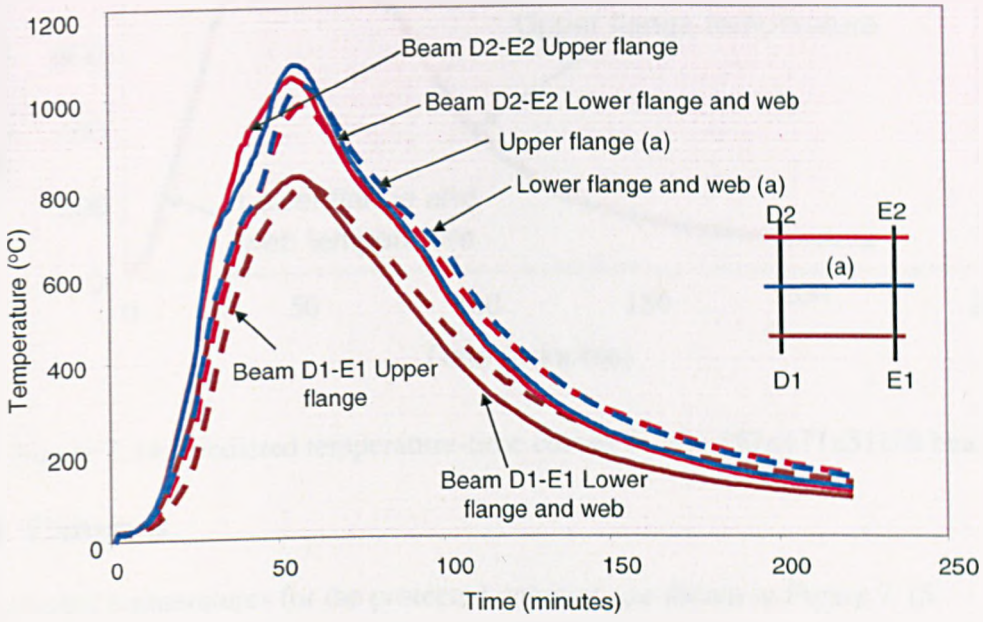

Figure 7.13: Measured temperature distribution for the edge beam (D1-E1) and secondary beams (D2-E2 & (a)).

Temperatures were recorded at mid-span of the beams on the upper flange, web, and bottom flange. The marked difference in temperature distribution between the internal secondary and edge beams is shown in the Figure 7.13. The maximum recorded temperature of 1072°C was attained after 50 minutes in the lower flange and web of internal beam D2-E2.

Unfortunately, no steel temperatures were recorded in the test for the 357x171x51UB primary beams. The temperature distributions for the flanges and webs of these beams were calculated using the iterative procedure for heat transfer set out in Eurocode 3 for unprotected beams. The temperature-time curves for the unprotected 357x171x51UB beams are shown in Figure 7.14. The maximum temperature of 1000°C was attained at approximately 52 minutes.

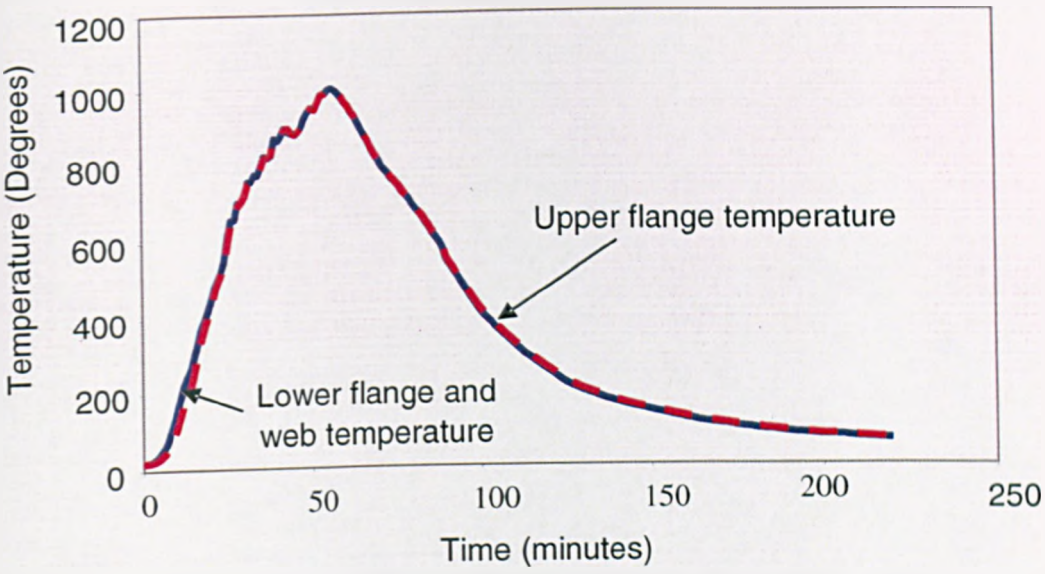

Figure 7.14: Predicted temperature-time curves for the 357x171x51UB beams

7.3.3 Columns

The recorded temperatures for the protected columns are shown in Figure 7.15.

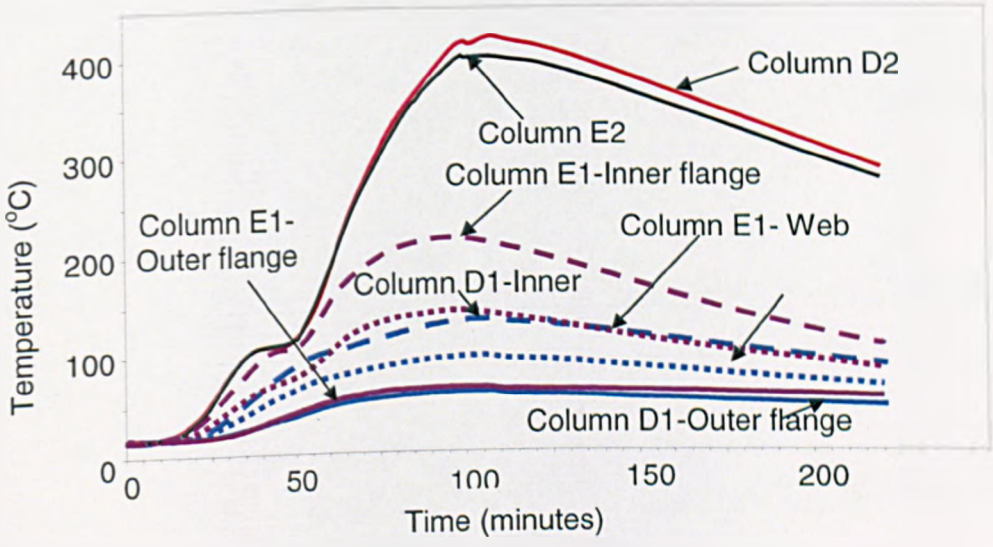

Figure 7.15: Measured temperature of columns in Cardington Test

Temperatures were recorded in the inner flanges, webs, and outer flanges. The maximum recorded steel temperature of 420°C occurred after 100 minutes of the fire in column D2. The recorded temperatures for the two edge columns show a logical variation between the inner and outer flanges, but for the two inner columns there was little variation in

temperatures and an average value was chosen. The columns were protected with a nominal 15mm thickness of Cafco300 vermiculite-cement spray.

7.4 Structural Behaviour

7.4.1 Observed Structural Behaviour

The maximum recorded slab displacement was approximately 1000mm, in the central zone of the compartment. Unfortunately, the actual slab displacement exceeded the allowable travel on the gauges, but has been estimated to have been approximately 1200mm [67].

It was observed, after the fire had finished and the structure had cooled, that the composite slab had extensive cracking in both the longitudinal and transverse directions. A plan of the visible cracking on the upper surface of the slab is shown in Figure 7.16. From this detail, it can be seen that the main longitudinal crack is off-centre of the bay of the column grid.

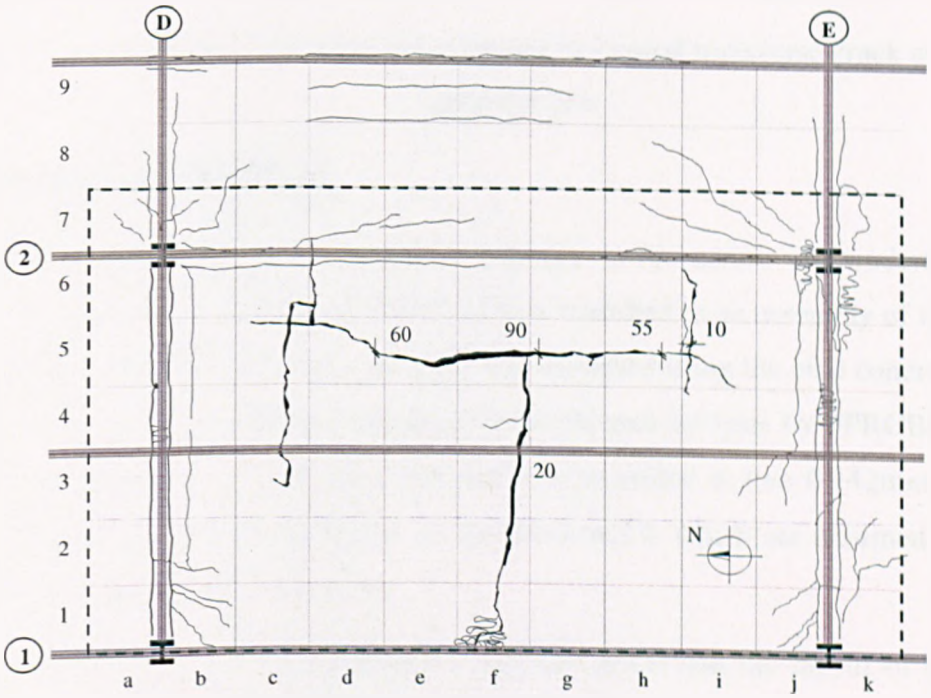

Figure 7.16: Detail of cracking of composite slab after fire test

The main longitudinal and transverse cracks penetrated the full depth of the slab, as shown in Figures 7.17(a) and (b), and the longitudinal crack was 90mm wide near to their intersection. This extent of rupture is unusual without a complete failure of the slab, but it can be seen in Figure 7.17(a) that the ends of the reinforcing bars in two sheets of mesh had slipped relative to one another across the crack. This was clearly due to inadequate

overlap of the adjacent sheets of mesh during construction of the building, so that only "fingers" of undeformed bars were overlapping, and that the anchorage which might have been achieved by overlapping the welds to the orthogonal reinforcement was not achieved. This situation would also have dictated the location of the longitudinal crack.

(a) (b)

Figure 7.17: a) Slipping of the reinforcement and b) Central transverse crack at mid-span after fire test

7.4.2 Numerical Modelling

The numerical modelling of the structural response to fire action was undertaken using *Vulcan*. The composite steel-framed building was modelled as an assembly of finite beam-column, spring, and slab elements. The slab was modelled using the nine concrete and two steel reinforcement layers which were used in the thermal analysis by FPRCBC-T, which are shown in Figure 7.11. The reinforcement was modelled as two 0.142mm thick steel layers, aligned with the bar directions, as Layers 3 and 4, which are assumed to be fully bonded to the adjacent concrete layers.

The extent of the structure incorporated within the model and the layout of the detailed finite element mesh are shown in Figures 7.18 and 7.19.

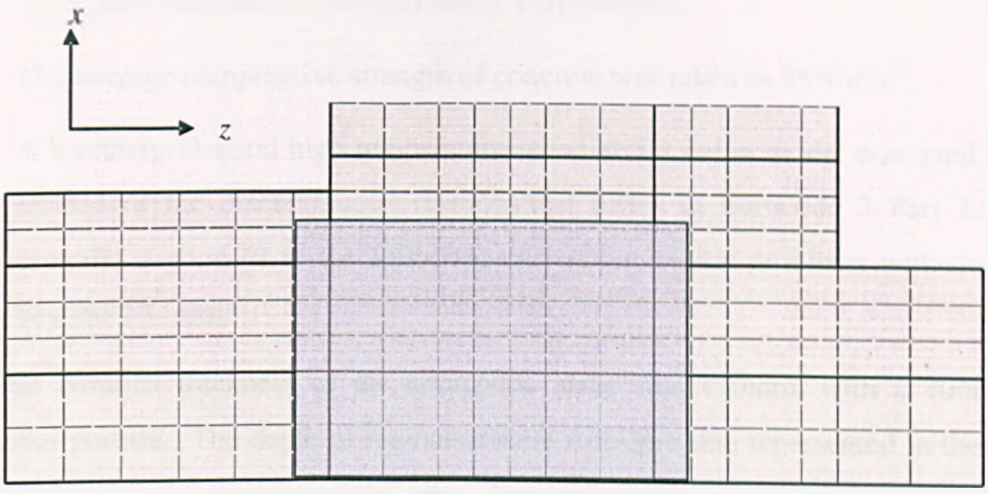

Figure 7.18: Finite element mesh used for floor system in structural analysis of the test.

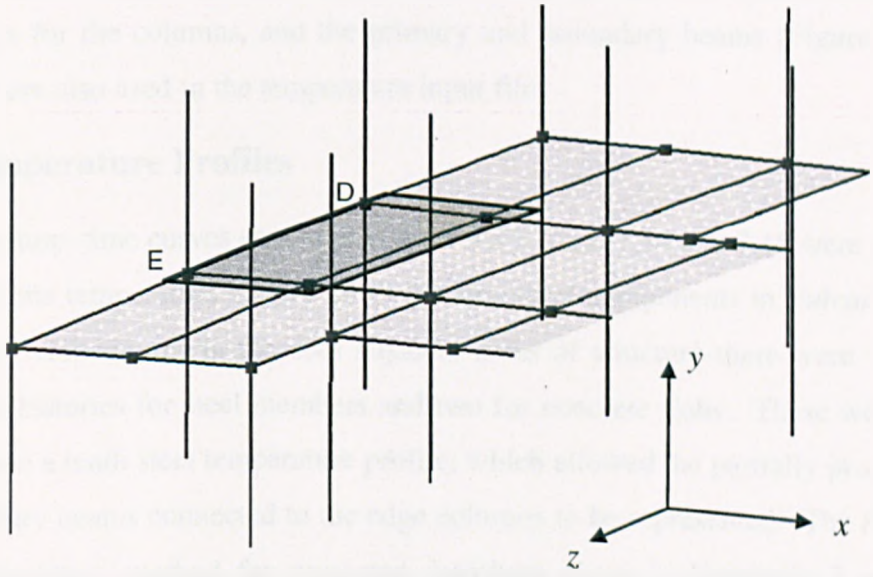

Figure 7.19: Perspective view of sub-frame used for analysis.

A uniform imposed load of 3.19kN/m^2 was applied to the whole floor area above the compartment, giving a total slab load of 6.01kN/m^2 and this was assumed in the modelling. The ambient-temperature material properties used in the modelling, which were based on test values from the original Cardington series wherever these were available, are as follows:

- The yield strength of the steel used in the anti-crack reinforcement mesh was assumed to be 460N/mm^2 ,
- The yield strength of the steel members was 308N/mm^2 for Grade 43 steel (S275) and 390N/mm^2 for Grade 50 steel (S355),

- The elastic modulus of the steel was $2.1 \times 10^5 N/mm^2$,
- The average compressive strength of concrete was taken as $35N/mm^2$,
- A Ramberg-Osgood high-temperature stress-strain curve model was used for steel instead of the discontinuous relationships given in Eurocode 3 Part 1.2. This provides a good fit to the Eurocode curves but avoids problems with the plateau beyond 2% strain.

The total nominal thickness of the composite slabs was 130mm, with a 70mm upper continuous portion. The depth of the continuous isotropic slab represented in the analysis was therefore 70mm, neglecting the ribs. The temperature distributions calculated from the thermal analysis (Figure 7.11) for the thin part of the slab above the troughs in the decking were incorporated into the temperature input file for the slab elements. The temperatures for the columns, and the primary and secondary beams (Figures 7.13, 7.14 and 7.15) were also used in the temperature input file.

7.4.3 Temperature Profiles

The temperature–time curves shown in Figures 7.11, 7.13, 7.14 and 7.15 were used as data to represent the temperature history of all the structural components in *Vulcan*. Including the constant temperatures in the cool adjacent areas of structure there were in total nine temperature histories for steel members and two for concrete slabs. These were extended to incorporate a tenth steel temperature profile, which allowed the partially protected zones of two primary beams connected to the edge columns to be represented. The iterative heat transfer calculation method for protected members given in Eurocode 3 was used to calculate the steel temperatures for the 1m protected lengths of these beams. It was assumed in these thermal calculations that the protection thickness was only 7.5mm, half the thickness applied to the columns. No measurements of the steel temperatures or the thickness of the partial protection on the primary beams had been taken, but observations suggest that a tapering protection thickness was applied by light spraying. Figure 7.20 shows how steel temperature profiles were assigned to specific structural members.

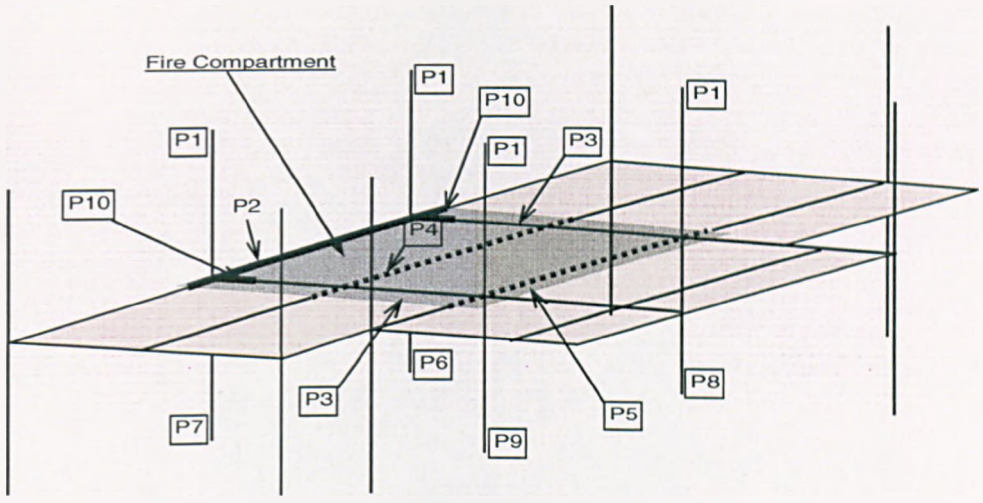

Figure 7.20: Temperature profiles used in modelling members of the sub-frame (Profile P1 is uniform 20°C; used for all steel outside the fire compartment).

7.4.4 Cases Studied

Six cases have been modelled, and displacement patterns compared with the test, given the large number of displacement measurements which were recorded at the grid of locations shown on Figure 7.21.

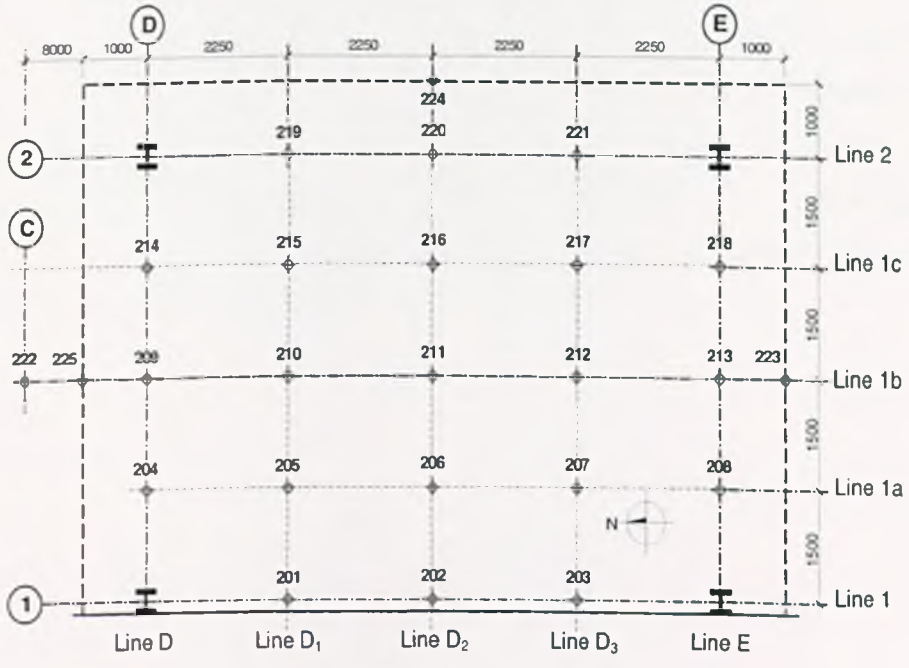

Figure 7.21: Positions of displacement gauges.

The background and rationale for each case is given below, but their essential differences are shown in Table 7.3.

Conditions	Case (*Vulcan* #)					
	1	2	3	4	5	6
Wind-post nodes unrestrained vertically.	✓		✓			
No vertical displacement of wind-post nodes.		✓		✓		
6m primary beam unprotected.	✓	✓				
45mm vertical movement allowed by non-linear spring at wind-posts.					✓	✓
6m primary beam has edge 1m protected.			✓	✓	✓	✓
Reinforcement layer strength reduced to 33% across longitudinal crack.						✓

Table 7.3: Conditions for the *Vulcan* analyses of the test.

In the test itself, wind-posts were attached to the edge beam at two locations. These are glazing support ties which are continuous along the face of the building and are bolted to each edge beam at 75mm slots. These were not modelled explicitly in this study, because the extra complication of the model was not justified by the potential benefits, given also that little data about the wind-post connections or their performance was available. In these cases their presence or absence were modelled by imposing boundary conditions on the beam nodes to which the wind-posts were attached. In *Vulcan* 1, the nodes representing the wind-posts were not restrained, but left free to move vertically. In *Vulcan* 2 these nodes were completely restrained against vertical movement. Both sets of results are shown in Figures 7.24-7.26.

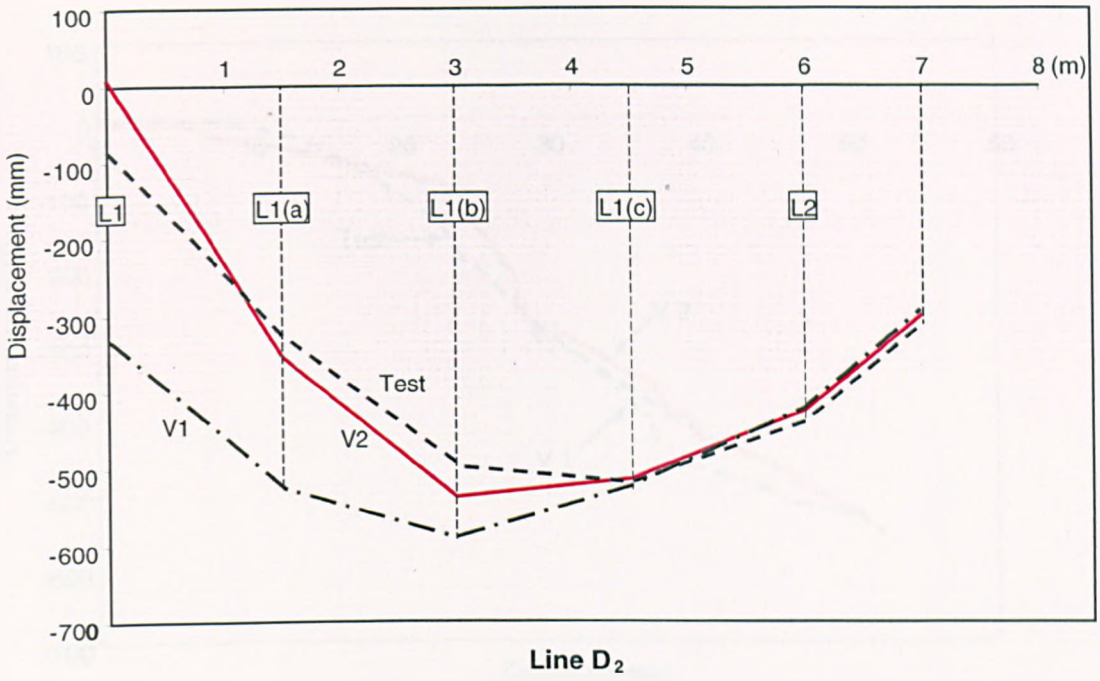

Figure 7.21: Transverse cross-section displacements on Line D_2 for *Vulcan* 1, *Vulcan* 2 and test at 49 minutes fire duration.

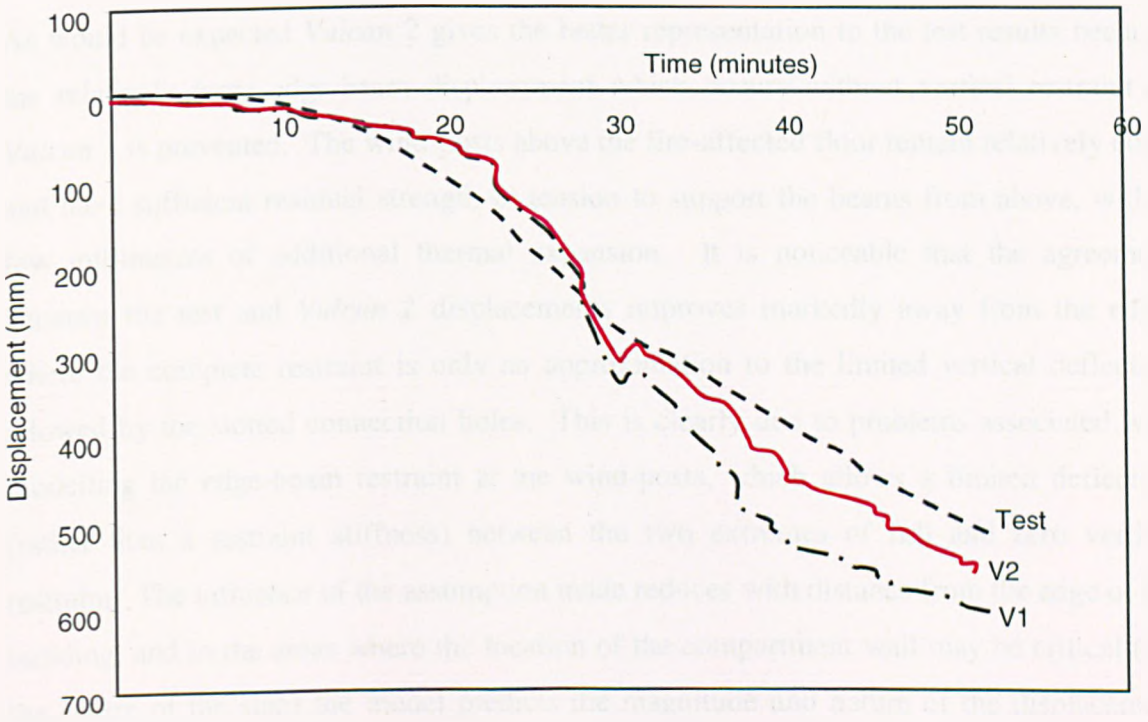

Figure 7.22: Comparison of displacements at node 211 between *Vulcan* 1, *Vulcan* 2 and test.

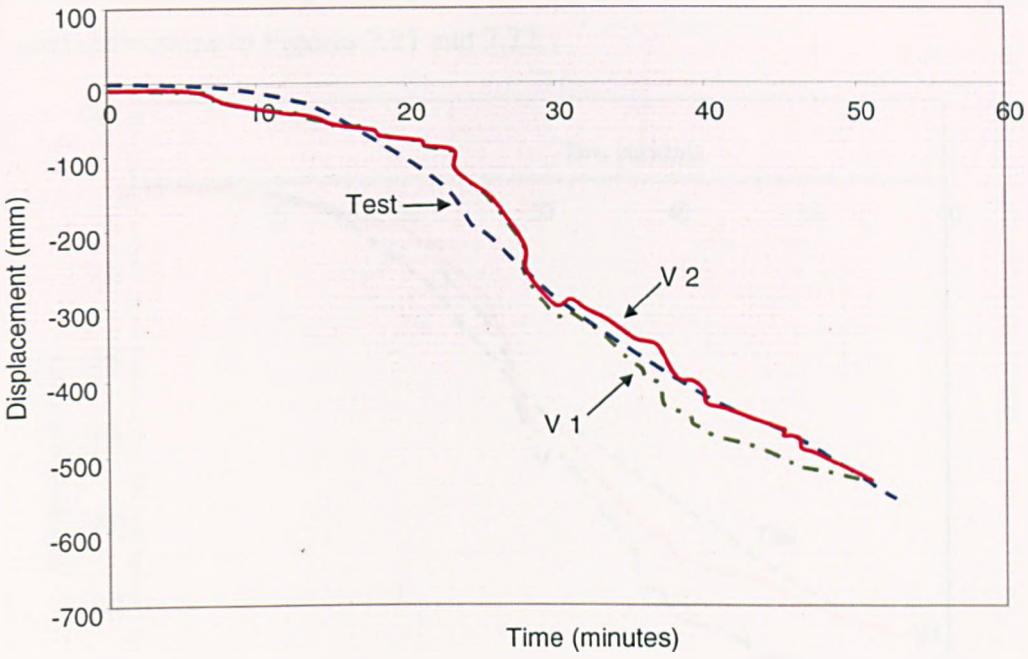

Figure 7.23: Comparison of displacements at node 216 between *Vulcan* 1, *Vulcan* 2 and test.

As would be expected *Vulcan* 2 gives the better representation to the test results because the relatively large edge-beam displacement which occurs without vertical restraint in *Vulcan* 1 is prevented. The wind-posts above the fire-affected floor remain relatively cool, and have sufficient residual strength in tension to support the beams from above, with a few millimetres of additional thermal expansion. It is noticeable that the agreement between the test and *Vulcan* 2 displacements improves markedly away from the edge, where the complete restraint is only an approximation to the limited vertical deflection allowed by the slotted connection holes. This is clearly due to problems associated with modelling the edge-beam restraint at the wind-posts, which allows a limited deflection (rather than a restraint stiffness) between the two extremes of full and zero vertical restraint. The influence of the assumption made reduces with distance from the edge of the building, and in the areas where the location of the compartment wall may be critical (i.e. the centre of the slab) the model predicts the magnitude and nature of the displacement with considerable accuracy.

As has been noted previously, beams D and E were partially spray-protected over a one-metre length from the connection with the edge beam using CAFCO 300. Cases *Vulcan* 3 and *Vulcan* 4 take into account the effect of the partial protection on the primary beams, as variants of cases *Vulcan* 1 and *Vulcan* 2 respectively. The results of the analyses *Vulcan* 3

and 4 are compared with *Vulcan* cases 1, 2 and the test results in terms of the mid-slab overall deflections in Figures 7.21 and 7.22.

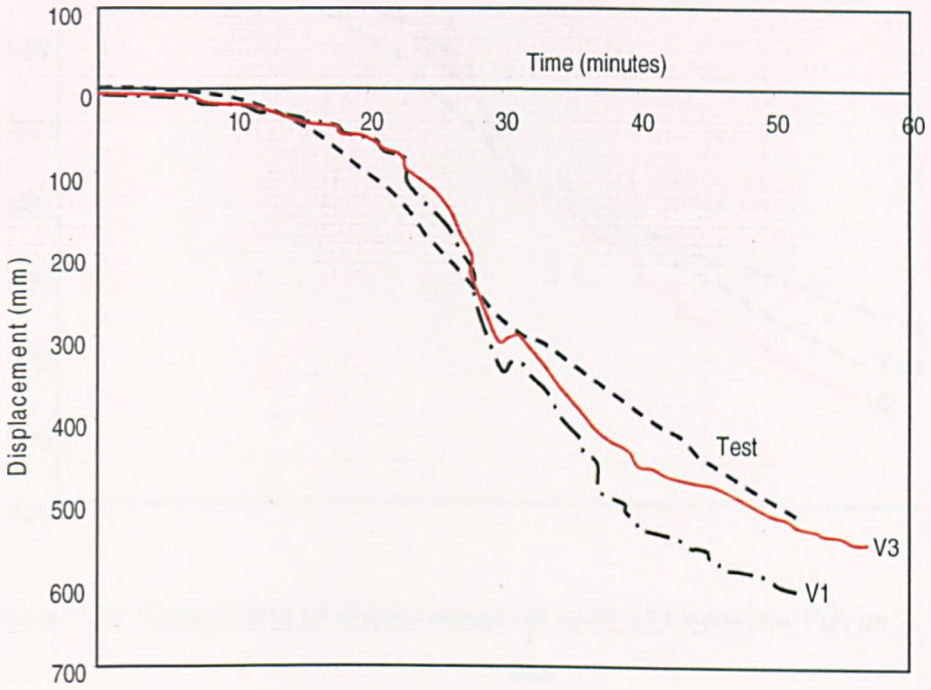

Figure 7.24: Comparison of displacements at node 211 between *Vulcan* 1, *Vulcan* 3 and test.

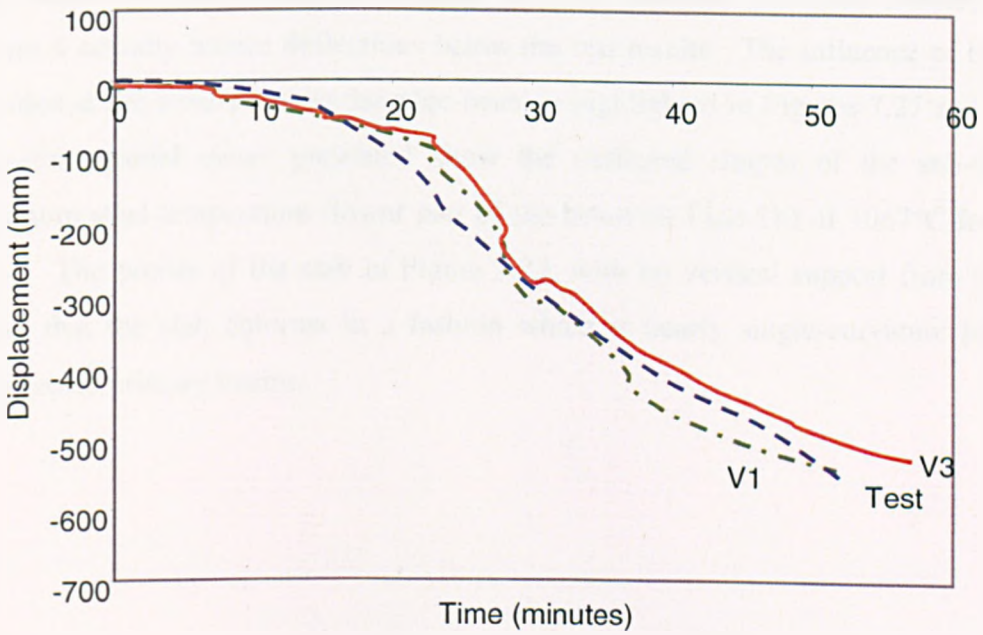

Figure 7.25: Comparison of displacements at node 216 between *Vulcan* 1, *Vulcan* 3 and test.

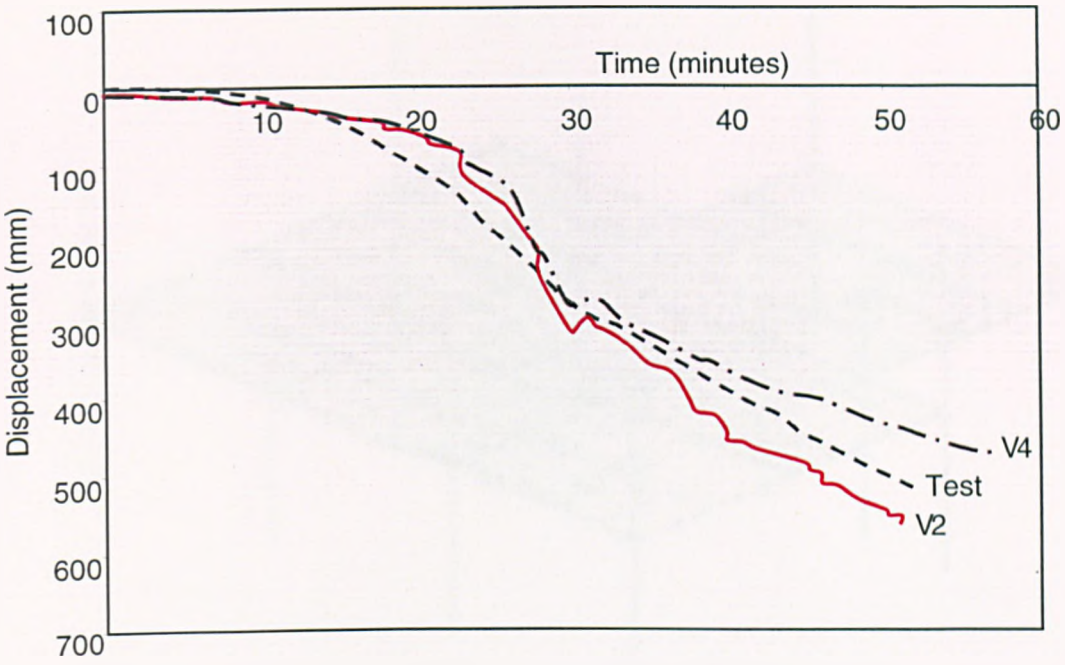

Figure 7.26: Comparison of displacements at node 211 between *Vulcan* 2, *Vulcan* 4 and test.

It can be seen from Figure 7.25 that the partial protection to the primary beams cause considerably lower vertical displacements at any given temperature, and these are brought close to the test results in *Vulcan* 3, without any support from wind-posts. When the wind-posts nodes are fully restrained (Figure 7.26) the partially protected primary beams of *Vulcan* 4 actually reduce deflections below the test results. The influence of the restraint provided at the wind-posts on the edge-beam is highlighted in Figures 7.27 and 7.28. The three-dimensional views presented show the deflected shapes of the sub-frame at a maximum steel temperature (lower part of the beam on Line 1b) of 1067°C for *Vulcan* 3 and 4. The profile of the slab in Figure 7.27, with no vertical support from wind-posts, shows that the slab deforms in a fashion which is nearly single-curvature between the unprotected primary beams.

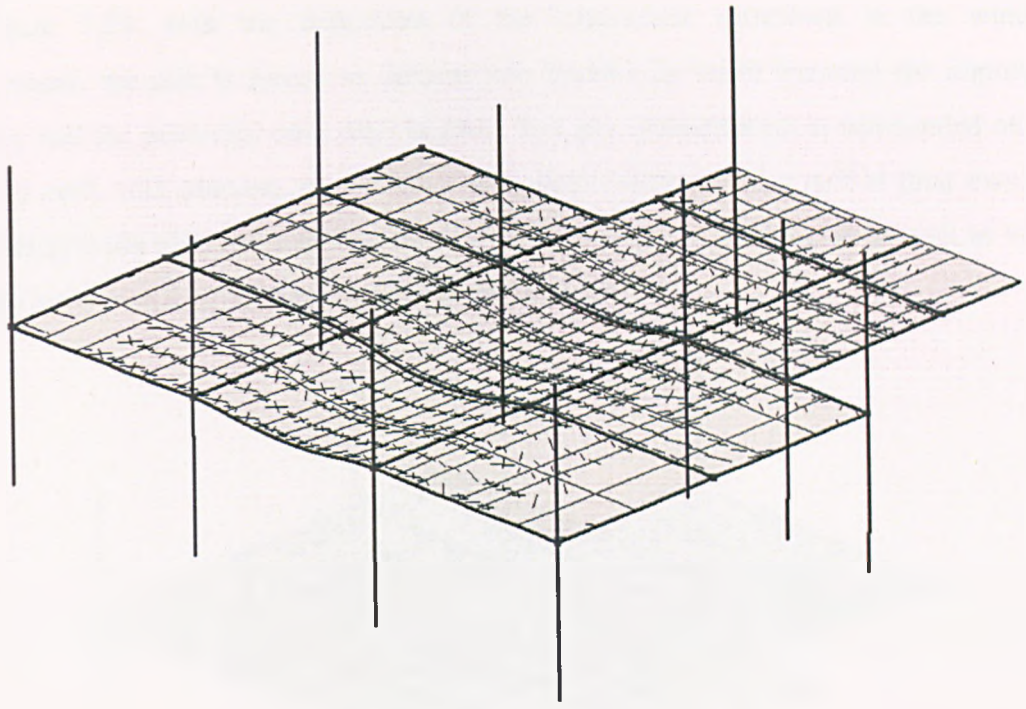

Figure 7.27: Deflection profile of the subframe in *Vulcan* 3 when maximum temperature of beam on Line 1b is 1067°C (52 minutes) (no wind post restraint).

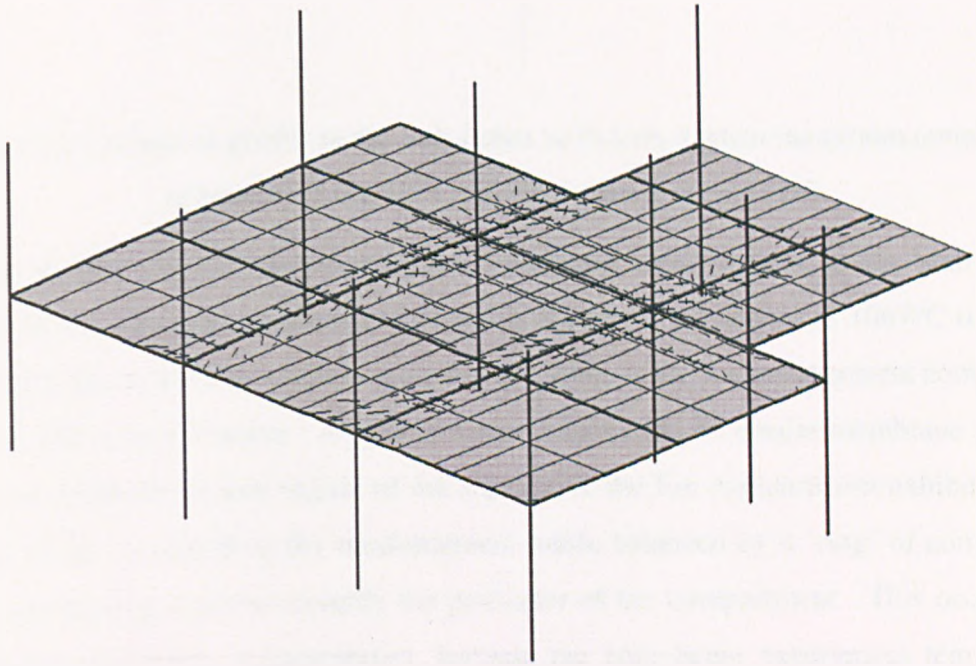

Figure 7.28. Deflection profile of the sub-frame in *Vulcan* 3 when maximum temperature of beam on Line 1b is 605°C (32 minutes) (wind post restraint).

At approximately 30 minutes, cracking starts to develop along the unprotected beams, Figure 7.28. This cracking is shown also in Figure 7.25 at approximately 32 minutes there is a marked jump in the deflection which corresponds to the cracking profile at this time.

In Figure 7.29, with the deflection of the edge-beam restrained at the wind-post connections, the slab is forced to deform into double-curvature between the unprotected primary and the relatively cool edge beams. The fire compartment is surrounded on three sides by cool, stiff structure, in particular slab areas which are very stiff in their own plane and thus provide high restraint to pull-in of the edges of the heated slab as well as vertical support similar to their ambient-temperature behaviour.

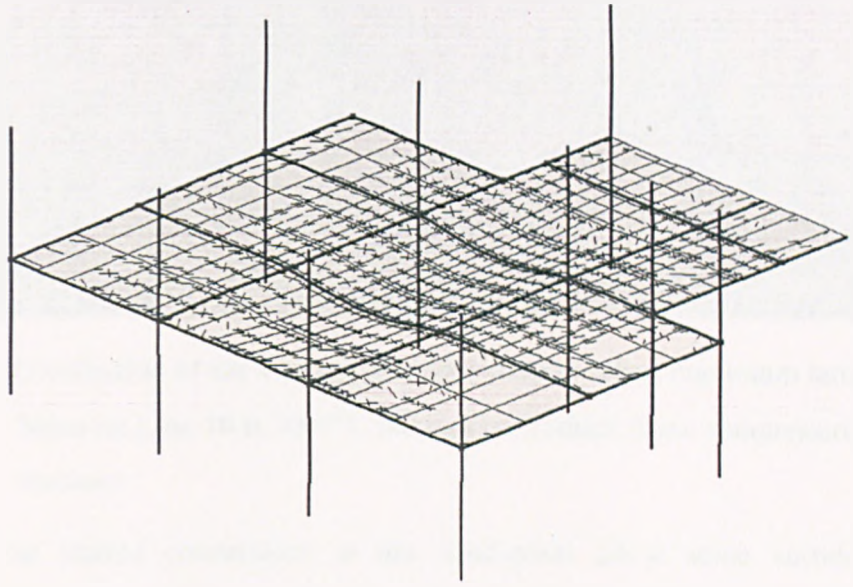

Figure 7.29: Deflection profile of the sub-frame in *Vulcan* 4 when maximum temperature of beam on Line 1b is 1067°C (wind post restraint).

In order to illustrate development of the membrane stress pattern in the slab at high deflections the principal membrane tractions in *Vulcan* 3 are shown at 1067°C on Figure 7.30, which shows the slab surface in plan view. Blue, thick vectors represent compression and thin, red vectors tension. A typical stress distribution of tensile membrane action is shown, in which the central region of the slab above the fire compartment exhibits biaxial tension, which is carried by the reinforcement mesh, balanced by a 'ring' of compression in the surrounding concrete towards the perimeter of the compartment. This occurs even though the edge-beam is unprotected, because the edge-beam experiences temperatures about 300°C lower (Figure 7.15) than the exposed unprotected steelwork within the compartment at this point and is therefore able to provide a reasonable degree of support to the edge of the slab.

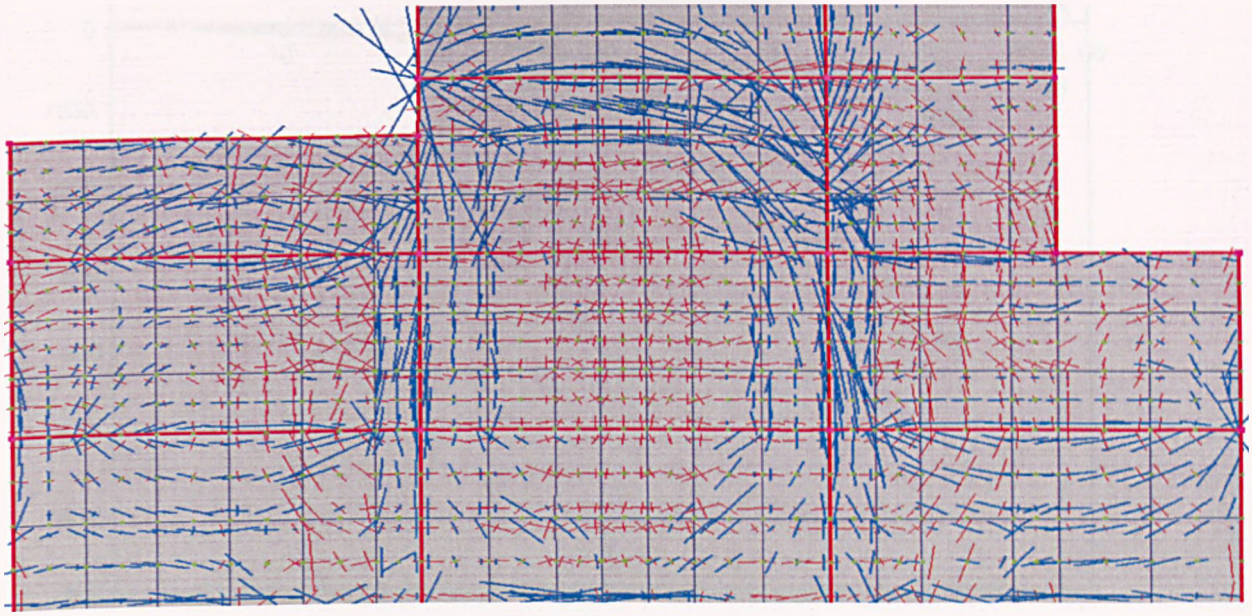

Figure 7.30: Distribution of the average principal stresses when maximum temperature of beam on Line 1b is 1067°C for *Vulcan* 3 (thick line= compression; thin line = tension).

In reality, the slotted connections at the wind-posts allow some vertical movement (between 0 and 75mm, depending on the bolt positions in the slotted holes) before applying restraint, and this needs to be considered in the model. To take some account of this vertical movement at the wind-post nodes, non-linear axial springs are incorporated between the wind-post nodes and rigid supports which allow vertical travel up to 45mm at very low stiffness before applying a high stiffness beyond this deflection which effectively prevents vertical movement. This new case, *Vulcan* 5, includes the partial protection of the primary beams at their ends towards the building edge which was included in *Vulcan* 3 and 4. The vertical movement at the wind-posts is shown in Figure 7.31, which plots the displacement of the edge-beam mid-span node for each of the cases *Vulcan* 1 to 5 and the test.

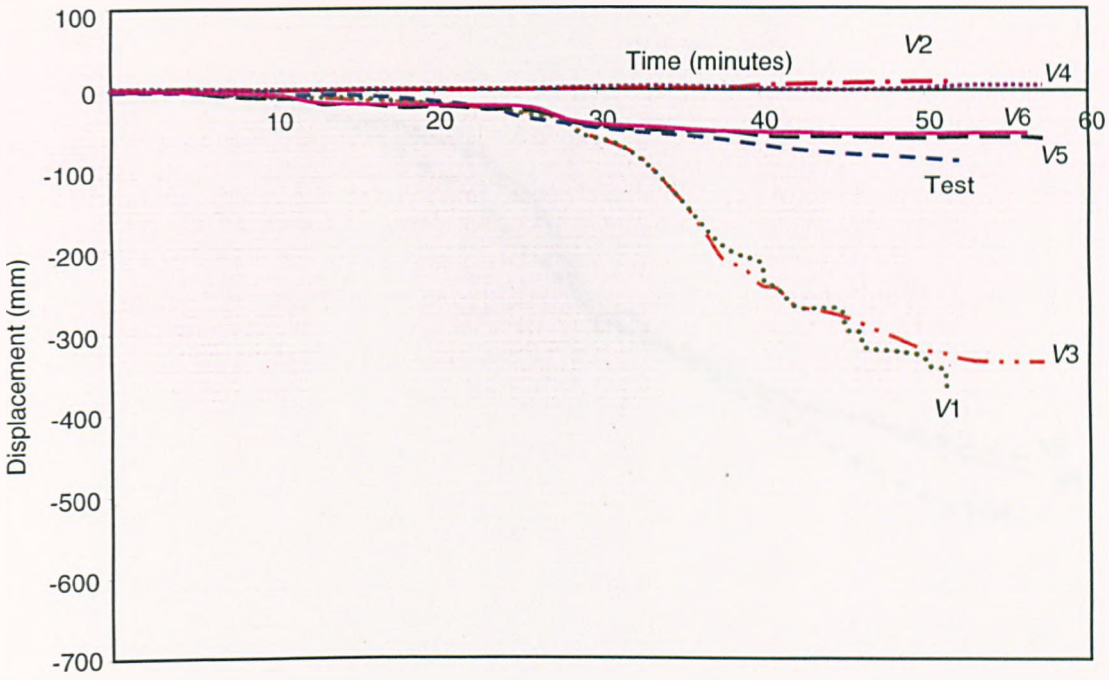

Figure 7.31: Comparison of displacements at edge-beam mid-span node 202 for *Vulcan* cases 1 to 5, 6 and test.

The graph shows that *Vulcan* 5 lies close to the test result, between the extremes given by the earlier cases. Although the accuracy of deflections at the edge beam thus greatly increases, it can be seen from Figure 7.32 that the mid-slab deflection differs little from that of *Vulcan* 4, and inspection of the deflection profile from *Vulcan* 5 in Figure 7.33 shows that it is qualitatively very similar to that shown in Figure 7.29 for *Vulcan* 4 which has full vertical restraint at the wind-posts.

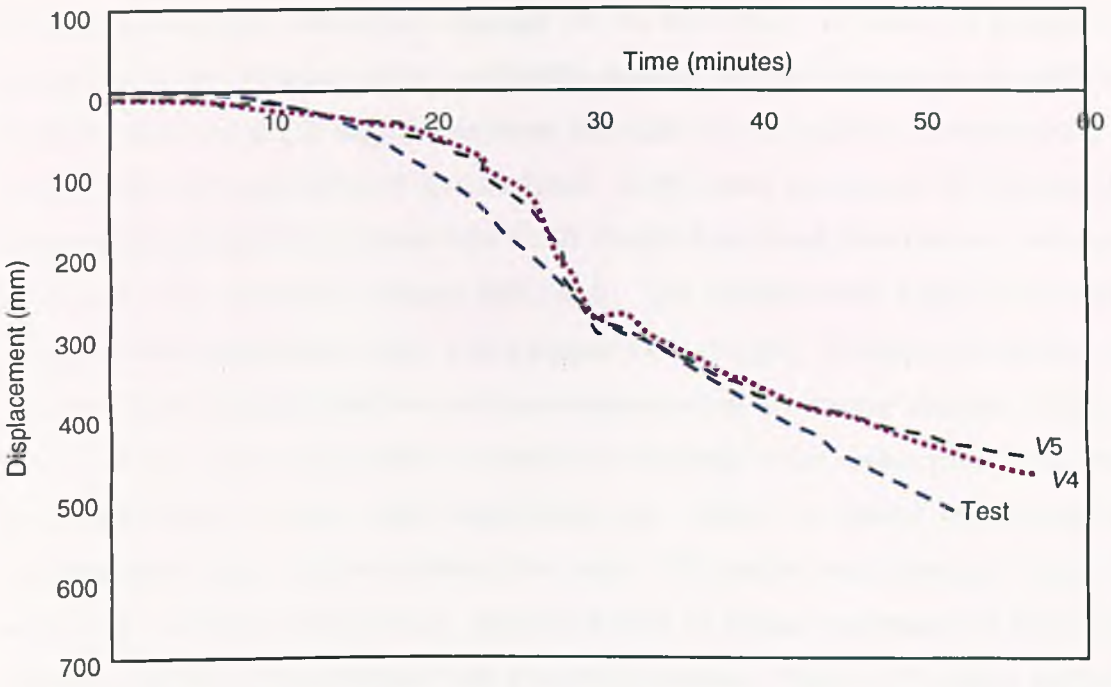

Figure 7.32: Comparison of displacements at node 211 between *Vulcan* 4, *Vulcan* 5 and test.

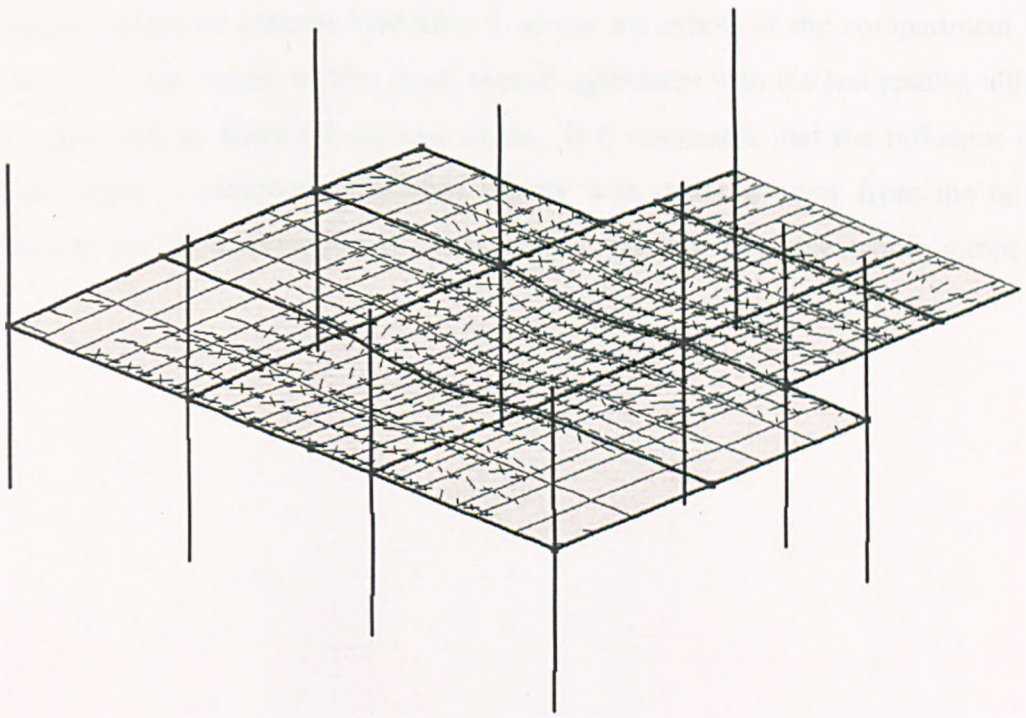

Figure 7.33: Deflection profile when maximum temperature of beam on Line 1b is 1067°C for *Vulcan* 5.

In the test, the major influence in the development of the wide longitudinal crack seems to have been inadequate overlap of sheets of the anti-crack mesh reinforcement leading to de-

bonding locally and subsequent slippage of the bar ends. In order to provide some indication of the influence of this artificially-induced line of weakness in the slab on its structural performance at high temperature, although it is not possible to reproduce it fully in the model, the case *Vulcan* 6 was analysed. In this case, the strength of the mesh layer with uniaxial properties perpendicular to the longitudinal crack direction was reduced by 67% in the slab elements spanning this crack. The reinforcement layer with properties parallel to the longitudinal crack was assigned full strength. A transverse tension crack across the short span of a slab in tensile membrane action is a normal integrity failure end-point, and there was no indication of similar bar slippage in the visible parts of the shorter crack perpendicular to the major longitudinal one. Hence, no similar amendment to the reinforcement layers was made along this crack. The model was based on *Vulcan* 5, in which the wind-post nodes were allowed 45mm of initial movement at low support stiffness and the primary beams were partially protected. Figure 7.31 shows deflections for the first six of the modelled cases compared with the test results at the edge node 202, and Figure 7.34 shows them for the other nodes 206, 211, 216 and 220 on the same line, as the time into the fire increases. These nodes progress from 1.5m from the edge-beam to the secondary beam on column Grid-Line 2 across the centre of the compartment (Line D_2). The results for *Vulcan* 6 show good overall agreement with the test results, although simpler cases such as *Vulcan* 2 are also close. It is noticeable that the influence of the edge-node support conditions diminishes rapidly with distance away from the building edge, making the deflections for all cases cluster together over the whole temperature range.

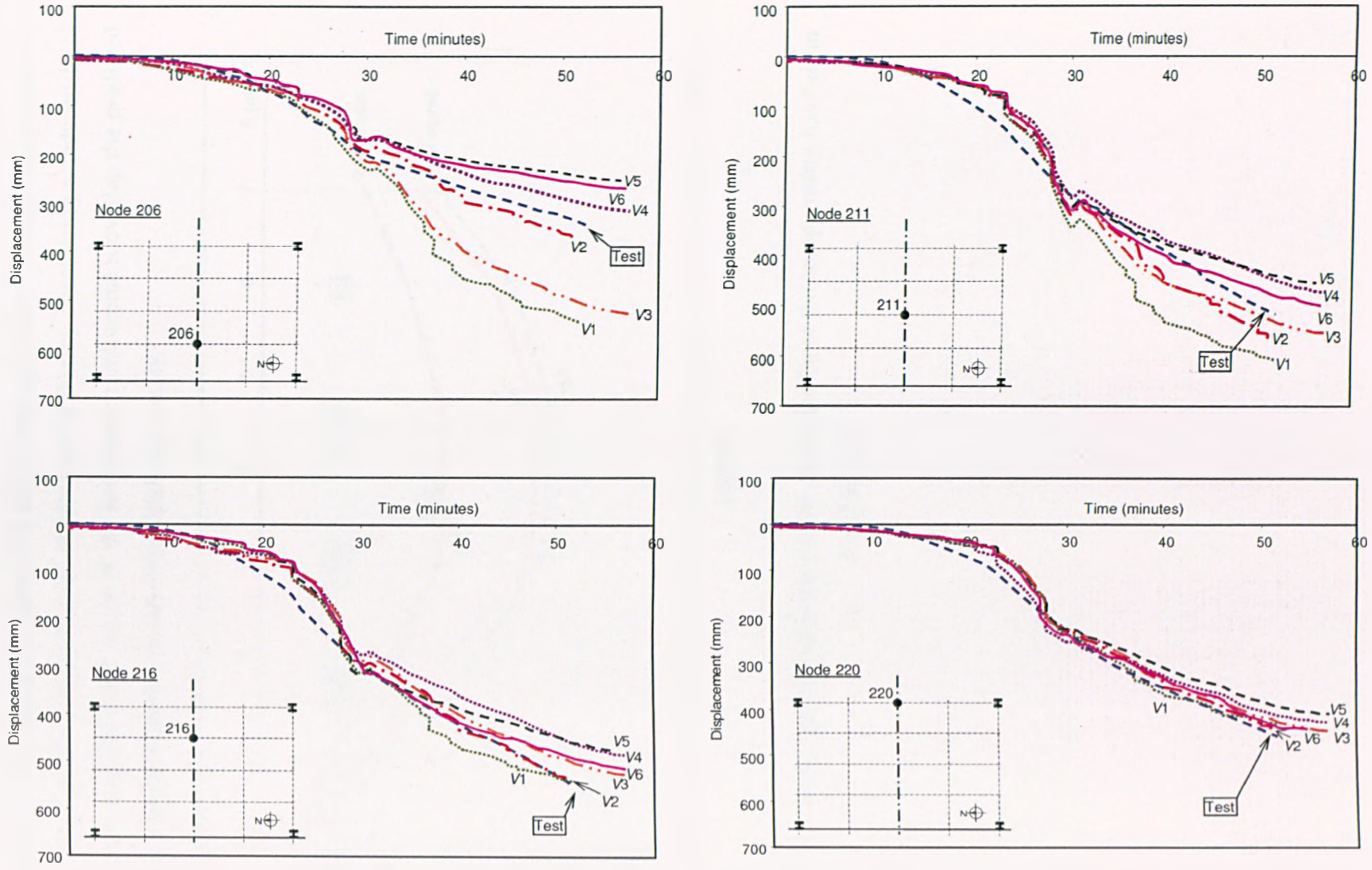

Figure 7.34: Comparison of displacements at nodes 206, 211, 216 and 220 between all *Vulcan* cases and the test .

Considering the case *Vulcan* 6 in Figure 7.34 it is difficult to predict the point at which the reinforcement bond in the region of incomplete overlap is lost and slippage occurs, forming the longitudinal crack and this has not been attempted here. The deflected shapes of the mid-span line D_2 of the slab at 30 and 45 minutes into the fire test are shown in Figures 7.35, 7.36 for *Vulcan* 6 only, demonstrating that by considering a reduced local reinforcement strength in the region of the inadequate reinforcement overlap the predicted deflections represent the test results surprisingly accurately.

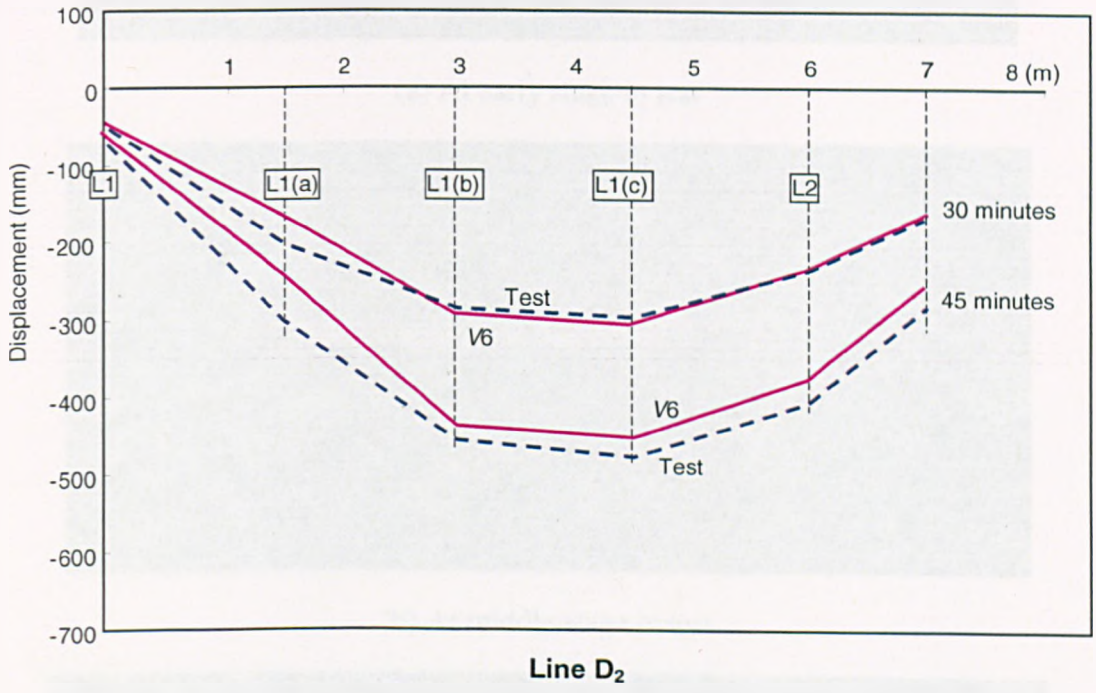

Figure 7.35: Transverse displacement profile along line D_2 of the compartment for *Vulcan* 6 and the test.

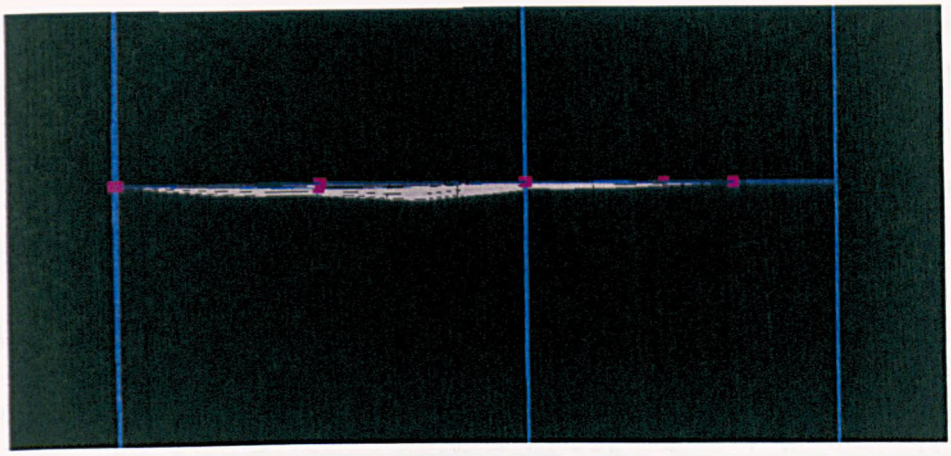

(a) At early stage in test

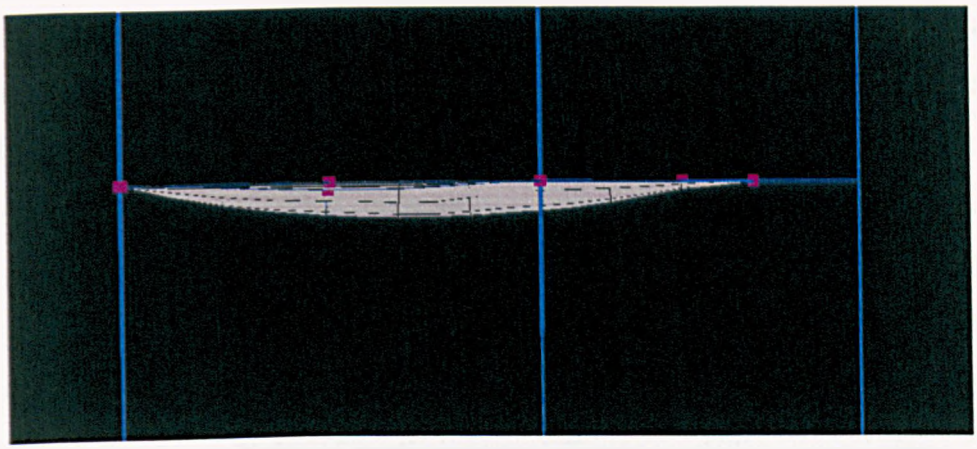

(b) At middle stage in test

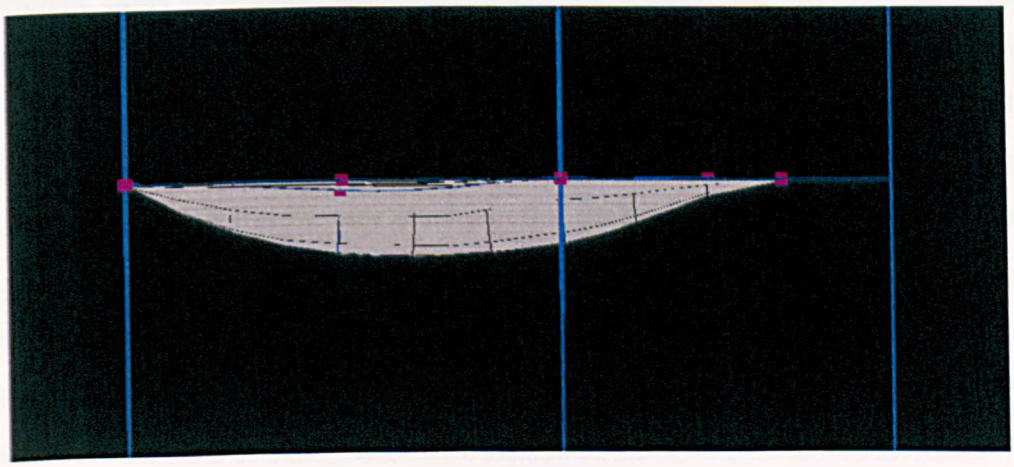

(c) At later stage in test

Figure 7.36: Longitudinal deflection profiles along line D_2 for *Vulcan* case 6.

It is also noticeable that, whereas the maximum displacement on Figure 7.21 occurs at the centre-line of the compartment (node 211) where the unprotected secondary beam is located, the maximum deflection of both *Vulcan* 6 and the test on Figures 7.35 and 7.36

actually occurs at node 216, 4.5m from the edge beam. At 30 minutes *Vulcan* 6 predicts displacements almost identical to the test result, whilst at 45 minutes the prediction is slightly less. This is consistent with the crack occurring suddenly between these two times in the test, as the loss of bond at the overlap occurs, which can not be modelled using the type of global analysis used here.

7.5 Concluding Remarks

The results have been presented from a series of thermal and thermo-structural numerical analyses of Fire Test 7 in a fire compartment of size 11m x 7m including a complete bay of the column grid of the multi-storey composite frame in the BRE Cardington laboratory. The fire compartment was subjected to a fire load of 40kg/m^2, and the slab above the compartment was loaded uniformly with an imposed load of 3.19kN/m^2. The objectives of the analyses were:

- To test the accuracy with which the behaviour can be predicted using the global analysis software *Vulcan*. This software used a relatively coarse grid of geometrically non-linear beam-column and shell elements and concrete constitutive relationships with a smeared cracking assumption.
- To check the sensitivity of predictions to different modelling assumptions.

Six different cases have been analysed. The results show that this type of modelling predicts the deflection behaviour with considerable accuracy, especially considering the uncertainties embodied in representing the biaxial properties of concrete at high temperatures, and using analysis which does not consider the formation of discrete cracks. All the cases modelled follow very much similar deflection patterns; even with boundary assumptions which neglect all edge support provided by the vertical wind-posts are relatively accurate away from the local vicinity of this edge. As the representation of the vertical restraint at these points becomes more realistic, firstly by providing total vertical support, and then by allowing slip at the slotted holes, up to a reasonable estimate of the slip provided, the deflection profile near to the edge becomes progressively more accurate. Accurate thermal modelling of the structure, particularly in this case by obtaining an accurate representation of the temperatures in the over-sprayed 1m zones at the outer ends of the primary beams, has a fairly major effect compared with weakening of the slab at the location of the observed longitudinal crack, suggesting that the deflection pattern is more a function of temperature distribution than of structure loading and strength.

The load-carrying mechanism is largely one of tensile membrane action at high deflection in all cases, and it is interesting to compare the principal traction plots of Figures 7.30 (*Vulcan* 3) and 7.37 (*Vulcan* 6). Although very similar tensile membrane action distributions are shown overall in these, the tensile vectors in the short-span direction are noticeably smaller in the crack region in Figure 7.37 than in Figure 7.30. The deflection profile for Vulcan case 6 is shown in Figure 7.38; the edge restraint allows slight vertical movement along the edge beam. Comparison with Figure 7.33 with full restraint shows greater deflections towards the centre of the compartment.

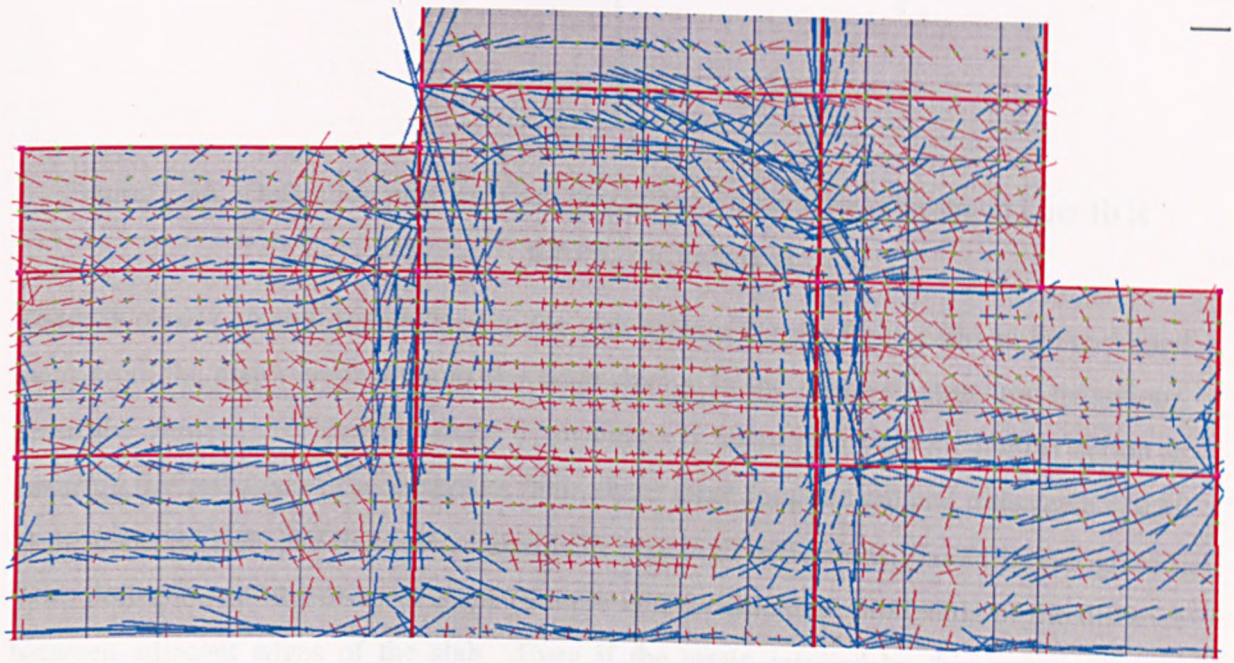

Figure 7.37: Distribution of the average principal stresses when maximum temperature of beam on Line 1b is 1067°C for *Vulcan* 6 (thick line = compression; thin line = tension).

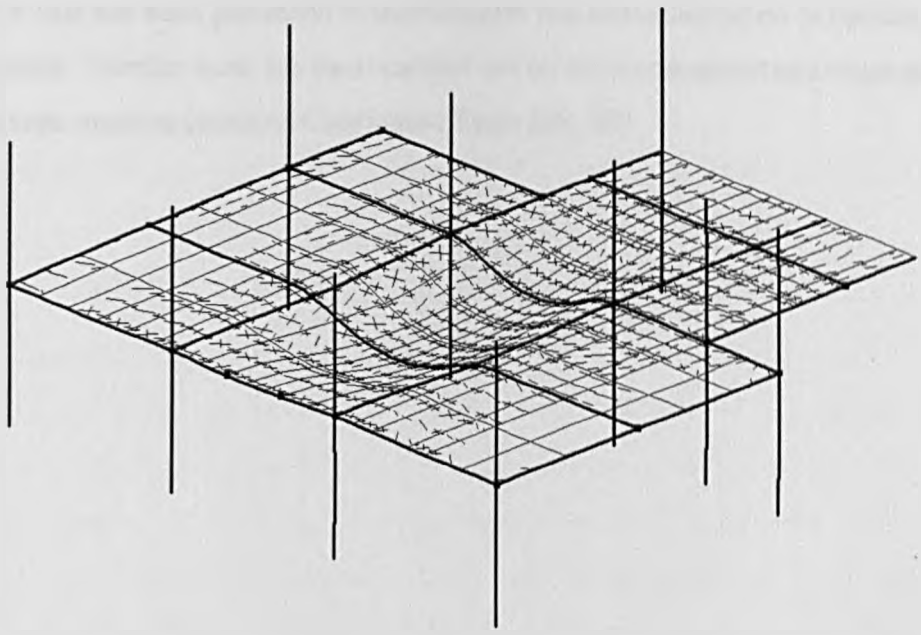

Figure 7. 38: Deflection profiles when maximum temperature of beam on Line 1b is 1067°C for *Vulcan* 6.

There is clearly enough redundancy in the slab system for the force paths to be re-routed away from the major crack without any large change in the observed structural behaviour. From the viewpoint of design, where it advantage is taken of tensile membrane action in ensuring fire resistance of a composite floor, these large longitudinal and transverse cracks in the concrete slab, and their association with very high deflections, should be recognised. With deflections of the order of *Span/10* there is a considerable shortening of the distance between adjacent edges of the slab. Even if the strain implied by this were tolerable, concrete is a brittle material in tension, and the shortening will inevitably localise into a very few discrete cracks rather than "smearing" as is assumed in the modelling. This may constitute an integrity failure of the slab as a separating element, even if no structural instability is caused.

The cameras above the fire compartment recorded the loss of the integrity limit state of the concrete slab at 54 minutes [68]. Before this time, there will have been the onset of cracking and although by no means definitive, this seems to tie in between these two times. The loss of bond between the steel and concrete has not been modelled using the type of global analysis used here.

The work that has been presented in this Chapter has concentrated on behaviour of the floor system. Further work has been carried out on the connection behaviour with comparisons made to previous Cardington Tests [69, 70].

Chapter 8

Discussion, Conclusions and Recommendations

8.1 Discussion

8.1.1 Ambient temperature tests

The complete ambient-temperature experimental programme consisted of 15 tests on horizontally unrestrained model-scale reinforced concrete slabs. The slabs had aspect ratios of 2.09 or 1.55 and either isotropic or orthotropic reinforcement. Table 8.1 shows the comparisons between design load and test load at design limit of vertical displacement.

Test	Size (mm)	Aspect Ratio	μ	t (mm)	fy (N/mm^2)	Bar Type	Design limit on vertical displacement (mm)	Design load	Test load	Design / Test
2	1150× 550	2.09	1.0	20.0	265	Smooth	18.1	2.89	2.76	**1.05**
5	1150× 550	2.09	1.0	18.0	258	Smooth	17.9	2.51	3.17	0.79
16	1150× 550	2.09	1.0	15.0	240	Deformed	17.3	2.00	3.18	0.63
4	850× 550	1.55	1.0	14.0	265	Smooth	13.4	2.53	2.30	**1.10**
10	850× 550	1.55	1.0	19.5	256	Smooth	13.2	3.23	4.41	0.73
15	850× 550	1.55	1.0	16.0	248	Deformed	13.0	2.65	2.81	0.94
6	1150× 550	2.09	0.2	18.0	262	Smooth	18.0	2.43	3.00	0.81
8	1150× 550	2.09	0.2	18.5	242	Deformed	17.3	2.16	2.52	0.86
11	850× 550	1.55	0.2	14.0	260	Smooth	13.3	2.83	2.86	0.99
14	850× 550	1.55	0.2	15.0	255	Deformed	13.1	2.87	7.09	0.40
7	1150× 550	2.09	5.0	18.5	252	Smooth	17.7	2.59	3.23	0.80
9	1150× 550	2.09	5.0	17.5	245	Deformed	17.4	2.37	3.83	0.62
9A	1150× 550	2.09	5.0	20.0	245	Deformed	17.4	2.72	4.07	0.67
12	850× 550	1.55	5.0	20.0	256	Smooth	13.2	3.13	3.72	0.84
13	850× 550	1.55	5.0	15.0	245	Deformed	12.9	2.24	2.10	**1.07**

Table 8.1: Comparison between design load and test load at design limit of vertical displacement.

For the six tests conducted on isotropically reinforced concrete slabs there was no significant difference in the observed load-displacement behaviour between those reinforced with smooth or deformed wire, up to displacements of the order of twice the thickness of the slab. It has been shown (Chapter 3) that the Simple Design Method, which assumes that the reinforcement crossing the eventual central tension crack across the short

span is still intact but is at its ultimate strength, yields results that compare very well with the experimental results beyond the initial range of displacements where the main concrete cracking occurs. However, at displacements above 30 mm *(short span/18* or double the slab thickness) Test 15, the isotropically reinforced slab with deformed wire and an aspect ratio of 1.55, showed a progressively reducing load carrying capacity with further increases of vertical displacement, thus diverging from the predictions of the Simple Design Method. This can be associated with the progressive fracture of the reinforcing wires across the main tension crack, which was observed shortly beyond 30 mm deflection.

Orthotropically reinforced concrete slabs were also tested, with the total area of reinforcement in both directions being equal to that contained in the isotropically reinforced slabs in all cases. Four tests were conducted in which a greater area of reinforcement was placed in the longer span of the slab, thus increasing the reinforcement across the final short-span tension crack. These tests showed clearly that different responses were obtained from the slabs reinforced with smooth wires in comparison with slabs reinforced with deformed wires. In the case of smooth reinforcement, the load capacity of the slab continued to increase with increasing displacement, beyond the initial peaks which occur before the major cracking occurs. However, when using deformed reinforcement the load capacity of the slab decreased consistently with increasing displacement in the same range. The post-peak behaviour of the slabs reinforced with smooth wire compared well with the predictions obtained using the Simple Design Method, but the capacities of the slabs progressively decreased after the peak, and the predictions became unconservative at high deflections, for those reinforced with deformed wire. Observations from the tests indicated that the difference between these types of behaviour was due to progressive fracture of the deformed wires across the tension cracks. The fact that the smooth wire did not extensively fracture was probably due to its relatively poor bond with the concrete, increasing the lengths over which the post-yield strains could act, combined with its higher fracture strain.

Although the predicted load-displacement response of slabs with deformed wires generally fell below the prediction of the Simple Design Method at large displacements, the maximum allowable vertical displacement of the method ensured that the predicted load-carrying capacity was in nearly all cases conservative compared with the test results. This allowable displacement currently takes no account of the bond between the reinforcement and concrete. Although the predicted load-capacity using the maximum allowable vertical

displacement is generally conservative compared with the test results it is based on an assessment of the average mechanical strain in the long-direction bars, which in effect assumes that the corresponding reinforcement is not bonded to the concrete. As has been observed in slabs reinforced with deformed wire, reinforcement may only de-bond over short lengths adjacent to the major tension crack, and thus may fracture progressively as the deflection increases. It is therefore apparent that the prediction of maximum allowable vertical displacement needs to be modified to incorporate the loss of bond between the reinforcement and the concrete. This would allow the difference in behaviour between smooth and deformed bars to be incorporated.

Further modifications to the design method have been suggested following an by examination of the post-test photographs (Chapter 3) of slabs having an aspect ratio 1.55, in which the tension cracks formed at the intersection of the diagonal yield line with longitudinal yield line. The Simple Design Method was revised and comparisons with the experimental results showed that for these types of slabs, the method was under-predicting the load capacity of the slab. This was later substantiated by the numerical results included in Chapter 4.

The slabs containing a greater amount of reinforcement in the long span were observed to fail by a mechanism that was different to that previously assumed. In these tests, the short-direction tension crack, the assumed failure mode, did not occur. Instead, the central long-direction yield-line crack developed into a tension crack, since this direction was more lightly reinforced. The Simple Method was revised for this type of failure mechanism but the theoretical results predicted higher enhancements than were actually attained in the tests.

The slabs were not pre-loaded and therefore had minimal micro cracks. Additionally, the slab was likely to have utilised more of its concrete tensile strength than would normally occur in practice. Normal slabs are subjected to loading and therefore have less tensile capacity due to micro cracking, shrinkage etc.

The steel reinforcement across the cracks started to fracture due to the high bond strength between the concrete and reinforcement, which then led to high straining over a very short length. Fracture of the steel initiated an 'unzipping effect' along the crack which progressed quickly, resulting in integrity failure of the slab. In the slabs reinforced with smooth wire, localised de-bonding between the steel and concrete took place as the crack

formed, and as the load was progressively applied, further de-bonding occurred. This phenomenon was observed along the full length of the crack. Subsequently, the load became distributed between the wires and, towards the end of the test, the slab was held together by the wires alone. The wire was rarely observed to have fractured, because of the progressively increasing length over which it strained.

The slabs modelled with zero concrete tension were assumed to have already cracked and the tension forces carried by the reinforcement. The *Vulcan* predictions, which considered no contribution of concrete tension, compared well with the experimental and theoretical predictions for the isotropic slabs and slabs that had more reinforcement placed in the shorter span (μ=5). The *Vulcan* predictions for slabs containing more reinforcement in the long span did not correspond well with the experimental and theoretical predictions.

In the *Vulcan* predictions where concrete tension was incorporated into the model, the calculated peak load exceeded the experimental peak load by ratios in the region of 1.1-1.6. The discrepancies between the experimental results and those of *Vulcan* are likely due to the fact that the slab will have a gradual development of micro-cracks, which is complex to model. The dramatic increase in displacement with no increase in load that was modelled in *Vulcan* was due to the large loss of stiffness suffered by the slab; currently the post peak behaviour of concrete slabs cannot be modelled due its complexity.

The experimental results, combined with *Vulcan* predictions, demonstrated that the important factors for deciding the load capacity of the slab are the tensile strength of the concrete at small displacements and the tensile strength of the reinforcement at large displacements.

For the isotropic slabs, membrane traction plots showed the development of compression forces normal to the long span within the central zone of the slab. The observed behaviour of these tests, under increasing load, showed that the slab facets started to 'jam' in the middle once the yield line and transverse cracks had formed (F'), Figure 8.1.

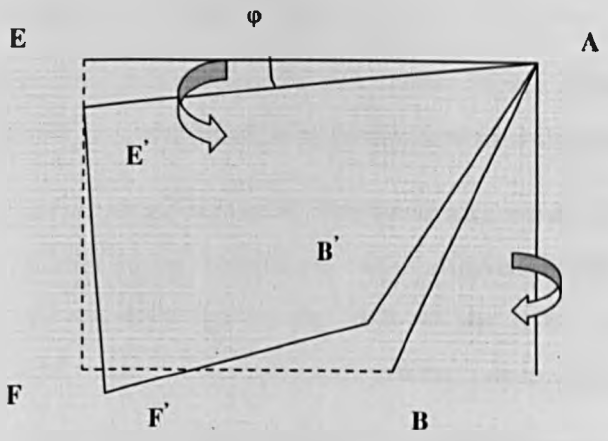

Figure 8.1: Rotation of AEFB

The Simple Design Method is assumed to have uniform tension along the longitudinal crack (F-B). In reality as the slab deflects, there are several phases in which these stresses will change depending on the geometry, reinforcement distribution and displacement of the slab. It was also shown for slabs of aspect ratio 1.55 that the *Vulcan* predictions (ft=0 N/mm^2) compared well to the modified Simple Method which took into consideration the observed failure mode for this particular type of slab (two crack mode of failure), Figure 8.2.

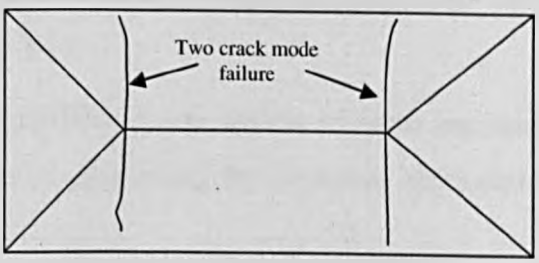

Figure 8.2: Two crack mode of failure

The existing mode of failure adopted in the Simple Method does raise some concerns as to its applicability for a range of slabs with differing aspect ratio and reinforcement distribution. It has been shown that the method remains conservative but questions must be raised concerning the level of conservatism utilised within the simple approach. Depending upon the aspect ratio and reinforcement distribution of the slab, a correct mode of failure and resulting stress distributions must be adopted. Therefore, the Simple Design Method for the assumed singular mode of failure that can be applied to a wide range of slabs is far from correct, but seems to be conservative.

Numerical studies undertaken have shown that:

- By placing more reinforcement in the long span, higher enhancements are gained. However, these are only apparent at large displacements (*span/5).*
- Decreasing the slabs cross-sectional reinforcement values between 0.05%-0.18% increases the enhancement factors at large displacements. However, further investigations are required due to the lack of test data.. Future studies should incorporate a wide range of slab sizes and reinforcement percentages.
- Concrete strength is not a significant factor at high displacements and the strength and type of wire used is important as this affects the load capacity of the slab.
- The work highlights the fact that the *Vulcan* is currently unable to model the bond behaviour between concrete and reinforcement or account for different reinforcement surface types.. The results show that both the Simple Method and numerical models for the deformed wire slabs are unconservative at displacements greater than *span/30.*
- The tensile strength of concrete is significant at low deflections but is very difficult to calculate, as shown from the *Vulcan* predictions. The models assumes pure tension with subsequent brittle failure and large loss of stiffness which *Vulcan* cannot currently model..
- The Simple Design Method was shown to yield unconservative predictions for certain types of slabs, questioning the universal applicability of this Upper Bound approach.

8.1.2 High Temperature Tests

Chapter 5 presented the main results from a number of loaded high-temperature tests conducted on horizontally unrestrained slabs. An electrical heating system and self-supporting frame was developed to enable the slabs to be heated up to lower-surface temperatures in the region of 800°C.

The major objective of these tests was to investigate the influence of thermal curvature on the failure mechanisms of rectangular slabs. Observations from the high-temperature tests have shown that the cracking mechanism differs in some respects from that observed at ambient temperature. At ambient temperature, four flat facets of the slab rotate about the edge supports and yield line cracks are formed as a low-deflection mechanism which is

forced into membrane action at high deflections, Figure 8.3. At high temperatures, the slab initially deflects into double curvature, generating full-depth cracking across its short span, and may later form a less distinctive yield line mechanism, Figure 8.4.

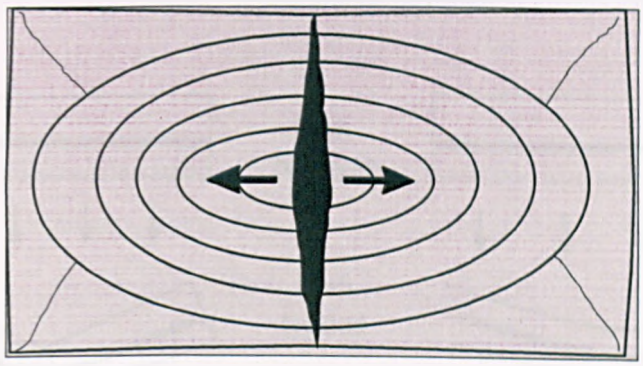

- Rectangular slab with no horizontal restraint
- Formation of yield line cracks
- Development of tension crack

Figure 8.3: Slab failure mechanism at ambient temperature

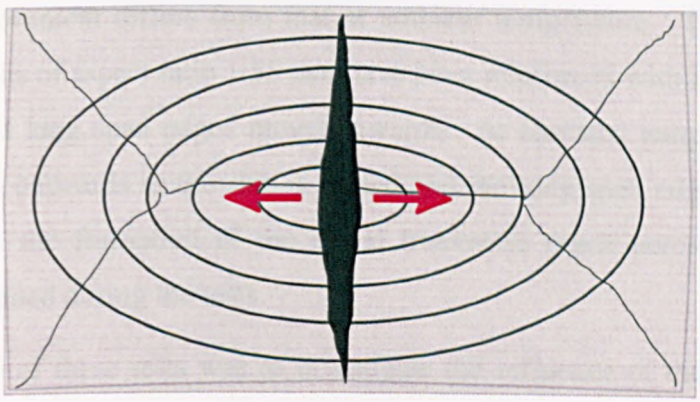

- Rectangular slab with no horizontal restraint
- Development of transverse crack
- Formation of yield lines

Figure 8.4: Slab failure mechanism at elevated temperature.

The Simple Method is based on the principle of yield lines forming, the concrete cracking and tension forces being carried by the reinforcement, Figure 8.5. The reinforcement is assumed to carry the entire tension force as the concrete has cracked and has no contribution from its tensile strength. The tension in the concrete is conservatively ignored as in practice normal slabs undergo micro cracking due to imposed load and the normal effects of creep and shrinkage. At elevated temperatures, with the absence of plastic

hinges initially forming, the tension force is carried by the reinforcement (which has not yielded) and the concrete, as shown in Figure 8.5. At increasing temperatures, the concrete starts to lose its strength and micro-cracks start to form. At larger displacements and dependent on load, due to the concrete's weakened state, the yield line mechanism forms which is dependent on the geometry and boundary conditions of the slab.

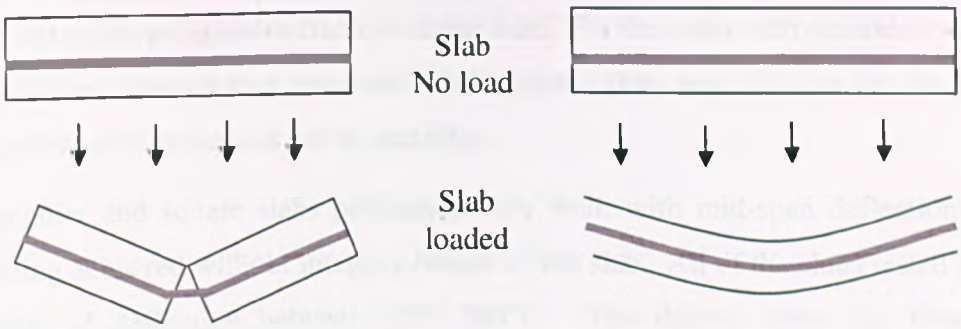

(a) Ambient temperature (b) High temperature

Figure 8.5: Explanation of failure modes at ambient and elevated temperature.

The slab edge movement differs from that at ambient temperature. The *Vulcan* models showed that in slabs of aspect ratio 1.55 that have been reinforced with isotropic wire, both the short span and long span edges moves inwards. At elevated temperatures, the short span edges moves outwards as the slab is heated and the long span edges moves inwards. This may explain the formation of the initial transverse crack across the slabs which progressively widened during the tests.

A major objective of these tests was to investigate the influence of thermal curvature on the failure mechanisms of rectangular slabs. Observations from the high-temperature tests have shown that the cracking mechanism differs in some respects from that observed at ambient temperature. At ambient temperature, four flat facets of the slab rotate about the edge supports and yield line cracks are formed as a low-deflection mechanism which is forced into membrane action at high deflections. At high temperatures, the slab initially deflects into double curvature, generating full-depth cracking across its short span, and may later form a less distinctive yield line mechanism, Figure 8.5.

The heated slabs, in general, performed very well, with enhancements of up to 3.5 times the yield (temperature dependent) achieved. This enhanced resistance is attributed to membrane forces, which assist in maintaining the structural integrity through diaphragm

action. The majority of the slabs supported the imposed loads for the entire duration of the fire test without collapse, despite the large slab deflections (*span/10*) attained in some of the tests. The slabs had much greater load capacity than predicted by yield line theory.

The slabs reinforced with smooth bars performed better than those reinforced with deformed bars. The tests showed that once the transverse crack had opened, the wire was exposed to the hot furnace temperatures which resulted in a loss of strength, which ultimately led to the progressive fracture of the wire. For the slabs with deformed wire, the fracturing of the exposed wire occurred much quicker than was the case for the smooth wirethe smooth, as it possessed lower ductility.

The rectangular and square slabs performed very well, with mid-span deflections up to *span/12* being achieved without integrity failure of the slab. All of the slabs tested showed similar rates of deflection between 20°C-300°C. The thicker slabs, *i.e.* those with reinforcement placed at 7.5mm from the bottom of the slab, deflected less than the 15mm thick slabs. The rate of deflection for a slabs reinforced with smooth wire (Test 15 and 13) could be seen to be less than that for the equivalent slab using deformed wire (Test 17 and 12). This seems to indicate that once the slab has cracked, the exposure of the deformed wire (which exhibited less ductility than the smooth wire) causes reduction in strength which leads to fracturing of the reinforcement.

The slabs showed that they had much greater fire resistance than predicted by yield-line theory and that the deflection limits of *span/30* or *span/20* imposed by current standards and the simplified approach are conservative. The maximum displacement using the Simple Design Method always gave a lower-bound value when compared with *span/30* and the actual deflection.

The square slabs performed in a similar manner to the rectangular slabs up to temperatures of approximately 300°C, and performed better at higher temperatures. The theoretical calculations predict the enhancements above yield load for square slabs much greater than for the corresponding rectangular slabs.

The enhancements for the heated rectangular tests with reinforcement at half depth showed that membrane action commences at displacements greater than approximately 15mm. In the thicker slabs with reinforcement placed at 7.5mm from the bottom, membrane action starts to develop earlier at approximately 10mm. For the square slabs, the development of membrane action started between 5-10mm.

Overall, the tests showed that slabs containing small amounts of reinforcement (0.05%) yield greater enhancements than corresponding slabs with greater reinforcement. The reasons for this are most likely due to the way in which enhancement is calculated, *i.e.* by dividing the applied load by the calculated reduced yield line load. As discussed previously, the yield line calculations ignore any tensile contribution from the concrete. Therefore, the calculations predict greater enhancements as the yield line load would be reduced for slabs that have small area of reinforcement (0.05%).

The overall predictions given by the simplified approach show a clustering of results. The test predictions showed a greater range of enhancement, dependant upon the area of reinforcement within the slab. The magnitude of enhancement in the tests was also much greater than that determined using the simplified method, probably due to the fact that concrete tension is ignored in the latter.

Comparisons between the numerical model *Vulcan* and the experiments have shown that *Vulcan* predicts deflections accurately, despite the fact that it does not model discrete cracking. Further studies were undertaken, using *Vulcan* to illustrate the mechanics involved in the high-temperature slab behaviour.

The *Vulcan* models accurately predicted the slab displacements up to approximately 550°C, after which the *Vulcan* predictions diverged from the test results. Possible reasons for this are as follows:

- Loss of bond between the reinforcement and concrete, leading to fracture of the reinforcement and progressive failure of the slab.
- Inaccuracy of the measured temperature profiles through the slab.
- The assumed contribution of the reduced concrete tensile strength in *Vulcan*.

The influence of the thermal strains within the slab were investigated by re-running the test models with zero applied load. It was shown that loaded and unloaded slabs displaced at a similar rate, indicating that the initial displacements are dominated by thermal expansion of the slab. Comparisons were made between the displacements attained in both the ambient and heated tests; this highlighted the steep initial rise in displacements of the heated slabs due to the thermal expansion of the slab.

At ambient temperatures, the membrane traction plots showed small compression force bands developing across the central region of the slab. This was determined, from the

observed slab behaviour and assumptions of the Simplified Method, as being caused by the trapezoidal facets rotating about the slab corners as they hinge about the diagonal yield lines, and impinging on one another in the central area of the slab. At elevated temperatures, initial compressive forces within the central zone of the slab were seen to develop. However, as the slab temperatures rapidly rose, these compressive forces were relieved with increasing displacement. At temperatures above 300°C, compressive forces across the short span start to develop and increase in magnitude as temperatures increase.

Further studies were carried out to investigate the influence of the temperature distributions through the slab on the slab displacements and membrane forces. It was shown that, at the beginning of the tests, the steep increase in the rate of displacements is due to large thermal displacements within the slab, which become less steep as the top surface temperatures of the slab increases, which decrease the thermal bowing. The initial steep thermal gradients are due to the poor conductivity of the concrete. The membrane traction plots for the temperature studies were compared and the results highlighted that the thermal gradient and resultant vertical displacements does indeed appear to influence the development of the compressive band within the central zone of the slab.

The development of the compressive band was also influenced by the percentage of reinforcement. In Tests 12 and 13, the slabs included 0.25% reinforcement and the resulting membrane force plots showed that the internal compressive forces within the central zone were not as pronounced as in the other tests, which had less reinforcement. It was suggested that the higher reinforcement and larger displacements resulted in the higher tension forces within the central zone of the slab.

Several of the test results (14 and 16) showed no difference in the rate of displacements for slabs reinforced with the alternate types of reinforcement. In these tests, the slabs had not suffered any major cracks and the wires were not exposed to the hot furnace temperatures. Towards the end of the tests, both types of wire would have behaved similarly. Due to high temperatures within the slab, a progressive loss of bond between the steel and concrete would occur as the strength of the materials reduces.

Numerical studies were undertaken to investigate the influence of concrete tension at high temperatures on the overall slab performance (with zero applied load). At ambient temperatures, the influence of concrete tension contributed to the initial load carrying capacity of the slab. The results from the study showed that up to temperatures of 200°C,

the influence of concrete tension on the displacements is negligible and the thermal gradient and resultant thermal expansion dominates the slab behaviour. At temperatures above 200°C, the tensile strength of the concrete does influence the slab displacements.

Similar numerical studies were undertaken which incorporated an applied load. It was shown that in slabs containing less reinforcement, the influence of the concrete tension is greater. This seems logical, as the slab that has a reduced reinforcement is, in effect, utilising its concrete tensile strength to resist the applied load.

The *Vulcan* predictions for the slabs of thicker depth were generally accurate up to temperatures of 550°C. However, after this point the actual slab behaviour is not predicted correctly. The *Vulcan* predictions are very good during the period in which the slabs exhibit no major cracking and undergo thermal bowing. However, the predictions diverge from actuality once the slab has cracked and the reinforcement has fractured, leading to an 'unzipping' effect and runaway failure of the slab. These slabs had less overall deflection in the early stages, and exulted smaller displacements than the thinner slabs due to their decreased thermal bowing.

The membrane traction plots for the square slabs showed membrane forces symmetrical about the diagonal axis, which was logical. The development of the compressive band within the central zone did not occur and the slabs had acquired full membrane action.

From the enhancement plots for these tests, it was noticable that the square slabs started to developed tensile membrane action at lower vertical displacements when compared to the rectangular slabs. It appears that the geometry of a slab plays an important role in the development of the compressive forces within the central zone of the slab.

8.1.3 Structural Behaviour of a Full Scale Test

This Chapter presented a numerical investigation of the thermal and structural results from a compartment fire test, conducted in January 2003 on the full-scale multi-storey composite building constructed at Cardington, United Kingdom. This building was erected in 1994 for an original series of six tests during 1995-96. The fire compartment's overall dimensions were 11m x7m with one edge at the building's perimeter, using largely unprotected steel downstand beams, and including within the compartment four steel columns protected with cementitious spray. The compartment was subjected to a natural fire of load 40 kg/m^2 timber, in common with the original test series. However, the

composite slab forming the ceiling was subjected to an increased uniform applied load of 3.19 kN/m^2.

Numerical modelling studies have been performed using 1) the numerical software *FPRCBC* in order to analyse temperature distributions in slabs, 2) Eurocode 3 Part 1.2 calculations for beam temperatures, and 3) *Vulcan* to model the structural response to thermal and mechanical loading. These are compared with the quite comprehensive test data, and a series of cases have been analysed in order to develop a comprehensive picture of the sensitivity of the behaviour to different assumed conditions.

The comparison between the modelling of basic cases and the test results shows very good correlation, indicating that such modelling is capable of being used to give a realistic picture of the structural behaviour of composite flooring systems in scenario-related performance-based design for the fire limit state. The extended studies demonstrate the influence of extra protection to the connection zones of primary beams, and the effects of different vertical support conditions at the perimeter of the fire compartment. The effect of incomplete overlapping of the reinforcing mesh in the slab, which is believed to have occurred in one region, was also considered.

The load carrying mechanism at high displacements is largely tensile membrane action in all cases. The maximum displacement calculated using the simplified approach was 771.5mm; the maximum measured displacement was 919mm. The ratio of the BRE maximum displacement to measured displacement is therefore 0.84. This value than for the model tests.

8.2 Conclusions

The aim of this research was to extend the knowledge of the performance of slabs at ambient and elevated temperatures, and to look at their failure mechanisms and the influence of temperature on their performance. An in-depth investigation of the BRE Simplified Design Method was undertaken. This involved undertaking a series experimental work in which a series of model-scale slabs were tested in a custom made loading rig at ambient and elevated temperatures.

The main objective was to investigate the influence of tensile membrane action on the behaviour of reinforced concrete slabs subject to fire. However, before this could be undertaken, a series of tests was carried out at ambient temperature to allow the basic engineering principles embodied in the developed design method to be checked, and to

validate the small-scale test methodology. The Simplified Design Method assumed that the basic behaviour observed at ambient temperature would remain the same at elevated temperatures.

Ambient Tests

This thesis presents the results from 15 small-scale tests conducted on horizontally unrestrained slabs which were subjected to large vertical displacements. All the tested slabs showed a load-carrying capacity far greater than the design capacity as calculated using the well-established yield-line theory. The purpose of these tests was to investigate the influence of isotropic and orthotropic reinforcement, together with reinforcement bond strength, on the degree of mobilisation of tensile membrane action, and thus on the load-capacity of the slab. The results of the tests have been compared to those found using the Simplified Design Method, which incorporates membrane action of composite floor slabs into the estimation of their load capacity in fire and where large vertical displacements are acceptable if compartmentation is maintained. This comparison shows that the design method compares well with experimental results and is generally conservative. However, in slabs reinforced with deformed wire, the theoretical predictions were less conservative. The reason for this is that the simple design method does not consider the bond and fracture of the reinforcement.

The maximum allowable vertical displacement computed using the design method ensured that the predicted load-carrying capacity was in nearly all cases conservative compared with the test results. This allowable displacement currently takes no account of the bond between the reinforcement and concrete. It is therefore apparent that the prediction of maximum allowable vertical displacement needs to be modified to incorporate the loss of bond between the reinforcement and the concrete. This would allow the difference in behaviour between smooth and deformed bars to be incorporated.

Further modifications to the design method have been prompted by examination of the photographs (Chapter 3) for slabs of aspect ratio 1.55, in which tension cracks formed at the intersection of the diagonal yield line with longitudinal yield line.

The numerical and experimental studies undertaken have shown that;

- By placing more reinforcement in the long span, higher enhancements are gained. However, these are only apparent at large displacements (*span/5*).

- Decreasing the slabs cross sectional reinforcement values between 0.05%-0.18% increases the enhancement factors at large displacements. Further investigations are required to fully validate this theory, due to the lack of test data. The studies should incorporate a wide range of slab sizes and reinforcement percentages.
- Concrete tensile strength is not a significant factor at high displacements and the strength and type of wire used is important as it affects the load capacity of the slab.
- *Vulcan* is unable to model the bond behaviour and the subsequent fracture of the reinforcement. The results show that both the Simple Method and numerical models for the deformed wire slabs are unconservative at displacements greater than *span/30.*
- The tensile strength of concrete is significant at low deflections but is very difficult to calculate, as shown in the *Vulcan* predictions. The models assume pure tension with subsequent brittle failure and large loss of stiffness when, in reality, slabs undergo micro cracking .

Heated Tests

An electrical heating system and self-supporting frame have been developed to enable slabs to be heated up to lower-surface temperatures of approximately 700°C. Test slabs have, in general, performed very well and supported loads well in excess of the predicted yield line loads.

A major objective of these tests was to investigate the influence of thermal curvature on the failure mechanisms of rectangular slabs. Observations from the high-temperature tests have shown that the cracking mechanism differs in some respects from that observed at ambient temperature. At ambient temperature, four flat facets of the slab rotate about the edge supports and yield line cracks are formed as a low-deflection mechanism which is forced into membrane action at high deflections. At high temperatures, the slab initially deflects into double curvature, generating full-depth cracking across its short span, and may later form a less distinctive yield line mechanism.

The experimental and numerical studies have shown that:

- The design method predicted the enhancements conservatively over the permitted deflection range. Enhancements of up to 4.5 times the yield load have been

achieved; this enhanced resistance has been attributed to membrane forces which assist in maintaining the structural integrity of the slab through diaphragm action

- Slabs reinforced with smooth wire perform better than those reinforced with deformed wire.
- Comparisons between results from the numerical model *Vulcan* and those from the experiments have shown that *Vulcan* predicts deflections accurately, even though it does not model discrete cracking.
- Numerical studies were undertaken to investigate the influence of concrete tension at high temperatures on the overall slab performance (with zero applied load). At ambient temperatures, the influence of concrete tension contributed to the initial load carrying capacity of the slab. The results from the study showed that up to temperatures of 200°C, the influence of concrete tension on the displacements is negligible and the thermal gradient and resultant thermal expansion dominates the slab behaviour. At temperatures above 200°C, the tensile strength of the concrete does influence the slab displacements.
- From the enhancement plots for these tests, it was shown that square slabs started to develop tensile membrane action at lower vertical displacements than the rectangular slabs. The development of the compressive forces within the central zone of the slab was apparent in the rectangular tests but not the square tests. It seems that the geometry of a slab plays an important role in the development of compressive forces within the central zone of the slab.
- The square slabs performed in a similar way to the rectangular slabs up to temperatures in the region of 300°C, and performed better at higher temperatures. The theoretical calculations predict that the enhancements above yield load for square slabs is much greater than for corresponding rectangular slabs.

The *Vulcan* models accurately predicted the slab displacements up to approximately 550°C after which the *Vulcan* predictions diverged from the test results. There were two likely reasons for this:

- Loss of bond between the reinforcement and concrete, leading to fracture of the reinforcement and progressive failure of the slab.
- Inaccuracy of the measured temperature profiles through the slab.

A summary is provided below which compares the failure mechanisms of the model slabs at ambient and elevated temperature.

Ambient Temperature	Elevated Temperature
• Development of yield line cracks • Rigid plastic behaviour	• Thermal bowing of the slab, which is temperature dependent • No development of yield line cracks
• Development of transverse crack	• Development of transverse crack
• Onset of tensile membrane action	• Depending on the load ratio slab may form yield line cracks • Tensile membrane action

Recommendations for future research

The following areas should be investigated:

- The contribution of the secondary beams to the load capacity of the slab should be considered. The Simple Design Method assumes that two plastic hinges are formed in the beam which causes the yield line mechanism. From the studies presented in this thesis, no consideration has been given to any beneficial effects from the unprotected secondary beams or that the secondary beams influence the failure mechanism of the slab and the results show the method to be conservative. However, it must be investigated as to whether plastic hinges are formed at high temperatures due to strength reduction. From the Cardington Test results, it seems that this proposed failure mechanism is incorrect as thermal bowing dominates at initial displacements due to steep thermal gradients through the slab.

- The Simple Method permits the prediction of enhancements of a slab by postulating a collapse mechanism which is compatible with the boundary conditions. The slab sections are assumed ductile enough to allow plastic rotation to occur at critical sections along the yield line. It was shown at ambient temperatures that the method can be unconservative if an incorrect collapse mechanism is used. In addition, as the level of reinforcement in the slab increases the collapse mechanism will be different from that assumed. The slab will be 'over-reinforced' and concrete

crushing will occur. This needs to be investigated further by experimental work. Work recently carried out by May and Lodi have shown that the yield line method is unconservative for slabs that have reinforcement greater than 0.75% [71].

- The inclusion of de-bonding criterion into *Vulcan.*
- Further investigations of concrete tension at elevated temperatures.
- The Simplified Method currently does not check the connection strength. The beams are checked for extra load and can be increased in size but the connections remain unchecked.
- Investigation of heated orthotropic slabs and slabs of varying span/depth ratios.

The experimental and numerical investigations that have been undertaken at ambient temperature have proven that the proposed design method is not always conservative and is only based on one pre-determined collapse mode. At high temperatures, the experimental and numerical work has shown that the slab behaviour is dominated by different mechanisms. The design method is based on the final failure mechanism of the slab and this was observed in the tests. The *Vulcan* predictions did predict with accuracy at elevated temperatures even though bond effects are not considered.

References

1. ISO 834 Fire resistance tests-elements of building construction, International Organisation for Sandardisation, Switzerland, (1975).
2. Law M.A review of formulae for T-equivalent. Proceedings of the Fourth International Symposium on Fire Safety Science, Melbourne, Australia, pp 985-996, (1997).
3. Pr EN 1991-1-2:2002, Eurocode 1: Actions on structures-Part 1.2: General actions-actions on structures exposed to fire, British Standards Institution, London, (2002).
4. Wickstrom U. A very simple method for estimating temperatures. Fire exposed structures, in New Technology to Reduce Fire Losses and Costs. Elsevier Applied Science, London, UK, pp 186-194, (1986).
5. Kirby B.R. and Preston R.R. High temperature properties of hot-rolled structural steels for use in fire engineering design studies. Fire Safety Journal, **13**, 27-37. (1988).
6. PrEN 1993-1-2 Eurocode 3: Design of steel structures-Part 1.2: General rules-structural fire design, European Committee for Standarisation, Febrauary (2002).
7. Irving J. The effect of elevated temperatures on concrete and concrete structures: a review of literature. Slough: Federation Internationale de la Precontrainte, (1975).
8. PrEN 1992-1-2 Eurocode 2: Design of concrete structures-part 1.2: General rules-Structural fire design, European Committee for Standardisation, (October 2002).
9. PrEN 1993-1-2, Eurocode 4: Design of composite steel and concrete structures-Part 1.2: General rules-structural fire design, European Committee for Standardisation, (December 2002).
10. Anderberg Y. and Thelandersson S. Stress and deformation characteristics of concrete at high temperatures, Bulletin 54, Division of Structural Mechanics and Concrete Construction, Lund Institute of Technology, Lund, Sweden, (1976).
11. British Standards Institution., BS 5950: Part 8, Code of practice for fire resistant design, British Standards Institution, London, (2003).

12. Steel Construction Forum. Investigation of Broadgate phase 8 fire. The steel Construction Instiute, (1991).

13. The Building Regulations., Approved Document B. Fire Safety. HMSO (2000).

14. Kruppa J. Some results on the fire behaviour of external steel columns. Fire Safety Journal, 2, **4**, pp247-257, (1981).

15. Rubert A and Schaumann P. Structural steel and plane frame assemblies under fire action. Fire Safety Journal, (1986), **10**, pp173-184.

16. Moore, D.B. and Lennon, T. Fire engineering design of steel structures. Progress in Structural Engineering and Materials, **1**, 1pp4-9, (1997).

17. Bailey, C. G, and Newman, G. N. The design of steel framed buildings without applied fire protection, The Structural Engineer, **76**(5): pp77-81 (1998).

18. Bailey, C. G, Lennon, T. and Moore, D.B. The behaviour of full-scale steel-framed building subjected to compartment fires. The Structural Engineer, 77(8), pp15-21, (1999b). .

19. Huang, Z. H., Burgess, I.W. and Plank, R.J., Non-linear modelling of three full-scale structural fire tests. Proceedings of First International Workshop on Structures in Fire, Copenhagen, Denmark, June, (2000b).

20. Newman, G. M., Robinson, J. T., Bailey, C. G., SCI-P288: Fire Safe Design, A new approach to multi-storey steel framed buildings, Steel Construction Institute, (2000).

21. Park, R., 'Tensile membrane behaviour of uniformly loaded rectangular reinforced concrete slabs with full restrained edges', Magazine of Concrete Research, **16** (46), pp39-44,(1964),.

22. Brotchie, J.F. and Holley, M.J., Membrane action in slabs: Cracking, deflection and ultimate load of concrete slab systems. Publication SP-30, American Concrete Institute, Detroit, Paper 30-16, pp345-377, (1971).

23. Park R., 'Ultimate strength of rectangular concrete slabs under short-term uniform loading with edges restrained against lateral movement', Proc. Institution of Civil Engineers, **28**, pp125-150, (1964).

24. Sawczuk, A. and Winnicki, L., 'Plastic behaviour of simply supported reinforced concrete plates at moderately large deflections', Int. J. Solids Structures, **1**, pp97-111, (1965).

25. Hayes, B., 'Allowing for membrane action in the plastic analysis of rectangular reinforced concrete slabs', Magazine of Concrete Research, **20** (65), pp205-212, (1968)

26. Bailey, C. G., The structural behaviour of steel frames with composite floor slabs subject to fire, Part 1: Theory, The Structural Engineer, **78**(11):19-27, (2000a).

27. Bailey, C. G., The structural behaviour of steel frames with composite floor slabs subject to fire, Part 2: Design, The Structural Engineer, **78**(11):28-33, (2000b).

28. Haung Z. H., Burgess I.W. and Plank R. J., "Nonlinear analysis of reinforced concrete slabs subjected to fire"., ACI Structural Journal **96**(1):127-135, (1999a).

29. Johansen, K. W., Yield line theory, Cement and Concrete Association, (1962).

30. Wood, R.H., Plastic and elastic design of slabs and plates, with particular reference to reinforced concrete floor slabs, Thames and Hudson, London. (1961).

31. Park, R. T., and Gamble, W. L., Reinforced Concrete Slabs, John Wiley & Sons (2000).

32. British Standards Institution, BS 476: Fire Tests on building materials and structures: Part 20, Method for determination of the fire resistance of elements of construction (general principle), British Standards Institution, London, (1987).

33. Ockleston, A. J., Load tests on a 3 storey reinforced concrete building in Johannesburg, The Structural Engineer, **33**(10), pp.304-322, (April 1955),.

34. Lim, L. Experimental Fire Tests of Two-Way Concrete Slabs. Fire Engineering research Report 02/12. University of Canterbury, New Zealand, 2001.

35. Hayes, B. and Taylor, R., Load-Testing of RC slabs. The Consulting Engineer, pp46-47, (Nov. 1969).

36. Taylor, R. and Hayes, B., An appraisal of reinforced concrete slab design., The Consulting Engineer, pp. 58-60, (May 1968).

37. Westergaad, H. M., and Slater, W. A., Moments and stresses in slabs. Proc. Am. Concrete Institution, **17**, pp.415-538, (1921).

38. Taylor R., A note on a possible new method of ultimate load design of reinforced concrete slabs, Magazine of Concrete Research, **17**(53), 1965, pp.183-186.

39. Powell D.S. The ultimate strength of concrete panels subjected to uniformly distributed loads. Thesis submitted to Cambridge University for the degree of M.Sc., (1956).

40. Kemp K O. Yield of a square reinforced slab on simple supports allowing for membrane forces. The Structural Engineer, **45**(7), (July 1967), pp.235-240.

41. Usmani A.S. and Cameron, N.J.K., Limit capacity of composite floor slabs in fire. Cement and Concrete Composites Journal, in press (2003).

42. Timenshenko S and Goodier J N, Theory of Elasticity, 2nd ed., McGraw-Hill, New York, (1951).

43. Bailey C. G., Efficient arrangement of reinforcement for membrane behaviour of composite floor slabs in fire conditions. Journal of Constructional Steel Research, **59**:p31-49, (2003).

44. C.P.114: The structural use of concrete in buildings (now withdrawn), BSI, London.

45. Clifton G. C., Hinderhofer M. D. and Schmid, R. Design of multi-storey steel framed buildings with unprotected secondary beams in serve fire. HERA Steel Design and Construction, Bulletin No. 60, HERA, Manukau City, New Zealand, (2001).

46. Foster S. J., Bailey C.G., Burgess I.W., and Plank R.J. Experimental behaviour of concrete floor slabs at large displacements., Journal of Engineering Structures, **26**(2004) pp 1231-1247.

47. Middleton C.R. Concrete Bridge Asessment Using Plastic Collapse Analysis, Presented at the Bridge Surveyor Conference, Cambridge University, March, (1998).

48. Bartos, P., Bond in Concrete., International Conference on Bond in Concrete, Applied Science Publishers, London, (1982).

49. Izzuddin, B. A, Elghazouli, M., Failure of lightly reinforced concrete members under fire, I: analytical modelling. Journal of Structural Engineering, 130, pp3-18, (2004).

50. Izzuddin, B. A, Elghazouli, M., Failure of lightly reinforced concrete members under fire, II Parametric studies and design considerations, 130, pp18-32, (2004).

51. Haung, Z., Burgess, I. W., and Plank, R.J. Modelling membrane action of concrete slabs in composite buildings in fire. Part I: Theoretical development. Journal of Structural Engineering, ASCE, 129(8), (2003), pp1093-1102.

52. Haung, Z., Burgess, I. W., and Plank, R.J. Modelling membrane action of concrete slabs in composite buildings in fire. Part II: Validations. Journal of Structural Engineering, ASCE, 129(8), (2003), pp1103-1112.

53. Barzegar-Jamshidi, F. Non-linear finite element analysis of reinforced concrete under short term monotonic loading, PhD Thesis, University of Illinois at Urbana-Champaign, (1987).

54. Rots, J. G. et al. The need for fracture mechanics options in finite element models for concrete structures, Proc. International Conference on Computer Aided Analysis and Design of Concrete Structures, F. Damjanic et al, Eds., Pineridge Press, Part 1, pp19-32. (1984)

55. Hoi Yan YIM, R. A new design calculation for the fire resistance of composite frames, MSc Thesis, University of Sheffield, May, (2002).

56. Foster, S.J., Burgess, I.W. and Plank, R.J. Experimental Behaviour of Model-Scale Concrete Floor Slabs at High Displacement, Paper S5-5, 3rd International Workshop on Structures in Fire, Ottawa, Canada, (2004), pp259-270.

57. Foster, S.J., Burgess, I.W. and Plank, R.J. Experimental Behaviour of Model-Scale Concrete Floor Slabs at Large Displacement and High Temperatures, Proc. Second International Conference on Steel and Composite Structures, Seoul, Korea, (2004) pp1268-1282. ISBN 89-89693-1

58. Foster, S.J., Burgess, I.W. and Plank, R.J. Investigation of Membrane Action in Model-Scale Slabs Subject to High Temperatures, ICASS '05, Shanghai, China, (2005).

59. Huang, Z., Platten, A. and Roberts, J. 'Non-linear finite element model to predict temperature histories within reinforced concrete in fires', *Building and Environment,* **31** (2), (1996) pp109-118.Schleich J.-B.,Cajot L.-G.

60. Huang, Z, Burgess, I. W. and Plank, R. J. 'Modelling of six full-scale fire tests on a composite building', *The Structural Engineer,* **80** (19), (2002) pp30-38.

61. Sanad, A.M., Rotter, J.M., Usmani, A.S. and O'Connor, M., 'Composite beams in large buildings under fire – numerical modelling and structural behaviour', *Fire Safety Journal,* **35** (3), (2000) pp165-188.

62. Wang, Y.C. 'Tensile membrane action in slabs and its application to the Cardington fire tests', *Second Cardington Conference,* BRE, Watford, UK, (1996).

63. Federal Emergency Management Agency, '*World Trade Center building performance study: Data collection, preliminary observations and recommendations*', FEMA 403, Washington, DC, (2002).

64. Foster S, J., Chladná M., Hsieh Y-C., Burgess I.W. and Plank R.J. Thermal and Structural Behaviour of a Full-Scale Composite Building Subject to a Severe Compartment Fire. Awaiting publication in Fire Safety Journal.

65. Petersson O., Magnusson S.E. and Thor J. *'Fire engineering design of steel structures'*, Publication 50, Swedish Institute of Steel Construction, Stockholm, (1976).

66. Karpaš J., Zoufal R. "*Požární odolnost ocelových a železobetonových konstrukcí (Fire Resistance of Steel and Concrete Structures)*", Zabraňujeme škodám, Svazek 28. Česká státní pojišťovna, Praha (1989).

67. Wald, F., Santiago, A., Chladná, M., Lennon, T., Burgess, I.W. and Beneš, M.,'*Tensile membrane action and robustness of structural steel joints under natural fire'* Internal report, Part 1-Project of Measurements; Part 2- prediction; Part 3- Measured data; Part 4- Behaviour, BRE, Watford, (2002-2003).

68. Wald F., Simões da Silva L., Moore D., Santiago A. Experimental Behaviour of Steel Joints under Natural Fire in "*Proceedings of ECCS and AISC meeting*" Amsterdam, (2004).

69. Wald F., Silva S., Moore D.B, Lennon T. Structural integrity fire test, in *Proceedings Nordic Steel Conference*, Copenhagen, (2004).

70. Wald F., Silva S., Moore D.B, Lennon T., Chladná M., Santiago A., Beneš M., Experiment with structure under natural fire, *The Structural Engineer*, (2004).

71. May, I. M. and Lodi S. H, Deficiencies of the normal moment yield criterion for RC slabs, *Proceedings of the Institution of Civil Engineers*, Structures and Buildings 158, Issue SB6,pp371-380, (December 2005).

Bibliography

1. Digest 02-Structural Aspects of Life Safety Issues, Building Research establishment, Swindon.

2. Digest 03- Fire Development- Calculation of Compartment Time-Temperature Response, Building Research Establishment, and Swindon.

3. Digest 04- Fire and Thermal Response Development- Calculation of Compartment Time-Temperature Response, Building Research Establishment, and Swindon.

4. Digest 05- Materials Behaviour, Steel and Composite-Calculation Procedures For the Design and Composite Construction Subject to Fire, Swindon.

5. Digest 06- Materials behaviour: Concrete-Calculation Procedures for the Design of Reinforced Concrete Construction Subject to Fire, Building Research Establishment, and Swindon.

6. Buchanan, A.H., Structural Design for Fire Safety, John Wiley & Sons, (2001).

Appendix A

A.1 Calculation of Yield Line Load for rectangular slab with uniformly distributed load

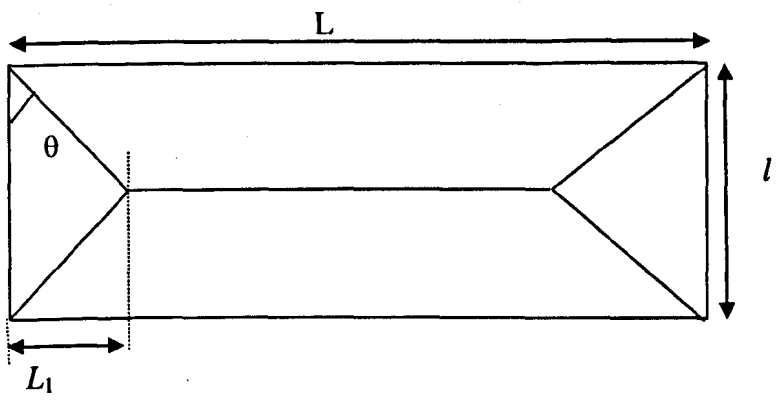

Using Wood's approximation [30]:

For a slab of aspect ratio 2.09 the yield load can be calculated as follows;

$$\frac{Pl^2}{m} = 13.986$$

l = 0.55m

L = 1.15m

m = 42.47 Nm/m

P = 1.963 kN/m^2

Total load = 1.242 kN

Calculation of L_1

$$\tan\theta = \sqrt{3 + \frac{1}{2.09^2}} - \frac{1}{2.09}$$

$$\theta = 52.8°$$

$$L_1 = \tan 52.8 . \frac{0.55}{2} = 0.363m$$

A.2 Calculation of Yield Line Load for rectangular slab for 12 point loading system

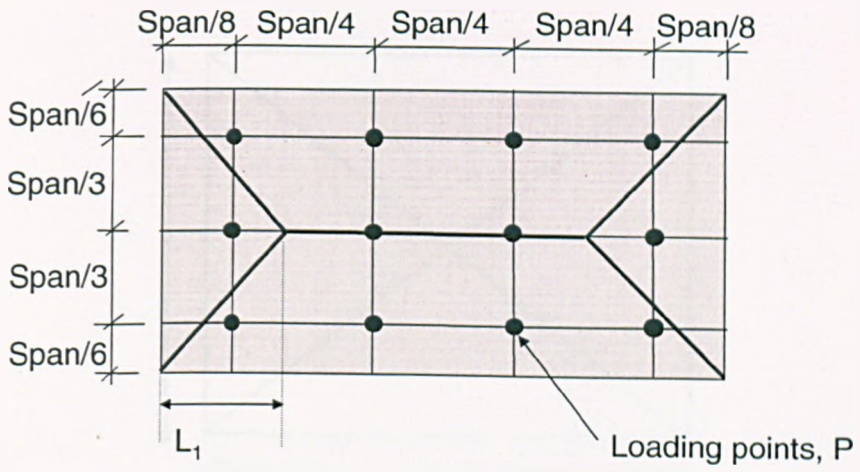

External work done = Internal work done

External work done:

$$\left(\sum(2P\delta_{\max})+\left(8P\frac{\delta_{\max}}{3}\right)+(0.396P\delta_{max}.2)\right)=5.46P\delta_{\max}$$

Internal Work Done:

$$\sum\left(\left(2m1.15.\frac{\delta_{\max}}{0.55/2}\right)+\left(2.0.55.m\frac{\delta_{\max}}{0.363}\right)\right)$$

Equate:

P = 88.6 N

Total Load

12 * 88.6 = 1.06 kN

Yield load calculated assuming distributed loading over -estimates actual yield by 14.7%

A.3 Calculation of Yield Line Load for square slab with uniformly distributed load

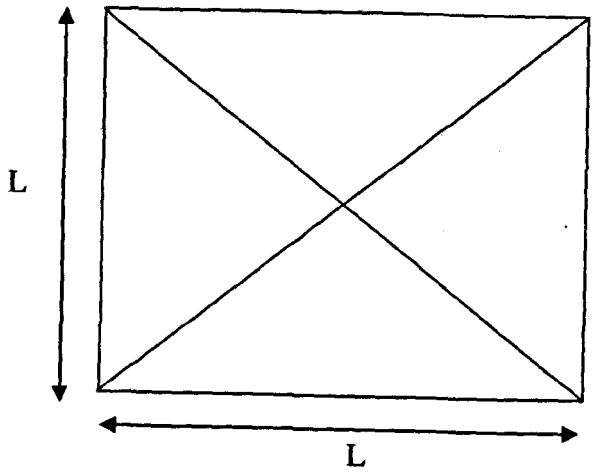

$$P = \frac{24m}{L^2}$$

L= 0.55m

L_1 = 0.275m

m = 42.47 Nm/m

P = 3.33 kN/m^2

Total load = 1.008 kN

A.3 Calculation of Yield Line Load for square slab for 4 point loading system

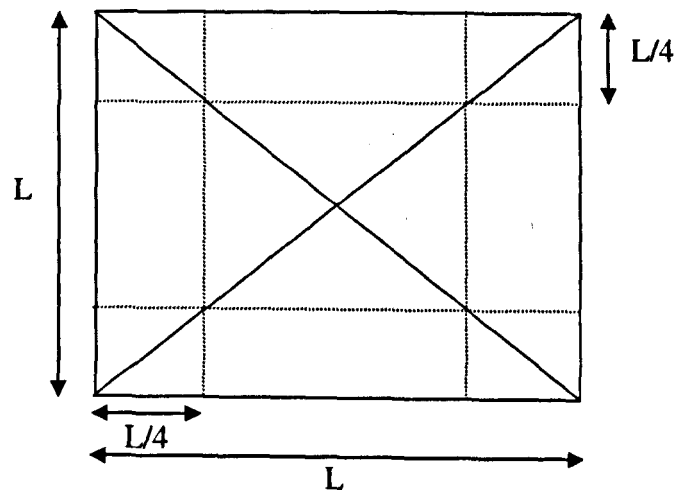

External work done:

$$\sum\left(4.\frac{1}{2}P\delta_{max}\right)$$

Internal work done:

$$\sum 4.L.m.\frac{\delta_{max}}{(L/2)}$$

Equate:

$$P=\frac{8m}{2}=169.6N$$

Total load = 4*169.6 = 0.6784kN

Yield load calculated assuming distributed loading over -estimates actual yield by 33%

A.4 Calculation of Yield Line Load for orthotropic rectangular slabs for 12 point loading system

A.4.1 Coefficient of Orthotropy 0.2

External work done = Internal work done

For UDL load

$$P = \frac{24 m_{uy}}{l^2 \left(\left[3 + (m_{ux}/m_{uy})(l/L)^2 \right]^{0.5} - (l/L)(m_{ux}/m_{uy})^{0.5} \right)^2}$$

Where m_{ux} is the reinforcement in the long span of the slab.

m_{ux} = 70.2 Nm

m_{uy} = 14.88 Nm

Total load = 0.78kN

For 12 point loading system: using affine transformation theory

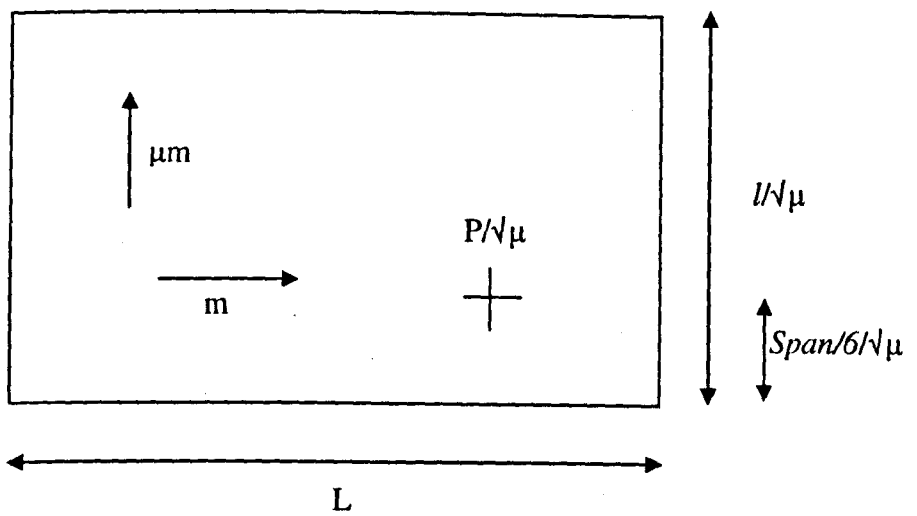

$$\frac{2P\delta_{max}}{\sqrt{\mu}} + \frac{8P\delta_{max}}{3\sqrt{\mu}} + 0.396\frac{P\delta_{max}}{\sqrt{\mu}} = 2.m\ 1.15.\frac{\delta_{max}}{0.275/\sqrt{\mu}} + 2.m\ .\frac{0.55}{\sqrt{\mu}}\frac{.\delta_{max}}{0.363}$$

11.345P=10.48m

m = 70.2 Nm/m

Total load = 0.778 kN

Yield load calculated assuming distributed loading over -estimates actual yield by 0.26%

A.4.1 Coefficient of Orthotropy 5

UDL;

$$P = \frac{24m_{uy}}{l^2\left(\left[3+(m_{ux}/m_{uy})(l/L)^2\right]^{0.5}-(l/L)(m_{ux}/m_{uy})^{0.5}\right)^2}$$

Where m_{ux} is the reinforcement in the long span of the slab.

m_{ux} = 14.26 Nm

m_{uy} = 73.3 Nm

Total load = 1.56 kN

For 12 point loading system: Using Affine transformation theory

m = *14.3* Nm/m

Use same equation as for slab with coefficient of orthotropy of 0.2 but substitute 5 into equation.

2.26P = 18.7 + 1.4m

Total Load = 1.52 kN

Yield load calculated assuming distributed loading over -estimates actual yield by 2.56%